Emergence of temperature and salinity changes in the ocean interior in response to climate change : timescales and mechanisms

Yona Silvy

THÈSE DE DOCTORAT DE SORBONNE UNIVERSITÉ

École doctorale : « 129 - Sciences de l'Environnement d'Île-de-France »

Spécialité : **Océanographie Physique**

réalisée au

Laboratoire d'**O**céanographie et du **C**limat **E**xpérimentations et **A**pproches **N**umériques

présentée par

Yona SILVY

pour obtenir le grade de

Docteure de Sorbonne Université

Titre de la thèse :

Emergence des changements de température et de salinité dans l'océan intérieur en réponse au changement climatique : échelles de temps et mécanismes

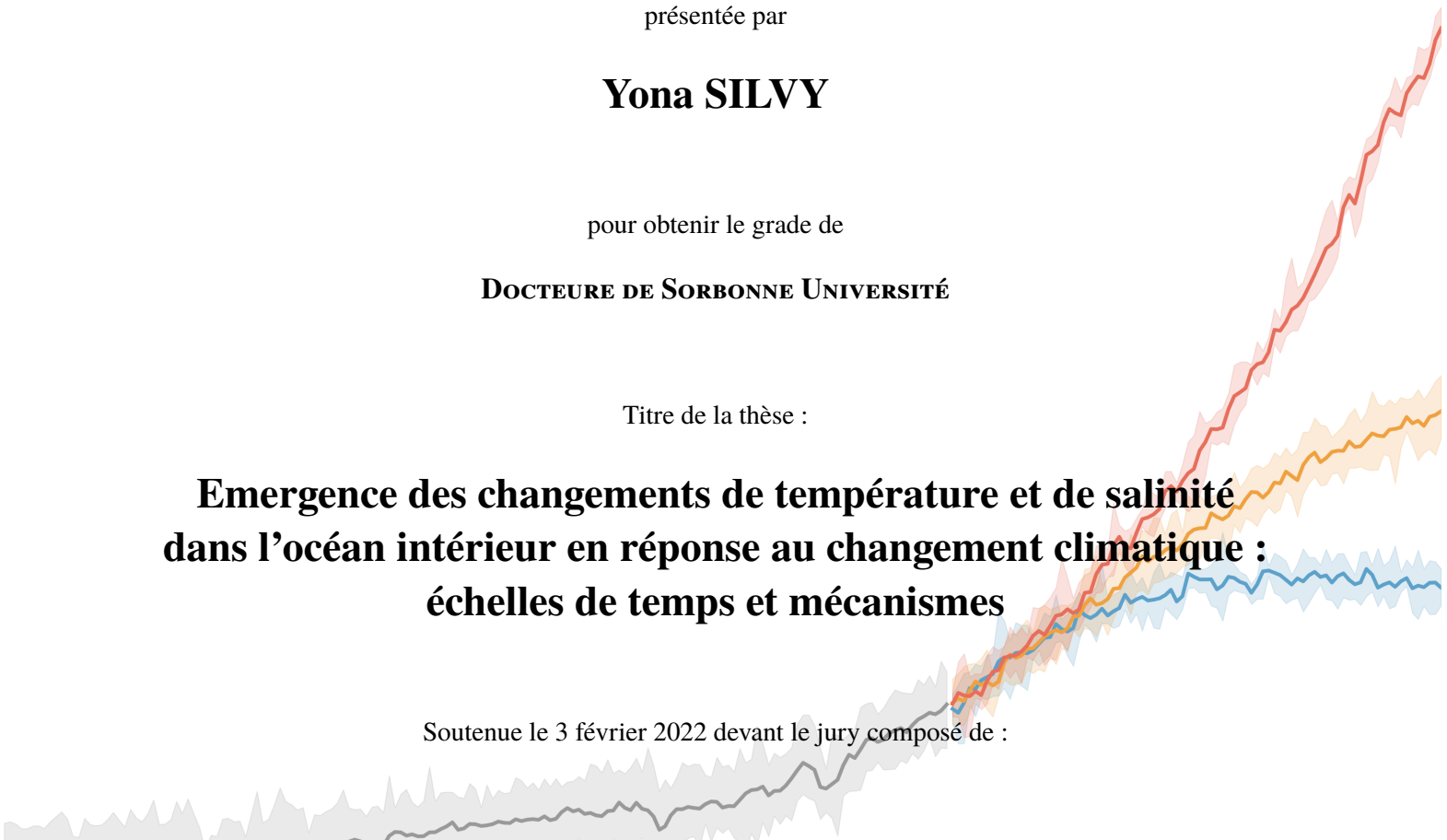

Soutenue le 3 février 2022 devant le jury composé de :

Rapportrice	Helene Hewitt	Met Office Hadley Center, Exeter, Royaume-Uni
Rapporteur	Laurent Terray	CNRS, CERFACS, Toulouse, France
Examinateur	Francis Codron	Sorbonne Université, LOCEAN, Paris, France
Examinatrices	Anne-Marie Tréguier	CNRS, LOPS, Brest, France
	Laure Zanna	NYU, Courant Institute, New York, Etats-Unis
Directeurs de thèse	Eric Guilyardi	CNRS, LOCEAN, Paris, France
	Jean-Baptiste Sallée	CNRS, LOCEAN, Paris, France

Abstract

Abstract : Human-induced climate change is already affecting every inhabited region of the planet. Yet, over 90% of the excess heat associated with human activities has been absorbed by the ocean since the 1970s, which acts to largely damp atmospheric warming, but has large impacts on human societies and marine life. In this thesis, I explore when and where thermohaline changes in the ocean interior become large enough to be unambiguously set apart from internal variability and investigate their associated physical drivers, using ensembles of climate models and dedicated numerical experiments. We find that the climate signal in the upper ocean water-masses emerges between the late 20th century and the first decades of the 21st. The Southern Hemisphere mid-latitude Mode Waters emerge before their Northern Hemisphere counterparts. The associated warming at these timescales is mostly caused by the uptake of heat from the atmosphere, passively transported into the ocean interior. In the deeper parts of the ocean, circulation changes play a more important role in the emergence timescales of the climate signals. Increased buoyancy gain at the surface in the subpolar areas cause a slowdown in the meridional overturning circulation. This warms the subsurface and abyssal waters in the Southern Ocean as soon as the mid-20th century, adding up to the weaker passive uptake of heat, but counteracts it in the deep North Atlantic over the 21st, delaying the emergence. Although climate models miss some important aspects of the ocean response to climate change, they allow to shed light on the balance of processes at play, and suggest anthropogenic influence has already spread to large parts of the ocean.

Key words : Thermohaline changes, emergence, anthropogenic signal, ocean interior, modelling

Résumé : Le changement climatique d'origine humaine impacte déjà toutes les régions habitées de la planète. 90% de l'excès de chaleur associé aux activités humaines a été absorbé par l'océan depuis les années 1970, atténuant en grande partie le réchauffement atmosphérique, mais impactant fortement les sociétés humaines et la vie marine. Dans cette thèse, j'explore à l'aide d'ensembles de modèles de climat et de simulations numériques dédiées, où et quand les changements de température et de salinité dans l'océan intérieur deviennent assez grands pour être différenciés de la variabilité interne, ainsi que les mécanismes physiques associés. Nous trouvons ainsi que le signal climatique dans les masses d'eau de l'océan supérieur émerge entre la fin du XX^{ème} et les premières décennies du XXI^{ème} siècle. Les eaux modales des moyennes latitudes de l'hémisphère Sud émergent plus tôt que leurs homologues de l'hémisphère Nord. Le réchauffement associé à ces échelles de temps est principalement du à une absorption de chaleur transportée passivement dans l'océan intérieur. Dans les profondeurs de l'océan, les changements de circulation jouent un rôle plus important aux échelles de temps d'émergence du signal climatique. Le gain de flottabilité en surface dans les régions subpolaires provoque un ralentissement de la circulation méridienne de retournement. Cela réchauffe les eaux intérieures et abyssales de l'Océan Austral dès le milieu du XX^{ème}, venant s'ajouter au faible transport passif de chaleur, alors que cela le contre dans les profondeurs de l'Atlantique Nord et retarde l'émergence. Bien que les modèles de climat passent à côté de certains aspects importants de la réponse océanique au changement climatique, ils permettent d'apporter des éléments sur l'équilibre de processus en jeu, et suggèrent que l'influence humaine impacte déjà de grandes parties de l'océan.

Mots clés : Changements thermohalins, émergence, signal anthropique, océan intérieur, modélisation

Remerciements

I would like to start by thanking the members of the jury for accepting to be part of this process, and particularly Helene and Laurent for accepting to review this thesis. I appreciate your time and energy!

Cette thèse s'est construite avec l'aide de beaucoup de monde que j'aimerais prendre le temps de remercier.

Un merci de l'espace à mes directeurs de thèse Eric et JB de m'avoir accompagnée et soutenue dans cette aventure. Eric, merci de m'avoir donné l'opportunité de démarrer dans la recherche et de rencontrer tellement de collègues passionné.e.s et stimulant.e.s. Merci pour ta bienveillance, ton investissement permanent et le temps que tu m'as généreusement donné. Merci aussi de m'avoir poussée à participer à toutes ces conférences et workshops même quand j'avais vraiment trop la flemme (que j'ai toujours un peu d'ailleurs), et de m'avoir donné confiance en moi quand je n'y arrivais pas. Merci d'en avoir tant fait pour la communication au grand public et de continuer à le faire.

JB, merci pour la science et merci pour les conneries (je dirais qu'on est sur du 50-50) ! Merci pour tous les échanges à en perdre la boule parfois, pour la pertinence de tes propos et pour ton humilité. Merci pour tout ce que tu m'as transmis même s'il me reste tant à apprendre encore, et de m'avoir communiqué ta passion pour la recherche et pour raconter des histoires, toujours en prenant de la hauteur. Je n'ai pas encore complètement choppé ta vibe d'adoration des intros, mais j'espère que ce n'est pas peine perdue. Merci pour les valeurs que tu portes. Merci pour la team et les réus du jeudi matin, pour ce cadre solidaire pendant les multiples confinements et après, qui nous a permis d'échanger tous ensemble, d'éveiller notre curiosité et culture scientifique tout en se marrant bien.

Merci aux zozos de la team polaire, j'ai appris beaucoup de choses grâce à vous, notamment que l'Océan Austral était clairement le meilleur océan. Merci pour toutes les discussions, les conseils, le soutien, les rires, les photos-montages, les emojis. Merci pour les réus composées à 90% de récits de sorties vélo et aux 10% restants d'insultes des ministres de l'intérieur successifs. Merci d'avoir rendu la science plus belle par cet esprit d'équipe et par toutes les bêtises qu'on a pu se raconter !

Un merci du fond du cœur à Juliette, pour ton aide sur ma thèse, les réus, les relectures de chapitre, le SAV émotionnel. Mais aussi pour ton humanité, ta générosité et pour tout ce que tu apportes à ce labo avec tant d'humilité. Merci pour ton engagement dans climactions et dans la société, et pour tous les moments de réflexion qui nous ont rapprochées.

Papi Clément, comment te remercier pour les mois qu'on a passés ensemble à mettre en place ces satanées simus, de ne m'avoir jamais lâchée malgré mon incompréhension totale de Fortran et de Jean

Zay (quoi ? déclarer des variables ??) et d'avoir réussi à m'amener au bout de ce projet, en prenant le temps de faire les choses comme il faut. J'ai appris tellement de cette expérience, ça m'a (presque ?) fait aimer la modélisation et donné envie de recommencer. Merci aussi pour ton amitié, pour les discussions engagées, pour ton écoute, pour tous les moments où je suis venue me plaindre dans ton bureau, pour les bières, pour les rigolades.

Paul, thanks for welcoming me in Livermore, for your excitement about the science that is so contagious and for teaching me all kinds of fun words from Down Under!

Un grand merci à Christian pour toute ton aide et le temps que tu as pu me consacrer sur la mise en place des simulations et pour les réponses aux milliers de questions que j'ai pu te poser ensuite ! Un grand merci aussi à Gurvan pour les réunions et discussions qui ont ponctuées mes années de thèse ; merci pour ta réflexion et merci d'avoir pu me guider à travers ces différentes étapes, avec toujours beaucoup de bienveillance. Merci plus généralement à tous les collègues du labo à qui je suis allée poser des questions et qui m'ont aidée pendant ces années de thèse. Merci aussi pour la convivialité des pauses café, pour les discussions de couloir, les apéros. Merci aux équipes support du LOCEAN et de l'IPSL, de permettre à la vie scientifique de fonctionner, et merci à l'équipe plateforme et l'équipe du mesocentre de nous fournir des outils et des formations pour pouvoir mieux travailler. Merci à Jean-Benoît pour tout ce que tu fais pour ce labo, avec toujours beaucoup d'humanité, et merci d'avoir porté à son terme le vote carbone. Premier labo de France !

En parlant carbone, merci aux méchants militants de climactions (vous savez qui vous êtes, toutes générations confondues) pour cette aventure de folie, pour cette dynamique de groupe, pour cette envie d'y aller ensemble. Merci pour les débats passionnés, pour les échanges, pour la solidarité pendant les confinements, pour la formation à tellement d'enjeux et de sujets, pour la stimulation intellectuelle que tout cela a procuré. Merci de m'avoir permis de trouver du sens, d'avoir toujours écouté les « jeunes », notre frustration du statu quo, notre envie parfois naïve de tout renverser, et de nous avoir donné un cadre pour nous exprimer et proposer des choses (et big up à la branche des jeunes radicalisés « la révolution » !). Et merci Serge et les autres pour la co-organisation des mois thématiques.

Merci aux copains et copines du labo, d'avoir rendu la vie de tous les jours enjouée, merci pour le soutien et l'entreaide, pour les pauses chez les uns et chez les autres dans les énormes moments de flemme, pour les apéros et les soirées (parfois clandestines), sans oublier le molkky ! Merci au meilleur bureau 426, à ma Sara, ma voisine de toujours, merci pour tes bêtises, pour les fous-rires, pour ta générosité et ta gentillesse, pour ton écoute, merci pour ces 3 ans ensemble !! Merci à Antoine et Gaston, mes traducteurs personnels de Jean Zay et NEMO, merci pour tous les tips, pour les photos-montages du tonnerre, merci pour les supers pauses goûter et pour la pile d'assiettes à dessert volées de la cantine.

Merci aux copains de toujours, d'être là, de grandir ensemble, d'évoluer, se révolter (et parfois se faire arrêter), s'amuser, s'élever, apprendre les uns des autres. Vous connaissez l'autre version des remerciements !

Merci à tous les professeur.e.s que j'ai pu avoir tout au long de ces longues études, qui m'ont donné goût à l'apprentissage, à la science (mais pas que), et une soif de connaissances qui j'espère ne s'en ira jamais. Merci à Michèle Fieux pour ses cours d'océanographie à l'ENSTA si inspirants qui m'ont donné envie d'en savoir plus. And huge thanks to Janet Sprintall, my first research advisor, for this wonderful first internship at Scripps that made me want to pursue doing research in physical oceanography, for giving me a chance and for your support and encouragements.

Un merci qui n'a pas de prix à toute ma famille, et tout particulièrement à mes parents. Merci de m'avoir donné le privilège d'avoir pu faire les études que j'ai faites, de m'avoir soutenue tout du long, d'avoir été fiers (même si Bubie est imbattable à ce poste), d'avoir toujours pris des nouvelles et de m'avoir encouragée. Maman, merci pour ton dévouement, merci de m'avoir trimballée à travers Paris à tous les cours de danse, de violoncelle, de piano, à l'école, durant toute mon enfance, et d'avoir donné autant de

toi, et de toujours continuer à le faire. Merci d'avoir été un modèle pour la jeune chercheuse que je suis (même si j'ai grandi en pensant que les réunions de recherche se faisaient toujours autour d'un carrot cake !). Papa, merci pour ton aide sur les DMs de maths, peut-être que c'est ce qui m'a poussée à continuer dans la science qui sait; merci de m'avoir accompagnée au bac d'abord, puis tous les matins pendant les longues semaines de concours (on ne dira pas que c'était en voiture dans Paris, je risque de me faire renier du labo); merci pour les multiples déménagements; merci pour ta douceur, et merci pour ton engagement qui a marqué les prémices du mien. Bubie, merci de t'être battue pour ta vie !!! Et merci pour ta joie de vivre contagieuse. Merci à ma complice végé de la famille, Emma, pionnière dans la lutte contre le statu quo ! Merci à Noam, mon immense petit-frère, compagnon de toute la vie, des bagarres d'enfants aux (presque) adultes que nous sommes maintenant, merci pour les meilleures randos sous la pluie pour oublier le boulot, les duos, le Gershwin, le frisbee le dimanche (sans se pêter les genoux si possible !!).

Merci à mes beaux-parents Claude et Jacky, de nous avoir accueillis pendant ce deuxième confinement si ensoleillé dans le Lot. Merci de nous avoir donné un cadre si serein, agréable et chaleureux.

Enfin, merci à Joël. Merci d'avoir été là dans les meilleurs moments comme dans les plus difficiles. Merci pour ton soutien inconditionnel, merci de croire en moi, de me faire toujours réfléchir et de me pousser à ne jamais me reposer sur mes acquis (que ce soit dans la vie, au volley ou dans la thèse !). Merci de m'avoir débugué mes scripts Python et LaTeX, avec un air seulement à moitié dépité. Merci de grandir et d'évoluer avec moi et merci de partager ma vie.

Aucun remerciement pour Slackbot qui n'a vraiment fait aucun effort. Cette thèse a donc été rédigée et corrigée intégralement par des humains (pour le meilleur ou pour le pire), preuve à l'appui.

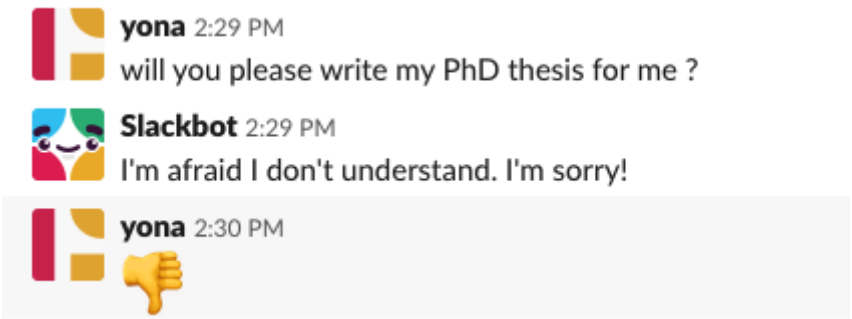

Scientific life and other contributions during the PhD

Teaching at Sorbonne Université

- 48h License 2 « Développement Durable » (course organizer: Hervé Le Treut)
- 24h License 1 « Atelier de Recherche Encadré: Océan » (course organizer: Guillaume Gastineau)

Outreach

- Presentation in a high-school classroom (climate and climate change), Sept 2019
- Science Fair - IPSL booth (ocean practical experiments for school kids), Oct 2019
- Invited on national French radio for the program "La Terre au Carré", France Inter, April 2021 https://www.franceinter.fr/emissions/la-terre-au-carre/la-terre-au-carre-06-avril-2021
- Training session for an educational kit on low-carbon lifestyles "Inventons Nos Vies Bas Carbone", April 2021
- Invited submission of a general public paper for www.climanosco.org in the series "Oceans on the rise", June 2021

Publications

- **Silvy, Y.**, Guilyardi, E., Sallée, JB., Durack, P.J. (2020) Human-induced changes to the global ocean water masses and their time of emergence. Nature Climate Change 10, 1030–1036 https://doi.org/10.1038/s41558-020-0878-x
- Mignot, J., Hourdin, F., Deshayes, J., Boucher, O., Gastineau, G., Musat, I., Vancoppenolle, M., Servonnat, J., Caubel, A., Chéruy, F., Denvil, S., Dufresne, JL., Ethé, C., Fairhead, L., Foujols, MA., Grandpeix, JY., Levavasseur, G., Marti, O., Menary, M., Rio, C., Rousset, C., **Silvy, Y**. (2021) The tuning strategy of IPSL-CM6A-LR. Journal of Advances in Modeling Earth Systems, 13, e2020MS002340. https://doi.org/10.1029/2020MS002340
- **Silvy, Y.** et al. What causes ocean warming to emerge from internal variability in a global climate model? (in prep)

Conferences, seminars and workshops

- Ocean Salinity Science Conference, 2018, Paris, France (oral)
- EGU General Assembly, 2019, Vienna, Austria (poster)
- CMIP6 Workshop, 2019, Bordeaux, France (poster)
- Archange kickoff meeting, 2020, Paris, France (oral)

- Ocean Sciences Meeting, 2020, San Diego, US (poster)
- PCMDI seminar, 2020, Livermore, US
- EGU General Assembly, 2020, online
- Varclim team seminar, LOCEAN, 2020 (online)
- Archange mid-term meeting, 2021, Paris, France (online)
- WCRP Workshop on attribution of multi-annual to decadal changes in the climate system, 2021, online (oral)
- SMILE webinar, 2021 (online) https://large-ensemble.github.io/webinars/archive/
- NCAR Climate and Global Dynamics Laboratory webinar, 2021 (online) https://youtu.be/mL4nJ6XZK3E

Reviewer for

- IAPSO ECS AR6 Second Order Draft group review (spring 2020)
- Journal of Climate (Oct 2020, Sept 2021)

Training courses

- ModNumOA: Modélisation Numérique pour l'Atmosphère et l'Océan (one week winter school on atmospheric and ocean modelling), Nov 2018
- Seminar series "Changement climatique et société", 2019-2020, 2020-2021
- Media training (2 days), Sept 2019
- IPSL training for the use of libIGCM (IPSL numerical modelling environment), Jan 2020
- Diverse Sorbonne Université trainings (S-Biblio, Biblio Zotero, Veille documentaire, Prévention et secours civique, Gestion du stress, Règles de publication d'un article scientifique, Thèse en LaTeX)

Life in the lab

- Creation and organization of the "month of" series of scientific events around a main topic in oceanography: early-career journal club animated by a permanent researcher, lab seminar, and an informal discussion session around coffee
- PhD student representative at the Lab Council

Climactions

Active participation since the creation of the working group (fall 2018) - see appendix F - aiming to rethink our research practises and start a low-carbon transition in the lab. Major steps in which I was involved:

- Regular meetings since 2018
- Co-writing and coordination of an early-career contribution to the IPSL General Assembly on July 2nd 2019; preparation and animation of a discussion session
- Co-writing of an open letter with other early-career scientists at the lab to the AGU and EGU, promoting a cultural change of scientific conferences, Sept 2019
- Preparation and participation to the climactions 2-day workshop, Nov 2019
- Presentation of climactions progress to the IPSL management, Dec 2019
- Realization of a poster on the carbon footprint of the lab and measures put to a general vote to reduce it, July 2020
- Lab seminar to prepare the vote, Sept 2020 https://colibris-wiki.org/empreinteClocean/?TexteVote
- Presentation at the poster session at the Labos1.5 workshop with Juliette Mignot, Nov 2020
- Invited talk at the Grand Séminaire de l'Observatoire Midi-Pyrénées with Xavier Capet, March 2021 https://www.youtube.com/watch?v=4tMNPw_6IE8
- Invited at a round-table at a PhD day organized by the CNAM on Planetary Health, May 2021

Contents

List of Figures

List of Tables

Acronyms

AABW Antarctic Bottom Water.
AAIW Antarctic Intermediate Water.
ACC Antarctic Circumpolar Current.
AMOC Atlantic Meridional Overturning Circulation.
AR6 Sixth Assessment Report.

CDW Circumpolar Deep Water.
CMIP Coupled Model Intercomparison Project.
CMIP5 Coupled Model Intercomparison Project Phase 5.
CMIP6 Coupled Model Intercomparison Project Phase 6.

D&A Detection and Attribution.
DAMIP Detection and Attribution Model Intercomparison Project.

EEI Earth's Energy Imbalance.
EOF Empirical Orthogonal Function.

FAFMIP Flux-Anomaly-Forced Model Intercomparison Project.

GCMs Global Climate Models.
GHGs greenhouse gases.
GSAT Global Surface Air Temperature.

IPCC Intergovernmental Panel on Climate Change.
IPSL Institut Pierre-Simon Laplace.

MMM Multi-Model Mean.
MOC Meridional Overturning Circulation.

NADW North Atlantic Deep Water.

OHC Ocean Heat Content.
OSC Ocean Salt Content.

PA Pattern Amplification.
PC Principal Component.

piControl Pre-Industrial Control.

SAM Southern Annular Mode.
SAMW Subantarctic Mode Water.
SC Salinity Contrast.
SROCC Special Report on the Ocean and Cryosphere in a Changing Climate.
SSS Sea Surface Salinity.
SST Sea Surface Temperature.

ToE Time of Emergence.

General Introduction

Contents

"It is unequivocal that human influence has warmed the atmosphere, ocean and land" [IPCC, 2021b]. These resounding words are part of the opening statement in the Summary for Policymakers presenting key findings of the Working Group I contribution to the Intergovernmental Panel on Climate Change (IPCC)'s Sixth Assessment Report (AR6). This statement draws upon over 150 years of climate science research, from the first discoveries and theories of the role of greenhouse gases in the climate system (e.g. Foote [1856], Tyndall [1861], Arrhenius [1896]), the deployment of instruments enabling the first signs and observations of such warming (e.g. Callendar [1938]), the development of climate models simulating the response to a doubling in atmospheric carbon dioxide concentration [Manabe and Wetherald, 1975], to the theoretical premises of detection and attribution (e.g. Hasselmann [1979]). Today, there have been considerable advances in observing, modelling and overall understanding the climate system and its response to ongoing human-induced climate change. In this thesis, we will explore the response of the ocean, a major piece of the climate system, to increasing anthropogenic forcings, and its modulation by internal variability. We will particularly try to link the question of signal-to-noise and emergence of the climate signal from internal variations with a large-scale understanding of the physical processes at play in the ocean. In this General Introduction, I will first rapidly present some broad characteristics of the global ocean that make it such a unique subject to study, and the tools at our disposal to do so. Then, I will draw upon the scientific literature to present how temperature and salinity have already changed today in the ocean from observations and how they are expected to continue changing, whether these changes are of anthropogenic origin, and finally the large-scale physical mechanisms possibly causing these changes. This literature review will lay the groundwork to the scientific questions and aims of this thesis, addressed in the last section of this introductory chapter.

1 On the importance of studying the ocean to understand Earth's climate

The World Ocean is the largest body of water on Earth, with five major interconnected basins of salty water, constituting 97% of Earth's water reservoir and 71% of its surface. Its mass is 250 times larger than the atmosphere's, its volumic mass 1000 times larger, and, combined to its very large heat capacity, makes it a huge reservoir of heat for the climate system, with great thermal inertia. It is also a central player in the Earth carbon cycle, sequestering about 50 times more carbon than the atmosphere. The ocean is much wider than it is deep (its mean depth is 3700m while the Earth's circumference is about 40 000km) and is warmed (and thus stabilized) by the sun at its upper surface, making vertical movements almost everywhere much more difficult than horizontal movements. This gigantic body of water is however in perpetual movement (from very small to very large spatial and temporal scales), caused primarily by exchanges of heat, water and momentum with the atmosphere, allowing the connection of surface conditions to the deepest parts of the ocean. How do these connections occur and why are they important for climate? In this first section, I will briefly expose why the ocean is such an important piece of the climate system - mainly through its physical aspects - and describe what tools exist to study it at global scale through international community efforts.

1.1 Connecting the atmosphere to the abyss

One of the ocean's main role in regulating climate is to transport the extra solar heat received in the tropics to the poles via its circulation, where heat is then partly lost to the atmosphere (e.g. Trenberth and Caron [2001]). The upper layers of the ocean are in direct contact with the overlying atmosphere, exchanging water through evaporation and precipitation, heat through shortwave and longwave radiation, sensible and latent turbulent fluxes, momentum through the winds and other elements such as carbon dioxide and oxygen. The properties acquired at the surface are mixed vertically by turbulent motions within this surface layer, which acts to integrate and modulate air-sea exchanges, having a direct role on climate variability [Frankignoul and Hasselmann, 1977]. The surface mixed layer has very homogeneous

properties on the vertical including its volumetric mass (or "density"). It is thus a bridge between the atmosphere and the deeper parts of the ocean. Below the surface mixed layer lies a large, less variable body of water not in direct contact with the atmosphere. The boundary between these two layers is a thin layer manifested by a very high density gradient (intense stratification), the pycnocline, preventing strong vertical exchanges between surface and depth [Fieux, 2010]. When the mixed layer deepens (e.g. in winter) because of strong winds (enhancing mixing), surface cooling or evaporation (making the surface waters cooler and/or saltier thus denser, creating vertical motion), properties in the underlying layer are mixed with those of the surface layer. When the mixed layer depth shoals, the deeper parts are disconnected. The surface mixed layer has varying depth over the globe, its connection to the deeper ocean is thus very different depending on the region of the ocean [de Boyer Montégut, 2004, Sallée et al., 2021]. Between 40ºN and 40ºS where surface waters are warm and more stable (figure 0.1 and 0.3), the pycnocline lies around tens to several hundred meters. At higher latitudes, where waters are much colder and where there is the presence of floating sea-ice at the surface, the ocean is less stable, vertical density gradients are weaker and isopycnals (lines of constant density) are almost vertical. In these regions, if the surface waters temporarily lose enough buoyancy (i.e., become heavier), vertical motions in the water-column called convection can reach the bottom of the ocean [Fieux, 2010]. This can occur via two processes during winter. Either surface waters lose enough heat to the atmosphere, and become cool enough (that is, dense enough) to break the stratification barrier. Or, when sea-ice is formed, it captures fresh water, making the liquid water saltier and dense enough to engender vertical motions. Large holes in the sea-ice called polynias, associated with strong winds that keep pushing the newly-formed sea-ice away, can reinforce these convection processes, by further letting the ocean release its heat directly to the very cold atmosphere, resulting in cooling the water-column and enhancing deep convection [Morales Maqueda, 2004]. The entire water column is thus homogenized and the surface is directly connected to the deep ocean, transferring the properties it has exchanged with the atmosphere (e.g. heat, carbon and oxygen) at depth, where it can be transported and stored for decades to centuries.

The exchange of properties with the atmosphere, their mixing over varying depths and their transport in the ocean interior along different layers of density is the process of water-mass formation and subduction (see the long arrows in figure 0.1). Water-masses are defined by a volume of water with unique temperature and salinity characteristics, acquired in the same location by air-sea and sea-ice exchanges and propagated in the surface mixed layer. At the end of winter when the mixed layer has reached its maximum depth defined by the water-mass density, they can flow and spread in the ocean interior along equal density lines, under lighter layers [Fieux, 2010] (figure 0.1). Their properties will change only by slowly mixing with surrounding water-masses. Water-masses are thus the memory of climate variations. The global ocean circulation, generated by the combination of winds and density gradients (the latter being the "thermohaline" component) transports these water-masses and their properties acquired at a specific time and location all over the globe, connecting all ocean basins, descending to the bottom of the ocean at high latitudes and transported back at the surface along different routes. The majority of the ocean volume is filled with deep and abyssal water-masses formed at high latitudes, in small convection regions of the subpolar North Atlantic and Southern Ocean, and spread equatorward from their formation site (Johnson [2008], DeVries and Primeau [2011] and see in figure 0.1: Antarctic Bottom Water (AABW) and North Atlantic Deep Water (NADW)). A water-mass is considered to be young if it has been in recent contact with the atmosphere (i.e. just formed, or "ventilated"), and old when it has spread in the ocean interior, transported and mixed by the circulation. The time scales of the circulation and thus of the age of water-masses can range from seasonal in the surface mixed layer, 10-20 years in the well-ventilated subtropical gyres and 100-1000 years in deeper layers. It is considered to take hundreds of years for properties to be transmitted along the ventilation and circulation routes of the "great conveyor belt" [Broeker, 1991], although this representation of a unique looping pathway has been "deconstructed" [Lozier, 2010], and other processes have been added [Marshall and Speer, 2012], improving the global understanding of this large-scale circulation.

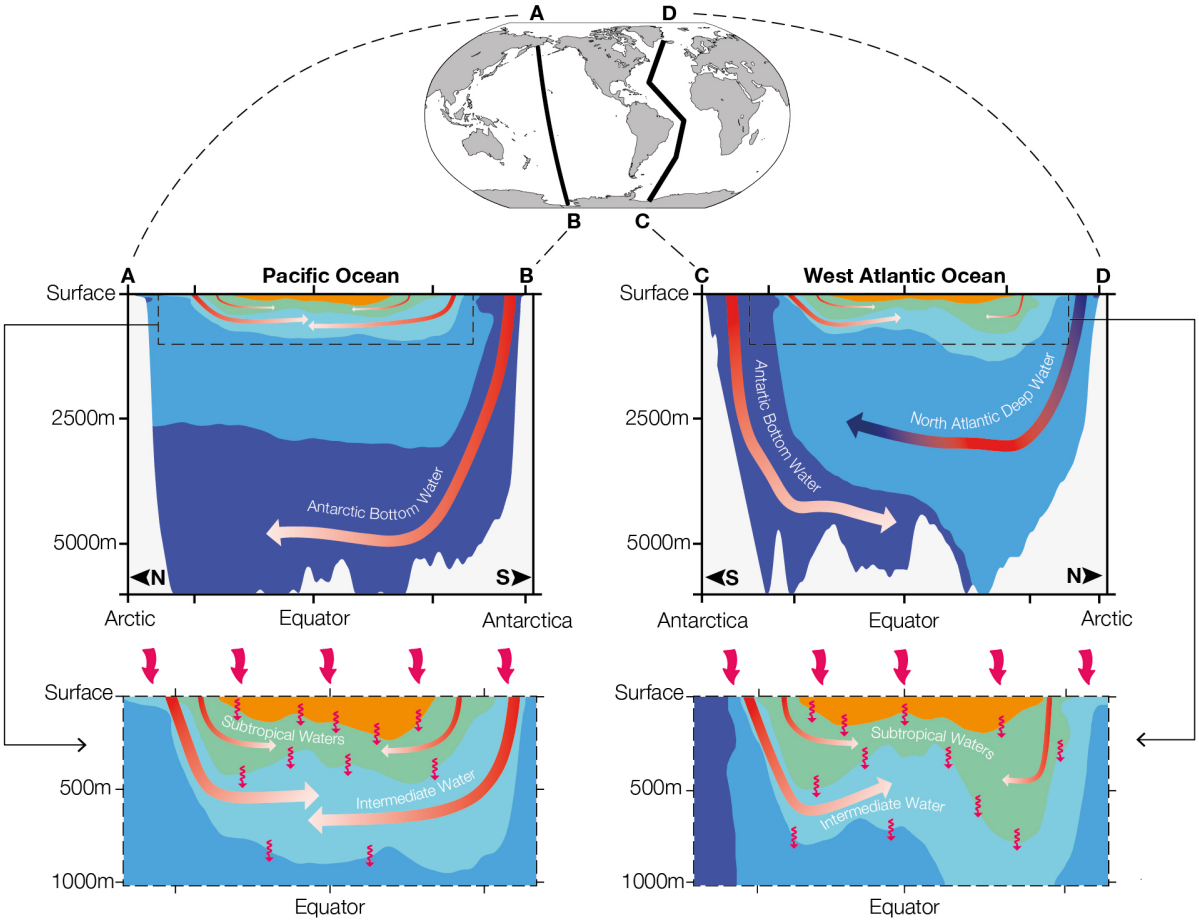

Figure 0.1: Ocean heat uptake pathways. From IPCC AR5 FAQ3.1 Figure 1 [Rhein et al., 2013]

1.2 Temperature and salinity: two markers of climate variability and change

Together with pressure (p), temperature (T) and salinity (S) determine the ocean's density through the equation of state $\rho = f(T,S,p)$. They are thus crucial tracers for ocean water-masses and for the global thermohaline circulation, and can be modified by exchanges with the atmosphere, sea-ice and land or by interior mixing.

Salinity is the oceanic signature of the Earth freshwater cycle: in regions where precipitation (P) exceeds evaporation (E) (E-P<0 near the equator and at high latitudes, blue regions in figure 0.2, panels C and D) there is a net input of freshwater, making surface waters less salty (blue regions in panels A and B), and in subtropical regions where evaporation exceeds precipitation (red regions), there is a net loss of freshwater, impacting how salt is distributed in the surface (figure 0.2) and subsurface (figure 0.3) waters [Durack, 2015]. Since about 80 % of evaporation and precipitation fluxes occur at the ocean surface [Baumgartner and Reichel, 1975] (with the remaining 20% over land), any change in the water cycle is reflected in ocean surface salinity patterns. Because of vertical exchanges within the surface mixed layer and horizontal currents, salinity integrates the highly-variable P-E fluxes and gives a smoother view of the evolution of P-E. Moreover, since the rise of satellite observations, Sea Surface Salinity (SSS) has been much easier to observe than evaporation and precipitation fluxes [Yu et al., 2020]. Salinity is also modified by sea-ice melt and formation, by river runoffs at river mouths (arriving as a freshwater flux with near-zero salinity) and by the melting of the Antarctic and Greenland ice sheets through iceshelf basal melt and calving. Salinity's role is particularly important at high latitudes where its influence on the equation of state and thus on the ocean's stability (with consequences on deep convection) is stronger

than at lower latitudes, where temperature variations mainly control variations in density.

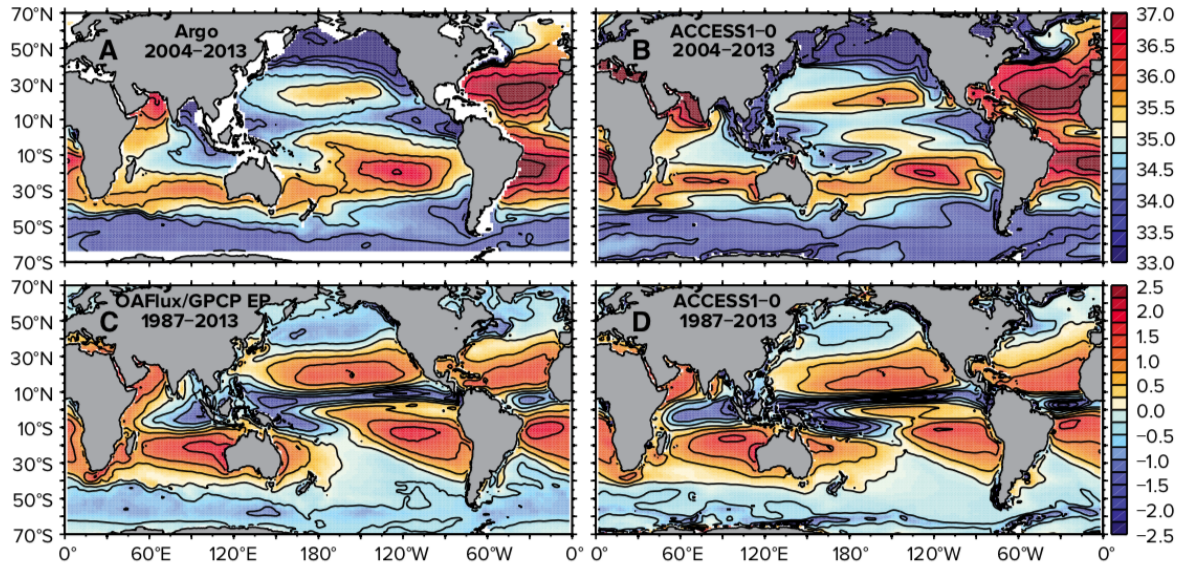

Figure 0.2: From Durack [2015]. Climatological mean 2004–2013 near-surface salinity (SSS; PSS-78; A, B) and 1987–2013 evaporation minus precipitation (E–P; m yr–1; C, D) in modern observations (A, C) and a representative model (ACCESS-1.0; B, D) from the CMIP5 suite.

The latitudinal distribution of Sea Surface Temperature (SST) primarily reflects the latitudinal dependence of solar radiation, with the warmest waters in the tropics, decreasing as we go towards the poles. As depth increases, temperature rapidly decreases, especially at low latitudes where the thermal stratification is strong (figure 0.3, with temperature contours very close together between 40ºN and 40ºS). SST is a key element both constrained by and determining the amplitude of net surface heat fluxes, but also impacts freshwater fluxes and carbon and oxygen exchanges with the atmosphere. It thus has an important impact on coupled air-sea processes. Integrated over the entire ocean volume, sea water temperature gives an indication of the Ocean Heat Content (OHC). In an equilibrium state where the heat entering the ocean is compensated by heat lost, OHC should be constant. When the climate system energy budget is not closed (which is in fact never the case on multi-centennial time scales because of fluctuations in internal variability and external forcings), there is an imbalance in radiation fluxes at the top of the atmosphere (TOA), named Earth's Energy Imbalance (EEI). On mutli-decadal time scales, due to the ocean's large heat capacity compared to other components of the Earth system (atmosphere, cryosphere, land), the majority of the imbalance is found in the OHC [Levitus et al., 2001, Meyssignac et al., 2019]. Tracking OHC change is thus a way to estimate the state of the EEI.

1.3 What tools do we have to study the ocean and its changes at global scale?

1.3.1 Observation systems to monitor the ocean

In situ measurements of ocean temperature and salinity have been collected by oceanographic vessels since the 19th century, with a larger coverage of the upper ocean starting in the 1960s, using primarily Mechanical Bathythermographs (MBTs), Expandable Bathythermographs (XBTs) and Conductivity-Temperature-Depth (CTD) instruments. Sampling has been historically biased towards the upper ocean (see figure 0.4), Northern Hemisphere, coastal regions and summer seasons due, among other factors, to instrument and accessibility reasons. Considerable efforts were lead during the 1990s with the World Ocean Circulation Experiment (WOCE) program, a global hydrographic survey which produced atlases of ocean physical and chemical properties (http://woceatlas.ucsd.edu). Since then, the Global Ocean Ship-

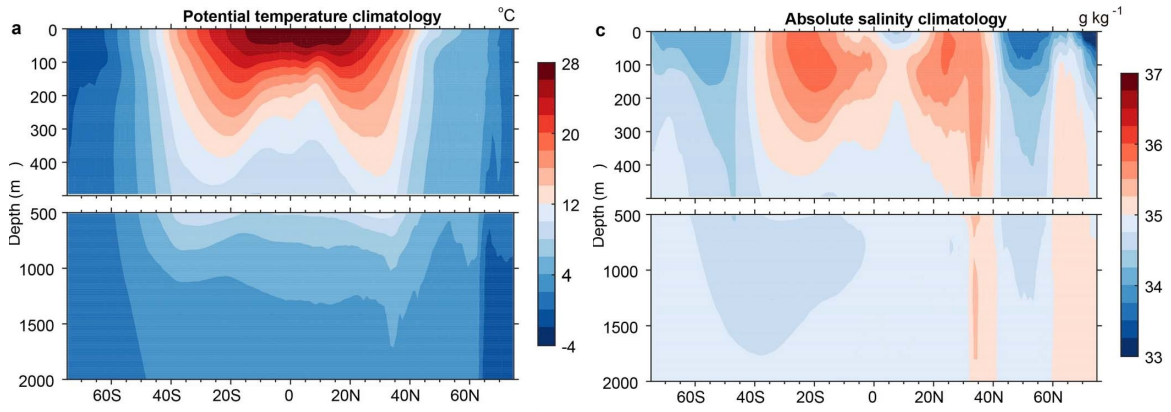

Figure 0.3: From Li et al. [2020]. Climatological mean zonally-averaged temperature and salinity, 1960-2018.

based Hydrographic Investigations Program (GO-SHIP, https://www.go-ship.org) has been coordinating repeat hydrographic sections and data access.

Ship-based measurements have been complemented by other means of *in situ* observations which do not need continuous human presence including moorings, gliders, and since the early 2000s, the extensive deployment of autonomous Argo floats sampling the upper 2000m of the ocean. The Argo program (https://argo.ucsd.edu) has drastically improved the spatio-temporal coverage of the ocean observing system, as seen in figure 0.4. In the Southern Ocean, large data gaps in ice-covered regions have been filled in the past couple decades by instrumented marine mammals with biologging techniques, coordinated by the Marine Mammals Exploring the Oceans Pole to Pole consortium (MEOP, https://www.meop.net). Some animals like elephant seals can dive several hundred meters underwater to feed, which is an opportunity to measure vertical profiles of temperature, salinity and pressure otherwise difficult to obtain.

The deep and abyssal ocean (>2000m) is still largely under-sampled (figure 0.4). Observations there consist for the most part of hydrographic sections. The recent development and deployment of deep-Argo floats, designed to profile down to 4000m and even 6000m, provides a way towards a complete full-depth observing system, necessary to close the heat and freshwater budgets of the ocean [Jayne et al., 2017].

An extensive review of historical oceanographic measurements of temperature and bias corrections is provided by e.g. Abraham et al. [2013]. Using all available temperature and salinity profiles, monthly multi-decadal globally-gridded products have been developed, using different types of objective analyses and data correction, and are often updated with the addition of new profiles (e.g. Levitus et al. [2012], Good et al. [2013], Ishii et al. [2017], Cheng et al. [2017, 2020]). These objectively-mapped products can significantly underestimate OHC trends as they tend to relax to climatological values in data-sparse regions [Durack et al., 2014b], and the different mapping choices lead to large uncertainties. However, as coverage increases, the different estimates of OHC are more consistent with each other. These globally-mapped products can therefore be very useful, but must be manipulated with caution when examining long-term historical trends in regions where data gaps exist.

Observing the ocean hydrology and dynamics from space has been possible since 1979 for SST, 1992 for sea level anomaly (SLA) and 2010 for SSS. Since there are very few observations of ocean currents below the surface, sea level anomaly is a particularly useful quantity to observe as it gives an indication of geostrophic currents (geostrophy being the main equilibrium of the ocean, between the effect of the Earth rotation and horizontal pressure gradients).

Because of the predominant role of the Atlantic Meridional Overturning Circulation (AMOC) in

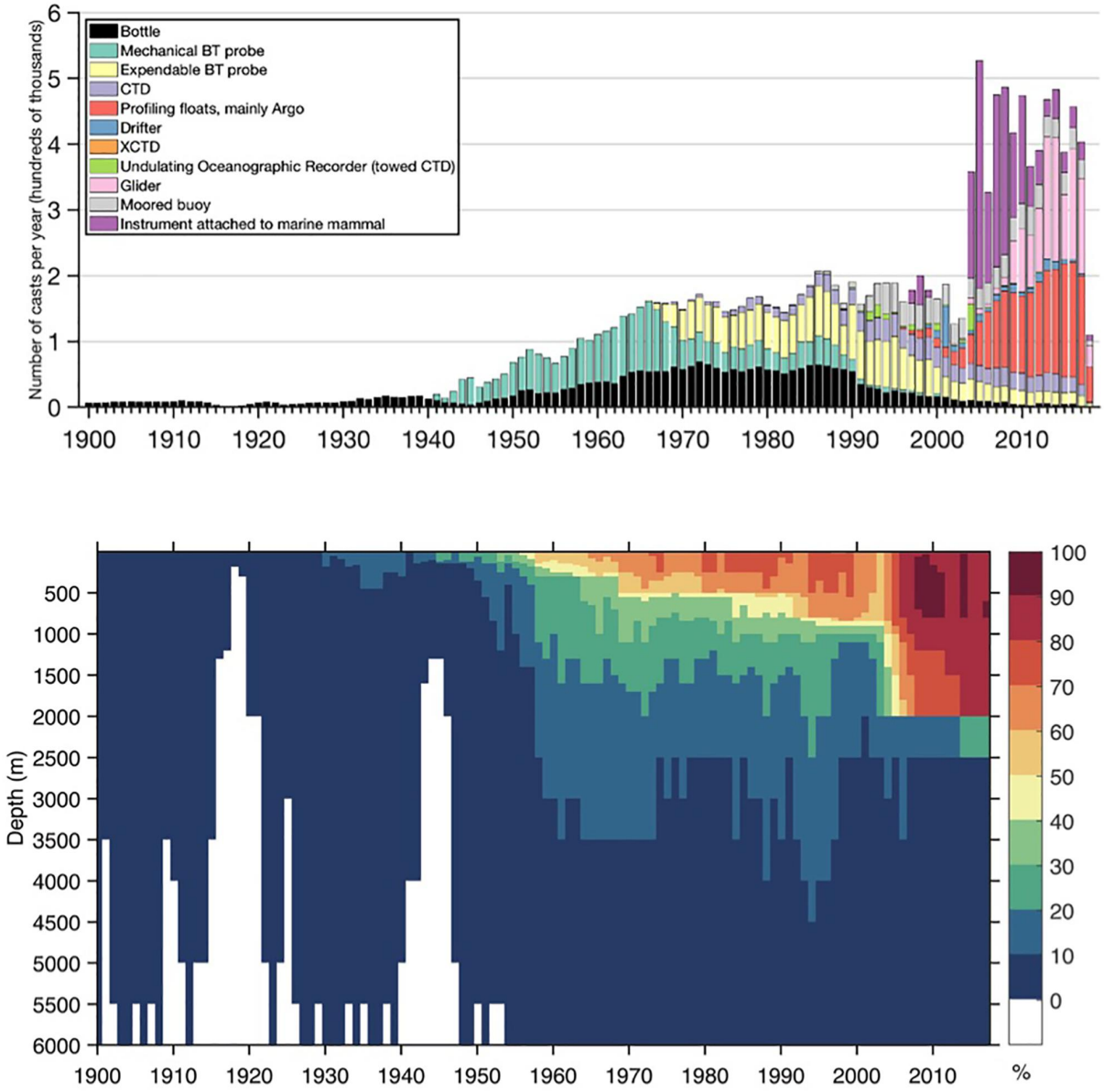

Figure 0.4: (Upper) Number of subsurface ocean temperature profiles per year by instrument type 1900–2017. [BT, Bathythermograph; CTD, Conductivity-Temperature-Depth; XCTD, Expendable CTD]. (Lower) Percentage (%) of data coverage for 3 × 3 boxes over the global ocean area from 5 to 6000 m. From Meyssignac et al. [2019].

regulating climate, sustained observing programs have been led in the North Atlantic to directly monitor the circulation and heat transport, such as the RAPID array, measuring the overturning circulation at 26ºN since 2004 (https://rapid.ac.uk/index.php) and the OSNAP array measuring the circulation in the North Atlantic subpolar gyre since 2014 (https://www.o-snap.org).

1.3.2 Theoretical frameworks of the ocean circulation

The ocean is a salty, stratified fluid on a rotating sphere. Its motions are governed by the general laws of mechanics associated to the laws of thermodynamics, translated into the Navier-Stokes equations (momentum conservation), the conservation of mass, salt and heat, and the equation of state of seawater (relating density to temperature, salinity and pressure). The forces acting on any parcel of the ocean are

gravity, pressure gradients, the Coriolis force (induced by the rotation of the Earth) if the parcel is moving, friction forces, and tidal forces. Well before observations of the ocean were collected and made available, theories of the ocean circulation were developed by making a number of simplifying assumptions and solving the equations of motion, to progressively uncover the complexity of this fluid environment. The theories of geophysical fluid dynamics and its applications to the ocean have been presented in several textbooks over the years (e.g. [Vallis, 2017]). Here, I give a few examples of central theoretical advances made in the 20th century, with applications on the gyre circulation, largely based on my first oceanography course given by Michèle Fieux, whose book has been a reference for French students for years [Fieux, 2010].

Most often, the hydrostatic approximation is made in the ocean, so that the vertical pressure gradient is balanced by gravity. When the horizontal pressure gradient is balanced by the Coriolis force, geostrophic balance is satisfied (in a stationary state). The geostrophic balance generally applies at large spatial scales in the ocean interior below the surface layer directly influenced by the winds, away from land boundaries where friction forces are important and away from the equator where the Coriolis force is null.

The surface layer influenced by the winds has been theorized by Ekman [1905], who considered the effect of a constant wind on a homogenized ocean, where the Coriolis force is in balance with frictional forces. At the ocean surface, the wind transmits a horizontal frictional force by turbulent viscosity, which engenders a horizontal current, directly deviated by the Coriolis force. The balance between these two forces results in a surface horizontal current 45º to the right (left) of the direction of the wind in the Northern (Southern) Hemisphere. This surface layer similarly generates a motion in the underlying layer by turbulent viscosity, deviated by the Coriolis force, and so on going down in the water column. The momentum transmitted by the winds at the surface penetrates in the ocean and is progressively rotated compared to the direction of the winds (the "Ekman spiral"). The strength of the current generated by the overlying layers decays exponentially, so that when it reaches the depth where it has rotated 180º, its magnitude is very small. The water column above that depth is called the Ekman layer, i.e. the layer directly influenced by the overlying wind, which, integrated over the vertical, yields a transport that is perpendicular to the right (left) of the wind and proportional to the wind stress. This Ekman transport results in convergence and divergence of water which lead to areas of downwelling and upwelling, with particular cases at the equator and at the coast. The vertical velocity at the base of the Ekman layer is proportional to the curl of the wind stress, thus, spatial variations in the winds can cause upward and downward motion. The influence played by the winds on the surface layer of the ocean can explain most of the oceanic surface horizontal circulation.

The wind can also impact the ocean circulation below the Ekman layer. Sverdrup [1947] considered a stationary, homogenized ocean below the Ekman layer, and using the geostrophic balance, derived the meridional transport in this layer as a function of the curl of the wind stress and the Coriolis parameter. This relation is very useful to explain the basin-scale subsurface ocean circulation such as the gyre circulation forced by the winds. However, it applies in a non-stratified deep ocean, away from physical boundary conditions and considering no bottom boundary layer.

Stommel [1948] extended the Sverdrup balance by adding a linear friction term at the bottom and found a solution including the westward intensification of the ocean currents now well-observed in the gyre circulation (e.g. Gulf Stream, Kuroshio, Brazil current), that could be explained by the latitudinal variation of the Coriolis parameter and by meridional boundaries. Munk [1950] further extended this work by adding a lateral boundary friction term, more important than the bottom one, as well as a more realistic distribution of the wind forcing, and derived a generalized solution of the wind-forced gyre circulation.

The intensification of the Western boundary currents can also be explained by the conservation of potential vorticity in the subtropical gyres, considering the balance between the wind forcing, the latitudinal dependence of the Coriolis parameter and lateral boundary friction (that depends on the strength of the

boundary current) [Fieux, 2010].

Many other theoretical frameworks were proposed over the years to explain other components of the ocean circulation such as the Antarctic Circumpolar Current (ACC), or the abyssal circulation, and to put these different pieces together. This is still an active area of research.

The growing number and means of oceanic observations, with higher time and space resolutions, has enabled to confirm or reject historical theories. Acoustic drifters released in the Atlantic were, for instance, able to confirm the existence of a deep western return current in the Atlantic ocean, theorized by Stommel [1957]. Observations of the deep and abyssal ocean have also allowed to revisit the way abyssal mixing and the returning upward branch of the circulation were thought to be forced (e.g. Munk [1966], Munk and Wunsch [1998]).

The more processes are considered, at different scales, the more complex the systems become. Technical advancements have allowed to solve certain problems numerically. We now present how numerical models can be important tools to study the ocean and its variations within the climate system.

1.3.3 Modelling the climate system and its changes

Numerical modelling of the ocean and climate

As mentioned before, the ocean is governed by the laws of physics. Its motion and properties can be solved and studied by making a number of assumptions to simplify the complex set of equations. These assumptions depend on the application and scientific questions. To solve the system under consideration, the equations of motion and the thermodynamic relations are discretized in time and space, coded, and solved by a computer, for each grid point and time step of the domain considered. This discretization step relies on mathematical tools, and several methods exist. Depending on the spatial and temporal resolution of the numerical model, different physical processes can be resolved or not by these equations, according to their characteristic time and space scales. Those that cannot be resolved are said to be parameterized, i.e. small-scale unresolved quantities are related to large-scale resolved quantities. The ocean model has to be provided boundary conditions, i.e. values or fluxes exchanged at the limits of its domain, such as heat, mass flux and momentum. When studying the ocean at global scale, its physical boundaries are the atmosphere, sea-ice, land, and the bathymetry (the shape of the ocean floor). The ocean model can also be coupled to other model components of the climate system, in which case the boundary conditions are calculated interactively with the other components. A model has to first be initialized before it can run, i.e. prognostic variables have to be provided at the initial time step. In the ocean, the temperature and salinity fields are usually initialized to climatological observed values, and the velocity field is initialized to rest. The model can then be run forward, and it can take several hundred to thousand simulated years for an equilibrium to be reached when simulating the global ocean, considering the time scales of the ocean circulation [Bryan, 1969].

Numerical models (of the ocean and the atmosphere) have many different applications, for diverse research questions but also for societal services, such as weather forecast or met-ocean services for industrial purposes. One application of these numerical models that has been developed in the past decades are Global Climate Models (GCMs), also called General Circulation Models, which we will take interest in here.

GCMs aim to represent the dynamics of the atmosphere and the ocean as well as the physical, chemical and biological processes within the climate system and their variability from seasonal, interannual, decadal to multi-decadal and centennial time scales. They are constituted of different components of the climate system that are developed separately and coupled to each other through their physical and biogeochemical interactions. Most GCMs today are composed of an ocean model, sea-ice model, atmospheric model and land surfaces model. Once the components are coupled to each other, the GCM handles all the energy exchanges, the carbon cycle and the water cycle across the components. Closure of the energy and

water budgets is an important step of model development but is not necessarily verified due to numerical losses by, e.g., the coupling interfaces and regridding between the model components. The spatial and temporal resolution adopted depends on the scientific question and application. To simulate the evolution of global climate since the industrial revolution to today and even in the future, the latest generation of GCMs have a horizontal resolution of about 1º and a temporal time step of the order of 30 minutes to an hour in the ocean and 15 minutes in the atmosphere. Scaling down the resolution (to possibly better represent the oceanic and atmospheric circulations) demands more computing time, and is thus generally applied today to regional climate modelling and shorter temporal periods.

Sources of climate variability and change

The climate system is chaotic and has internal variations, inherited from the non-linear equations governing its motion and thermodynamics, acting on a range of time and space scales [Franzke and O'Kane, 2017]. This means two particles initially side by side can end up, after a period of time, at two completely unrelated locations. Or put another way, a climate initialized infinitesimally differently than a first one will end up in two significantly different states (within the range of possible internal variations).

The climate system also responds to "external forcings", i.e. drivers of physical or biochemical change coming from outside the realm of the ocean/sea-ice/atmosphere/land components. On time scales important for current human societies (decadal to centennial time scales), two natural external forcings play a role on climate interannual to multi-decadal variability: solar incoming radiation, which has a cycle of about 11 years, modulating the amount of shortwave radiation received by the Earth [Lean, 2010], and volcanic eruptions, which act to temporarily cool the climate system by releasing sulphate aerosols in the stratosphere, reflecting part of the shortwave radiation [Cole-Dai, 2010]. Since about 1750, and mostly since the industrial revolution, humans have increasingly contributed to introducing other external forcings in the climate system ("anthropogenic forcings"). The dominant ones are the emissions of additional greenhouse gases (GHGs), with the major two gases being carbon dioxide and methane, released in the atmosphere by the combustion of fossil fuels extracted from the ground, by enteric fermentation (through livestock farming), rice cultivation, deforestation and land use [Friedlingstein et al., 2020, Saunois et al., 2020]. These additional GHGs act to increase the greenhouse effect, trapping more infrared radiation within the atmosphere, creating an imbalance between incoming and outgoing energy fluxes at the top of the atmosphere, resulting in a warming of the troposphere and cooling of the stratosphere [Forster et al., 2021]. Other anthropogenic forcings include aerosols, small polluting particles released in the atmosphere, which tend to reflect the sun's radiation and thus cool the surface climate. Finally, ozone-depleting substances like chlorofluorocarbons (CFCs) were largely released in the second half of the 20th century (they were used in e.g. aerosol sprays and refrigerants), creating what is known as the "ozone hole" in the stratosphere, observed since the late 1970s [Solomon, 1999]. The ozone hole was found to have important consequences for the climate of the Southern Hemisphere (e.g. Thompson et al. [2011]). After the Montreal protocol in 1996 which banned the use of these substances, the ozone hole started slowly recovering [Solomon et al., 2016].

Simulating the historical climate

To simulate the evolution of the climate system from the pre-industrial era to today, observations of all these external forcings (natural and anthropogenic) and their evolution are prescribed to global climate models. Such simulations are called "historical" experiments, and run from ∼1850 to ∼today (depending on when they were conducted). The Coupled Model Intercomparison Project (CMIP) [Taylor et al., 2012, Eyring et al., 2016] provides a common framework and protocol for climate models of all modelling institutions to simulate (among else) the climate of the historical period, with prescribed fields of historical radiative forcings, and common standardized outputs for multi-model studies. Before a historical simulation can start, the climate model has to be (quasi-)equilibrated (it is often not the case as this can take several hundred to thousand simulated years, which can be computationally constraining). To do

that, GCMs are initialized from climatological data and run forward without any external forcings. This is called a "spin-up" simulation. Once a quasi-equilibrium has been reached, the model simulates the "unforced climate" in what is called a Pre-Industrial Control (piControl) simulation. The historical simulation is branched from a piControl, with historical external radiative forcings now prescribed. However, exact conditions in 1850 were largely unknown, especially in the ocean. Initializing the historical simulations from an unknown state thus means it is not possible to correctly reproduce the phases of internal variations observed today. Consequently, in an endeavour to span the possible variations present in 1850, historical simulations can be run multiple times by the same model (each simulation is called a "member", which together form an "ensemble"), starting from a different climate state simulated by the model in the piControl simulation. The different members then provide multiple realizations of possible climates; in the real world, the observations correspond to one realization of the climate, of which we don't know all the conditions in 1850. The ensemble of members also provide a range of internal variability, and averaging across members (when a large enough number of members have been performed) provides the best estimate to retrieve the "forced response" (i.e. the long-term response to external forcings) as it damps the variability [Deser et al., 2012].

GCMs have to be evaluated for their capacity to reproduce relevant observations and to reproduce physical processes. There are several particularly useful metrics (which measure a distance between the model and observations) or indicators to look at when evaluating a climate model: the mean state and the annual cycle (compared to climatological observations) and the response to external forcings (the trend in key variables in the historical period compared to the trend in observations). Differences in the climate mean state are called biases. Multi-model biases are evaluated for each CMIP exercise and for different parts of the climate system. For zonal mean potential temperature and salinity, the Coupled Model Intercomparison Project Phase 5 (CMIP5) and Coupled Model Intercomparison Project Phase 6 (CMIP6) broadly show a warm and salty bias at mid and intermediate depths (and in the Southern Ocean for temperature), and a cold and fresh bias in the surface layers [Eyring et al., 2021]. The origin of these biases can be complex, depend on the resolution and are model-dependent. Getting a global climate model to correctly reproduce the mean observed state is an entire research area. The coupling itself between components can entirely modify the mean state obtained previously with a forced ocean or atmosphere alone. The procedure relies on tuning a number of model parameters (associated to unresolved processes) to adjust the response of the model and make it as close as possible to an observed target (the targets are usually a number of defined climate indices such as global surface air temperature, sea-ice cover, etc...). The tuning process can be extremely time and energy (cpu time) consuming and rely a lot on ad-hoc methods (e.g. Mignot et al. [2021]), so modelling groups are now shifting towards machine learning methods to more objectively explore the space of parameter values yielding acceptable targets (e.g. Williams et al. [2021], Hourdin et al. [2021]).

Attributing observed changes to climate drivers

Simulations over the historical period can also be run without anthropogenic forcings (natural forcings only: "historicalNat" experiments), or without variations in natural forcings, or with only some anthropogenic forcings (figure 0.5). This allows the evaluation of the climate impact of individual or groups of forcings. When external forcings are constant, the climate system is referred to as being "unforced" (piControl experiments). During the historical period, the climate forced with natural forcings alone cannot reproduce the observed warming of global mean surface temperature (figure 0.5, Eyring et al. [2021]) and human activities are found to be the sole cause of the observed long-term warming since 1850.

These simulations are part of the Detection and Attribution Model Intercomparison Project (DAMIP). Indeed, CMIP consists in core simulations (called the "Deck" in CMIP6) that have to be performed by all the modelling centers to understand and compare the unforced simulated climates of different models (piControl experiments), and their response to idealized (e.g. abrupt quadrupling or 1% per year increase in atmospheric CO_2 concentration) and historical forcings. Then, other specific MIPs are proposed to

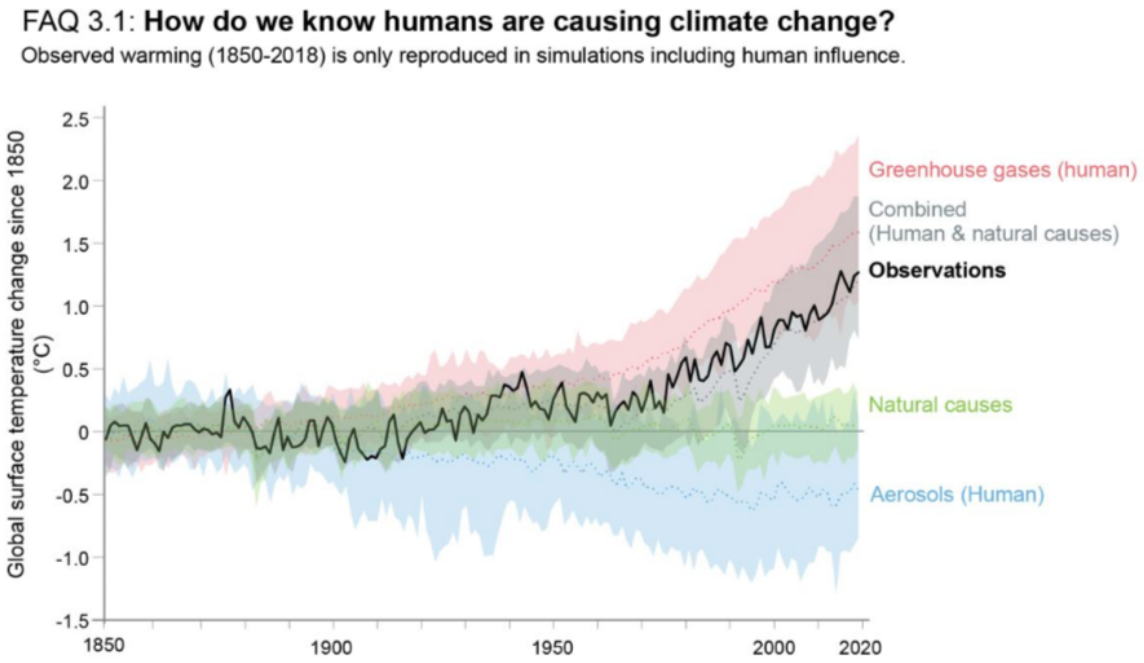

Figure 0.5: Observed warming (1850-2018) is only reproduced in simulations including human influence. From IPCC AR6 FAQ3.1 Figure 1 Eyring et al. [2021]

explore specific aspects and answer targeted questions [1].

Projecting the evolution of future climate

To project the possible evolution of future climate (usually until 2100 but also on longer time scales), different scenarios of the 21st century are constructed under a range of socio-economic and mitigation assumptions (i.e. what will society decide to do in response to man-made climate change), yielding GHGs and pollutants emissions or concentrations in the atmosphere [Gidden et al., 2019]. The information provided by climate model historical experiments and projections is (and has been for decades already) crucial to understand the anthropogenic origin of current climate change and its impacts on societies and ecosystems, and to inform citizens and decision makers.

When considering climate model projections, three sources of uncertainty have been reported: internal variability, model representation and scenarios [Hawkins and Sutton, 2009]. The uncertainty in scenarios (i.e. which future will actually happen) is explored by constructing different pathways of emissions; the choice of scenario is not visible right away on, for example, Global Surface Air Temperature (GSAT), because of internal variability, but after a couple of decades [Lee et al., 2021]. The uncertainty in model physics (do models realistically reproduce the "real" climate) is explored by considering the projections provided by multiple climate models, to span different alternative realities depending on modelling choices. This is done through the CMIP exercises which provide precise protocols for model forcings and outputs so that the intercomparison can be made successfully. In the past couple years, the 6th phase of the project has seen the light with climate modelling institutions releasing their model data progressively as the experiments were being conducted, and is still ongoing. Finally, uncertainty in internal variability arises from the chaotic nature of the climate system and its internal modes of variability, and is large on decadal time scales. Internal variability can indeed temporarily mask or amplify long-term trends in response to anthropogenic forcings. The uncertainty in climate projections due to internal variability can

1. See e.g. https://www.wcrp-climate.org/modelling-wgcm-mip-catalogue/modelling-wgcm-cmip6-endorsed-mips

be estimated from the spread between members of a single model initialized from different climate conditions. This uncertainty is problematic when trying to provide relevant climate projections in the next 10 years or so, especially at regional scale. Research in decadal climate predictions aims to use observed variability to constrain climate simulations and to provide skilful forecasts of climate variations from a year to a decade ahead, primarily through the use of hindcasts (e.g. Boer et al. [2016]).

Before digging more into how we can use global climate models to explore possible future climates, we now turn to oceanic changes already observed today.

2 The thermohaline structure of the ocean is changing

Since we started observing the ocean, clear multidecadal changes have surfaced in the thermohaline characteristics of the ocean. In this section, I will give an overview of these large-scale multidecadal observed changes, before assessing their significance - relative to natural climate variations - and their anthropogenic origin in section 3 and the physical mechanisms causing them in section 4.

Since the focus of this introduction chapter is closely related to what was reported in several chapters of the IPCC Working Group I AR6 [IPCC, 2021a], released in August 2021, I present when relevant the confidence level they have assigned to the different ocean changes and their origin.

Note many changes are occurring in the ocean physical, chemical, biological properties, in their long-term mean evolution but also in the frequency and intensity of extreme events [Bindoff et al., 2019]. Here, the focus will be put on long-term changes in temperature and salinity and related quantities.

2.1 Changes in temperature and heat content

2.1.1 A broad surface warming

Since the beginning of the 20th century, the ocean surface has warmed broadly (figure 0.6): based on the mean of four observation-based products (COBE1 [Ishii et al., 2005], COBE2 [Hirahara et al., 2014], HadISST [Rayner, 2003], ERSST [Huang et al., 2017]), the warming trend in globally-averaged SST has been evaluated at 0.62 ± 0.12 °C/century for the period 1900-2018 [Garcia-Soto et al., 2021], with accelerated warming in the last decade (2.56 ± 0.68 ºC/century for 2009-2018). The AR6 evaluates that "it is now *very likely* that global mean SST changed by 0.88°C [0.68-1.01°C] from 1850-1900 to 2011-2020, and 0.60°C [0.44-0.74°C] from 1980 to 2020". This warming is not uniform, with the fastest trends observed in the tropics and even some regions with observed cooling in the subpolar North Atlantic (referred to as the "warming hole" or "cold blob") and the subpolar Southern Ocean.

2.1.2 A warming present on all vertical levels with varying horizontal patterns

Already in the early 2000s, broad, consistent ocean warming since the mid-20th century had been observed in the subsurface and at depth [Levitus, 2000, Levitus et al., 2005, Gille, 2002, 2008]. Since around 2005, the Argo array has allowed much better monitoring of the warming in the upper 2000m (e.g. Roemmich et al. [2015], Wijffels et al. [2016]), while we still rely mostly on repeat hydrographic sections to explore the deeper ocean >2000m [Purkey and Johnson, 2010, Desbruyères et al., 2016, 2017, Purkey et al., 2019].

The most pronounced patterns of warming are located in the upper layers and follow the structures of ventilation pathways, with a deeper penetration of warming in the subtropical gyres [Levitus et al., 2012, Roemmich et al., 2015, Häkkinen et al., 2016, Desbruyères et al., 2017], see figure 0.7. Strong multi-decadal warming is observed in the upper North Atlantic ocean along the Gulf Stream and North Atlantic Current [Levitus et al., 2012, Häkkinen et al., 2016], but weaker warming or even cooling is observed at depth [Desbruyères et al., 2016]. The Southern Ocean is contrasted in terms of warming trends, with

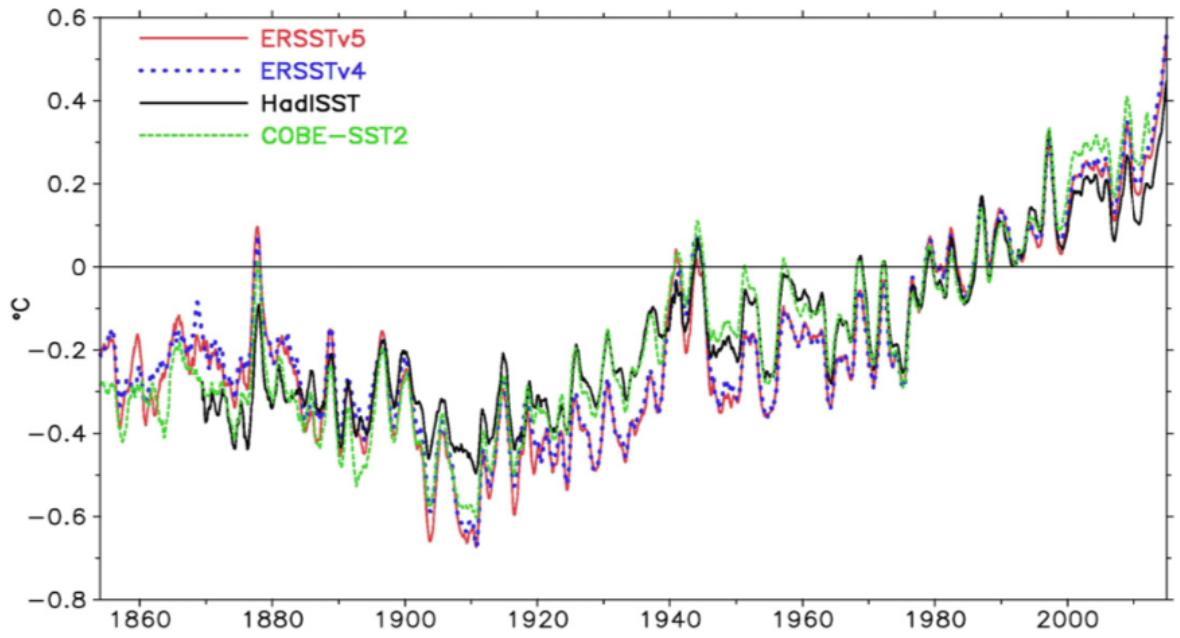

Figure 0.6: From Huang et al. [2017]. Observed global mean SST anomaly relative to 1971-2000 for different reconstructed products.

delayed warming in the upwelling region south of the ACC [Armour et al., 2016] but more rapid warming in the top 2000m in and north of the ACC compared to global rates [Sallée, 2018, Roemmich et al., 2015]. Southern Ocean Mode and Intermediate Waters have warmed at a rate of 0.1-0.2ºC/decade [Sallée, 2018]. Changes in surface winds have caused enhanced southward and upward transport of Circumpolar Deep Water (CDW), which have also warmed due to upper ocean increased stratification acting to decrease mixing of CDW with the overlying surface waters, all of which with potential important consequences for access to the continental shelf and iceshelf basal melt [Schmidtko et al., 2014, Auger et al., 2021, Fox-Kemper et al., 2021].

Repeat hydrographic sections over all ocean basins since the 1980s have allowed the assessment of deep (2000-4000m) and abyssal (4000-6000m) warming (Purkey and Johnson [2010], extended by Desbruyères et al. [2016]). The warming observed in these layers was found to be equivalent to a 0.065 $\pm$ 0.040 W.m^{-2} heat flux for 1991-2010, with significant trends at every pressure levels and with 2/3 of this warming contained between 2000-4000m, although the less voluminous abyssal layer (>4000m) warmed at a faster rate. The subpolar Southern Ocean was found to have a dominant role for both deep and abyssal warming, contributing 67% of the global trend despite its small volume, and being the only region where the deep warming trend is statistically significant from zero. A consistent warming was found in regions of formation or fed by AABW, highlighting their key role as a clear pathway of ocean warming (and also investigated by e.g. Purkey and Johnson [2013] and Purkey et al. [2019]). Combining Argo data in the top 2000m and repeat hydrography below 2000m, Desbruyères et al. [2017] estimate the global ocean warming in the last decade to amount to a 0.71 $\pm$ 0.09 W.m^{-2} heat uptake (applied over the Earth area) with 90% of that warming taking place above 2000m. They also confirm that ocean warming is present at every pressure level, with local maxima at the surface, at 1000m and at 4200m.

The AR6 assesses that "it is *virtually certain* that the upper ocean (0-700m) has warmed since 1971, that ocean warming at intermediate depths (700-2000m) is *very likely* since 2006, and that it is *likely* that ocean warming has occurred below 2000m since 1992". Furthermore, it gives "*high confidence* that deep ocean warming below 2000m has been larger in the Southern Ocean than in other ocean basins due to widespread AABW warming".

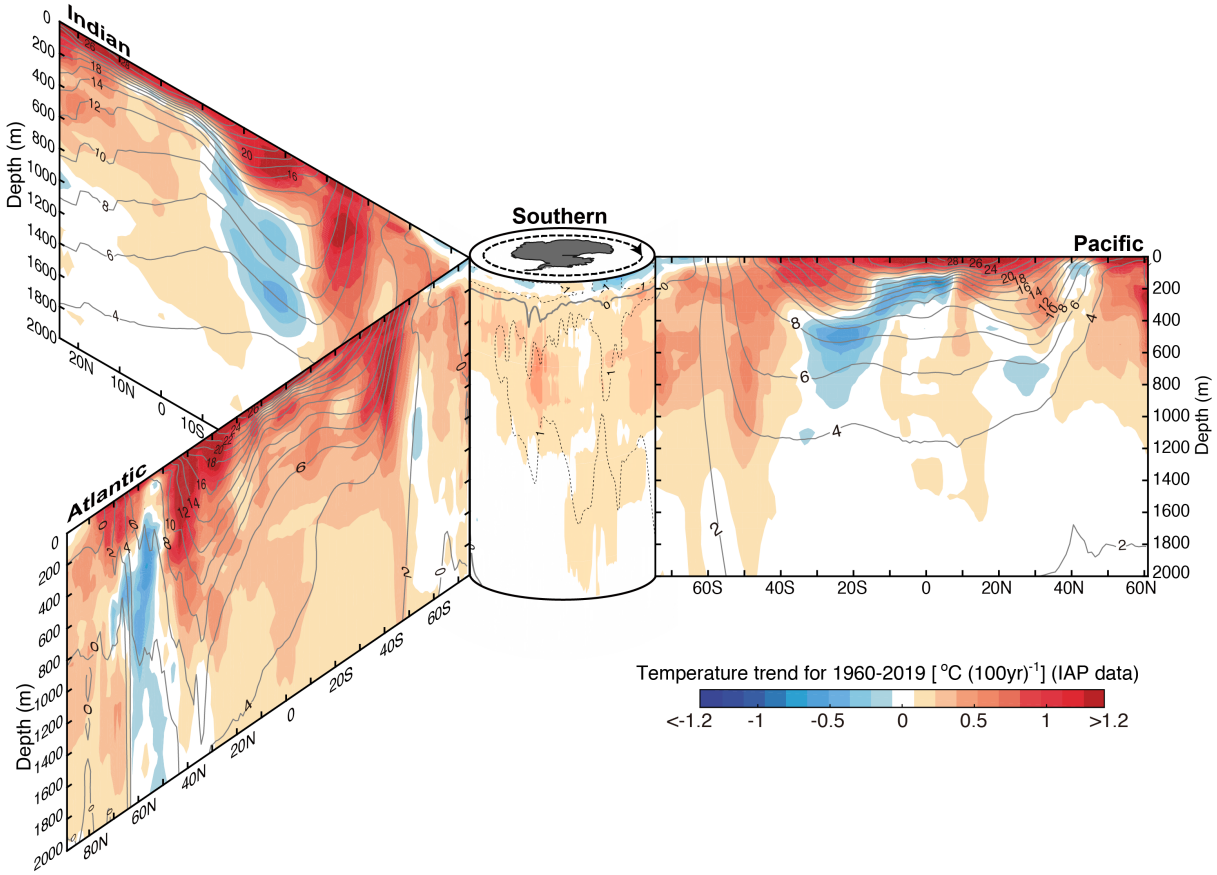

Figure 0.7: Figure downloaded from http://159.226.119.60/cheng/, based on IAP gridded data [Cheng et al., 2017]. Mean ocean warming rate (0-2000m, linear trend) from 1960 to 2019. Figure shows vertical section of the ocean temperature trends within 1960 to 2019 from sea surface to 2000 m (60-year Ordinary Least Squares linear trend). Shown are the zonal mean sections in each ocean basin organized around the Southern Ocean (south of 60°S) in the center. Black contours show the associated climatological mean temperature with intervals of 2°C (In the Southern Ocean, 1°C intervals are provided in dashed contours).

2.1.3 A globally-integrated warming that reflects the energy imbalance of the climate system

Additional greenhouse gases released by human activities in the atmosphere are trapping more heat in the climate system, creating an energy imbalance at the top of the atmosphere. The global trend of OHC reflects this earth energy imbalance, with 91% of the total energy gained in the climate system from 1971 to 2018 stored in the ocean (see figure 0.8, right panel) [Forster et al., 2021]. The remaining energy went to heating the atmosphere (1%), land (5%) and melting ice (3%) (figure 0.8). OHC integrates the natural variations within the climate system and better reflects long-term changes, compared with only upper-ocean or surface temperature (compare figures 0.6 and 0.8) which can hide periods of ocean heat absorption at depth while surface temperature is not rising, such as the warming "hiatus" of the 2000s [Storto et al., 2021]. This makes OHC one of the key variables we ought to closely monitor to track the evolution of ongoing climate change [Meyssignac et al., 2019].

The IPCC AR5 report [Rhein et al., 2013] estimated the rate of ocean heat uptake for the upper 2000m ranging from 0.20 to 0.32 W.m^{-2} for 1971-2010, and about 0.5 W.m^{-2} for 1993-2010. However, these rates were probably underestimated, as Cheng et al. [2019] highlighted recent studies with extended observation-based OHC estimates ranging from 0.36 to 0.39 W.m^{-2} for 1971-2010, and 0.55 to 0.68 W.m^{-2} in the decades after 1991. The 2nd World Ocean Assessment [Garcia-Soto et al., 2021] reports a rate of 0.34 $\pm$ 0.08 W.m^{-2} for 1955-2018 in the upper 2000m (mean rate from observation-based datasets Ishii

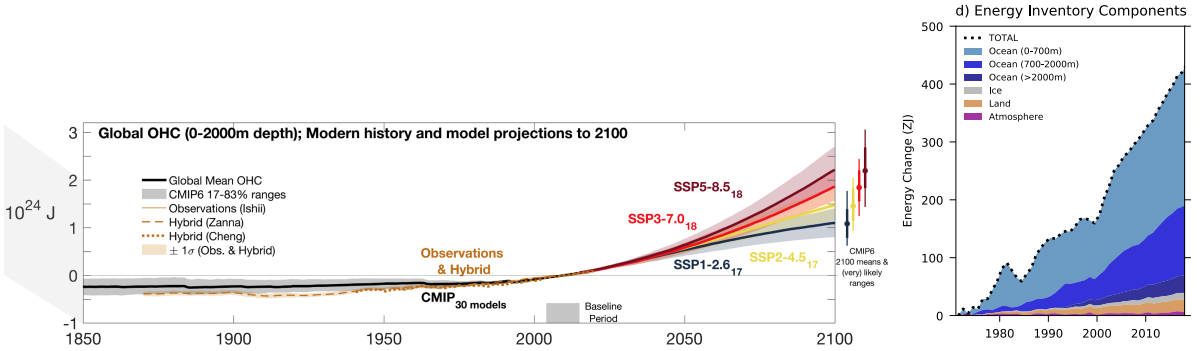

Figure 0.8: (Left) From Fox-Kemper et al. [2021], Figure 9.6: global OHC anomalies in the upper 2000m, from observation-based estimates and CMIP6 multi-model means. (Right) From Forster et al. [2021] box7.1 Figure 1: estimate of the net cumulative energy change (ZJ = 10^{21} Joules) for the period 1971–2018, per component of the Energy Inventory.

et al. [2017] and Cheng et al. [2017]). This rate has increased in the recent decades to 0.62±0.05 W.m^{-2} for 1999-2018 (mean of Ishii et al. [2017], Cheng et al. [2017] and a combination of Domingues et al. [2008] and Levitus et al. [2012]). For 2009-2018, the mean rate rises to 0.65 ± 0.07 W.m^{-2}. Finally, the latest figures reported by the IPCC AR6 [Forster et al., 2021] give a corresponding warming rate of 0.34-0.62 W.m^{-2} for 1971-2018 in the upper 2000m, 0.43-0.73 W.m^{-2} for 1993-2018 and 0.40-0.89 W.m^{-2} for 2006-2018.

A reconstruction of the full-depth OHC evolution since 1871 was proposed by Zanna et al. [2019b], using observed SST fed to a representation of time-independent ocean transport processes, giving unprecedented information about OHC below 2000m and at these time scales. Their reconstruction agrees well with observation-based estimates in the upper 2000m (0.30 ± 0.06 W.m^{-2} for 1955-2017) and they indicate a warming rate of 0.028 ± 0.026 W.m^{-2} below 2000m on the same period. New information provided by this study also includes an OHC increase during 1921-1946 as large as during 1990-2015.

Global climate models from the CMIP5 and CMIP6 exercises simulate consistent multi-decadal OHC increase compared to the latest observational estimates (see e.g. figure 0.8), with coherent vertical warming although they have a tendency to produce stronger trends than observed at depth and weaker trends in the upper ocean [Eyring et al., 2021, Fox-Kemper et al., 2021]. Global ocean warming is projected to continue in the coming decades under all GHG emissions scenarios with *very high confidence*, following observed patterns of change with an uptake of heat particularly pronounced in the subtropical gyres, mode waters, AABW, delayed warming in the upper subpolar Southern Ocean and in the deep subpolar North Atlantic [Fox-Kemper et al., 2021]. The AR6 concludes on ocean warming projections: "there is *high confidence* that there is a long-term commitment to increased OHC in response to anthropogenic CO_2 emissions, which is essentially irreversible on human timescales".

2.2 Changes in salinity

Global, multi-decadal patterns of salinity change have been observed at the surface and subsurface since the 1950s and confirmed by several independant studies [Boyer et al., 2005, Hosoda et al., 2009, Helm et al., 2010, Durack and Wijffels, 2010, Skliris et al., 2014, Cheng et al., 2020]. These global surface observations have shown intensified salinity patterns along the mean salinity field, with evaporation-dominated regions getting saltier (e.g. the subtropical gyres and the entire Atlantic basin) and precipitation-dominated regions getting fresher (e.g. the Pacific Warm Pool and the high latitudes), consistent with an amplification of the water cycle. Coherent changes have also been observed in subsurface waters, with anomalies penetrating in the upper 1000m, freshening the high latitude waters (e.g. the Antarctic Intermediate Water (AAIW)) and enhancing the already salty subtropical gyres (see figure

0.9). The inter-basin contrast between the salty Atlantic and fresh Pacific basins has also amplified at the surface and in the subsurface. This intensification of the climatological field in the subsurface suggests that persistent surface anomalies of several decades have already propagated into the ocean interior. We note however that on shorter timescales (interannual to decadal), the relationship between salinity change patterns and water cycle amplification is not evident, due to ocean circulation, salt transport and natural variability [Vinogradova and Ponte, 2017].

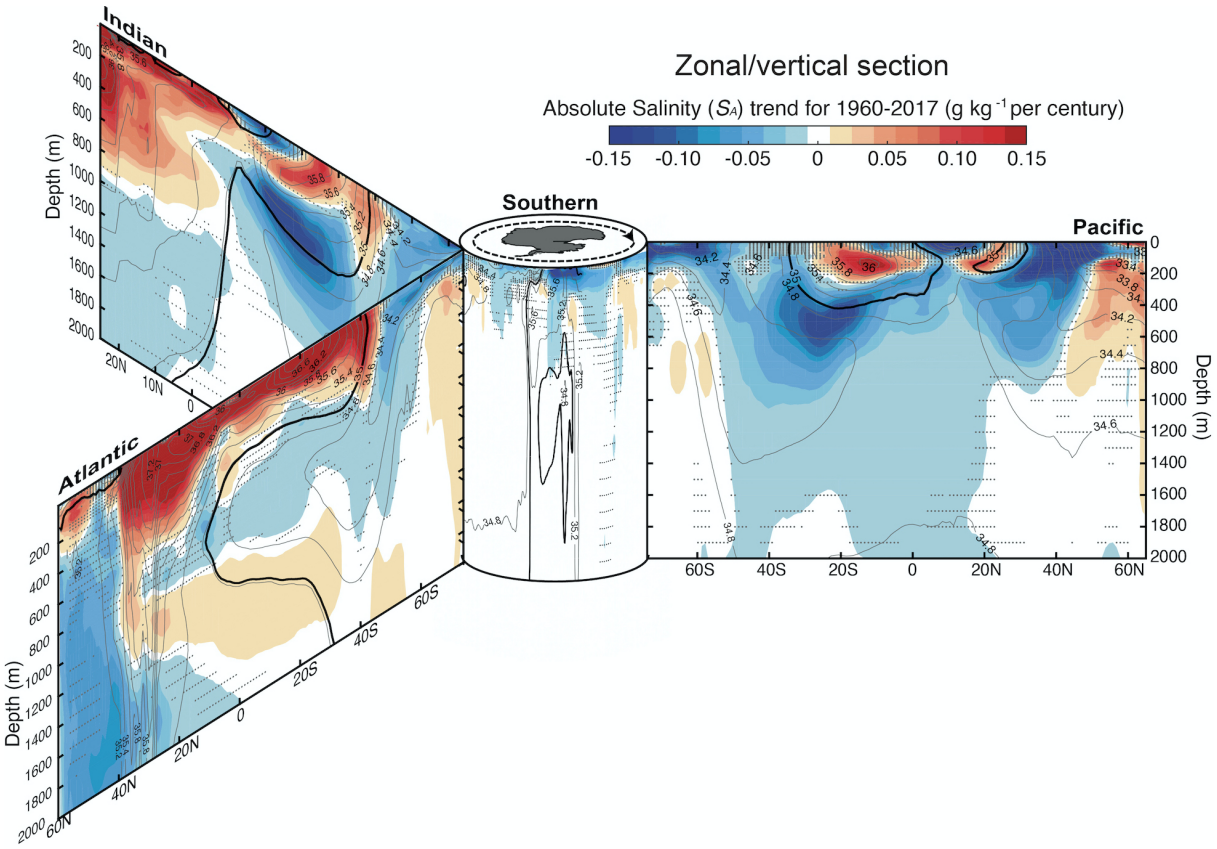

Figure 0.9: From [Cheng et al., 2020]. Ocean salinity trends for 1960–2017 from sea surface to 2000 m as the zonal mean sections in each ocean basin organized around the Southern Ocean in the center. Gray contours show the climatological mean salinity, with intervals of 0.2 g kg^{-1}. The thick black contour shows the global median of the climatological salinity.

The multi-decadal SSS Pattern Amplification (PA) has been estimated to range from 5-8% from observed estimates [Hosoda et al., 2009, Durack et al., 2012, Skliris et al., 2014, Zika et al., 2018, Cheng et al., 2020]. The spread in these estimates is suggested to come from errors in the different datasets [Cheng et al., 2020]. However, the E-P (Evaporation – Precipitation) PA inferred from full-depth salinity observations and water-mass transformation theory is much lower, around 3%/K (Skliris et al. [2016], based on Zika et al. [2015]). Climate models also predict SSS PA at twice the rate of E-P PA [Durack et al., 2012]. In investigating the cause of this ratio between SSS and E-P PA, idealized model studies have shown that ocean warming, by increasing near-surface stratification, was partly responsible for the amplification of the SSS pattern [Durack et al., 2012, Zika et al., 2018], and could explain close to half of the observed SSS pattern changes between 1957-2016 [Zika et al., 2018]. The E-P fluxes are subject to more high-frequency variability compared to ocean salinity, which acts as an integrator of the freshwater fluxes. Furthermore, SSS is better observed (and easier to) than E-P, particularly since the satellite era, with more coherence and less discrepancies in the pattern trends of various reconstructions [Skliris et al., 2014]. Yu et al. [2020] provide an extensive review of water-cycle amplification estimates, both from direct E and P measurements and from ocean salinity. Recently, using an improved estimate of upper

ocean salinity since 1960 and correlation between salinity and E-P in CMIP5 models, Cheng et al. [2020] derived an estimate of the water cycle amplification of 2.6%-3.2%/K.

The AR6 concludes on salinity changes and their cause with the following statement: "[...] subsurface salinity trends are connected to surface trends *(very likely)*, which are in turn linked to an intensifying hydrological cycle *(medium confidence)* and increasing evidence from updated observational records indicates it is now *virtually certain* that surface salinity contrasts are increasing".

There is little observational evidence of salinity changes in the deeper ocean, however a persistent freshening of AABW below 1000m and in the deep and abyssal ocean was observed by repeated hydrographic sections between the 1980s and 2000s in the South Pacific and Indian oceans with the strongest trends near their formation site (i.e. near the Antarctic continental slope), a probable consequence of increased continental ice melt [Rintoul, 2007, Purkey and Johnson, 2013, Jullion et al., 2013]. Overlying salinification of CDW was also observed by these repeated transects. Another decade of hydrographic sections provided additional evidence for recent AABW freshening [Menezes et al., 2017, Purkey et al., 2019].

CMIP5 and CMIP6 models simulate similar consistent patterns of basin-scale surface and subsurface salinity pattern amplification over the past decades, and the AR6 assesses the following for future changes: "overall, projections confirm the SROCC assessment that fresh ocean regions will continue to get fresher and salty ocean regions will continue to get saltier in the 21st century *(medium confidence)*"[Fox-Kemper et al., 2021, Eyring et al., 2021].

2.3 Changes in stratification

Global ocean warming and high-latitude freshening has resulted in an increase in ocean stratification, particularly in the upper ocean. There have been multiple ways of defining ocean stratification and reporting its multi-decadal changes. The IPCC AR5 [Rhein et al., 2013] reported a 4% increase in global mean thermal stratification between the 0 and 200m layers between 1971 and 2010. The Special Report on the Ocean and Cryosphere in a Changing Climate (SROCC) [Bindoff et al., 2019] based its definition of stratification on the square buoyancy frequency N^2 (or Brünt-Vaisala frequency, proportional to the vertical density gradient), and reported a 2.18-2.42% increase in globally-averaged N^2 defined between 0-10m and 190-210m between the periods 1971-1990 and 1998-2017. Li et al. [2020] report N^2 changes for 1960-2018 in the upper 2000m of the ocean using new gridded products of 3D temperature and salinity [Cheng et al., 2017, 2020]. They find that N^2 is increasing almost everywhere in the upper 2000m of the ocean and in all basins, with the strongest trends in the top 200m and in the tropics. They report a 6.9% increase in globally-averaged 0-200m N^2, and 5.3% in the total 0-2000m layer. With the AR5 definition, their product gives a 5.1 $\pm$ 2.1 % increase in upper 200m stratification during 1971-2010 (compared to 4% reported in AR5). And when adopting the SROCC definition, they obtain a 4.3% increase from 1971-1990 to 1998-2017 (compared to the 2.3% reported in SROCC). They explain the underestimation of previous reports by conservative biases in the datasets due, in part, to sparse observational sampling in certain regions which results in infilled grid cells by climatological values and underestimated trends. In investigating the relative importance of temperature and salinity in the stratification increase, Li et al. [2020] find that temperature changes largely dominate the observed stratification increase but that salinity changes can still play a role locally, especially in polar regions.

In an endeavour to follow the changes in stratification between the upper and deep ocean (i.e. in the pycnocline) more closely, and to account for the different dynamical regimes across the ocean and their evolution in time, Sallée et al. [2021] computed the multi-decadal evolution in mixed-layer depth and in N^2 at the base of the mixed layer, from a large combination of in-situ temperature and salinity profiles between 1970 and 2018. They report a global mean summertime pycnocline stratification increase of 8.9 $\pm$ 2.7%/dec, compared to the much lower value of 1.3 $\pm$ 0.3%/dec when computing stratification in the fixed 0-200m layer (a value consistent with annual-mean estimates of previous studies, e.g. the 1.2 $\pm$

0.1%/dec of Li et al. [2020]). This suggests computing stratification changes over a fixed layer can hide substantial increases in pycnocline stability (see the difference in trends at local scale in figure 0.10). Sallée et al. [2021] also find that the contribution of temperature changes to the increased stratification has been dominant due to global surface warming, except in the subpolar Southern Ocean; and they find an intensification of the contribution of salinity to stratification mirroring the amplifying hydrological cycle (i.e. the evaporation-dominated gyres are getting saltier thus increasing their destabilizing contribution to upper ocean stratification, while precipitation-dominated regions especially in the cold Southern Ocean are getting fresher, thus increasing the salinity-induced stability). This summertime increased stratification of the pycnocline is associated with a reported deepening of the summer mixed layer of 5m-10m/dec across the ocean, equivalent to a deepening of 2.9 ± 0.5%/dec compared to the local MLD climatology. This result is new and counters the intuitive assumption that mixed layer depths are shoaling as surface warming increases. A suggested explanation to this multi-decadal mixed layer deepening is an increase of upper ocean turbulence driven by intensifying winds, large enough to counteract the expected shoaling by surface buoyancy fluxes.

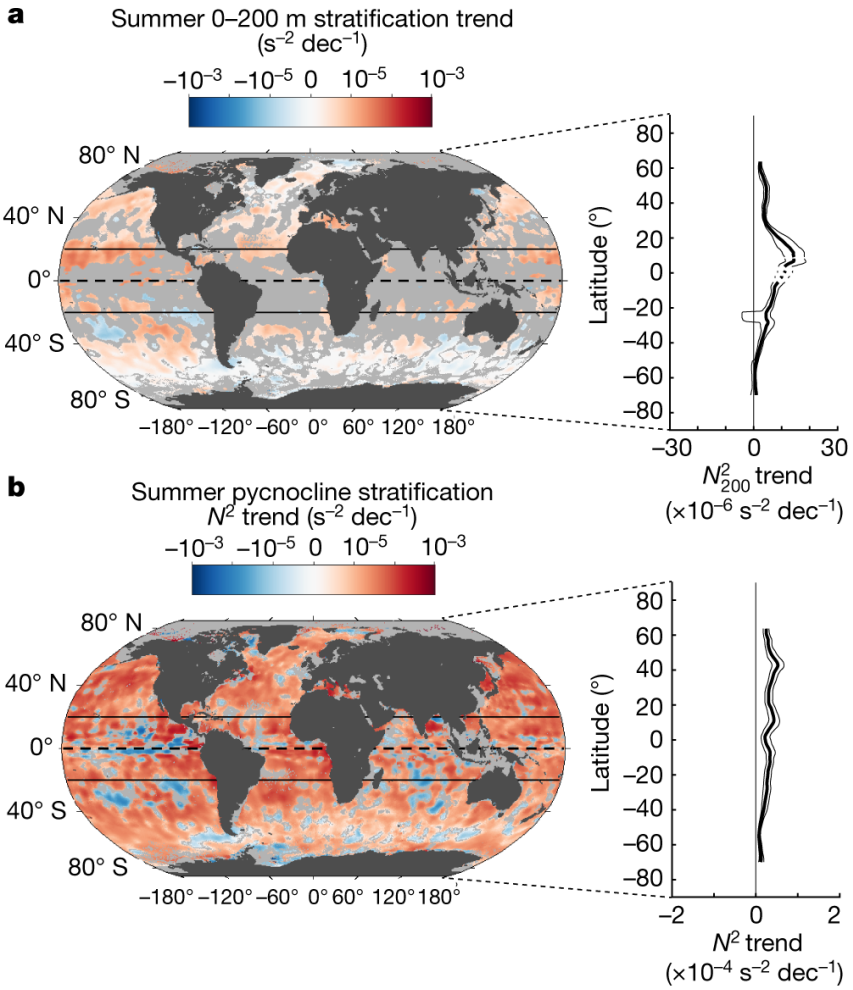

Figure 0.10: From [Sallée et al., 2021]. 1970-2018 trends in summer upper-ocean stratification (a) 0-200m N^2_{200} and (b) pycnocline stratification N^2.

Overall, the multi-decadal upper ocean increased stratification is assessed to be *virtually certain* in the AR6, with a reported rate of 4.9 ± 1.5 % from 1970 to 2018 for the upper 200m with *high confidence*.

As the depth and strength of the pycnocline strongly control vertical mixing and the availability of biochemical properties between the surface and deep layers, increased stratification of the ocean and

changes in mixed layer depth have potential impacts for nutrient, oxygen, carbon and heat fluxes between the upper and deep ocean, thus on water-mass ventilation and formation, with important biological and climatic consequences [Bindoff et al., 2019, Li et al., 2020, Sallée et al., 2021].

In CMIP models, the upper ocean increase in stratification of the past decades is projected to continue in the 21st century over most ocean basins, with a likely decrease in abyssal stratification [Bindoff et al., 2019]. Contrarily to the observed deepening of summer mixed-layer depth, CMIP6 models project a shallowing of the mixed layer by the end of the century [Fox-Kemper et al., 2021].

3 Are these changes significant compared to climate variability and are they human-induced?

3.1 Disentangling internal variability from external forcings

The reported observed changes presented in section 2 point towards a robust and increasing influence of human activities on the ocean over the past several decades. However, other factors can modulate the response to anthropogenic forcings, such as strong internal variability and the response to natural forcings, especially to volcanic eruptions. These other factors are not uniform and vary in space and time. For example, the strong decadal warming observed in the Southern Ocean in the early 2000s-2010s was proposed to be caused both by human activity and by an internal inter-hemispheric mode of variability that temporarily strengthened the forced signal, but that already started to shift, thus slowing down the ongoing decadal warming [Rathore et al., 2020, Wang et al., 2021, Zika et al., 2021].

How can we make sure the observed changes are related to a human-induced climate change signal? How can we know when a reported change is large enough to surpass internal variability or variations due to natural forcings? One application of global climate models in climate change studies is to formally detect a change in the available observations, and attribute it to cause, using forced and unforced experiments. Detecting an externally-forced change means that it cannot be explained by internal variability alone (identified by long unforced pre-industrial control experiments). The attribution process aims to evaluate whether the observed change is consistent with the externally-forced model-produced change, and the relative contributions of the external forcings. Different statistical methods have been applied for Detection and Attribution (D&A) studies [Eyring et al., 2021]. The basic idea is first to define a model-based fingerprint, representing the forced climate response (to a single or multiple external forcings). How this fingerprint is defined in time and space and how it is then related to observations is method-dependent. Two major techniques on which most of the studies presented below are based are the regression-based method and the pattern-based method [Eyring et al., 2021].

In the regression-based method, the fingerprint $\boldsymbol{X}$ represents the space-time pattern of the change predicted by the model, following some spatial and temporal averaging of the variable in question, and generally normalized using a long control run. The observations $\boldsymbol{Y}$ (with similar averaging as the fingerprint definition) are regressed against the single or multiple fingerprints (one-signal or multiple-signal regression), yielding a regression coefficient β and residuals $\boldsymbol{\epsilon}$ representing internal variability, so that $\boldsymbol{Y} = \beta\boldsymbol{X} + \boldsymbol{\epsilon}$ (for a simple linear regression). A control run is also projected onto this fingerprint, yielding a distribution of regression coefficients based on which a confidence level can be computed. If the regression coefficient is significantly different from zero, the change in the observations is said to have been detected. Furthermore, if the regression coefficient is close to one (within the confidence interval), the observed change can be partly attributed to the forcing represented in the fingerprint. A statistical test can be run on the residuals $\boldsymbol{\epsilon}$ to evaluate their consistency with internal variability as defined from the control run.

In the pattern-based method, the fingerprint is defined as the first Empirical Orthogonal Function (EOF) from the externally-forced model simulation(s) (usually from a multi-model mean), thus reflecting

the spatial change only. The observations are projected onto this fingerprint, yielding a time-evolving pseudo-principal component, measuring the degree of spatial pattern similarity with the fingerprint. Long control runs are also projected onto the fingerprint to evaluate internal variability. The linear trend can be calculated in these pseudo Principal Component (PC) time series, and detection is found if the trend in the pseudo-PC of the observations statistically surpasses the distribution of trends in the pseudo-PCs of the control run. Another detection method consists in regressing the pseudo-principal component onto the PC associated with the fingerprint and testing for significance on the regression coefficient.

Some of the reported temperature and salinity observed changes have already exceeded the range of internal climate variability and have been partly attributed to human activity. We will here review the main conclusions concerning the D&A of temperature and salinity changes in the ocean. Because the D&A analyses rest upon different definitions of fingerprints, the results are tricky to compare to each other, and it is important to understand what they represent.

3.2 Detection and attribution of thermohaline changes in the ocean

3.2.1 Temperature and ocean heat content

In 2000, Levitus [2000] released a multi-decadal gridded product of observed global OHC change in the upper 3000m from the World Ocean Database (WOD). Following the publication of this product, several modelling groups compared the simulated multi-decadal ocean warming in their coupled model to the warming of this new estimate and tested whether it could be explained by unforced internal variability alone or not. Levitus et al. [2001] showed that the globally-integrated 0-3000m 60ºS-60ºN OHC trend over the period 1955-1996 from Levitus [2000] was consistent with that of an ensemble of fully-forced simulations (temporal variations in GHGs, sulfate aerosols, volcanic activity and solar irradiance) run with the GFDL ocean-atmosphere coupled model; that the simulated positive radiative forcing of the second half of the twentieth century came from the increase in emissions of anthropogenic GHGs, compensated by a cooling caused by volcanic eruptions, and that the simulated warming trend was inconsistent with internal variability alone estimated from all 41-year trends in a control run, providing evidence for a possible human influence on observed warming of the ocean. Sun and Hansen [2003] also found comparable ocean warming to the Levitus estimate in another fully-forced coupled model (GISS SI2000 atmosphere coupled to the HYCOM ocean model), as well as Gregory et al. [2004] with the Hadley Center (HadCM3) model. It was noted however that even though the models reproduced the magnitude of the long-term observed warming, none of them reproduced the strong decadal variability present in the Levitus dataset, although this decadal variability was found to have large uncertainties due to sparse sampling and infilling method [Gregory et al., 2004], and later found to be falsely augmented by instrumental biases [Levitus et al., 2009].

It was Barnett et al. [2001] who conducted the first formal detection study of OHC change, using the Levitus [2000] dataset and the Parallel Coupled Model (PCM) subsampled in grid boxes where there were observations. They defined a fingerprint from the ensemble mean of GHG-forced simulations of the PCM, based on 5 decadal averages (1955-2000) of temperature vertically integrated from 0 to 3000m and horizontally-averaged in each of the 6 ocean sub-basins, concatenating the resulting 6 time series to form a unique fingerprint representing the space/time patterns of OHC change. Projecting the GHG-forced ensemble, a long control run and the observations onto this fingerprint, they found that a climate change signal had occurred in the model and that observations were consistent with the anthropogenically-forced model results.

Using the ECHAM4/OPYC3 coupled model forced by anthropogenically varying GHGs, sulphate aerosols and tropospheric ozone, and an identical definition of the space/time fingerprint of OHC change, Reichert et al. [2002] found similar results, with a simulated climate change signal detected both in the upper 300m and 3000m of the ocean in the observations and attributed to anthropogenic forcings.

A few years later, using an updated version of the observed dataset [Levitus et al., 2005], Barnett [2005] and Pierce et al. [2006] extended the former D&A studies by looking for signals on every depth level of the ocean in each oceanic sub-basin, instead of the former vertically-averaged single time series of 6 concatenated sub-basins, using both the PCM and HadCM3 models. This allowed to illustrate the geographical variations and vertical penetration of the warming signal. They found that the observed warming in the top ∼100m of all ocean basins was stronger than that expected by internal variability, reaching ∼300m in the North Atlantic and even deeper in the South Atlantic; that this warming could not be explained by natural external forcings (solar fluctuations and volcanic activity, which were found to present a signal indistinguishable from internal variability); and that the observed warming signal was consistent with the anthropogenically-forced warming, illustrating the responsibility of human influence in the warming of the upper layers of the ocean. Interestingly, Pierce et al. [2006] found that their model fingerprint explained 80% of the variance of the observed signal in the top 75m, dropping to a minimum at 150m, and rising again to significant levels between 250 and 600m, indicating promising attempts to look for anthropogenic signals below the thermocline, even though they did not formally detect it yet at these depths.

Pierce et al. [2012] further extended this work by defining a model warming fingerprint based this time on 20 models from the CMIP5 archive to look for anthropogenic warming in the updated and corrected (for instrumental bias, Levitus et al. [2009]) observed estimate of Levitus et al. [2012], for the period 1955-2004. In addition, instead of defining their fingerprint by averaging temperature per sub-basin, they used 10°x10° latitudinal and longitudinal boxes to better capture the spatial variations. In the global 3D (upper 700m) observed temperature field, they find a detectable signal of climate change, that cannot be explained by internal variability nor natural external forcings, but that is consistent with the anthropogenically-forced signal (although the inter-model spread can be large). When the fingerprint is calculated independently at each depth level, the observed warming is detected in the top 300m of the ocean.

Gleckler et al. [2012] strengthened the evidence for a human-induced observed upper ocean warming using a different approach of D&A where the spatial and temporal aspects are separated (pattern-based method) when defining their fingerprint. They focus on vertically (0-700m), sub-basin averaged temperature anomalies, in the CMIP3 archive and in 3 observational products corrected for instrumental biases [Levitus et al., 2009, Domingues et al., 2008, Ishii and Kimoto, 2009]. The fingerprint is defined as the first Empirical Orthogonal Function (EOF) of the multi-model mean response to fully-forced simulations, and each observational dataset, model control run and ensemble mean is projected onto this time-invariant fingerprint to produce pseudo-principal component time series, representing the time-dependent correspondence between the fingerprint and each dataset. These time series are then used to derive signal and noise estimates (linear trends) as a function of time, and a resulting signal-to-noise ratio (SNR). They define the detection time as the year when this SNR exceeds and remains above a given confidence level. When starting the detection analysis in 1970, they detect a human-induced warming signal in the 1980s in all 3 observational datasets (at the 5% and 1% confidence level; in the 1990s with a 1960 start date) with SNRs above 4 by 2003, indicating a well-established anthropogenic fingerprint of ocean warming by the end of the 20th century in the upper ocean.

Continuing more recently on the detection of the large-scale warming, Tokarska et al. [2019] focus on global mean temperature anomalies in 3 depth layers (0-300m, 300-700m, 700-2000m) using CMIP5 models to look for a climate change signal in the observed estimate of Levitus et al. [2012], during 1955-2012. They conduct multiple Regularized Optimal Fingerprinting (ROF, Ribes and Terray [2013]) analyses to estimate the influence of individual forcings (especially separating GHGs from other anthropogenic forcings). Their results indicate that the observed warming is detected and attributed to the full anthropogenic contribution as well as the GHG forcing alone, and point to no detection of the signal in response to natural forcings alone.

Bilbao et al. [2019] also look at temperature anomalies in the upper 2000m, in an ensemble of CMIP5

models and in 4 different observational datasets, for the period 1960-2005, and conduct a standard optimal fingerprinting analysis (two signal and three-signal analyses), considering variations in both vertical layers and time in their fingerprints. Their results strengthen the anthropogenic origin of the ocean warming in the upper ocean, that cannot be explained by natural external forcings or internal variability alone. They also provide information on individual forcings, with a detected signal for the natural forcings, GHGs and other anthropogenic forcings, due to their accounting of the spatial-temporal structure of the response. They found that the D&A analysis gave more positive results when the fingerprints were refined to take into account both the vertical and regional structure rather than global means.

Two studies provided a dynamical constraint on their D&A analysis, by considering temperature changes in an isotherm layer rather than within a fixed depth layer, thus removing isotherm displacement which they argue lowers the influence of ocean circulation changes and dynamically-driven variability. Comparing the temperature either vertically-averaged in the upper 220m or vertically-averaged above the 14ºC isotherm, in the EN3 observed estimate [Ingleby and Huddleston, 2007] and HadCM3 model, with a fingerprint defined spatio-temporally over 5 sub-basins, Palmer et al. [2009] detected both the anthropogenic and natural forcings influence in the temperature above the 14ºC layer, but neither of them were detected in the fixed-depth layer. Weller et al. [2016] extended this analysis by applying it in the more recent EN4 dataset [Good et al., 2013] compared to a CMIP5 ensemble of models and over a longer period. They detect the influence of anthropogenic and natural forcings in both indicators of upper-ocean temperature, but robust detection of the anthropogenic forcings is found only for the isotherm-following indicator.

Two recent studies focused more specifically on detecting climate change signals in the Southern Ocean, historically the most poorly sampled region. Swart et al. [2018] used the CanESM2 large ensemble and all available hydrographic profiles between 1950-1980 and 2006-2015 to investigate the warming in zonal-mean upper 2000m between 30ºS and 60ºS, as a function of depth and latitude. They show that the observed changes are inconsistent with internal variability alone or natural forcings, and attribute them primarily to the anthropogenic GHG forcing and secondarily to stratospheric ozone depletion, consistent with the current comprehension of forced changes in the Southern Ocean. Hobbs et al. [2021] extended this work by considering an ensemble of CMIP5 models selected based on their accurate representation of Southern Ocean water-masses, instead of a single model, and by including the deeper ocean (0-5000m) and all latitudes south of 30ºS (including >60ºS) in their D&A analysis. They confirm the evidence of an anthropogenically-forced observed warming in the Southern Ocean, strongest in the Subantarctic Mode Water (SAMW) and AAIW layers but also detected in the denser waters (CDW and AABW) for the first time (although interpretation should be made carefully as the processes associated with AABW formation are not well represented in CMIP5 models [Heuzé et al., 2013]). They find that the attribution of some of the observed temperature change to non-GHG anthropogenic forcings such as stratospheric ozone depletion and aerosols is model-dependent and so less robust than the GHG-forced response. These non-GHG forcings are found to have possibly mitigated the GHG-induced warming, which alone is greater than the total observed change (with possibly a warming induced by ozone depletion offset by a cooling induced by aerosols).

Overall, we see that in the past couple decades, a number of studies using a variety of methods, models and observational datasets have given hard evidence pointing to a warming signal that has been distinctly detected from natural internal variability since the mid-20th century in observations of ocean temperature and heat content, and consistently attributed to anthropogenic forcings, with a predominant role of GHGs. We note that the influence of natural forcings (primarily volcanic eruptions) on upper ocean temperature has been detected in the observations only when the temporal resolution adopted was high enough (i.e. yearly or 2-year averages) [Palmer et al., 2009, Weller et al., 2016, Bilbao et al., 2019].

The AR6 concludes "it is extremely likely that human influence was the main driver of the OHC increase observed since the 1970s, which extends into the deeper ocean *(very high confidence)*".

Besides the generalized warming, the observed subpolar North Atlantic "warming hole" was found to be of anthropogenic origin and to have recently emerged from internal variability, in a pattern-based study by Chemke et al. [2020].

3.2.2 Salinity

A number of studies mentioned above [Pierce et al., 2012, Swart et al., 2018, Hobbs et al., 2021] also considered salinity in addition to multi-decadal temperature changes, in their respective regions and datasets, and found that they were also inconsistent with internal variability alone and of anthropogenic origin. Furthermore, Pierce et al. [2012] showed that conducting the D&A analysis on joint temperature and salinity changes yielded stronger human-induced signals than temperature or salinity alone. Based on global means on individual levels, they detected human-induced salinity changes in the top 125m of the ocean (compared to 300m for temperature, and 250m for joint the joint temperature-salinity analysis).

The first formal D&A analysis on multi-decadal salinity changes was conducted by Stott et al. [2008] who focused on the vertically-averaged top 500m of the Atlantic basin per 10º latitudinal band, using the observed estimate of Boyer et al. [2005] and Smith and Murphy [2007] and the HadCM3 model. They show a persistent increase in salinity in the 20ºN-50ºN band, inconsistent with internal variability. Their fingerprint of spatially-varying trends is detected in the observations and attributed to human forcings for the period 1967-2006, but it isn't for 1957-1996, displaying the progressive emergence of the anthropogenic signal in the observations.

Another regional D&A study was led by Terray et al. [2012], who analysed near-surface salinity data in the tropical Atlantic and Pacific oceans in a compilation of multi-decadal observed SSS datasets compared to an ensemble of CMIP3 models. They aim to investigate whether the observed Pacific freshening, Atlantic salinification and increasing inter-basin contrast are consistent with internal variability or attributable to external forcings. They find that human influence on the mean Pacific freshening is detected (i.e. inconsistent with internal variability) using two different detection methods (the temporal approach indicating a detection starting in the late 1990s), as well as on the strengthening inter-basin contrast but with one method only, while the mean Atlantic SSS change remains within the range of internal variability. With a more regional approach, they find a robust human influence on the freshening of the whole Pacific fresh pool, and on the salinification of the subtropical North Atlantic alone.

Using their new objective analysis of multi-decadal 0-2000m ocean salinity, Cheng et al. [2020] investigate the evolution of the observed surface and subsurface salinity contrast (the difference in salinity between salty and fresh regions) compared to that of an ensemble of CMIP5 models. They find that the salinity contrast between 1960-2017 has clearly emerged from natural variability, i.e. the mean salinity pattern has amplified, with less contamination of interannual variability when integrated over the top 2000m than when just estimated at the surface.

Finally, the AR6 assesses the following: "at the global scale it is *extremely likely* that human influence has contributed to observed surface and subsurface salinity changes since the mid-20th century (strengthened from the *very likely* AR5 assessment)". They add: "All available multi-decadal assessments have confirmed that the associated pattern of change corresponds to fresh regions becoming fresher and salty regions becoming saltier *(high confidence)*. CMIP5 and CMIP6 models are only able to reproduce these patterns in simulations that include greenhouse gas increases *(medium confidence)*. Changes to the coincident atmospheric water cycle and ocean-atmosphere fluxes (evaporation and precipitation) are the primary drivers of the basin-scale observed salinity changes *(high confidence)*".

Looking for anthropogenic climate change in the ocean in the past two decades has provided additional evidence of human influence on the climate system. Considering multiple variables such as temperature and salinity when detecting and attributing observed change to human influence strengthens the overall assessment, reduces uncertainties and provides information on the many ways human activities have

already perturbed the climate system.

3.3 Looking for remaining undetected change in the ocean interior

While the D&A studies reviewed here have brought robust evidence of an anthropogenic signature in upper ocean temperature and salinity changes, they have also revealed that such changes were detected only in the top hundred meters of the ocean at basin or global scale, or when vertically-averaging throughout multiple layers. No change has been detected, for instance, on a single depth layer lower than 300m. We can think of several reasons why. First, current temperature and salinity changes are much weaker at depth compared to the upper ocean, it is possible that they haven't emerged from natural variability yet (although natural variability is also much lower there, meaning the signal-to-noise ratio is potentially still low). Second, observations before the Argo period remain sparse below the first hundred meters of the ocean, uneven sampling can thus bias the total signal. Third, detecting an observed change on single vertical levels or at more regional scales relies on models to have a correct representation of water-masses and ocean circulation regionally or locally. This is not often the case (e.g. Sallée et al. [2013], Heuzé et al. [2013], Heuzé [2017]), making such diagnostics at finer geographical scales difficult. The temperature and salinity evolution in many regions of the ocean thus remains undetected. We can wonder when and if, in the model world, they will emerge from internal variability of the climate system.

In the past decades, several studies have used global climate models to diagnose the Time of Emergence (ToE) of the climate signal of different variables from internal variability noise, to search for the time when a climate change signal becomes permanently greater than a noise (or the evolution of the signal-to-noise ratio). Remaining in the model world allows such analyses to be led at global, regional and local scales. Past studies have focused mainly on unraveling ToE for surface air temperature using different methods and ensembles of models [Diffenbaugh and Scherer, 2011, Mahlstein et al., 2011, Deser et al., 2012, Hawkins and Sutton, 2012, Mora et al., 2013, Lyu et al., 2014, Diffenbaugh and Charland, 2016, Lehner et al., 2017], revealing that although high latitudes are warming faster, earlier emergence is found in the tropics because of the low noise level (i.e. weak internal variability). ToE has also been investigated for precipitations [Giorgi and Bi, 2009, Deser et al., 2012, Mahlstein et al., 2012, Mora et al., 2013], sea level rise [Lyu et al., 2014] and marine carbon cycle and marine ecosystem stressors [Keller et al., 2014, Rodgers et al., 2015, Frölicher et al., 2016, Henson et al., 2017, Schlunegger et al., 2019]. The underlying important implications of looking for emerging signals at local scale is whether or not a signal becomes perceptible enough for a local observer (endemic species, crops, a fish, my grandmother) to be aware of it, meaning are they already adapted to large interannual to decadal changes. This will depend on their own individual vulnerability to ranges of different environmental variables characterising their habitat, and their capacity to adapt to large and rapid changes. It also raises the question of which noise to take into account (i.e. which envelope of variability), which can differ greatly when considering different time scales (interannual, monthly, daily, hourly, etc...).

Emerging signals in temperature and salinity in the ocean interior have not been investigated yet in the framework of ToE analyses. An early coupled model study has examined in which ocean variables and where the earliest anthropogenic signal could be found, and concluded that subsurface temperature and salinity were the best candidates, both on pressure and density levels, giving indications on which ocean observations to focus on when wanting to detect change on a 30-year period [Banks and Wood, 2002]. They have also found that the signal to noise ratios of ocean temperature and salinity were spatially-dependent, indicating that emergence of the anthropogenic signal is not uniform. Using repeated hydrographic sections in the Indian sector of the Southern Ocean, Banks et al. [2000] showed that the observed multi-decadal cooling and freshening of SAMW and AAIW on density levels between the 1960s and the 1980s-1990s [Bindoff and Mcdougall, 2000] was reproduced in a coupled model including anthropogenic forcings, and that the observed and simulated trends could not be explained by the simulated internal variability alone. They also found that compared to Northern Hemisphere Mode Waters, SAMW was a particularly good indicator of anthropogenic climate change with higher signal to noise ratios and

earlier detection of trends, confirming that signal to noise ratios are not spatially uniform. They suggested this was because SAMW has much weaker decadal variability than its Northern Hemisphere counterparts, because it is formed in large volumes with homogeneous density, thus averaging along density surfaces allows a clearer detection of climate change signals, and because their changes give an integrated view of surface forcings. In idealized experiments using the same coupled model, the surface forcings causing this cooling and freshening were found to be predominantly the increased surface warming for SAMW, with an important role of surface freshening (increased precipitation) for AAIW [Banks et al., 2002]. More generally, the subsurface cooling and freshening along isopycnals at midlatitudes, and warming and salinification at lower and higher latitudes, was found to be a fingerprint of anthropogenic change in the Indo-Pacific basin in the same coupled model, and caused by an overall surface warming [Banks and Bindoff, 2003].

One aim of this thesis will be to extend this earlier work with ensembles of more recent climate models (multi-model ensembles and single-model initial condition large ensembles) to robustly identify regions and timings of anthropogenic emergence of ocean subsurface temperature and salinity change. We will try to understand why changes in some regions such as the formation and export of SAMW and AAIW can be detected earlier, and re-examine the drivers of change and their timing. Particular interest will also go towards the deeper parts of the ocean, where there are few observations of multi-decadal temperature and salinity changes. We will explore whether climate models show detectable changes in the deep and abyssal ocean, how they compare to signals of the upper ocean, to what forcings they respond and on which time scales, and what are the mechanisms driving these changes.

4 What physical mechanisms are causing thermohaline changes in the ocean?

While diagnosing robust, human-induced multi-decadal thermohaline changes is an important question, understanding how these changes take place in the ocean, i.e. what the physical processes involved in driving these long-term changes are, is crucial to our comprehension of the ocean response to climate change.

The ocean is forced at its surface and lateral boundaries by exchanges with the atmosphere, sea-ice and land in the form of heat fluxes (shortwave and longwave radiation and turbulent fluxes), freshwater fluxes (evaporation, precipitation, river runoffs and ice melt from sea-ice, icebergs and land ice) and momentum (wind stress). Heat fluxes directly affect (and depend partly on) SST while freshwater fluxes directly affect SSS. SST and SSS anomalies are mixed within the mixed layer and subducted in the ocean interior by the circulation at different spatial and time scales, which constitutes the process of water-mass formation. Heat and freshwater fluxes, by affecting ocean temperature and salinity, also drive variations in density and thus on the thermohaline circulation, which can affect how heat and salt are transported within the ocean interior. Similarly, winds drive part of the ocean circulation thus temperature and salinity variability as well.

In this section, I will first give an overview of what we know about recent and projected changes in these drivers of temperature and salinity variability, namely surface fluxes and the large-scale ocean circulation. We will see that, in fact, we know much less about the changes in these drivers than in the changes in ocean temperature and salinity characteristics, due partly to lack of historical observational data, and poor model representation and agreement. Furthermore, it is difficult to relate past or future thermohaline changes directly to changes in these drivers from observations or model outputs as the processes interact with each other and the resulting changes are blended together. Thus, several frameworks have been developed to propose a decomposition of these physical mechanisms driving temperature and salinity changes in the ocean, and to diagnose them separately. In the second and third part of this section, I present the results from the application of two main frameworks of decomposition (passive heat uptake

vs. circulation changes, and individual flux forcings), that rely mostly on model studies that I will use in this thesis.

4.1 Changes in the drivers of temperature and salinity variability

We have seen that changes in temperature and salinity in the ocean can be caused by changes in surface fluxes and in the ocean circulation. What do we actually know in the observations and projections, about the evolution of these drivers of thermohaline changes?

4.1.1 Surface fluxes

Surface fluxes are harder to observe directly than ocean surface variables and their potential reported changes come with more uncertainty [Cronin et al., 2019, Yu et al., 2020]. Since there are very little observations of long-term air-sea fluxes, the AR6 [Fox-Kemper et al., 2021] assessed that direct observed trends in heat fluxes, freshwater fluxes and wind stress have not emerged and are overwhelmed by spatial and temporal internal variability. Changes in large-scale heat and freshwater fluxes are more reliably inferred from changes in OHC and salinity, which is another reason why continuous observations of the ocean are so crucial. Here we try to give a rapid overview of the few indications that we do have concerning the changes in surface fluxes.

In global climate models, trends in heat fluxes are much weaker than observed for the multi-model mean, suggesting low model agreement, although some regional patterns are reproduced such as the heat uptake increase in the Southern Ocean and North Atlantic, which amplify and become more robust in terms of model agreement by the end of the 21st century [Fox-Kemper et al., 2021]. Overall, we now have a clear picture of globally-integrated ocean heat uptake from in-situ temperature measurements (as described in section 2.1), as well as rather well constrained future increase. However, the regional patterns of ocean heat uptake are less well understood and depend on ocean circulation and its changes.

Evaporation and Precipitation constitute the main fluxes of water seen by the ocean. In a warmer climate, E-P is expected to amplify [Held and Soden, 2006]. Theoretically, saturation water vapor pressure increases at a rate of 7%/ºC following the Clausius-Clapeyron relation under constant relative humidity (this means a warmer atmosphere can hold more water). This rate has been verified in observations of atmospheric moisture content (i.e. precipitable water; Trenberth et al. [2005], Chung et al. [2014]). Under a number of assumptions, including an unchanged large-scale atmospheric circulation, it is expected that E-P amplifies at a similar rate as atmospheric moisture content, meaning that E-P spatial patterns remain the same but the contrast between dry and wet regions increases as temperature increases [Yu et al., 2020]. However, modeled amplification in the hydrological cycle shows a rate closer to about 2%/ºC (e.g. Allen and Ingram [2002]). Direct observations of E-P over the last 30 years show an effective upward trend, with E increasing at 9±3%/ºC and P increasing at 2±3%/ºC, however these trends are very uncertain and inconsistent with reanalysis products [Yu et al., 2020]. The AR6 gives "*low confidence* in direct estimates of trends in surface freshwater fluxes". Some coherent regional patterns are still present within several products, with an intensification of the intertropical convergence zone (ITCZ) as well as increased rainfall in the Southern Hemisphere high latitudes, and intensified subtropical dry zones in the South Pacific and Atlantic, as expected from the "dry gets drier, wet gets wetter" paradigm [Yu et al., 2020]. In CMIP6 models, 21st century trends still show large areas of low model agreement, although some regional patterns become more robust, such as a wetter equatorial Pacific and high latitudes, and drier Atlantic and southern subtropical Pacific and Indian oceans [Fox-Kemper et al., 2021].

Available wind speed estimates over the ocean show large disagreements in trends of the past decades, but a convergence is found over the Southern Ocean with a strengthening of the wind speed, the largest trend observed globally, alongside smaller positive trends in the western North Atlantic and tropical eastern Pacific since the 1980s [Gulev et al., 2021].

The principal mode of variability in the Southern Hemisphere atmospheric circulation is the Southern Annular Mode (SAM), defined as the difference in zonal-mean pressure between the mid and high latitudes, reflecting the strength and position of the westerly winds. Variations in the SAM are thus important for the meridional overturning ocean circulation in the Southern Ocean. A trend towards the positive phase of the SAM (i.e. stronger westerly winds) has been observed throughout the second half of the 20th century, along with direct measurements of intensified and poleward-displacing zonal winds during the satellite-observing era, and linked to stratospheric ozone depletion (e.g. Thompson and Solomon [2002], Marshall [2003], Thompson et al. [2011], Abram et al. [2014], Jones et al. [2016b]). Increased concentrations of atmospheric greenhouse gases have the same fingerprint of change for the SAM index and associated atmospheric circulation: the recent evolution of the SAM is thus driven by the balance between decreased ozone-depleting gases and increased greenhouse gases, both of which are of anthropogenic origin [Banerjee et al., 2020]. In the future, the increase in SAM is projected to continue in response to GHG forcings [Bracegirdle et al., 2013, 2020].

Concerning overall regional trends in surface winds, the AR6 assesses that "there is only *low confidence* in observed and projected wind stress trends in most regions because trends in oceanic wind stresses during the satellite era have not emerged or are inconsistent with historical simulated changes."

4.1.2 Large-scale ocean circulation

The oceanic circulation constitutes a complex interplay of processes, of different time and space scales. A schematic of the "global conveyor belt" revisited by Marshall and Speer [2012] is presented in figure 0.11. Important large-scale features include the Meridional Overturning Circulation (MOC), a construction to look at the circulation in a depth-latitude frame. Its Atlantic wing (the AMOC) brings heat northward along its upper branch and is associated, in the dominant and simplistic paradigm, with the formation of NADW in the subpolar areas that return south along the lower branch [Lozier, 2010]. In the Southern Ocean, there are two overturning cells, associated with the upwelling of CDW, which on the northern side are exported north of the ACC and subducted as SAMW and AAIW, and on the southern side feed the lower branch with deep convection and export of AABW [Speer et al., 2000]. The global MOC thus connects deep and shallow layers as well as the opposite subpolar regions. How these circulation systems change can affect the ventilation of the ocean and its physical characteristics in the deepest regions. Large-scale horizontal (or barotropic) features are also important for the global circulation, with the predominance of the ACC which flows around the Antarctic continent with no continental barriers, and the wind-driven subtropical gyres in every basin.

Direct measurements of the AMOC strength and variations at 26ºN by the RAPID array since 2004 have shown a slowdown in overturning in the first years of observations, associated with a well-documented long-term subpolar SST cooling [Smeed et al., 2014, 2018]. However, this short period of observations doesn't provide enough evidence to know whether this weakening is the subject of a long-term trend or part of the strong decadal variability characterising the North Atlantic. Caesar et al. [2018] propose a fingerprint of the AMOC constructed from North Atlantic subpolar SST to reconstruct the AMOC evolution since the pre-industrial era, and show that according to this AMOC index, there has been a slowdown since the mid-twentieth century (i.e. a subpolar gyre cooling in SST, due to reduced northward heat transport and northward shift of the Gulf Stream). Combining proxy data and paleo reconstructions, Caesar et al. [2021] suggest the overturning is currently at its minimum in the last millenium. However, due to the limited observational evidence and the disagreement between observations and models on North Atlantic mechanisms and drivers, the AR6 assesses this AMOC weakening with *low confidence*. More years of direct observations will be needed to assess the evolution of the AMOC with more certainty.

Future projections of AMOC evolution in climate models reveal a *very likely* weakening over the 21st century as assessed in the SROCC and in AR6, in all emissions scenarios. However, large uncertainties lie in the timing and magnitude of this decline, which results in "*low confidence* in quantitative projections

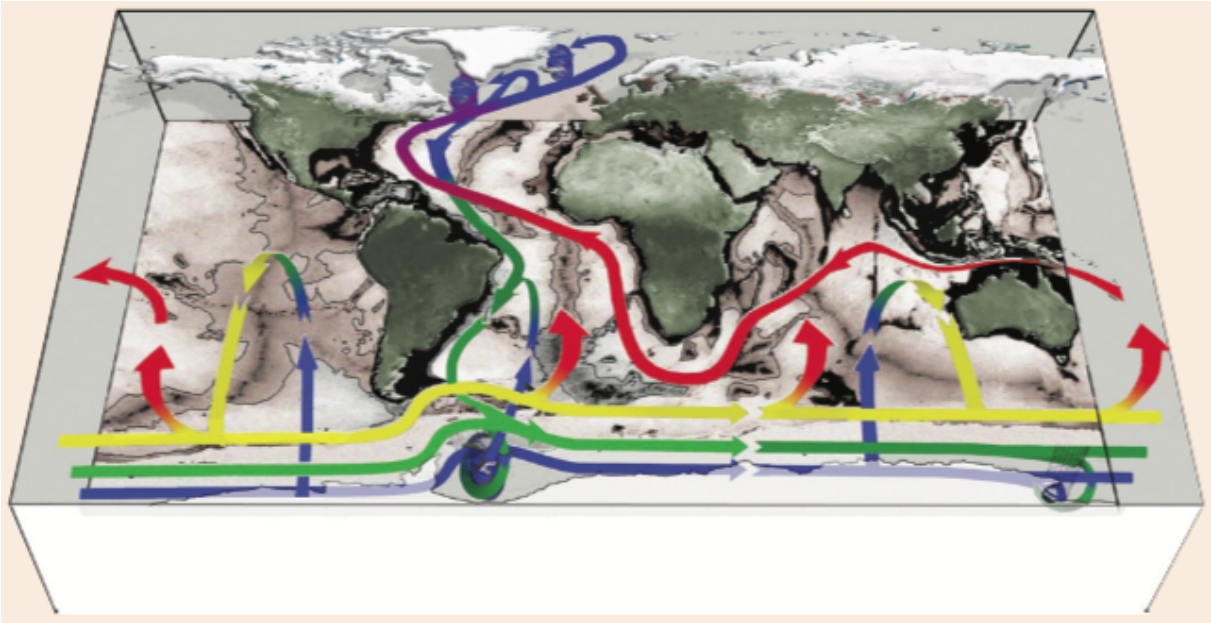

Figure 0.11: Schematic of the updated global "conveyor" by Marshall and Speer [2012]. Cooler colours indicate denser water masses, ranging from warmer mode and thermocline waters in red to bottom waters in blue.

of AMOC decline in the 21st century, despite the *high confidence* in the future decline as a qualitative feature based on process understanding" [Fox-Kemper et al., 2021].

NADW forms either by deep convection (upper NADW) or deep overflows (lower NADW) in the subpolar Atlantic. Observed evidence of very large climate variability in this region gave the following assessment in AR5 "it is *very likely* that the temperature, salinity, and formation rate of the Upper NADW is dominated by strong decadal variability related to the North Atlantic Oscillation (NAO)" and AR6 assessed "it is *likely* that any observed changes in temperature, salinity, and formation rate of the Lower NADW are dominated by decadal variability". The long-term cooling previously reported in lower NADW [Rhein et al., 2013] is then to be taken carefully considering this strong decadal variability.

Intensifying westerly winds in the Southern Ocean raise many questions concerning potential circulation shifts in this region, since winds are an important driver of the Southern Ocean circulation [Rintoul, 2018]. The ACC's mean position has been shown to be only weakly sensitive to intensifying westerly winds [Bindoff et al., 2019, Fox-Kemper et al., 2021]. The upper cell however is expected to be reinforced in response to intensifying winds, but the SROCC assessed there is only *low confidence* in an observed long-term increase in its transport, and climate models only project a moderate increase. Mirroring the upper cell's potential increase, a slowdown in the lower overturning cell is expected and is consistent with the observed decrease in AABW volume [Bindoff et al., 2019, Fox-Kemper et al., 2021]. Indeed, the export of AABW down from the Antarctic continental slope and northward constitutes the lower limb of the deep overturning cell and there is observational evidence that AABW volume has decreased in recent decades, possibly due to a slowdown in formation rate and/or freshening and warming of AABW (i.e. a renewal with lighter deep waters) [Purkey and Johnson, 2012, Azaneu et al., 2013]. The AR6 assessed the slowdown in AABW circulation since the 1990s with *medium confidence*, although they also assessed with *medium confidence* the existence of short periods of lower-cell increases [Fox-Kemper et al., 2021]. The formation and export of AABW will continue to decrease in the future due to warming and freshening of surface waters in the subpolar Southern Ocean, which has been assessed with *medium confidence* in the AR6 [Fox-Kemper et al., 2021]. The projected decrease in the lower cell in climate models might be enhanced by increasing iceshelf basal melt [Bindoff et al., 2019].

Overall, the recent changes in AMOC and Southern Ocean circulation rely on a too-short observational record to determine whether the anthropogenic response has overcome internal variability or natural forcings [Eyring et al., 2021].

There is observational evidence from satellite altimetry of an intensification, expansion and poleward shift of the subtropical gyres alongside with Western Boundary Currents since 1993, with the exception of the Gulf Stream and the Kuroshio [Fox-Kemper et al., 2021]. Future projections indicate a continued intensification and poleward extension of all subtropical gyres, along with an intensification of the East Australian and Agulhas Current Extension and weakening of the Gulf Stream and Indonesian Throughflow coherent with projected trends in winds [Fox-Kemper et al., 2021].

4.2 The role of passive transport of added heat vs. redistribution by the changing circulation in ocean heat storage

The uptake of extra heat in the climate system by the ocean can be viewed as a passive process, transmitted from the atmosphere to the ocean surface and transported in the ocean interior passively by a range of processes (advection, diffusion, mixing), i.e. acting like a passive tracer which does not affect ocean density. However, when ocean transport is perturbed, it can spatially redistribute pre-existing heat which also ends up affecting OHC change locally (although this redistributive OHC change is equal to zero when globally-averaged since it doesn't encompass the additional heat that enters the ocean).

Untangling the relative roles played by the passive and redistributive components of ocean heat storage has predominantly been investigated by modelling studies, either by introducing passive heat tracers [Banks and Gregory, 2006, Xie and Vallis, 2012, Marshall et al., 2015, Armour et al., 2016, Gregory et al., 2016, Garuba and Klinger, 2016, 2018, Todd et al., 2020, Dias et al., 2020, Couldrey et al., 2021], by comparing experiments in which currents are fixed to climatological values to experiments where currents evolve freely [Winton et al., 2013, Bronselaer and Zanna, 2020], by integrating tracer budgets [Williams et al., 2021] or decomposing heat divergence into a mean-circulation effect and a changing circulation effect [Hu et al., 2020] or by using a representation of climatological transport processes to trace passive ocean heat storage from SST anomalies [Zanna et al., 2019b, Newsom et al., 2020]. These studies have used coupled or ocean-only models generally forced by idealized scenarios of increased radiative forcing (such as 1pctCO2/year, abrupt 4xCO2 and others).

The questions they aimed to answer was: can heat be considered as a passive tracer when it is being uptaken by the ocean in a warming climate? Put another way, what role does the changing circulation play in shaping ocean heat content change patterns? How do these two processes respond regionally?

In figure 0.12 we show a ventilation tracer (a), the passive heat tracer anomaly (b) and the temperature anomaly (c) from Marshall et al. [2015] and in figure 0.13, the temperature anomaly in a fixed currents (left) and freely-evolving currents (right) simulation from Winton et al. [2013]. The patterns of passive (or "excess"/"added") warming, modelled by a passive tracer (e.g. figure 0.12b) or by fixed-current experiments (e.g. figure 0.13 left), resemble closely those of a ventilation tracer (e.g. figure 0.12a). That is, the amplitude of the patterns reflects that of the forcing modulated by the ventilation time scales of the ocean (years to decades in the well-ventilated gyres, to centuries in the deeper ocean). Temperature anomaly was found to act like a passive tracer (i.e. to follow these patterns) mostly in regions where the oceanic circulation is primarily forced by winds like the subtropical gyres and where it is not too dependent on temperature. In the Southern Ocean in particular (in and north of the ACC), heat uptake was thus found to be largely passive [Marshall et al., 2015, Gregory et al., 2016, Garuba and Klinger, 2016, Armour et al., 2016, Liu et al., 2018, Zanna et al., 2019b, Newsom et al., 2020, Bronselaer and Zanna, 2020, Couldrey et al., 2021]. In this region, anomalous heat is largely taken up at $\sim$60ºS at the southern flank of the ACC, is transported northward by the background MOC, where it vertically accumulates at $\sim$45ºS [Marshall et al., 2015, Frölicher et al., 2015, Gregory et al., 2016, Armour et al., 2016, Liu et al., 2018, Dias et al., 2020, Couldrey et al., 2021]. This was found to be a feature of the ocean's response to GHG forcing

independently of geographic variations in the radiative forcing or changes in wind and freshwater fluxes, shown in ocean-only studies where the radiative forcing imposed was constant and uniform with only a damping term allowed [Armour et al., 2016, Marshall et al., 2015]. These two studies also concluded that delayed warming in the subpolar Southern Ocean was fundamentally controlled by the background ocean circulation (circumpolar upwelling of old water originating in the North Atlantic that haven't seen climate signals yet and surface northward transport) rather than processes within the atmosphere. This control applies on time scales of decades to centuries, which means warming of these subpolar surface waters is probably set by the time it takes for deep ocean waters to be warmed themselves [Marshall et al., 2015, Armour et al., 2016].

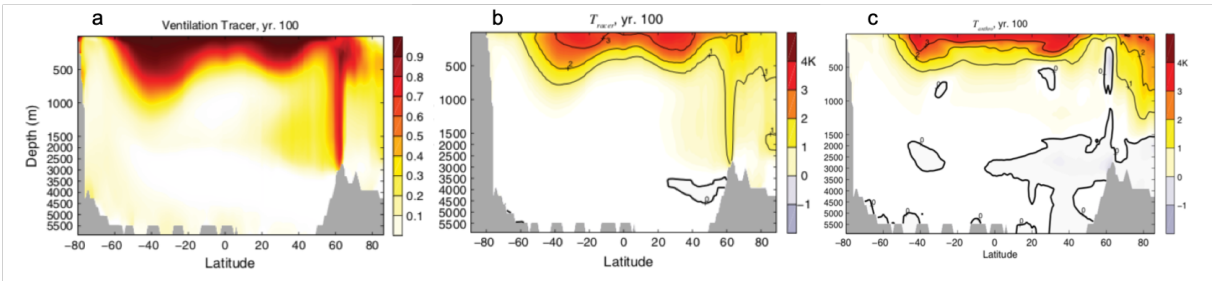

Figure 0.12: From Marshall et al. [2015]. Zonal mean (a) Idealized ventilation tracer whose value at the surface is set to unity (b) Passive temperature tracer anomaly (c) Temperature anomaly, after 100 years of a simulation forced with homogeneous radiative forcing and a constant climate feedback parameter.

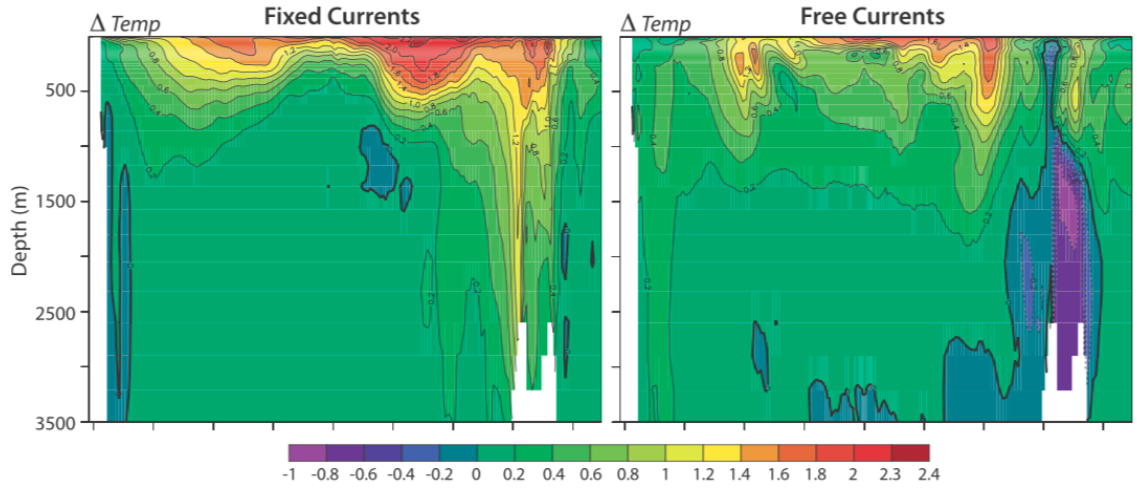

Figure 0.13: From Winton et al. [2013]. Zonal mean temperature anomaly in years 81-100 of a 1pctCO2 simulation with fixed currents (left, corresponding to passive heat) and freely-evolving currents (right, standard simulation).

However, redistribution of background temperature by the changing circulation and other transport processes plays an important role in setting the regional patterns of heat storage on decadal to multi-decadal time scales [Banks and Gregory, 2006, Xie and Vallis, 2012, Winton et al., 2013, Marshall et al., 2015, Garuba and Klinger, 2016, 2018, Zanna et al., 2019b, Bronselaer and Zanna, 2020, Dias et al., 2020, Williams et al., 2021, Zika et al., 2021]. Consequently, excess heat entering the ocean passively cannot be used as a sole indicator of heat uptake patterns. The North Atlantic is a good example of a region where excess and redistributed heat both play an important and opposing role on total ocean warming. There, in response to the positive surface heat flux, large amounts of added heat accumulate deep in the subsurface (due to the intense vertical mixing characterising this region), in addition to which the region sees a strong redistributive cooling brought by a weakened AMOC resulting in less northward

heat transport (see figures 0.12 and 0.13) [Xie and Vallis, 2012, Winton et al., 2013, Marshall et al., 2015, Gregory et al., 2016, Garuba and Klinger, 2016, 2018, Bronselaer and Zanna, 2020, Todd et al., 2020, Dias et al., 2020, Williams et al., 2021, Couldrey et al., 2021]. The AR6 assesses with "*high confidence* that projected weakening of the AMOC will cause a decrease in northward OHT in the northern hemisphere mid-latitudes" [Fox-Kemper et al., 2021].

At low latitudes, the anomalous surface heat uptake is small but there is positive heat storage, explained by a redistributive warming brought by anomalous equatorward heat transport (AMOC weakening in the Northern Hemisphere and enhanced upper cell in the Southern Ocean, along with a reduced upwelling of cold waters at low latitudes), enhanced by an anomalous uptake of heat at high latitudes stored at lower latitudes [Xie and Vallis, 2012, Winton et al., 2013, Gregory et al., 2016, Garuba and Klinger, 2018, Hu et al., 2020, Bronselaer and Zanna, 2020, Dias et al., 2020, Couldrey et al., 2021].

A few studies found that redistribution allowed heat to penetrate deeper in the ocean than passive warming alone [Banks and Gregory, 2006, Xie and Vallis, 2012, Garuba and Klinger, 2016]. However, Armour et al. [2016] found that this was not the case in the Southern Ocean in an ocean-only experiment forced with a uniform radiative forcing, because of upper ocean stratification acting to reduce mode water formation, thus constraining heat in the surface layers, a result also found more generally by Marshall et al. [2015] in a similar experiment (figure 0.12).

Bronselaer and Zanna [2020] used a series of fixed and free-current numerical experiments (similar to Winton et al. [2013], see figure 0.13) to derive a constant relation between passive heat (difficult to diagnose from observations or historical model simulations) and anthropogenic carbon (which is possible to retrace). This relation allowed them to reconstruct the passive component of heat storage in observations and CMIP5 historical experiments and scenarios, from the diagnosed anthropogenic carbon in these datasets. They found that over the historical period, redistribution has a dominant effect on heat storage patterns, but that over the 21st century, excess heat is projected to become increasingly important in shaping ocean warming patterns since the warming signal will be increasingly important under increasing GHG emissions.

When excess heat is taken up at the surface, it is transported in the ocean by the background circulation (passive heat) as well as by the perturbed circulation (non-linear term). By comparing their passive heat tracer in a control and warming experiment, Gregory et al. [2016] found that this non-linear term was of second order for total added heat, confirmed by another study by Hu et al. [2020] when examining the decomposition for ocean heat divergence. However, Couldrey et al. [2021], using the same methodology as Gregory et al. [2016] and investigating more closely this term, found that it could be locally important, particularly in the Arctic.

Studies that jointly investigated the role of the changing circulation on heat and carbon storage, found that the effect of redistribution was much more important for heat than for carbon [Winton et al., 2013, Bronselaer and Zanna, 2020, Williams et al., 2021]. Indeed, changes in the circulation redistribute pre-existing gradients in the variable considered, which are far greater for heat than for carbon compared to their individual change.

In modelling studies that use coupled climate models or ocean models forced in a way that allows a feedback of the SST on air-sea fluxes (instead of fixed fluxes), SST anomalies arising from redistributed heat can feedback on the surface heat flux, modulating the amount of heat being uptaken at the surface and thus on global ocean heat storage. By implementing passive tracers that take specifically this effect into account in an ocean-only model forced with restoring boundary conditions, Garuba and Klinger [2016] find that this redistribution feedback increases heat uptake globally by about 25%, while Garuba and Klinger [2018] find it amounts to 13% in slightly different experiments where all surface fluxes are perturbed (see next section). In the Flux-Anomaly-Forced Model Intercomparison Project (FAFMIP) protocol [Gregory et al., 2016], the SST coupled to the atmosphere to compute the heat flux is the SST

impacted by redistribution only, so that ocean warming by added heat does not feedback on the heat flux to dampen it [Bouttes and Gregory, 2014]. This means redistribution can feedback on the air-sea anomalous heat flux. Dias et al. [2020] estimate this effect in FAFMIP simulations to account for 33% of global ocean heat storage in an ocean model forced with bulk formulas. On the other hand, Couldrey et al. [2021] find that the feedback is responsible for 10% more heat content change than the heat flux perturbation should yield in an ensemble of coupled models. This additional heat input into the ocean is explained by a weakening AMOC cooling the subpolar North Atlantic by decreasing northward heat transport. This cooling feedbacks on the heat flux, causing more positive heat uptake in this region, which further weakens the AMOC. This process thus creates a positive retroaction in the North Atlantic.

These processes can occur at different time scales. On decadal time scales, ocean circulation variability can be strong thus influencing redistribution patterns. One example is the decadal variability of ocean heat storage in the Southern Ocean. Ocean heat uptake and ocean heat content have been documented as important in the Southern Ocean compared to other regions of the ocean (e.g. Roemmich et al. [2015], Frölicher et al. [2015]). However, recent work suggests this particularly high heat storage has been partly reinforced by decadal variations but has not been as important compared to the Northern Hemisphere in the most recent years because of a different phase of these decadal variations [Rathore et al., 2020, Wang et al., 2021].

One recent study proposed a new framework based on water-mass transformation to diagnose passive and redistributive warming from observations only [Zika et al., 2021]. By considering the change in the temperature-salinity volumetric distribution between two periods, they could infer and isolate the added heat necessary to warm each water-mass (since in volumetric temperature-salinity space, pure spatial redistribution of heat is not represented), and convert it back to vertically-integrated OHC change geographically. They found that over the period 2006-2017 (the Argo-sampled period), there was a clear widespread and spatially coherent added warming, but that the magnitude of redistribution patterns were much larger on the time scales considered and explained much of the total OHC change patterns. This reinforces the role of redistribution on decadal time scales because of internal variability, and the potential for larger magnitudes of added heat patterns with increasing global warming.

In assessing the ability of climate models to correctly reproduce these relative patterns of change, the AR6 concluded: "climate models have more skill in representing OHC change from added heat than from ocean circulation change *(high confidence)*. Since added heat dominates over redistributed heat on a centennial scale (especially under high emissions scenarios) confidence in future modelled OHC patterns at the end of the 21st century is greater than at decadal scale" [Fox-Kemper et al., 2021].

None of these studies, except Zanna et al. [2019b] and Bronselaer and Zanna [2020] to some degree, explored the relative time scales of the passive and redistributive mechanisms under realistic long-term radiative forcing such as happened since the pre-industrial era, nor their emergence from internal variability noise. There is also a lack of investigation of the passive and redistributive component of salinity change. The idea is the same than with heat, except the added component takes the form of an increasing contrast in salinity, with both positive and negative anomalies (saltier/fresher regions) depending on the sign of the change in Precipitation-Evaporation+Runoffs regionally, in response to the hydrological cycle amplification. The AR6 assesses “there is *high confidence* that, at annual to decadal timescales, regional salinity changes are driven by ocean circulation change superimposed on longer term trends”. More work is needed to investigate the regional patterns of salinity change and their attribution to passive/active processes.

4.3 The role of individual surface fluxes

Changes in the circulation and other ocean transport processes (acting to redistribute heat and salt in the ocean) necessarily originate from changes in buoyancy fluxes or wind stress. To investigate the role of individual surface fluxes on circulation, temperature and salinity long-term changes in the ocean,

a number of idealized modelling study have been led in which surface flux perturbations are imposed separately, using coupled [Mikolajewicz and Voss, 2000, Fyfe et al., 2007, Gregory et al., 2016, Lago et al., 2016, Liu et al., 2018, Shi et al., 2020, Todd et al., 2020, Couldrey et al., 2021] and ocean-only models [Armour et al., 2016, Garuba and Klinger, 2018, Zika et al., 2018, Todd et al., 2020, Dias et al., 2020, Patara et al., 2021].

Heat flux perturbation

Other than causing a widespread ocean warming (see figure 0.14 middle panel) explaining the main patterns of the total response, the heat flux perturbation is the principle cause of an AMOC slow-down [Mikolajewicz and Voss, 2000, Gregory et al., 2016, Garuba and Klinger, 2018, Todd et al., 2020]. There is some disagreement as to the role of other surface fluxes: Mikolajewicz and Voss [2000] find that three quarters of the AMOC weakening can be attributed to the heat flux perturbation and one quarter to the freshwater flux, while Gregory et al. [2016] and Todd et al. [2020] find that the AMOC is not significantly affected by freshwater and wind stress change. Coupled models reveal a clear feedback in the North Atlantic reinforcing this AMOC weakening, with subpolar SST cooling enhancing the positive heat flux perturbation into the ocean, which is itself enhancing AMOC weakening. Todd et al. [2020] quantified this atmosphere-SST feedback to amount to 10% more AMOC weakening in coupled vs. ocean-only models.

Allowing a feedback between the SST and the prescribed heat flux in their ocean model, Garuba and Klinger [2018] show that imposing a surface heat flux perturbation leads to a 12% global heat loss (they call this "active heat loss" i.e. due to the redistribution feedback) due mainly to surface warming in the tropical Pacific caused by a weakening of the subtropical cells.

Looking at the response of SSS to a surface warming perturbation, Mikolajewicz and Voss [2000] and Zika et al. [2018] show there is a pattern amplification of the SSS similar to the response to a hydrological cycle amplification, in zonal mean patterns of SSS [Mikolajewicz and Voss, 2000] or for the full latitude/longitude SSS patterns [Zika et al., 2018]. Zika et al. [2018] conclude that upper-ocean warming (and the consequent increased stratification) was responsible for one third of the total SSS pattern amplification, underlying the important role of both surface fluxes in setting the global patterns and amplitude of SSS.

Freshwater flux perturbation

The freshwater flux perturbation imposed alone causes a global redistributive surface cooling (see figure 0.14, right panel), particularly in the subpolar North Atlantic and Southern Ocean [Mikolajewicz and Voss, 2000, Gregory et al., 2016, Garuba and Klinger, 2018, Zika et al., 2018, Couldrey et al., 2021]. Garuba and Klinger [2018] find that the freshwater perturbation causes a large redistributive heat gain (34% of total heat uptake) because of this surface cooling in the North Atlantic caused by a weakening of the subpolar gyre. In the Southern Ocean, where the freshwater perturbation is positive into the ocean (increased precipitation), the stratification of the surface layer is increased. This increased stratification isolates the layer of warm waters below the surface (figure 0.14) and reduces vertical mixing between the two layers, thus reduces the release of the underlying heat to the atmosphere as well as deep convection near the Antarctic coast and the associated downward flush of cold waters, which creates the SST cooling and subsurface warming [Gregory et al., 2016, Armour et al., 2016, Todd et al., 2020].

Wind stress perturbation

Just like changes in freshwater fluxes, if no redistribution feedback is taken into account, changes in wind stress don't directly add heat to the ocean. Changes in OHC due to wind stress arise from a reorganization of the pre-existing ocean temperature field (i.e. pure redistribution displacing isotherms),

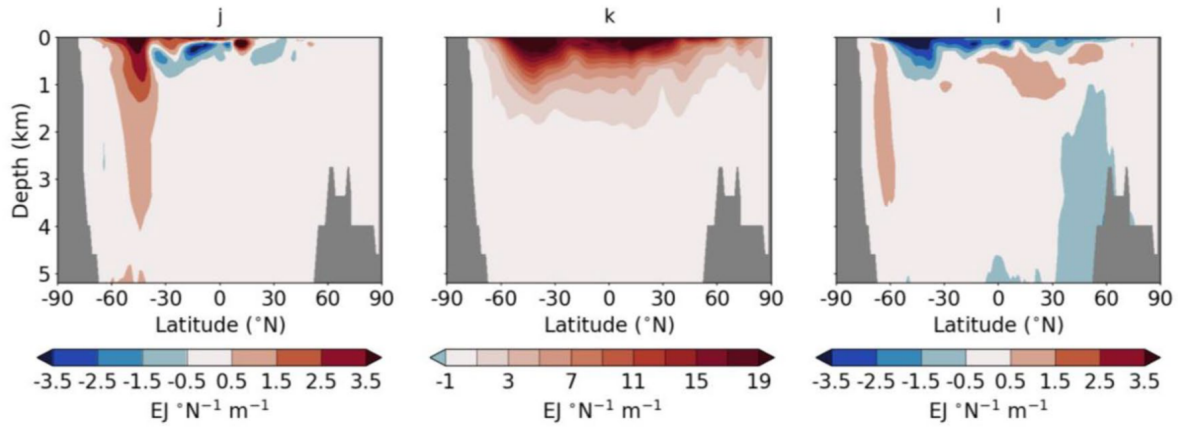

Figure 0.14: From Couldrey et al. [2021]. Zonally-integrated OHC change in the final decade of FAF-stress (left), FAF-heat (middle) and FAF-water (right); mean of 12 AOGCMs. 1EJ = 10^{18}J. The FAFMIP flux perturbations are computed as a multi-model mean from 1pctCO2 simulations at a time of doubling CO_2 concentration relative to piControl state. They are applied to each AOGCM similarly, as a constant forcing for the full 70 years of each experiment, with no time-variation except for the annual cycle.

so that changes in OHC due to wind stress perturbations can be important regionally but compensate when globally-integrated.

Changes in wind stress create the largest response in the Southern Ocean (see figure 0.14 left panel), where increased and poleward-intensifying westerly winds enhance the northward Ekman transport and subduction of heat between 40-50ºS, yielding a subsurface redistributive warming around 45ºS, surrounded by a cooling at higher latitudes (brought by the Ekman-intensified upwelling south of 60ºS and enhanced deep convection), and at lower latitudes (where there is reduced downward Ekman pumping) [Mikolajewicz and Voss, 2000, Fyfe et al., 2007, Armour et al., 2016, Gregory et al., 2016, Liu et al., 2018, Garuba and Klinger, 2018, Todd et al., 2020, Shi et al., 2020]. These patterns of change are consistent with an intensification of the wind-driven Southern Ocean upper cell attributed to wind stress changes [Liu et al., 2018, Patara et al., 2021]. Several studies conclude that the total Southern Ocean warming at mid-latitudes and its structure are caused by a combination of wind stress (active heat uptake) and heat flux changes (passive warming), with a dominance of the response to heat fluxes although the wind stress change is key to set the latitudinal structure of the warming [Fyfe et al., 2007, Liu et al., 2018, Shi et al., 2020]. Liu et al. [2018] find that wind stress changes are responsible for 1/8 of total basin-integrated (south of 30ºS) ocean heat storage, and 20% of the total heat storage maximum (latitudinally). Shi et al. [2020] find that 20% of total ocean heat storage south of 30ºS is due to wind stress changes.

For salinity, wind stress changes in the Southern Ocean have an opposite effect compared to freshwater fluxes, partly damping the total response: surface waters get saltier due to the wind-intensified upwelling of salty circumpolar deep waters and surface northward Ekman transport, while increased precipitation at high latitudes tend to freshen the upper layer, creating a competition between these two forcings [Shi et al., 2020]. More generally, there is often an opposing effect between changes in wind stress and buoyancy fluxes, as increased buoyancy fluxes tend to weaken ocean ventilation while an increased wind stress tends to strengthen ventilation [Patara et al., 2021].

Wind stress changes are found to more widely impact ocean circulation in these idealized numerical experiments, with e.g. an intensification of the North Atlantic subpolar gyre [Mikolajewicz and Voss, 2000] and a poleward shift of the subtropical gyres and of the ACC [Mikolajewicz and Voss, 2000, Garuba and Klinger, 2018]. The ocean warming found at the edge of the poleward-shifting subtropical gyres creates active heat loss to the atmosphere when the redistribution feedback is accounted for, amounting

to a global 12% heat loss in an experiment where only the wind stress perturbation is activated [Garuba and Klinger, 2018].

Attributing ocean changes to individual surface flux perturbations as done by such modelling studies relies on the linear additivity of the forcings, i.e. the response to all forcings applied together should replicate that of the sum to individual forcings. Several studies argue it is the case at the first order [Mikolajewicz and Voss, 2000, Fyfe et al., 2007, Lago et al., 2016, Zika et al., 2018, Shi et al., 2020], however [Couldrey et al., 2021] show that in coupled models, non-linear interactions between individual fluxes are non-negligible in the Arctic and subpolar North Atlantic and small in most of the ocean, although the non-linear response is model-dependent.

We note many other processes and surface forcings not discussed here are also important to better understand the causes of observed and future changes, such as the role of sea-ice (e.g. Haumann et al. [2020]) and iceshelf melt (e.g. Bronselaer et al. [2018], Lago and England [2019], which is not yet represented interactively in climate models).

A question of time scales

Tackling the question of the role of individual surface flux perturbation in altering ocean temperature and salinity patterns has mostly been done from idealized radiative scenarios mimicking an increase of CO_2 concentration in the atmosphere, in which the forcings time scales are not representative of the evolution of actual emissions since the pre-industrial period, nor take into account the possible counteracting effects of other anthropogenic forcings such as aerosols. The transient response in temperature and salinity changes is not explored, rather only the long-term changes and their cause are investigated. Consequently, we can wonder how these different surface fluxes compete under realistic time scales of human forcings and what it implies for the evolution of ocean temperature and salinity patterns: does the response change sign because one mechanism temporarily overwhelms the others? As an example, Southern Ocean increased ventilation was found to be mainly driven by wind stress changes since the mid-20th century, but this process will only hold as long as the wind stress response surpasses the increased stratification caused by increased buoyancy fluxes [Patara et al., 2021, Sallée et al., 2021]. Will this balance be disrupted, and if so, when? Furthermore, do temperature and salinity changes generated by individual fluxes surpass internal variability? Would a climate change signal significantly emerge in the absence of other fluxes?

5 Scientific problem and aim of this thesis

Summary

In this General Introduction, I have tried to put forward pieces of evidence from the scientific literature exposing the significant changes that the ocean has undergone in its thermohaline structure in the past decades. Such changes have been observed thanks to years of repeated efforts to sample the global ocean, from oceanographic cruises, to the deployment of autonomous floats and instrumented marine mammals. Large sampling biases still exist, especially at depth and at high latitudes, and new programs are underway to fill these gaps for the future of the ocean observing system.

Still, some of these changes have already been attributed to human activities disturbing the natural variations of the climate system since the industrial revolution. The detection of multi-decadal temperature and salinity changes and their attribution to human activities has been made possible by combining ocean observations with simulations of the climate system including - or not - the influence of human-induced greenhouse gases, aerosols, and other forcings. However, due to poor historical coverage, this attribution has essentially been done at relatively global scale and in the upper ocean. We still don't know if, when or where, at more local scale, long-term temperature and salinity changes have exceeded or will

exceed natural climate variations in the ocean interior. Moreover, the mechanical studies that proposed to isolate the causes of these large scale temperature and salinity changes in the ocean have mostly looked at the equilibrium or long-term response. However, the balance between different mechanisms can differ in the transient response compared to what happens at equilibrium, such as the competition between buoyancy fluxes and winds.

Questions

In this thesis, I will broadly investigate the emergence of large scale ocean temperature and salinity changes, particularly under the mixed layer where the ocean has larger inertia and is further away from the influence of rapid exchanges with the atmosphere. We will explore where and when we can expect to detect forced changes, thus proposing a spatial mapping of the timing of emerging signals in the ocean interior. We will examine the origin of these emerging signals in terms of physical processes, as well as the time scales of potential physical drivers.

Keeping this general aim in mind throughout this thesis, I propose to address three targeted questions which I briefly lay out here, and which will be further discussed at the end of the manuscript.

1. What is the balance of mechanisms that makes the region associated with SAMW and AAIW such a key place for the detection of thermohaline changes of anthropogenic origin?
These water-masses have long been of particular interest as they play a fundamental role in upper ocean ventilation and overturning [McCartney, 1977, Hanawa and Talley, 2001, Sallée et al., 2010, Morrison et al., 2022]. This interest stemming from ocean observations has been confirmed by the repeated evaluation of these water-masses (their formation and hydrology) in the successive generations of climate models as well as their sensitivity to projected climate change [Sloyan and Kamenkovich, 2007, Downes et al., 2009, 2010, Sallée et al., 2013, Hong et al., 2021, Meijers et al., 2021]. SAMW and AAIW are of great relevance for the climate system and its changes, as they have been identified as dominant pathways of anthropogenic heat and carbon uptake and storage [Khatiwala et al., 2009, Roemmich et al., 2015, Frölicher et al., 2015, Zanna et al., 2019b, Morrison et al., 2022]. As they integrate fluctuations in surface forcings at the density outcrops on large and homogeneous volumes subducted beneath the mixed layer, they have been found early on to be key indicators of anthropogenic climate change signals, which can possibly be detected earlier than in the Northern Hemisphere [Banks et al., 2000]. The detection of multi-decadal observed subsurface temperature and salinity changes in these water-masses and their attribution to human activity has been confirmed recently by two independent studies, using a large initial-condition ensemble [Swart et al., 2018] and a CMIP5 multi-model ensemble [Hobbs et al., 2021]. If heat is taken up as a passive process in SAMW and AAIW regions, we can expect the time scales of the emergence of subsurface temperature changes to depend on the time scales of the surface heat input at high latitudes, modulated by the typical time scale of the upper ocean overturning, as the overturning strongly controls the rate of anthropogenic heat ventilation [Morrison et al., 2022]. However, depending on how quickly or whether the overturning increases in response to poleward and amplifying westerly winds, these time scales might be affected. Increased buoyancy fluxes might also play a role in stratifying the upper layers, preventing heat from penetrating as deeply along the original heat uptake pathway. How these opposing forcings interact in the transient response will determine if the emergence of the heat content change arises earlier or is delayed compared to the passive uptake.

2. What can we learn from climate models about deep and abyssal changes and their timing?
AABW and NADW, formed in relatively small areas in the high latitudes, fill large volumes of the ocean in the deep and abyssal layers [Johnson, 2008]. Changes in their rate of formation and in their characteristics can thus fundamentally change the thermohaline structure of the ocean deep interior. This has consequences for the storage of heat, carbon and nutrients. Deep thermohaline changes have already been observed (e.g. Purkey and Johnson [2010], Desbruyères et al. [2016], Purkey et al. [2019]), although observations are still sparse and the significance of these changes compared to internal variations is largely

unknown. We will explore when, in climate models, changes at depth are predicted to emerge from internal variability and how they relate to high latitude processes. However, global climate models are known to misrepresent the formation of these deep and abyssal water-masses [Heuzé et al., 2013, Heuzé, 2017, 2021, Mohrmann et al., 2021], as high latitude processes result from complex interactions and feedback processes between the ocean, atmosphere and cryosphere which are poorly represented or not represented at all, such as deep overflows and iceshelf basal melt. We will discuss what we can learn from these models for our understanding of deep ocean thermohaline changes, their timescales and drivers of change, keeping all their limitations in mind.

3. What does emergence mean in different methodological frameworks, how do they compare and what do we learn from them?
Finally, we will address a more analytical aspect, and aim to uncover whether some frameworks can help detect earlier changes in the ocean. We will look at different methods, compare a local and global approach, different estimates of climate variability, and different frameworks to analyse thermohaline changes separately or together.

Approach and tools

We will tackle these questions largely with the use of global ocean and climate models, and use gridded observation-based products as validation tools. We will first adopt a multi-model approach and explore an ensemble of CMIP5 models. The multi-model analysis allows to reveal common features and patterns of change among diverse representations of the climate system. In particular, averaging across models can reveal forced climate changes, compared to uncertainties in internal variability and across models. Then, we will turn to a single-model initial condition large ensemble, to more specifically isolate the forced signals in one model world, and identify uncertainties relating exclusively to internal variability. Finally, we will take on a more mechanistic approach, by performing numerical experiments with a global ocean model - the same ocean component as used in the coupled model large ensemble. A global view of ocean processes will be adopted throughout this thesis. We will look at large-scale patterns of change and their drivers, and use rather simple diagnostics to uncover the time scales and mechanisms at play in the ocean interior.

Structure of the thesis

The results will be presented in four chapters, followed by a closing chapter where we will try to discuss the implications of the work conducted across this thesis in a broader context. The first two chapters will focus on providing diagnostics of time of emergence of temperature and salinity changes in the ocean, while in the other two chapters, we propose a numerical framework to tackle more mechanistic aspects and understand the underlying processes causing these global-scale changes to emerge.

In Chapter I, we present a CMIP5 multi-model analysis of thermohaline changes along density surfaces and their time of emergence. This work was published in the journal *Nature Climate Change* in August 2020 [Silvy et al., 2020]. Supplementary material to this first paper is included in Appendix A. We then extend the analysis of these density-compensated changes to the Institut Pierre-Simon Laplace (IPSL) coupled model large ensemble, before discussing the implications of the density framework.

In Chapter II, we focus on this IPSL initial condition large ensemble, and look for ocean thermohaline changes and their emergence from internal variability in different frameworks of analysis and with different methodologies. This work was not written for scientific publication, but to present temperature and salinity changes and their time scales in the large ensemble before trying to understand their origins in the following chapters. This chapter is also meant as a place to discuss possible frameworks to analyse temperature and salinity changes, and what we can learn from each of them. A few supplementary figures on ocean drift are provided in Appendix B.

In Chapter III, we describe the numerical framework developed during the second part of the thesis. The goal of this framework is to understand the forcing mechanisms of transient thermohaline changes in the IPSL large ensemble in response to individual drivers of change. This meant implementing a new configuration of ocean-only experiments. In this chapter, we try to present the main steps and a comprehensive view of the modelling work done. More specific considerations and sensitivity tests are addressed in Appendix C. The work done on the heat budget of the ocean model was published in Appendix B of Mignot et al. [2021]. Furthermore, the development of this numerical framework and the associated code has benefited a team led by Matthieu Lengaigne at UMR Marbec, working on forced surface processes in the Indian ocean. The code of the numerical configuration will be made freely available.

In Chapter IV, we use the numerical experiments presented in Chapter III to investigate, in a first section, the processes and time scales of anthropogenic heat emergence in the ocean, in the context of the IPSL large ensemble. This work is presented in the form of a manuscript that will be submitted to the *Journal of Climate* in the weeks or so following submission of this thesis. Supplementary Material to be submitted along with this manuscript is provided in Appendix D. In a second section, we present ongoing work and perspectives for a study on the drivers and time scales of salinity changes, particularly on the amplification of salinity climatological patterns. A few additional figures are featured in Appendix E.

These four chapters are meant to be understandable almost independently from one another, which is why there might be some redundancies at times in presenting the IPSL model.

Finally, I was involved in a group effort at LOCEAN to quantify the carbon footprint of our research practises, interrogate it in the light of the climate crisis, and propose low-carbon pathways for the lab. A summary of the different steps that took place during the two years of fall 2018 - fall 2020 is presented in Appendix F, based on a draft written collectively with colleagues of the working group "Climactions" in the fall of 2020.

Chapter

I

Emergence of density-compensated forced changes in the ocean in a multi-model analysis

Contents

1 Introduction

In this first chapter, we will focus on long-term thermohaline changes analyzed in density space in the CMIP5 archive of global climate models, compare them to observations of change since 1950, and diagnose their associated time of emergence from climate variability. Before diving into this study, I come back in this brief introduction to a few reasons why the density space has been commonly adopted to investigate climate trends. Particularly, I present the Bindoff and Mcdougall [1994] theoretical framework that has been introduced to trace back mechanisms of ocean change to surface drivers, from the observations of temperature and salinity changes along both pressure and density surfaces. Considering density as a coordinate is often employed as an oceanographic tool as it defines how the ocean is organized. Other frameworks that have adopted a density approach include, for instance, looking at how surface heat and freshwater fluxes convert water from one density range to another to quantitatively estimate the formation rates of water-masses [Walin, 1982, Speer and Tziperman, 1992]; or computing meridional ocean transport that cannot be explored along standard pressure levels [Döös and Webb, 1994, Speer et al., 2000].

1.1 A theoretical framework to investigate the mechanisms of ocean ventilation

Bindoff and Mcdougall [1994] introduced a theoretical framework to explain subsurface temperature and salinity changes in response to separate atmospheric forcings. They proposed three ventilation mech-

anisms, under a number of hypotheses, by which ocean properties could change below the mixed layer on a given pressure surface.

- First, the "pure warming" process in which surface waters are warmed by an increased heat flux into the ocean and subducted below the mixed layer, resulting in a temperature increase at a given pressure level, no salinity change, and a density-compensated temperature and salinity change along a given isopycnal due to its downward displacement in the water column caused by the surface warming. These changes along isopycnals depend on the stability ratio of the water column R_ρ, i.e. on the relation between the vertical gradients of temperature θ_z and salinity S_z. In the subtropics, $R_\rho = \frac{\alpha\theta_z}{\beta S_z} > 1$ (where α and β are respectively the thermal expansion and haline contraction coefficients) which means the pure warming results in a cooling and freshening along isopycnals.
- Second, the "pure freshening" process where surface waters are freshened by a change in Precipitation-Evaporation and subducted, resulting in a freshening and no temperature change at a given pressure level, and, similarly as the pure warming, a density-compensated temperature and salinity change along a given isopycnal (also depicted as a cooling and freshening in the subtropics where waters are saltier and warmer in the upper ocean than below).
- Third, the "pure heaving" process where isopycnals can move vertically in response to a change in subduction rate (which was assumed constant in the two previous processes) caused e.g. by a wind stress perturbation, resulting in a temperature and salinity change on a given pressure surface but no signature on a given isopycnal.

We note here, isopycnal refers to a neutral surface [McDougall, 1987], and the term neutral density is employed. In reality, these three ventilation processes often occur concurrently. In that sense, this framework enables the decomposition of temperature and salinity changes to retrace their origin. Indeed, at a given location and for each of the three processes, the changes in temperature and salinity along a given pressure and a given density level can be constrained by a set of equations relating them to each other, to the change in depth of the given isopycnal and to R_ρ, α, β, θ_z and S_z. This yields a system of 6 quantities (with 2 independent variables), each of them due to a linear combination of the 3 processes, that can be written in matrix form. Using an inverse method, it is then possible to estimate, under a choice of assumptions (e.g. minimizing each process or considering the percentage variance of only one process at a time), the proportion of each process responsible for the total temperature and salinity changes observed at the same location (on pressure and neutral density surfaces) between two time periods (see Bindoff and Mcdougall [1994]).

Using a repeated section at 34ºS in the Tasman Sea, Bindoff and Mcdougall [1994] show that pure heave processes dominate on the seasonal timescale in the upper ocean, but pure warming dominates decadal changes in the SAMW, illustrated by a warming at fixed depth, cooling and freshening on isopycnal layers and a downward displacement of these isopycnals. They also find that at decadal timescales, pure freshening dominates on denser levels, in a water-mass that outcrops ∼60ºS. It is interesting to see that although the multi-decadal precipitation trend was unknown over the Southern Ocean (although they already expected precipitation to intensify at these high latitudes according to numerical climate change experiments), they already found evidence of a possible perturbation in the freshwater flux, expressed as a freshening of surface water-masses at high latitudes that had been subducted equatorward, consistent with the multi-decadal freshening of AAIW observed today. These findings (dominance of pure warming in the SAMW and pure freshening in the AAIW) were confirmed in a subsequent study looking at multi-decadal changes along a section at 32ºS in the Southern Indian Ocean [Bindoff and Mcdougall, 2000] and later in an idealized scenario of increasing CO_2 forcing in a global climate model [Banks and Bindoff, 2003].

To draw a possible link with the passive/redistributive framework presented in the General Introduction, since pure warming and pure freshening are defined under a stationary circulation (at fixed subduction rates), we could relate pure warming to passive warming (i.e. subduction of warmer surface waters

due to increased heat flux into the ocean by the unperturbed circulation), pure freshening to passive freshening (subduction of fresher waters due to increased freshwater flux into the ocean by the unperturbed circulation) and pure heave to all processes related to dynamic redistribution of pre-existing heat and salt by the perturbed circulation, i.e. wind stress changes but also circulations changes caused by heat and freshwater flux perturbations. Keeping in mind that these processes are idealized.

The Bindoff and McDougall framework is thus particularly interesting in observations or historical simulations where the individual role of surface flux perturbations and of passive and redistributive processes can't be separated as they can be in dedicated numerical experiments. However, the linear system of observables to solve pure warming, pure freshening and pure heave is underdetermined (as only two variables are independent). Consequently, there are several mathematical solutions to this system, so an understanding of physical processes is needed to correctly interpret the different possible solutions.

1.2 The density binning approach

This sparked interest in many subsequent studies to investigate observed thermohaline changes both on density and pressure surfaces, although not always to solve the processes mentioned above. Here, we present results from a project in collaboration with Paul Durack at the PCMDI in Livermore (and others), that aimed to draw from the observed change along density surfaces [Durack and Wijffels, 2010] and revisit them in a multi-model approach. All the binning code and outputs were developed before this PhD. Because each model can have a different equation of state, the choice was made to transform all the temperature and salinity CMIP5 outputs to a common density label: γ_a, an approximation of neutral surfaces [McDougall and Jackett, 2005], much less costly than the γ_n computation [Jackett and McDougall, 1997]. As shown by the agreement of long-term changes along density levels found across studies that did not necessarily use the same density coordinate, this choice does not impact the large-scale features investigated here. This density coordinate zooms on upper ocean water-masses, essentially highlighting Mode and Intermediate waters, leaving the deeper ocean to reside in only a few density classes. For a more intuitive visualization, the results are shown in this first study by remapping back to pressure levels after all computations were done in density space, using a climatology to define a density-depth relationship.

The following section presents the CMIP5 study published in *Nature Climate Change* in August 2020. The Supplementary Material published alongside the paper is attached in Appendix A. Then, we extend the work to the large ensemble of historical members of the IPSL coupled model that was used for CMIP6 and that will be further analysed in the next chapter. Finally, we discuss the limits and interpretation of the density binning approach.

2 Paper: Human-induced changes to the global ocean water-masses and their time of emergence

nature climate change

ARTICLES

https://doi.org/10.1038/s41558-020-0878-x

Human-induced changes to the global ocean water masses and their time of emergence

Yona Silvy[1]✉, Eric Guilyardi[1,2], Jean-Baptiste Sallée[1] and Paul J. Durack[3]

The World Ocean is rapidly changing, with global and regional modification of temperature and salinity, resulting in widespread and irreversible impacts. While the most pronounced observed temperature and salinity changes are located in the upper ocean, changes in water masses at depth have been identified and will probably strengthen in the future. Here, using 11 climate models, we define when anthropogenic temperature and salinity changes are expected to emerge from natural variability in the ocean interior along density surfaces. The models predict that in 2020, 20–55% of the Atlantic, Pacific and Indian basins have an emergent anthropogenic signal; reaching 40–65% in 2050 and 55–80% in 2080. The well-ventilated Southern Ocean water masses emerge very rapidly, as early as the 1980–1990s, while the Northern Hemisphere water masses emerge in the 2010–2030s. Our results highlight the importance of maintaining and augmenting an ocean observing system capable of detecting and monitoring persistent anthropogenic changes.

Observed ocean temperature and salinity changes have been partially attributed to human activities, with global ocean heat content change identified in the early 2000s[1,2] and temperature and salinity changes in the upper (0–700 m) and intermediate (700–2,000 m) ocean in more recent times[3–11]. A few studies focused on more specific regions, with detected human-induced changes to ocean salinity in the Tropical Pacific[9], Atlantic[10] and Southern Ocean[11] regions. However, there are still vast regions of the World Ocean, particularly at depth, where anthropogenic change remains undetected. The lack of positive attribution can be due to poor observational coverage, weak changes or because natural variability is large and is hiding forced changes. Because of the slow transport of heat and salt in the ocean interior, some regions in the deep ocean may be isolated from human-induced changes for a long time, as the climate signal propagates from the surface to the ocean interior. Other regions, which are more directly connected to the surface by atmosphere–ocean exchanges, ocean circulation and mixing, may respond more quickly. On the basis of anthropogenically forced climate model simulations, it is possible to estimate where and when the human-induced signal emerges against the background variability in the ocean interior.

While investigating the timescale of anthropogenic signal emergence in the climate system, past studies have focused on surface temperature[12–17], precipitation[18,19] and sea level rise[20] as well as marine ecosystem drivers and ocean carbon cycle indicators[21–26]. It was shown that temperature and salinity are potentially good indicators for detecting anthropogenic change in the next few decades[27]. Here, we investigate the emergence of human-induced salinity changes at depth, in basin-scale zonal means, using a multimodel framework. We focus on the ocean interior below the 'bowl' (that is, below the deepest winter mixed layer) and we use climate models participating in the fifth phase of the coupled model intercomparison project (CMIP5). Ocean circulation below the bowl primarily flows along density surfaces. Density surfaces can move vertically (heave) for several reasons including transient dynamical changes unrelated to atmosphere-forced and ocean-ingested heat or freshwater changes, that manifest as temperature and salinity changes when assessed on a given pressure level. In an endeavour to detect the earliest time of emergence (ToE), we remove from our analysis this transient dynamical change by investigating temperature and salinity changes on neutral density levels (see Methods). On a density surface, changes of salinity and temperature are by definition correlated, so to avoid redundancy we will hereafter only discuss salinity changes.

Observed zonally averaged salinity changes along density surfaces show remarkably similar structures across different basins in the Southern Hemisphere (Fig. 1a)[28,29]. These features include a subtropical freshening in the upper 1,000 m in the density range of subantarctic mode and intermediate waters (26.5–27.0 kg m^{-3}), surrounded by a relatively strong salinity increase in the tropical shallow cells and a slightly more moderate salinity increase in the range of upper circumpolar deep waters (~50°–60° S, ~27.5 kg m^{-3}). The Northern Hemisphere Pacific presents a similar geographical salinification/freshening/salinification pattern of change. The North Atlantic features a subpolar freshening extending into the subtropics along the 27.7–28.0 kg m^{-3} isopycnals as well as a freshening along the 27 kg m^{-3} isopycnal from the subtropics to the equator and southward, capped by a strong salinity increase in the upper ocean and smaller increase at depth. Strong salinification is observed in the North Indian region, spanning almost all density ranges and suggesting that the influence of marginal sea outflows of high salinity dominates.

These large-scale patterns of multidecadal change have been proposed to be caused by regional surface changes in freshwater fluxes[29–32] (wet regions get wetter and dry regions get dryer), as well as from surface warming shifting isopycnal outcrops poleward and along which the signal penetrates the ocean interior[30–32].

Although the amplitude of the change is weaker in the multimodel mean (MMM of 11 models; Fig. 1b) than in the observation-based estimate—which is expected for a multimodel ensemble mean as it washes out change patterns of water masses with slightly different geographies thus not exactly aligned—the main patterns of change

[1]LOCEAN-IPSL, Laboratoire d'Océanographie et du Climat: Expérimentation et Approches Numériques, Sorbonne Université/CNRS/IRD/MNHN, Paris, France. [2]NCAS-Climate, University of Reading, Reading, UK. [3]Program for Climate Model Diagnosis and Intercomparison, Lawrence Livermore National Laboratory, Livermore, CA, USA. ✉e-mail: yona.silvy@icloud.com

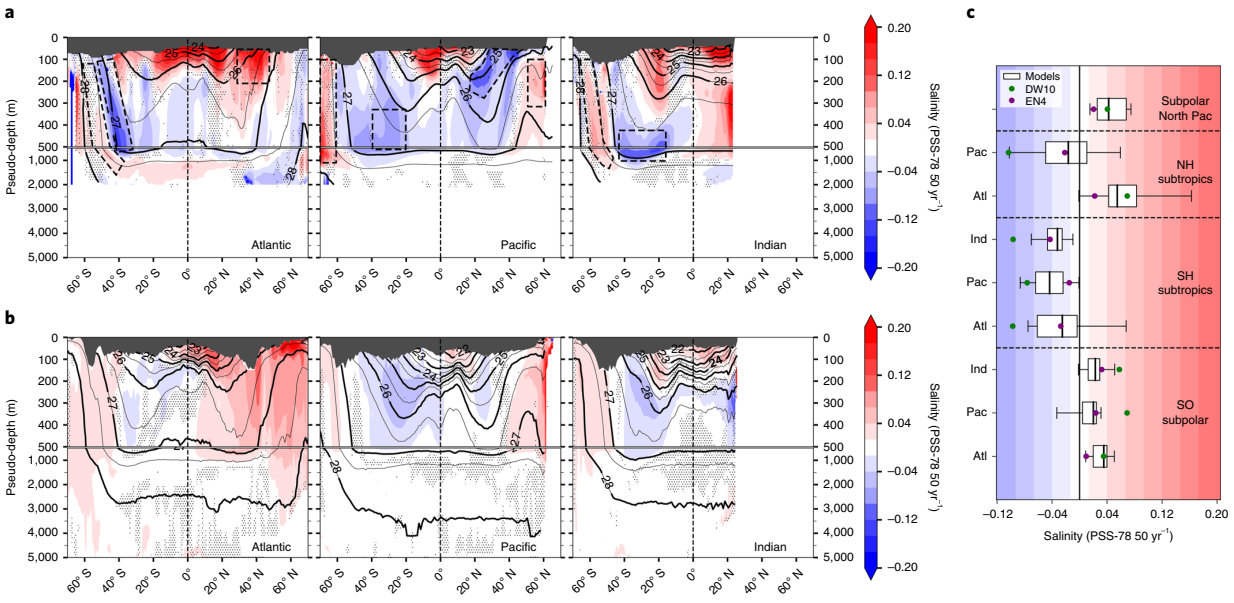

Fig. 1 | Observed and simulated salinity changes between 1950 and 2008, shown in patterns of 50-yr salinity changes, analysed on density surfaces. For ease of reading, all figures of this paper are projected back from density to pressure as vertical coordinate (see Methods). **a**, From Durack and Wijffels[29] observation-based analysis. Contours show isopycnals and stipples where the trend is not significant at the 90% confidence level. **b**, From the MMM CMIP5 historical experiments. Contours show isopycnals and stipples indicate where less than 60% of models agree on the sign of the trend. The changes in original density coordinate are shown in Supplementary Fig. 1. **c**, Trend averaged in nine regions (approximate boxes shown in **a**) for two observational estimates (DW10 and EN4) and for the model distribution (boxes indicate first and third quartiles and the median; whiskers indicate the minimum and maximum outliers). The shading in **c** corresponds to the colour scale of **a** and **b**. The exact regions in density space as used for each observational dataset and model are plotted in Supplementary Figs. 1a, 2a and 4 (same coordinates for both observational datasets). The greyed-out regions at the surface correspond to data trimming above the bowl—see text. Pac, Pacific; Alt, Atlantic; Ind, Indian; NH, Northern Hemisphere; SH, Southern Hemisphere; SO, Southern Ocean.

are reproduced. Indeed, the observed salinification/freshening/salinification from equator to pole in the Southern Hemisphere of all three basins and in the Northern Hemisphere Pacific is replicated in the models, although we note the mode water freshening in the Southern Hemisphere tends to appear on slightly lighter density classes in the models than in the observations (around 26 kg m^{-3} in the models versus 26.5–27.0 kg m^{-3} in the observations), consistent with past studies[11,31,33]. The magnitude of change within the individual model ensembles is equivalent to observed estimates (Supplementary Fig. 3) and the change is robust across models in regions where the observed signal is the strongest, indicative of a coherent forced change. The Northern Indian region shows a change pattern of opposite sign in the MMM than in observations, as models probably have trouble reproducing the two competing sub-basin regimes in this region (the fresh Bay of Bengal and the very salty overflows of Red Sea and Persian Gulf waters). The subpolar North Atlantic also shows disagreement between the observations and model change. This is also a region that the models struggle to simulate correctly as it has large regional differences, numerous interactions with the ice and land, and many competing sources of ocean change and variability[34]. As the Durack and Wijffels 2010[29] (hereafter DW10) analysis ends in 2008 (Fig. 1a), we also compute the 1950–2017 change using the EN4 (ref. [35], v.4.2.1) observation-based objective analyses (Supplementary Fig. 2a). The EN4 spatial patterns of change are extremely similar to those of DW10, giving confidence in the robustness of these identified observed patterns. In the MMM, the patterns of change identified during 1950–2008 (Fig. 1b and Supplementary Fig. 1b) become more robust when extending the period to 2017 and the amplitude of the change increases (Supplementary Fig. 2b).

To more quantitatively compare the observed and simulated trends in water masses regionally, a diagnostic of the trends is shown in nine regions of interest, where the simulated change is coherent in sign with the observations (Fig. 1c); we thus don't consider the North Indian and subpolar North Atlantic, as the observed change there is not captured by the models. In both observations and models, the nine regions correspond to the salinity increase in the subpolar Southern Ocean, the freshening in the Southern Hemisphere subtropics, the increase (freshening) in the northern subtropical Atlantic (Pacific) and the increase in the subpolar North Pacific. The coordinates are chosen to best capture these patterns and tailored to the water-mass ranges of each model, as those are not necessarily reproduced at the same locations. Approximate boxes are shown in Fig. 1a; the exact boxes can be found in Supplementary Fig. 1a for the observations and Supplementary Fig. 4 for each model. We also run the same diagnostic for EN4. Regional trends in the observational estimates and models (Fig. 1c) are within the same order of magnitude, although the DW10 values tend to lie systematically on the higher end of the model distribution or even outside in some sections of the poorly sampled Southern Hemisphere, suggesting that the models might simulate a conservative estimate of the change. In the well-sampled Northern Hemisphere, both observational estimates fall within the model distribution. In all regions, EN4 yields a smaller trend than DW10, consistent with the respective methods of these estimates (in data-sparse regions, EN4 is restored towards the climatology, thus providing a very conservative estimate of change).

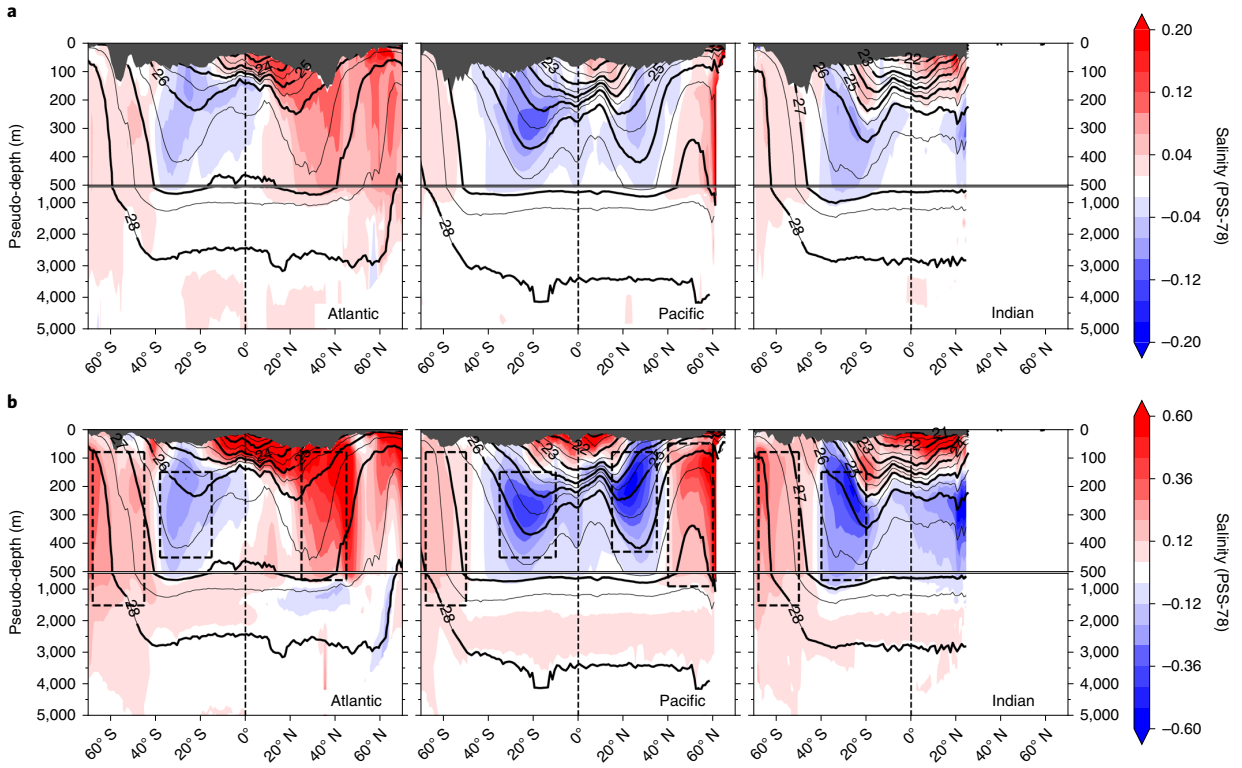

Fig. 2 | Anthropogenic salinity change along density surfaces. a, At the end of the twentieth century (MMM difference between the CMIP5 historical and historicalNat experiments in the last 20 yr (1986–2005)—to account for potential decadal variability). **b**, At the end of the twenty-first century (MMM difference between the last 20 yr (2081–2100) of the CMIP5 RCP 8.5 scenario and the average of the whole historicalNat experiment). Boxes in **b** represent the approximate regions in which salinity trends are computed in Fig. 1c and in which ToE is calculated in Fig. 4. The same signal as in **b** is shown in Supplementary Fig. 4 for each model in density space with the exact box locations.

Overall, this gives us confidence in the ability of models to reproduce these regional patterns of change.

On the basis of the same model suite, we now determine the 'anthropogenic' component of the change by subtracting from the salinity computed in the historical simulations, the salinity computed in idealized coincident simulations where human-induced forcings are removed (historicalNat). At the end of the twentieth century, it is striking that the simulated historical change (Fig. 1b) is very close to the estimated 'anthropogenic' contribution (Fig. 2a), with a Pearson's spatial correlation coefficient of 0.88, suggesting that human-induced forcings are responsible for most of the observed salinity change during the second half of the twentieth century[5,9–11]. The pattern of the historical anthropogenic signal is further amplified from 2006 and into the twenty-first century under a high-emission scenario (representative concentration pathway RCP 8.5; Fig. 2b), confirming the robustness of the structures of the anthropogenic forced change over the observed time period. As this signal appears qualitatively robust and human-induced, we now investigate when it can be statistically unambiguously distinguished from natural background variability over the 1861–2100 period.

We define the ToE of salinity change as the year when the anthropogenic signal (defined over 1861–2100) exceeds and never falls back below twice the typical natural variability 'noise' threshold (the interannual standard deviation of the historicalNat experiment), such that emergence is detected within the 95% confidence interval (see Methods). Unlike previous studies, we choose 'natural' (CMIP5, historicalNat) rather than 'unforced' (piControl) simulations from which to calculate our noise envelope. This choice encompasses the effects of natural forcings (including volcanic eruptions) in the noise in addition to the internal variability of the climate system, which ensures that a conservative temporal estimate of forced signal emergence is calculated (see Methods and Supplementary Discussion). Nevertheless, early detection is found: in all regions showing a robust pattern of change, the multimodel median ToE falls between the late twentieth century and the first decades of the twenty-first century (Fig. 3a) and there is a noteworthy agreement between models on the sign of the signal (see also intermodel spread in Supplementary Fig. 5). Regions that do not emerge show no agreement between models (grey areas in Fig. 3a). In 2020, most of the identified forced patterns have already emerged in the ocean interior, with 20–45% of the zonally averaged basin emerged in the Atlantic, 20–55% in the Pacific and 25–50% in the Indian (Fig. 3b, first to third quartiles). These numbers rapidly increase, reaching 35–55% in the Atlantic in 2050 to 55–65% in 2080; 45–65% to 60–75% in the Pacific; 45–65% to 60–80% in the Indian.

The earliest ToE are found in the Southern Hemisphere subtropical (40°–20° S) and subpolar (60°–40° S) areas, with a median ToE as early as the 1980s and overall earlier than 2020. The subtropical Southern Ocean is a dominant region for heat uptake associated with the formation and subduction of water masses ventilating the subtropical gyres with mode and intermediate waters[33,36]. The early emergence of the human-induced signal in this region is consistent with the observed changes that have been detected and attributed to anthropogenic forcings[11]. Model agreement in the southern

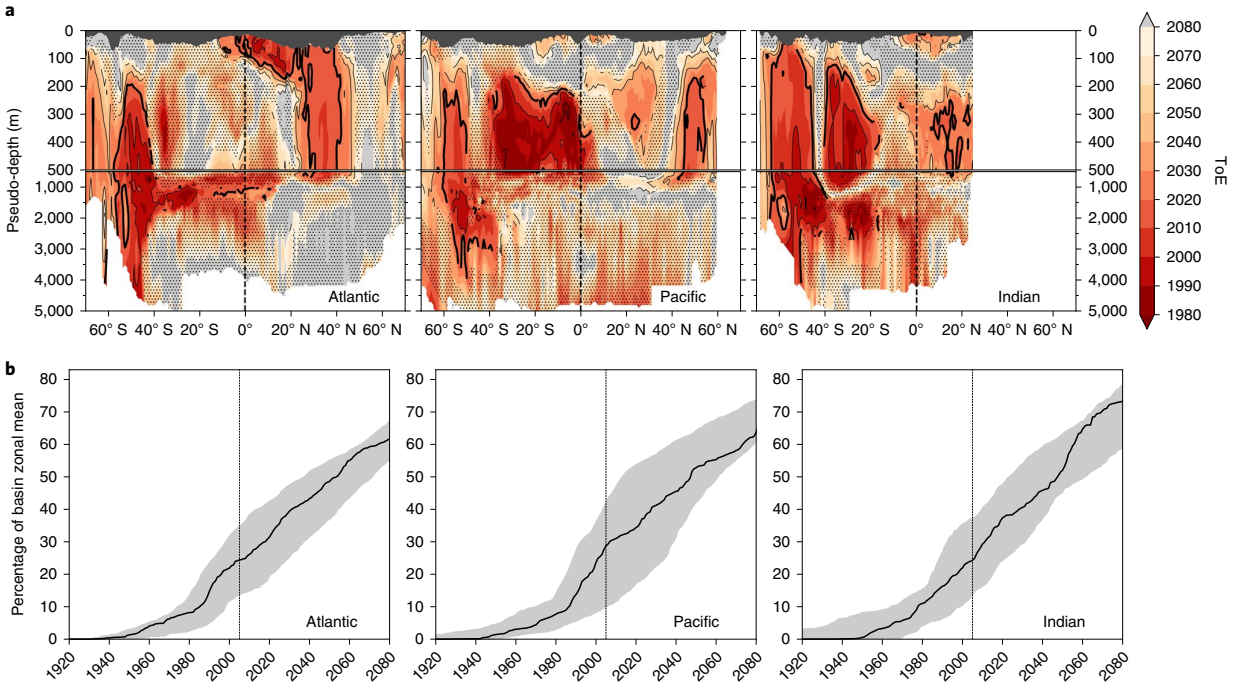

Fig. 3 | ToE and percentage of emergence in basin zonal means. a, Multimodel median ToE of the anthropogenic salinity change, calculated for an ensemble of 11 models. Light grey regions mean no emergence of the signal, while stippled regions show where the models do not agree on the sign of the signal (see Methods). Bold contour is year 2020. **b**, Percentage of basin emergence in zonal means under the bowl (see Methods). The black line is the median, the grey shading is the interquartile range.

subtropical Atlantic from 40° S to 20° S is weak in the upper 1,000 m, reflecting that unlike the Indian and Pacific basins, this basin is not associated with a well-ventilated layer of subantarctic mode water[36]. Instead, the upper 1,000 m in the Southern Ocean Atlantic basin is populated with newly ventilated intermediate waters[36], whose circulation and subduction are poorly represented by the CMIP5 models[33]. The model spread is relatively narrow for the Southern Hemisphere subtropics (two to three decades for the interquartile range in the Pacific and Indian sectors; Supplementary Fig. 5) and slightly larger for the subpolar Southern Ocean. We note that the emergence in the subpolar Southern Ocean is to be assessed cautiously, with most models rapidly limiting spurious open ocean deep convection due to near-surface freshening[37,38], therefore arguably warming at depth (1,000–2,000 m) much faster than in the real world (in the subpolar Southern Ocean, deep convection acts to extract heat from the interior ocean and release it to the atmosphere[39]). The other regions featuring an emergent signal in the first decades of the twenty-first century are the northern Pacific between 10°–30° N and 40°–60° N, with a median ToE from the 2010s to 2040 and an intermodel range of a few decades. The signal in the North Atlantic also emerges in the early decades of the twenty-first century, mostly before 2020, with an interquartile range of two to four decades. The intermodel range gives a measure of the uncertainty that the climate models are providing and so a spectrum of possibilities for the real world to lie within. There is decadal to multidecadal variability between realizations and between models, as well as model errors, which means it is difficult to get that range below zero (10 yr).

Because each model can represent a given water mass at slightly different latitude or density, we again delineate model-specific water mass ranges that are uniquely defined for each model, so a clearer, quantitative water-mass-centric model intercomparison can be performed (same regions as Fig. 1c; see approximate regions in Fig. 2b and exact boxes for each model in Supplementary Fig. 4 in density space). Additionally, and again to increase the signal-to-noise ratio, because each model can have a different climate sensitivity, here we associate, for each model member, the ToE of the anthropogenic signal in all nine regions to the corresponding global mean surface warming at that time under the RCP 8.5 scenario (global mean surface air temperature (GSAT) increase relative to the pre-industrial era, Fig. 4). Supplementary Fig. 6 shows the same analysis, as a function of time (ToE axis instead of GSAT anomaly).

Most models predict that salinity change signals emerge between +0.5 °C and +2 °C of global mean surface warming, corresponding to a ToE between the late twentieth century and the first decades of the twenty-first century (Fig. 4). According to this distribution, there is a 100% probability for the anthropogenic signal in the Northern subpolar Pacific and in the Southern Hemisphere Pacific and Indian subtropics to emerge before a +2 °C warming, and over 75% probability to emerge before +1.5 °C—and even before +1 °C for the Pacific southern subtropics (note observed global mean surface warming to 2018 is about 1 °C; ref. [40]). The subpolar Southern Ocean sectors have a relatively early median emergence (~0.8–1.3 °C) but a wide model spread, especially in the Pacific, probably reflecting model deficiencies in representing this part of the ocean[37,38]. The Northern Hemisphere subtropical water masses emerge slightly later than their Southern Hemisphere counterparts (except in the Atlantic basin), with about 75% probability to emerge before +2.25 °C. We expect the dependence of these results to slower warming scenarios to be limited, as most models present a signal emerging before there is a notable difference between scenarios (see comparison of the RCP 4.5 and RCP 8.5 warming in Supplementary Fig. 7).

We repeat the same analysis on an idealized emission scenario where CO_2 concentration in the atmosphere increases by 1%

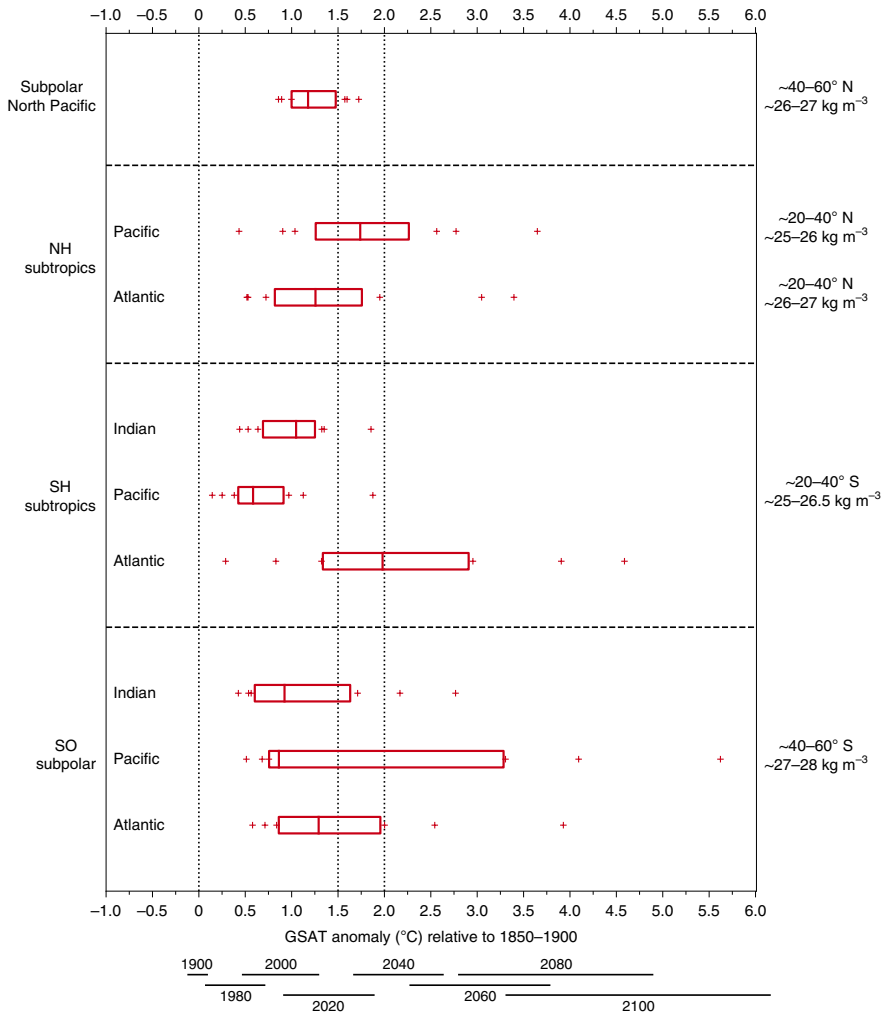

Fig. 4 | Distribution of GSAT at emergence. Calculated from the anthropogenic salinity signal and noise for each of the 11 models in nine regions of interest: the Southern Ocean subpolar range, the Southern Hemisphere subtropical range, the Northern Hemisphere subtropical range and the subpolar North Pacific (the exact coordinates for each model are shown in Supplementary Fig. 4). Red boxes indicate first quartile, median and third quartile. A date reference was added below the warming axis, spanning the range of the historical and RCP 8.5 simulations.

every year (1pctCO_2); that is, a much faster forcing than observed in the twentieth century or projected for the twenty-first century (see Supplementary Figs. 6 and 8 and CO_2 signal patterns in Supplementary Fig. 9). The overall agreement in the emergence of a climate signal in different water masses across the different models and the two types of very different timing of forcing scenarios (RCP 8.5, 1pctCO_2) offers confidence in simulated emergence patterns and confirms the dominant role of CO_2 emissions.

In analysing emergence timescales in the climate system, previous studies[20,21] showed that spatial patterns of ToE are strongly determined by the unforced variability, meaning that an earlier ToE arises in regions of weaker noise and vice-versa. We investigate whether this is the case by examining the relative contributions of signal and noise to the ToE regional pattern for each model, as well as the regional intermodel spread (see Supplementary Discussion and Supplementary Figs. 12 and 13). We find that the time-independent noise level is not sufficient to explain the ToE spread, which seems predominantly explained by the signal across regions and models; that is, either its strength or its decadal to multidecadal variability. This suggests that the low noise level of the ocean interior makes it a unique place for early detection of human-induced changes, even with the conservative estimate used here. Indeed, although the anthropogenic climate signal might appear at the surface first, strong background variability there can delay its emergence and counterintuitively earlier emergence can be found in the ocean interior, with geographical differences compared to the surface. Surface air temperature and sea surface temperature in the RCP 8.5 scenario were found to emerge mainly within the early-to-middle twenty-first century, showing strong regional differences with earlier emergence in the tropics due to the low noise level there than at higher latitudes[14,15,20]. ToE is especially late in the Southern Ocean for surface temperature, whereas we find the earliest emergence in this part of the world in the ocean interior. Half of the ocean area is expected to have emergent thermosteric sea level rise in the 2040s and, when including additional effects such as ice mass loss, as early as 2020[20]. It is interesting to see that the timing of emergence of

changing patterns occurs differently for different variables, probably a testimony of their distinctive interactions and feedbacks in the Earth system. This is clearly illustrated by the very diverse patterns and timing of emergence of the change in the different components of the ocean carbon cycle[26]. The diversity of climate variables investigated collectively provides a comprehensive understanding of the ToE of human-induced change in the Earth system, into which this study is contributing additional insight.

This work suggests that a large portion of the observed change patterns in the ocean interior is human-induced and will continue to intensify with continuing CO_2 emissions. If these patterns have been suggested to be primarily driven by an increased surface warming and water-cycle amplification[29,31] (two processes that directly affect heat and salt in the ocean thus density and circulation), understanding how these patterns will continue to amplify in the future in a more stratified upper ocean[41] and with possibly modified ocean circulation and mixing requires further investigation. In particular, deciphering which of the changing surface fluxes is likely to play a larger role, where and on what timescales, can be explored with model-specific flux-anomaly-forced model intercomparison project (FAFMIP)-like[42,43] mechanistic studies.

The hemispheric asymmetry in emergence, with earlier ToEs in the Southern Hemisphere subtropics is reminiscent of a number of recent studies stressing the importance of the Southern Ocean for ocean heat and carbon storage, associated with the overturning circulation[44–46]. It is noteworthy that this part of the world is historically the most poorly sampled and therefore the worst positioned for detecting a forced climate signal in observations[47,48]. The global pattern of human-induced fingerprint of ocean interior change can be used to guide the future development of a targeted global ocean observing system focused at monitoring and detecting future ocean change. The maintenance of this observing system along with continued investment in climate and ocean model development and evaluation, will provide the necessary measurements and model tools to best inform adaptation and mitigation strategies and policies going forward.

Online content

Any methods, additional references, Nature Research reporting summaries, source data, extended data, supplementary information, acknowledgements, peer review information; details of author contributions and competing interests; and statements of data and code availability are available at https://doi.org/10.1038/s41558-020-0878-x.

Received: 17 October 2019; Accepted: 16 July 2020;
Published online: 17 August 2020

References

1. Barnett, T. P., Pierce, D. W. & Schnur, R. Detection of anthropogenic climate change in the world's oceans. *Science* **292**, 270–274 (2001).
2. Reichert, B. K., Schnur, R. & Bengtsson, L. Global ocean warming tied to anthropogenic forcing. *Geophys. Res. Lett.* **29**, 20–4 (2002).
3. Barnett, T. P. et al. Penetration of human-induced warming into the world's oceans. *Science* **309**, 284–287 (2005).
4. Palmer, M. D., Good, S. A., Haines, K., Rayner, N. A. & Stott, P. A. A new perspective on warming of the global oceans. *Geophys. Res. Lett.* **36**, L20709 (2009).
5. Pierce, D. W., Gleckler, P. J., Barnett, T. P., Santer, B. D. & Durack, P. J. The fingerprint of human-induced changes in the ocean's salinity and temperature fields. *Geophys. Res. Lett.* **39**, L21704 (2012).
6. Gleckler, P. J. et al. Human-induced global ocean warming on multidecadal timescales. *Nat. Clim. Change* **2**, 524–529 (2012).
7. Tokarska, K. B., Hegerl, G. C., Schurer, A. P., Ribes, A. & Fasullo, J. T. Quantifying human contributions to past and future ocean warming and thermosteric sea level rise. *Environ. Res. Lett.* **14**, 074020 (2019).
8. Bilbao, R. A. F., Gregory, J. M., Bouttes, N., Palmer, M. D. & Stott, P. Attribution of ocean temperature change to anthropogenic and natural forcings using the temporal, vertical and geographical structure. *Clim. Dynam.* **53**, 5389–5413 (2019).
9. Terray, L. et al. Near-surface salinity as nature's rain gauge to detect human influence on the tropical water cycle. *J. Clim.* **25**, 958–977 (2012).
10. Stott, P. A., Sutton, R. T. & Smith, D. M. Detection and attribution of Atlantic salinity changes. *Geophys. Res. Lett.* **35**, L21702 (2008).
11. Swart, N. C., Gille, S. T., Fyfe, J. C. & Gillett, N. P. Recent Southern Ocean warming and freshening driven by greenhouse gas emissions and ozone depletion. *Nat. Geosci.* **11**, 836–841 (2018).
12. Mahlstein, I., Knutti, R., Solomon, S. & Portmann, R. W. Early onset of significant local warming in low latitude countries. *Environ. Res. Lett.* **6**, 034009 (2011).
13. Diffenbaugh, N. S. & Scherer, M. Observational and model evidence of global emergence of permanent, unprecedented heat in the 20th and 21st centuries. *Climatic Change* **107**, 615–624 (2011).
14. Hawkins, E. & Sutton, R. Time of emergence of climate signals. *Geophys. Res. Lett.* **39**, L01702 (2012).
15. Mora, C. et al. The projected timing of climate departure from recent variability. *Nature* **502**, 183–187 (2013).
16. Diffenbaugh, N. S. & Charland, A. Probability of emergence of novel temperature regimes at different levels of cumulative carbon emissions. *Front. Ecol. Environ.* **14**, 418–423 (2016).
17. Lehner, F., Deser, C. & Terray, L. Toward a new estimate of 'Time of Emergence' of anthropogenic warming: insights from dynamical adjustment and a large initial-condition model ensemble. *J. Clim.* **30**, 7739–7756 (2017).
18. Giorgi, F. & Bi, X. Time of emergence (TOE) of GHG-forced precipitation change hot-spots. *Geophys. Res. Lett.* **36**, L06709 (2009).
19. Mahlstein, I., Portmann, R. W., Daniel, J. S., Solomon, S. & Knutti, R. Perceptible changes in regional precipitation in a future climate. *Geophys. Res. Lett.* **39**, L05701 (2012).
20. Lyu, K., Zhang, X., Church, J. A., Slangen, A. B. A. & Hu, J. Time of emergence for regional sea-level change. *Nat. Clim. Change* **4**, 1006–1010 (2014).
21. Keller, K. M., Joos, F. & Raible, C. C. Time of emergence of trends in ocean biogeochemistry. *Biogeosciences* **11**, 3647–3659 (2014).
22. Rodgers, K. B., Lin, J. & Frölicher, T. L. Emergence of multiple ocean ecosystem drivers in a large ensemble suite with an Earth system model. *Biogeosciences* **12**, 3301–3320 (2015).
23. Frölicher, T. L., Rodgers, K. B., Stock, C. A. & Cheung, W. W. L. Sources of uncertainties in 21st century projections of potential ocean ecosystem stressors. *Glob. Biogeochem. Cycles* **30**, 1224–1243 (2016).
24. Henson, S. A. et al. Rapid emergence of climate change in environmental drivers of marine ecosystems. *Nat. Commun.* **8**, 14682 (2017).
25. Turk, D. et al. Time of emergence of surface ocean carbon dioxide trends in the North American coastal margins in support of ocean acidification observing system design. *Front. Mar. Sci.* **6**, 91 (2019).
26. Schlunegger, S. et al. Emergence of anthropogenic signals in the ocean carbon cycle. *Nat. Clim. Change* **9**, 719–725 (2019).
27. Banks, H. & Wood, R. Where to look for anthropogenic climate change in the ocean. *J. Clim.* **15**, 879–891 (2002).
28. Helm, K. P., Bindoff, N. L. & Church, J. A. Changes in the global hydrological-cycle inferred from ocean salinity. *Geophys. Res. Lett.* **37**, L18701 (2010).
29. Durack, P. J. & Wijffels, S. E. Fifty-year trends in global ocean salinities and their relationship to broad-scale warming. *J. Clim.* **23**, 4342–4362 (2010).
30. Durack, P. J., Wijffels, S. E. & Matear, R. J. Ocean salinities reveal strong global water cycle intensification during 1950 to 2000. *Science* **336**, 455–458 (2012).
31. Lago, V. et al. Simulating the role of surface forcing on observed multidecadal upper-ocean salinity changes. *J. Clim.* **29**, 5575–5588 (2016).
32. Zika, J. D. et al. Improved estimates of water cycle change from ocean salinity: the key role of ocean warming. *Environ. Res. Lett.* **13**, 074036 (2018).
33. Sallee, J.-B. et al. Assessment of Southern Ocean water mass circulation and characteristics in CMIP5 models: historical bias and forcing response. *J. Geophys. Res. Oceans* **118**, 1830–1844 (2013).
34. Heuzé, C. North Atlantic deep water formation and AMOC in CMIP5 models. *Ocean Sci.* **13**, 609–622 (2017).
35. Good, S. A., Martin, M. J. & Rayner, N. A. EN4: quality controlled ocean temperature and salinity profiles and monthly objective analyses with uncertainty estimates. *J. Geophys. Res. Oceans* **118**, 6704–6716 (2013).
36. Sallée, J.-B., Speer, K., Rintoul, S. & Wijffels, S. Southern Ocean thermocline ventilation. *J. Phys. Oceanogr.* **40**, 509–529 (2010).
37. de Lavergne, C., Palter, J. B., Galbraith, E. D., Bernardello, R. & Marinov, I. Cessation of deep convection in the open Southern Ocean under anthropogenic climate change. *Nat. Clim. Change* **4**, 278–282 (2014).
38. Heuzé, C., Ridley, J. K., Calvert, D., Stevens, D. P. & Heywood, K. J. Increasing vertical mixing to reduce Southern Ocean deep convection in NEMO3.4. *Geosci. Model Dev.* **8**, 3119–3130 (2015).
39. Dufour, C. O. et al. Preconditioning of the Weddell Sea polynya by the ocean mesoscale and dense water overflows. *J. Clim.* **30**, 7719–7737 (2017).

40. IPCC *Special Report on Global Warming of 1.5 °C* (eds Masson-Delmotte, V. et al.) (WMO, 2018).
41. Yamaguchi, R. & Suga, T. Trend and variability in global upper-ocean stratification since the 1960s. *J. Geophys. Res. Oceans* **124**, 8933–8948 (2019).
42. Gregory, J. M. et al. The flux-anomaly-forced model intercomparison project (FAFMIP) contribution to CMIP6: investigation of sea-level and ocean climate change in response to CO_2 forcing. *Geosci. Model Dev.* **9**, 3993–4017 (2016).
43. Todd, A. et al. Ocean-only FAFMIP: understanding regional patterns of ocean heat content and dynamic sea level change. *J. Adv. Model Earth. Syst.* https://doi.org/10.1002/essoar.10501557.1 (2020).
44. Gille, S. T. Decadal-scale temperature trends in the southern hemisphere ocean. *J. Clim.* **21**, 4749–4765 (2008).
45. Khatiwala, S. P. et al. Global ocean storage of anthropogenic carbon. *Biogeosciences* **10**, 2169–2191 (2013).
46. Frölicher, T. L. et al. Dominance of the Southern Ocean in anthropogenic carbon and heat uptake in CMIP5 models. *J. Clim.* **28**, 862–886 (2015).
47. Roemmich, D. et al. Unabated planetary warming and its ocean structure since 2006. *Nat. Clim. Change* **5**, 240–245 (2015).
48. Durack, P. J., Gleckler, P. J., Landerer, F. W. & Taylor, K. E. Quantifying underestimates of long-term upper-ocean warming. *Nat. Clim. Change* **4**, 999–1005 (2014).

Methods

Density binning of CMIP5 simulations. In this study, we use a suite of CMIP5 climate models binned into a neutral density framework, using the McDougall and Jackett[49] routine, to examine anthropogenic signals in the ocean on approximated neutral surfaces (γ^a) compared with natural climate variability. Zonal means are computed for each oceanic basin along neutral density surfaces, which allows for a more water-mass-centric assessment than is possible using a standard pressure level analysis. We note that some vertical movement (heave) of density surfaces can be due to climate change[50,51] but we don't investigate those here. In addition to providing a cleaner signal and reducing the noise, the density framework provides several other benefits, including a view of the ocean interior delineated by its water masses, useful for intermodel comparison[33,52], as water masses can be defined by their density range. Additionally, along density surfaces, salinity and temperature changes compensate and thus have the same structure and sign, and consequently the same emergence timescale.

To allow for a simpler and more intuitive visual representation, zonally averaged values are then remapped back to a pseudo-depth coordinate using a γ^a to pressure relationship derived from the observation-based product EN4 (ref. [35]) by a surface-to-bottom mapping of the ocean per density layer. Note that all remapping of this paper, irrespective of whether we are in the context of past, contemporary or future, is done with the exact same γ^a to pressure relationship which is based on contemporary observations. The remapping is purely a visual tool here, which does not introduce any signal: all signal, noise and ToE computations are done in γ^a space. All the data are trimmed at the bowl (that is, below the winter mixed layer depth), indicated by a dark grey shading in the figures.

ToE definition. ToE is computed both locally (for each gridpoint; Fig. 3) and regionally in a number of determined regions, using a manual fingerprint (that is, regional model-specific boxes fixed in time) to track the signal (Fig. 4). We use an ensemble of 11 models with a total of 35 realizations for the anthropogenic ToE and 13 single-member models for the CO_2 ToE (see Supplementary Table 1). The ToE is computed for each individual member, then intermember medians are derived, yielding a multimodel distribution with the same weight for each model and thus an estimate of the uncertainty.

The anthropogenic signal is 240 yr long, ranging from 1861 to 2100. Over the historical period (1861–2005), it is defined at each yearly time step as the salinity difference between the CMIP5 historical experiment (fully forced) and the time-averaged CMIP5 historicalNat value (natural forcings only: solar fluctuations and volcanic eruptions). Over the projection period (2006–2100), it is defined at each yearly time step as the salinity difference between the CMIP5 RCP 8.5 scenario ('business as usual') and the time-averaged historicalNat value (same baseline for both periods to ensure continuity). For each historical + RCP 8.5 ensemble member, the historicalNat time series used as the baseline of the signal is the ensemble mean if multiple members exist.

We note that the correct term for the signal defined above should be 'externally forced' as the influence of external natural forcings can be present during the historical period; however, considering the greater influence of human-induced forcings over time and especially in the ocean interior, we therefore refer to this signal as 'anthropogenic'. The possible influence of external natural forcings in the signal during the historical period will occur in terms of additional decadal to multidecadal variability.

The noise represents the bounds of background climate variability and is built from the interannual standard deviation of the historicalNat experiment (1861–2005, over 145 yr). Within several historical + RCP 8.5 members of a model, the noise is the same and is defined using the maximum standard deviation of all available historicalNat realizations within that model. The threshold of signal exceedance over noise is chosen at two on the basis of the large consensus in existing literature and because it represents a 95% confidence of signal emergence but sensitivity to this threshold is discussed in the Supplementary Information (see Supplementary Fig. 10). Overall, this definition makes it a rather high (thus conservative) estimate of the noise envelope (interannual noise, historicalNat choice instead of an annual mean pre-industrial control, two standard deviations as the threshold and picking the maximum among historicalNat members). The signal is considered to have emerged if it definitively exceeds the noise threshold at least 20 yr before the end of the projection to account for potential 'false' emergence—that is, if the signal were to go back within the bounds of climate variability afterwards[20,53]. Note that some internal variability (and natural variability over the historical period due to volcanic and solar forcings) remains in our signal definition, which is not exactly the purely forced response to anthropogenic forcings such as can be identified with the MMM of a large ensemble but is rather a change and thus more similar to what real observational time series would look like.

The historicalNat experiment is a coherent choice for estimating natural climate variability as it accounts for internal variability as well as external natural forcings, both included in the forced experiments. However, we do test how our results are affected by using the pre-industrial control (no external forcings) instead of the historicalNat experiment in defining the noise, as is often done, and do not find the ToE distributions to be much altered (see Supplementary Fig. 11). The change driven by the CO_2 forcing alone can be estimated in a similar way, by taking the salinity difference between the yearly idealized 1pctCO_2 experiment (140 yr) and the mean value of the pre-industrial control. The noise for CO_2 ToE is then defined as the standard deviation of the pre-industrial control over the last 240 yr (to have the same noise definition as done in Supplementary Fig. 11 for the turquoise boxes).

ToE distribution of basin zonal means. The gridpoint-per-gridpoint ToE distribution is calculated on the basis of the methodology described by Lyu et al.[20]. A signal is considered to have emerged if its ToE is at least 20 yr earlier than the end of the time series (2080 for the RCP 8.5, 120 for the 1pctCO_2). At each gridpoint, the signal of each model realization can emerge with either a positive (salinity increase) or negative (freshening) change, or not emerge at all and stay within the bounds of natural climate variability. The distribution can be calculated if at least half of the runs emerge with the same sign of the signal or at least half of the runs show no emergence and if the outliers that have a different direction of change are less than 5 (5 for the anthropogenic signal, 1 for the pure CO_2). We then compute the distribution by excluding the outliers, first by computing the intermember medians, then the multimodel distribution using these medians so as to give each model the same weight. If the conditions are not met, the location is labelled as 'no agreement'. See supplementary material of ref. [20] for details and examples.

Manual fingerprint. The regional ToEs are calculated by averaging both signal and noise in selected regions (see Fig. 2b). Namely, we defined: the Southern Ocean subpolar range, encompassing signal associated with upper circumpolar deep water (around 40°–60° S; 27–28 kg m^{-3}); the Southern Ocean subtropical range, encompassing signal associated with mode and intermediate waters (around 20°–40° S; 25.0–26.5 kg m^{-3}); the Northern Hemisphere subtropical range, encompassing signal associated with Atlantic and Pacific mode waters (around 20°–40° N; 25–26 kg m^{-3} in the Pacific; 26-27 kg m^{-3} in the Atlantic) and the subpolar North Pacific, encompassing signal associated with the North Pacific intermediate waters (around 40°–60° N; 26-27 kg m^{-3}). The boxed coordinates are model-specific and were fixed (in γ^a space) on the basis of the zonally averaged spatial pattern of the signal at the end of the time series (see Supplementary Fig. 4). The regional emergence of the signal (Fig. 4) is based on a manual fingerprint for each region displayed, thus slightly sensitive to the precise boxes used. The patterns of change that already exist in the historical forced simulations continue to exist in the same locations and enhance in the twenty-first century simulations, giving us confidence in using boxes fixed in time.

Warming scale. Global surface warming at emergence was computed by taking each run's GSAT (historical + RCP 8.5) smoothed with a 10-yr running mean, at the ToE in each region. GSAT anomaly is calculated relative to the 1850–1900 period. The same was done for the 1pctCO_2 GSAT (Supplementary Fig. 8).

Percentage of basin emergence. We define the percentage of emerged area in basin zonal means and under the surface bowl at each time step by computing the cumulative sum over each basin of the number of grid cells that have emerged before that time step, weighted by the thickness of their respective density layer; and dividing it by the cumulative sum of each grid cell's isopycnal thickness of that same basin zonal mean. The result is given in terms of area as the latitudinal grid is regular with a 1° resolution (all models were interpolated on that same horizontal regular grid). This is done for every model simulation, then the intermember medians are computed. Shown in Fig. 3b are the median, first and third quartiles of the multimodel distribution.

Data availability

All CMIP5 model data used in this paper are available through the Earth System Grid and freely available for download (https://esgf-node.llnl.gov/search/cmip5/).

Code availability

The analysis code for this paper is written in Python and is available on GitHub (https://github.com/ysilvy/ocean_toe_2020)[54]. The density binning code and data are available upon request to the authors.

References

49. McDougall, T. J. & Jackett, D. R. The material derivative of neutral density. *J. Mar. Res.* **63**, 159–185 (2005).
50. Häkkinen, S., Rhines, P. B. & Worthen, D. L. Warming of the global ocean: spatial structure and water-mass trends. *J. Clim.* **29**, 4949–4963 (2016).
51. Desbruyères, D., McDonagh, E. L., King, B. A. & Thierry, V. Global and full-depth ocean temperature trends during the early twenty-first century from argo and repeat hydrography. *J. Clim.* **30**, 1985–1997 (2017).
52. Iudicone, D. et al. Water masses as a unifying framework for understanding the Southern Ocean carbon cycle. *Biogeosciences* **8**, 1031–1052 (2011).
53. Hawkins, E. et al. Uncertainties in the timing of unprecedented climates. *Nature* **511**, E3–E5 (2014).
54. Silvy, Y. ocean_toe_2020 v1.0.0. Github repository (2020); https://doi.org/10.5281/zenodo.3944613

Acknowledgements

We thank C. de Lavergne, A. Fedorov, P. Gleckler, J. Gregory, E. Hawkins, G. Madec, H. Mercier, J. Mignot, B. Santer and L. Terray for helpful discussions. We acknowledge the support from the Make Our Planet Great Again project ARCHANGE (Agence Nationale pour la Recherche project no. ANR-18-MPGA-0001) from the European Research Council under the European Union's Horizon 2020 research and innovation programme (grant no. 637770) and from the Centre National de la Recherche Scientifique. We also acknowledge the CMIP5 modelling groups, the ESGF and IPSL/ESPRI-MOD data distribution systems. The work of P.J.D. was prepared by Lawrence Livermore National Laboratory (LLNL) under contract no. DE-AC52-07NA27344 and is a contribution to the US Department of Energy, Office of Science, Climate and Environmental Sciences Division, Regional and Global Modeling and Analysis Program (LLNL release no. LLNL-JRNL-794900).

Author contributions

The density binning of CMIP5 data was designed and performed by E.G. and P.J.D. All subsequent analysis for this paper was performed by Y.S. and supervised by E.G and J.-B.S. Observational data were provided by P.J.D. All authors contributed to interpreting the results and writing the manuscript.

Competing interests

The authors declare no competing interests.

Additional information

Supplementary information is available for this paper at https://doi.org/10.1038/s41558-020-0878-x.

Correspondence and requests for materials should be addressed to Y.S.

Peer review information *Nature Climate Change* thanks Veronique Lago, Nadya Vinogradova-Shiffer and the other, anonymous, reviewer(s) for their contribution to the peer review of this work.

Reprints and permissions information is available at www.nature.com/reprints.

3 Extension to the IPSL-CM6A-LR large ensemble

The Institut Pierre Simon Laplace (IPSL) participated in CMIP6, with the development and configuration of a new coupled model, IPSL-CM6A-LR [Boucher et al., 2020, Mignot et al., 2021], using it to run the many experiments requested by CMIP6, through a large community effort that lasted over several years.

32 historical members were run with the IPSL-CM6A-LR model, enabling a large sampling of internal variability (each member was initialized at a different year of the 2000-year pre-industrial control simulation). The idea behind is that very little is known about the oceanic conditions in 1850; starting the historical simulations from different initial conditions of internal variability (such as different phases of the AMOC) allows to span a range of possible initial states [Hawkins et al., 2016]. Averaging across members is a way to remove (some of) the noise of internal climate variability and isolate the forced response since all members have the same external forcings but different initial states of internal variability. The historical simulations are defined for the period 1850-2014 and the scenarios for 2015-2100 (scenarios in CMIP6 changed from RCPs to SSPs - Shared Socioeconomic Pathways). An extended set of simulations (entitled historical-EXT) outside of the CMIP6 request was run with the same 32 historical members for the period 2015-2059 following ssp245 [Bonnet et al., 2021a]. This is a considerable addition since the regular scenario experiments with IPSL-CM6A-LR have 6 to 11 members depending on the scenario.

In chapter II, we will explore different ways of investigating forced changes in this ensemble of historical extended simulations. Here, we extend the work of the study presented above by running similar analyses with this large ensemble of 30 members (2 members had data transfer problems) and different ssp scenarios to fully test the dependence of the ToE results on the emissions scenario.

We find similar structures of change in IPSL-CM6A-LR (figure I.1, middle panels) compared to the CMIP5 models and ensemble mean of the previous published study (figure I.1, top panels; note we compare different amplitudes of change: the CMIP5 Multi-Model Mean (MMM) is computed for the end of the century under RCP8.5 instead of the mid-century under SSP2-4.5 for IPSL-CM6A-LR). One main difference lies in the sign of the change in the northern tropical Atlantic where there is a clear subsurface freshening in IPSL-CM6A-LR instead of the opposite change in the CMIP5 MMM, illustrating a possible strong bias of this model. The freshening in the southern subtropical Pacific ocean is also much weaker compared to the CMIP5 MMM, in which it was the most prominent pattern. Associated to the changing structures in IPSL-CM6A-LR, we find structures of ToE (figure I.1, bottom panel) with very similar time scales as in the CMIP5 study, i.e. an emerged signal between the late 20th century and the early decades of the 21st century, with much of the patterns already emerged by 2020 (bold black line). The southern subtropical Pacific ocean shows little emerging signal, consistent with the weak freshening.

Note here for data reasons we have used the intermember standard deviation for the noise estimate instead of the piControl standard deviation. We will see in chapter II that this makes little difference, provided deep ocean drift has been removed (see below and chapter II for the discussion on drift).

This time, with the IPSL-CM6A-LR model, we compare the ToE in different emissions scenarios, shown in figure I.2 for ssp245, ssp460 and ssp585, with 6 members each (branching from the same historical members). We note the historical-EXT (30 members following ssp245, figure I.1 bottom panels) and ssp245 (6 members, figure I.2 upper panels) patterns of ToE are very similar, showing a good intermember coherence and almost no hidden emergence by the historical-EXT experiment which is limited to 2059. Furthermore, we see very little differences in the structures and the timing of emergence between the 3 ssp scenarios (figure I.2), confirming that when a change pattern emerges in the ocean, it does so before there are significant differences in surface warming scenarios. Additionally, when there is no emergence (grey areas), a stronger warming scenario doesn't induce one. This suggests human influence and its continued emissions have already set the patterns of signal emergence in the ocean for the 21st century.

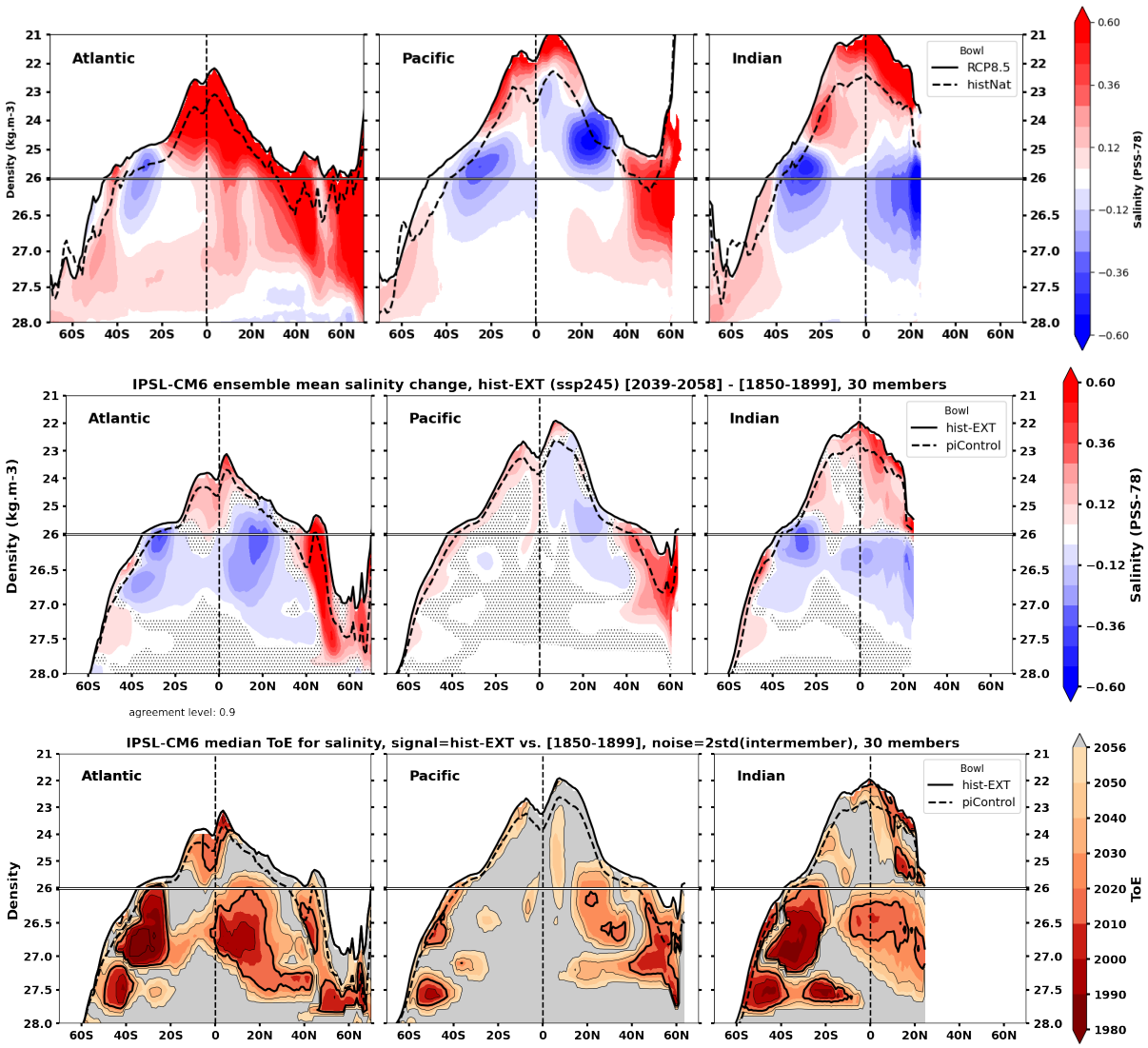

Figure I.1: (Top) Same as Fig. 2b of Silvy et al. [2020] but in the original density space: CMIP5 multi-model mean salinity change in the last 20 years of RCP8.5 [2081-2100]. (Middle) IPSL-CM6A-LR (historical-extended) ensemble mean salinity change in the mid-21st century and (bottom) ensemble median time of emergence, in basin zonal means. The bold black lines in the bottom panel indicate year 2020. Note emergence is capped at year 2056 since the historical-EXT experiment does not continue further than 2059 in the 21st century and due to a few years missing after the density binning.

4 Caveats and discussion

4.1 Model drift

One significant limit of this study lies in the fact that model drift was not removed before conducting the ToE analysis. This choice was made in the density binning project, as the density projection provides a zoom on the upper ocean with very little drift. Residual drift can indeed persist in climate models, particularly in the deep and abyssal ocean, even after a long spin-up, when the ocean is still not in equilibrium with the atmospheric forcing [Gupta et al., 2013, Irving et al., 2020].

Since drift in temperature or salinity is rarely significant in the upper ocean, omitting to remove it from the CMIP5 outputs should not impact (or very little) the ToE analysis in the water-masses delineated in our study. However, drift is often non-negligible below 2000m (i.e. in the very last density bins) in a number

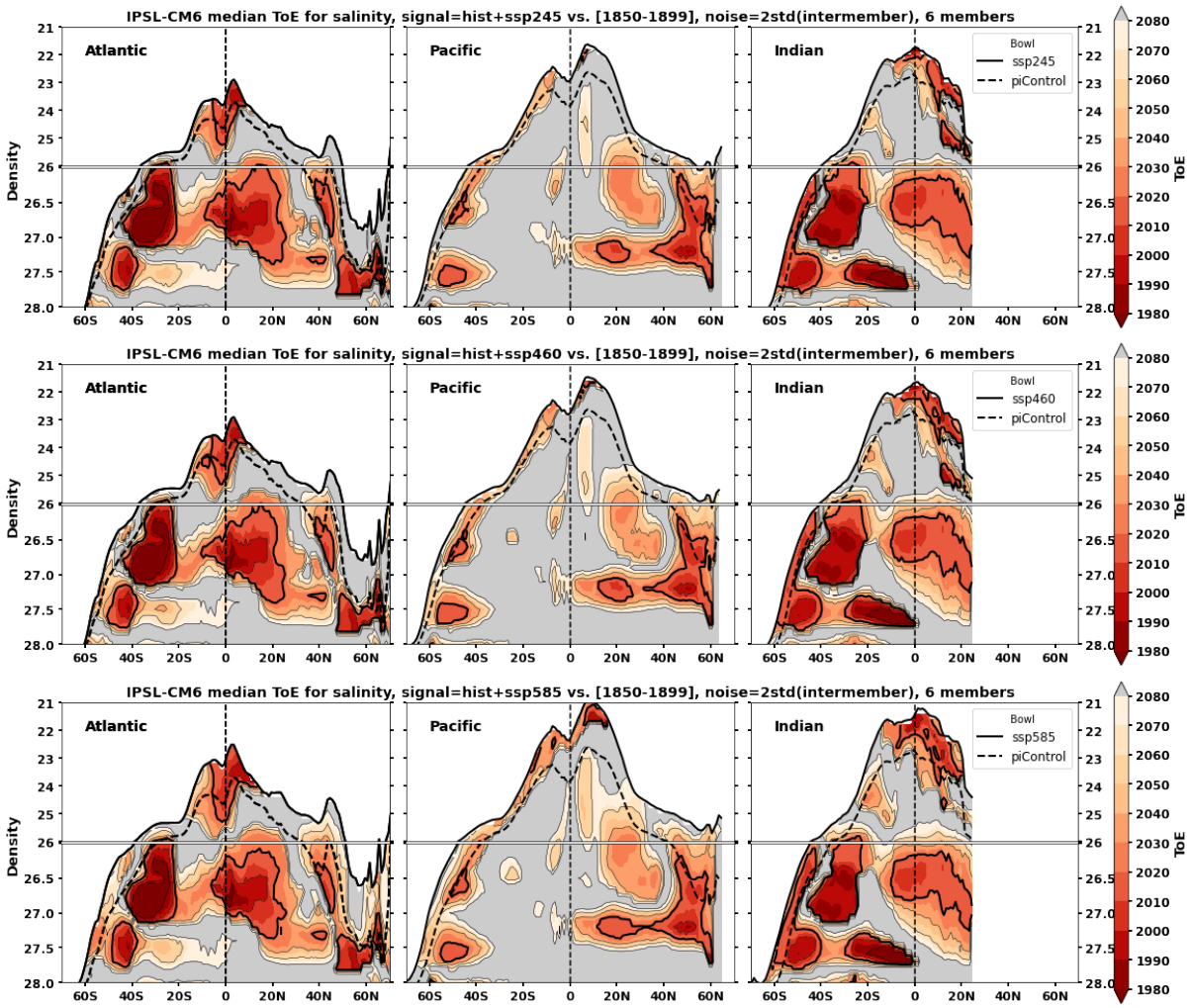

Figure I.2: Ensemble median Time of Emergence for the ssp245, ssp460 and ssp585 scenarios (6 members each).

of models, contaminating the forced signal in the historical simulations as well as the noise envelope from piControl runs, and thus the time scales of emergence of this signal from internal variability noise. For example, the IPSL-CM6A-LR model has a quasi-linear cooling drift in global mean ocean temperature of about -0.13 W.m^{-2} in the 2000-year pre-industrial control experiment (see Mignot et al. [2021] and also the next chapters of this thesis). Signs of this drift can be seen in figure I.1 in the middle panels, where there is a consistent sign in the change between members in the deep Pacific Ocean (no stipples between 27.5-28 kg.m^{-3}), but no emergence because of the large spread in the member's initial state leading to an anomalously large intermember standard deviation (see chapter II). This drift arises from a negative net surface heat flux into the ocean over the piControl experiment (the heat budget of the ocean component is closed, the drift is thus purely physical and not due to e.g. numerical errors), illustrating an imbalance between the atmospheric and ocean physics in the coupled model, and is transmitted to the deeper ocean below 2000m (i.e. upper ocean temperatures don't drift but the deep ocean does as anomalies are stored there on long time scales). Interestingly, when the same ocean model used in IPSL-CM6A-LR (NEMO3.6) is forced with reanalysis atmospheric forcing instead of the LMDz atmospheric model, the same drift exists in the first hundred years of the simulation but is slowly reduced after over a thousand years of simulation (Casimir de Lavergne, personal communication), which is not the case in the coupled model. A debate is undergoing to determine whether the cooling drift will eventually disappear if the coupled model is run long enough. We examine the impact of this drift in chapter II.

4.2 The heave-spice decomposition

Looking at zonal mean temperature and salinity on density levels instead of pressure has a number of advantages for better capturing water-mass geographies. Namely, computing zonal means along isopycnal layers has more physical sense than on pressure levels, which also holds for a model inter-comparison exercise where the water-masses are better aligned in that framework (although models don't necessarily produce water-masses with identical densities due to different mean states). Changes along density levels are also commonly extractable from observations (e.g. Durack and Wijffels [2010], Helm et al. [2010], Purkey and Johnson [2013], Desbruyères et al. [2014], Häkkinen et al. [2016], Desbruyères et al. [2017], Wang et al. [2021]) and so comparable to model outputs.

However, adopting this framework also means we are not capturing the full signal (for a local observer) but only the density-compensated part ("spice"), commonly conceptually explained as "water-mass property changes" (that is, if water-masses are defined and centered on constant densities through time, which is only a partial view of what a water-mass is). The other part of the signal, "heave", is manifested on multi-decadal time scales as a widespread deepening of almost all isopycnals in response to global warming bringing additional heat into the ocean [Häkkinen et al., 2016, Desbruyères et al., 2017]. A local observer, like a fish, will perceive both spice and heave signals, i.e. the total change at a given depth. For a complete impacts study, the total change should thus be considered, although every framework has its limits (such as zonal means along pressure levels that mix different water-masses together).

The isopycnal displacement signal at the end of the 21st century is shown in figure I.3 (top) in density space for the CMIP5 MMM, displaying an almost widespread deepening (positive downward). The associated ToE of this heave signal is also presented here (figure I.3, bottom), showing similar time scales as those found in the spice signal, with more widespread emergence and more robust features (i.e. better model agreement on the sign of the signal). The Southern Ocean Mode and Intermediate waters stand out again as the regions with the earliest emergence of the deepening signal ($\sim$1980s), although the strength of the signal is similarly as large at the end of the century in other regions such as the subpolar North Atlantic where the stronger noise delays the emergence.

The main advantages usually presented when looking at property changes along isopycnals is that it removes the effect of dynamically-driven isopycnal displacements (caused by e.g. eddies, internal waves) that can change properties on pressure surfaces without any changes along density surfaces. However, we have seen that on multi-decadal time scales, the main cause of isopycnal deepening is the widespread warming of anthropogenic origin. We note long-term changes in the winds can also add to the isopycnal deepening. Hence, heave is also a marker of long-term changes in surface fluxes. For example, a warming originating from an increased heat flux into the ocean, propagating from the surface to the interior (the "pure warming" process from the Bindoff and Mcdougall [1994] framework), has a signature both on isopycnal displacement and on along-isopycnal changes. The spice and heave mathematical decomposition, in this context, does not provide a sufficient framework to separate different physical mechanisms, as they can be related to the same driver. However, solving the system for pure warming, pure freshening and pure heave, as proposed by Bindoff and Mcdougall [1994], is a useful application to interpret sources of change from temperature and salinity analyzed on both pressure and density levels.

Lyu et al. [2020] applied the Bindoff and Mcdougall [1994] framework to understand the processes driving Southern Ocean upper ocean temperature and salinity changes in the CMIP5 ensemble of the 21st century RCP8.5 scenario. They solved the proportion of pure warming, pure freshening and pure heave and found that the mid-latitude warming and deepening of isopycnals could be explained by a combination of pure warming and pure heave, coherent with the additional heat input into the ocean at high latitudes transported northward and subducted by the background circulation and with the response to enhanced and poleward shifted westerly winds. They also found that the mid-latitude freshening was coherent with the pure freshening process, driven by excess precipitation at high latitudes and northward subduction of the freshened waters.

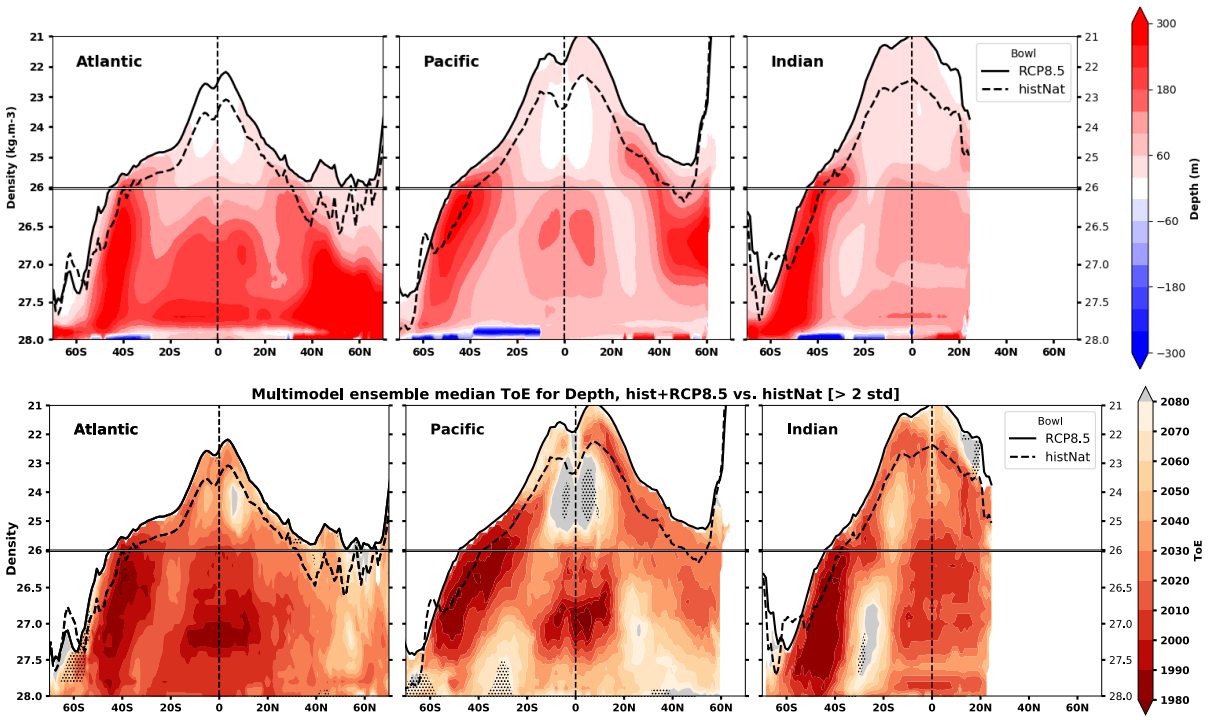

Figure I.3: (top) Multi-model ensemble mean change in isopycnal depth (positive downward) and (bottom) median time of emergence. Same method as in the paper.

Overall, I have found that looking at changes along density surfaces alone has a certain ambiguity. Indeed, the drivers of change in terms of physical mechanisms remain entangled, and the density-compensating framework makes it hard to understand which variable -temperature or salinity- is leading, or whether the appeared sign of the change is simply a consequence of the heave/spice decomposition. Furthermore, density space gives more emphasis to the upper ocean (which has strong density gradients) than to the deep and abyssal ocean (with very low gradients, i.e. contracted to a few bins). Since the observational analyses have mainly focused on the top 2000m of the ocean, this was appropriate. But when looking at changes deeper than 2000m, the density space compresses these parts of the ocean, making it harder to interpret changes in their geographical structure. The heave/spice framework and the sign of the possible changes according to the stability ratio of the ocean have been detailed in earlier papers from the 1990s and 2000s.

Overall, our understanding is that decomposing thermohaline changes into changes along density surfaces and vertical movement of isopycnals is not necessarily a way to separate physical mechanisms but it is a mathematical decomposition, that mixes the pure warming, pure freshening and pure heave processes. For instance, a downward displacement of an isopycnal layer (heave) can result both from a pure warming signal which will change the temperature along both pressure and density surfaces, but also from a pure heave signal related to circulation changes. Breaking down temperature and salinity changes on pressure surfaces into spice and heave components is thus not enough to allow for a formal decomposition into heat, freshwater and wind stress individual perturbations. Solving the pure warming, pure freshening and pure heave mechanisms however requires to know both changes on pressure and density surfaces, as well as the vertical gradients and isopycnal displacements.

5 Key points

- In this chapter, we presented a multi-model analysis of anthropogenic salinity changes along density levels in the ocean, in basin zonal means.
- We have found that models generally reproduced the observed large scale structures of change, although on lighter density levels, and with important differences in basins where the zonal average potentially mixes up different sub-basin signals, such as the northern Indian ocean and the subpolar North Atlantic.
- Using Time of Emergence diagnostics, we showed that in the regions that already expressed robust changes across models in the historical period, these changes were found to emerge from background climate variations between the late 20th century and the first decades of the 21st century in the multi-model median, with an inter-model range of several decades.
- We focused on a few regions, with a manual delineation to take into account each model's specific water-mass geography, and looked at the emergence as a function of global mean surface warming as well as time, finding that some regions emerged before the 1.5ºC threshold with weaker inter-model spread in mid-latitude water-masses (except for the southern Atlantic basin) than in the southern high latitudes, where model agreement is lower.
- Consistent with Banks et al. [2000], we found earlier emergence of the anthropogenic signal in the Southern Hemisphere mode waters than in their Northern Hemisphere counterparts. This feature is also found when looking at the isopycnal long-term displacement in the water column.
- We find similar time scales of emergence in the IPSL-CM6A-LR model, although the internal organization of water-masses is different in some places than in the CMIP5 multi-model mean.
- Overall, these results point to the ocean Mode Waters as particularly good places to detect anthropogenic climate signals, with earlier detection in the Southern Ocean, providing a different view than just looking at the surface, mapping out how these signals are spread and organized in the ocean interior.

Chapter

II

Detecting forced ocean changes in the IPSL-CM6A-LR large ensemble

Contents

1 Introduction

When looking at changes in climate variables, a multi-model analysis, such as the one presented in Chapter I, can mix up different types of uncertainties, essentially uncertainties originating from internal variability and from model-to-model differences [Hawkins and Sutton, 2009]. Especially in the case where there are few members of the historical and scenario simulations per model, the difference between the realizations of two different models could be due to either different phases of internal variations or different model physics (including how internal variations are represented and how much a model warms in response to increasing greenhouse gases). How much of the spread in Time of Emergence presented in the previous chapter is due to model differences or internal variability is thus not quantifiable with the

small number of members that were available. In this Chapter, we address the uncertainty associated with internal variability in a single model, leaving out model-to-model differences.

Members in an ensemble are forced by the same external forcings and differ only by their initial conditions, so that when a large enough number of members are performed, internal variability can be averaged out. Large initial-condition model ensembles (also referred to as SMILEs - Single Model Initial-condition Large Ensembles, see https://large-ensemble.github.io) provide a robust way to isolate the forced response across members, and estimate the intrinsic climate variability within a single model in transient simulations [Deser et al., 2020]. Large ensembles have been used for many purposes in identifying forced long-term signals compared to internal variability. These include investigating the uncertainty in the emergence of surface warming (e.g. [Deser et al., 2012, Lehner et al., 2017]), detecting the warming pattern in atmospheric observations [Santer et al., 2019] and detecting trends in ocean biogeochemical variables [Rodgers et al., 2015, Schlunegger et al., 2019]. One study used a large ensemble to detect and attribute observed changes in upper ocean temperature and salinity in the Southern Ocean [Swart et al., 2018]. Some mechanistic studies have also been lead to understand the role of internal variability on decadal time scales [Maher et al., 2020, Bonnet et al., 2021b]. Furthermore, estimating internal variability by the across-member spread in externally-forced simulations enables to account for potential effects of external forcings on internal variability (e.g. Maher et al. [2015], Swingedouw et al. [2017]) which are not taken into account in unforced pre-industrial simulations. Large ensembles have thus proven to be very useful tools, and quite relevant for the questions raised in this thesis.

How the members in such ensembles are initialized, their number and the period on which they are run varies from one model to the other. Initialization can be performed by branching the historical members start date from different states in a multi-century piControl simulation (e.g. the MPI grand ensemble [Maher et al., 2019]), as in the CMIP protocol. This is referred to as macro-initialization, and spans different possible oceanic as well as atmospheric conditions. Micro-initialization refers to applying infinitesimal perturbations in the initial atmospheric state (such as air temperature) of each member (e.g. the CESM large ensemble [Kay et al., 2015], where the members are branched in 1920 from a historical simulation that started from 1850 conditions). The range of internal variations expressed in a macro-initialized ensemble is larger than when initializing from atmospheric conditions alone [Hawkins et al., 2016]. Another similar initialization method consists in branching the members from a given year in a historical simulation, and use consecutive days of a given month as the start date. For example, the GFDL-ESM2M large ensemble [Rodgers et al., 2015] used conditions from 1-29 January 1950 as the initial state for January 1st for each of the 29 members, meaning different initial conditions for both the atmosphere and ocean components. One ensemble using the CanESM2 model has used both micro and macro initialization [Kirchmeier-Young et al., 2017]. With CMIP6 taking place in recent years, many other modelling groups have now run ensembles of a "large" number of historical members (often 30-50 members, sometimes followed by many members of the SSPs), all macro-initialized from piControl conditions (see a temporary table of the CMIP6 models with more than 15 historical members here: https://www.cesm.ucar.edu/projects/community-projects/MMLEA/). Finally, some ensembles have also run single-forcing simulations for the historical+future period, enabling attribution analyses.

Here, I will focus on the IPSL-CM6A-LR large ensemble of historical-extended simulations published partly for CMIP6 [Bonnet et al., 2021a], which was briefly introduced in Chapter I and will be one of the tools for the second part of this thesis (Chapters III and IV). Before exploring some of the mechanisms causing the emergence of oceanic thermohaline changes in the ensemble in Chapter IV, I will discuss here possible methods and frameworks with which we can investigate the emergence or detection of forced signals in the context of this large ensemble. This transitional chapter is meant as a bridge between the multi-model analysis of chapter I using only one method to look at the emergence of thermohaline changes in the ocean interior, and the single model, more mechanistic approach used in the next chapters. Here, I will more fully introduce and explore the framework of the large ensemble to look at ocean interior temperature and salinity changes in response to increasing anthropogenic forcings.

There have been multiple ways proposed in the literature to investigate the emergence or the detection of long-term changes, and many definitions of signal and noise (computing linear trends or running means, applying low-pass filters, extracting an ensemble average, regressing onto a searched-for fingerprint, and many more statistical tools). Here, I will not go over all these possible methods, but the idea is to show a couple of examples of the methods that can be applied to the large ensemble, in different analysis frameworks, and discuss the advantages and drawbacks of each, and what understanding they bring. The first part will be dedicated to a local approach as adopted in Chapter I (Time of Emergence analysis), and the second to a pattern-based approach which I will introduce. The coordinate systems and spatial averaging frameworks used here will be more simple or intuitive than the density framework employed in Chapter I, namely zonal mean temperature and salinity (along standard pressure surfaces) and vertically-integrated heat and salt contents, which we will work with again in Chapter IV. The patterns of thermohaline changes in these frameworks will not be described in details or given too many possible mechanistic interpretations since this is the subject of Chapter IV. Before presenting these analyses, I will briefly introduce the ensemble again and the drift removal procedure.

2 Model and drift removal

IPSL-CM6A-LR [Boucher et al., 2020] is the coupled model developped by the Institut Pierre-Simon Laplace modelling center for CMIP6 [Eyring et al., 2016]. It is composed of the LMDZ6A-LR atmospheric model [Hourdin et al., 2020], the ORCHIDEE land surface model [Krinner et al., 2005] version 2.0 and the NEMO3.6 ocean model [Madec et al., 2017]. The atmospheric component has a horizontal resolution of 2.5ºx1.3º on a regular latitude-longitude grid and 79 vertical layers, while the ocean component uses the eORCA1 tripolar grid with a nominal horizontal resolution of 1º refined to 1/3º at the equator, with 75 vertical levels with varying thicknesses. The ocean physics component of NEMO3.6 is coupled to the LIM3 sea-ice model [Rousset et al., 2015] and to the PISCES-v2 biogeochemical model [Aumont et al., 2015]. The oceanic equation of state is estimated with a polynomial representation of TEOS-10 [Roquet et al., 2015]; the model prognostic fields are thus conservative temperature and absolute salinity.

An ensemble of 32 extended historical simulations was performed with the IPSL-CM6A-LR model (see Bonnet et al. [2021a] for the presentation of the ensemble), following the CMIP6 protocol for the historical period 1850-2014 and extended to 2059 following the ssp245 scenario - apart from the ozone field which was kept constant to its 2014 values due to missing forcings at the time when the extensions were performed. The 32 members were initialized at different branch points of a long piControl experiment, spaced 20 to 40 years apart (macro-initialization). Some files were missing for member r2i1p1f1 and r16i1p1f1, so we only considered the other 30 members for the analysis. The initialization procedure enables the ensemble to adequately sample the dominant, low-frequency mode of variability present in the model. Indeed, the IPSL-CM6A-LR model has a bi-centennial mode of variability affecting the AMOC and linked to low-frequency variability in the freshwater exchanges between the North Atlantic and the Arctic basins (this is explored by Jiang et al. [2021]). As a result, this bi-centennial variability modulates Global Surface Air Temperature (GSAT) trends [Bonnet et al., 2021a]. We illustrate this in figure II.1, showing global mean SST and the AMOC evolution in the 2000-year piControl and in each historical-extended simulation branched at a different point in the piControl. The first decades of the historical simulations are driven by the low-frequency oscillations of the piControl. Because the members sample different phases of these oscillations, averaging across them removes the effect of the decadal and centennial oscillations and isolates the forced signal (bold orange line in the inset plots in figure II.1). When the effects of greenhouse gases rapidly rise up in the 21st century, the ensemble spread around the mean decreases as the forced signal takes over internal variations.

The observed GSAT anomaly has been found to lie within the spread of the ensemble [Boucher et al., 2020], although the ensemble mean warms more towards recent years. Observed global ocean heat content change in the upper 2000m fits with the ensemble mean for the period 1970-2018, although the

ensemble mean warms more than observations in the 0-700m range and has lower warming in the 700-2000m [Bonnet et al., 2021a], a feature possibly explained by the overestimated stratification of the model [Boucher et al., 2020].

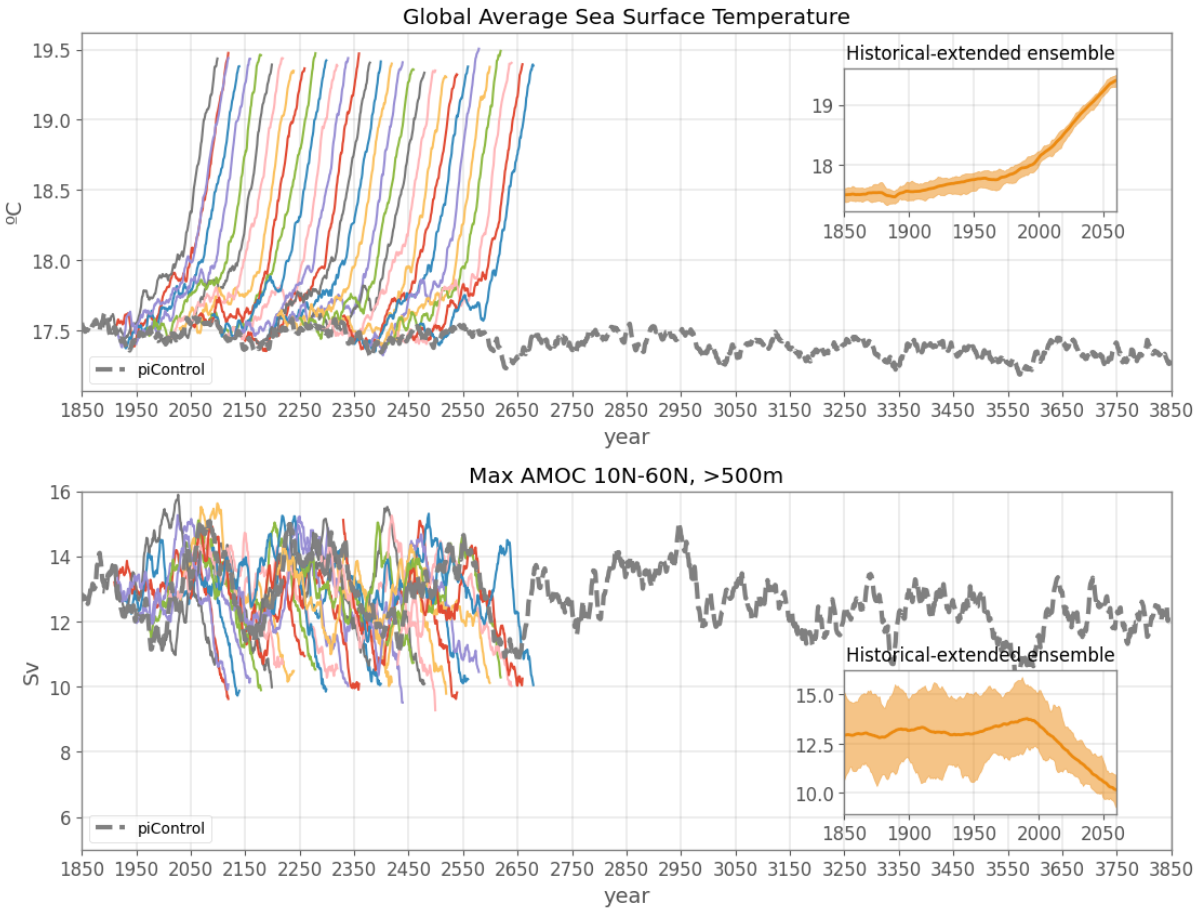

Figure II.1: Global mean SST (top) and maximum of the meridional overturning streamfunction between 10ºN and 60ºN in the Atlantic basin (bottom) in the 2000-year piControl run (grey) and in the historical-extended members (colored lines, plotted from their branch point in the piControl). The historical-extended ensemble is also shown in the inset plots, put back on the 1850-2100 axis.

The piControl in IPSL-CM6A-LR has a quasi-linear cooling drift in global mean ocean temperature (corresponding to a heat flux of about -0.13 W.m^{-2}), particularly marked below 2000m, originating from a mean net surface heat loss [Mignot et al., 2021]. This drift is propagated in the historical simulations branching from different points in the piControl and strongly influences the temperature evolution of the deep ocean, as shown in figure II.2 (top left panel and inset plot top right panel). The drift in salinity has a more quadratic shape at the global scale and is much less important than the temperature drift (0.7ºC difference in temperature below 2000m during the 2000-year piControl, versus 0.02 pss between the low and high points). Removing the temperature and salinity drift is necessary before analyzing any long-term changes and trends. Because we will use information at the grid point level in the following analyses, the drift needs to be removed at each grid point.

We show in Appendix B the time series for a few example grid points in the 2000-year piControl and at different depths. This reveals that the drift in temperature and salinity is mostly present at depth. In regions of strong low-frequency internal variability, such as the Atlantic ocean, the cooling trend is superimposed on the (bi)-centennial variations characterising this model. In regions less affected by internal variability, such as the deep Pacific ocean, the evolution of temperature is quasi-linear with very

small variations around the cooling trend. The sign of the drift in salinity depends on the region of the ocean. In the North Atlantic for instance, the evolution of salinity has a negative trend on top of the large low-frequency variations (similarly to temperature), when in the South Atlantic it has a positive trend. In the Pacific and Indian oceans, deep ocean salinity has a marked quadratic drift. For consistency between temperature and salinity, we thus fitted a 2nd order polynomial to the 2000-year piControl annual means at every grid point, knowing that the quadratic fit captures the linear trends anyways. Fitting over the longest possible period allows to isolate the drift without mistakenly picking low-frequency modes of internal variability (such as the bi-centennial mode in the North Atlantic) [Gupta et al., 2013]. Moreover, in the upper ocean where there is barely any drift, the quadratic fit will simply capture no change.

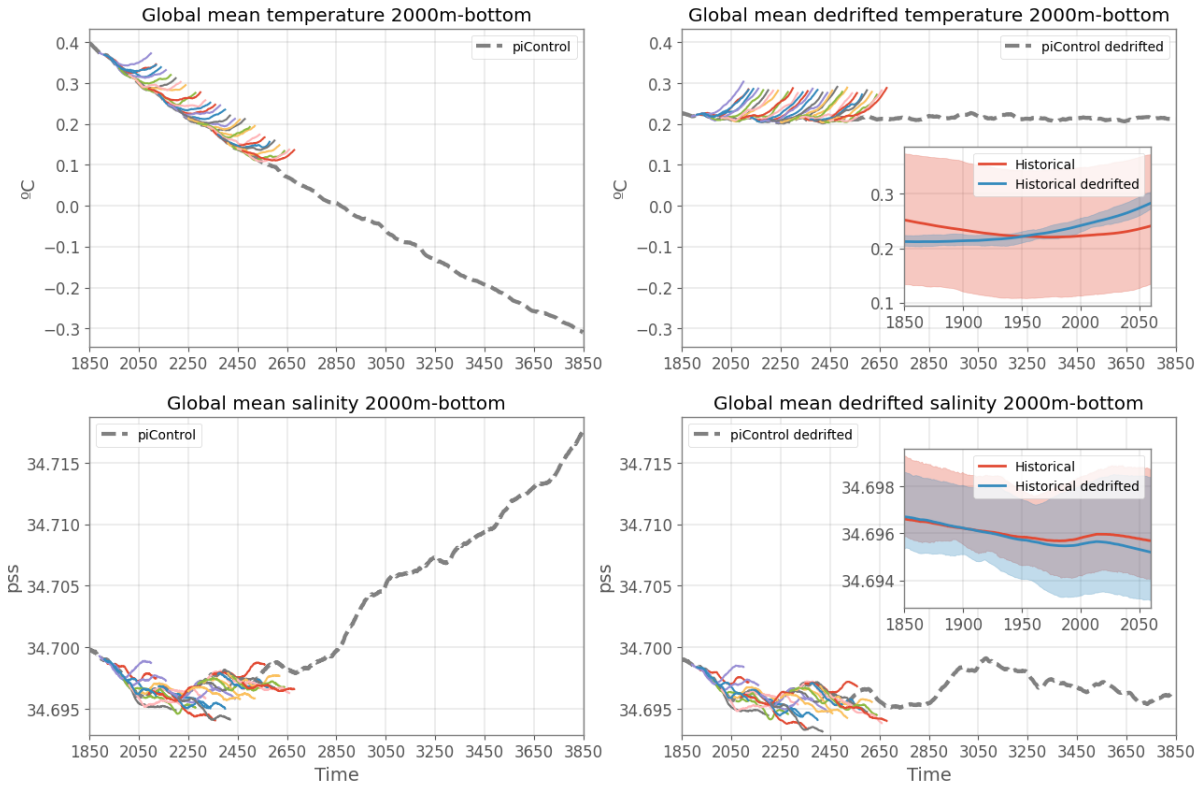

Figure II.2: Global mean ocean temperature (top) and salinity (bottom) below 2000m in the 2000-year piControl run (grey) and in the historical-extended members (colored lines), before (left) and after (right) the gridpoint-by-gridpoint dedrifting procedure.

We remove the corresponding 210-year period (corresponding to the historical-extended 1850-2059 period) of this quadratic fit from every member, that is, on each member's respective period of the piControl. Then, we add the same mean state back to each member. This mean state is defined as the mean of the piControl calculated over the period where the historical-extended simulations were performed, i.e. 1870-2680 in piControl time (figures II.1 and II.2). This mean state is added so as to keep physical values of temperature and salinity as opposed to anomalies after removing the drift. Note also that with this procedure, all 30 members are ensured to have exactly the same mean state, and they only differ by their different phasing of internal variability set by the initial conditions from the piControl. Figure II.2 shows global mean temperature and salinity below 2000m before and after removing the drift at the grid point level in the piControl and the historical-extended simulations. This has an important impact for temperature as the cooling drift is quite intense (-0.1ºC in 200 years below 2000m, same order of magnitude as the forced signal, figure II.2). We can see how before dedrifting, the historical ensemble mean didn't show a clear warming below 2000m because of the opposing cooling inherited from piControl in the first hundred years. Moreover, the spread is large before dedrifting because as the piControl drifts, the

initialization of the historical members puts each of them at a different mean state. Removing the drift and realigning each member on a similar mean state allows the warming signal to be clearly marked and the intermember spread to be reduced and much more coherent to real differences in internal variability rather than differences in climatic mean states. At global scale, removing the drift in salinity does not have much effect, as internal variations in the historical simulations seem to be larger than their drift, and the drift in piControl is strongest after the period when the historical members were launched (figure II.2).

Unless otherwise stated, all results will be presented for data in which the drift has been removed from the original outputs (piControl and historical-extended ensemble).

3 Local approach: time of emergence

Here, we investigate the ToE of externally-forced ocean changes (in the sense of chapter I) at local scale in two simple averaging frameworks: zonally-averaged temperature and salinity (on regular pressure levels), and vertically-integrated heat and salt contents. We choose these frameworks because they are most often adopted to look at changes in the ocean interior on a 2D plane and complement each other rather well.

The definition of ToE used here is similar to the one used in chapter I, but we adjust it to the large ensemble and to better compare the effect of drift removal. Namely, for each member and each grid point (in the zonal mean or vertically-integrated framework), the signal is now defined as the anomaly relative to the 1850-1899 reference period and the noise is defined as the intermember spread (although we test the sensitivity to using the noise from the long piControl). Defining the anomaly in this way instead of relatively to a piControl mean state ensures that it is centered around zero at the beginning of the period. On the contrary, in a situation where the piControl is drifting (thus on a different mean state), the first approach yields an uncentered anomaly which can end up outside of the noise envelope already in the beginning of the simulation, wrongly passing the threshold exceedance test. Of course, this situation only occurs in some regions of the deep ocean and not after removing the drift.

3.1 Zonal mean temperature and salinity

3.1.1 Results

The ensemble mean salinity in global and basin zonal means (figure II.3) shows strong opposing anomalies in the upper ocean, penetrating in the top hundred meters, with overall freshening at high latitudes and salinification in the subtropics, although the "fresh gets fresher, salty gets saltier" patterns are not clear. We will see in chapter IV that circulation changes influence salinity changes by breaking the fingerprint of hydrological cycle amplification transmitted by the freshwater fluxes.

In the deeper ocean, a small but significant (compared to the intermember spread; no stipples) freshening appears along the formation and export pathway of Antarctic Bottom Waters, all the way to the bottom of the ocean and spreading northward. This freshening is consistent with observations from these parts of the deep and abyssal ocean (e.g. Purkey et al. [2019]). A larger freshening appears on the entire water column in the Nordic Seas (around 70ºN in the Atlantic basin), where deep convection is strong in the model pre-industrial mean state. In chapter IV, we will show that deep convection shuts down in the subpolar North Atlantic (particularly in the Greenland and Labrador Seas where the mixed layer is deepest in the piControl).

The internal variability as estimated by the intermember spread (second row in figure II.3) is largest in the subtropical gyres and in the interior North Atlantic where the overturning circulation and deep convection are strong. Large values are also found near the surface at high latitudes where internal variations of salinity are partly driven by the exchange of freshwater with the sea-ice. On the edge of the continental slope near Antarctica where deep water formation is intense (with unrealistic open-ocean deep convec-

tion, as global climate models regularly convect too much in the open ocean compared to what is observed [Heuzé, 2021]), the large values penetrate to 1000m.

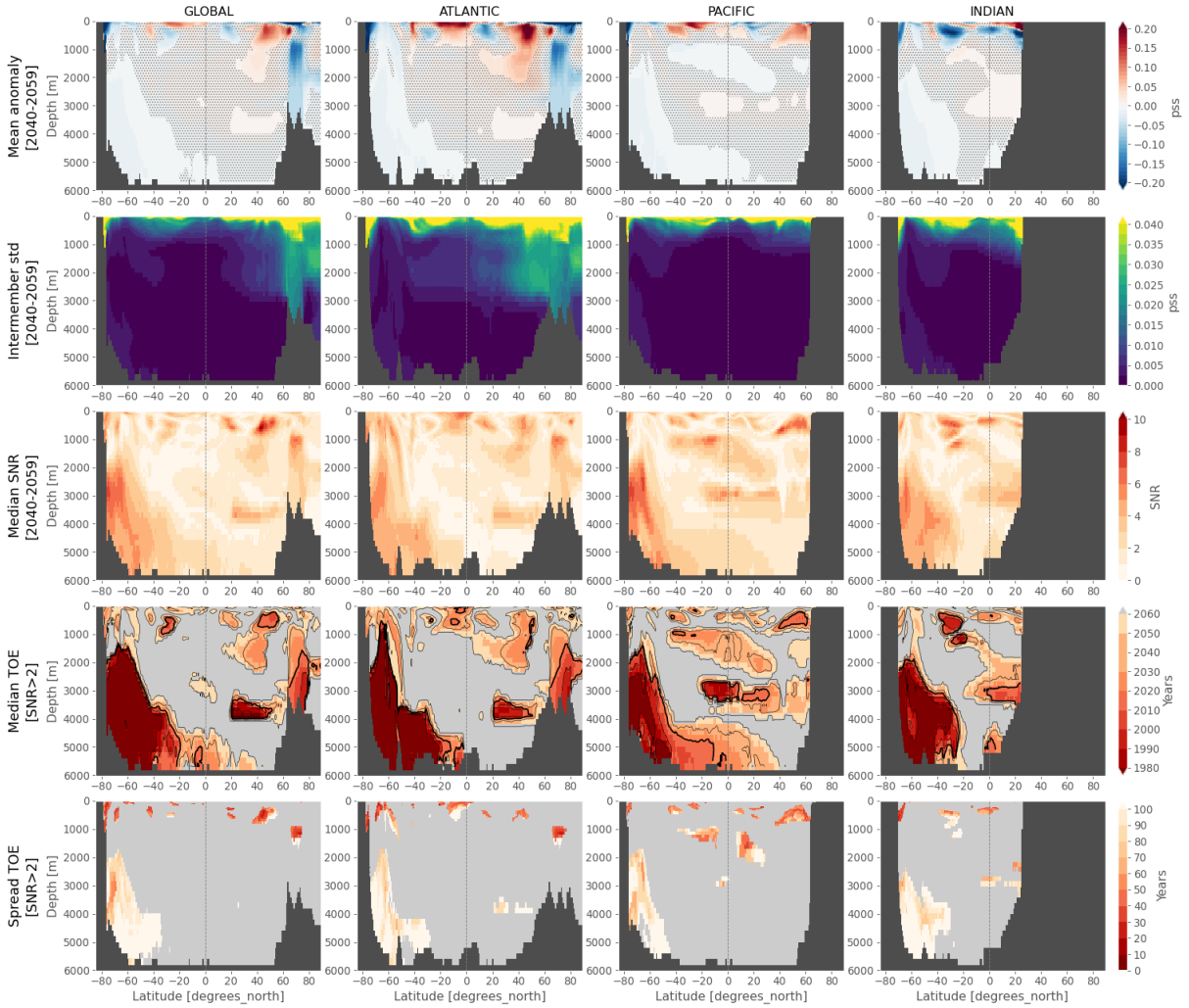

Figure II.3: (Top row) Zonal mean salinity anomalies in the ensemble mean for [2040-2059] relative to [1850-1899]. Stipplings show where the absolute value of the anomaly is lower than twice the intermember spread. (Second row) Intermember spread in [2040-2059]. (Third row) SNR in [2040-2059]. (Fourth row) Median Time of Emergence for SNR>2. Grey shading means no emergence. (Bottom row) Spread (max-min) in Time of Emergence for SNR>2. Grey shading means at least one member in the ensemble has not emerged.

By dividing the anomalies by the intermember spread, we obtain the signal-to-noise ratio (SNR, third row in figure II.3) and associated ToE when the SNR exceeds a threshold of 2 (and remains above it). This reveals broken out patterns of emerging signal in the 21st century in the subsurface (for the median ToE, fourth row), with even earlier emergence (before 2000) in the Nordic Seas at depth, and in the deep layers of the three basins (around 3000m in the Pacific and Indian and around 4000m in the North Atlantic). The earliest emergence is revealed to be for the export of AABW, from 1500m south of 60°S to the abyssal ocean, with a median emerging well before 1980. However, this is contrasted by a very large intermember spread in the ToE (close to 100 years, fifth row), suggesting the emergence is influenced by internal variability within each member, so that a SNR of 2 is too low to isolate the emergence of the forced signal. This also suggests that the region associated with the export of AABW in the model is very sensitive to small changes. The large grey areas in the ToE spread shows that it is frequent to find members that have not emerged by 2059.

Now we look at the changes and associated emergence for zonal mean temperature (figure II.4). The sign of the change is now much more homogeneous as compared to salinity, with widespread warming, strongest in the upper ocean in the subtropical gyres and in the subpolar North Atlantic and Pacific. The warming spreads at depth with coherent signals in the abyssal layer. The few regions expressing significant cooling are the subpolar North Atlantic at depth, and the Atlantic and Pacific sectors of the Southern Ocean in what could be the range of old upwelling Lower Circumpolar Deep Waters, albeit with weaker cooling. Overall there is a collocation of large changes and large noise levels, as these are set in regions most influenced by atmospheric variability, and are similar to those found for salinity variability (apart from sea-ice covered regions).

The earliest emergence of the warming signal is found, as for the freshening signal, in the export pathway of AABW, with even wider patterns than for salinity. Areas showing an emerged signal by 1980 spread beyond the equator. Again, this very early emergence is associated with a very large intermember spread in ToE, highlighting once more this interesting part of the World Ocean as possibly very sensitive to forced changes, but governed by mechanisms associated with strong dependence to initial conditions in internal phases of variability. More coherent emergence in the full ensemble with narrower intermember spread in the ToE distribution is found in the regions associated with the subduction of SAMW and AAIW in all three basins (emerged signal by 2020 in the median), down to almost 2000m. Their counterparts in the North Atlantic and Pacific subtropical gyres are contained in the upper 500-800m. A notable feature is the emergence by 2020 of a large portion of the deep Pacific basin (2000-4000m) from 40ºS to its northern bound, the least ventilated region of the ocean (DeVries and Primeau [2011] and see figure V.1 showing the water-mass age in the model). The inter-member spread however is almost as large as for the AABW.

In the following subsections we test the sensitivity of these results (for temperature only) to the choice of SNR threshold, of noise (comparing the piControl to the intermember spread), and to the effect of drift removal.

3.1.2 Sensitivity to the SNR threshold

We now look at the patterns of emergence in zonal mean temperature for a larger threshold of SNR (figure II.5). A threshold of 5 SNR naturally shifts the emergence of the warming signals later in time, with smaller areas of the ocean emerging before 2060. It also highlights which regions have shifted away from the piControl distribution with more certainty. Various features in the upper ocean (the SAMW and AAIW, the subtropical gyres, the subpolar Pacific and subsurface equatorial Pacific and Atlantic) now have a very narrow intermember spread in the ToE (a couple of decades), indicating that the forced signal is coherent in the entire ensemble and internal variability acts to modulate the forced component on time scales of maximum 20 years in these regions. Some parts of the AABW still emerge quite early, at the turn of the century for the earliest grid points. But the earliest emergence is still associated with a wide spread or no emergence of the full ensemble, confirming that these areas are potentially dominated by internal variability on centennial time scales. On the opposite, the gridpoints in the AABW that emerge later in the 21st century (the upper contours) are associated with a narrow spread of 10-20 years. In these regions, the forced signal in the full ensemble is not masked by internal variability.

Overall, this shows that some regions of the ocean require a larger SNR to fully isolate the forced signal from large internal variability, while others have a distinct and rapid enough warming in all members for the forced signal to be clearly identified in the full ensemble for low threshold values. In regions such as the subpolar Southern Ocean, the larger spread could be understood because of different timings in deep convection events in-between members, possibly modulating the response to anthropogenic changes on time scales of several decades. To surpass the choice of SNR threshold, we could add a criterion on the intermember spread in ToE, and look at the ToE when the spread becomes lower than e.g. 20 years.

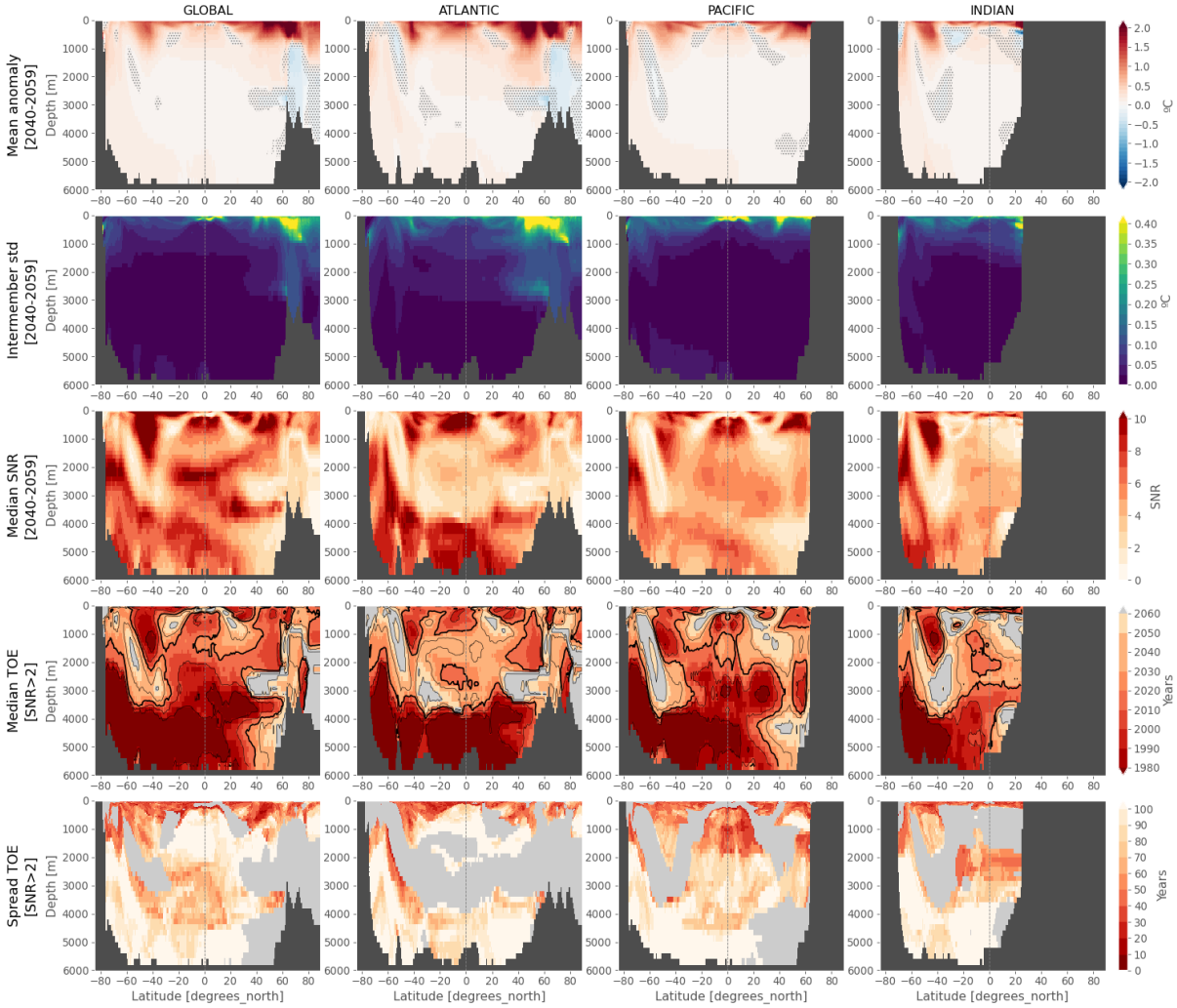

Figure II.4: As in figure II.3 but for zonal mean temperature.

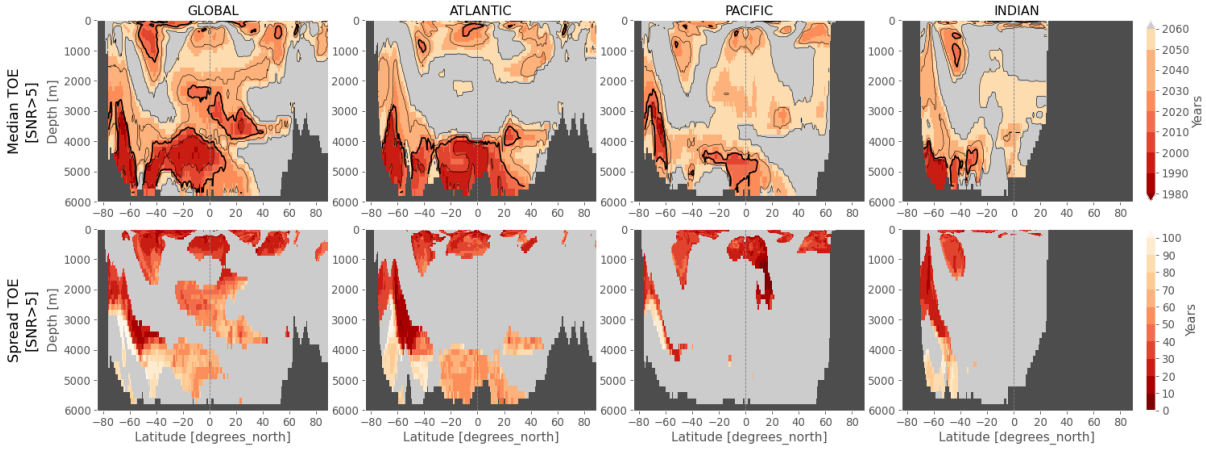

Figure II.5: Ensemble median (top) and min-max spread (bottom) Time of Emergence for SNR>5.

3.1.3 Sensitivity to the choice of noise

We show in figure II.6 the intermember standard deviation in zonal mean temperature (as in figure II.4 but averaged over the entire historical-extended period) compared to the 2000-year interannual standard

deviation in the piControl. The two estimates are almost identical (spatial correlation of 0.99 in the global zonal mean and spatial root mean square error of 0.018ºC), yielding similar patterns and values of ToE (not shown). The only difference in ToE between the two methods is essentially in the Nordic Seas below 1000m where the internal variability as estimated from the intermember spread is clearly reduced in the 21st century (compare figure II.4, second row with figure II.6, first row). Consequently, the cooling in this region emerges with the intermember noise and not with the piControl noise. Note however for a SNR of 5 the cooling hasn't emerged (figure II.5).

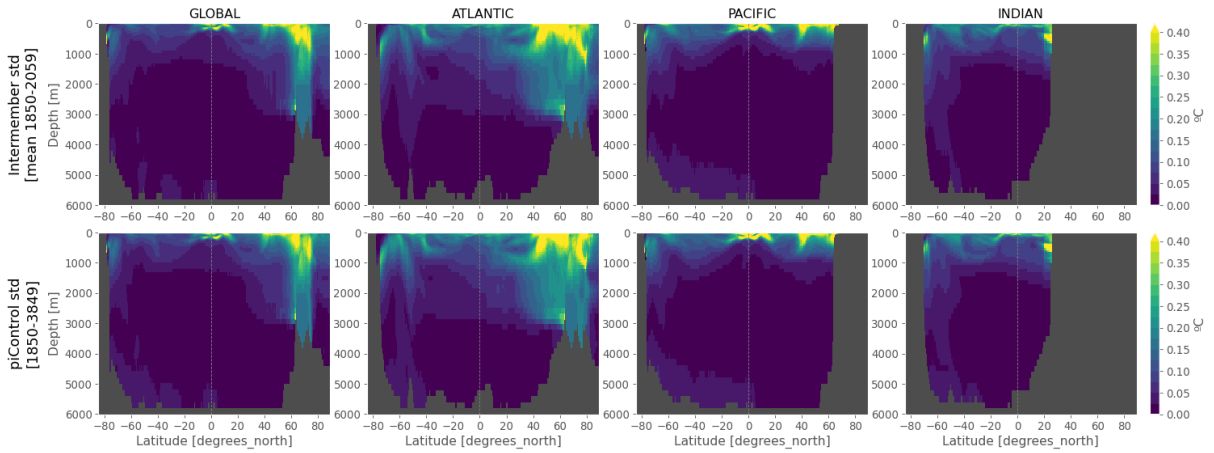

Figure II.6: (Top row) Intermember standard deviation averaged over [1850-2059]. (Bottom row) Inter-annual standard deviation from the 2000-year piControl.

3.1.4 Sensitivity to drift removal

We now show in figure II.7 what the analysis of figure II.4 would have given if the drift had not been removed. Essentially all the signal that emerged below 2000m in the dedrifted analysis is now masked by the much larger intermember spread due to the different initialization times in a drifting piControl. The time series for two example grid points in the deep and abyssal Pacific ocean are shown in figure II.8. The ensemble mean (not dedrifted, red line) shows the clear cooling drift in the deep ocean (left panel), that doesn't emerge because of the large intermember spread caused by the different mean states in each member. After removing the drift, the ensemble mean reveals a small warming trend and because the spread is then much reduced, the ensemble mean exceeds the noise envelope during the late 20th century. The intermember noise envelope now coincides well with the dedrifted piControl envelope. Similarly, in the abyssal ocean (right panel in figure II.8), the intermember spread is reduced when removing the drift. In this region there is a warming trend appearing in the ensemble mean already in the initial data, but it is delayed by the drift.

The upper ocean on the other hand is not much affected by the drift and thus by drift removal. Because the deep and abyssal oceans are represented by a small density range, the ToE analysis in density presented in chapter I is only affected in the very last density bins ($\sim$27.7-28 kg.m^{-3}) by the impact of the drift, or not at all, depending on the definition of ToE chosen (not shown).

3.2 Vertically-integrated heat and salt contents

The same analysis is now shown in figure II.9 for vertically-integrated Ocean Heat Content (OHC) and Ocean Salt Content (OSC). OHC shows broad warming except in some parts of the Southern Ocean, with intensified patterns in the subpolar North Atlantic and in the zonal band at the northern bound of the ACC. OSC shows freshening over the entire subpolar Southern Ocean, over the Atlantic sector of the Arctic, and over the Western Indian ocean. Salinification is found mostly in the Atlantic basin with a

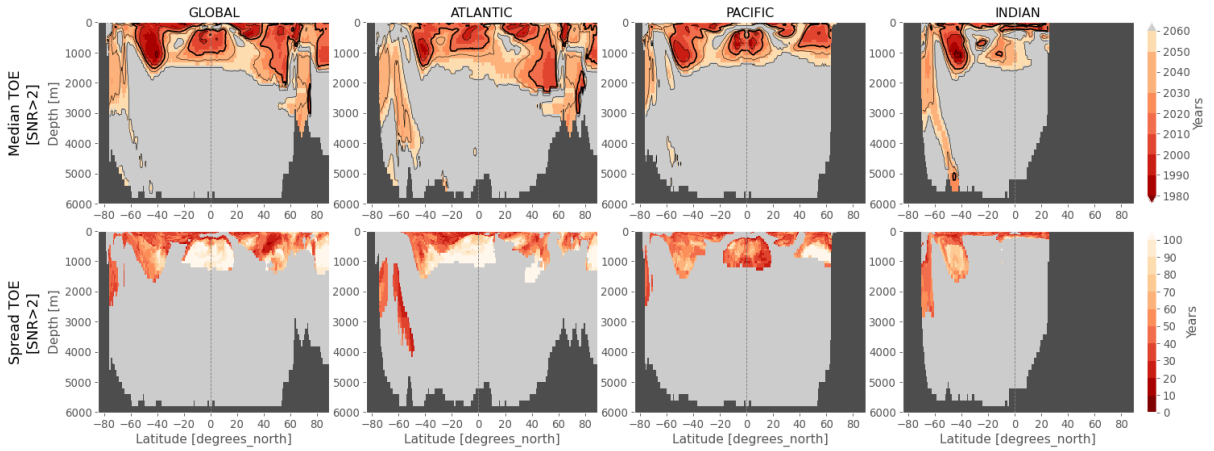

Figure II.7: Ensemble median (top) and min-max spread (bottom) Time of Emergence for SNR>2. As in figure II.4 bottom panels but the analysis was applied on the data prior to removing the drift.

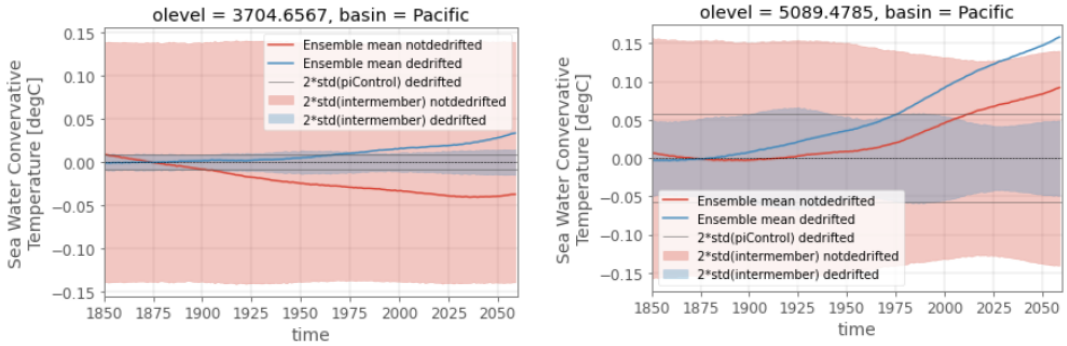

Figure II.8: Time series of the ensemble mean temperature anomaly at 3ºS in the deep (∼3700m, left) and abyssal (∼5000m, right) Pacific ocean, before and after removing the drift.

strong signal along the North Atlantic Current, and in the Western part of the south Pacific subtropical gyre. Overall the salinity signal is less clearly identified than the heat signal, which we can see by the lower SNRs. There are similar features shared between OHC and OSC, such as the positive change in the subpolar North Atlantic, tropical Atlantic and western parts of the Pacific and Atlantic subtropical gyres. This points to possible common changes driven by changes in the circulation.

Internal variability in OHC is larger at high latitudes. For OSC, there is a hemispheric asymmetry: it is dominated by the Arctic and North Atlantic, with relatively low values in the ACC compared to OHC.

As already found in the zonal mean framework, the signal in salinity emerges in much less area than for temperature. Their common feature is the early emergence (1980s for OHC, 2000s for OSC) in the Eastern tropical Atlantic, but associated with a particularly large (>100 years) intermember spread. This signal integrates the warming at different vertical levels, with large SNRs in the upper ocean and in the abyssal ocean for heat (see figure II.4). Whereas for salt content, it mainly represents the positive salinity changes in the upper ocean, with much smaller SNRs below (figure II.3). Otherwise, the salinity emerging patterns are scattered and emerging towards the mid-21st century. A notable exception is very early emergence of the freshening signal near the Antarctic continent, in regions associated with deep convection, but also associated with several decades of intermember spread. OHC emerges by 2020 all around the Southern Ocean with patterns centered around 40ºS, in almost the entire Atlantic basin, the northern Indian ocean, the northern and north-eastern bounds of the Pacific basin and part of the Arctic ocean. The intermember spread is larger than a century in the tropical and North Atlantic, and about

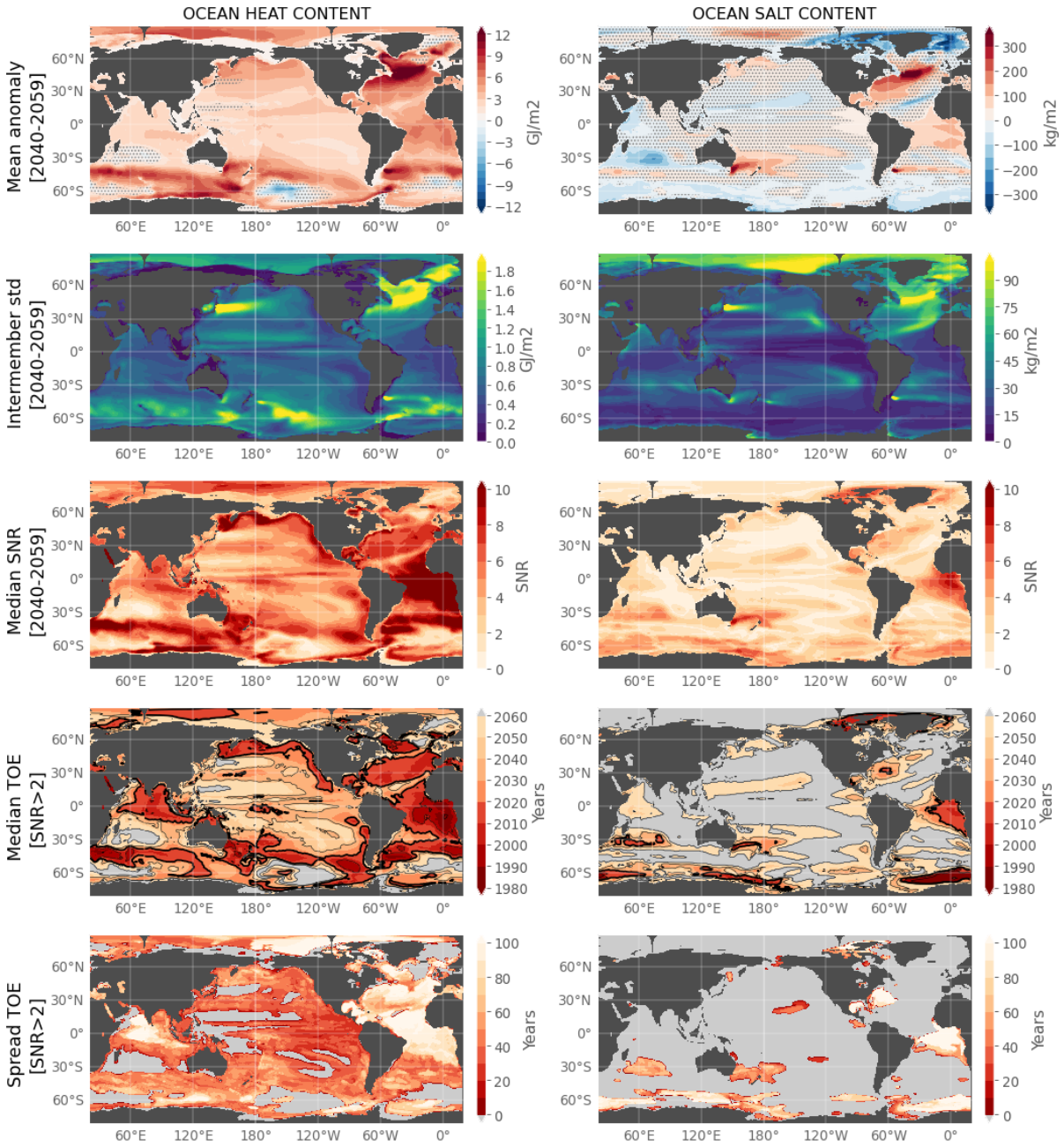

Figure II.9: (Top row) Vertically-integrated heat and salt contents in the ensemble mean for [2040-2059] relative to [1850-1899]. Stipplings show where the absolute value of the anomaly is lower than twice the intermember spread. (Second row) Intermember spread in [2040-2059]. (Third row) SNR in [2040-2059]. (Fourth row) Median Time of Emergence for SNR>2. Grey shading means no emergence. (Bottom row) Spread (max-min) in Time of Emergence for SNR>2. Grey shading means at least one member in the ensemble has not emerged.

30-50 years in most of the other regions, apart from those where the full ensemble hasn't yet emerged. The large spread in the Atlantic basin may be linked to the model's bicentennial variability.

4 Pattern-based approach: detection times

I will now present another method that can be employed to investigate the time when a forced change can be detected in a large ensemble. This is largely based on the study by Santer et al. [2019] who apply the method to two large ensembles and look at the warming around the globe in the lower and mid to upper troposphere and at the cooling in the lower stratosphere. The general idea is to define a spatial fingerprint of change based on the ensemble mean and to search for this fingerprint in each member as well as in observation-based products to determine the "detection times", i.e. the time when the fingerprint can be significantly detected in the large ensemble and in the observations. This kind of pattern-based analysis has also been applied to multi-model ensembles on different climate variables, also in the context of climate change detection (e.g. Gleckler et al. [2012], Bonfils et al. [2020]). Here, I will try to briefly present the method, before applying it to the zonal mean and vertically-integrated frameworks in the IPSL-CM6A-LR large ensemble. Finally, I will apply this method to another framework: the volumetric distribution of temperature and salinity in the ocean.

The ToE presented above gave local results, at the grid point scale. Here, the distribution of "detection times" in the large ensemble will be given for an entire spatial pattern, a more global approach although taking into account information at the grid point scale through Principal Component Analysis.

4.1 Method

Fingerprint definition The method is based on an estimate of the "true" climate change signal in response to a set of forcings. Here, we use the historical-extended simulations, so the forcings include both natural and anthropogenic influences. The fingerprint $F(x)$ is defined as the leading Empirical Orthogonal Function (EOF) of the centered ensemble mean, for a given variable (e.g. after all sorts of spatial averaging: here zonal means and vertically-integrated values). We will use the historical-extended period 1850-2059 to determine this fingerprint, with annual values. $F(x)$ is time-independent (x represents the spatial dimension).

Signal time series and trends The goal is then to determine the similarity over time of this fingerprint with the geographical patterns of change in each member of the ensemble. The change H in each member i is thus projected onto the fingerprint $F(x)$, yielding time-varying pseudo-principal components:

$$Z(i,t) = \sum_{x=1}^{N_x} H(i,x,t)F(x) \tag{II.1}$$

with N_x the length of the spatial dimension, and t the time. The pseudo-PCs $Z(i,t)$ are called the signal time series, defined here over 1850-2059 and give an indication of the strength of the fingerprint in each member, and of its evolution over time. For each signal time series $Z(i,t)$ we fit a linear trend over increasing lengths of time L, starting with a 10-year trend. If the start date is 1850, the first trend (L=10) will be fitted over 1850-1859 in $Z(i,t)$. L is increased by one year until the time period reaches the final year (e.g. 1850-2059, L=210). The signal $S_i(L)$ is then defined as the L-year trend over the increasing L-year periods.

Noise estimates To determine whether the time-varying pattern similarities (the signal time series) show a statistically significant increase, we need an estimate of internal variability noise in which there is a priori no expression of the fingerprint except by chance. We will test several estimates of internal variability. The first estimate is simply deduced from the intermember standard deviation of the L-year trends across members: $N_1(L) = \sigma_{S_i(L)}$. The second estimate is derived from the long 2000-year piControl

run, which we project onto the fingerprint to obtain a 2000-year pseudo-PC:

$$N(t) = \sum_{x=1}^{N_x} C(x,t)F(x) \tag{II.2}$$

with $C(x,t)$ the change in the piControl relative to the mean state. $N(t)$ is referred to as the noise time series. $N_2(L)$ is defined as the standard deviation of the distribution of all possible L-year trends in the piControl noise time series $N(t)$. Santer et al. [2019] use all non-overlapping trends in the noise time series but other versions of this method include all possible L-year segments. We have tested the impact of the increment. If we use all possible non-overlapping segments, the 210-year distribution does not have enough realizations to give a confident estimate of a null distribution, meaning we need to use overlapping segments. Using overlapping segments shifted by one year or 10 years yields similar results, so to speed up the computation, we have used all segments shifted by 10 years. A third estimate that will be used later on is derived similarly as the piControl estimate, but instead of the long piControl, we construct a long time series by concatenating each historical members' difference to the ensemble mean, and project it on the fingerprint. We also obtain a noise time series, compute the distribution of L-year trends and deduce the standard deviation of this distribution $N_3(L)$.

Detection times To determine the time at which the fingerprint can be unambiguously detected in each member, we compute the time-dependent signal-to-noise ratio $S_i(L)/N(L)$. The signal is detected when the SNR exceeds for the last time a chosen threshold (we will show the results for 2σ, 3σ and 5σ). The detection time is then defined as the final year of the trend length at which detection occurred (e.g. if detection is found for L=100 and the start year was 1850, the detection time is 1949). The detection time is calculated for each member of the ensemble, so that the results are presented as a distribution.

As opposed to the definition of ToE calculation presented in section 3, we now have an estimate of the noise which is time-dependent and accounts for the period over which the signal trends are computed (the L-year periods), meaning a decreasing noise level with time, as the period considered increases.

Different choices could have been made in the definition of signal and noise. For instance, Bonfils et al. [2020] use linear regression coefficients between the signal/noise time series and the PC associated with the ensemble mean fingerprint $F(x)$, instead of the trends of signal/noise time series themselves.

Detecting observed changes Finally, the goal of such analyses is to project observational estimates onto the model fingerprint to try to find a detection time in the observations (the time and space covered would be adapted to the observational coverage). The method is the same as for individual members: the observations are projected onto $F(x)$, yielding on observation-based signal time series. L-year trends are calculated and compared to the same estimates of noise, and a detection time is determined, and can then be compared to the distribution of detection times in the large ensemble. I have not yet tested that on ocean observation-based products. This requires treatment of the data in similar ways in the observations and the model (such as temporal and spatial data coverage), but it is a possible perspective of this exploratory work. This however relies on the assumption that the IPSL-CM6A-LR model simulates a realistic response to external forcings in the ocean, which is a strong assumption, especially when using grid point level data. This is why multi-model ensembles can potentially be better-suited to capture the across-model response, and why large spatial averaging such as sub-basin and vertical averages are usually applied (e.g. Gleckler et al. [2012]).

4.2 Zonal-mean fingerprint

4.2.1 Absolute changes

We start by investigating the fingerprint of change for zonal mean temperature and salinity (in the global zonal mean for brevity). The dedrifted annual values have been bilinearly interpolated to a regular

1ºx1º grid before zonally averaging, and then linearly interpolated on a regular vertical grid every 100m. This way, each grid point, in the zonal mean framework, has the same weight and all parts of the zonal mean ocean are represented equally in the computations as we don't want the upper ocean to be over-represented in its number of grid points in the EOF. This treatment was not applied in the local ToE analysis as the grid point results are independent. Note we don't further weight by the longitudinal volume as a weighting has already been applied in the zonal average: the goal is simply to choose a first way to average or integrate to look at a two-dimensional change, and then simply make sure that the gridding within that framework is regular. The piControl noise is tested in the next section on vertically-integrated heat and salt content; here we simply use the intermember spread in the trends as our noise estimate.

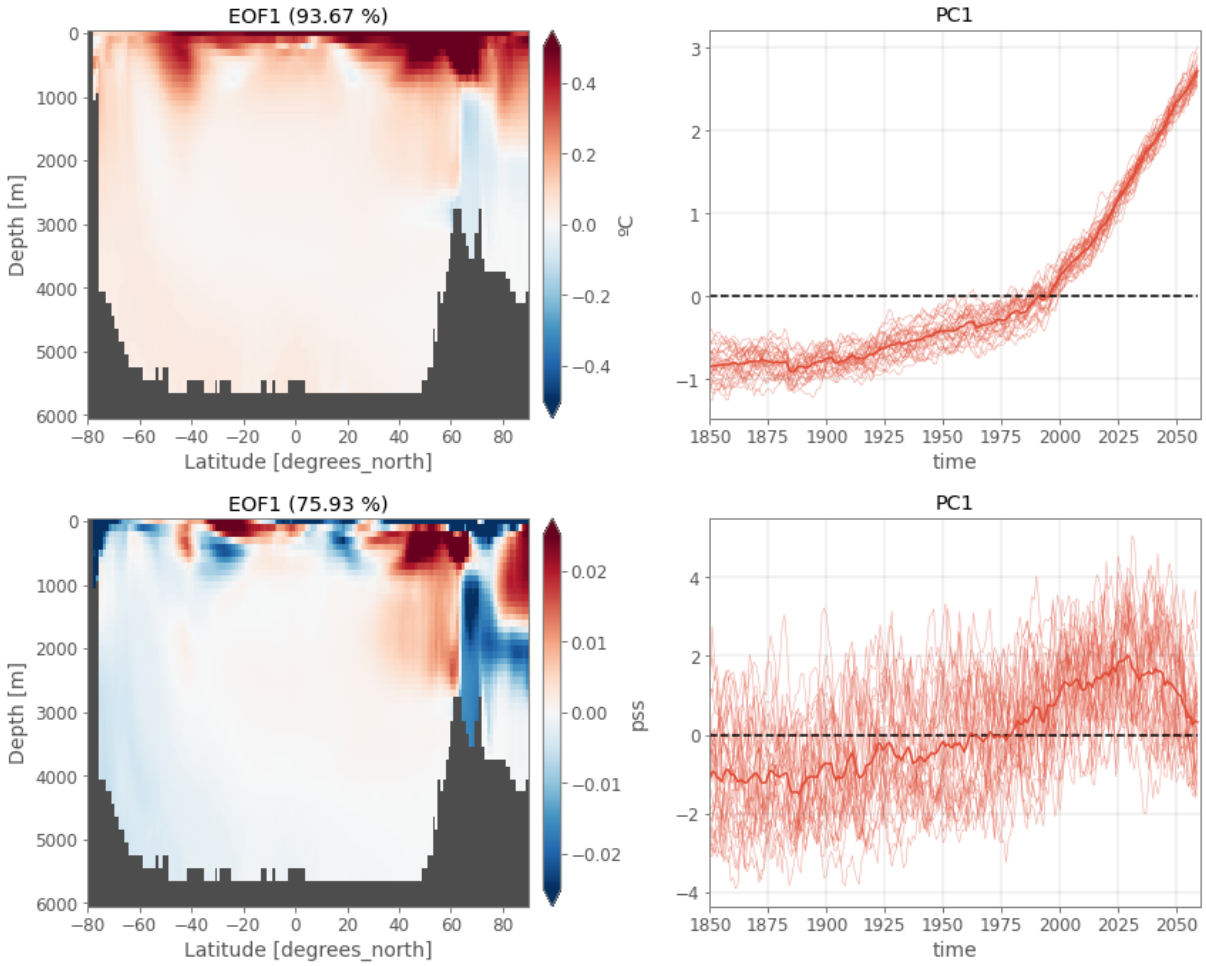

Figure II.10: Zonal mean temperature (top) and salinity (bottom). Leading EOF of the ensemble mean change relative to its mean state (the fingerprint, left) and associated PC (right, bold line). The numbers in the titles on the left represent the percentage of variance explained by this first mode. Thin solid lines on the right are the signal time series (pseudo-PCs) of individual members, i.e. the projection of the zonal mean change onto the fingerprint. A scaling is applied so that the PC has unit variance (divided by the square-root of its eigenvalue).

In figure II.10 we show the fingerprint for temperature (top left) and salinity (bottom left) change (the leading EOF of the ensemble mean). On the right panels, the associated PC to the fingerprint is plotted in the bold line and the thin lines are the signal time series (pseudo-PCs) of the individual members, that is the projection of each member onto the fingerprint [1].

1. The analysis is run with the Python package eofs.xarray: https://ajdawson.github.io/eofs/latest/index.html [Dawson, 2016].

The fingerprint clearly resembles the global zonal mean temperature anomaly in the large ensemble shown in the previous section (figure II.4), although the vertical resolution has been strongly downgraded in the upper 1000m and slightly upgraded in the deeper ocean. The time evolution of this fingerprint largely resembles that of global mean SST (figure II.1), a testimony of the upper ocean driving the co-variance of the zonal mean temperature change. This is also revealed by the clear influence of volcanic eruptions creating temporary cooling steps in the increasing curves.

The zonal mean salinity fingerprint also represents the anomaly as shown in figure II.3, but there is much larger internal variability in-between ensemble members in the signal time series, with a decrease in the last couple decades of the period. This time evolution is in fact representative of the Arctic change with a surface freshening and subsurface salinification (the latter which is showing here larger magnitudes than in figure II.3), as expressed by the grid points time series between 80-90ºN (not shown). This shows, again, that the analysis is dominated by grid points that have the largest signals.

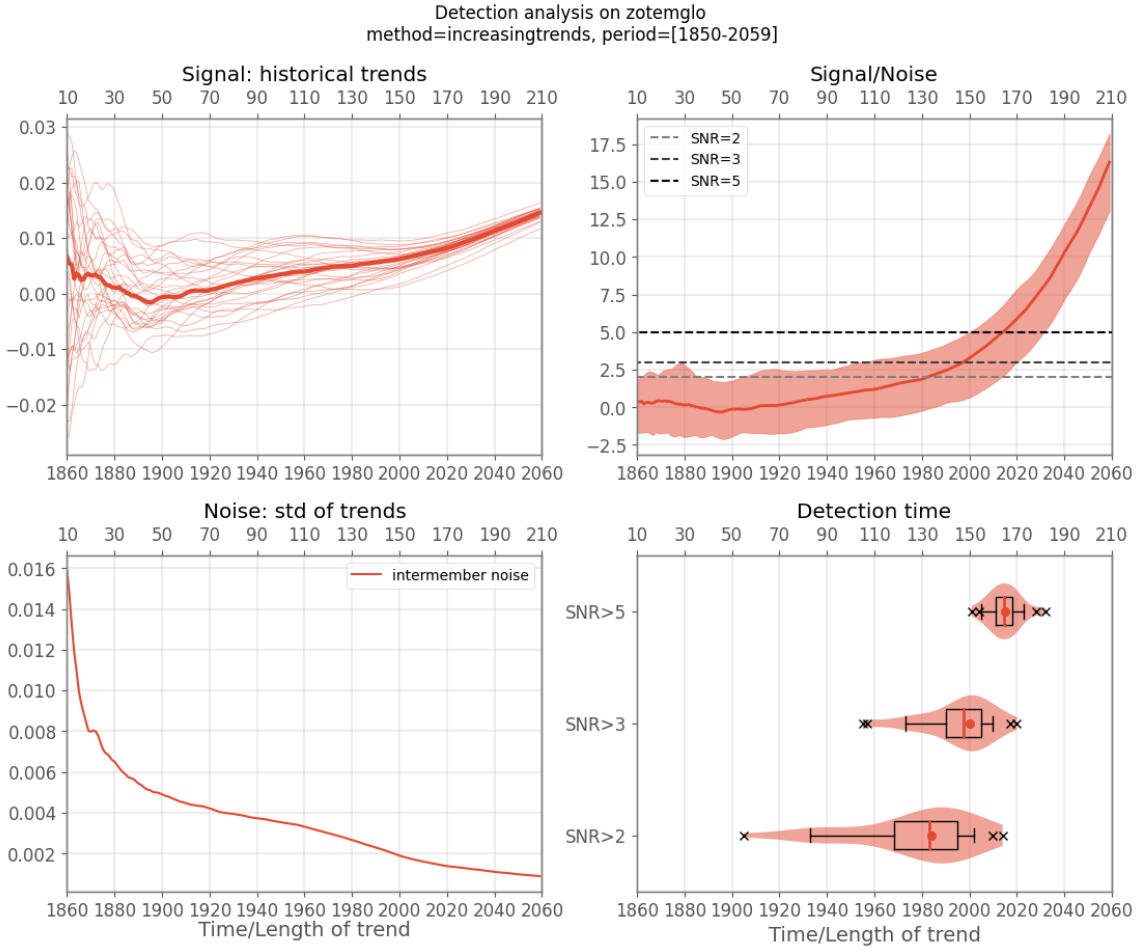

Figure II.11: Signal trends, noise, SNR and detection times for zonal mean temperature change. The analysis is conducted on the entire period 1850-2059, starting the trend analysis in 1850. The xaxis shows the length of the trends L on the top spine and the corresponding year (last year of the trend) on the bottom spine. The whiskers in the bottom right plot show the 5-95 percentiles of the distribution, with the crosses representing the outliers. The box shows the 25-75 percentiles, the red line the median and the red dot is the detection time computed from the mean of the signal distribution. The red shading is the violin plot of the distribution of detection times.

We show the detection results for temperature in figure II.11, with the evolution of the signal trends, standard deviation of these trends, SNR and detection times. For trend lengths of 10 to 50 years (1860-

1900), the intermember spread is large, with trends of both signs in the ensemble. The intermember spread quickly decreases (divided by 2 in 10 years), broadly following an exponential decay as the individual signal trends grow more coherent to each other and increase over time. This yields increasing SNRs from 1900 to 2059. The distribution of detection times is extremely wide for the 2σ threshold (SNR>2, about 110 years), with a median detection time in 1985 but a quarter of the distribution detected before 1970. This is not too surprising considering there is an early warming in the 20th century in the signal time series (figure II.10) followed by a brief pause, which makes the warming in some members detectable while others have different phases of internal variability which delay the detection of the forced signal to a later point when the warming is strongest. The SNR>3 threshold reduces the spread of the distribution in detection times (now 65 years for the full distribution) and shifts the median to 1995. A SNR of 5 further reduces the spread (30 years) and may thus be a more suitable diagnostic to detect the long-term, clearer warming in the full ensemble with more intermember coherence, with detection in the first couple decades of the 21st century for 75% of the ensemble, and detection in the full ensemble by 2030.

Compared to the local approach (figure II.4), the median detection time for SNR>2 (1985) is found earlier than most grid points ToE in the upper ocean. This could be explained by the decreasing noise level with time in the present method, which was not the case for the ToE method. This could also suggest that a fingerprint at global scale, although its signal is mostly representative of the surface signal, can be an interesting method to detect early signs of anthropogenic warming. However, a better comparison would imply applying the trends method at local scale to see whether the difference found is attributable to the use of trends instead of time series, or to the global fingerprint.

4.2.2 Normalized changes

Because temperature (and salinity) don't vary with the same orders of magnitude in different parts of the ocean, the upper ocean, or more generally regions which have the highest absolute changes, are dominating in the fingerprint and are thus over-represented in the time-varying pseudo-components (the signal time series). Instead, now we want to see how the fingerprint can represent the evolution of the ocean temperature relatively to its local variability. This is a similar question as what we did in the ToE analysis by dividing by the intermember spread to obtain a SNR. This is translated for the EOF analysis into normalizing the input data (after centering it, as was already done before), i.e. dividing the variable at each grid point by its standard deviation. This is often done when the fingerprint is defined using joint fields of different climate variables: because they don't have the same unit, the data is normalized (e.g. Bonfils et al. [2020]). Here, for coherence, instead of dividing the ensemble mean and each member by its interannual standard deviation, we divide all the data by the intermember spread. This is equivalent to dividing by the piControl interannual variability (as shown in the previous section), which gives an estimate of each grid point's internal variability without the climate change trend in the envelope.

We show the analysis on the normalized data (denoted as "reduced" on the figures) in figure II.12 for temperature and II.13 for salinity. The zonal mean temperature fingerprint is now unitless and reflects the change compared to the local variability, which is why we find similar patterns as the SNR in figure II.4, with the largest values located in the SAMW and AAIW. The evolution of the strength of this fingerprint in time in each member, expressed by the pseudo-PCs signal time series, now shows a much smoother and almost exponential increase. There are fewer effects of volcanic forcings, and less "pollution" by internal variability. The signal trends still show a wide spread in the first several decades before gradually decreasing. The median detection time for the 2σ level is shifted by 40 years earlier (1940-45) with a distribution spread out over much of the 20th century (and even late 19th century), but already less so than the previous analysis without normalizing the data (<100 years). Detection in the full ensemble is reached by 1970. The 3σ threshold shows similar values as 2σ for the median and last member, shifted by about 10 years later, but the spread is narrower (50 years, first member to be detected in 1930). For 5σ, the entire distribution shows detection times between 1960 and 2000, with a median in 1985, about 30 years earlier than previously found. This suggests that considering the entire ocean depth-latitude structure, normalized

by the local variability, can lead to much earlier detection of the global fingerprint of temperature change in the ocean under increasing anthropogenic forcings, compared to not normalizing, which pulls the weight of the analysis towards the more variable surface ocean. The deeper ocean, because of its low internal variability, is a particularly interesting place to look for forced changes. This also reinforces the fact that the deep and abyssal parts of the ocean seem particularly sensitive to small thermohaline changes in IPSL-CM6A-LR. Unfortunately, it is virtually impossible to verify whether the model correctly reproduces internal variability in the ocean deeper than 2000m, due to lack of continuous observations at these depths.

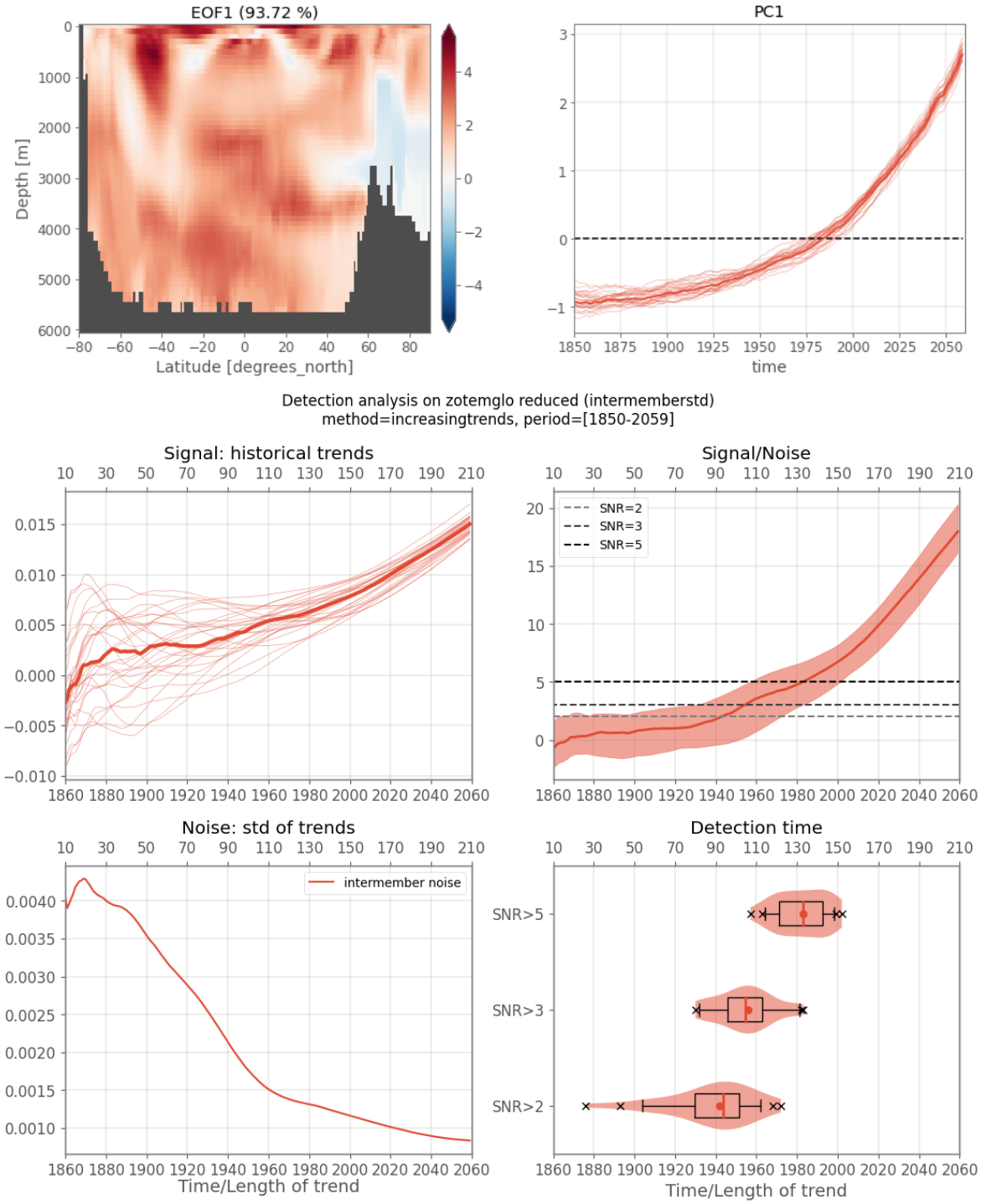

Figure II.12: As in figure II.10 and II.11 but for the analysis where all the input data is divided by the intermember standard deviation.

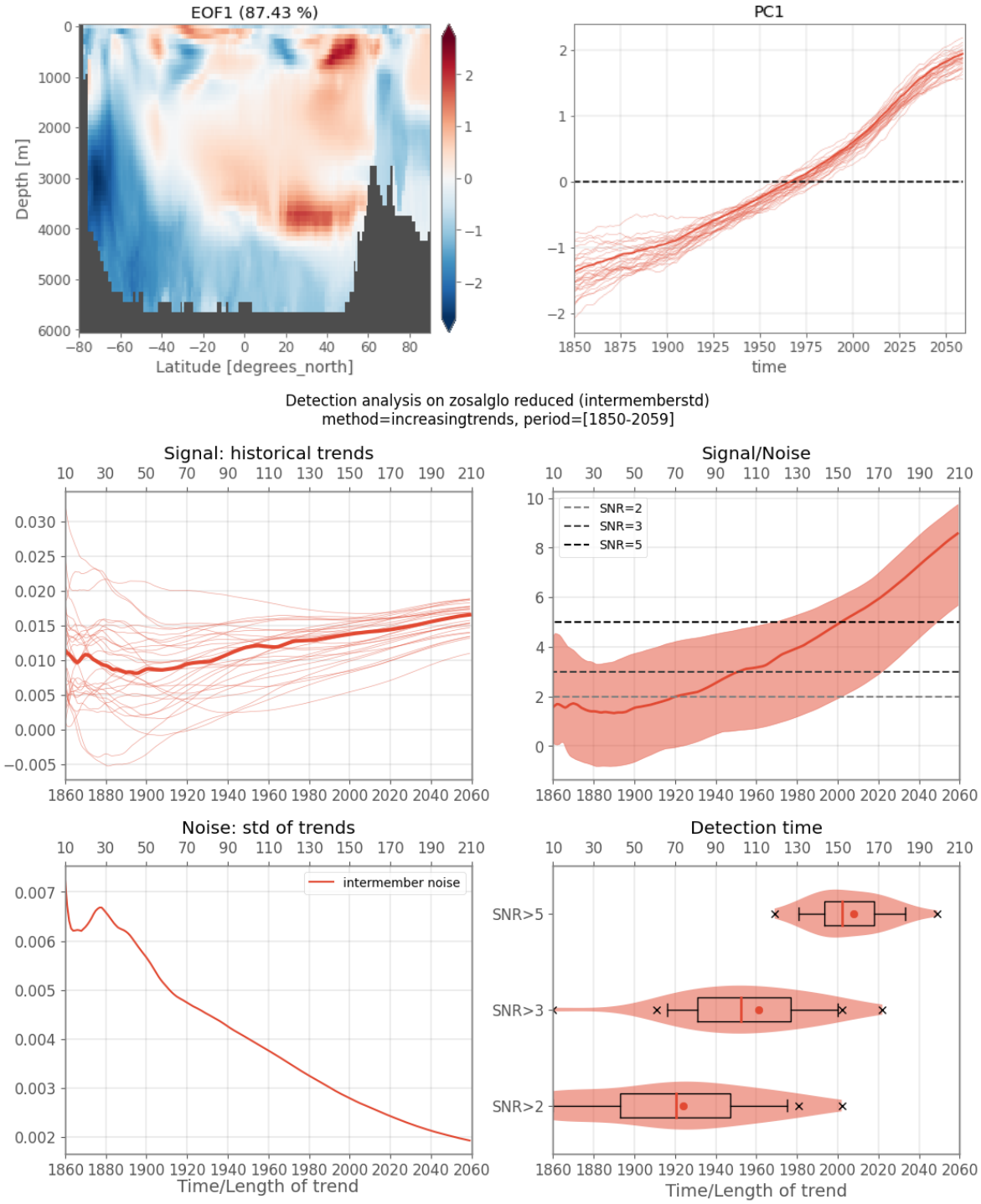

Figure II.13: As in figure II.12 but for salinity.

The fingerprint for normalized salinity (figure II.13) clearly highlights the overall freshening in AABW and abyssal waters, and salinification at intermediate and deep levels. The upper ocean doesn't show more pronounced values than the deeper parts, unlike some regions for temperature. The time evolution of this fingerprint in the ensemble shows a marked positive trend starting in the beginning of the simulations in the ensemble mean, although associated with large intermember spread which decreases after 1880 and over the historical-extended period. The cause of the positive trend in the early decades of the simulations is unknown, but since this feature is absent when repeating the analysis in the upper 2000m only, its origin is in the deep ocean. It could be due to residual drift there, although the amplitude of the changes in

the historical members below 2000m proved to be small - of the order of 0.01 pss over several centuries (figure II.2) -, and not much affected by the dedrifting procedure. It is possible that the small drift in salinity shown in figure II.2 for the global mean actually averages larger opposing signals. The resulting detection times are spread out from 1860 to 2000-2020 for SNR>2 and SNR>3, evidence that the early trends are large enough in some members to be detected while the large internal variability can hide detection for 100+ years in others. The SNR>5 threshold starts to give slightly more consistent detection in the ensemble, much later than the other two, although detection is still widely spread out in time, between 1970 and 2050, with a median around 2005.

There is thus much more uncertainty concerning the salinity fingerprint than for temperature, related partly to the early positive trends which we cannot yet explain, associated with large intermember spread in the detection times. For a fixed threshold of 5σ for signal detection, the median trend is detected about 20 years later for salinity than for temperature, and the tail of the distribution extends 50 years later in time. This is coherent with the local ToE approach where we also found overall earlier emergence of the temperature signals compared to salinity, and less parts of the ocean emerged by the mid-21st century for salinity. These two approaches are thus complementary, the pattern-based method giving a time when the global fingerprint can be detected, and the local ToE method pointing to which regions more specifically show a detectable change.

Note another approach to be tested would be to define a joint temperature-salinity fingerprint, as done by e.g. Pierce et al. [2012] for their detection and attribution study (with a different method). This allowed them to detect larger signals than with the separate temperature or salinity fingerprints.

4.2.3 Sensitivity to the trends definition

Based on the same signal time series (pseudo-PCs) for normalized zonal mean temperature (figure II.12), we now test two other ways to compute the signal trends and their impact on detection times. Let's refer to method 1 as the one we have previously been applying, i.e. trends are calculated for increasing periods of time, starting with the 10-year period 1850-1859 and incremented by one year until we reach the period 1850-2059. The detection times calculated with method 1 are reproduced again in red in figure II.14. The signal time series don't increase linearly in time, especially over the 1850-2000 period with barely any change at the end of the 19th century, while the noise decreases as the period considered for trend calculations increases. We can thus see that whether a signal has been detected or not at a given year can depend on how much time has passed since the beginning of trend calculation, and on the amplitude of the signal.

We test whether there are large differences or not by applying a similar method but starting the trend calculation in 1950 (method 2, blue distributions in figure II.14). Indeed, starting trend calculations in 1850 to detect signals in the ocean is of course delusional when applied to actual observations. The model and large ensemble framework is simply a way to test when we could have detected a change if we had a "perfect/complete" observational system going all the way back to the preindustrial era - provided the model faithfully reproduces the ocean response to forced changes, which is questionable. Furthermore, when looking at the detection of climate change signal trends in a large ensemble, past studies have also proposed to compute the signal with a moving L-year trend window (e.g. Rodgers et al. [2015] with L = 30 years), to see when a multi-decadal trend could be detected. We test this method by computing 30-year trends on our signal time series, from 1850 to 2059 (i.e. the first signal value will be the trend over 1850-1879, for year 1879; the second value for the trend over 1851-1880, etc..). Since it is now a fixed window moving in time, there is no dependence on the start date of the analysis. We don't further test the sensitivity to the window length here. A period of 30 years usually corresponds to the interval on which values are averaged to define climate indicators where the impact of internal variability has been largely removed. The detection times for this method 3 are plotted in purple in figure II.14.

Method 2 (blue distributions) has its first signal values in 1959 by definition. We can see that for

SNR>2 and SNR>3, more than half of the ensemble already detects a change in the 10-year trend calculated over 1950-1959. This is coherent with the results of the 30-year trends, that express a median detection time around 1950 and an 80-year intermember spread for SNR>2. This distribution is shifted about 10 years later for SNR>3, with slightly shorter spread (70 years). For SNR>5, methods 2 and 3 (blue and purple) show aligned distributions of detection times. Compared to method 1 presented earlier and shown in red here, these results are systematically about 10-15 years later, hence a more conservative estimate explained by more contamination by internal variability since the trend periods are shorter than in method 1. But overall, these 3 methods give very consistent results with one another.

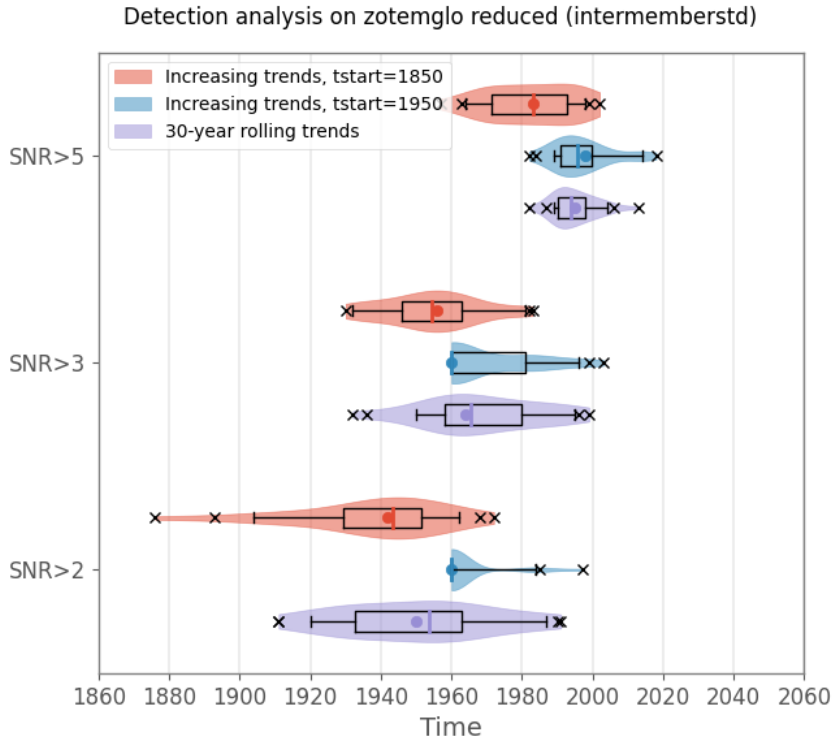

Figure II.14: Detection times of the zonal mean temperature fingerprint for the normalized analysis (figure II.12), with three different methods for the calculation of the signal trends. (Red) As described before, trends are calculated from the signal time series (pseudo-PCs), starting from 1850 and increasing in period length. (Blue) As red, but the trend calculation starts in 1950. (Purple) Moving 30-year trends are calculated from the same signal time series.

4.2.4 A thought experiment: what application for the Argo observing system?

To toy with this thought a little bit further, I wanted to see if I could answer the following question: if we started our "observations" (in the model world, i.e. the start date of the trend computations) around the beginning of the Argo era, and over the ocean area covered by Argo (i.e. roughly about 0-2000m, 60ºS-60ºN) when could these fingerprints of temperature and salinity change be detected? To answer this simply, I now run the analysis with the fingerprints defined from 0 to 2000m, 60ºS to 60ºN, and start the trend calculation in 2005.

Detection times are presented in figure II.15 for the normalized and non-normalized changes. By 2021, both the normalized and non-normalized fingerprints of zonal mean temperature change in the upper 2000m can be detected in the full ensemble (already by 2014 for the normalized analysis), showing how fast the temperature signal is in the 21st century. For the salinity fingerprint, the detection is successful for SNR>2 in 75% of the ensemble by 2021 in the normalized analysis, but for greater thresholds there is

still no detection by 2059. Note that for the upper 2000m, the evolution of the fingerprint is not associated anymore with a positive trend as soon as the beginning of the historical period (as seen in figure II.13). Instead, the PC and pseudo-PCs show barely any evolution until the late 20th century followed by a sharp increase, and with much more intermember variability than temperature (not shown). Less variability is associated with the detection times of the non-normalized salinity fingerprint, with detection of the full ensemble by 2040 for SNR>2.

If we consider that the model's variability and response to anthropogenic forcings is realistic, we can, today, already detect the zonal mean fingerprint of temperature change in this realization with "observations" of the upper 2000m ocean over the 2005-2021 period. For salinity however, it would take 10-20 more years.

A natural perspective to this example is to search for these fingerprints in actual observations of the ocean. Data is available before 2005 but these products often tend to fill missing data with climatological values, giving conservative estimates of potential changes. How the observations would project onto these model-based fingerprints is yet unknown.

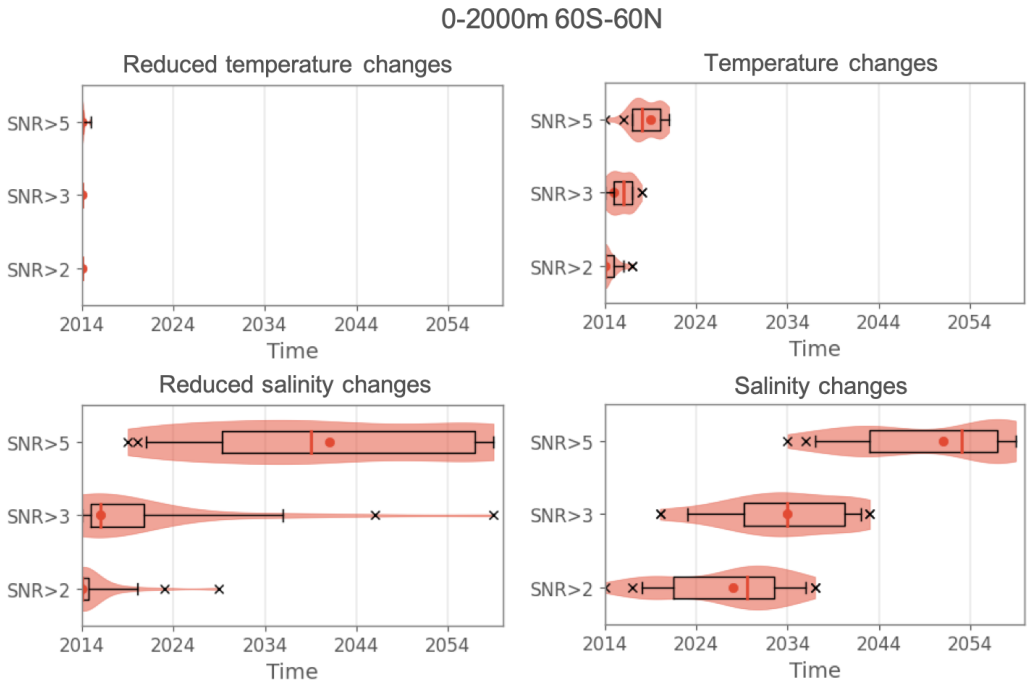

Figure II.15: Detection times of the zonal mean temperature and salinity fingerprints defined over 0-2000m, 60ºS-60ºN, for the normalized ("reduced") and non-normalized analysis with 2005 as the start year for the trends calculation.

4.3 Vertically-integrated fingerprint

The detection analysis is now applied to vertically-integrated ocean heat and salt contents and briefly discussed (figures II.16 and II.17). The yearly data is also bilinearly interpolated here on a regular 1ºx1º horizontal grid, and the EOF analysis is weighted by the gridpoint area.

The non-normalized fingerprints (figure II.16, first and third rows) show similar patterns as the ensemble mean anomaly presented for the local approach in figure II.9, and the normalized fingerprints (second and fourth rows) similar patterns as the SNR in figure II.9, except the sign of the change is now taken into account. By normalizing the initial data, one feature that stands out is the subpolar North Atlantic,

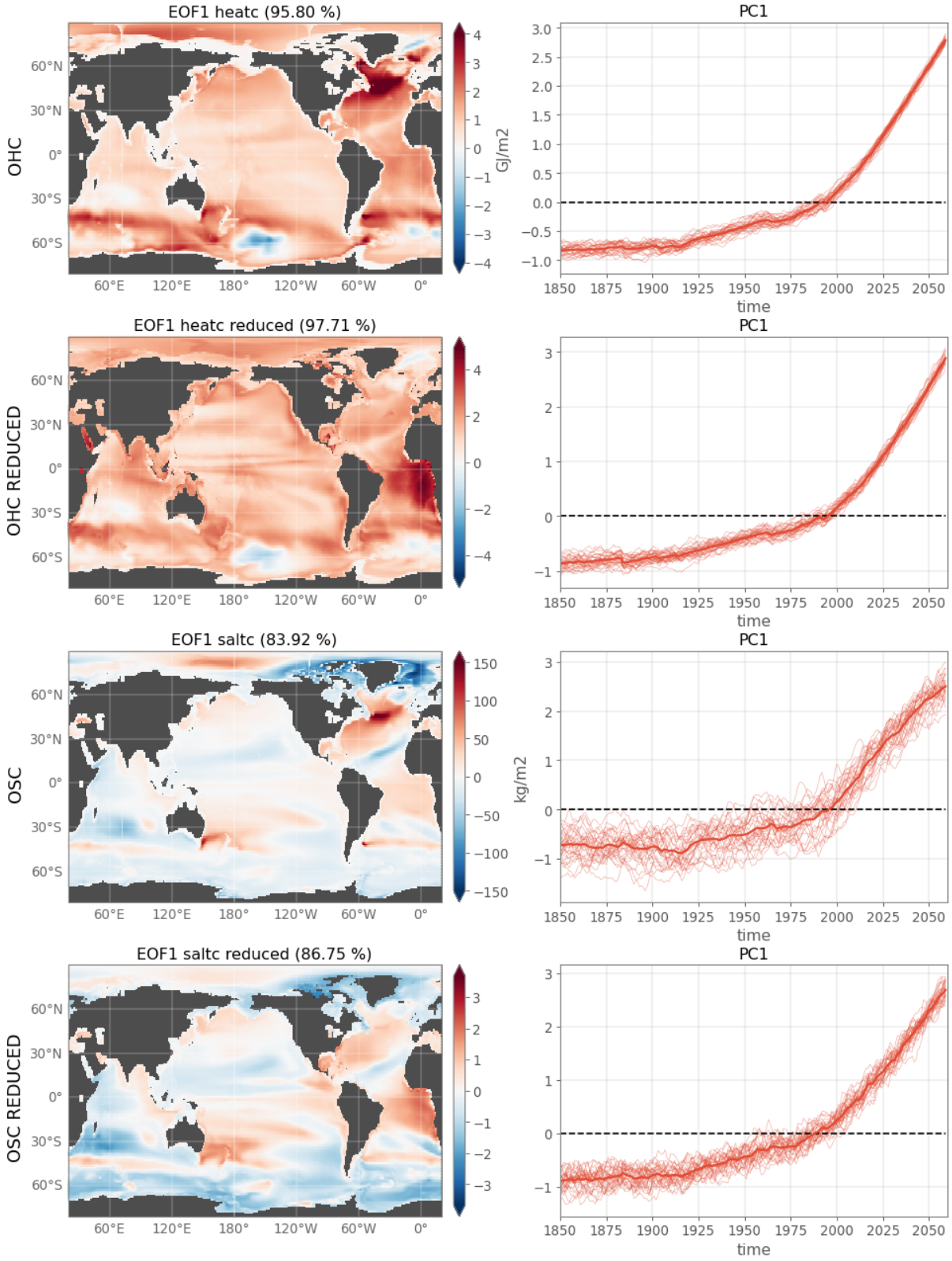

Figure II.16: Vertically-integrated ocean heat and salt content fingerprints (left) and associated signal time series (right, projection of individual members onto the fingerprint). The EOF analysis is weighted by the gridpoint area. The data is normalized (divided by the time-mean intermember standard deviation) prior to running the EOF analysis in the second and fourth rows.

which originally displayed the largest change over the globe for both OHC and OSC, and now has a much more weaker change relative to its large local internal variations. Note that normalizing the data with the piControl standard deviation gives the same results (not shown).

The evolution of all four fingerprints show similarities with that of global mean SST: a marked increase starting in the early decades of the 20th century, a pause between 1960-1980, and a much stronger increase afterwards. The non-normalized OSC presents much more intermember variability in the signal time series than the normalized OSC, but there doesn't seem to be much difference for OHC, and the reasons are unclear. A possible explanation resides in the unconstrained nature of salinity compared to temperature: ocean salinity is forced by air-sea interactions and mixed by the ocean circulation, but it does not feedback on the air-sea fluxes like temperature does. This could - partly - explain the larger intermember variability in the evolution of salinity compared to temperature.

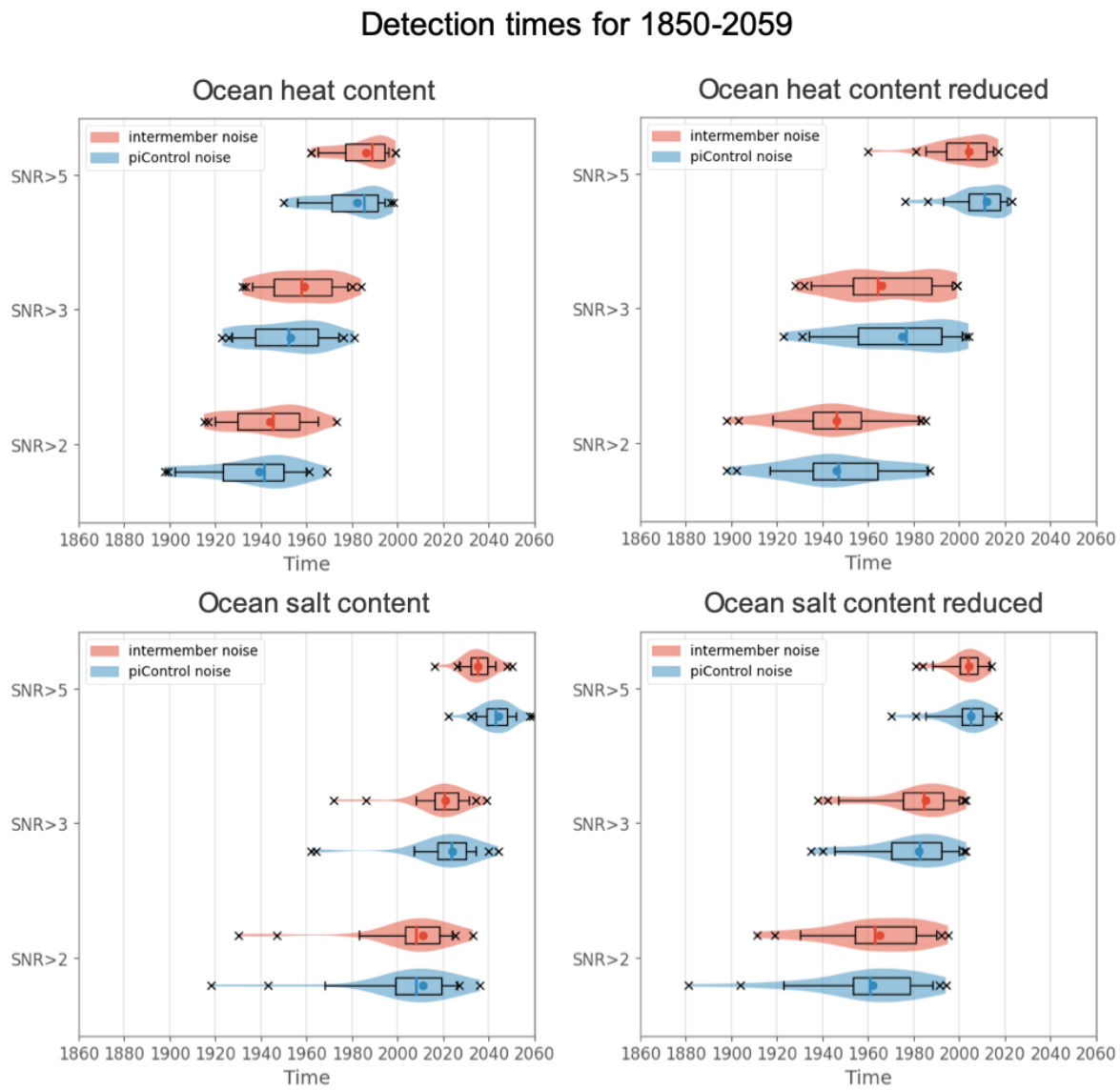

Figure II.17: Detection times of the vertically-integrated ocean heat and salt content fingerprints, for the normalized ("reduced") and non-normalized analysis data. Red distributions indicate when the analysis uses the intermember noise (same in the zonal mean framework), and blue distributions when the piControl noise is used instead.

The detection times for these four analyses are shown in figure II.17. The start year for the trends computation is 1850. The results for the SNR>2, SNR>3 and SNR>5 thresholds are shown but we will mainly comment on the SNR>5 detection times for brevity. Detection of the ocean heat content fingerprint is found in the ensemble between 1960 and 2000, with a median around 1985. This corresponds to what was found for the normalized zonal mean temperature fingerprint (figure II.12). However, for the normalized ocean heat content fingerprint, this distribution is shifted by about 20 years later in time (omitting the outlier member in 1960). This suggests the SNR increases faster in the non-normalized case, where the fingerprint is naturally dominated by the largest changes. For ocean salt content, the opposite occurs: detection is found earlier in the normalized case, by about 30 years (between 1980-2015 with a median in 2005, compared to 2015-2050 with a median in 2035). There is now much more intermember coherence in the detection of these salinity fingerprints than found in zonal means (reduced intermember spread), with a similar median detection time in the normalized case but much earlier detection for the last member (2015 vs. 2050, see figure II.13).

Overall, it seems that these vertically-integrated fingerprints reveal mostly the upper ocean signal (as seen by the expression of volcanic eruptions in the signal time series of OHC and by the early 20th century signal), but with less internal variability, a mark of the integrated signal over several levels. It would be interesting to compare the detection timing of the SST and SSS fingerprint. For SST, it would probably be close to what was found for the non-normalized zonal mean temperature fingerprint (figures II.10 and II.11), dominated by the first levels of the ocean and detected between 2000 and 2030 for SNR>5.

We also computed the detection analysis with the piControl noise as described in the methods section: the 2000-year piControl is projected onto the fingerprint, giving an estimate of the amplitude of the fingerprint in an unforced simulation in which it would *a priori* be present only by chance. This gives us a 2000-year noise time series oscillating around zero, on which linear trends are computed on all possible L-year segments shifted by 10 years. The noise N is then the standard deviation of this distribution of trends for each increasing L-year period. The distributions of detection times computed with the piControl noise (blue in figure II.17) are aligned with those computed with the intermember noise (red) in almost all cases, with a shift in their respective medians of maximum ten years across analyses and threshold. This further supports the fact that the unforced interannual variability as extracted from a long piControl experiment is well estimated by the 30-member spread in the large ensemble.

Compared to the local ToE approach (figure II.9), the pattern-based method allows earlier detection of the climate change signal, although the intermember spread is still large for the SNR>2 threshold. The two approaches don't target the same questions and are in fact complementary. With the pattern-based method, we aim to investigate whether the global pattern of change has been detected, whereas in the local method, we can distinguish the time scales of signal detection between different regions and identify "hot spots" of climate change signal emergence.

4.4 Application to the volumetric Temperature-Salinity framework

We now move forward to another analysis framework: the volumetric distribution of the ocean in temperature-salinity (T-S) space. This type of quantification is not new in physical oceanography and has been used in past studies to make a volumetric census of the world ocean water-masses in bivariate discrete classes of temperature and salinity, and discuss their origin (e.g. Worthington [1981]). It is a way to represent the entire volume of the ocean on a plane, and is essentially a 2-dimensional histogram. This kind of representation has been applied to study, among else, the thermohaline circulation and investigate the different processes of water-mass formation [Zika et al., 2012, Döös et al., 2012, Groeskamp et al., 2014, Hieronymus et al., 2014, Evans et al., 2014, 2018]. In more recent years, Zika et al. [2021] used this volumetric census with Argo data at two different time periods to diagnose the excess heat entering the ocean in response to long-term climate change, as opposed to changes in the circulation redistributing the background temperature. Indeed, the addition and mixing of heat in the ocean is reflected in the

volumetric T-S distribution by the creation of new T-S classes (or bins). The pure advection in space of a water parcel of volume V and of given T-S characteristics will not change the T-S values of that volume of water, and thus will not be reflected as a change in the volumetric T-S distribution.

Here, we are also interested in how this volumetric distribution evolves in time under increasing anthropogenic forcings. That is, how the water-masses evolve in T-S space and in time, and whether and when we can detect these changes, still in the framework of the IPSL-CM6A-LR ensemble.

The T-S "binning" has been performed with the xhistogram Python package [2] on the historical-extended and piControl dedrifted annual outputs. The ocean model of IPSL-CM6A-LR, uses a variable volume formulation, which means the vertical grid has time-varying levels (the variation in grid-cell thickness is several orders of magnitude smaller than the thickness itself). Consequently, we took the precaution to use the time-evolving grid-cell thickness output (thkcello) at each time step in the weights information (along with grid-cell area), although the time dependence doesn't seem to impact the distributions (not shown). The bin resolution was chosen at 0.25ºC for temperature and 0.025 g.kg^{-1} for salinity following Evans et al. [2014] (note that we use Conservative Temperature and Absolute Salinity). This is a good compromise, for exploratory work, between a large enough resolution to resolve changes in temperature and salinity between most bins, and the time it takes for the binning code to run.

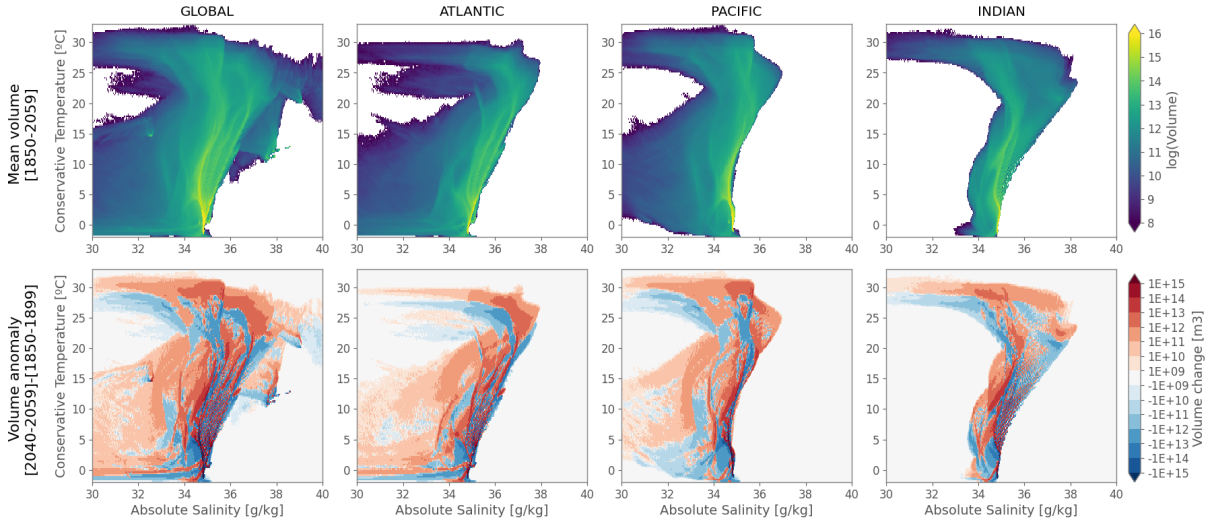

Figure II.18: Temperature-Salinity volumetric distribution in the ensemble mean for the global, Atlantic, Pacific and Indian oceans (note semi-enclosed seas are not included in the basin histograms). (Top) Mean volume (shown in logarithmic scale) over the historical-extended period. (Bottom) Anomaly in [2040-2059] relative to [1850-1899].

The mean global volume for the IPSL-CM6A-LR historical-extended ensemble mean is shown in figure II.18 (upper left panel) along with its change in [2040-2059] relative to [1850-1899] (lower left panel). The ocean volume per bin can vary by several orders of magnitude. Indeed, the majority of the ocean volume is distributed along "branches" that all converge towards a small number of bins containing large amounts of ocean water, around -1ºC to 3ºC and 34.8 g.kg^{-1}. On the opposite, numerous bins are occupied by smaller amounts of water, especially at the surface and in the low to mid-latitudes where the water is warmest and spans a wide salinity range. As the climate warms, ocean waters are globally warmed while salinity changes are various. As a result, the volumetric distribution shows dipoles of change (bottom panels in figure II.18): volumes of water move from one T-S class to another, and the distribution, overall, expands. One marked example that visually stands out is the warming of surface tropical waters, which overall gain a couple of degrees Celcius, from the 27-29ºC range moving to the

2. https://xhistogram.readthedocs.io

30-32ºC range (blue-red dipole in figure II.18). The warming of the Arctic is also well made out (below-0ºC waters at low salinities <34 g.kg^{-1}). Other parts of the ocean are more difficult to distinguish in the dominant branches of ocean volume. The largest changes in volume magnitude are collocated with the largest quantities of mean volume. Of course, this distribution can mix water-masses of similar T-S characteristics coming from two very different parts of the world, geographically speaking. We show the T-S distributions of the 3 main ocean basins (Atlantic, Pacific, Indian) in figure II.18 as an example of how water-masses are distributed and how they can overlap on one another in this framework.

We can see how changes analyzed uniquely at the grid point level (as in section 3) in this framework are not satisfactory as 1) volume is a positive quantity 2) hence, when some bins are emptied, there is a volume threshold value of 0 which cannot be surpassed 3) some T-S bins are emptied over time, others are filled, and others stand in-between. What we are interested in here is the T-S spatial pattern itself, and not the local changes which cannot be analyzed similarly as intensive quantities. Thus, we will apply the pattern-based method introduced in the former section to extract the dominant mode of long-term variability in the thermohaline structure of the ocean and look for detectable changes. Here, we will present results at global scale and for a few cases only so as to give a taste of the possible applications of the detection method in this framework. Interesting perspectives would be to discretize the geographical ocean in sub-basins as in Zika et al. [2021] before performing the analysis, to prevent water-masses of very different geographical origins to be mixed together in single bins.

The fingerprint for global ocean volume (first EOF of the ensemble mean, 1850-2059) and associated signal time series (projection of individual members onto the fingerprint) are shown in figure II.19. The pattern is the same as the ensemble mean anomaly shown in figure II.18. Surprisingly, the time evolution of this fingerprint (figure II.19, upper right panel) shows an increase almost from the start of the historical period, probably too early to be a sign of human-induced climate change. This evolution is in fact representative of the deep ocean, which encloses large quantities of water in very few T-S bins compared to the number of bins covered by the global ocean. We prove that by showing the fingerprint of change for the global ocean below 2000m only (figure II.19, lower panels). The analysis for the 0-2000m ocean will be shown later. In the deep ocean, the change of volume in the T-S bins are several orders of magnitude larger than for the bins covering the ocean surface. The signal time series for the deep ocean below 2000m have the exact time evolution as those for the global ocean, meaning the global fingerprint is completely dominated by the deeper ocean. In fact, this drift-like evolution is determined more precisely from the change occurring in the coldest bins. Indeed, the analysis restricted to volumes of positive temperatures only reveals a much more coherent evolution with a progressive increase, while the analysis applied only to volumes of negative temperatures yields the time evolution of figure II.19 (not shown). These very cold waters show the largest volume changes with a shift of the distribution towards fresher waters. This is coherent with what looked like a residual drift in salinity when investigating the zonal mean normalized salinity fingerprint (figure II.13). The potential residual drift seems to originate from the export of AABW. This suggests this issue should be addressed before examining deep ocean changes in salinity in this model, with a more efficient drift removed in salinity. Note that the analysis before removing any drift in temperature and salinity yields a much steeper increase of the time evolution of the fingerprint (for the global and deep ocean alike, not shown) until the late 20th century, proof that some drift was indeed removed in the analysis presented here.

Even without a residual deep ocean drift, the global fingerprint of the changing volumetric distribution would emphasize the deep ocean because of the order of magnitude of ocean volume (and volume change) in these bins. This residual drift prevents an accurate detection of actual change in the volumetric distribution. To ignore it we can either do the analysis in the upper 2000m of the ocean where there is no influence of the remaining drift, or do the analysis on the normalized volume. We will present these two cases here and apply the detection analysis.

If we normalize the T-S volume prior to performing the EOF analysis (i.e. center and divide by the

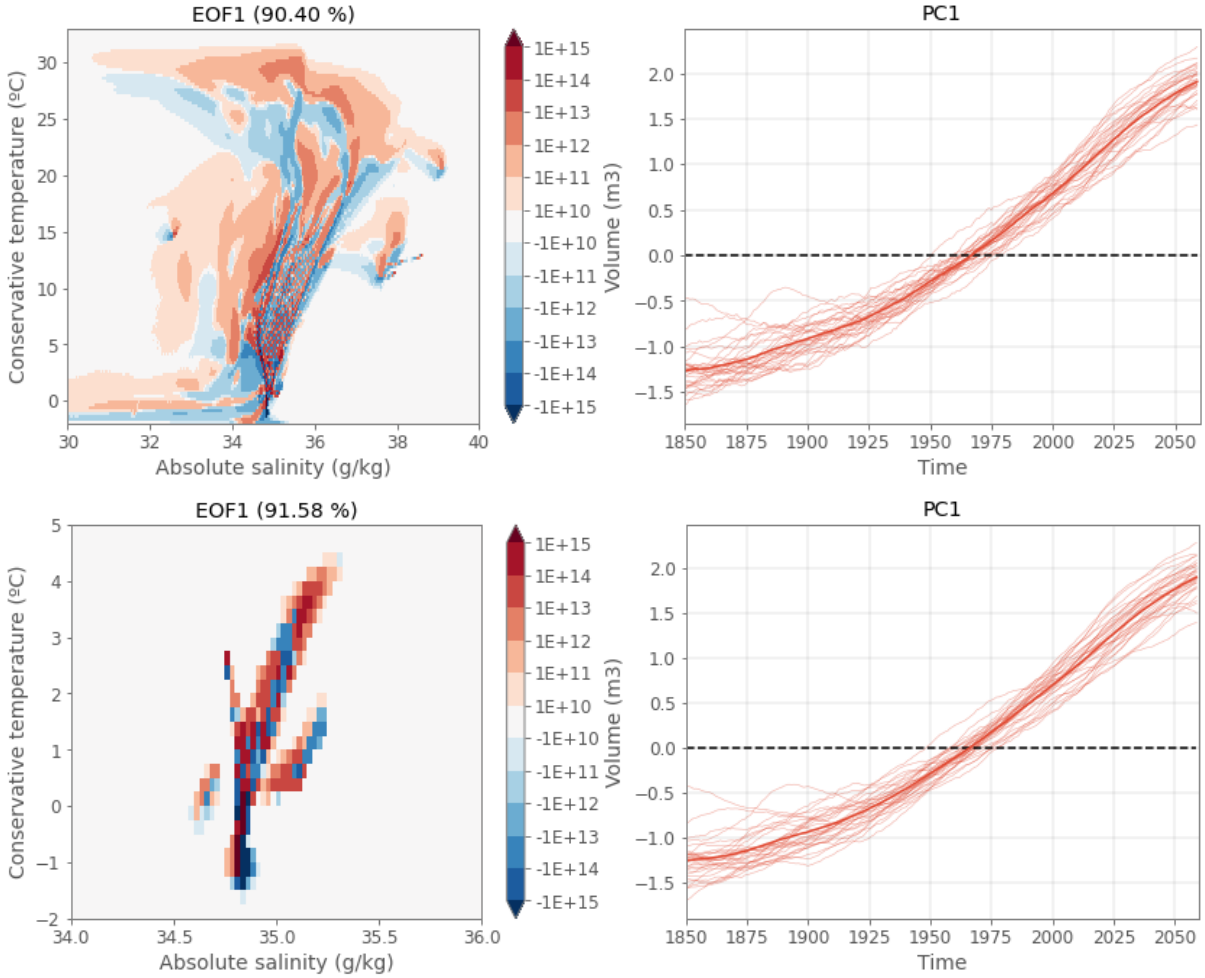

Figure II.19: Fingerprint and signal time series of the volumetric distribution of the ocean in T-S space. Upper panels show the analysis for the global ocean volume, and lower panels for the volume below 2000m.

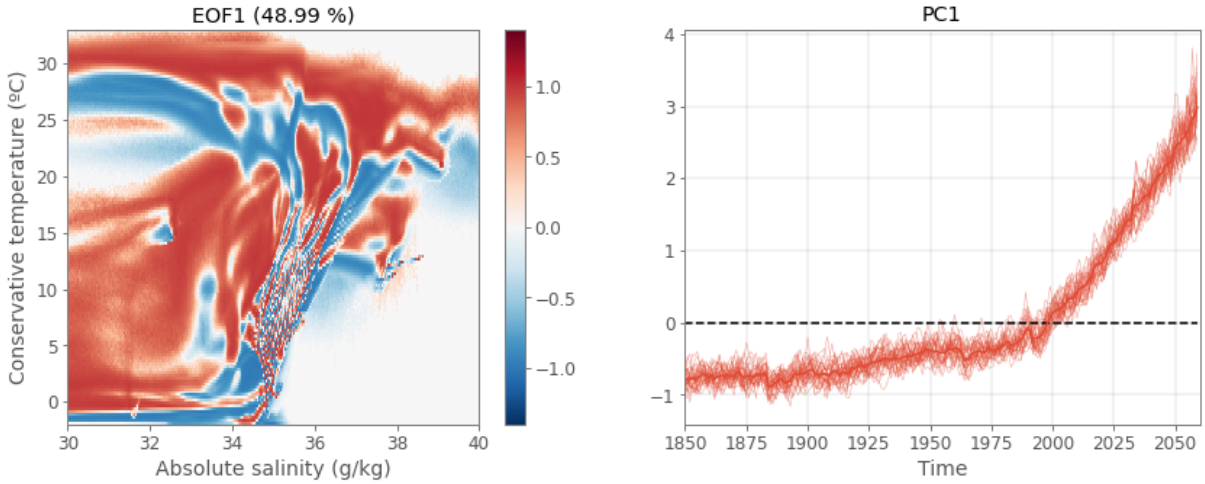

Figure II.20: Fingerprint and signal time series of the normalized volumetric distribution of the ocean in T-S space, for the global ocean.

ensemble mean interannual standard deviation for each bin), we obtain a volumetric T-S distribution weighted by the order of magnitude of volume contained in each bin (figure II.20). Consequently, this is somewhat equivalent to a T-S diagram of the ocean, without taking into account the ocean volume as weights. The new normalized fingerprint (figure II.20) has similar patterns of change as the regular fingerprint (figure II.19). Thus, a surface bin ends up having the same weight as a deep ocean bin, although these two bins don't represent the same volume of water. The fingerprint is now more representative of the surface signal since surface waters take so much space in this T-S framework. Here, we don't mean to imply this is a better way to look at changes in this T-S space, but explore the possibilities given the current limitations. Note that normalizing by the piControl interannual standard deviation or intermember standard deviation would make more sense in a regular geographical framework (as done for the zonal means or vertically-integrated contents presented before), but because new T-S classes are created with ongoing climate change (e.g for the warmer surface waters) and because these classes can slightly differ between members, the piControl or intermember standard deviation would be zero in some classes, which does not make sense to study the change.

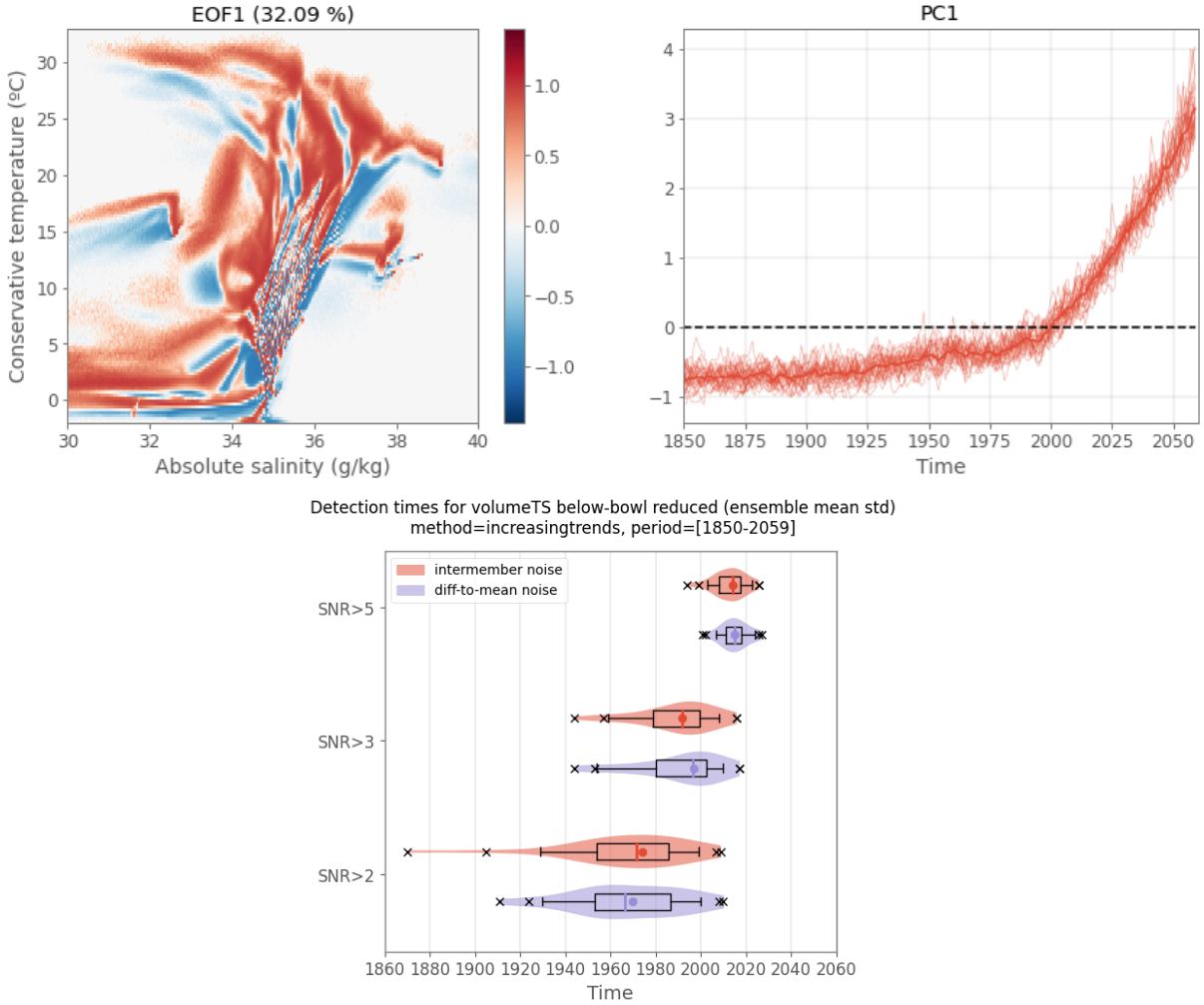

Figure II.21: Fingerprint, signal time series and detection times of the normalized volumetric distribution of the ocean in T-S space, for the global ocean below the maximum mixed layer depth. Purple and red distributions stand for two different estimates of the noise, see text for details.

In an endeavor to remove some of the surface noisier signals and numerous T-S bins, we look at this normalized fingerprint but for the global volume under the mixed layer depth, which was calculated from the maximum MLD in the 2000-year piControl at each geographical grid point. The fingerprint now

looks similar but with less T-S space occupied (figure II.21 compared to figure II.20). The evolution of this fingerprint in time is also slightly smoother than for the global ocean volume, with less impact of volcanic eruptions on the interannual time scale (the sudden drops following large volcanic eruptions are smoothed out). This signal is detected between ∼2000 and 2025 in the large ensemble for SNR>5. This timing is very coherent with the detection of the zonal mean temperature fingerprint (non-normalized), representative of the upper ocean warming (figure II.11). Note that the analysis applied to the entire ocean volume including the mixed layer actually shifts the SNR>5 distribution by about 20 years earlier than without the mixed layer (not shown), since these surface points shift so much in T-S space over the historical-extended simulations.

We also tested the third method to estimate the noise here from the large ensemble: we first calculate, for the T-S volume, each member's difference to the ensemble mean and concatenate in time these 30 fields. The resulting 3D (time, temperature, salinity) volume field is normalized similarly as the ensemble mean (centered and divided by the ensemble mean standard deviation) and projected onto the fingerprint. We obtain a 6300-year noise time series (pseudo-PC), on which we calculate the distribution of increasing L-year trends (as we would for the piControl noise method presented earlier in this chapter). This noise estimate yields almost identical detection time distributions (purple shading in figure II.21) as those obtained from using the intermember standard deviation of the signal trends (red shading).

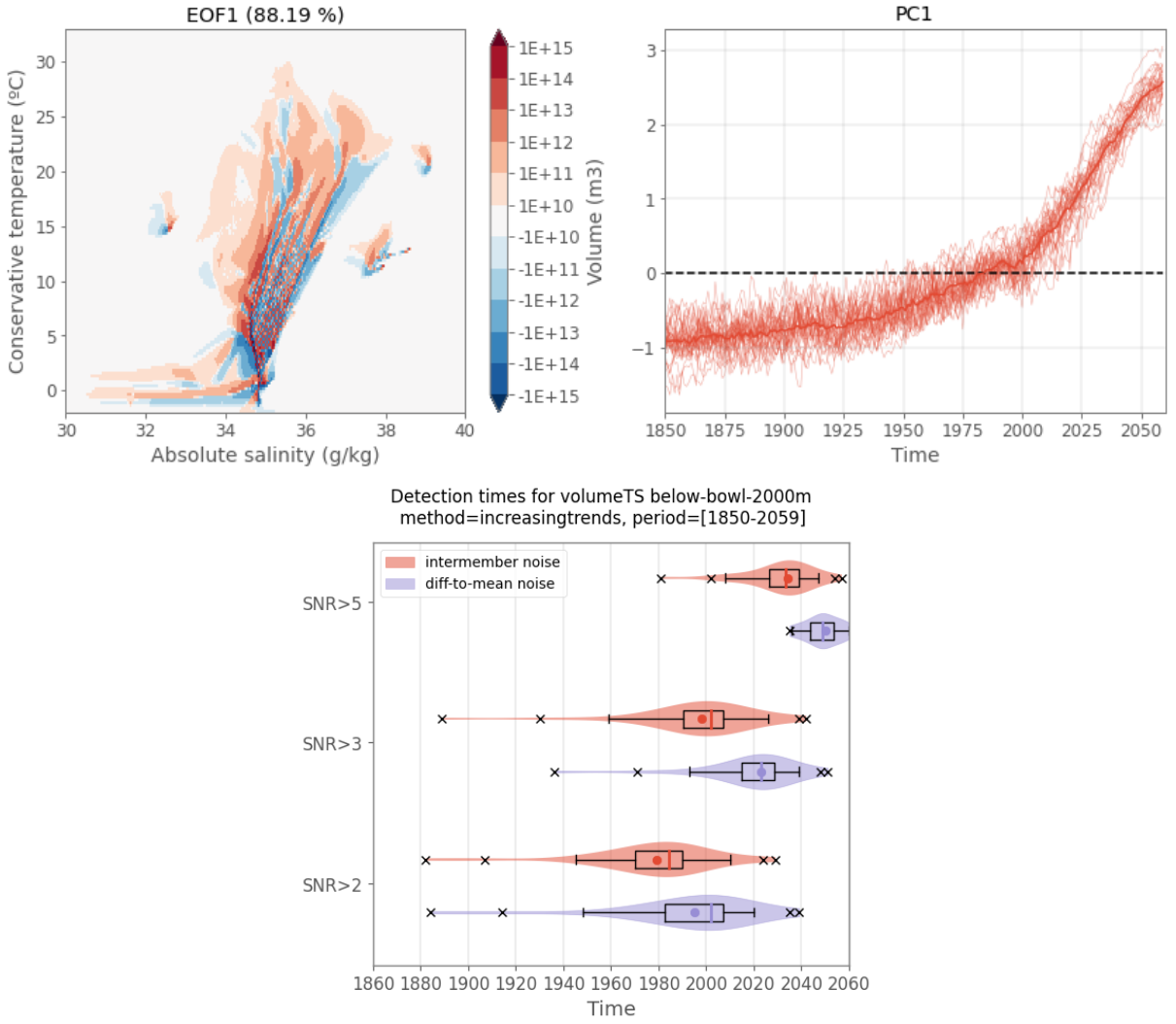

Figure II.22: Fingerprint, signal time series and detection times of the volumetric distribution of the ocean in T-S space, for the global ocean in the upper 2000m and below the maximum mixed layer depth.

We now apply the analysis without normalizing the volume, on the global ocean above 2000m depth and below the mixed layer (figure II.22; note that removing the mixed layer volume does not change the detection results). Now, the change in the T-S volumetric distribution is detected much later and with wider intermember spread, with a median detection time around 2030 for SNR>5 and individual members detected from 1980 to the very last years of the period. The alternative noise estimate (purple shading, computed from each member's difference to the mean, see explanation above) yields this time slightly delayed distributions, with a median shifted by about 20 years later in time, meaning it is a more conservative estimate when the volume is not normalized.

Overall, in this framework, it is easier to follow and detect changes coming from the upper layers of the ocean, as these waters express the largest changes in temperature and salinity, and are thus displaced over larger "distances" in T-S space. In this case, the "unweighted" T-S space (i.e. the normalized analysis) provides an interesting tool to track the change in the thermohaline structure of surface ocean water-masses. The deeper ocean on the other hand is compressed to fewer T-S classes. It is also prone to changes in its thermohaline structure, but the distances covered in T-S space are much smaller, and the volume is more subject to reorganization within the bins than creation of new bins. It makes it harder to detect these changes: the detection is delayed to the 21st century and with much more internal variability modulating the timing of detection. Furthermore, a possible residual drift in salinity found in the coldest waters is "polluting" the global ocean fingerprint. A more adapted dedrifting procedure for salinity is needed to fully explore the possibilities offered by this framework, along with more adapted bin resolution in the deepest water-masses.

5 Key points

- In this chapter, I aimed to investigate the emergence of anthropogenic ocean temperature and salinity changes in the IPSL-CM6A-LR large ensemble of historical-extended simulations, by testing different methods and frameworks.
- First, a local Time of Emergence approach similar to Chapter I was applied to zonal mean temperature and salinity changes along regular pressure levels, and to vertically-integrated heat and salt content changes. Second, a pattern-based method was applied to the same variables, looking for when a global fingerprint of change could be detected. Finally, the pattern-based method was tested on the evolution of the temperature-salinity volumetric census of the global ocean.
- These different configurations allowed to test the sensitivity of signal detection when considering the influence of the upper, deeper or global ocean with different weights.
- While the local and pattern-based methods were different, the results were similar: overall, they point to an emergence/detection of the ocean warming patterns in all members of the ensemble by the early 21st century, while the emergence of salinity changes at global scale are delayed, with more internal variability masking the forced signal and less regions individually emerging.
- When considering the patterns of locally-weighted signal to noise ratios, i.e. not just the absolute change which benefits more to the upper ocean, the global warming pattern is detected earlier. This is coherent with the local ToE approach which points to the AABW and its northward spread in the abyssal ocean as the region emerging earliest, both in temperature and salinity. This highlights the relevance of looking in the deep ocean interior for forced change because the noise levels are very low, although it is also where the influence of initial conditions is the largest.
- These results point to a particular sensitivity of the deep ocean in the model, which shows very early emerging signals in the 20th century even in the least ventilated regions. The short time scales on which the warming is found in these areas suggest the temperature anomalies are not transmitted passively along the pre-existing ventilation routes of the ocean interior, but probably testify of an internal reorganisation of the ventilation which seems to cause rapid subsurface changes. This point will be more specifically addressed in Chapter IV with dedicated simulations presented in Chapter III to test these hypotheses.
- Examining deep ocean changes needs to be done carefully as significant drift can exist. We successfully removed the quasi-linear cooling drift in temperature, but a regional freshening drift in salinity seems to have persisted. This point should be tackled before going further in potential deep ocean salinity analyses.
- In agreement with what we found in Chapter I, the region associated with SAMW and AAIW stands out with the largest SNR in the zonal mean temperature framework, especially in the Indian sector, where the patterns penetrate almost to 2000m depth. This highlights these water-masses as a preferred pathway for the uptake of anthropogenic heat.
- Using 30 macro-initialized historical members, we have seen that the intermember spread is an excellent estimate of unforced interannual variability of the model when compared to piControl. In addition, this estimate takes into account the impact of external forcings on internal modes of variability which a piControl simulation does not.

- All in all, the final interesting result is not necessarily a precise year of signal emergence, as we have seen that there are many subjective criteria on which that depends, but rather what these criteria reveal. One prominent aspect is how initial conditions can modulate the detection of the forced signal, with a difference of several decades over the 20th century between individual members. Indeed, although the climate change signal (the ensemble mean) can be detected as early as the 1940s when considering the deep ocean low noise level, it is slow and thus more exposed to intermember modulations that can be as large as the temperature anomaly itself, delaying or enhancing the exceedance of a significance threshold in individual members.
- The volumetric T-S framework is an interesting oceanographic tool to get a sense of the water-masses distribution. However, it reduces the deep ocean to a very small number of T-S classes, which makes it more difficult to track the changes occurring there. Upper ocean water-masses on the other hand are spread out in T-S space, which makes it easier to understand their shifts. For a more in-depth investigation into deeper ocean changes in this framework, finer resolution of T-S classes would be needed, and separating into a few geographical regions prior to computing the histogram would probably help better discriminate the nature of the water-mass changes.

Chapter

III

Configuration of the simulations

Contents

1 Goal

In the first two chapters of this thesis, we diagnosed an externally-forced, multi-decadal change in the ocean temperature and salinity simulated fields, in different analytical frameworks, that could be unambiguously distinguished from internal variability starting in the second half of the 20th century, with very region-dependent structures and timings of emergence. In this third part of the thesis, we will use a more mechanistic approach to understand how these signals emerge. In the General Introduction, we presented the potential drivers of thermohaline changes in the ocean: changes in surface heat, freshwater, and momentum fluxes causing additional warming/freshening entering the ocean and/or causing circulation changes redistributing pre-existing temperature and salinity gradients. A number of studies have addressed the question of the relative role of these processes for the ocean heat storage in response to

rising greenhouse gases, revealing important mechanisms at play. They were however conducted mostly in idealized scenarios in terms of time scales of emissions and considering almost always CO_2 as the only external forcing.

Here, we are interested in unraveling the relative role and time scales of these drivers of human-induced temperature and salinity emergence, on historical time scales of forcings (i.e. since the pre-industrial era) and into the 21st century under realistic scenarios of emissions. Are all of the drivers equally important to let temperature and salinity exceed their range of internal variability? How do they interact? What are their relative role in setting the timing and location of emergence ? To tackle these questions, we designed numerical experiments in which air-sea flux perturbations during the period 1850-2100 are imposed together and separately on a stand-alone configuration of an ocean model. This allows the investigation of the individual role of surface flux changes in modifying ocean temperature and salinity. Furthermore, to separate patterns of change due to the perturbed circulation from those due to passive transport of heat and salt into the ocean, we implemented passive tracers of temperature and salinity forced by identical surface flux perturbations as the corresponding oceanic properties. More details of the experimental protocol are given in section 2.

This chapter has two purposes. First, to introduce and describe this experimental protocol which will be the basis for the study presented in chapter IV of this thesis. Second, to document the modelling work done in the hope that it can, at some point, be of use to others. I am not describing all the technical details of the NEMO routines and configuration here, but rather trying to describe the system, present the approach taken, discuss the choices that were made and validate the simulations. For more details, the code of the configuration and a short technical documentation can be found here: https://github.com/ysilvy/simus_orca1_fluxforced.

The modelling environment is set up by the IPSL "platform team", who provides technical guidance in running the models. All simulations were run by myself on the French Jean Zay supercomputer held at the IDRIS center (http://www.idris.fr/jean-zay/cpu/jean-zay-cpu-hw.html). The configuration was developped with tremendous help and support from Clément Rousset and Christian Ethé, and with regular guidance from Gurvan Madec. My gratitude also goes to Juliette Mignot for introducing me to the general modelling framework at IPSL, for her advice on the coupled model, and for her support all along this long process.

2 Ocean model and experimental design

The ocean model

We use the ocean physics component (OPA) of the NEMO model version 3.6 [Madec et al., 2017] for our experiments, as NEMO3.6 is the ocean – sea-ice – biogeochemical component of the IPSL-CM6A-LR coupled model [Boucher et al., 2020], developed here at IPSL, which took part in the CMIP6 exercise. The configuration used is the eORCA1 tripolar grid, with a nominal horizontal resolution of 1º (down to 1/3º latitudinal refinement at the equator) and 75 vertical levels with layer thicknesses varying from 1m at the surface to 200m at the bottom. The vertical layers are time dependent, with a nonlinear evolving free surface using the variable volume formulation. The equation of state is estimated with a polynomial representation of TEOS-10 [Roquet et al., 2015]; the model prognostic fields are thus conservative temperature and absolute salinity. The different schemes and parameterizations employed in the eORCA1 configuration and used in IPSL-CM6A-LR are described in Boucher et al. [2020] and all details can be found in Madec et al. [2017]. The ocean model can be forced at its boundaries in a number of ways. The most current ones include forcing with:

- bulk formulae: the user provides a number of key atmospheric variables and lets the model compute the physical fluxes between the ocean and the atmosphere. The forcings are usually provided by reanalysis products, such the Coordinated Ocean–Ice Reference Experiments (CORE, Large and

Yeager [2009]) and the Japanese 55-year Reanalysis (JRA-55, Kobayashi et al. [2015]). In this configuration, the forcings are provided at the ocean+sea-ice interface with the atmosphere, and feedbacks of the model SST are allowed on the computed fluxes since bulk formulae need the SST.

- fixed fluxes: the user directly provides all the physical fluxes at the ocean interface. In this configuration, there are no feedbacks of the ocean state on the flux forcings, unless a relaxation is activated.
- a coupled atmospheric model, such as in the IPSL-CM6A-LR configuration: in this framework, the ocean and atmospheric model feedback on each other by sending their respective surface variables through a coupler which provides the corresponding fluxes on the oceanic and atmospheric grids.

Experimental design

This work is set within the simulated climate of the IPSL-CM6A-LR coupled model. For the purpose of the CMIP6 exercise, 2000 years of pre-industrial control run were conducted (after a long spin-up), along with 32 members of the historical experiment (1850-2014), extended to 2059 under the ssp245 scenario, and multiple scenarios for 2015-2100 with fewer members. In this study, we want to investigate and isolate the mechanisms responsible for temperature and salinity emergence from natural variability in the IPSL-CM6A-LR historical+ssp ensemble. In order to do that, we choose to reproduce the 1850-2100 full ocean response with the same surface forcings as in the coupled model, to then be able to isolate the response to each forcing perturbation in different experiments.

Furthermore, as demonstrated in Chapters I and II, internal variability plays an important role in determining the timing of emergence of the anthropogenic signal within members of a model ensemble. Hence, we want our different numerical experiments to have a same reference in terms of phasing of internal variability if we are to compare the temporal evolution of the patterns of change and their associated timing of emergence in each of the simulation. This means we want the background internal variability of the surface fluxes to be similar in each experiment, which entails preventing retroactions between the ocean and the surface fluxes, including when perturbations are applied. Thus, forcing the ocean with fixed fluxes is a coherent choice for the objectives of these simulations (compared to an ocean coupled to an atmospheric model or forced with bulk formulae, which enable a retroaction that we want to avoid). As a co-benefit, running the ocean model in a stand-alone configuration is computationally much less expensive in cpu and elapse time (and consequently less energy and CO_2 emissions) than running a coupled model. Still, these experiments have contributed to emit their fair share of CO_2 (see Appendix F).

We first set up an ocean-only CTL experiment forced with fluxes from a pre-industrial control simulation (piControl, no external forcings) of the IPSL-CM6A-LR coupled model (see the simplified schematic of the experiments in figure III.1). The goal is for this ocean-only CTL to inherit the mean climate and internal variability of the coupled model piControl, to provide a background climate for the sensitivity experiments. The piControl fluxes are thus imposed at high frequency (3-hourly) at the liquid ocean interface (below the atmosphere and the sea-ice), during 251 years. The sea-ice component is excluded. We go into more details over the forcing methodology in the next sections. We then run perturbation experiments, forced with the same fluxes as CTL, plus a perturbation component (figure III.1). The perturbation components are constructed from the monthly-mean anomalies (relative to 1850-1899) of the ensemble mean of the IPSL-CM6A-LR historical+ssp245 experiments to obtain a good estimate of the externally-forced signal over the 1850-2100 period (32 members over 1850-2059, 11 members over 2060-2100). The ALL experiment has the perturbation on all fluxes (heat, freshwater+salt, wind stress). The HEAT, STRESS and WATER experiments only have the perturbation component on respectively the heat fluxes, wind stress, and freshwater+salt fluxes. The BUOY experiment has both the heat flux and the freshwater+salt flux perturbations. All experiments are thus aligned on the piControl internal variability, with the perturbation (forced) components on top slowly taking effect. The ALL experiment is designed to reproduce the historical+ssp245 forced response. It is initialized as any historical member from a parent

piControl state, with its own internal variability. The sensitivity experiments decompose the response of the ALL experiment while keeping identical phases of internal variability.

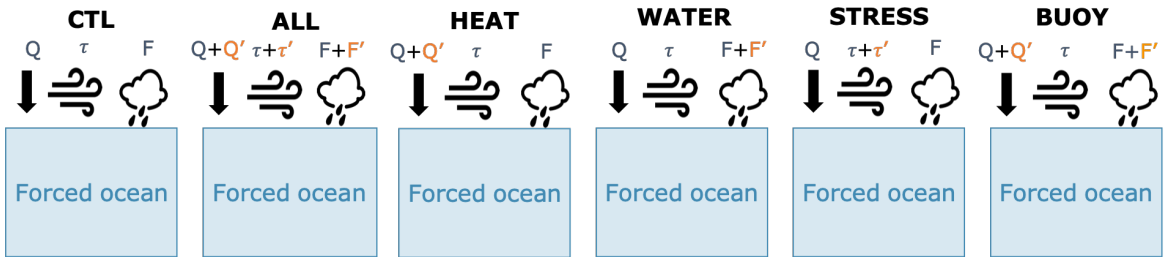

Figure III.1: Schematic of the simulations. Grey letters represent the "background" fluxes at 3-hourly outputted from the piControl. Orange letters are the perturbation fluxes (anomalies) extracted from the historical+ssp245 experiments of IPSL-CM6A-LR.

Configuring these experiments was undertaken in two main steps:

1. Setting up the CTL experiment from the piControl fluxes. This required enumerating all the components needed to force the ocean from the coupled model, in order to reproduce as closely as possible the piControl variability for 251 years, and adapt the code as to enable the flux forcing. This step is described in section 3.
2. Setting up the ALL experiment by adding the perturbation components, and making sure the response was similar to that of the historical+ssp large ensemble. This is described in section 4.

With these experiments, we thus aim to reproduce, with an ocean-only model, the unforced and forced response of a coupled model. We also added two passive tracers in each of these experiments, described in section 5.

Because the piControl of the IPSL-CM6A-LR published for CMIP6 did not have all needed high frequency outputs, we also had to run before-hand another piControl simulation with the IPSL-CM6A-LR coupled model to save the fluxes at the liquid ocean interface at 3-hourly frequency as well as other components. The piControl is initialized from the same spin-up simulation used as restart state in the piControl r1i1p1f1 published for CMIP6, but ran on a different machine, and saving fluxes at 3-hourly at the atmosphere-ocean interface and ocean-ice interface. Our piControl ran for 401 years, but only the fluxes from the last 251 years are used in the forced experiments.

The IPSL-CM6A-LR has a systematic quasi-linear drift in ocean global-mean temperature (see figure III.2 and Mignot et al. [2021]), passed on to the CTL experiment, due to a negative incoming heat flux (see heat budget in figure III.7). In the analysis of the simulations (chapter IV), all outputted data is thus dedrifted before any computation (see chapter II for the methods).

Our protocol closely resembles that of the ocean-only Flux-Anomaly-Forced Model Intercomparison Project (FAFMIP, Gregory et al. [2016], Todd et al. [2020]). Our CTL simulation corresponds to their faf-passiveheat simulation, ALL to faf-all, HEAT to faf-heat, etc. However, significant differences exist since we don't aim at answering the same questions. First, the (monthly) perturbation component used in FAFMIP (available here: fafmip.org) has a seasonal cycle but no interannual variation. It is constructed from idealized simulations at a time when CO_2 concentration has doubled in the atmosphere. Each experiment is run for 70 years. Consequently, they immediately impose constant strong anomalies and are not interested in the transient ocean response to human-induced radiative forcing but more in long-term patterns of change. Second, they use different initial conditions depending on the ocean model used. For most ocean models (including NEMO3.4), they perform a spin-up of several thousand years to equilibrate the ocean, integrated with a prescribed climatology, varying air-sea fluxes or bulk formulae, including a relaxation term both in SST and in SSS towards climatological values. After spin-up, the faf-passiveheat

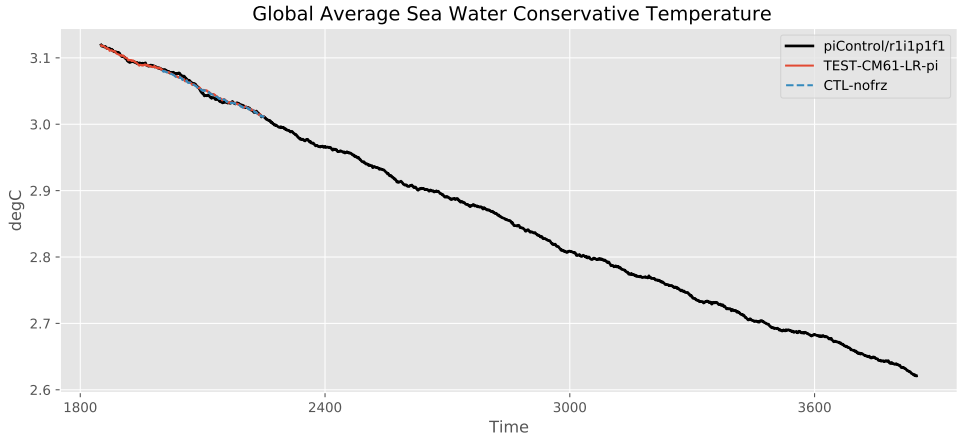

Figure III.2: Drift in global mean ocean temperature in the IPSL-CM6A-LR piControl r1i1p1f1 (black), the reference coupled simulation for the protocol (red) and the forced CTL experiment (dashed blue).

(i.e. control experiment) is performed by first diagnosing 70 years of high-frequency surface buoyancy and momentum fluxes (including restoration terms) under the same climatological conditions, and then re-running 70 years by prescribing those saved fluxes without any restoration. The only exception is HadOM3 which directly used fluxes from the 70-year control experiment (after spin-up) of its parent coupled model HadCM3 to produce the faf-passiveheat simulation. This is similar to what we do here, with our parent experiment being the IPSL-CM6A-LR piControl. Third, since the FAFMIP protocol is not meant to be model-specific, the perturbation fluxes are not decomposed precisely (e.g. solar vs. non-solar heat flux, E-P vs. runoffs, no salt flux). Since we are working with only one ocean model and its parent coupled model from which the fluxes and their perturbation components are extracted, we can be more precise in how we force the ocean and add more forcing components (see next sections).

3 Setting up the CTL experiment with fixed fluxes: an odyssey

In this section, I present how to set up the ocean-only CTL simulation (Figure III.1) from the outputs of a coupled piControl. To understand how the ocean model is forced, I present more generally the physical fluxes exchanged at the ocean boundaries in NEMO3.6, in the eORCA1 configuration, and indicate which variables are needed to force the NEMO3.6 ocean at the liquid-ocean interface (i.e. on the oceanic grid, under sea-ice). Synthetic schematics are shown in figures III.3 and III.4. Understanding what fluxes were needed to force the ocean was an essential step of the work, as well as verifying whether the freshwater and heat budgets closed, which was an indicator of the consistency of the code. Orders of magnitude of the fluxes are shown, their variability, and the associated budgets. Since we force the ocean with the fluxes from a coupled piControl with the same ocean model, the oceanic global budgets should be quasi-identical in piControl and ocean-only CTL. The only difference is in global ocean area, as the coupled configuration comprises closed seas which are masked in the ocean-only setup. Thus the globally-averaged surface fluxes have slightly different values in piControl and CTL.

The reference configuration is ORCA1_LIM3_PISCES (as in IPSL-CM6A-LR) but removing the sea ice (LIM3) and the biogeochemistry (PISCES) components. All the modified fortran routines to include in MY_SRC and the namelist_cfg (which includes the parameters for the modified configuration) can be found here: https://github.com/ysilvy/simus_orca1_fluxforced as well as a technical documentation (in French).

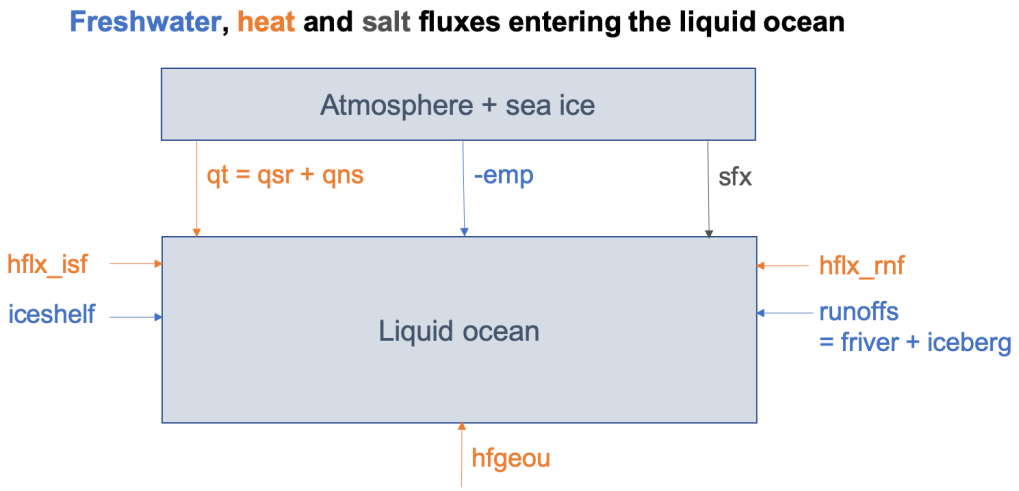

Figure III.3: Freshwater (blue), heat (orange) and salt (grey) fluxes entering the liquid ocean in the eORCA1 configuration.

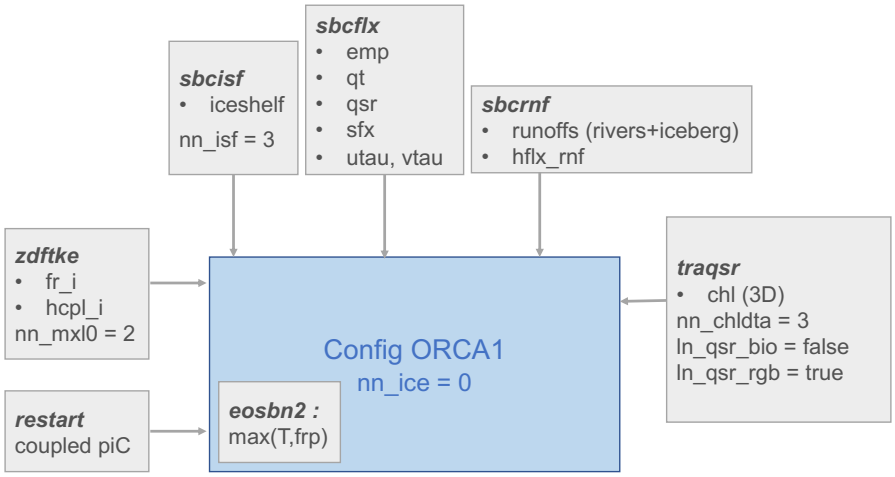

Figure III.4: Schematic of the code components modified to force the ocean.

3.1 Freshwater fluxes

The ocean receives and loses water from liquid and solid precipitation, evaporation, sea ice melting and freezing, river runoffs, iceberg melting and iceshelf melting. Under-iceshelf cavities are closed in the configuration of the ocean used here and there is no dynamical interaction between the ocean and the icesheets. Note this is one of the main limitations of climate models in projecting possible future changes in the ocean since melting contributions from the Antarctic and Greenland icesheets are expected to play a significant and increasing role during the 21st century [Golledge et al., 2019], but development is underway in NEMO to open interactive under-iceshelf cavities.

Instead, in the current version of the model, the mass of water contained in the icesheets is conserved, and all excess precipitation falling on the icesheets eventually returns to the ocean through different melting terms. In the Southern Hemisphere, 50% of the mass goes into iceshelf melting along the coast, and 50% into iceberg melting along a climatological map. In the Northern Hemisphere, all the mass goes into a calving term uniformly distributed along the coast. The freshwater flux from rivers, icebergs and

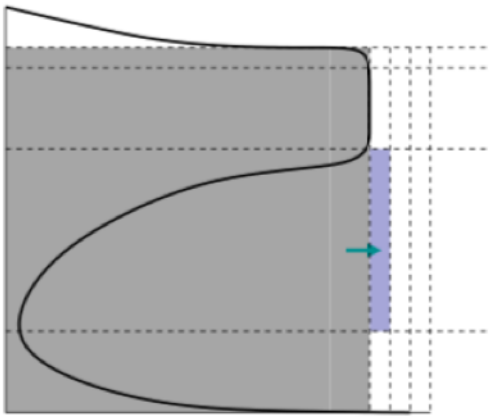

Figure III.5: From Madec et al. [2017], their figure 7.1. Schematic of the iceshelf representation used in the forced and coupled experiments. The black line is the shape of the cavity, the grey shading is the masked area (land, iceshelf and closed iceshelf cavity), the purple shading is the location of the prescribed iceshelf melt input.

iceshelf melt are geographically distributed according to a prescribed map and vertically distributed until a prescribed depth. Note the vertical distribution of these freshwater fluxes is done inside the code, the model outputs are the 2-dimensional unchanged fields. Table III.1 presents how these terms are grouped and defined in the model.

Table III.1: Freshwater flux terms at the ocean interface in NEMO3.6

Short name	**Signification**	**Unit**
emp	Evaporation - Precipitation - Calving (>0 upward)	kg.m^{-2}.s^{-1}
runoffs	River runoffs + iceberg melting (>0 into ocean) = friver + iceberg	kg.m^{-2}.s^{-1}
iceshelf	Iceshelf melting (>0 into ocean)	kg.m^{-2}.s^{-1}

The net amount of water entering the ocean liquid interface is given by -emp + runoffs + iceshelf (figure III.3). For a given time period Δt, the global ocean volume change (in m^3) should verify:

$$\Delta V = \frac{\Delta t}{\rho_0} * \overline{\sum_{x,y} ((\text{-emp(x,y,t)+runoffs(x,y,t)+iceshelf(x,y,t))*areacello(x,y))}^{t} \quad \text{(III.1)}$$

Where ρ_0=1026 kg.m^{-3} is the ocean volumic mass of reference, areacello is the ocean grid cell area, and x and y are the horizontal coordinates. All three terms emp, runoffs and iceshelf outputted from the piControl are needed to force the ocean. Averaged over the ocean area (see figures III.6 and III.7), the contribution from iceshelf melt and icebergs are very small (41 mSv, mean over the entire simulation; 1 mSv = 10^3 m^3.s^{-1}) with very low variability, compared to the much larger terms competing against each other, namely emp (1718 mSv in CTL) and friver (1636 mSv). Summing all these terms, the net incoming freshwater flux for the simulation period is close to zero ($\sim$1 mSv, equivalent to a total volume change of $\sim$9086 km^3 of water over the simulation).

To check the closure of the freshwater budget over the period 1850-2100, the left hand term and right hand term in equation III.1 are computed separately (figure III.7). ΔV is computed as the difference in

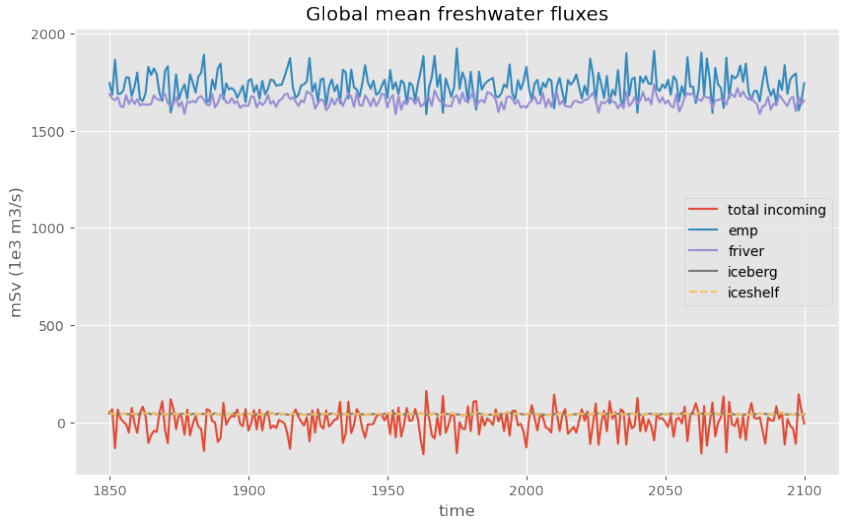

Figure III.6: Evolution of the globally-averaged freshwater fluxes in the piControl and CTL experiments (annual means).

global ocean volume V between the last and first days of the simulation. To compute accurate budgets, this global scalar V was outputted at daily frequency, as monthly values can introduce large errors especially with such small quantities. In the piControl we even outputted at 3hourly frequency. The right hand term in equation III.1 is computed from annually-averaged freshwater fluxes. The ocean freshwater budget closes almost perfectly in piControl and CTL. The difference of 0.002 or 0.016 mSv between the two terms is probably explained by precision errors introduced during the data analysis, and a larger error in CTL due to daily scalar values compared to 3hourly values for the piControl. piControl and CTL have different globally averaged values in the fluxes as the area in piControl is larger due to the presence of closed seas, which are masked in the ocean-only configuration. This doesn't however affect the values read locally in the CTL.

3.2 Heat fluxes

The ocean exchanges heat at its upper boundary with the atmosphere and sea-ice components, from shortwave radiation (not used to melt sea-ice), long-wave radiation and all other non-radiative fluxes (sensible and latent heat from evaporation, precipitation and ice thermodynamics). It also receives heat from river runoffs (sensible heat), iceberg melting in the Southern Hemisphere (sensible+latent heat; melting is considered at SST), calving in the Northern Hemisphere (latent heat; melting is considered at 0ºC) and iceshelf melting (sensible+latent heat; melting considered at -1.9ºC). As for the freshwater fluxes, the heat fluxes associated to runoffs and iceshelf melting are distributed on the vertical inside the code. Finally, there is also a constant, spatially-varying geothermal heating at the bottom of the ocean [Goutorbe et al., 2011]. These terms are synthetized in table III.2 together with notations used in the model.

The total heat input into the ocean is qt + hflx_rnf + hflx_isf + hfgeou (figure III.7). For a given time period Δt, the global ocean heat content change (in Joules) should verify:

$$\Delta OHC = \Delta t * \overline{\sum_{x,y} (\text{(qt(x,y,t)+hflx\_rnf(x,y,t)+hflx\_isf(x,y,t)+hfgeou(x,y))*areacello(x,y))}}^{t} \quad \text{(III.2)}$$

With $OHC(t) = \rho_0 * cp * \sum_{V_{ocean}} \theta(t) * dV$; $cp \approx 3981.\text{K}^{-1}.\text{kg}^{-1}$ the ocean specific heat; θ the ocean

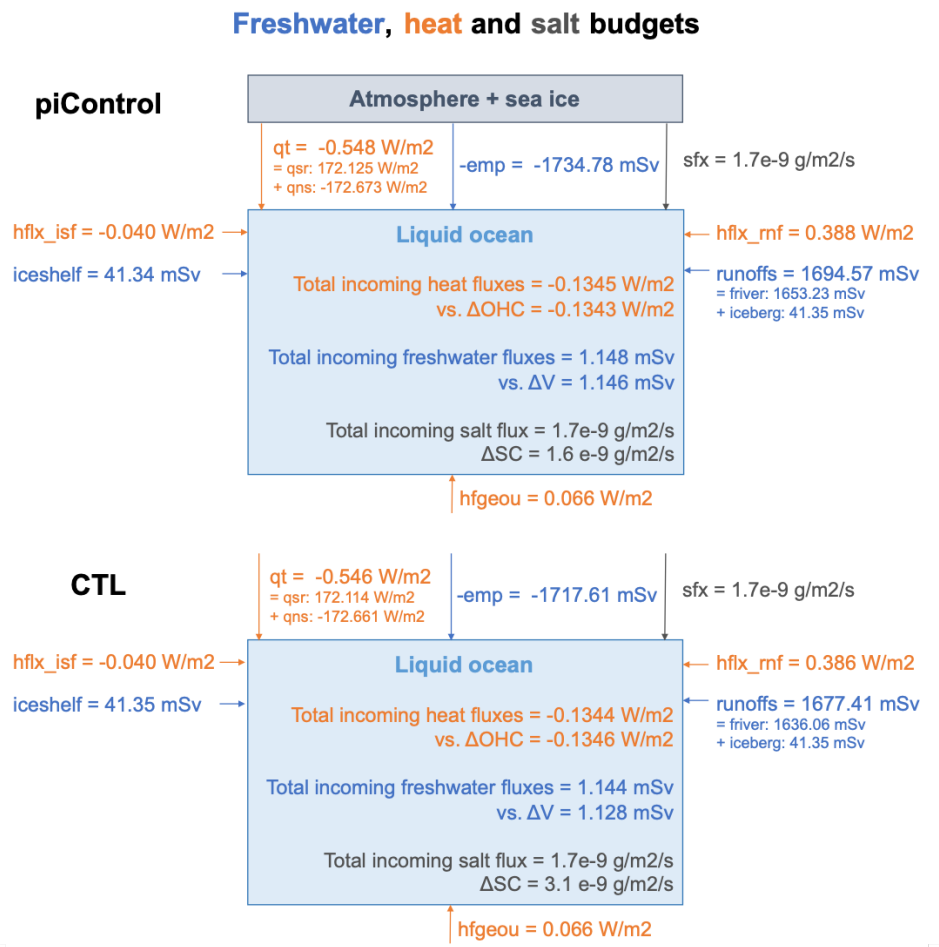

Figure III.7: Heat (orange), freshwater (blue) and salt (grey) budgets in the piControl (top) and CTL (bottom). The ocean area in the piControl is slightly larger due to closed seas included in the coupled simulation and masked in the CTL, which explains the small differences in globally-averaged surface fluxes.

conservative temperature with grid cell volume dV.

The model needs to read qt, qsr, hflx_rnf and hfgeou to force the ocean (hfgeou is a constant field). hflx_isf is reconstructed online from the freshwater flux term (iceshelf, see table III.1) and the freezing point temperature. The shortwave radiation qsr needs to be specified separately as it is vertically distributed in the top hundred meters of the ocean depending on the chlorophyll concentration field (see subsection 3.5.2 on chlorophyll prescription).

Globally-averaged, solar (qsr) and non-solar (qns) heat fluxes are very large and variable terms of opposite signs (figure III.7) that almost compensate to yield the net downward heat flux qt (=-0.55 $W.m^{-2}$ averaged over the simulation length). The runoffs sensible heat flux (hflx_rnf) and iceshelf heat flux (hflx_isf) have much weaker interannual variability (see figure III.8) and mean values of 0.39 $W.m^{-2}$ and -0.040 $W.m^{-2}$ respectively. The net incoming heat flux at the ocean interface sums up to -0.13 $W.m^{-2}$ during the 251 years, illustrating the disequilibrium found in the long piControl (figure III.2). By evaluating the left and right-hand side terms of the heat budget (equation III.2) separately, we find a perfect closure of the budget, with an error of 0.002 $W.m^{-2}$ both in the piControl and CTL. By exploring heat budgets in the coupled model, we found that although the ocean-only component has a closed heat budget, the sea-ice model does not [Mignot et al., 2021]. The ocean+sea-ice system thus doesn't perfectly conserve heat.

Table III.2: Heat flux terms at the ocean interface in NEMO3.6

Short name	Signification	Unit
qt	Net downward heat flux = qns + qsr	W.m^{-2}
qsr	Downward shortwave flux	W.m^{-2}
qns	Downward non solar heat flux (includes hflx_icb and hflx_cal)	W.m^{-2}
hflx_rnf	Sensible heat flux from river and iceberg runoffs (at SST)	W.m^{-2}
hflx_icb	SH iceberg latent heat loss (<0), included in qns	W.m^{-2}
hflx_cal	NH calving latent heat loss (<0), included in qns	W.m^{-2}
hflx_isf	Heat flux from iceshelf melting (Sensible+latent)	W.m^{-2}
hfgeou	Geothermal heat flux	W.m^{-2}

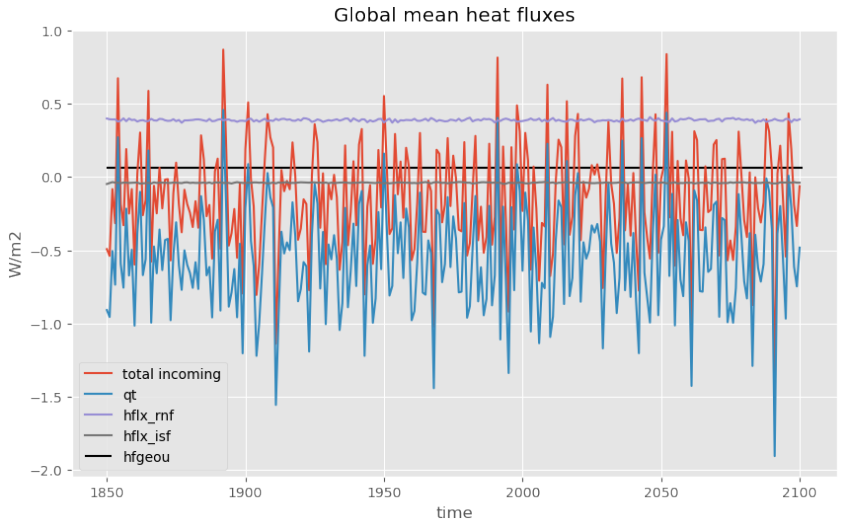

Figure III.8: Evolution of the globally-averaged heat fluxes in the piControl and CTL experiments (annual means).

3.3 Salt flux

When the ocean is coupled to a sea-ice model, there is a salt flux exchanged between the two components, as the ice salinity is different from zero (e.g. when ice melts, there is a downward flux of both freshwater and salt).

Table III.3: Salt flux at the ocean/sea-ice interface in NEMO3.6

Short name	Signification	Unit
sfx	Downward salt flux into sea water	g.m^{-2}.s^{-1}

This salt flux sfx is thus needed to correctly reproduce the piControl with the ocean-only configuration. For a given time period Δt, the global ocean salt content change (in g of salt) should verify:

$$\Delta SC = \Delta t * \overline{\sum_{x,y} (\text{sfx(x,y,t)*areacello(x,y)})}^{t} \quad \text{(III.3)}$$

With $SC(t) = \rho_0 * \sum_{V_{ocean}} S(x,y,z,t) * dV$; S the ocean absolute salinity (in g.kg^{-1}) with grid cell volume dV.

The globally-averaged salt flux oscillates around zero during the entire simulation with a very large interannual variability (figure III.9). It has a mean value of 1.7*10^{-9} g.m^{-2}.s^{-1} (equivalent to 619 kg.s^{-1} integrated over the ocean surface, or to a total of 4.9*10^{12} kg of salt exchanged) over the simulation period. Evaluating the left-hand term in equation III.3 separately (see figure III.7), we find an equivalent flux in salt content change equal to 1.6 *10^{-9} g.m^{-2}.s^{-1} in the piControl and 3.1*10^{-9} g.m^{-2}.s^{-1} in the CTL. These numbers correspond to very small and variable quantities and are thus very sensitive to the computation method (e.g. frequency of the global scalar outputs).

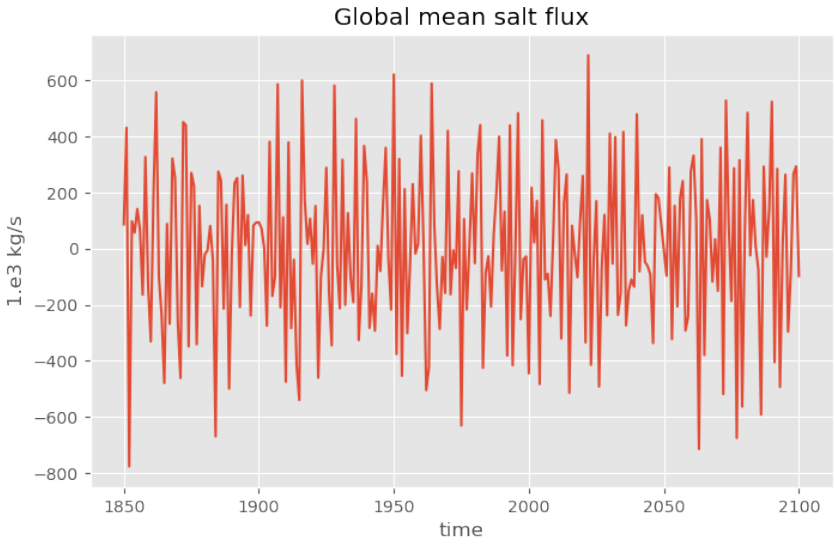

Figure III.9: Evolution of the globally-averaged salt flux in the piControl and CTL experiments (annual means).

3.4 Wind stress

Wind stress is prescribed to the ocean via its zonal (utau) and meridional (vtau) components (table III.4). The model needs to read both terms to force the ocean.

Table III.4: Wind stress components at the ocean interface in NEMO3.6

Short name	Signification	Unit
utau	Surface downward x stress	N.m^{-2}
vtau	Surface downward y stress	N.m^{-2}

All the above-mentioned fluxes (heat, freshwater, salt, wind stress) are outputted from the piControl at 3-hourly frequency and provided to the forced experiments without time interpolation.

3.5 Other components

3.5.1 Vertical mixing

The parameterization of ocean vertical mixing depends on sea ice concentration and thickness in the IPSL-CM6A-LR configuration, in particular the mixing length scale. Thus, we read both fields (sea ice fraction and thickness) from the piControl to keep the CTL experiment as close to piControl as possible.

Sensitivity tests were conducted to find at what frequency these sea-ice fields should be read. We found that providing the information with monthly means conducted to immediate differences in the first month of the CTL experiment compared to the piControl. We thus chose to read them at 3hourly similarly to the previous fields.

3.5.2 Chlorophyll field

The shortwave flux penetrates in the top layers of the ocean. The penetration of that flux is modulated by the concentration of total chlorophyll in the ocean, the only biogeochemical component that has an effect on the ocean physics in NEMO. When the biogeochemistry model (PISCES, Aumont et al. [2015]) is activated (which is the case in the coupled piControl experiment), the chlorophyll concentration is directly read online. When PISCES is deactivated (which is the case for our forced experimental setup), the solar radiation vertical profile in the ocean is defined through 3 wavebands (RGB) and depends on a read chlorophyll field.

The pre-existing options in the code for the prescribed chlorophyll field include (2D figures in Appendix C):

- imposing a constant and uniform chlorophyll field (=0.05 mg.m^{-3}): parameter nn_chldta=0, figure C.3;
- reading a 2D surface file and imposing the same values in the subsurface than in the surface: nn_chldta=1, figure C.4,
- or reading a 2D file that is then vertically interpolated to reconstruct a more realistic chlorophyll profile in the top layers: nn_chldta=2.

The 2D file can either be a climatology (figure C.2) or a time-varying field (figure C.1).

We first used the third option (nn_chldta=2, as it was supposedly an improvement from nn_chldta=1), reading the surface chlorophyll field from the piControl (outputted from PISCES at monthly frequency) but it didn't give satisfying results: the SST in CTL diverged too quickly away from the piControl (see figures III.10 and C.1). A fourth option (parameter nn_chldta=3) was thus implemented to read the 3D field in our simulations. Indeed, we have found through a series of first sensitivity tests that to best reproduce the piControl, the full 3D chlorophyll field needs to be read. The temperature was found to be very sensitive to the different options, as they have different effects on solar penetration, see figure III.10 and figures C.1-C.4.

Hence, in our final CTL simulation, we read the 3D time-dependent chlorophyll data from the piControl (at monthly frequency).

Note that, a posteriori, by running an additional sensitivity test, we found that in the case where we impose only the surface time-dependent chlorophyll field from PISCES without activating the vertical reconstruction (nn_chldta=1), the results were very similar to imposing the 3D field in the first year (figures III.10 and C.4). This was surprising as the vertical interpolation (nn_chldta=2) was developped specifically to better represent the vertical profile of chlorophyll. This option should thus probably be investigated as there seems to be a problem with this representation, both when reading a time-dependant field or a climatology. We don't know if the good results obtained for nn_chldta=1 hold for a longer simulation, but in the future it is useful to know that the surface field alone seems to be as good as the 3D

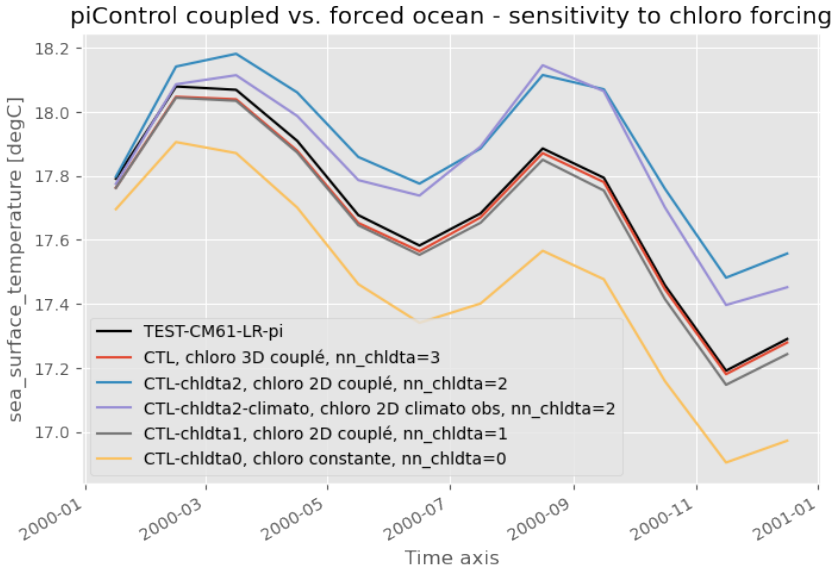

Figure III.10: Monthly global mean SST the first year of the simulation, for the: coupled piControl (black), CTL with the 3D chlorophyll read from the piControl (red), CTL with the 2D chlorophyll read from the piControl and interpolated vertically (blue), CTL with a surface climatological chlorophyll field read and interpolated vertically (purple), CTL with the 2D chlorophyll read from the piControl and the same values imposed in the subsurface (grey), and CTL with a constant and uniform chlorophyll value (yellow).

field (with much lighter storage demand), as long as the vertical interpolation is not activated.

3.5.3 Temperature below freezing point

Because of the ocean-only configuration (no sea-ice) with a flux formulation and no restoring term on the SST, it is possible for the temperature to locally fall below freezing point in polar regions, in all the ocean-only simulations including CTL. We implemented part of the solution proposed by Todd et al. [2020] in our experiments, namely we let the temperature evolve without any changes so as to conserve heat in the model. However, as to not create any un-physical convection events, if the temperature falls below freezing, in the computation of the equation of state and of the Brünt-Vaisala frequency, we replace the temperature by the freezing point temperature so that the model still sees a physical density. In that configuration, temperature can still fall below freezing point (in the ALL simulation it can reach below -7ºC in polar areas because of the negative heat flux perturbation especially in the Arctic, see section 4). This represents only very small areas of the ocean and doesn't directly affect the circulation because of the modification to the equation of state, but heat transport can still be affected. We thus tested several cases for the treatment of the freezing point to confirm this choice (see Appendix C).

3.6 Diagnostics and validation

The forcing frequency of the CTL experiment is at 3 hours with the fluxes from piControl. This frequency was chosen for the physics in CTL to remain very close to the piControl (see below). The coupling frequency in the coupled model between the ocean and atmosphere is 1.5 hours [Boucher et al., 2020], so small errors are still introduced in the CTL all along the simulation and can be amplified due to non-linearities of the system. Furthermore, we are also introducing errors by reading the monthly chlorophyll field (instead of an interactive chlorophyll) and by reading the sea-ice fields at lower frequency than the coupling frequency for the vertical mixing parameterization. Here, we present several diagnostics to test and validate our CTL experiment against the reference coupled piControl in the context of this study.

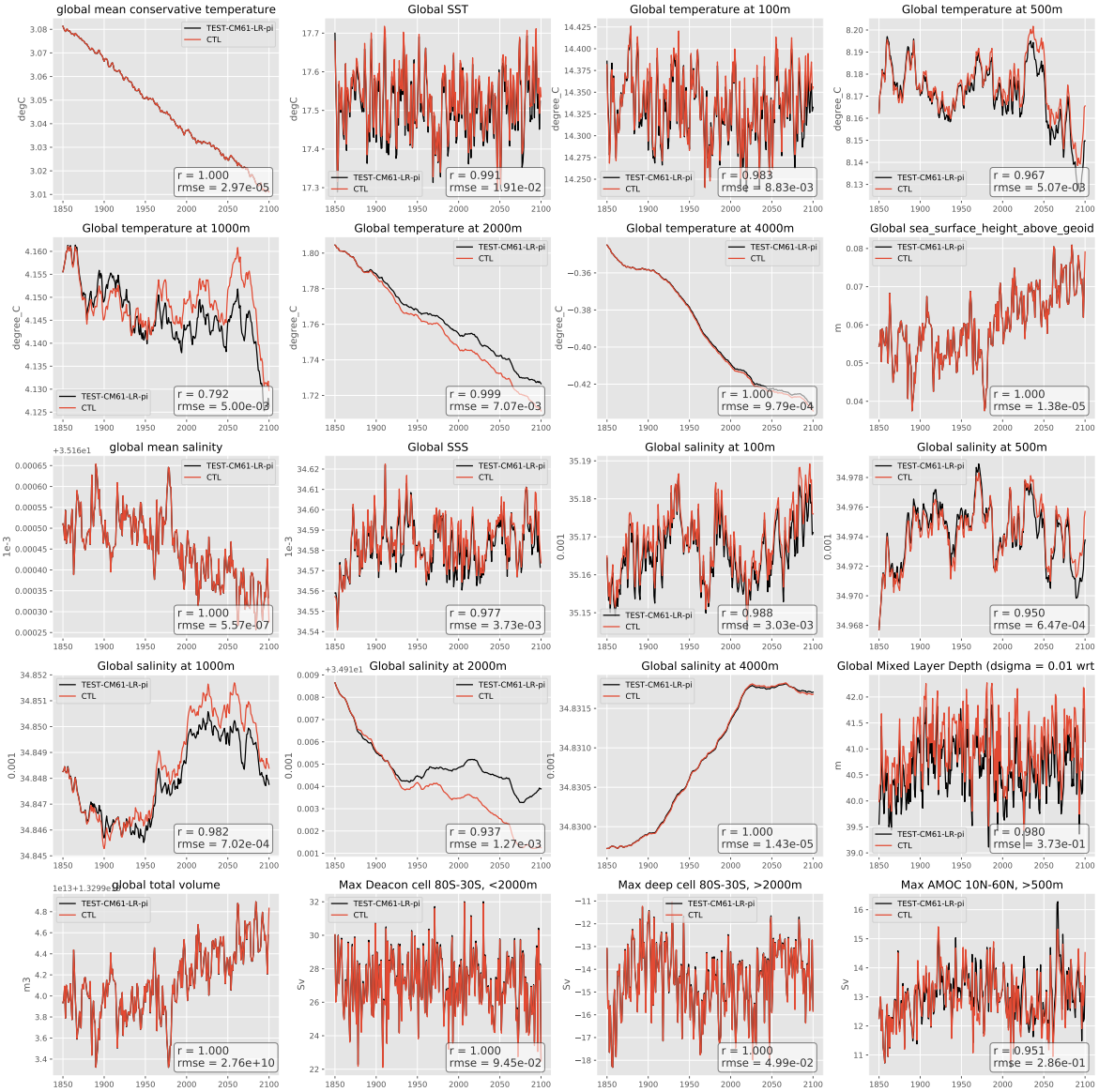

Figure III.11: Intermonitoring of 1D variables (annual means) for the coupled piControl (black) and the flux-forced CTL (red). The values in the bottom right corner correspond to the Pearson correlation coefficient (no unit) and to the root mean square error (in the unit of each variable) between the two time series.

Several 1D variables are presented in figure III.11 for the piControl (black) and the CTL experiment (red). Global ocean heat, volume and salt are almost perfectly conserved between piControl and CTL (see the budgets in Figure III.7) as illustrated by the respective superimposed time series in global mean conservative temperature, salinity and total volume. In the surface and bottom waters, temperature and salinity in the CTL reproduce the piControl variability and values, with small differences in the peak values at the surface (the root mean square error is an order of magnitude weaker than the interannual variability). Overall there is no drift away from the piControl even after 250 years of simulation in these variables. However, there is some small readjustment slowly appearing in the intermediate layers, with warmer and saltier waters at 500m-1000m and colder and fresher at 2000m. The differences are nevertheless very small at the end of the simulation (rmse about the same order of magnitude than interannual variability). In terms of large scale circulation proxies, we show the maximum (in absolute value to account for the sign of the overturning) in the global meridional streamfunction for the deacon (above

2000m, 30°S-80°S) and deep (below 2000m, 30°S-80°S) cells in the Southern Ocean, and the maximum in Atlantic meridional streamfunction (below 500m, 10°N-60°N). The similarity between the 2 experiments is striking during the entire length of the simulations, both in terms of magnitude and of variability, especially for the Southern Ocean cells where the two curves are almost perfectly superimposed (rmse 2 orders of magnitude weaker than interannual variability). The AMOC time series is also very well reproduced, even though some extremes are not perfectly replicated in terms of amplitude (rmse one order of magnitude smaller than interannual variability). The global mixed layer depth presents an rmse of 0.37m between CTL and piControl, with differences present very early on in the simulation but that don't increase in time.

We now look at the difference in 2D-fields for sea surface temperature (figure III.12), salinity (figure III.13) and mixed layer depth (figure III.14) at different periods of the simulations. The main differences in SST are localised in the subpolar North Atlantic with a warm patch surrounded by cooling centered on the maximum differences of mixed layer depth, which corresponds to a deep convection zone and to the sea-ice margins, which is a region of complex physical processes and exchanges between the ocean, atmosphere and sea-ice. It is also where slightly below freezing temperatures locally occur in the CTL (not shown) which can explain the cool/warm dipoles since any heat loss is compensated by a heat gain somewhere else as the heat is globally conserved in the CTL as in the piControl (figure III.7 and figure III.11). These discrepancies in the subpolar North Atlantic do not however seem to impact the rest of the ocean and are even smaller by the end of the simulation (2090-2100) than at other time periods which could indicate strong internal variability governing the differences. In other parts of the globe, we note a slightly warmer Pacific in CTL compared to piControl and cooler Atlantic, although these patterns remain small (<0.5ºC difference locally) during the entire experiment.

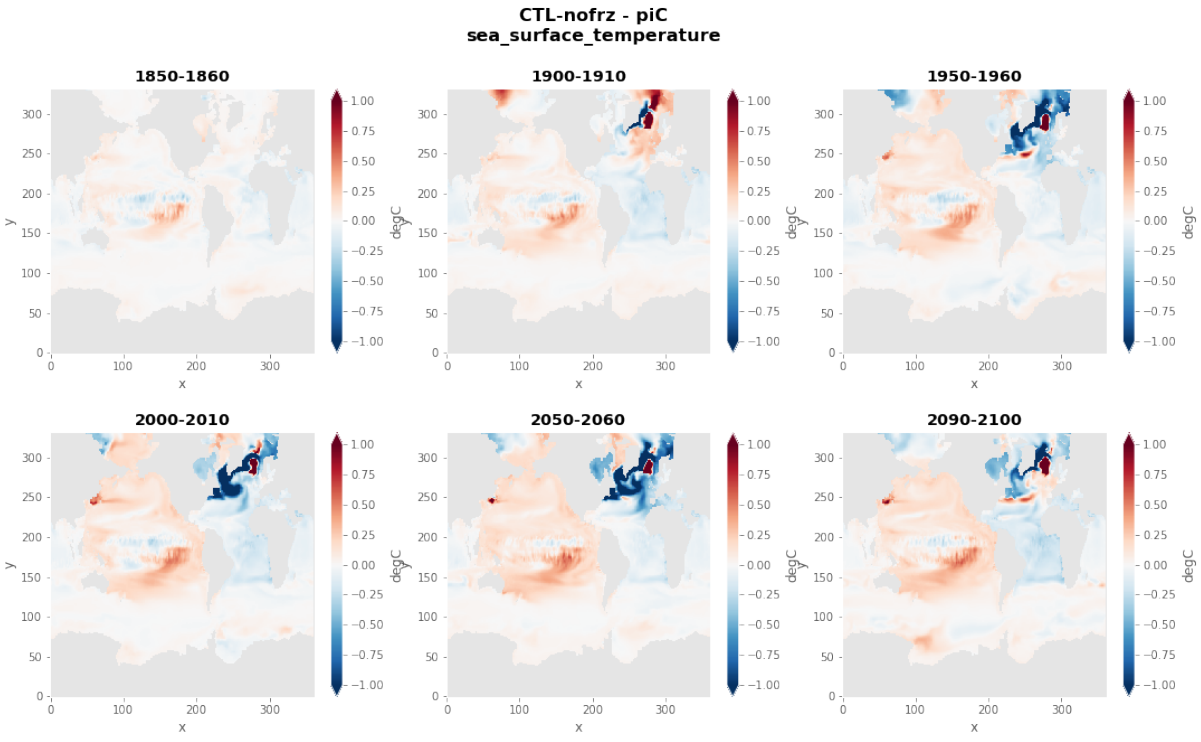

Figure III.12: Difference in SST between the coupled piControl and the flux-forced CTL at different periods of the simulations (10-year means).

The largest SSS differences (figure III.13) are localised in the Arctic with very strong dipoles (>0.5 g.kg^{-1} difference) which are not constant in time and seem to stay well within the ice-covered region without impacting other areas of the ocean where differences remain very small (<0.1 g.kg^{-1}) without

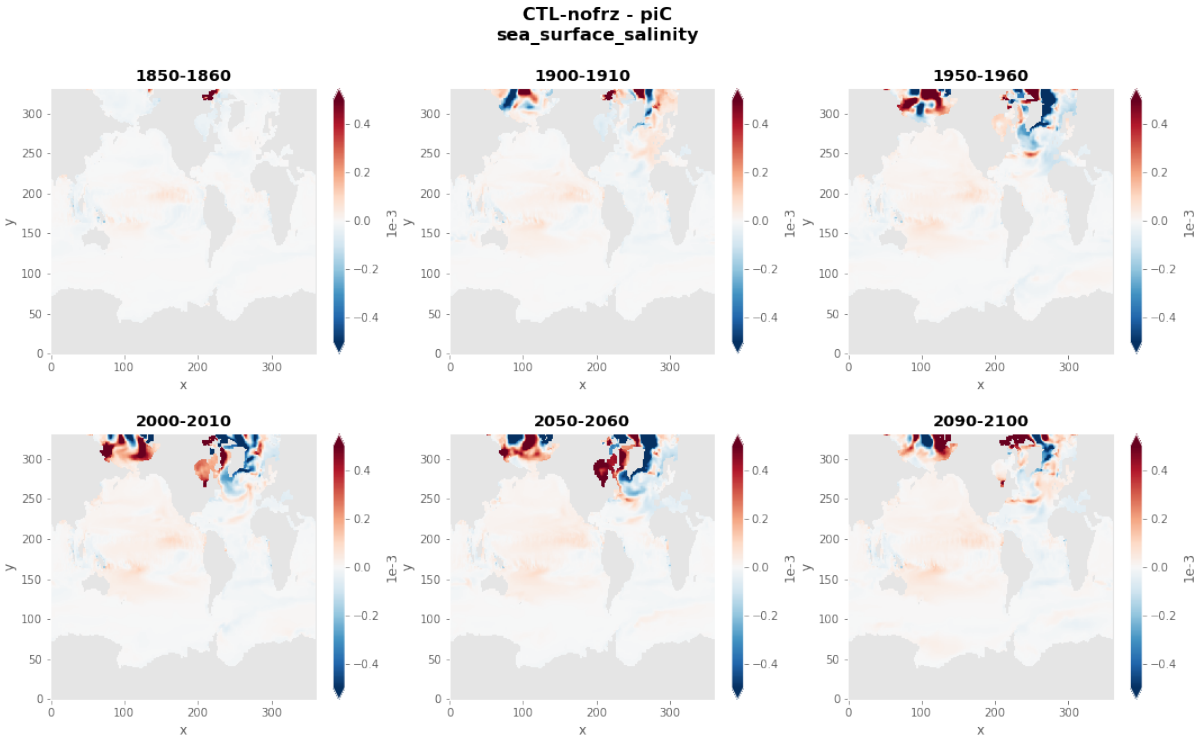

Figure III.13: Difference in SSS between the coupled piControl and the flux-forced CTL at different periods of the simulations (10-year means).

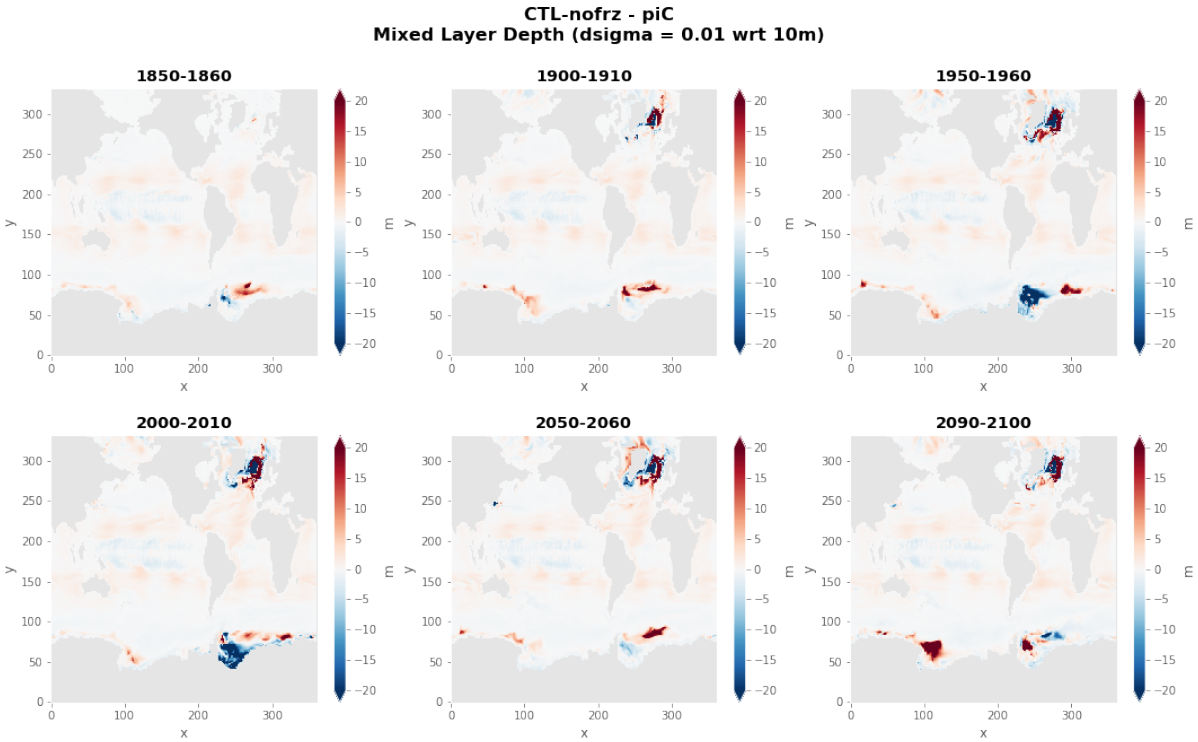

Figure III.14: Difference in mixed layer depth between the coupled piControl and the flux-forced CTL at different periods of the simulations (10-year means).

increasing much in time.

The largest mixed layer depth differences (figure III.14, >20m difference) occur in regions of deep convection in the subpolar North Atlantic and Southern Ocean close to Antarctica, although there is a lot of variability in time in the latter.

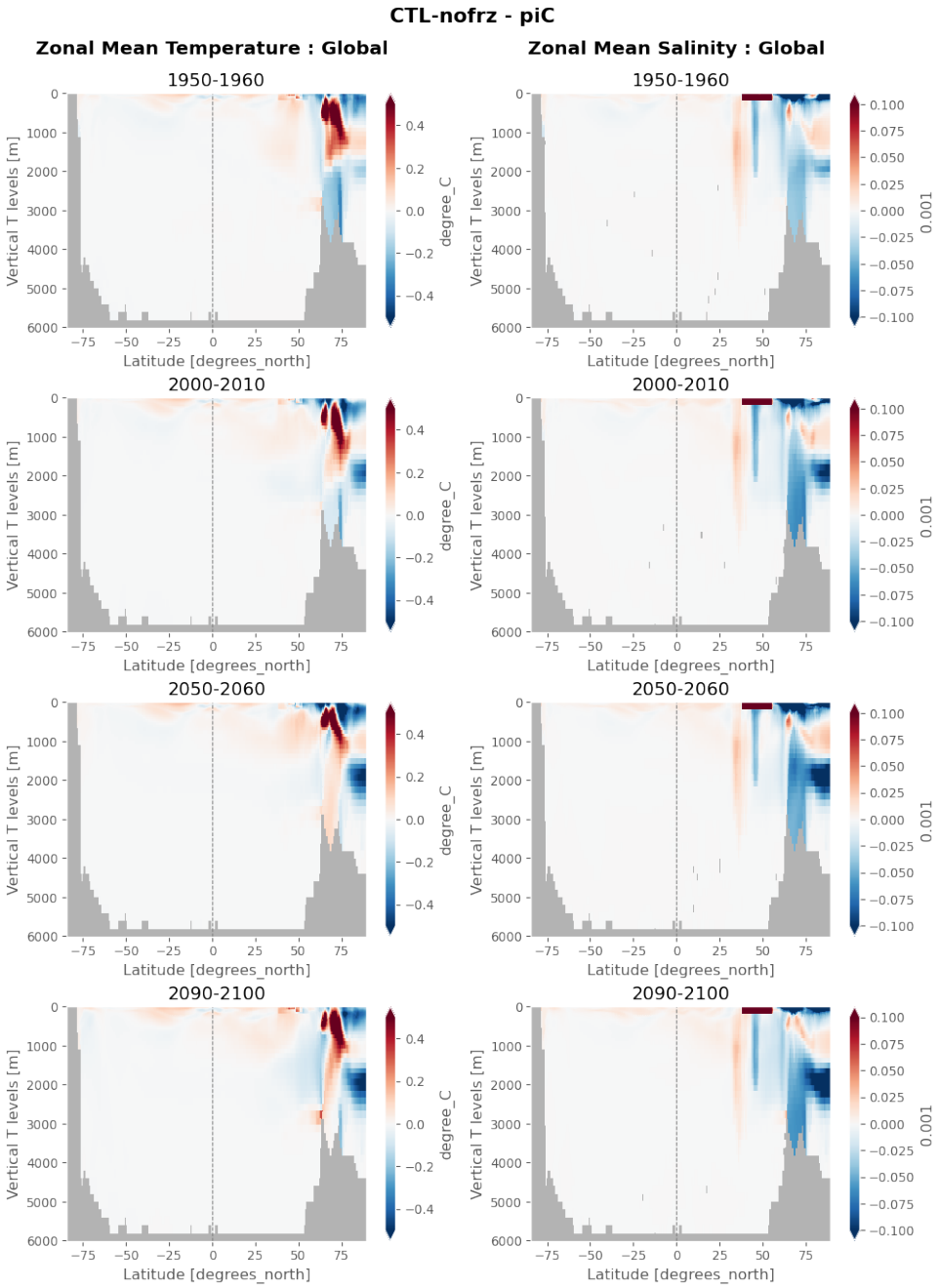

Figure III.15: Difference in zonal mean temperature (left column) and salinity (right column) between the coupled piControl and the flux-forced CTL at different periods of the simulations (10-year means). Due to an unknown issue in the piControl outputs for salinity, a large difference appears at the surface around 40ºN, which should be ignored.

The differences in zonal mean temperature and salinity (figure III.15) between the CTL and the reference piControl confirm that the largest errors (>0.5ºC and 0.1g.kg^{-1} difference) are located in the Arctic and subpolar North Atlantic. The dipolar structure indicates vertical re-adjstment. There is some propa-

gation at depth especially in the deep convection zone between 60-70ºN, but the differences don't increase in time after they are installed. This also confirms that the CTL stays very close to the piControl in all other parts of the ocean, with very small differences between the two experiments (<0.05ºC and <0.01g.kg^{-1} outside the surface subtropical gyres). The errors seem to mostly propagate along the main ocean ventilation pathways except in the Antarctic Bottom Water (AABW) formation regions where the differences remain small (or haven't had enough time to propagate in the deeper ocean).

Overall, these results are very satisfying for the purpose of this study and allow us to validate our CTL experiment, which will become our new reference for the analysis of the different experiments.

4 Adding the perturbation components

In the ALL experiment, we use the same configuration as CTL and add an anomalous component to all surface fluxes needed to force the ocean (see table III.5). The anomalous component is constructed as follows:

$$Q'(x,y,t) = Q(x,y,t) - \overline{Q(x,y,t)}^{t=1850-1899} \tag{III.4}$$

with $Q(x,y,t) = \overline{Q(x,y,t,i)}^{i}$ the ensemble mean flux over all available members i of the IPSL-CM6A-LR large ensemble. There are 32 members for most variables over the historical-extended period 1850-2059, and 11 members over 2060-2100, following the ssp245 scenario from 2015.

Table III.5: NEMO and equivalent CMIP6 short names for the heat, freshwater and wind stress fluxes read in the forced experiments

Name NEMO	Corresponding CMIP6	Unit	Comment
qt	hfds	W.m^{-2}	
qsr	rsntds	W.m^{-2}	
hflx_rnf	hfrunoffds	W.m^{-2}	In the published CMIP6 outputs of IPSL-CM6A-LR, hfrunoffds is not included in hfds (hfds=qt), unlike the budgets in Griffies et al. [2016]
emp	wfo+friver+ficeberg	kg.m^{-2}.s^{-1}	In the published outputs of IPSL-CM6A-LR, wfo (=water flux into sea water) is of opposite sign of what it should be and is thus positive upward (=E-P-R)
runoffs	friver + ficeberg	kg.m^{-2}.s^{-1}	
iceshelf	flandice	kg.m^{-2}.s^{-1}	In Emon CMIP6 outputs
sfx	sfdsi	g.m^{-2}.s^{-1}	sfdsi is specified in kg.m^{-2}.s^{-1} in the CMIP6 outputs, however it is outputted in g.m^{-2}.s^{-1} in IPSL-CM6A-LR since sfx is in g.m^{-2}.s^{-1} in the code
utau	tauuo	N.m^{-2}	
vtau	tauvo	N.m^{-2}	

Here, we present the orders of magnitude, temporal evolution and spatial patterns of the flux anomalies.

4.1 Perturbations budgets

Table III.6 summarizes the orders of magnitude of the flux perturbations compared to the corresponding mean values in CTL.

Table III.6: Globally-averaged heat, freshwater and salt fluxes. Mean values over 1850-2100 for the perturbation components (left column) and the fluxes in CTL imposed from piControl (right). The mean values of the anomalies are also presented for 1950-2100 to show the evolution in time.

	Anomalies 1850-2100	**Anomalies 1950-2100**	**CTL 1850-2100**
qt	0.712 W.m^{-2}	1.129 W.m^{-2}	-0.546 W.m^{-2}
qsr	-0.411 W.m^{-2}	-0.659 W.m^{-2}	172.114 W.m^{-2}
qns	1.123 W.m^{-2}	1.788 W.m^{-2}	-172.661 W.m^{-2}
hflx_rnf	0.038 W.m^{-2}	0.061 W.m^{-2}	0.386 W.m^{-2}
hflx_isf	-0.003 W.m^{-2}	-0.005 W.m^{-2}	-0.040 W.m^{-2}
qt+hflx_rnf+hflx_isf	**0.747 W.m^{-2}**	**1.186 W.m^{-2}**	**-0.2 W.m^{-2}**
hfgeou	0	0	0.066 W.m^{-2}
emp	91.37 mSv	148.13 mSv	1717.61 mSv
runoffs	92.14 mSv	148.78 mSv	1677.41 mSv
iceshelf	2.94 mSv	4.68 mSv	41.35 mSv
-emp+runoffs+iceshelf	**3.71 mSv**	**5.33 mSv**	**1.14 mSv**
sfx	**14 326 kg.s^{-1}**	**21 243 kg.s^{-1}**	**622 kg.s^{-1}**

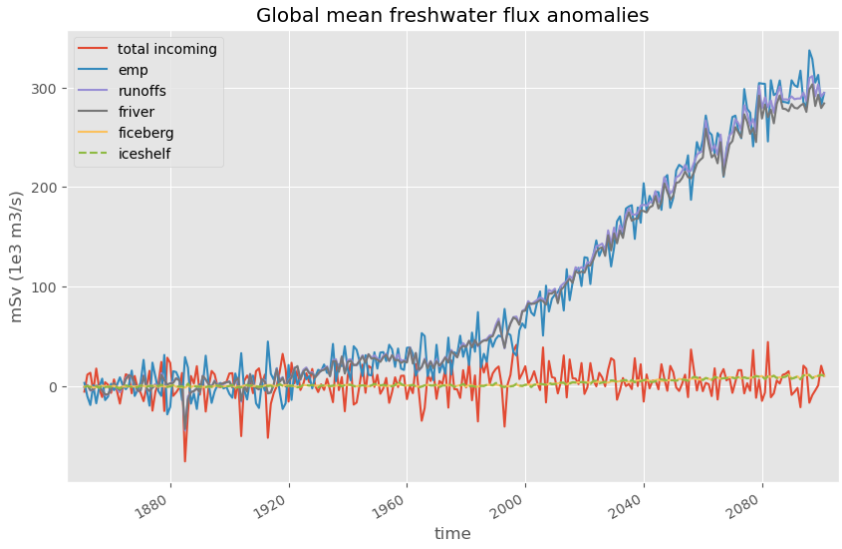

Figure III.16: Evolution of the globally-averaged freshwater flux anomalies as computed from the IPSL-CM6A-LR ensemble mean anomalies relative to 1850-1899.

The evolution of global mean freshwater flux anomalies (figure III.16) is a balance between two opposing terms increasing very rapidly and at the same rate (emp and runoffs; both increasing to reach about 300 mSv in 2100), with an additional much smaller contribution from iceshelf melting (reaching about 10 mSv in 2100). The latter is however very significant in the total balance since the two large terms almost balance each other out to yield an order of magnitude similar to the iceshelf term, as in the freshwater

flux budget in CTL (figure III.7 and table III.6). The iceberg melt (included in runoffs) is equal to the iceshelf melt term by definition. Each freshwater flux anomaly has a lower globally-averaged value than its CTL counterpart. After summation there is a net positive input of water in the ocean by the freshwater flux perturbations. Note that the interannual standard deviation of this total flux is larger than its mean (figure III.16).

The increase in global mean surface heat flux anomaly (qt') is dominated by the increase in non-solar heat flux term (qns') and damped by the decrease in solar heat flux (qsr'), see table III.6 and figure III.17. There is a clear signature of the impact of volcanic eruptions in the qsr' and qt' terms. The anomalous component hflx_rnf' is more than one order of magnitude smaller than qt', and hflx_isf' 2 orders of magnitude smaller. Still, there is a significant increase in hflx_rnf' owing to the large increase in river runoffs (figure III.16), but only a small decrease in hflx_isf' (reconstructed from iceshelf').

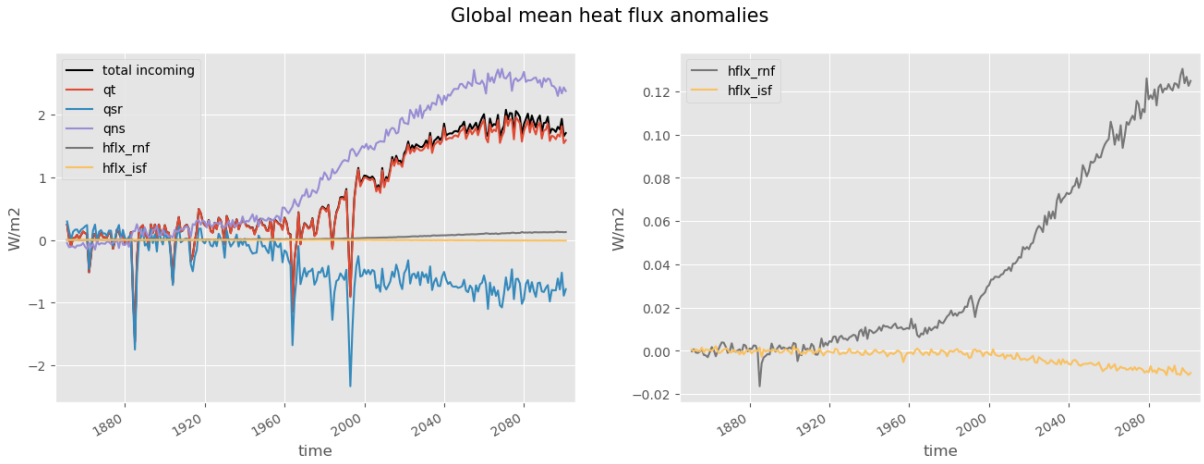

Figure III.17: Evolution of the globally-averaged heat flux anomalies as computed from the IPSL-CM6A-LR ensemble mean anomalies relative to 1850-1899.

Globally integrated, the salt flux anomaly has a small positive trend with a much higher interannual variability (table III.6 and figure III.18), hiding marked spatial patterns of opposite signs (not shown).

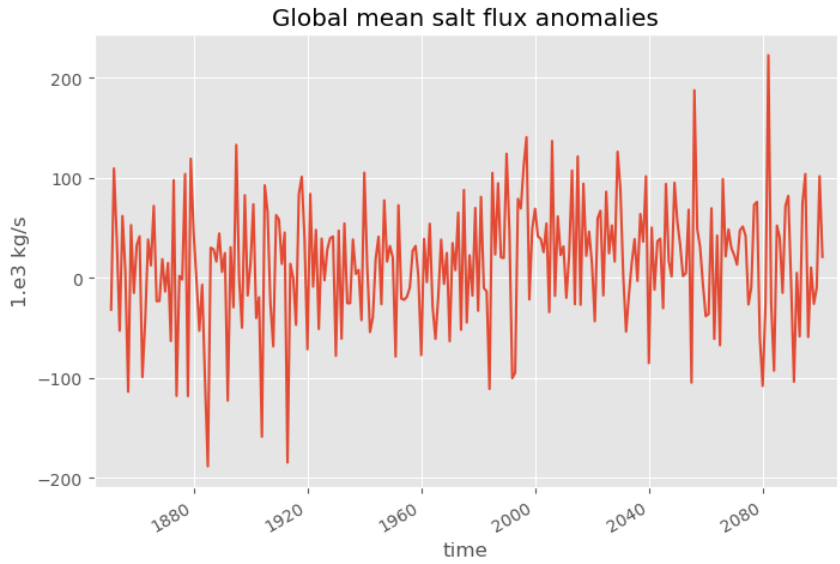

Figure III.18: Evolution of the globally-averaged salt flux anomaly as computed from the IPSL-CM6A-LR ensemble mean anomalies relative to 1850-1899.

4.2 Anomalies spatial patterns

Here, we present the spatial patterns of the anomalies averaged in the last 20 years of the period: 2081-2100 (figure III.19). These patterns largely agree with those of the FAFMIP anomalies [Gregory et al., 2016] which are constructed from a multi-model mean of 1%CO2 idealized experiments and reproduced in figure III.20 for comparison purposes. This similarity gives confidence in the response of the IPSL-CM6A-LR model to external forcings relatively to other coupled models in terms of surface fluxes.

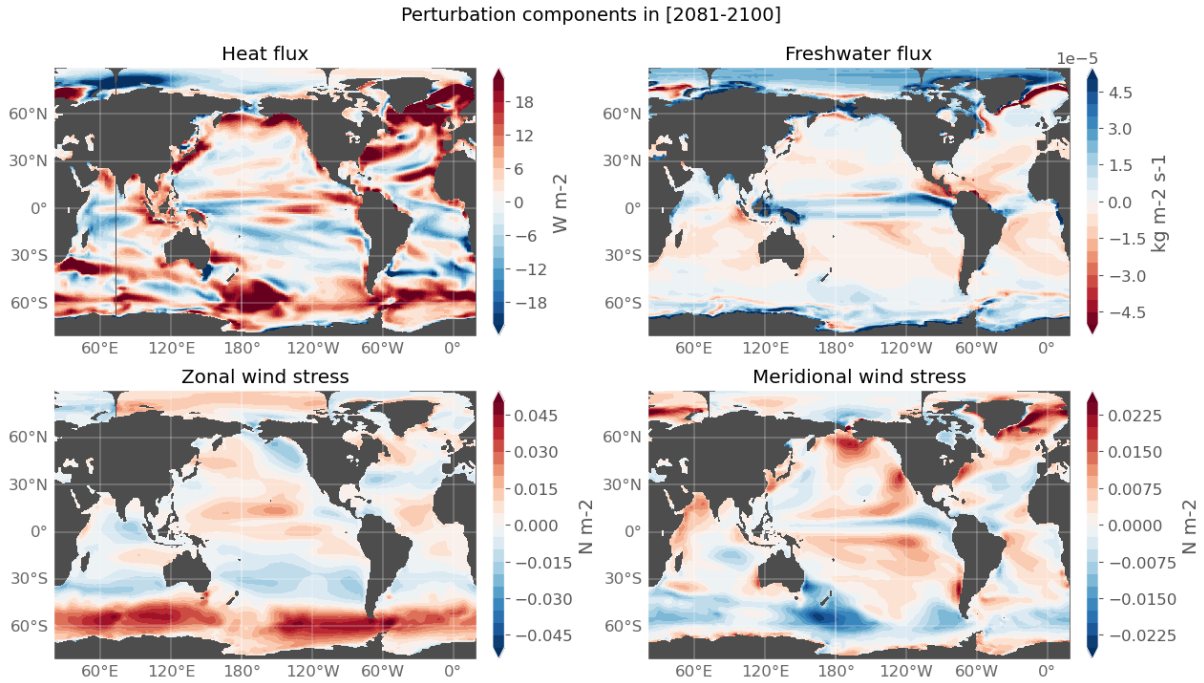

Figure III.19: Total heat flux, freshwater flux, and wind stress perturbations averaged over 2081-2100, as computed from the ensemble mean anomaly of IPSL-CM6A-LR historical+ssp245.

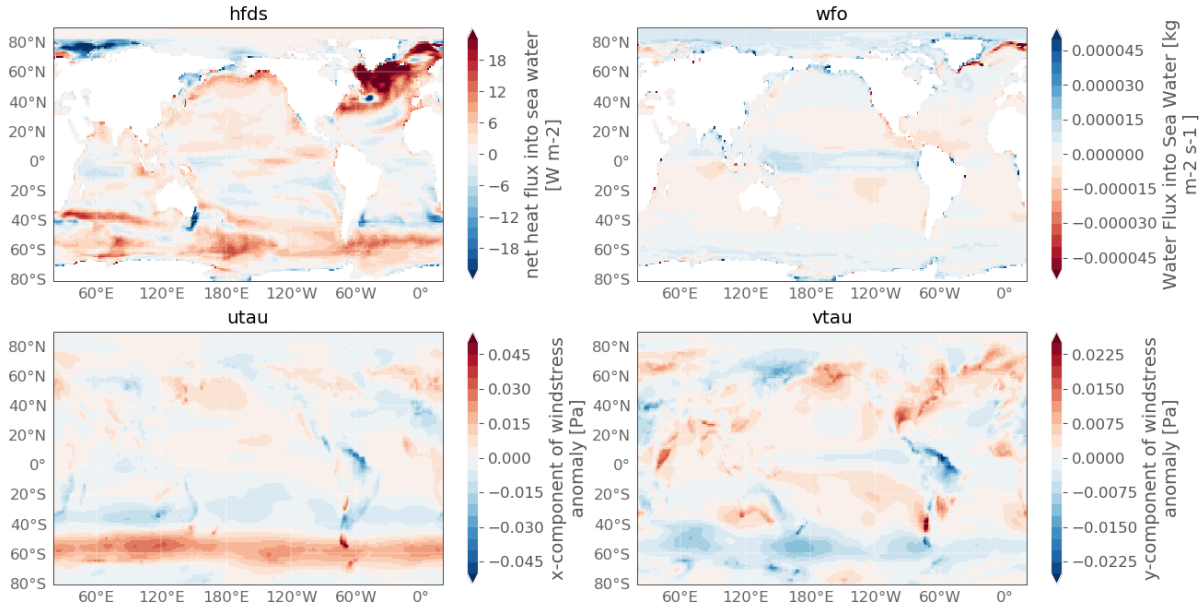

Figure III.20: FAFMIP perturbations (data downloaded from http://www.fafmip.org).

4.3 The ALL experiment: diagnostics and validation with the IPSL-CM6A-LR large ensemble

The goal for the ALL experiment is to simulate a similar response to the IPSL-CM6A-LR historical+ssp245 ensemble since it is forced with all the flux anomalies from these experiments. Errors are however inevitably introduced for several reasons. First, we impose the anomalous components at monthly frequencies without restoration. Thus, any small arising difference can amplify and will not be corrected. This is what happens with below-freezing temperatures in the Arctic, helped by the absence of the sea-ice model (see section 3.5.3). Second, the absence of the sea-ice model also prevents the correct parameterization of vertical mixing under sea-ice covered areas. We kept the same configuration as in the CTL experiment (section 3.5.1), i.e. we read ice fraction and thickness from the piControl to parameterize vertical mixing, which means different mixing rates than in a situation where sea-ice is increasingly melting (anthropogenic response). Indeed, even though we could have provided the ice information from the IPSL-CM6A-LR historical+ssp245 ensemble for the vertical mixing of the ALL experiment, we cannot provide this information to the HEAT, WATER, STRESS and BUOY experiments since they are idealized cases with no reference for sea ice. The only variables which we wish to differ between these experiments are the anomalous surface fluxes. Since all other components should remain identical, as to better compare the experiments and test their linear additivity, we have decided to use only the information of sea-ice from the piControl in every experiment. Third, we have the exact same problem with the chlorophyll field, which certainly changes under anthropogenic forcing, while we do not wish to change that component either in the perturbed experiments.

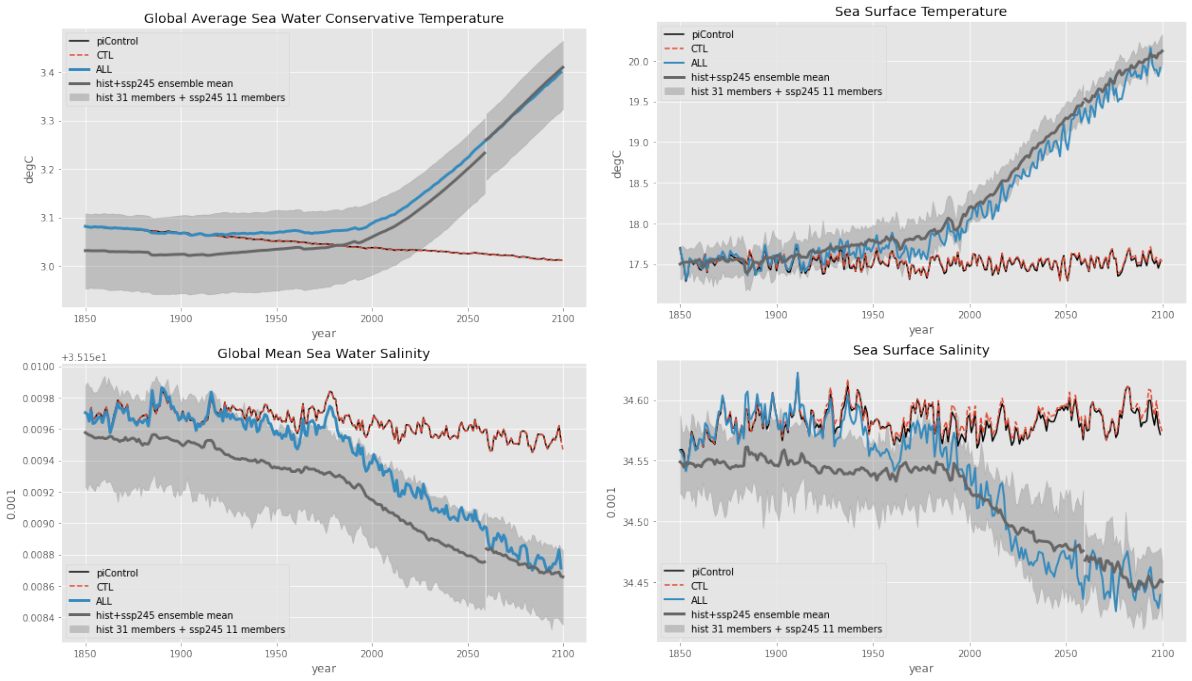

Figure III.21: Evolution of global mean temperature (top left), salinity (bottom left), SST (top right) and SSS (bottom right) for the IPSL-CM6A-LR ensemble (grey), piControl (black), CTL (dotted red) and ALL (blue).

Nevertheless, the global response and patterns of change of the ALL experiment very closely resemble that of the IPSL-CM6A-LR historical+ssp245 ensemble. This is illustrated by several global diagnostics (figures III.21 and III.22) showing that the ALL experiment follows the response and stays within the range of the large ensemble during the entire simulation (apart from a few peaks in interannual variability). It acts as an individual member, with its own initial state and internal variability phased on the coupled piControl (and thus on the ocean-only CTL as well) because of the 3-hourly flux forcing, with the

additional response to external forcings especially marked by long-term increasing anthropogenic emissions. Because of the flux-forced ocean-only configuration, there is no feedback to the atmosphere when adding a perturbation, thus all our experiments are aligned with the piControl internal variability and can be compared appropriately in time.

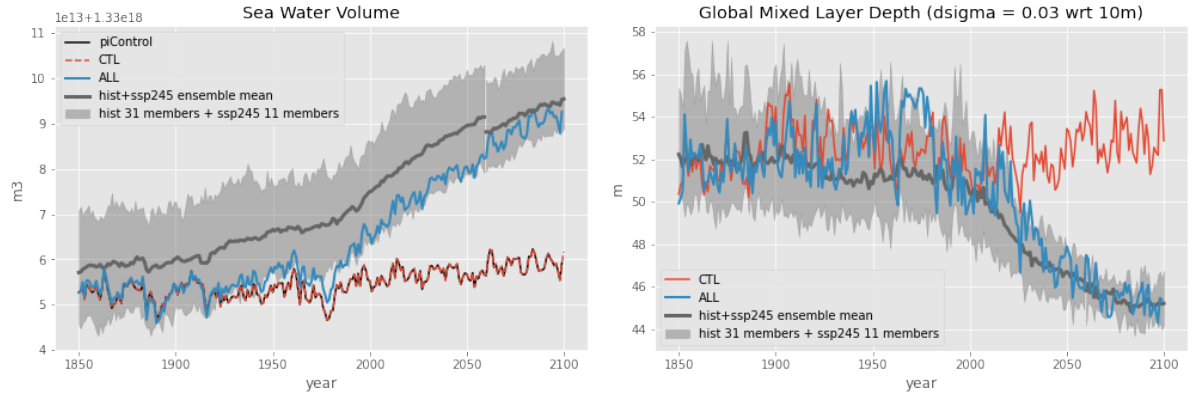

Figure III.22: Evolution of global ocean volume (left) and global mean mixed layer depth (right) for the IPSL-CM6A-LR ensemble (grey), piControl (black), CTL (dotted red) and ALL (blue).

We also compare the ALL experiment to the ensemble mean response for the zonal mean temperature and salinity anomalies in the mid-21st century (figures III.23 and III.24). The response of the ALL experiment in both temperature and salinity is strikingly similar to the response of the IPSL-CM6A-LR ensemble mean, validating the coherence of this experiment (Pearson correlation coefficient in global zonal mean of 0.88 for salinity and 0.92 for temperature).

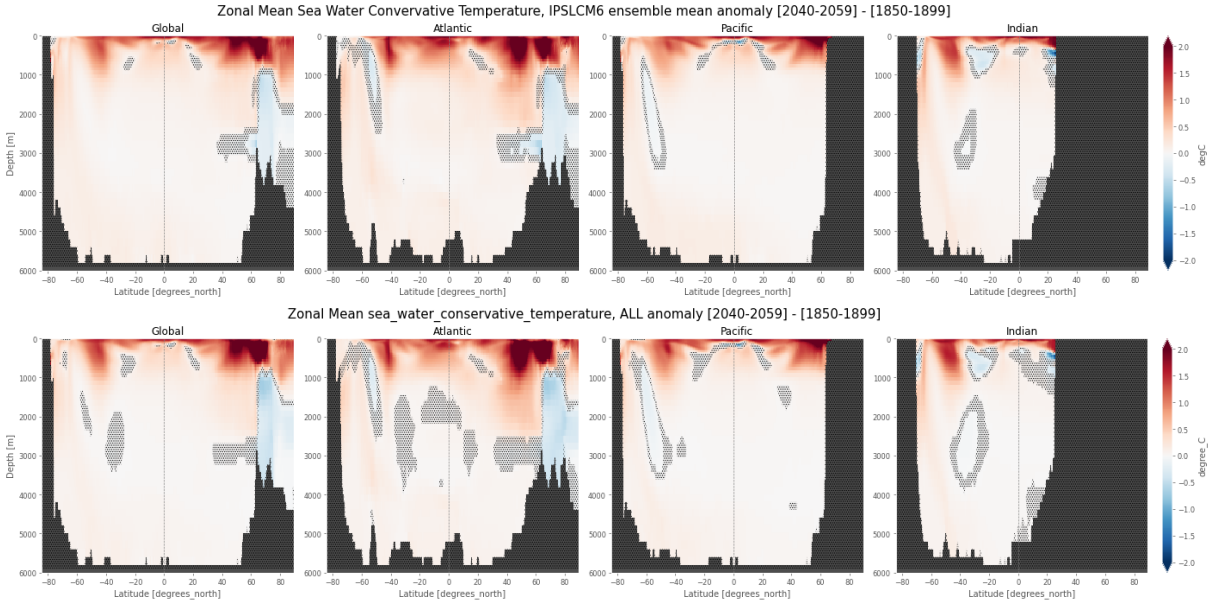

Figure III.23: Zonal mean temperature anomaly in 2040-2059 relative to 1850-1899, for the IPSL-CM6A-LR ensemble mean (top) compared to the ALL experiment (bottom). Stippling indicates when the anomaly is lower than the standard deviation (in absolute value) of the 2000-year piControl published for CMIP6.

The only notable discrepancy is seen for the SST anomaly in the Arctic (figure III.25) where surface temperatures fall below the freezing point in the ALL experiment (due to the absence of the sea-ice component), creating negative anomalies unlike in the IPSL-CM6A-LR historical+ssp245 response where

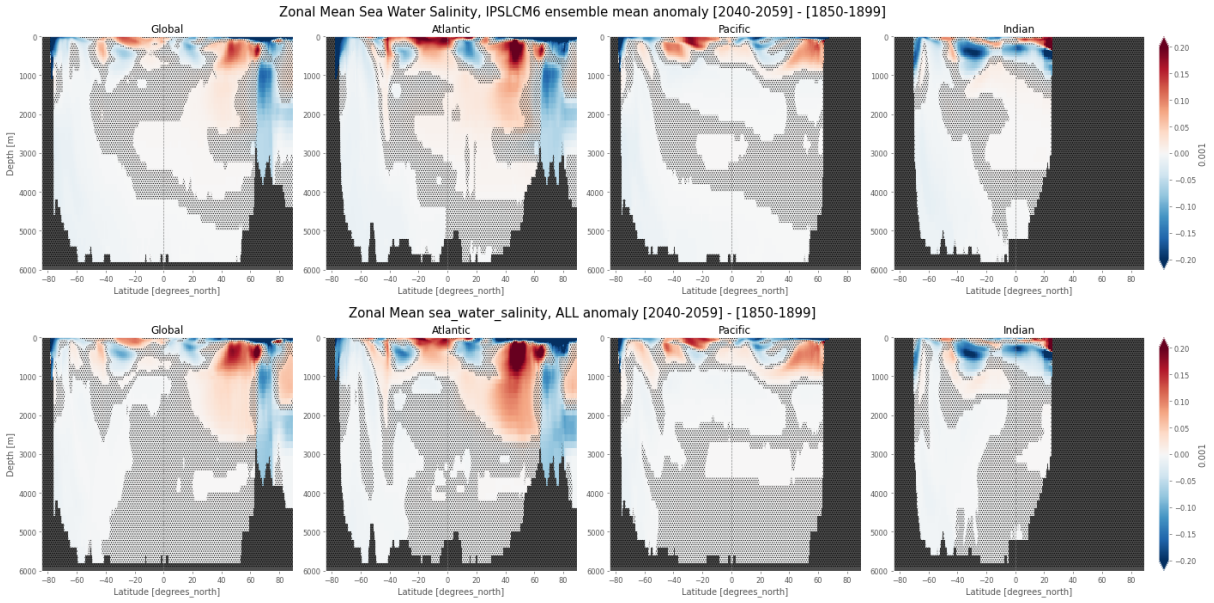

Figure III.24: Zonal mean salinity anomaly in 2040-2059 relative to 1850-1899, for the IPSL-CM6A-LR ensemble mean (top) compared to the ALL experiment (bottom). Stippling indicates when the anomaly is lower than the standard deviation (in absolute value) of the 2000-year piControl published for CMIP6.

there is a small warming. We ran different sensitivity experiments to the treatment of the temperatures below freezing in our forced experiments (presented in Appendix C) and concluded that overall, letting the temperature fall freely below the freezing point (while constraining the equation of state and Brünt-Vaisala frequency) gave the best response in the CTL and ALL experiments relatively to our objective (i.e. gave the closest response to the piControl and to the large ensemble respectively). These negative anomalies are only located in the Arctic surface layers and don't seem to impact the rest of the ocean, as illustrated by the previous figures.

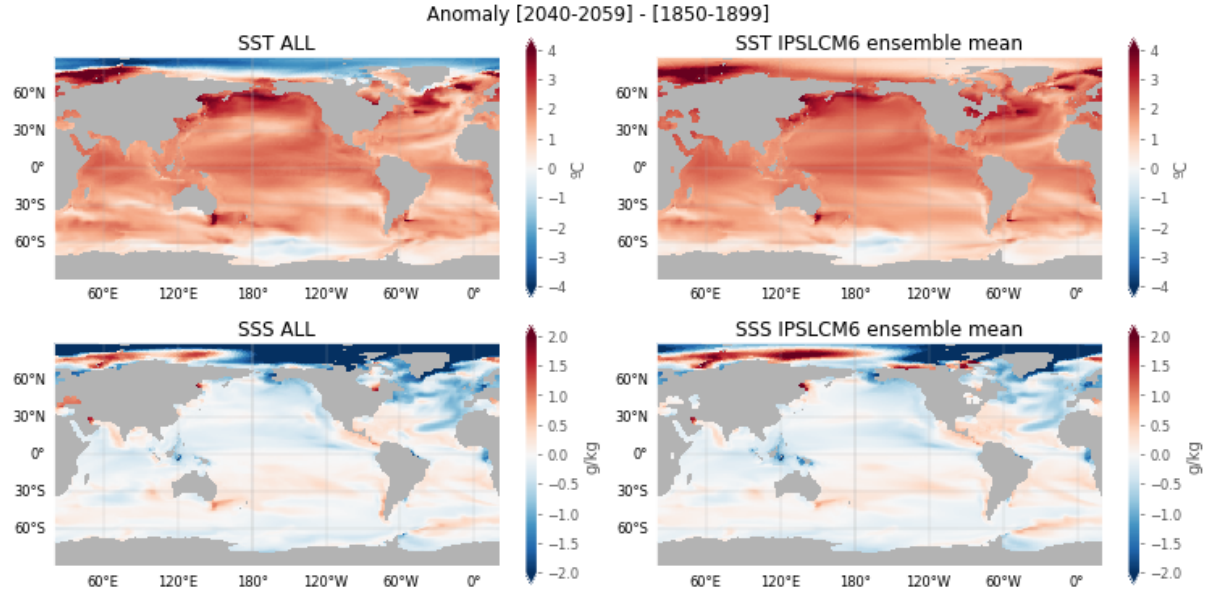

Figure III.25: SST (top) and SSS (right) anomalies in 2040-2059 relative to 1850-1899, for the IPSL-CM6A-LR ensemble mean (right) compared to the ALL experiment (left).

The SSS anomaly patterns are well reproduced in the ALL experiment apart from the Arctic freshen-

ing spreading too much West, North of the Bering Strait compared to the large ensemble.

We note the Arctic is the region of the World where we have the most difficulties reproducing the response of the coupled model, both in the CTL and in the ALL experiments, due to the absence of a sea-ice model in our simulations. This work is thus not designed to study the mechanisms at play in the Arctic Ocean in the IPSL-CM6A-LR model, and any result in this region should be interpreted carefully.

In all other regions, we have managed to reproduce very satisfactorily the IPSL-CM6A-LR large ensemble response with an ocean-only model and can coherently decompose the individual flux anomalies to investigate the different physical mechanisms within this framework.

5 Passive tracers

Two passive tracers are implemented using the TOP component in NEMO3.6 (Tracers in the Ocean Paradigm). Here, we define them conceptually and quickly present their implementation in the code. The definition of these tracers is largely based on the one first introduced by Banks et al. [2002] and later more explicitly by Banks and Gregory [2006], before being more widely applied by several other studies (see the General Introduction).

Let us write a simplified evolution of the ocean temperature θ:

$$\frac{\partial \theta}{\partial t} = Q - \underline{\nabla}.(\underline{u}\theta), \tag{III.5}$$

with Q the net downward heat flux at the ocean surface (let's note that "downward" is to be interpreted as "toward the liquid ocean"); and $\underline{u}$ a fictional velocity field representing all processes associated with ocean circulation (resolved and parameterized). By decomposing each variable into a stationary and an anomalous component (e.g. $\theta = \overline{\theta} + \theta'$), we have:

$$\frac{\partial \theta'}{\partial t} = Q' - \underline{\nabla}.(\underline{\overline{u}}\theta') - \underline{\nabla}.(\underline{u'}\theta') - \underline{\nabla}.(\underline{u'}\overline{\theta}). \tag{III.6}$$

By considering that the stationary components can represent the CTL mean state and the anomalous components the evolution of the perturbed state in each of our simulations, we can interpret each of these terms as follows: Q' represents the total heat flux anomaly (qns'+qsr'+hflx_rnf'+hflx_isf'), $\underline{\nabla}.(\underline{\overline{u}}\theta')$ is the transport of the anomalous heat θ' by the CTL circulation $\overline{u}$, $\underline{\nabla}.(\underline{u'}\overline{\theta})$ is the transport of the pre-existing heat in CTL $\overline{\theta}$ by the changing circulation u' in the new experiment, and the non-linear term $\underline{\nabla}.(\underline{u'}\theta')$ is the transport of the anomalous heat by the changing circulation. The first term in the right-hand side of equation III.6 is commonly referred to as "passive heat" as it forces excess heat into the ocean without any change to the dynamics, and the last term as "redistributed heat" as it accounts for temperature anomaly due to anomalous currents redistributing the mean temperature field. The non-linear second-order term is often neglected. To properly separate the effect of anomalous heat directly transported into the ocean and the effect of redistribution, the following decomposition is proposed: $\theta' = \theta'_A + \theta'_R$ with θ_A the "added" or "excess" heat initialized at 0 and θ_R the redistributed heat initialized at θ in each of the simulations. The evolution of θ'_A and θ'_R can be written as follows:

$$\begin{aligned} \frac{\partial \theta'_A}{\partial t} &= Q' - \underline{\nabla}.(\underline{\overline{u}}\theta'_A) - \underline{\nabla}.(\underline{u'}\theta'_A) \\ \frac{\partial \theta'_R}{\partial t} &= -\underline{\nabla}.(\underline{\overline{u}}\theta'_R) - \underline{\nabla}.(\underline{u'}\theta'_R) - \underline{\nabla}.(\underline{u'}\overline{\theta}) \end{aligned} \tag{III.7}$$

θ'_A is forced only by the heat flux anomaly Q' and transported in the ocean by the total circulation $\underline{\overline{u}} + \underline{u'}$, while θ'_R is forced by the redistribution term $\underline{\nabla}.(\underline{u'}\overline{\theta})$ and transported by the total circulation as

well. Consequently, we can see that if Q'=0 (no additional heat), $\theta'_A = 0$ (since it is initialized at 0) and if $\underline{u}' = 0$ (the circulation remains constant), θ'_R=0.

Here, we note PAT (Passive Anomaly Tracer, such as in Banks et al. [2002]) = θ'_A. In our simulations, PAT is expressed in ºC, forced with the perturbation heat flux components (qns', qsr', hflx_rnf' and hflx_isf') and advected by the model circulation. All the forcing terms are applied to the tracer trend in the same way as for temperature, i.e. qns' is applied in the first level of the ocean; qsr' is applied on the vertical with the same absorption coefficient calculated in the model physics; hflx_rnf' and hflx_isf' are also applied vertically. Even though the perturbation components are applied to the model physics only in ALL, HEAT and BUOY, we read these perturbations to force PAT the same way in all the experiments. PAT is the passive additional heat, that is, it does not affect the equation of state, it has the same source in all experiments, and is transported in the ocean by the circulation of the different experiments. The only difference in PAT between the 6 experiments will be the non-linear term $\underline{\nabla}.(\underline{u}'\theta'_A)$. The "passive heat" as characterized in Gregory et al. [2016], Todd et al. [2020] and Couldrey et al. [2021] corresponds to PAT in the CTL experiment (i.e. the excess heat transported into the ocean by the background circulation).

Similarly, the Passive Anomaly Salinity (PAS) tracer is implemented and forced with the anomalous freshwater flux components (emp', runoffs', iceshelf') and anomalous salt flux (sfx') in every simulation. However, PAS is trickier to implement than PAT because of the variable volume formulation. In the model physics, only the salt flux is applied in the salinity trend. The effect of the freshwater fluxes (Evaporation-Precipitation-Runoffs-Iceshelf) is applied directly in the volume trend, and salinity is then affected by the concentration/dilution effect in each layer: adding more water in a layer means decreasing the salt concentration. The same concentration/dilution effect by the freshwater fluxes applies to PAS. However, we only want PAS to be affected by the anomalous components emp', runoffs' and iceshelf'. Moreover, in some experiments (CTL, HEAT, STRESS), the freshwater and salt flux perturbations are not applied to the model physics while it is the case in other simulations (ALL, WATER, BUOY). Thus, we also apply freshwater fluxes in the PAS trend (similarly as for salinity in the fixed z-levels formulation) to correct for what is present or not in the physics. That is:

— We remove from the PAS trend the effect of the piControl fluxes (emp, runoffs, iceshelf, without the anomalies) to balance the concentration/dilution effect
— If freshwater flux anomalies are not activated in the physics (CTL, HEAT and STRESS experiments), we add the anomalies in the PAS trend
— Otherwise, the anomalies (present in the volume trend in the model physics) will have an effect on PAS through the concentration/dilution effect

As in the physics, emp is applied on the first ocean level, and runoffs and iceshelf are vertically distributed. See the code here (trcsms_my_trc.F90): https://github.com/ysilvy/simus_orca1_fluxforced/tree/main/MY_SRC.

PAS is initialized to the ocean mean salinity (34.7 g.kg^{-1}) because the trend formulation needs to see a value consistent with salinity, and this value is removed in all post-processing analyses to obtain an anomaly.

6 Key points

- In this chapter, I described the numerical framework developed for the analysis of chapter IV.
- This framework aims to decompose a number of physical mechanisms driving temperature and salinity changes in the ocean interior, in the context of the IPSL-CM6A-LR simulations of human-induced global warming.
- First, we reproduced a pre-industrial control experiment of the IPSL-CM6A-LR, using an ocean-only configuration of the NEMO3.6 model with a fixed-flux forcing.
- Then, in a sister simulation, we added perturbation components to the surface fluxes that isolate the externally-forced signal, and were able to replicate the ocean's response of the IPSL-CM6A-LR historical+ssp ensemble.
- Sensitivity experiments were conducted, applying the perturbation components individually to decompose the ocean's response to separate surface forcings.
- This framework provides an interesting way to separate relatively well - or at least as cleanly as possible in this modelling framework - the internal variability from the externally-forced signal in ocean-only simulations.
- Passive tracers were implemented to separate the effect of the excess heat and freshwater from the redistribution of pre-existing heat and salt by the changing circulation.

Chapter

IV

Decomposing mechanisms of temperature and salinity changes and their emergence from internal variability

Contents

1 Foreword

In Chapter II, we saw that IPSL-CM6A-LR presents spatially-varying time scales of emergence for temperature and salinity changes. Using a novel numerical framework described in Chapter III, we will explore in this present chapter the physical mechanisms associated with these time scales. Many directions were offered when analyzing these simulations, and many possibilities still remain. I have chosen to focus first on processes and time scales of ocean heat storage. This analysis is presented below as a paper that we plan to submit to the *Journal of Climate*. It results from a collaboration including input from my PhD advisors Jean-Baptiste Sallée and Eric Guilyardi as well as from Clément Rousset, Juliette Mignot, Christian Ethé and Gurvan Madec. The Supplemental Material to this manuscript is in Appendix D. This paper aims to qualitatively validate the long-term response obtained in our ocean-only experiments against the patterns found by previous studies under more idealized forcing or nearing equilibrium, and to exploit the novelty of the framework to investigate the transient response at regional scale.

Next, I present a few perspectives for a study focused on salinity changes. Salinity is forced by an overall signal of water-cycle amplification: its passive component is organized into positive and negative anomalies over regions climatologically associated with waters saltier and fresher than the global mean, respectively. The transient response of ocean interior salinity, its increasing contrast, mechanisms and time scales are still largely unknown. This second section aims to give a few prospects to fill this knowledge gap.

2 Paper: What causes anthropogenic ocean warming to emerge from internal variability in a global climate model?

What causes anthropogenic ocean warming to emerge from internal variability in a global climate model?

1. Introduction

Global ocean warming is a key indicator of human-induced climate change, accounting for 91% of the observed energy increase in the climate system between 1971 and 2018 (IPCC 2021). Multi-decadal increase in global ocean heat content results from a net global air-sea heat flux into the ocean. Ocean heat content change has, however, not been uniformed over the global ocean, with some regions experiencing rapid heat content increase while others have experienced no change, or a slight decrease in the past 50 years (Fox-Kemper et al. 2021). Processes shaping this regional distribution of heat content change control local ocean temperature change relevant for impacts on ecosystems and societies, and control timescales at which climate change signals penetrate into the ocean.

Spatial patterns of heat content change are caused by a combination of (i) air-sea heat flux perturbation causing surface temperature anomalies, which are then transported into the ocean interior by the ocean circulation; and (ii) changes in ocean circulation redistributing temperature internally in the ocean. Various methodologies have been proposed to decompose temperature change into these two processes, assuming that (i) is a purely passive process where surface temperature anomalies are advected by the climatological mean circulation; and that (ii) is a purely redistributive process where circulation variability transports the climatological mean temperature tracer (Banks and Gregory 2006; Xie and Vallis 2012; Winton et al. 2013; Marshall et al. 2015; Armour et al. 2016; Gregory et al. 2016; Garuba and Klinger 2016; Zanna et al. 2019b; Bronselaer and Zanna 2020). The relative contribution of passive versus redistributive processes on ocean temperature change varies largely with the timescales considered. At decadal timescale, redistribution dominates temperature variability in response to large internally-generated variations in the ocean circulation (Zika et al. 2021; Rathore et al. 2020). On longer timescales, as the surface heat flux forcing accumulates in response to climate change, passive storage of heat becomes larger (Bronselaer and Zanna 2020). This is particularly clear in regions of large subduction such as the Southern Ocean and the North Atlantic basins, where passive heat accumulates in ventilated watermasses, with some modulation in response to forced ocean circulation change (Piecuch et al. 2017; Zanna et al. 2019b; Bronselaer and Zanna 2020).

At multi-decadal timescales in the Southern Ocean, surface heat excess associated to climate change enters the ocean at the southern flank of the Antarctic Circumpolar Current (ACC), before being passively transported northward and subducted in the ocean interior along the ventilation pathways of Subantarctic Mode and Antarctic Intermediate Waters (SAMW, AAIW) (Marshall et al. 2015; Frölicher et al. 2015; Gregory et al. 2016; Armour et al. 2016; Liu et al. 2018; Dias et al. 2020; Couldrey et al. 2021). The redistribution signal is, in comparison, weaker and associated with intensifying and poleward-shifting westerly winds, driving increased northward Ekman transport and consequently increased heat subduction and storage at mid-latitudes (Fyfe et al. 2007; Liu et al. 2018; Shi et al. 2020).

In contrast, the North Atlantic basin is associated with a larger redistribution signal, even at long timescales, due to a slowdown in the Atlantic Meridional Overturning Circulation (AMOC), which itself is largely caused by an increasing heat flux (Mikolajewicz and Voss 2000; Gregory et al. 2016; Garuba and Klinger 2018; Todd et al. 2020). The slowdown of the AMOC weakens the poleward heat transport, causing a redistributive cooling in the subpolar North Atlantic, feeding back on the surface heat flux and increasing the initial heat uptake by the ocean, which further weakens the AMOC. This creates a positive loop clearly identified in coupled models with a prescribed heat flux perturbation (Gregory et al. 2016; Todd et al. 2020). In parallel to this redistributive cooling, positive heat flux perturbation causes heat to passively accumulate and to be transferred at depth by deep convection in the subpolar North Atlantic (Xie and Vallis 2012; Winton et al. 2013; Marshall et al. 2015; Gregory et al. 2016; Garuba and Klinger 2016, 2018; Bronselaer and Zanna 2020; Todd et al. 2020; Dias et al. 2020; Williams et al. 2021; Couldrey et al. 2021).

Most studies that investigated temperature change in the framework of passive vs. redistribution have focused on the long-term multi-decadal response to idealized forcings. For instance, to isolate the passive and redistributive components, Banks and Gregory (2006), Xie and Vallis (2012), Marshall et al. (2015), Armour et al. (2016), Gregory et al. (2016), Garuba and Klinger (2016, 2018), Todd et al. (2020), Dias et al. (2020), Couldrey et al. (2021) have investigated century-scale response of the ocean by introducing passive temperature tracers in idealized climate change experiments where CO_2 forcing is instantly doubled or quadrupled, or where CO_2 forcing grows at 1% or 2% per year. Others, have proposed to compare the century-scale response of the ocean in experiments in which currents are fixed to climatological values to experiments where currents evolve freely under a 1% CO_2 per year scenario

(Winton et al. 2013; Bronselaer and Zanna 2020). One study proposed a reconstruction of passive heat storage from a representation of climatological transport processes passively advecting observed SST anomalies (Zanna et al. 2019b). Another reconstructed the passive component of temperature change in observations of the 20th century and model projections, using the relation diagnosed between anthropogenic carbon and passive heat in idealized simulations and applying it to observations of anthropogenic carbon (Bronselaer and Zanna 2020). Another decomposition that has been proposed on the long-term response to radiative forcing scenarios aimed to trace total changes in temperature to separate contributions from individual air-sea flux perturbations: changes in the surface heat flux, freshwater flux and wind stress, which can all cause circulation changes and consequently redistribution (Mikolajewicz and Voss 2000; Fyfe et al. 2007; Armour et al. 2016; Gregory et al. 2016; Liu et al. 2018; Garuba and Klinger 2018; Shi et al. 2020; Todd et al. 2020; Dias et al. 2020; Couldrey et al. 2021).

Today, it remains unclear how these passive/redistributive processes and their relative time scales compete with each other and with internal variability in the transient response to realistic *historical* forcings (CO_2 and other forcings) and 21st century scenario. In this study, we are interested in what processes cause not only heat storage at the end of the 21st century (i.e. the long-term response) but also which processes cause temperature changes to emerge from local internal variability in the ocean interior, which can occur much earlier than 2100 in climate models (Silvy et al. 2020). We will use the notion of Time of Emergence (ToE) of climate signals (e.g. Hawkins and Sutton (2012)), that is, the time when a signal (e.g. a temperature change) last exceeds and remains above a significance threshold representing the internal variability noise envelope, and apply this notion to ocean interior changes.

We will explore whether the emergence of the subsurface temperature anomalies relies on the rate of increased surface heat flux modulated by the time scales of the unperturbed ocean circulation; or on circulation changes themselves, which can fundamentally change the way water-masses are ventilated in some regions and re-organize the temperature distribution. The influence of circulation changes acting on the transport of excess heat into the ocean will also be explored, with a non-negligible role found in some regions and on different time scales.

We investigate the mechanisms of ocean heat storage and their time scales in response to increasing anthropogenic forcings in the framework of the coupled model IPSL-CM6A-LR large ensemble of *historical* simulations and *ssp245* scenario. In section 2 we present the ensemble and its long-term changes in temperature and ocean heat content with their emergence from internal variability. In section 3 we introduce a modelling framework designed to decompose these changes with a set of sensitivity experiments with an ocean-only model. We present the results of these experiments, with a focus on the long-term changes in section 4, confirming the validity of our results with past studies, and investigate the more regional and temporal aspects in section 5 focusing on a few important ventilation pathways. The approach and the general results of this study are finally summarized and discussed in section 6.

2. Long-term changes in the IPSL-CM6A-LR large ensemble

a. Model and data

IPSL-CM6A-LR (Boucher et al. 2020) is the coupled model developed by the Institut Pierre-Simon Laplace modelling center for the 6th phase of the Coupled Model Intercomparison Project (CMIP6, Eyring et al. (2016)). It is composed of the LMDZ6A-LR atmospheric model (Hourdin et al. 2020), the ORCHIDEE land surface model (Krinner et al. 2005) version 2.0 and the NEMO3.6 ocean model (Madec et al. 2017). The atmospheric component has a horizontal resolution of 2.5ºx1.3º on a regular latitude-longitude grid and 79 vertical layers, while the ocean component uses the eORCA1 tripolar grid with a nominal horizontal resolution of 1º refined to 1/3º at the equator, with 75 vertical levels with varying thicknesses. The ocean physics component of NEMO3.6 is coupled to the LIM3 sea-ice model (Rousset et al. 2015) and to the PISCES-v2 biogeochemical model (Aumont et al. 2015). The oceanic equation of state is estimated with a polynomial representation of TEOS-10 (Roquet et al. 2015); the model prognostic fields are thus conservative temperature and absolute salinity. All results are presented for conservative temperature, but for simplicity we will simply use the generic term "temperature" in the remainder of the paper.

An ensemble of extended *historical* simulations was performed with the IPSL-CM6A-LR model (see Bonnet et al. (2021a) for the presentation of the ensemble), following the CMIP6 protocol for the *historical* period 1850-2014 and extended to 2059 following the *ssp245* scenario - apart from the ozone field which was kept constant to its 2014 values due to missing forcings at the time when the extensions were performed. The ensemble has 32 members, initialized at different branch points of a long pre-industrial control experiment (*piControl*) performed for CMIP6, spaced 20 to 40 years apart so that the ensemble samples the phases of the low-frequency variability present in the model (see Boucher et al. (2020) or Jiang et al. (2021) for a description of this long-term variability). In the extended period (2015-2059), some files were missing for member r2i1p1f1 and r16i1p1f1, so we only considered the other 30 members for the analysis on the entire period.

The *piControl* in IPSL-CM6A-LR (ran for 2000 years: 1850-3849) has a quasi-linear cooling drift in global mean ocean temperature (corresponding to a heat flux of about -0.13 W m^{-2}), particularly marked below 2000m, originating from a mean net surface heat loss (Mignot et al. 2021). This drift is propagated in the *historical* simulations and strongly influences the temperature evolution of the deep ocean, temporarily masking the warming signals, thus detrimental to the goals of this study. Removing this drift in ocean temperature outputs is necessary before analyzing any long-term changes. We fitted a 2nd order polynomial to the 2000-year *piControl* annual means at every grid point. Fitting over the longest possible period allows to isolate the drift without mistakenly picking low modes of internal variability (such as the bi-centennial mode in the North Atlantic present in the model, Jiang et al. (2021)) (Gupta et al. 2013). We remove the corresponding 210-year period of this quadratic fit from every member, that is, on each member's respective period of the *piControl*, and add the same mean state back to each member. This mean state is defined as the mean of the *piControl* calculated over the period where the historical-extended simulations were performed, i.e. 1870-2680. This mean state is added so as to keep full physical values of temperature as opposed to anomalies after removing the drift. Note that with this procedure, all 30 members are also ensured to have exactly the same mean state, and they only differ by their different phasing of internal variability set by the initial conditions from the *piControl*.

Large ensembles are useful tools to isolate the forced response from internal variability of the climate system, by averaging across multiple members sampling the uncertainty in internal variability (e.g. Deser et al. (2020)). Internal variability can thus be estimated by the intermember spread (usually measured by its standard deviation), a measure that varies over time, as opposed to estimating the internal interannual variability from a *piControl* which is fixed in time. One advantage of estimating a time-dependent internal variability stems from the fact that it can be impacted in future scenarios compared to the late 19th century, which is particularly true in the IPSL-CM6A-LR large ensemble where the spread is reduced (Bonnet et al. 2021a), highlighting an influence of anthropogenic external forcings on internal modes of variability.

b. Patterns of temperature and heat content changes

Here, we present the ensemble mean change in vertically-integrated ocean heat content (OHC) and zonal mean temperature (Figure 1a,b), with the corresponding signal-to-noise ratio (SNR, Figure 1c,d). The 'signal' is here defined as the ensemble mean, and the 'noise' as the intermember standard deviation. The Time of Emergence (ToE) is also calculated for each of the 30 members as the time when the SNR becomes definitively greater than a chosen significance threshold (i.e. the time when the forced signal can be unambiguously distinguished from internal variability). Each member's SNR is calculated as the anomaly relative to 1850-1899 (the signal) divided by the intermember standard deviation (the noise). The ensemble median ToE is presented (Figure 1e,f) for a SNR threshold of 3.

Panels 1a and 1b show a broad-scale warming in the ensemble mean by the mid-21st century, particularly pronounced in the subpolar North Atlantic and at the northern bounds of the ACC. The subsurface maximum warming penetrates deepest in the Southern Hemisphere subtropical gyres and in the Arctic (down to about 1000m). In addition, a weaker but significant warming signal (greater than twice the intermember noise) penetrates along the Antarctic Bottom Water (AABW) formation region and ventilation pathway (Figure 2). On the opposite, a subsurface (below 1000m) cooling is apparent in the deep convection region of the Greenland Sea between 65ºN and 80ºN (Figure 1b), but it is weaker than internal variability for vertically-integrated OHC (Figure 1a) as the subsurface cooling is mixed with upper-ocean warming. Another cooling region appears around 55-60ºS mainly in the Southern Pacific sector and also slightly in the Southern Atlantic (Figure 1a; Supplemental Material Figure 1). These cooling regions are associated with deep cooling of very old water-masses in the model (water-masses that have not been ventilated after 200 years of simulation; Figure 2). The overall regional patterns of OHC change are consistent with the multi-model mean CMIP5 and CMIP6 projected changes (Fox-Kemper et al. 2021)

Regions with the largest warming signal are not always those with the highest SNR. For instance, the warming in the tropical Atlantic stands out with a very large SNR exceeding 10 for vertically-averaged OHC (Figure 1c), because although the signal of change is not the largest, it is very large relative to the very weak noise of the region, particularly at depth (Figure 1d and Supplemental Material Figure 2 for the basin zonal means). Similarly, the weak warming in the AABW (Figure 1b) is in fact relatively pronounced in the subsurface when compared to the region's low internal variability (Figure 1d). The largest pattern of maximum SNR (>10) is located in the subtropical Southern Ocean along the ventilation pathway of SAMW and AAIW, reaching almost 2000m depth.

For a threshold of 3 for the SNR, a large portion of the Atlantic as well as the Southern Ocean band around 40-50ºS emerges between the late 20th century and the early 21st century. A narrow band along the North Pacific coasts and the Bering strait also sees an early emergence of its warming pattern, as well as the Eastern tropical Indian Ocean due to weak internal variability there (Figure 1e). The zonal mean view (Figure 1f) highlights the AABW in the deep and abyssal ocean as the most sensitive water-masses, with a warming signal emerging earlier than the

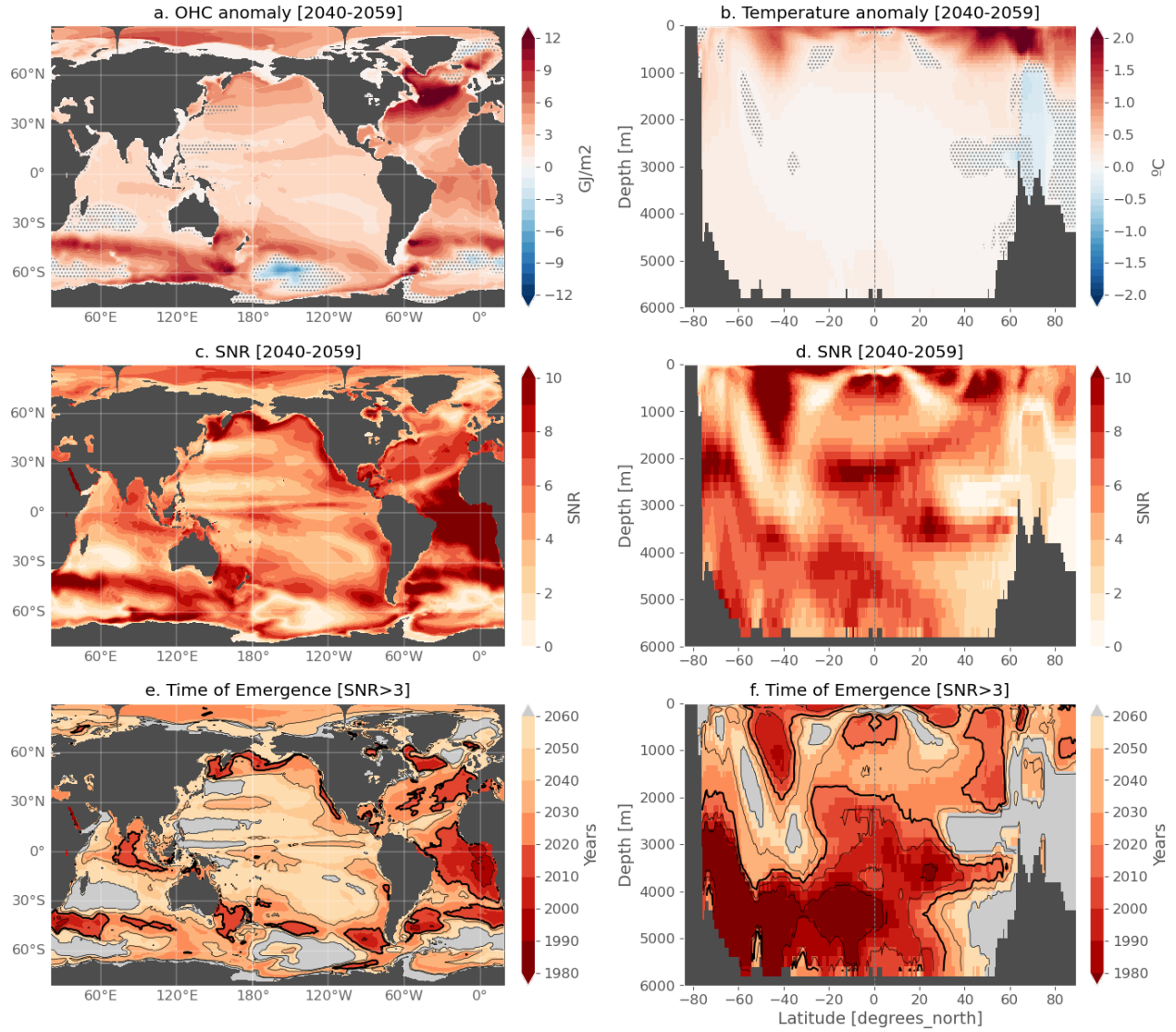

FIG. 1. IPSL-CM6A-LR ensemble mean anomaly relative to [1850-1899] (a,b) and signal to noise ratio (c,d) averaged between 2040-2059 (last 20 years of the historical-extended period) for ocean heat content (a,c) and zonal mean temperature anomaly (b,d). Ensemble median time of emergence (e,f) for a SNR>3 (grey shading indicates the signal has not emerged in the large ensemble for the chosen threshold; thick black line indicates year 2020). Stipples in panels a. and b. indicate where the anomaly is below twice the inter-member standard deviation.

1980s, although it is also where the intermember spread in ToE is the largest (>100 years for the full ensemble spread; see Supplemental Material Figure 2). This is a sign that in this region, internal variability acts to modulate the slowly-increasing forced signal over the 20th and possibly delay or advance its emergence in individual realizations. A larger SNR threshold could be better suited to more coherently detect the forced signal in the full ensemble, with smaller spread. This point will be further discussed in section 5. Near the surface, the strong warming in subtropical mode waters emerges before 2020 in both hemispheres, and early emergence before year 2000 is found at around 45ºS at 1000m depth (consistent with Silvy et al. (2020)). The emerging pattern before 2020 between 45-60ºN penetrating down to 2000m (Figure 1f) is located in the Greenland and Irminger Seas (Figure 1e), where deep convection occurs in the IPSL-CM6A-LR model (Boucher et al. 2020; Jiang et al. 2021). Regions of no emerging signal (i.e. where the SNR has not exceeded 3 before 2059) include the poorly ventilated lower Circumpolar Deep Water (CDW) where a slight cooling or delayed warming is identified, the surface waters near the Antarctic coast, and the deep ocean north of 40ºN.

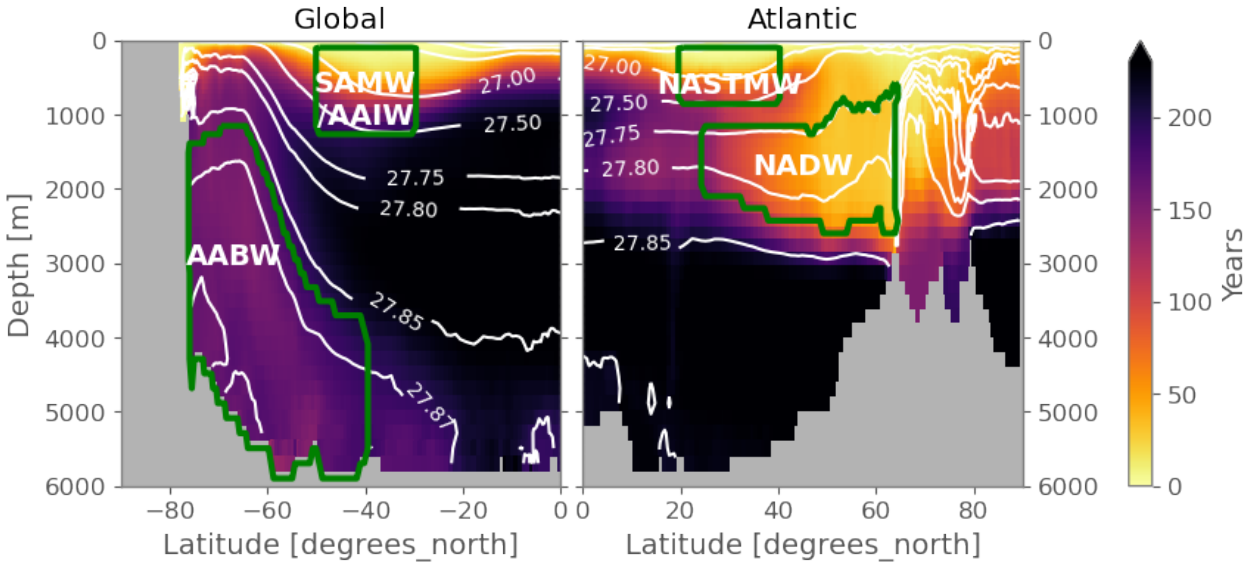

FIG. 2. Zonal mean Age tracer in the CTL experiment averaged over the last 20 years [2081-2100] (colors) and potential density (white contours, kg.m^{-3}). The Age passive tracer is initialized at 0 at the start of the simulation and incremented by one year every simulated year everywhere outside of the mixed layer. The four regions considered for the temporal analysis are drawn in green, corresponding broadly to the range of Antarctic Bottom Waters (AABW), Subantarctic Mode and Antarctic Intermediate Waters (SAMW/AAIW), North Atlantic Subtropical Mode Waters (NASTMW) and North Atlantic Deep Waters (NADW).

We are now interested in deciphering which processes cause these different patterns of change and their time scales of emergence from internal variability in the large ensemble, and start with the description of ocean-only simulations, which we specifically designed to address this question.

3. Experimental design

We use the ocean physics component (OPA) of the NEMO3.6 model (Madec et al. 2017), which is the ocean component of the IPSL-CM6A-LR coupled model (thereafter referred to as IPSL-CM6) presented above, under the same eORCA1 configuration, without the sea-ice model and the biogeochemical model. The goal of the modelling experiments is to reproduce the ocean response of the *historical+ssp245* simulations in the IPSL-CM6 model (over the period 1850-2100), and decompose that response into separate processes. Namely, we target the contributions from individual surface flux changes on the one hand, and the contributions from the passive transport of added heat and the redistribution of pre-existing heat by the changing ocean transport processes on the other hand. Since the protocol is closely related to the ocean-only FAFMIP protocol (Todd et al. 2020), we try to use similar terms, when relevant, to describe our experimental design.

a. Numerical experiments

We first set up a control experiment (CTL, see Figure 3) with the ocean-only model, forced at the ocean interface with the fluxes from the *piControl* experiment of the IPSL-CM6 model. The CTL is initialized from the *piControl* initial state, which itself starts after a multi-century spin-up of the coupled model. The surface fluxes from the *piControl* are outputted on the oceanic grid at 3-hourly frequency (at the ocean-atmosphere and ocean-sea ice interface), twice the coupling frequency. They are prescribed to the ocean-only model with no restoring: the ocean model is therefore forced with fixed fluxes. The high frequency of the forcings enables our CTL experiment to reproduce the internal variability and mean state of the coupled *piControl* very well with no deviation during the 251 years of simulations (see key validation diagnostics in Supplemental Material Figure 3). All the components of the surface fluxes are derived from the coupled model so that the oceanic heat and freshwater budgets close, as in the coupled model. Components of the heat flux, freshwater flux, salt flux and wind stress used to force the NEMO3.6 model are detailed in Appendix A, as well as other necessary fields to more faithfully reproduce the *piControl*.

We then set up the ALL experiment, which is configured exactly like the CTL, except that we now add a perturbation component to each surface flux (heat, freshwater, salt,

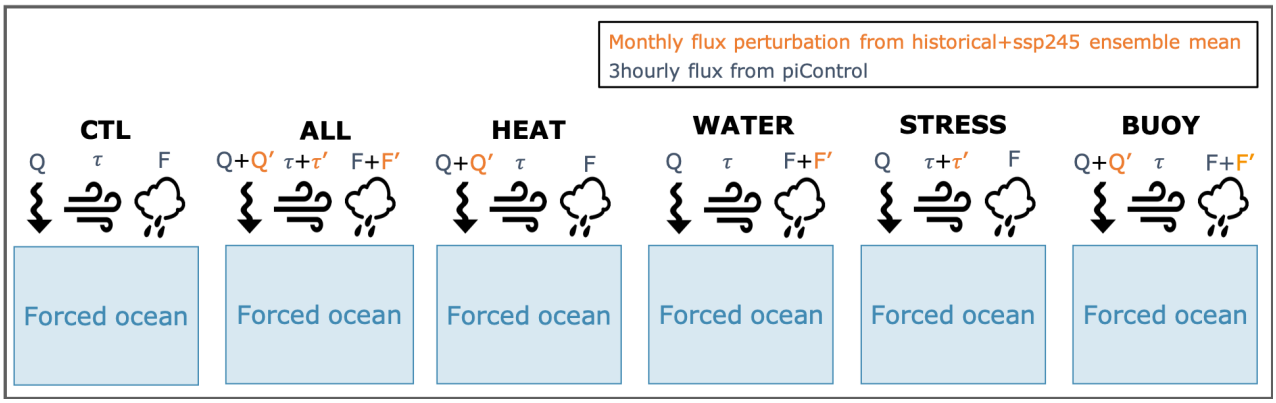

FIG. 3. Schematic of the fixed-flux forced ocean experiments

wind stress) to reproduce the externally-forced response in the *historical+ssp245* simulations. The perturbations for each flux component are taken as the ensemble mean anomaly relative to 1850-1899 from the IPSL-CM6 *historical*-extended simulations for the period 1850-2059 and *ssp245* scenario simulations for the rest of the 21st century (2060-2100, 11 members), at monthly frequency. By averaging across members, these perturbations isolate the forced *historical+ssp245* response in IPSL-CM6. Maps of the surface flux perturbations are shown in Supplemental Material Figure 4 averaged over the last 20 years (2081-2100). The ALL experiment thus has the internal variability of the CTL experiment (inherited from the *piControl* 3-hourly surface fluxes) and the time-dependent forced response from the *historical+ssp245* simulations (inherited from the monthly perturbations over 1850-2100). ALL thus acts as any *historical+ssp245* member, with its own initial conditions from a *piControl* state, and reproduces the response of the ensemble, which is within the ensemble spread (see Figure 5, 7-9 and Supplemental Material Figure 3).

Sensitivity experiments are in turn conducted with the same configuration (Figure 3), applying the perturbations on the surface heat fluxes only (HEAT), freshwater and associated salt fluxes (WATER), both buoyancy fluxes together (BUOY), and wind stress components (STRESS) respectively. These experiments allow for the total ocean response to be decomposed in separate contributions from individual surface fluxes, within the hypothesis of linear additivity of the components (e.g. hypothesis that ocean temperature changes in ALL is the sum of temperature changes in HEAT, WATER and STRESS (or BUOY and STRESS)). The validity of the linear additivity and its limits are addressed in the results sections.

As indicated above, all ocean-only experiments have similar internal variability because of the 3-hourly fixed fluxes from the *piControl*, so that they are directly comparable. All anomalies in the analysis are computed relative to the CTL on the same period of time, filtering out a majority of the internal variability. We note that since this internal variability is inherited from a *piControl* simulation, it isn't affected by the external forcings' eventual impact on modes of variability, unlike what occurs in the scenarios of the 21st century, illustrated by a reduced inter-member spread in the large ensemble on some variables of the climate system (Bonnet et al. 2021a).

All the experiments also inherit the cooling drift present in the *piControl*. As for the temperature field in the *historical*-extended simulations, the drift is removed from the experiments i.e. the corresponding period of the 2000-year quadratic fit on the 3D temperature field is subtracted and the CTL mean state is added back to all the simulations.

Because there is no sea-ice component in the flux-forced experiments, temperature can locally fall below the freezing point in polar regions. We implement a treatment to the equation of state in these regions, so that there is no impact of below-freezing temperatures on the dynamics. This point is discussed in Appendix A.

One of the main differences of our protocol with the ocean-only FAFMIP design (Todd et al. 2020) is in the surface perturbations we impose: FAFMIP provides monthly anomalies with no interannual variations, extracted from a multi-model mean in CMIP5 1pctCO2 experiments at a time when CO_2 concentration in the atmosphere has doubled. They are interested in the equilibrium response. Here, we impose on an ocean-only model the perturbations extracted from the *historical+ssp245* transient simulations in the IPSL-CM6 ensemble (which has the same ocean configuration as the stand-alone ocean component). This enables us to reproduce the response of these transient coupled simulations, with realistic historical and future external forcings. Furthermore, because we are conduct-

ing a single-model study, we can apply the perturbations with more degrees of precision (e.g. on each component of the surface fluxes, separating into those that need special treatments such as vertical distribution, see Appendix A).

b. Passive tracer and decomposition of temperature changes

A simple analytical framework is presented in Appendix B to decompose the evolution of the temperature anomaly T' in the ocean-only perturbed experiments relative to the CTL experiment. Briefly, T' is forced at the surface by the anomalous surface heat flux Q' and advected and mixed by the circulation in the perturbed experiment; but it also has a forcing term coming from the perturbed circulation acting on the CTL temperature. To virtually decompose these two effects, we introduce a passive temperature tracer as in Banks et al. (2002), Banks and Gregory (2006) and other subsequent studies. This passive "added heat" tracer T'_a is initialized at zero, forced at the surface by the same anomalous heat flux Q' as T', and advected by the circulation (CTL + perturbed components). Thus, integrated over the global ocean, T'_a amounts to the same storage of heat as T', but their local patterns can differ. The "redistributed heat" is diagnosed in the post-processing by $T'_r = T' - T'_a$ and represents the effect of the perturbed circulation redistributing the background temperature.

T'_a is implemented similarly in each experiment (forced by Q' and advected passively by the circulation specific to the experiment), so that T'_a between the perturbed experiments and CTL differs only by the effect of the perturbed circulation acting on the added heat (see Appendix B). We refer to this component as the non-linear added heat, diagnosed by $T'_a - T'_a|_{CTL}$.

To summarize, in the experiments where an anomalous surface heat flux is imposed (ALL, HEAT, BUOY), we can decompose the total temperature change T' (diagnosed from the output prognostic temperature field) into:

- An added heat component, diagnosed from T'_a calculated online, further decomposed into
  - A passive heat component, diagnosed from T'_a in CTL: $T'_a|_{CTL}$
  - The effect of the perturbed circulation on the added heat (what we refer to as the non-linear added heat component), diagnosed from $T'_a - T'_a|_{CTL}$
- A redistributed heat component, diagnosed from $T' - T'_a$

so that:

$$\begin{aligned} \underbrace{\text{Total}}_{T'} &= \underbrace{\text{Added}}_{T'_a} + \underbrace{\text{Redistributed}}_{T' - T'_a} \\ &= \underbrace{\text{Passive}}_{T'_a|_{CTL}} + \underbrace{\text{Non-linear added}}_{T'_a - T'_a|_{CTL}} + \underbrace{\text{Redistributed}}_{T' - T'_a} \end{aligned} \quad (1)$$

4. Decomposition of the long-term changes in the ocean-only experiments

Here, we present the decomposition of the long-term ocean warming patterns into contributions from individual surface flux perturbations (Figure 4 and Supplemental Material Figure 5 for the basin zonal means) and into contributions from the added and redistributed components in the ALL experiment, as described above (Figure 5, see Supplemental Material Figure 6 for the decomposition in the HEAT experiment). We show the anomaly averaged in the last 20 years of the simulations compared to CTL, so as to maximize the signal magnitude and to compare it with previous studies that used strong idealized forcings. We highlight here the main features that are common to past studies, to set this work in the light of past efforts, before adding new aspects in the next section.

First, we note that the ALL experiment reproduces faithfully the response of the IPSL-CM6 ensemble (Figures 1a,b and 4a,b), which fulfills its primary purpose. The anomalies in basin zonal means and calculated on the same time period (2040-2059) for both the IPSL-CM6 ensemble mean and the ALL experiment are shown in Supplemental Material Figure 1, as well as their difference relative to the ensemble spread, and further validate the consistence of the ALL experiment.

The heat flux perturbation explains the overall warming of the ocean as well as its main patterns, as illustrated by the HEAT and ALL experiments (Figure 4). Yet, some regional differences stand out, particularly in the North Atlantic and in the Southern Ocean, evidence for a non-negligible role played by other flux perturbations in setting the total warming patterns.

In the Southern Ocean, the wind stress perturbation alone (Figure 4g,h) causes a redistributive warming around 40-60ºS mostly pronounced in the Atlantic and Western Pacific Ocean, penetrating deeply in the ocean and surrounded by cooling patterns at lower and higher latitudes. These results are consistent with previous studies, which explained this warming pattern by the increased northward Ekman transport in response to the poleward and intensifying westerly winds and consistent with an intensification of the wind-driven upper cell (Figure 6b), acting to transport and subduct more heat north of the ACC (Fyfe et al. 2007; Armour et al. 2016; Gregory et al. 2016; Liu et al. 2018; Garuba and

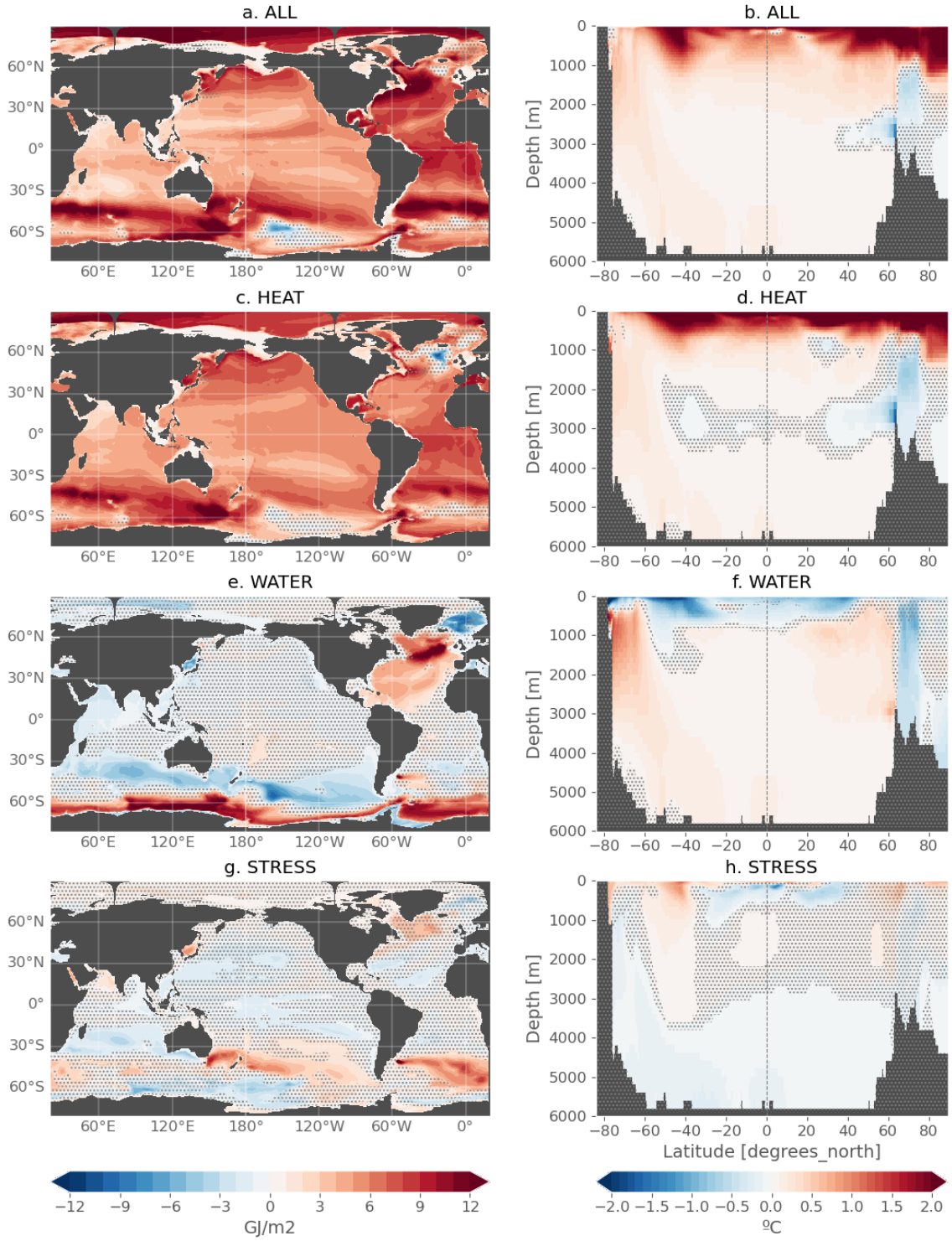

FIG. 4. Ocean heat content and zonal mean temperature anomaly in the ocean-only experiments, for the period [2081-2100] relative to the CTL experiment on the same period. Stipples indicate where the anomaly is below twice the interannual standard deviation of the CTL.

Klinger 2018; Todd et al. 2020; Shi et al. 2020). The northward Ekman pumping and ventilation can also be shifted to slightly higher latitudes in response to the wind stress perturbation (Waugh et al. 2019), creating the

dipole pattern in the Indian ocean (Figure 4g, cooling at 20-30ºS and warming at 40-50ºS). In southern high latitudes, the freshwater flux perturbation alone causes an intense redistributive cooling in the surface layers and a redistributive warming below from 500m to the bottom, especially intensified south of 60ºS (Figure 4e and f). This dipole has been explained by increased precipitation at high latitudes in the Southern Ocean, acting to stratify the surface layer, reducing vertical mixing between the upper and deep layers, decreasing the supply of cold newly formed waters into the deep and abyssal layers which causes a redistributive subsurface warming and surface cooling (Gregory et al. 2016; Armour et al. 2016; Todd et al. 2020). This is consistent with the decrease of more than 8 Sv in the Southern Ocean deep overturning cell found at the end of the WATER experiment (Figure 6c), also found by Todd et al. (2020) with model-dependent rates. On the opposite, the wind stress perturbation acts to strengthen the deep overturning cell (with a peak of 4 Sv in 2060, Figure 6c), cooling the waters in the subsurface southern high latitudes and along the export pathway of AABW (Figure 4). We will explore the temporal response of these regional features in more details in section 5.

More globally, there is a widespread surface cooling in the WATER experiment (Figure 4f), also found by e.g. Gregory et al. (2016), on top of a global subsurface warming. This cooling is consistent with increased stratification caused by the surface freshening in the subpolar Southern Ocean, as mentioned above, since surface waters are colder. Inversely, at mid-latitudes where the water-column is thermally stable, the surface cooling could be caused by an increase in evaporation over precipitation (Supplemental Material Figure 4), acting to de-stratify the water column, enhancing vertical mixing, thus cooling surface waters and warming the subsurface.

In the North Atlantic, the wind stress perturbation is about 4-5 times smaller than in the Southern Ocean (Supplemental Material Figure 4) and causes only small changes compared to internal variability, such as the warming south of Greenland (Figure 4g). We note there is no consensus between models in response to the FAFMIP wind stress perturbation in this region in Todd et al. (2020). The freshwater flux perturbation causes a much more significant warming than wind stress perturbation in the North Atlantic basin (greater than internal variability), particularly intensified at 45-50ºN, counteracting the subsurface cooling in HEAT at these latitudes (Figure 4e vs. 4c), and a cooling in the Nordic Seas that propagates on the entire water column (Figure 4f). This dipole is also present in the multi-model mean of Gregory et al. (2016) in their *faf-water* experiment, although the cooling spreads south of Greenland reaching 45ºN. The response to *faf-water* in Todd et al. (2020) (their Figure 13) reveals that the response patterns in the North Atlantic are very model dependent. The North Atlantic is also found to be the region of largest inter-model spread in total redistributed heat, possibly related to the spread in the magnitude of AMOC weakening (Todd et al. 2020; Couldrey et al. 2021).

As the climate system is inherently non-linear, some non-linearities arise from the interactions between the different surface perturbations. These are presented in Figure C1 and discussed in Appendix C. Overall, the largest non-linearities are found in subpolar areas where there are intense and different ventilation changes between the experiments. Caution should be considered when decomposing the total response in these areas, in that the sum of individual forcings is not exactly equal to the all-forcing response, although the decomposition is still relevant to investigate the potential different mechanisms and their respective time scales.

The passive warming component ($T'_a|_{CTL}$, Figure 5c and d) follows the shape of the main ocean ventilation pathways (see shading of the sea-water age tracer in Figure 2), that is we see some intense warming (>2ºC) along the subtropical gyres and along deep convection regions in the subpolar North Atlantic and Nordic Seas. Weaker but significant passive warming (compared to internal variability) is also exported down the AABW pathway. However, circulation changes in the ALL experiment act to decrease the penetration of the added heat in the subsurface (Figure 5h, non-linear added heat term, $T'_a|_{ALL} - T'_a|_{CTL}$): because of the upper ocean stratification, the added heat $T'_a|_{ALL}$ is partly trapped at the surface compared to $T'_a|_{CTL}$.

Although the passive component sets the main patterns of total warming, redistributed warming plays a key role in setting some more regional features. First, we note that the main patterns of redistributed change come from the heat flux perturbation (Supplemental Material Figure 6), meaning that the total HEAT patterns shown in Figure 4c and d arise from a mix of these two processes. A notable regional exception is the redistributive cooling pattern in the subtropical gyres (Figure 5f), particularly intense in the North Atlantic and southern Indian subtropical gyres around 30ºS (Figure 5e and see basin zonal means in Supplemental Material Figure 5). This redistributive cooling is set by all three flux perturbations (WATER, STRESS and the redistribution in HEAT) and counteracts a strong passive warming in the subtropical gyres. This passive warming is also particularly intensified in the North Atlantic gyre and southern Indian gyre, two important regions for ocean ventilation by subduction of newly-formed Mode Waters (Hanawa and Talley 2001; Morrison et al. 2022).

As in previous work, we find some redistributive warming at low latitudes, in the Atlantic and Pacific basins (Figure 5e). Some studies have attributed this to an anomalous positive equatorward heat transport, considering both the

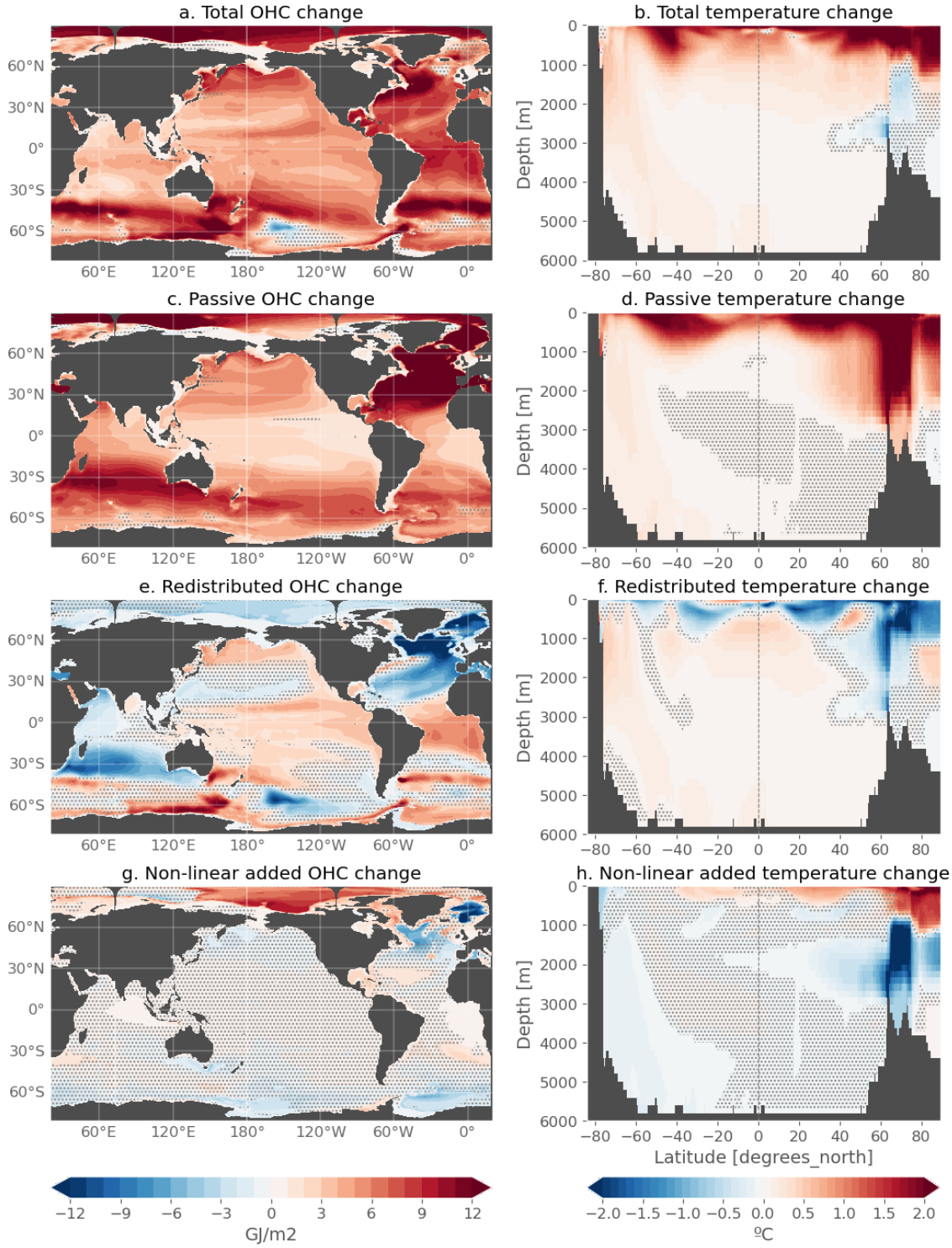

FIG. 5. Ocean heat content and zonal mean temperature anomaly in the ALL experiment for the period [2081-2100] relative to the CTL experiment. (a,b) total change, (c,d) passive component, (e,f) redistributed component and (g,h) non-linear part of the added component (i.e. perturbed transport acting on added heat). Stipples indicate where the plotted field is below twice the interannual standard deviation of the CTL.

AMOC weakening and the increased northward Ekman transport in the Southern Ocean (Xie and Vallis 2012; Winton et al. 2013; Gregory et al. 2016; Garuba and Klinger 2018; Hu et al. 2020; Bronselaer and Zanna 2020; Todd et al. 2020; Dias et al. 2020; Couldrey et al. 2021). However it seems that this vertically-integrated redistributive warming arises from warming at different levels in the water column (Figure 5f, no stipples in the tropical region under 500m, meaning the warming is greater than internal variability), coherent with the emerging patterns of the large ensemble (Figure 1d and f), with a potential important role for the abyssal redistributive warming.

In the North Atlantic, there is a strong passive warming component extending from the subtropical gyre to the Nordic Seas (Figure 5c), due to the positive surface heat flux perturbation (Supplemental Material Figure 4), partly compensated by a redistributive cooling in line with the AMOC weakening (Figure 6a) and particularly intense in the subsurface (Figure 5f), consistent with previous studies (Xie and Vallis 2012; Winton et al. 2013; Marshall et al. 2015; Gregory et al. 2016; Garuba and Klinger 2016, 2018; Todd et al. 2020; Bronselaer and Zanna 2020; Williams et al. 2021; Couldrey et al. 2021).

The overall agreement in the decomposition of the total temperature response to increasing anthropogenic forcings with previous findings under different or more idealized setups validates the coherence of our ocean-only experiments.

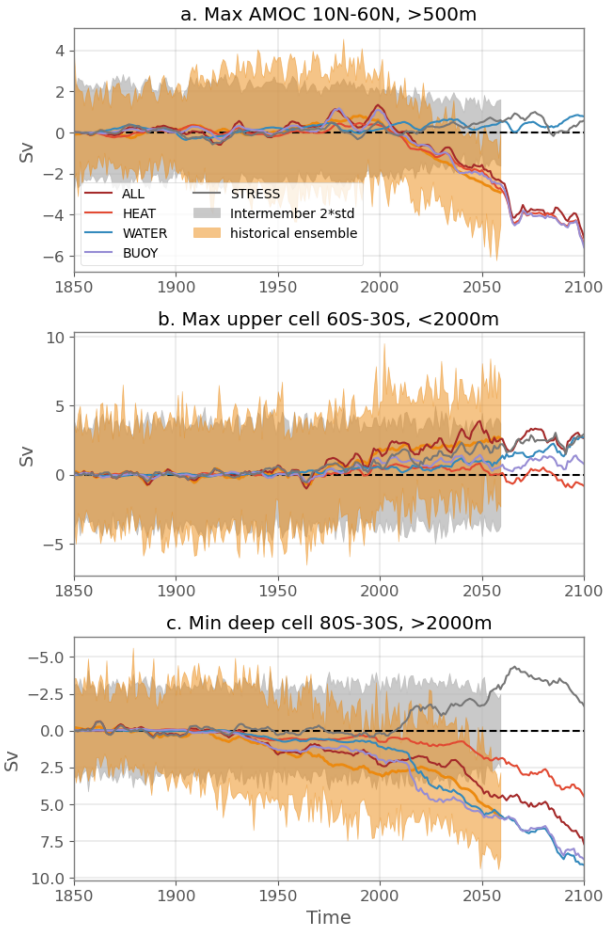

FIG. 6. Time series of circulation anomalies. (a) AMOC (maximum of the Atlantic meridional streamfunction between 10ºN and 60ºN, below 500m. (b) Southern Ocean upper cell (maximum of the global meridional streamfunction between 30ºS and 60ºS above 2000m. (c) Southern Ocean deep cell (minimum of the global meridional streamfunction between 30ºS and 80ºS below 2000m. We take the minimum as the deep cell turns anticlockwise, so has a negative sign. A positive anomaly thus means a decrease in the deep cell, so the y axis is reversed.) In the ocean-only simulations (colored lines) the anomalies are relative to the CTL experiment, with a 5-year running mean applied for visual purposes. The anomalies in the large ensemble (orange shading) are expressed relative to 1850-1899. The grey shading represents $2\sigma_{intermember}$.

5. Temporal response in the main ocean ventilation pathways

We now aim to explore the processes and the time scales which drive anthropogenic heat storage in the ocean interior. We thus proceed to investigate the temporal response of the contributions discussed above, in four significant regions for ocean ventilation. We have seen the important role played by the North Atlantic and Southern Ocean in setting ocean heat uptake patterns, not surprising considering their prominence for the global ocean overturning circulation.

First, we will focus below on upper ocean ventilation (upper two green boxes in Figure 2), associated with the subduction of Mode and Intermediate Waters feeding the subtropical gyres. We look at the region entitled "SAMW/AAIW" in the Southern Ocean (standing for Subantarctic Mode Waters and Antarctic Intermediate Waters), in a zonal average framework. These water-masses feed the upper limb of the Southern Ocean upper cell, subducting surface properties and change along their way (Morrison et al. 2022). In the North Atlantic, we look at the North Atlantic Subtropical Mode Waters (NASTMW), also known as Eighteen Degree Waters (Talley and Raymer 1982). These two regions are very well-ventilated in the model, as seen by the Sea-Water Age tracer (Figure 2).

Next, we will focus on the export pathways associated with the formation of Antarctic Bottom Waters (AABW) and North Atlantic Deep Waters (NADW) (see the lower two green boxes in Figure 2). AABW and NADW are the two most prominent water-masses found in the ocean (Johnson 2008), feeding the lower limbs of the MOC. They flow equatorward from their formation region, occupying the abyssal and deep layers respectively, before being

mixed with surrounding overlying water-masses or transported upwards by wind-induced upwelling (Marshall and Speer 2012). Note that we adopt an Eulerian view, with fixed geographical regions, to investigate how these climatologically well-ventilated areas of the ocean are affected in their heat storage response by different types of change, along with the time scales of emergence of these forced signals from internal variability. We leave a more specific water-mass tracking framework for potential future work.

a. Upper ocean ventilation

We present the evolution of temperature anomaly averaged in the SAMW/AAIW and NASTMW regions in Figure 7. The total warming is shown by the dark red curve representing the ALL experiment and by the orange spread representing the large ensemble. The ALL response in the SAMW/AAIW region is well within the spread of the large ensemble and has a similar evolution as the ensemble mean. This warming signal in SAMW/AAIW, starting early in the 20th century, is dominated by added heat (dark red dotted line). It is slightly damped by a small redistributive cooling (difference between the dotted and solid dark red lines). This redistributive cooling stems in the most part from the redistribution caused by the heat flux perturbation (difference between the dotted and solid light red lines), consistent with increased surface stratification preventing the downward spread of heat. Wind stress and freshwater perturbations redistribute heat in such a way that wind stress tends to warm SAMW/AAIW, while freshwater tends to cool them (consistent with Figure 4), almost compensating each other. But, we see here that, while their impact on temperature is significant (same order of magnitude as the heat flux) at the end of the 21st century, they start showing an influence on temperature decades after the heat flux perturbation does (Figure 7a).

The total warming significantly emerges at the turn of the century. As displayed by the spread in the large ensemble, the higher the SNR, the more coherent the ToE in the large ensemble is (i.e. the inter-member spread is smaller). This occurs because the warming in the 20th century is slow and subject to modulations by internal variability which can delay the emergence by several decades between members. When the warming signal picks up the pace at the turn of the century, the modulations by internal variability are too weak to slow down the forced signal as it did in the 20th century, and the emergence depends much less on the SNR threshold. All members emerge within maximum 35 years of each other for SNR>5 (1980 to 2015) and within two decades for SNR>7 (by 2020). Passive warming emerges earlier than the total response (black triangle, identical for the added component in the other simulations, not shown to lighten the figure) by about 10-15 years for SNR>7, illustrating the effect of the redistribution component in slightly delaying the emergence of the total signal. The passive warming, as well as the response in HEAT and BUOY, still emerge within the large ensemble ToE distribution, which indicates the effect of the redistributive processes on signal emergence are of the same order of magnitude as the uncertainty of internal variability on the emergence of the forced signal. The cooling in the WATER experiment and warming in STRESS both emerge in the 21st century but outside of the large ensemble distribution and with larger gaps between SNR thresholds because of the slower timing of the response.

On the North Atlantic side, the NASTMW region is also dominated by passive warming until the early 21st century. Redistributive cooling (difference between dotted and solid dark red lines) starts to counteract the passive signal in the 2010s and increases in the 21st century. The redistribution component is consistent with a heat-flux driven stratification tending to decrease ventilation in this region in the early 21st century (not shown), and might be related to the concurrent AMOC weakening (Figure 6a) reducing northward heat transport. In contrast to SAMW/AAIW, the temperature change implied by freshwater and wind stress perturbations is much smaller than the change due to the heat flux perturbation. There is nevertheless a weak cooling due to both these perturbations at the end of the 21st century. When combined with heat flux changes, the freshwater flux contribution appears however negligible since in the BUOY experiment (buoyancy flux perturbations combined) the warming is superimposed on the response in HEAT.

The response of the non-linear added heat component ($T'_a|_{ALL} - T'_a|_{CTL}$) and its timing are coherent with the decreased ventilation in the region (increase Age tracer, not shown), consistent with the increased surface heat flux stratifying the upper ocean, trapping the excess heat near the surface instead of the deeper heat transport in CTL (see also Figure 5h and Supplementary Figure 7).

Similarly to the SAMW/AAIW region, the large ensemble spread in ToE of the NASTMW warming reduces considerably between a SNR threshold of 2 and 5. The forced signal in the large ensemble has unambiguously emerged for the full distribution by 2020-2030 for a SNR>7. The emergence of the temperature signal is dictated by the heat flux perturbation, which is slightly delayed by redistribution, as indicated by the 10-year difference in ToE between the passive warming and the total warming (black triangle vs. dark red dot for SNR>5 and SNR>7). In contrast, the cooling caused by the wind stress or freshwater perturbations alone are barely significant compared to internal variability during the entire simulation (no emergence for SNR>5), but wind stress perturbations cause the ALL simulation to diverge from the BUOY simulation in the early 21st century, postponing the emergence of the warming by about 10

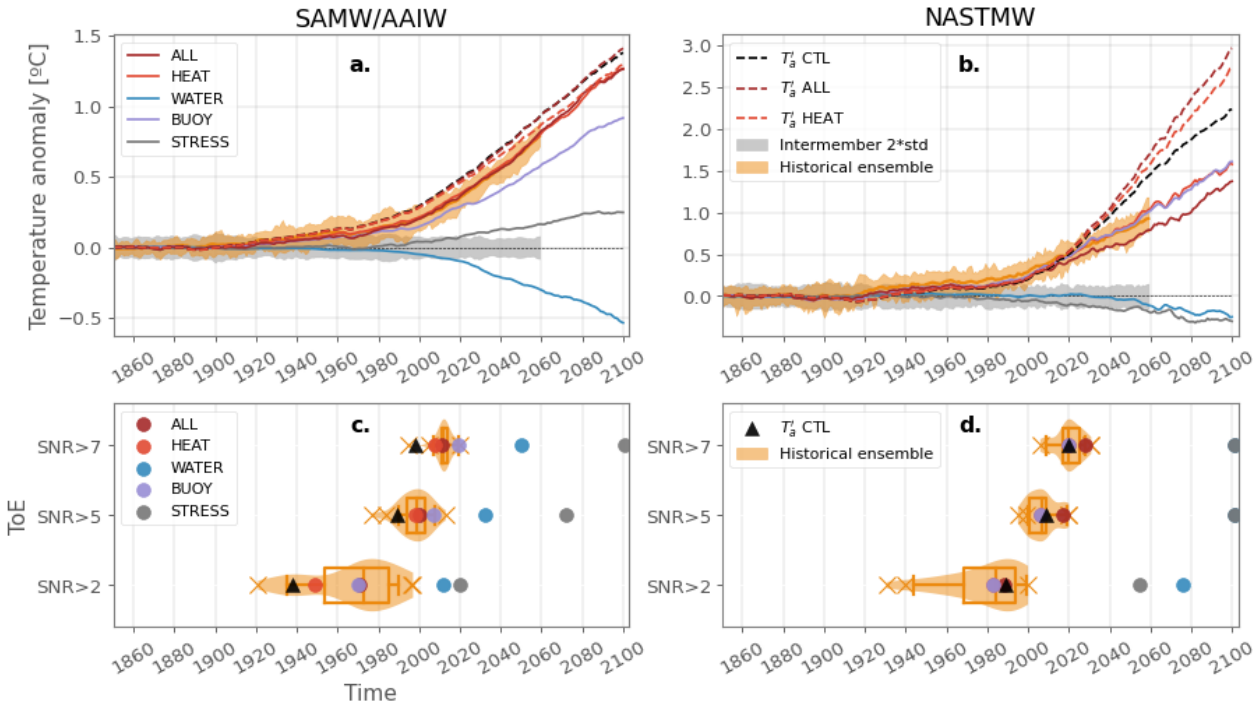

FIG. 7. Temperature anomalies (a,b) and corresponding ToE at different thresholds (c,d) in the SAMW/AAIW (left) and NASTMW (right) regions. The orange shading is the envelope of the large ensemble (LE). Each colored line/circle represents an ocean-only experiment (see legend). Anomalies in the experiments are expressed relative to the CTL at each time step to remove the maximum effects of internal variability, and expressed relative to 1850-1899 in the LE. The dotted lines in (a,b) are T'_a, representing the added heat in CTL (or passive heat; black), ALL (dark red) and HEAT (light red). The difference between T'_a in the perturbed experiments and CTL corresponds to the non-linear added heat (the effect of the perturbed transport acting on the added heat). The ToE is shown only for $T'_a|_{CTL}$ for visual purposes (black triangle). The grey shading in (a,b) is $\pm 2\sigma_{intermember}$ in the LE temperature, meaning when a temperature anomaly line crosses that threshold for the last time corresponds to the ToE for SNR>2 (we propagate the $\sigma_{intermember}$ value in 2059 in the last 41 years for signal detection in the ocean-only experiments). The distribution of ToE in the LE is shown both by the orange box plots (whiskers represent the 5th and 95th percentiles of the distribution, outliers are represented by orange crosses) and by the orange shaded violin plots.

years.

Overall, both regions present a similar temporal response in total warming, with an early signal starting around 1920, a slow increase until the late 20th century and a stronger warming trend during the 21st century, coherent with the temporal evolution of global mean near-surface air temperature in the model and in observations (Bonnet et al. 2021b), and with global mean SST in the model (Supplementary Figure 3). By the early 21st century, the warming of these Mode Waters is already outside the range of internal variability, with an emergence about 10 years earlier for the Southern Hemisphere compared to the North Atlantic. Redistribution plays a larger role in damping the magnitude of the warming brought by the transport of added heat in the North Atlantic (54% of the added heat in 2100) compared to the Southern Ocean (10%). However, the impact of redistribution occurs earlier in the Southern Ocean, because of the extra heat input which weakens the ventilation of the region. There are opposite effects of the wind stress changes in these two regions, which act to bring more warming in the Southern Ocean versus cooling in the North Atlantic, with an accelerating/slowing effect of about 10 years of the warming and its emergence from internal variability when comparing the all-forcing simulation (ALL) to the simulation without wind stress perturbations (BUOY). In both regions, a SNR of 2 still causes a large spread in the emergence of the large ensemble warming, which is much reduced for a larger threshold.

b. Deep water formation and their export pathways

We now move to the regions associated with the export of AABW and NADW, presented in Figure 8.

Unlike what occurs in the previous two regions, the AABW warming is due to contributions both from excess heat entering the ocean ($T'_a|_{ALL}$, dark red dotted line),

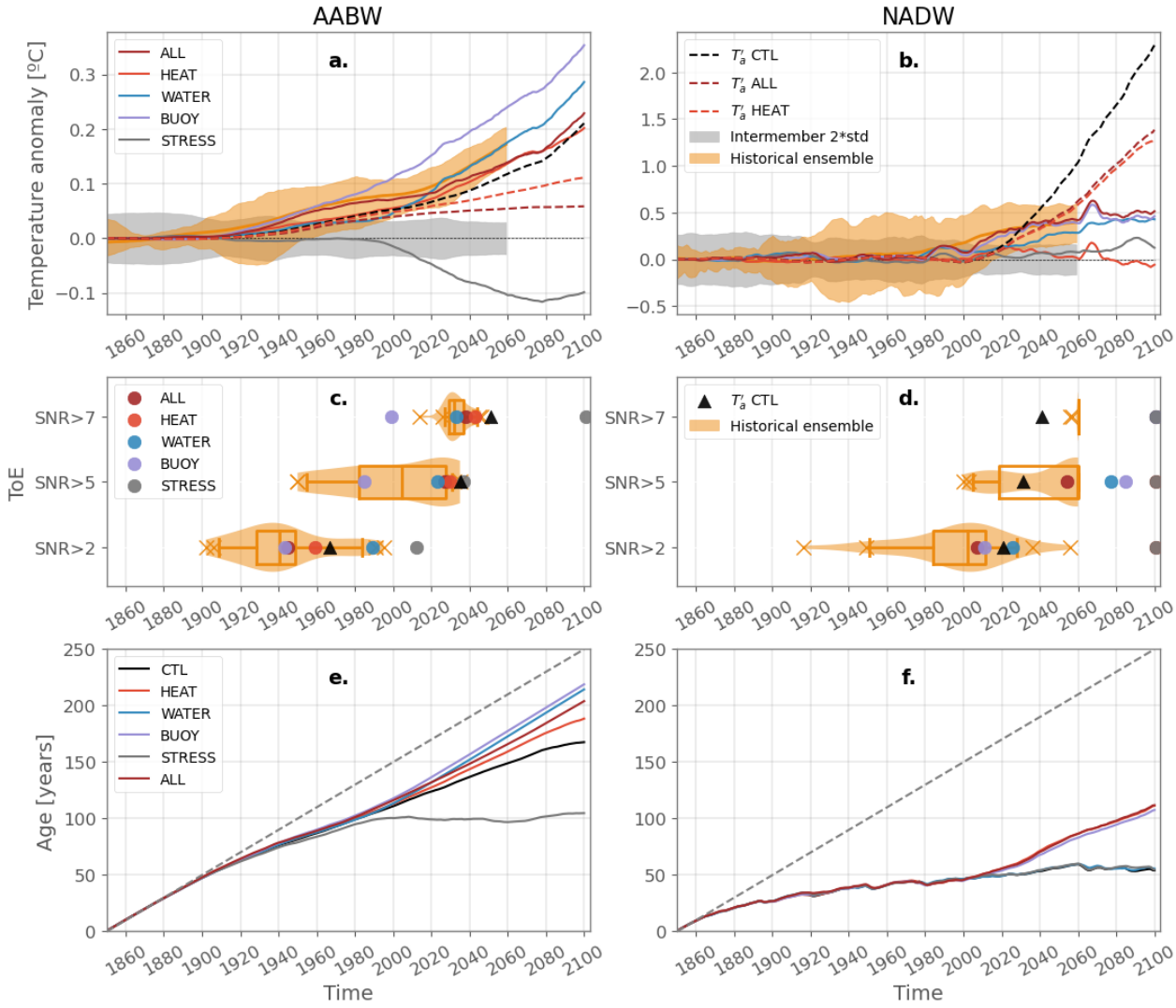

FIG. 8. (a,b,c,d) Same as Figure 7 but for AABW and NADW. (e,f) Age tracer in the ocean-only experiments. The grey dotted line represents the values of no ventilation.

passively transported, and to redistributive processes (difference between dark red solid and dotted lines). The redistributive warming is coherent with a weakening of the deep cell (Figure 6c) in response to an increase in both the surface freshwater and heat fluxes at southern high latitudes (Supplemental Material Figure 8). The deep cell weakening is indeed associated with a decrease in the ventilation of the region (Figure 8e), which prevents newly-formed cold waters at the surface from being mixed with the underlying layers, leading to subsurface warming and surface cooling (see Figure 4f). In the 21st century, the redistributive warming is primarily driven by the increased surface freshwater flux into the ocean (which contributes more to the buoyancy flux anomaly than the heat flux perturbation in this region, Supplementary Material Figure 8), competing with a redistributive cooling caused by wind stress changes. In contrast to heat and freshwater perturbations, wind stress perturbations result in an increase of the deep cell strength (Figures 6c and 8a,e). These circulation changes in the 21st century are coherent with the evolution of the mixed layer depth (MLD) south of 60ºS (Figure 9a). Indeed, they feature an abrupt shutdown of deep convection in the WATER and BUOY experiments at the end of the 20th century that is sustained in the rest of the simulations in response to the increased surface freshwater flux. This shutdown is compensated by a MLD deepening in response to the surface wind stress increase (Figure 9a). As a result of the competing effects between buoyancy fluxes and wind stress, the shoaling of the MLD in the ALL experiment does not show abrupt change but is more

gradual throughout the 21st century (consistent with the response of the large ensemble, Figure 9a). In summary, AABW warming results from a combination of added heat at the surface that is transported as part of the deep cell circulation, and reduction of strength of the deep cell. The deep cell slowing itself is caused by a balance of buoyancy fluxes that tend to push towards a rapid shut down of the circulation, and wind stress change that counterbalances this effect by reinforcing the circulation thereby avoiding a rapid shut down.

Changes in the AABW actually start early in the 20th century, as indicated by very early ToE (around 1940) when using a SNR threshold of 2. But this early emergence is actually explained by a noise envelope of temperature variations in the AABW export region that is very small so that a minor change in the circulation - on top of the passive warming slowly entering the ocean - leads to a temperature change that exceeds this noise, even though the circulation change might be small or temporary, and before the clear shutdown in deep convection occurs. The very large spread in the intermember ToE (almost one century wide for SNR>2) is a clear indication that the threshold of 2, combined with the slow warming of the 20th century, is too small to detect emergence of this early signal in all members of the ensemble in this water-mass. Even for SNR>5, the spread of the intermember ToE is large, and it is really only with a threshold of 7 combined with the more rapid forced warming that emergence is unambiguously detected in all members (i.e. small spread in the intermember ToE). This highlights the difficulty to isolate the forced signal in this region before the early decades of the 21st century, because of potentially sensitive mechanisms to the different phases of internal variability expressed in the individual members of the large ensemble which modulate the water-mass change signal (e.g. Abrahamsen et al. (2019); Silvano et al. (2020)). With SNR>7, the forced signal robustly emerges in the full ensemble by 2040, a timing consistent with the large changes in the circulation associated with the reduction in deep convection and decrease of the deep cell. In this case, the warming in the BUOY experiment emerges outside of the large ensemble distribution, about 40 years before the warming in ALL because in ALL the effects of buoyancy forcing are counterbalanced by the redistributive cooling associated with wind stress perturbations.

We here only discussed AABW changes very close to their sources around the Antarctic continent. But the model shows that AABW warming is transmitted along the export pathway of AABW further northward in the abyssal ocean, and even spread over the entire deep 2000-4000m ocean at global scale (Supplemental Material Figure 9). The timing of circulation from the AABW formation regions to its upward mixing in the 2000-4000m layer is arguably longer than our simulation (e.g. DeVries and Primeau (2011); Figure 2). It is therefore surprising to see abyssal warming spreading in the wider ocean at timescales from a few decades to a century. Our analysis presented in Supplementary Material Figure 9 shows that it is changes in circulation and deep ocean stratification that actually allow for a rapid spread of the climate signal in the deep ocean, with almost no contribution from the added heat passively transported at the century timescale.

The NADW region is much more ventilated than its Southern Hemisphere counterpart (AABW), as seen in the age tracer (Figures 2 and 8e,f), yet the warming signal emerges much later - or not at all depending on the SNR threshold - because of much larger internal variability but also because of warming signals starting later on than for AABW. Strong and rapid passive heat ($T'_a|_{CTL}$) arises starting in the 2000s and emerges after a few decades. The excess heat in the ALL simulation ($T'_a|_{ALL}$) is damped by almost half by 2100 compared to $T'_a|_{CTL}$, because of circulation changes in response to the heat flux perturbation ($T'_a|_{ALL} \approx T'_a|_{HEAT}$). These changes are consistent with AMOC weakening (Figure 6c), entirely driven by the heat flux perturbation (see Supplemental Material Figure 8 for the time evolution of the surface heat flux in the subpolar North Atlantic). This is coherent with the large reduction of deep convection in the subpolar North Atlantic as a response to heat flux perturbation (Figure 9a and see Supplemental Material Figure 10 for more specific time series showing a shutdown of deep convection in the Labrador Sea and decrease in the Greenland Sea). This leads to a decrease in the overall ventilation of the region (Figure 8f), preventing added heat from penetrating as deeply as in the CTL. All of these processes are consistent in terms of timing, starting in the early 21st century. Circulation changes also explain the large redistributive cooling in HEAT ($T'_a|_{HEAT}$ compared to HEAT in Figure 8b), entirely balancing the added heat component, so that the temperature anomaly in HEAT stays around zero for the entire period (Figure 8b). The wind stress perturbation has almost no effect in this region, however, as for the AABW, the freshwater flux perturbation causes a redistributive warming of almost the same intensity as the ALL warming at the end of the 21st century. Nevertheless the warming in response to the freshwater flux experiment cannot be explained by AMOC, MLD or ventilation changes as these remain very close to the CTL. Changes in the air-sea freshwater flux in this region are actually small compared to interannual variations of the heat flux in the context of their respective influence on buoyancy fluxes (Supplemental Figure 8).

In the large ensemble, the spread in the temperature anomaly is very large throughout the simulation. It only starts to narrow towards the end of the historical-extended period, with no emergence of the ensemble for SNR>7, the signal being still too weak compared to internal variations.

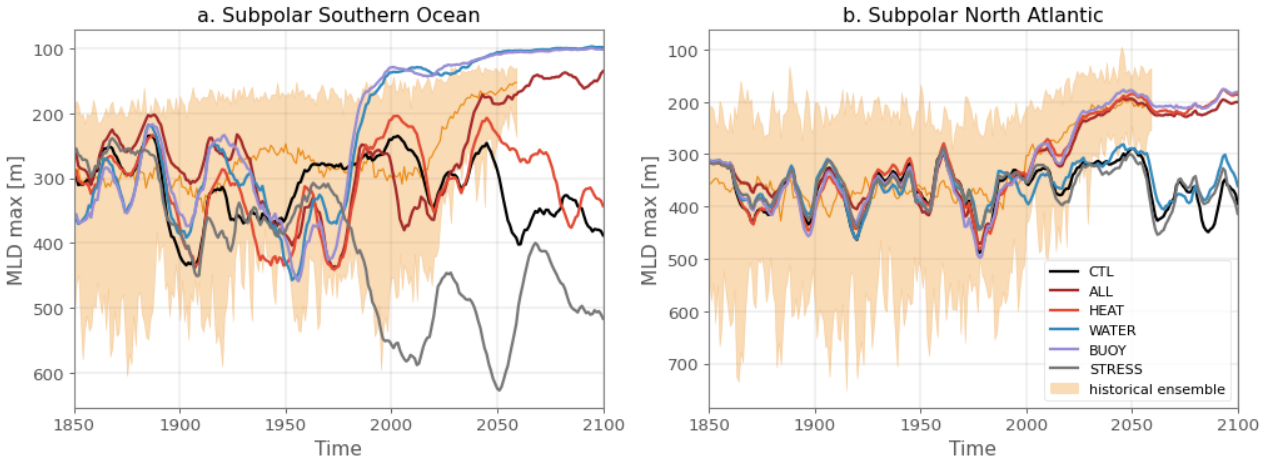

FIG. 9. Mixed layer depth (annual maximum) in the Southern Ocean south of 60ºS (a) and subpolar North Atlantic (b), in the large ensemble (orange shading) and in the ocean-only experiments (colored lines, with a 10-year running mean applied for visual purposes). The MLD is defined as the depth at which there is a 0.03 kg.m^{-3} difference in potential density relative to 10m. See Supplemental Material Figure 10 for the geographical delimitation of the subpolar North Atlantic, and for the time series in more specific deep convection regions.

6. Summary and Discussion

In this study, we introduced a new numerical framework to investigate the timescales of passive and redistributive processes and the role of individual surface flux perturbations on ocean temperature changes in response to climate change. With an ocean-only model forced with fixed fluxes, we proposed a set of experiments to examine the response of the ocean to the externally-forced signal of the IPSL-CM6A-LR large ensemble of *historical+ssp245* simulations. We force the model with climate change induced variations in all the buoyancy and wind stress fluxes together, as well as by isolating changes of individual fluxes, in an endeavour to disentangle and understand their respective role. A passive temperature tracer, forced with the heat flux perturbation, was implemented to isolate the signal and timescales of anthropogenically-added heat spreading passively in the ocean interior. This numerical framework is particularly adapted to isolate the emergence of externally-forced signals relative to internal variability, as all the ocean-only experiments are forced with the same background variability at 3-hourly frequency from a coupled unforced *piControl*.

Compared to previous studies that investigated these mechanisms under long-term radiative forcing, we focus on the transient response to climate change and on the timescales necessary for the forced signals to emerge from background internal variability. We highlight that the contribution of the passive and redistributive components to the emergence of the total warming signal from internal variability can be quite different from their contribution to the amplitude of the warming at the end of the 21st century.

In the Mode Waters of the mid-latitude Southern Ocean and North Atlantic (SAMW/AAIW, NASTMW), circulation changes produce a redistributive cooling which is small in the Southern Hemisphere but significant in the North Atlantic by the end of the century. This redistributive cooling delays the emergence of the total warming signal by about 10 years, which is already distinguishable from internal variability by the early 21st century. While the redistributive cooling in the Mode Waters of the North Atlantic has a significant impact on the intensity of their total warming, it is relatively slow to establish so that circulation changes only have a very minor role on the emergence of the warming.

In contrast to the upper ocean, circulation changes play a key role in warming the deep and abyssal waters of the subpolar Southern Ocean. Indeed, warming in this region results from a combination of added heat that is exported by the deep cell, and deep cell weakening warming the ocean by reducing cold water influx. The two are important and have similar timescales over the 20th century, but redistribution takes the upper hand over the 21st century, as it gets increasingly difficult to passively export the excess heat with the deep cell weakening. The warming induced by circulation changes is driven by a combination of buoyancy flux changes that increase the stratification, therefore shoaling the MLD and reducing ventilation of the deep ocean by cold water, which is counterbalanced by wind stress changes that tend to increase deep convection and ventilation. Overall, all fluxes are important in setting AABW warming: buoyancy fluxes

impact both added heat (mostly heat flux) and redistributed heat (mostly freshwater flux); and the wind stress impacts redistribution. The emergence is significantly delayed by the wind stress perturbation starting in the late 20th century.

While the redistribution component is important for the deep Southern Ocean warming signal to emerge before the added heat alone, the deep North Atlantic waters are cooled by the redistribution component in response to AMOC weakening, significantly counteracting the increasing passive warming in the 21st century. This is explained by an AMOC weakening driven by the heat flux perturbation in the 21st century, consistent with a decrease in deep convection found in all convective areas of the subpolar North Atlantic. As a result of these counteracting processes, the residual warming emerges decades later than in the Southern Ocean, or does not emerge with high significance thresholds, unlike its Southern Hemisphere counterpart. The fact that the forced signals (passive warming and AMOC weakening) do not significantly increase before the 21st century in the North Atlantic is consistent with a) large internal variability of the region and b) large aerosol radiative cooling in the Northern Hemisphere in the 20th century, temporarily offsetting the greenhouse gas (GHG) radiative warming (Naik et al. 2021). Scenario *ssp245* is associated with reduced aerosol forcing into the 21st century, while GHGs continue to increase (Gidden et al. 2019), so that GHG forcing is not counterbalanced anymore by the aerosol cooling effect. This is consistent with the AMOC temporal evolution, showing only small changes over the 20th century and decreasing rapidly in the 21st century in this model (Figure 6a) once the heat flux over the North Atlantic starts to increase (Supplemental Figure 8). Such AMOC response is similar to the CMIP5 and CMIP6 multi-model mean (Shi et al. 2018; Menary et al. 2020; Hassan et al. 2021). The impact of aerosols on heat fluxes in the North Atlantic has potential implications for detection and attribution studies of ocean interior changes, delaying the detectability of the observed changes in the North Atlantic, while the Southern Ocean observed warming has already been attributed to anthropogenic forcings, in the SAMW/AAIW but also at greater depths (Swart et al. 2018; Hobbs et al. 2021).

While the decrease in subpolar Southern Ocean deep convection in climate models in response to increasing CO_2 forcing is now well established (Gregory 2000; de Lavergne et al. 2014; Heuzé et al. 2020), how can we trust the timescales of the processes responsible for this deep convection shutdown uncovered here when such climate models don't accurately reproduce the observed processes of AABW formation (Heuzé et al. 2013; Heuzé 2021) nor include the amplified Antarctic iceshelf glacial melt contribution, which can significantly impact the ventilation (Lago and England 2019)? Indeed, an accurate representation of shelf processes is missing from global climate models, and although in the case of IPSL-CM6A-LR, there might be some dense water formed on the shelf, its export to the deep ocean is uncertain, and most of the bottom waters are formed by deep convection in the Weddell Sea, under sea-ice (Heuzé 2021; Mohrmann et al. 2021). As open-ocean deep convection controls the renewal of AABW and overturning circulation in the model world, decreases in this deep convection in response to increased freshwater and heat fluxes might thus lead to too rapid subsurface changes. The influence of the buoyancy fluxes here may be overestimated compared to the perturbation from the winds, that might act to delay the emergence. However, the iceshelf melt, which is not an interactive feature in this and other CMIP models, is expected to amplify the surface freshening and stratification, decrease AABW formation and progressively warm the subsurface and abyssal ocean waters, which can in turn create a positive feedback on the basal melt (Fogwill et al. 2015; Silvano et al. 2018; Bronselaer et al. 2018; Lago and England 2019). This might tend to move the emergence forward.

In turn, The North Atlantic has been shown to be the most model-dependent region in the response to increased CO_2 forcing and its decomposition into different flux perturbations (Todd et al. 2020; Couldrey et al. 2021). Large sources of heat uptake uncertainties across models have been identified in the spread of surface fluxes and ocean model formulations (Huber and Zanna 2017; Couldrey et al. 2021), leading to large uncertainties in projections of ocean circulation changes (Huber and Zanna 2017; Zanna et al. 2019a; Bronselaer and Zanna 2020).

The different processes discussed in the paper thus make sense for our understanding of future changes, however, the timescales and amplitude on which they occur in the real world, especially in the deeper areas of the ocean, are largely unknown, and remain a large object of uncertainty.

Here, we decompose the response to different drivers of change without allowing any feedbacks between the ocean and other components, as we use an ocean-only model with no sea-ice and fixed fluxes. We do this in an endeavour to decouple the components as much as possible and concentrate on the response of the individual flux perturbations actually received by the ocean during the *historical+ssp245* period in the coupled model. The balance of processes highlighted here may be different when perturbing an ocean coupled to a sea-ice model, which allows feedbacks on the air-sea fluxes (Dias et al. 2021). Subpolar areas are also where the strongest non-linearities between perturbation fluxes occur, and where, in the absence of a sea-ice model, the temperature can fall below freezing point, even though we changed the equation of state so that it doesn't affect the circulation.

These points show the limitation of these experiments in rigorously decomposing physical drivers of change in ice-covered and convective regions, although they bring an understanding of the response to separate processes.

Finally, the sensitivity of ocean warming timescales to initial conditions (large spread in ToE for SNR>2) uncovered here in the large ensemble suggests that a multi-large ensemble analysis would be a promising approach to identify whether these features are robust across models that have different representations of internal variability, and whether the sensitivity to initial conditions holds in the same regions. This could help better quantify the uncertainties in timescales of climate signal emergence in the ocean interior.

APPENDIX A

Forcing NEMO3.6 with fixed fluxes

a. Forcing terms from the piControl

To force NEMO3.6 with fixed fluxes, the ocean model needs to read the heat, freshwater, salt fluxes and wind stress components indicated in bold in Table A1. Heat fluxes include all radiative and turbulent fluxes exchanged with the atmosphere and the sea-ice, as well as the sensible and latent heat received or lost from river runoffs, iceberg melt and iceshelf melt. The total heat flux entering the ocean is qt + hflx_rnf + hflx_isf + hfgeou. hfgeou is constant in time, and hflx_isf is reconstructed online from the prescribed associated freshwater flux (iceshelf). The global heat budget closes, with an error of only 10^{-3} $W.m^{-2}$, with the same terms as the coupled model (Mignot et al. 2021). All terms are 2D fields, but hflx_rnf and hflx_isf are distributed along the vertical until a prescribed depth. The solar heat flux qsr is also read separately as it penetrates into the first hundred meters of the ocean, and is absorbed following an exponential decrease with depth and depends on the chlorophyll field prescribed to the model (see below). Freshwater fluxes include evaporation, precipitation, sea-ice formation and melt, river runoffs, iceberg melt and iceshelf melt. Runoffs (including iceberg melt) and iceshelf melt are distributed on the vertical similarly as their associated heat flux. The total freshwater flux into the ocean is -emp + runoffs + iceshelf. The salt flux only comes from exchanges with the sea-ice (it is a real salt flux, as sea-ice melt has a non-zero salinity).

In addition to these surface fluxes, the sea-ice fraction and thickness from the *piControl* are also read at 3-hourly frequency for the vertical mixing parameterization. Furthermore, in the coupled model the penetration of the shortwave heat flux into the first layers of the ocean in the *piControl* is modulated by the chlorophyll concentration calculated in the ocean biogeochemical model (PISCES, Aumont et al. (2015)). Only the ocean physics component is used in our experiments, PISCES is deactivated as it was estimated not necessary, and for computation time reasons. The 3D chlorophyll field outputted from PISCES in the *piControl* is thus read at monthly frequency to best reproduce the shortwave absorption in the ocean and consequently the temperature field. Indeed, large differences compared to the *piControl* were found as soon as the first year of the simulation when imposing a constant and uniform chlorophyll field instead of the 3D PISCES field.

Time series of a few diagnostic variables in *piControl* and in the ocean-only CTL experiment are shown in Supplemental Material Figure 3.

b. Perturbations

The perturbations constructed from the IPSL-CM6A-LR *historical+ssp245* ensemble mean anomaly are applied on each forcing term shown in bold in table A1. The corresponding CMIP6 terms for IPSL-CM6A-LR are also given in table A1. We show in Supplemental Material Figure 4 the maps of the heat flux, freshwater flux and wind stress perturbations for the last 20 years (2081-2100), which are qualitatively similar to the FAFMIP perturbations (http://fafmip.org). Note because we are using a single ocean model and forcing with outputs of a coupled model with the same ocean model, we can apply the perturbations much more precisely (i.e the vertical distribution of some fluxes, as mentioned above).

The heat flux perturbation is applied similarly on the passive temperature as it is on the model prognostic temperature: same vertical penetration of the solar heat flux on the vertical, as well as the vertical distribution for runoffs and iceshelf melt.

c. Temperature below freezing point

Because of the ocean-only configuration (no sea-ice) with a flux formulation and no restoring term on the SST, it is possible for the temperature to locally fall below the freezing point in polar regions in all the simulations including CTL. Sensitivity tests were conducted on the treatment of the prognostic temperature by e.g. imposing a relaxation to the freezing-point when temperature fell below it, but that meant adding heat in the system, leading in CTL to too much drift away from the parent *piControl* simulation even in regional diagnostics, and in ALL to drift away from the large ensemble envelope, overall losing the goals set in the protocol and benefits brought by the flux-forced experiments. Instead, to circumvent this potential problem, we implemented part of the solution proposed

TABLE A1. Freshwater, heat, salt flux and wind stress terms at the ocean interface in NEMO3.6. The bold terms indicate the fluxes needed to force the ocean from the coupled model outputs in a fixed-flux configuration. The corresponding CMIP6 terms are given in the right column.

Short name	Signification	Unit	CMIP6 equivalent
emp	Evaporation-Precipitation, includes sea-ice formation and melt, and calving in the NH	kg m^{-2} s^{-1}	**-(wfo+friver+ficeberg)**
runoffs	River runoffs + iceberg melting (> 0 into ocean) = friver + iceberg	kg m^{-2} s^{-1}	**friver+ficeberg**
iceshelf	Iceshelf melting (> 0 into ocean)	kg m^{-2} s^{-1}	**flandice**
qt	Net downward heat flux = qns + qsr	W m^{-2}	**hfds**
qsr	Downward shortwave flux	W m^{-2}	**rsntds**
qns	Downward non solar heat flux (includes hflx_icb and hflx_cal)	W m^{-2}	nshfls
hflx_rnf	Sensible heat flux from river and iceberg runoffs (at SST)	W m^{-2}	**hfrunoffds**
hflx_icb	SH iceberg latent heat loss (<0), included in qns	W m^{-2}	
hflx_cal	NH calving latent heat loss (<0), included in qns	W m^{-2}	
hflx_isf	Heat flux from iceshelf melting (Sensible+latent)	W m^{-2}	
hfgeou	Geothermal heat flux (constant in time)	W m^{-2}	
sfx	Downward salt flux into sea water	g m^{-2} s^{-1}	**sfdsi**
utau	Surface downward x stress	N m^{-2}	**tauuo**
vtau	Surface downward y stress	N m^{-2}	**tauvo**

by Todd et al. (2020) in our experiments: we let the temperature evolve without any changes as to conserve heat in the model, while in order not to create any un-physical convection events, if the temperature falls below freezing, we replace the temperature by the freezing point temperature in the computation of the equation of state and of the Brünt-Vaisala frequency. This procedure ensures that the circulation is not affected by an unrealistic density. In that configuration, temperature can still fall below freezing point, affecting heat transport, especially the Arctic ocean, where the heat flux perturbation is locally negative. However, these negative anomalies are concentrated at the surface and don't affect vertically-integrated OHC or other parts of the ocean.

APPENDIX B

Passive tracer and decomposition of temperature changes

To write a simplified equation of the evolution of the prognostic temperature in the model, we use a similar terminology as Gregory et al. (2016) and Couldrey et al. (2021): the convergence of temperature by the fully-resolved velocity and by all parameterized transport processes is symbolized by the transport operator Φ, acting on the temperature T, so that:

$$\frac{\partial T}{\partial t} = Q + \Phi(T) \tag{B1}$$

with Q the net heat flux at the ocean boundaries (see Appendix A for the details of the heat flux components in NEMO3.6). We can now decompose the temperature, surface heat flux and transport processes into a CTL (unperturbed) component, and a perturbed component relative to the CTL, so that $T = T_{CTL} + T'$, $\Phi = \Phi_{CTL} + \Phi'$, $Q = Q_{CTL} + Q'$ and the evolution of the temperature anomaly T' follows:

$$\frac{\partial T'}{\partial t} = Q' + \Phi_{CTL}(T') + \Phi'(T') + \Phi'(T_{CTL}) \tag{B2}$$

The temperature change T' arises from two sources, that is from the anomalous surface heat flux Q' (the "added heat") and from changes in the transport processes acting on the unperturbed temperature field ($\Phi'(T_{CTL})$ the "redistributed heat"). If $Q' = 0$ and $\Phi' = 0$ then there is no temperature change.

To decompose the total temperature changes into contributions from the passive uptake of added heat and the redistribution of pre-existing heat, we follow the now commonly-adopted approach first introduced by Banks et al. (2002) and Banks and Gregory (2006), that consists in implementing a passive temperature tracer representing the transport of added heat in the ocean without changing the density. This Passive Anomaly Temperature (PAT), or T'_a (for added heat) is initialized to 0, forced at the surface by the anomalous heat flux Q' (similarly as T', see Appendix A) and transported in the ocean by the full circulation $\Phi = \Phi_{CTL} + \Phi'$:

$$\frac{\partial T'_a}{\partial t} = Q' + \Phi_{CTL}(T'_a) + \Phi'(T'_a) \tag{B3}$$

The redistributed temperature change is then diagnosed by $T'_r = T' - T'_a$. Since there is no feedback on the surface

fluxes, all the excess heat Q' that enters the ocean acts to change the global ocean heat content, that is, over a period of time Δt,

$$\iint \overline{Q'}^{\Delta t} dA = \frac{\rho_0 cp}{\Delta t} \iiint T' dV = \frac{\rho_0 cp}{\Delta t} \iiint T'_a dV = \frac{\Delta OHC}{\Delta t} \tag{B4}$$

with dA a surface grid cell area and dV a grid cell volume. The redistribution component doesn't add any extra heat to the global ocean:

$$\frac{\rho_0 cp}{\Delta t} \iiint T'_r dV = 0 \tag{B5}$$

but it can change the temperature regionally. We note T'_a can be negative locally since Q' has both signs.

T'_a is implemented in all the ocean-only simulations. In CTL, $\Phi' = 0$ by definition, so $\Phi'(T'_a) = 0$ and T'_a in CTL is the added heat passively transported by the unperturbed circulation, corresponding to the passive tracer diagnosed in *faf-passiveheat* in the FAFMIP protocol (Gregory et al. 2016; Todd et al. 2020; Couldrey et al. 2021). It can also be compared to the temperature change in climate change simulations where the circulation is maintained at climatological values (Winton et al. 2013; Bronselaer and Zanna 2020). Consequently, we can decompose the evolution of the added heat T'_a in the ALL experiment into:

$$\left.\frac{\partial T'_a}{\partial t}\right|_{ALL} \approx \left.\frac{\partial T'_a}{\partial t}\right|_{CTL} + \Phi'|_{ALL}(T'_a|_{ALL}) \tag{B6}$$

The difference among the different T'_a (in-between experiments) allows to diagnose the effect of the perturbed circulation on the added heat, that is approximately the 2^{nd}-order term $\Phi'(T'_a)$.

APPENDIX C

Non-linear additivity of the ocean-only experiments

The non-linear interactions between the different surface perturbations are presented in Figure C1 by comparing the response to the all-forcing experiment to the sum of the responses to individual forcings. More specifically, we compare first BUOY to the sum of HEAT and WATER and then ALL to the sum of BUOY and STRESS, and again ALL to the sum of HEAT, WATER and STRESS. Significant non-linearities arise mainly in subpolar regions, where there are intense ventilation changes in the experiments and where the forced changes are large. In the subpolar North Atlantic, the non additivity is caused by non-linear interactions between the two buoyancy flux perturbations (right panels in Figure C1), while in the Southern Ocean non-linearities are dominated by interactions between the buoyancy flux and the wind stress perturbations (middle panels), and to a smaller degree by interactions between the buoyancy flux perturbations themselves. These regions have also been identified as the most difficult to reproduce the exact same convection events in the CTL compared to the coupled *piControl* (not shown), as these are very sensitive mechanisms to the surface fluxes, and the 3-hourly forcing (twice the coupling frequency in the coupled model) is still insufficient for these types of events. We note that overall the evolution of the CTL temperature doesn't diverge in time from the *piControl* (see Supplemental Material Figure 3) and validates the aims set for our scientific questions.

References

Abrahamsen, E. P., and Coauthors, 2019: Stabilization of dense Antarctic water supply to the Atlantic Ocean overturning circulation. *Nature Climate Change*, **9 (10)**, 742–746, https://doi.org/10.1038/s41558-019-0561-2, URL http://www.nature.com/articles/s41558-019-0561-2.

Armour, K. C., J. Marshall, J. R. Scott, A. Donohoe, and E. R. Newsom, 2016: Southern Ocean warming delayed by circumpolar upwelling and equatorward transport. *Nature Geoscience*, **9 (7)**, 549–554, https://doi.org/10.1038/ngeo2731, URL http://www.nature.com/articles/ngeo2731.

Aumont, O., C. Ethé, A. Tagliabue, L. Bopp, and M. Gehlen, 2015: PISCES-v2: an ocean biogeochemical model for carbon and ecosystem studies. *Geoscientific Model Development*, **8 (8)**, 2465–2513, https://doi.org/10.5194/gmd-8-2465-2015, URL https://gmd.copernicus.org/articles/8/2465/2015/.

Banks, H., R. Wood, and J. Gregory, 2002: Changes to Indian Ocean Subantarctic Mode Water in a Coupled Climate Model as CO2 Forcing Increases. *Journal of Physical Oceanography*, **32**, 12.

Banks, H. T., and J. M. Gregory, 2006: Mechanisms of ocean heat uptake in a coupled climate model and the implications for tracer based predictions of ocean heat uptake. *Geophysical Research Letters*, **33 (7)**, https://doi.org/10.1029/2005GL025352, URL https://agupubs.onlinelibrary.wiley.com/doi/abs/10.1029/2005GL025352.

Bonnet, R., O. Boucher, J. Deshayes, G. Gastineau, F. Hourdin, J. Mignot, J. Servonnat, and D. Swingedouw, 2021a: Presentation and Evaluation of the IPSL-CM6A-LR Ensemble of Extended Historical Simulations. *Journal of Advances in Modeling Earth Systems*, 25, https://doi.org/10.1029/2021MS002565.

Bonnet, R., and Coauthors, 2021b: Increased risk of near term global warming due to a recent AMOC weakening. *Nature Communications*, **12 (1)**, 6108, https://doi.org/10.1038/s41467-021-26370-0, URL https://www.nature.com/articles/s41467-021-26370-0.

Boucher, O., and Coauthors, 2020: Presentation and Evaluation of the IPSL-CM6A-LR Climate Model. *Journal of Advances in Modeling Earth Systems*, **12 (7)**, https://doi.org/10.1029/2019MS002010, URL https://onlinelibrary.wiley.com/doi/abs/10.1029/2019MS002010.

Bronselaer, B., M. Winton, S. M. Griffies, W. J. Hurlin, K. B. Rodgers, O. V. Sergienko, R. J. Stouffer, and J. L. Russell, 2018: Change in future climate due to Antarctic meltwater. *Nature*, **564 (7734)**, 53–58, https://doi.org/10.1038/s41586-018-0712-z, URL http://www.nature.com/articles/s41586-018-0712-z.

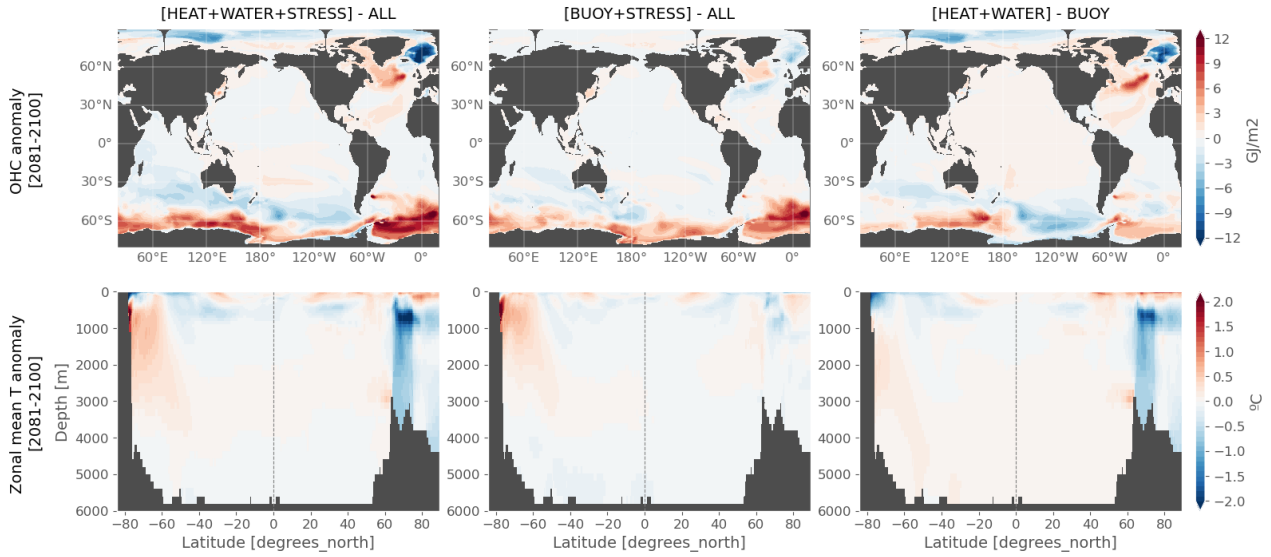

FIG. C1. Difference between the ALL experiment and the sum of HEAT, WATER and STRESS experiments (left panels), between ALL and the sum of BUOY and STRESS (middle panels), and between BUOY and the sum of HEAT and WATER (right panels), for ocean heat content and zonal mean temperature anomaly in [2081-2100] relative to the CTL.

Bronselaer, B., and L. Zanna, 2020: Heat and carbon coupling reveals ocean warming due to circulation changes. *Nature*, **584 (7820)**, 227–233, https://doi.org/10.1038/s41586-020-2573-5, URL http://www.nature.com/articles/s41586-020-2573-5.

Couldrey, M. P., and Coauthors, 2021: What causes the spread of model projections of ocean dynamic sea-level change in response to greenhouse gas forcing? *Climate Dynamics*, **56 (1-2)**, 155–187, https://doi.org/10.1007/s00382-020-05471-4, URL http://link.springer.com/10.1007/s00382-020-05471-4.

de Lavergne, C., J. B. Palter, E. D. Galbraith, R. Bernardello, and I. Marinov, 2014: Cessation of deep convection in the open Southern Ocean under anthropogenic climate change. *Nature Climate Change*, **4 (4)**, 278–282, https://doi.org/10.1038/nclimate2132, URL https://www.nature.com/articles/nclimate2132.

Deser, C., and Coauthors, 2020: Insights from Earth system model initial-condition large ensembles and future prospects. *Nature Climate Change*, **10 (4)**, 277–286, https://doi.org/10.1038/s41558-020-0731-2, URL http://www.nature.com/articles/s41558-020-0731-2.

DeVries, T., and F. Primeau, 2011: Dynamically and Observationally Constrained Estimates of Water-Mass Distributions and Ages in the Global Ocean. *Journal of Physical Oceanography*, **41 (12)**, 2381–2401, https://doi.org/10.1175/JPO-D-10-05011.1, URL http://journals.ametsoc.org/doi/10.1175/JPO-D-10-05011.1.

Dias, F. B., and Coauthors, 2020: Ocean Heat Storage in Response to Changing Ocean Circulation Processes. *Journal of Climate*, **33 (21)**, 9065–9082, https://doi.org/10.1175/JCLI-D-19-1016.1, URL https://journals.ametsoc.org/jcli/article/33/21/9065/353950/Ocean-Heat-Storage-in-Response-to-Changing-Ocean.

Dias, F. B., and Coauthors, 2021: Subpolar Southern Ocean Response to Changes in the Surface Momentum, Heat, and Freshwater Fluxes under 2xCO2. *Journal of Climate*, **34 (21)**, 8755–8775, https://doi.org/10.1175/JCLI-D-21-0161.1, URL https://journals.ametsoc.org/view/journals/clim/34/21/JCLI-D-21-0161.1.xml.

Eyring, V., S. Bony, G. A. Meehl, C. A. Senior, B. Stevens, R. J. Stouffer, and K. E. Taylor, 2016: Overview of the Coupled Model Intercomparison Project Phase 6 (CMIP6) experimental design and organization. *Geoscientific Model Development*, **9 (5)**, 1937–1958, https://doi.org/10.5194/gmd-9-1937-2016, URL https://gmd.copernicus.org/articles/9/1937/2016/.

Fogwill, C. J., S. J. Phipps, C. S. M. Turney, and N. R. Golledge, 2015: Sensitivity of the Southern Ocean to enhanced regional Antarctic ice sheet meltwater input. *Earth's Future*, **3 (10)**, 317–329, https://doi.org/10.1002/2015EF000306, URL https://onlinelibrary.wiley.com/doi/10.1002/2015EF000306.

Fox-Kemper, B., and Coauthors, 2021: Ocean, Cryosphere and Sea Level Change. *Climate Change 2021: The Physical Science Basis. Contribution of Working Group I to the Sixth Assessment Report of the Intergovernmental Panel on Climate Change*, Cambridge University Press.

Frölicher, T. L., J. L. Sarmiento, D. J. Paynter, J. P. Dunne, J. P. Krasting, and M. Winton, 2015: Dominance of the Southern Ocean in Anthropogenic Carbon and Heat Uptake in CMIP5 Models. *Journal of Climate*, **28 (2)**, 862–886, https://doi.org/10.1175/JCLI-D-14-00117.1, URL https://journals.ametsoc.org/doi/full/10.1175/JCLI-D-14-00117.1.

Fyfe, J. C., O. A. Saenko, K. Zickfeld, M. Eby, and A. J. Weaver, 2007: The Role of Poleward-Intensifying Winds on Southern Ocean Warming. *Journal of Climate*, **20 (21)**, 5391–5400, https://doi.org/10.1175/2007JCLI1764.1, URL http://journals.ametsoc.org/doi/10.1175/2007JCLI1764.1.

Garuba, O. A., and B. A. Klinger, 2016: Ocean Heat Uptake and Interbasin Transport of the Passive and Redistributive Components of Surface Heating. *Journal of Climate*, **29 (20)**, 7507–7527, https://doi.org/10.1175/JCLI-D-16-0138.1, URL https://journals.ametsoc.org/doi/10.1175/JCLI-D-16-0138.1.

Garuba, O. A., and B. A. Klinger, 2018: The Role of Individual Surface Flux Components in the Passive and Active Ocean Heat Uptake. *Journal of Climate*, **31 (15)**, 6157–6173, https://doi.org/10.1175/JCLI-D-17-0452.1, URL https://journals.ametsoc.org/doi/full/10.1175/JCLI-D-17-0452.1.

Gidden, M. J., and Coauthors, 2019: Global emissions pathways under different socioeconomic scenarios for use in CMIP6: a dataset of harmonized emissions trajectories through the end of the century. *Geoscientific Model Development*, **12 (4)**, 1443–1475, https://doi.org/10.5194/gmd-12-1443-2019, URL https://gmd.copernicus.org/articles/12/1443/2019/.

Gregory, J. M., 2000: Vertical heat transports in the ocean and their effect on time-dependent climate change. *Climate Dynamics*, **16 (7)**, 501–515, https://doi.org/10.1007/s003820000059, URL http://link.springer.com/10.1007/s003820000059.

Gregory, J. M., and Coauthors, 2016: The Flux-Anomaly-Forced Model Intercomparison Project (FAFMIP) contribution to CMIP6: investigation of sea-level and ocean climate change in response to CO2 forcing. *Geoscientific Model Development*, **9 (11)**, 3993–4017, https://doi.org/10.5194/gmd-9-3993-2016, URL https://www.geosci-model-dev.net/9/3993/2016/.

Gupta, A. S., N. C. Jourdain, J. N. Brown, and D. Monselesan, 2013: Climate Drift in the CMIP5 Models. *Journal of Climate*, **26 (21)**, 8597–8615, https://doi.org/10.1175/JCLI-D-12-00521.1, URL https://journals.ametsoc.org/jcli/article/26/21/8597/34545/Climate-Drift-in-the-CMIP5-Models.

Hanawa, K., and L. D. Talley, 2001: Chapter 5.4 Mode waters. *International Geophysics*, G. Siedler, J. Church, and J. Gould, Eds., Ocean Circulation and Climate, Vol. 77, Academic Press, 373–386, https://doi.org/10.1016/S0074-6142(01)80129-7, URL http://www.sciencedirect.com/science/article/pii/S0074614201801297.

Hassan, T., R. J. Allen, W. Liu, and C. A. Randles, 2021: Anthropogenic aerosol forcing of the Atlantic meridional overturning circulation and the associated mechanisms in CMIP6 models. *Atmospheric Chemistry and Physics*, **21 (8)**, 5821–5846, https://doi.org/10.5194/acp-21-5821-2021, URL https://acp.copernicus.org/articles/21/5821/2021/.

Hawkins, E., and R. Sutton, 2012: Time of emergence of climate signals. *Geophysical Research Letters*, **39 (1)**, L01 702, https://doi.org/10.1029/2011GL050087, URL http://doi.wiley.com/10.1029/2011GL050087.

Heuzé, C., 2021: Antarctic Bottom Water and North Atlantic Deep Water in CMIP6 models. *Ocean Science*, **17 (1)**, 59–90, https://doi.org/10.5194/os-17-59-2021, URL https://os.copernicus.org/articles/17/59/2021/.

Heuzé, C., K. J. Heywood, D. P. Stevens, and J. K. Ridley, 2013: Southern Ocean bottom water characteristics in CMIP5 models. *Geophysical Research Letters*, 1409–1414, https://doi.org/10.1002/grl.50287@10.1002/(ISSN)1944-8007.GRLCMIP5, URL https://agupubs.onlinelibrary.wiley.com/doi/abs/10.1002/grl.50287%4010.1002/%28ISSN%291944-8007.GRLCMIP5.

Heuzé, C., M. Mohrmann, E. Andersson, and E. Crafoord, 2020: Global decline of deep water formation with increasing atmospheric CO2. preprint, Environmental Sciences. https://doi.org/10.31223/X56K6D, URL http://eartharxiv.org/repository/view/1731/.

Hobbs, W. R., C. Roach, T. Roy, J.-B. Sallée, and N. Bindoff, 2021: Anthropogenic Temperature and Salinity Changes in the Southern Ocean. *Journal of Climate*, **34 (1)**, 215–228, https://doi.org/10.1175/JCLI-D-20-0454.1, URL https://journals.ametsoc.org/view/journals/clim/34/1/jcliD200454.xml.

Hourdin, F., and Coauthors, 2020: LMDZ6A: The Atmospheric Component of the IPSL Climate Model With Improved and Better Tuned Physics. *Journal of Advances in Modeling Earth Systems*, **12 (7)**, https://doi.org/10.1029/2019MS001892, URL https://onlinelibrary.wiley.com/doi/10.1029/2019MS001892.

Hu, S., S.-P. Xie, and W. Liu, 2020: Global Pattern Formation of Net Ocean Surface Heat Flux Response to Greenhouse Warming. *Journal of Climate*, **33 (17)**, 7503–7522, https://doi.org/10.1175/JCLI-D-19-0642.1, URL https://journals.ametsoc.org/doi/10.1175/JCLI-D-19-0642.1.

Huber, M. B., and L. Zanna, 2017: Drivers of uncertainty in simulated ocean circulation and heat uptake. *Geophysical Research Letters*, **44 (3)**, 1402–1413, https://doi.org/10.1002/2016GL071587, URL https://onlinelibrary.wiley.com/doi/abs/10.1002/2016GL071587.

IPCC, 2021: *Climate Change 2021: The Physical Science Basis. Contribution of Working Group I to the Sixth Assessment Report of the Intergovernmental Panel on Climate Change*. Cambridge University Press.

Jiang, W., G. Gastineau, and F. Codron, 2021: Multicentennial Variability Driven by Salinity Exchanges Between the Atlantic and the Arctic Ocean in a Coupled Climate Model. *Journal of Advances in Modeling Earth Systems*, **13 (3)**, https://doi.org/10.1029/2020MS002366, URL https://onlinelibrary.wiley.com/doi/10.1029/2020MS002366.

Johnson, G. C., 2008: Quantifying Antarctic Bottom Water and North Atlantic Deep Water volumes. *Journal of Geophysical Research*, **113 (C5)**, C05 027, https://doi.org/10.1029/2007JC004477, URL http://doi.wiley.com/10.1029/2007JC004477.

Krinner, G., and Coauthors, 2005: A dynamic global vegetation model for studies of the coupled atmosphere-biosphere system. *Global Biogeochemical Cycles*, **19 (1)**, https://doi.org/10.1029/2003GB002199, URL http://doi.wiley.com/10.1029/2003GB002199.

Lago, V., and M. H. England, 2019: Projected Slowdown of Antarctic Bottom Water Formation in Response to Amplified Meltwater Contributions. *Journal of Climate*, **32 (19)**, 6319–6335, https://doi.org/10.1175/JCLI-D-18-0622.1, URL http://journals.ametsoc.org/doi/10.1175/JCLI-D-18-0622.1.

Liu, W., J. Lu, S.-P. Xie, and A. Fedorov, 2018: Southern Ocean Heat Uptake, Redistribution, and Storage in a Warming Climate: The Role of Meridional Overturning Circulation. *Journal of Climate*, **31 (12)**, 4727–4743, https://doi.org/10.1175/JCLI-D-17-0761.1, URL https://journals.ametsoc.org/doi/10.1175/JCLI-D-17-0761.1.

Madec, G., and Coauthors, 2017: NEMO ocean engine. https://doi.org/10.5281/ZENODO.3248739, URL https://zenodo.org/record/3248739, publisher: Zenodo Version Number: v3.6-patch.

Marshall, J., J. R. Scott, K. C. Armour, J.-M. Campin, M. Kelley, and A. Romanou, 2015: The ocean's role in the transient response of climate to abrupt greenhouse gas forcing. *Climate Dynamics*, **44 (7-8)**, 2287–2299, https://doi.org/10.1007/s00382-014-2308-0, URL http://link.springer.com/10.1007/s00382-014-2308-0.

Marshall, J., and K. Speer, 2012: Closure of the meridional overturning circulation through Southern Ocean upwelling. *Nature Geoscience*, **5 (3)**, 171–180, https://doi.org/10.1038/ngeo1391, URL http://www.nature.com/articles/ngeo1391.

Menary, M. B., and Coauthors, 2020: Aerosol-Forced AMOC Changes in CMIP6 Historical Simulations. *Geophysical Research Letters*, **47 (14)**, https://doi.org/10.1029/2020GL088166, URL https://onlinelibrary.wiley.com/doi/10.1029/2020GL088166.

Mignot, J., and Coauthors, 2021: The tuning strategy of IPSL-CM6A-LR. *Journal of Advances in Modeling Earth Systems*, https://doi.org/10.1029/2020MS002340, URL https://onlinelibrary.wiley.com/doi/10.1029/2020MS002340.

Mikolajewicz, U., and R. Voss, 2000: The role of the individual air-sea flux components in CO2-induced changes of the ocean's circulation and climate. *Climate Dynamics*, **16 (8)**, 627–642, https://doi.org/10.1007/s003820000066, URL https://doi.org/10.1007/s003820000066.

Mohrmann, M., C. Heuzé, and S. Swart, 2021: Southern Ocean polynyas in CMIP6 models. *The Cryosphere*, **15 (9)**, 4281–4313, https://doi.org/10.5194/tc-15-4281-2021, URL https://tc.copernicus.org/articles/15/4281/2021/.

Morrison, A. K., D. W. Waugh, A. M. Hogg, D. C. Jones, and R. P. Abernathey, 2022: Ventilation of the Southern Ocean Pycnocline. *Annual Review of Marine Science*, **14 (1)**, null, https://doi.org/10.1146/annurev-marine-010419-011012, URL https://doi.org/10.1146/annurev-marine-010419-011012, _eprint: https://doi.org/10.1146/annurev-marine-010419-011012.

Naik, V., and Coauthors, 2021: Short-lived climate forcers. *Climate Change 2021: The Physical Science Basis. Contribution of Working Group I to the Sixth Assessment Report of the Intergovernmental Panel on Climate Change*, Cambridge University Press.

Piecuch, C. G., R. M. Ponte, C. M. Little, M. W. Buckley, and I. Fukumori, 2017: Mechanisms underlying recent decadal changes in subpolar North Atlantic Ocean heat content. *Journal of Geophysical Research: Oceans*, **122 (9)**, 7181–7197, https://doi.org/10.1002/2017JC012845, URL https://onlinelibrary.wiley.com/doi/10.1002/2017JC012845.

Rathore, S., N. L. Bindoff, H. E. Phillips, and M. Feng, 2020: Recent hemispheric asymmetry in global ocean warming induced by climate change and internal variability. *Nature Communications*, **11 (1)**, 2008, https://doi.org/10.1038/s41467-020-15754-3, URL http://www.nature.com/articles/s41467-020-15754-3.

Roquet, F., G. Madec, T. J. McDougall, and P. M. Barker, 2015: Accurate polynomial expressions for the density and specific volume of seawater using the TEOS-10 standard. *Ocean Modelling*, **90**, 29–43, https://doi.org/10.1016/j.ocemod.2015.04.002, URL https://linkinghub.elsevier.com/retrieve/pii/S1463500315000566.

Rousset, C., and Coauthors, 2015: The Louvain-La-Neuve sea ice model LIM3.6: global and regional capabilities. *Geoscientific Model Development*, **8 (10)**, 2991–3005, https://doi.org/10.5194/gmd-8-2991-2015, URL https://gmd.copernicus.org/articles/8/2991/2015/.

Shi, J.-R., L. D. Talley, S.-P. Xie, W. Liu, and S. T. Gille, 2020: Effects of Buoyancy and Wind Forcing on Southern Ocean Climate Change. *Journal of Climate*, **33 (23)**, 10 003–10 020, https://doi.org/10.1175/JCLI-D-19-0877.1, URL https://journals.ametsoc.org/doi/10.1175/JCLI-D-19-0877.1.

Shi, J.-R., S.-P. Xie, and L. D. Talley, 2018: Evolving Relative Importance of the Southern Ocean and North Atlantic in Anthropogenic Ocean Heat Uptake. *Journal of Climate*, **31 (18)**, 7459–7479, https://doi.org/10.1175/JCLI-D-18-0170.1, URL https://journals.ametsoc.org/doi/10.1175/JCLI-D-18-0170.1.

Silvano, A., S. R. Rintoul, B. Peña-Molino, W. R. Hobbs, E. van Wijk, S. Aoki, T. Tamura, and G. D. Williams, 2018: Freshening by glacial meltwater enhances melting of ice shelves and reduces formation of Antarctic Bottom Water. *Science Advances*, **4 (4)**, eaap9467, https://doi.org/10.1126/sciadv.aap9467, URL https://www.science.org/doi/10.1126/sciadv.aap9467.

Silvano, A., and Coauthors, 2020: Recent recovery of Antarctic Bottom Water formation in the Ross Sea driven by climate anomalies. *Nature Geoscience*, **13 (12)**, 780–786, https://doi.org/10.1038/s41561-020-00655-3, URL http://www.nature.com/articles/s41561-020-00655-3.

Silvy, Y., E. Guilyardi, J.-B. Sallée, and P. J. Durack, 2020: Human-induced changes to the global ocean water masses and their time of emergence. *Nature Climate Change*, https://doi.org/10.1038/s41558-020-0878-x, URL https://doi.org/10.1038/s41558-020-0878-x.

Swart, N. C., S. T. Gille, J. C. Fyfe, and N. P. Gillett, 2018: Recent Southern Ocean warming and freshening driven by greenhouse gas emissions and ozone depletion. *Nature Geoscience*, **11 (11)**, 836–841, https://doi.org/10.1038/s41561-018-0226-1, wOS:000448672100009.

Talley, L. D., and M. E. Raymer, 1982: Eighteen_degree_water_variability.pdf. *Journal of Marine Research*, **40**, 757–775.

Todd, A., and Coauthors, 2020: Ocean-Only FAFMIP: Understanding Regional Patterns of Ocean Heat Content and Dynamic Sea Level Change. *Journal of Advances in Modeling Earth Systems*, **12 (8)**, https://doi.org/10.1029/2019MS002027, URL https://onlinelibrary.wiley.com/doi/10.1029/2019MS002027.

Waugh, D. W., A. McC. Hogg, P. Spence, M. H. England, and T. W. N. Haine, 2019: Response of Southern Ocean Ventilation to Changes in Midlatitude Westerly Winds. *Journal of Climate*, **32 (17)**, 5345–5361, https://doi.org/10.1175/JCLI-D-19-0039.1, URL http://journals.ametsoc.org/doi/10.1175/JCLI-D-19-0039.1.

Williams, R. G., A. Katavouta, and V. Roussenov, 2021: Regional Asymmetries in Ocean Heat and Carbon Storage due to Dynamic Redistribution in Climate Model Projections. *Journal of Climate*, **34 (10)**, 3907–3925, https://doi.org/10.1175/JCLI-D-20-0519.1, URL https://journals.ametsoc.org/view/journals/clim/34/10/JCLI-D-20-0519.1.xml.

Winton, M., S. M. Griffies, B. L. Samuels, J. L. Sarmiento, and T. L. Frölicher, 2013: Connecting Changing Ocean Circulation with Changing Climate. *Journal of Climate*, **26 (7)**, 2268–2278, https://doi.org/10.1175/JCLI-D-12-00296.1, URL http://journals.ametsoc.org/doi/10.1175/JCLI-D-12-00296.1.

Xie, P., and G. K. Vallis, 2012: The passive and active nature of ocean heat uptake in idealized climate change experiments. *Climate Dynamics*, **38 (3)**, 667–684, https://doi.org/10.1007/s00382-011-1063-8, URL https://doi.org/10.1007/s00382-011-1063-8.

Zanna, L., J. M. Brankart, M. Huber, S. Leroux, T. Penduff, and P. D. Williams, 2019a: Uncertainty and scale interactions in ocean ensembles: From seasonal forecasts to multidecadal

climate predictions. *Quarterly Journal of the Royal Meteorological Society*, https://doi.org/10.1002/qj.3397@10.1002/(ISSN)1477-870X.25-Years-of-Ensemble-Forecasting, URL https://rmets.onlinelibrary.wiley.com/doi/abs/10.1002/qj.3397%4010.1002/%28ISSN%291477-870X.25-Years-of-Ensemble-Forecasting.

Zanna, L., S. Khatiwala, J. M. Gregory, J. Ison, and P. Heimbach, 2019b: Global reconstruction of historical ocean heat storage and transport. *Proceedings of the National Academy of Sciences*, **116 (4)**, 1126–1131, https://doi.org/10.1073/pnas.1808838115, URL https://www.pnas.org/content/116/4/1126.

Zika, J. D., J. M. Gregory, E. L. McDonagh, A. Marzocchi, and L. Clément, 2021: Recent Water Mass Changes Reveal Mechanisms of Ocean Warming. *Journal of Climate*, **34 (9)**, 3461–3479, https://doi.org/10.1175/JCLI-D-20-0355.1, URL https://journals.ametsoc.org/view/journals/clim/34/9/JCLI-D-20-0355.1.xml.

3 Perspectives: the role of ocean circulation changes in eroding the fingerprint of water-cycle amplification on salinity

On multi-decadal time scales, observations of sea surface and upper ocean salinity have shown a clear amplification of climatological patterns [Durack and Wijffels, 2010, Skliris et al., 2014, Cheng et al., 2020], in response to an intensification of the hydrological cycle which is much more difficult to infer from direct observations of precipitation and evaporation (see the General Introduction).

At global scale, the surface warming of the ocean was found to play a significant role, after the water cycle amplification, in driving the surface salinity pattern amplification because of its stabilizing effect, decreasing mixing with the ocean interior and between fresh and salty regions [Durack et al., 2012, Zika et al., 2018].

On the other hand, ocean circulation and mixing can locally damp the E-P signal. This is true for internally-generated circulation variability on interannual to decadal time scales [Vinogradova and Ponte, 2017], but also for forced multi-decadal circulation changes. Indeed, by comparing active and passive salinity tracers under an idealized scenario in which CO_2 increases at 2%/year, Banks et al. [2002] showed that in the Southern Ocean, the active salinity field responded to perturbations in surface freshwater fluxes but also to forced changes in the circulation. This was confirmed in another modelling study proposed by Shi et al. [2020], who forced the ocean with buoyancy fluxes and wind stress perturbations separately from an abruptly quadrupled CO_2 scenario. They found that increasing westerly winds over the Southern Ocean caused an increase in surface salinity driven by intensified Ekman upwelling of salty waters and northward advection, substantially offsetting the freshening in response to buoyancy forcings.

Unlike the substantial scientific literature that looked at processes of anthropogenic heat uptake, the physical processes causing ocean interior salinity changes at global scale have received much less attention. Furthermore, how the balance of forcings responds and evolves in the transient response to climate change is still to be investigated. In this section, I will show preliminary results for an on-going study focused on salinity, in the same framework as presented earlier, that is, the IPSL-CM6A-LR large ensemble of historical-extended simulations and the numerical simulations developed during this PhD. First, I will display the salinity counterparts of figures 4 and 5 of the manuscript presented in section IV.2: the long-term salinity response to individual surface flux perturbations, and the decomposition into passive and redistributive components. Then, I will propose to look at the global scale salinity contrast as introduced by Cheng et al. [2020] to identify how the salinity anomalies amplify the climatological mean field, and which processes act to intensify or dampen the effect of the water cycle. To conclude, a few other ideas will be briefly discussed, and we leave further work on this study to the coming months.

Long-term response

The vertically-integrated salt content anomalies and zonal mean salinity anomalies in 2081-2100 of each ocean-only experiment (relative to the same period in CTL) are presented in figure IV.1. Similarly as for temperature, we can decompose total salinity changes S' in the ALL/WATER/BUOY experiments using the Passive Anomaly Salinity (PAS; Banks et al. [2002]) tracer that we implemented (here denoted S'_a for added salt/freshwater). Note the added component takes both positive and negative signs, compared to the added heat which is predominantly positive. The decomposition is made in the following way:

$$\begin{aligned} \underbrace{\text{Total}}_{S'} &= \underbrace{\text{Added}}_{S'_a} + \underbrace{\text{Redistributed}}_{S' - S'_a} \\ &= \underbrace{\text{Passive}}_{S'_a|_{CTL}} + \underbrace{\text{Non-linear added}}_{S'_a - S'_a|_{CTL}} + \underbrace{\text{Redistributed}}_{S' - S'_a} \end{aligned} \tag{IV.1}$$

The decomposition in the ALL experiment is presented in figure IV.2 for years 2081-2100. We here discuss the main features of these two figures.

The experiment forced with the freshwater flux perturbation alone (WATER, figure IV.1e) features an overall amplification pattern of the climatological salinity field, with fresher high latitudes and saltier mid-latitudes. However, there are differences with the pure passive component (S'_a in CTL, figure IV.2c,d), showing that circulation changes in the WATER experiment itself tend to rearrange the signal of pattern amplification. Moreover, there are strong zonal asymmetries in the Northern Hemisphere, with large salinification in the entire North Atlantic basin and small freshening in the North Pacific mid-latitudes. Other than the stronger E-P perturbation in the North Atlantic basin (figure D.4), the outflow from the Mediterranean Sea, which is also getting saltier due to a decrease in the net freshwater flux, can explain this asymmetry with the North Pacific. These differences across basins generate mixed up patterns in the global zonal mean (see the zonal means per basin in figures E.1 and E.2 in appendix E).

The circulation changes driven by the heat flux and wind stress perturbations are important to set the total salinity change patterns in some regions. For instance, in the North Atlantic, the strong salinification in the WATER experiment (both in the subtropical and subpolar gyres) is offset by significant freshening in response to the heat flux perturbation in the subpolar gyre and to a lesser degree in the subtropical gyre. This heat-flux driven redistributed freshening is consistent with the redistributed cooling in the same region highlighted in the former section, and explained by a slow down in the AMOC (figure 6 in the heat storage manuscript), causing less northward transport of warm and salty water. Other common features of redistribution can be found between temperature and salinity, such as the temperature and salinity increase in the tropical Atlantic caused by the heat flux perturbation (figure IV.1c and D.6e), or the local patterns in the Southern Hemisphere induced by the wind perturbation, with increases in the southwestern Pacific and Atlantic basins, and the cooling/freshening around 30ºS in the Indian basin.

The salinity changes induced by circulation changes caused by the freshwater flux perturbation itself are non-negligible, with the most prominent features found at high latitudes (figure E.3e,f), very much resembling the freshwater-induced redistributed heat component (figure 5e,f in the previous section): a dipole of increasing salinity in the subpolar North Atlantic and freshening in the Nordic Seas, and overall salinification in the southern high latitudes, spreading at depth.

Circulation changes also act on the added component by damping the patterns of the passive tracer in the CTL (figure IV.2e,g vs. g,h). As we saw previously for heat, circulation changes are overall dominated by the buoyancy flux perturbations, acting to stratify the ocean and decrease the deep overturning cell and the AMOC. This causes a decrease in the ventilation at depth and thus less downward spread of the passive tracer.

The results from Shi et al. [2020] are consistent with these experiments, with a surface freshening in the subpolar Southern Ocean induced by the buoyancy perturbation (figure IV.1h) partly compensated by the increased salinity found in STRESS (figure IV.1j).

The AABW ventilation pathway is again identified as an important region for all components in response to forced changes, notably in STRESS and in the passive and redistributed components that show clear changes spreading northward and at depth (figures IV.1j and IV.2d,f). The passive component shows a freshening on the entire water-column in response to the increased freshwater flux at southern high latitudes (figure D.4). Indeed the CTL circulation is efficient for the ventilation of tracers in this region. However, when the overturning decreases in response to increased buoyancy fluxes, as seen in the previous section, the passive tracer is not ventilated as efficiently, creating the positive anomaly seen in the non-linear component (figure IV.2h, $S'_a|_{ALL} - S'_a|_{CTL}$). A similar mechanism applies in the deep convection regions of the North Atlantic, but with opposite signs. This is coherent with what we found for the passive temperature tracer.

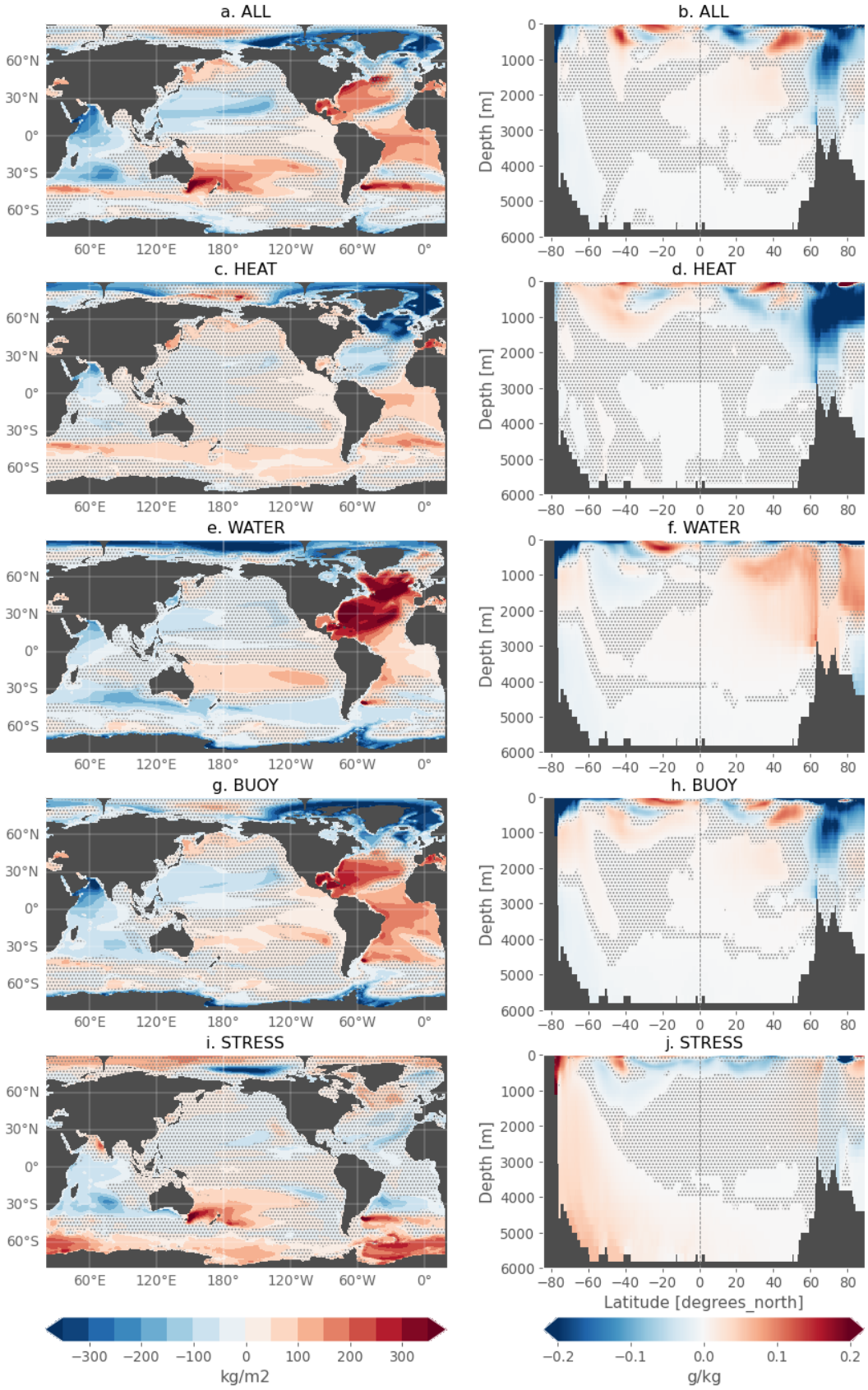

Figure IV.1: Vertically-integrated salt content anomaly (left) and zonal mean salinity anomaly (right) in the ocean-only perturbed experiments relative to CTL, averaged over [2081-2100]. Stipples indicate when the anomaly is below twice the interannual standard deviation of the CTL.

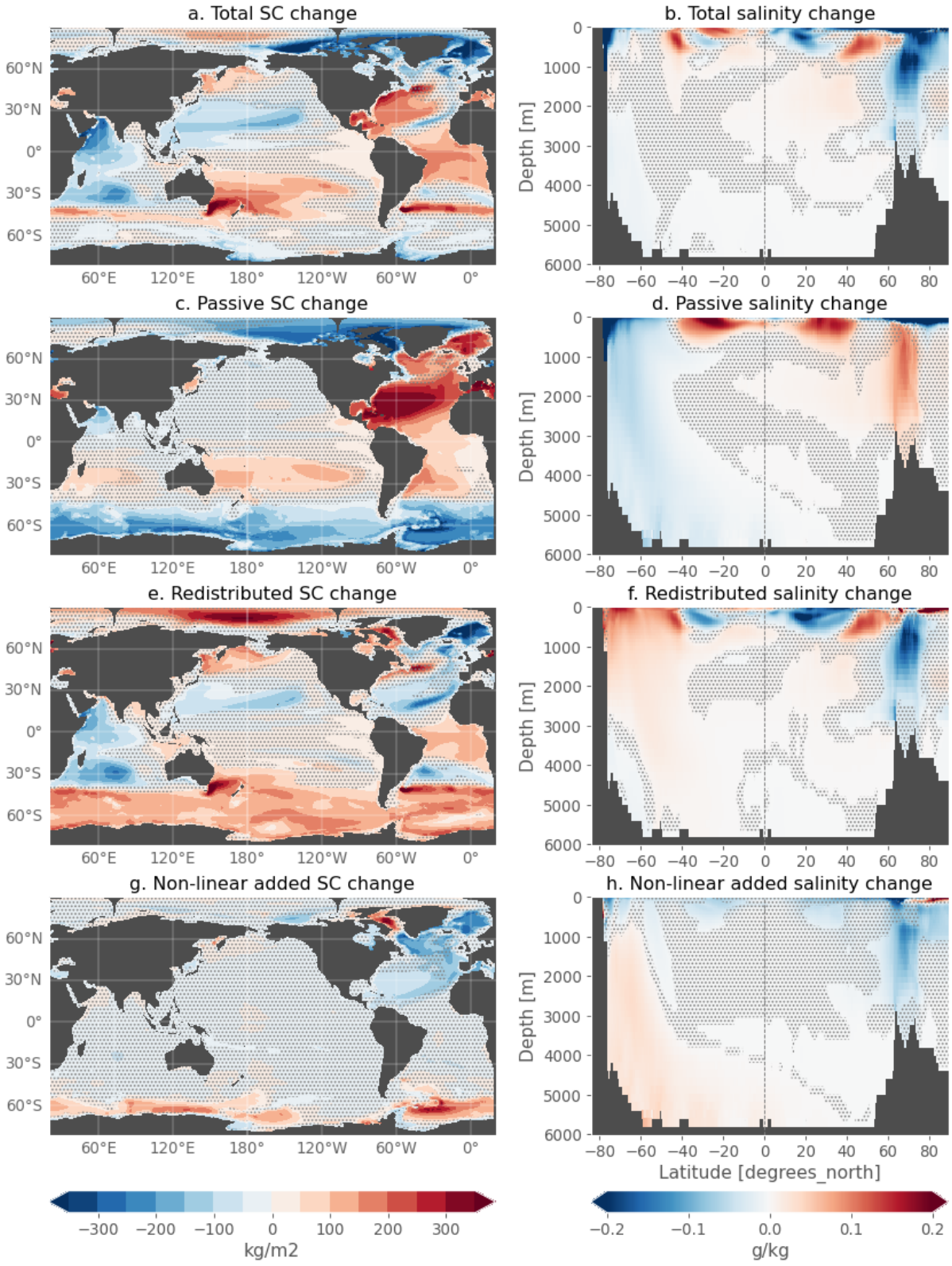

Figure IV.2: Vertically-integrated salt content anomaly (left) and zonal mean salinity anomaly (right) in the ALL experiment relative to CTL, for the total, passive, redistributed and non-linear added components, averaged over [2081-2100]. Stipples indicate when the anomaly is below twice the interannual standard deviation of the CTL.

Salinity contrast

The regional approach adopted in section IV.2 could be partially applied to salinity as well, but the upper ocean boxes can mix up opposing signals (freshening/salinification) and averaging across these structures is not what we are interested in. Other regions are more appropriate such as the export of AABW and will be investigated in future work. Instead, here we propose to adopt a more global approach and diagnose the evolution of the salinity pattern amplification, and its partial elimination by forced circulation changes. Different pattern amplification indices have been proposed to capture this global aspect. Here, we compute the Salinity Contrast (SC) metric as defined by Cheng et al. [2020]. This metric can be computed for the SSS only or for the 3D salinity field over a chosen depth. From a climatological salinity field, a global median salinity S_{clim} is defined over the chosen ocean volume, as well as the regions where salinity is greater than S_{clim} (V_{high}) and lower than S_{clim} (V_{low}). The salinity contrast is then computed at each time step as the difference in volume-weighted salinity between high salinity (V_{high}) and low salinity (V_{low}) regions, that is:

$$SC = \frac{\iiint_{V_{high}} S(x,y,z,t)dV}{\iiint_{V_{high}} dV} - \frac{\iiint_{V_{low}} S(x,y,z,t)dV}{\iiint_{V_{low}} dV} \tag{IV.2}$$

We downloaded the latest time series of salinity contrast computed from the observation-based IAP gridded dataset of Cheng et al. [2020], at the surface (SC0) and in the upper 2000m (SC2000), available for the period 1960-2020. S_{clim}, V_{high} and V_{low} are defined over 1960-2020 and the data is given relative to the 2008-2018 baseline. The annual mean values are plotted in figure IV.3 (black line) along with the lowess-filtered time series with a span width of 240 months (grey line). The observed SC0 and SC2000 show a clear increase from the 1970s, with interannual variations modulating this general positive trend. We note there can be some differences among gridded salinity products before the 2000s, as displayed in Figure 11 in Cheng et al. [2020]. We reproduce these two indices in the IPSL-CM6A-LR large ensemble, choosing the same period 1960-2020 from the ensemble mean to define the climatological field, and compute SC0 and SC2000 in individual members, shown with the same 2008-2018 baseline. The observed time series lie within the spread of the ensemble. The ensemble mean SC0 anomalous values and trend fit well those of the observed SC0. For SC2000 however the observed trend is larger than the ensemble mean's, but the observed time series is within the ensemble distribution. Member r1i1p1f1 is displayed here as an example and shows that depending on the initial conditions, the observed trend is one possible realization. In the large ensemble, SC0 continues to increase in the remainder of the 21st century simulations. On the other hand, SC2000 in the ensemble mean stabilizes around 2010 and barely changes afterward.

Because we have simulations that go back in time, and because we designed ocean-only experiments to specifically separate internal variability from forced signals, we now compute the SC0 and SC2000 indices in the ocean-only experiments, using the mean CTL experiment as the climatological state, so that the climatology is defined under unforced conditions. We then plot the anomaly in the perturbed experiments relative to the CTL. Note this is equivalent to computing SC0 from the salinity anomaly relative to CTL. We apply the same procedure with the passive salinity tracers. We also compute SC0 in the large ensemble, this time using 1850-1899 from the ensemble mean as the climatological state, and the SC anomaly is plotted relative to this same period. The resulting time series are shown in figure IV.4.

SC0 in the ALL experiment increases and evolves within the spread of the large ensemble, centered on the ensemble mean until about 2000 and greater thereafter. It starts to increase in the early decades of the 20th century, pauses from 1950 to 1980 and starts to increase more rapidly after the 1980s, mirroring the signal of global mean surface temperature increase. This global increase results from the freshwater flux perturbation (WATER experiment), acting to intensify the SSS contrast at a larger rate than in ALL in the 21st century. SC0 in the WATER experiment can itself be decomposed into an added salty/freshwater

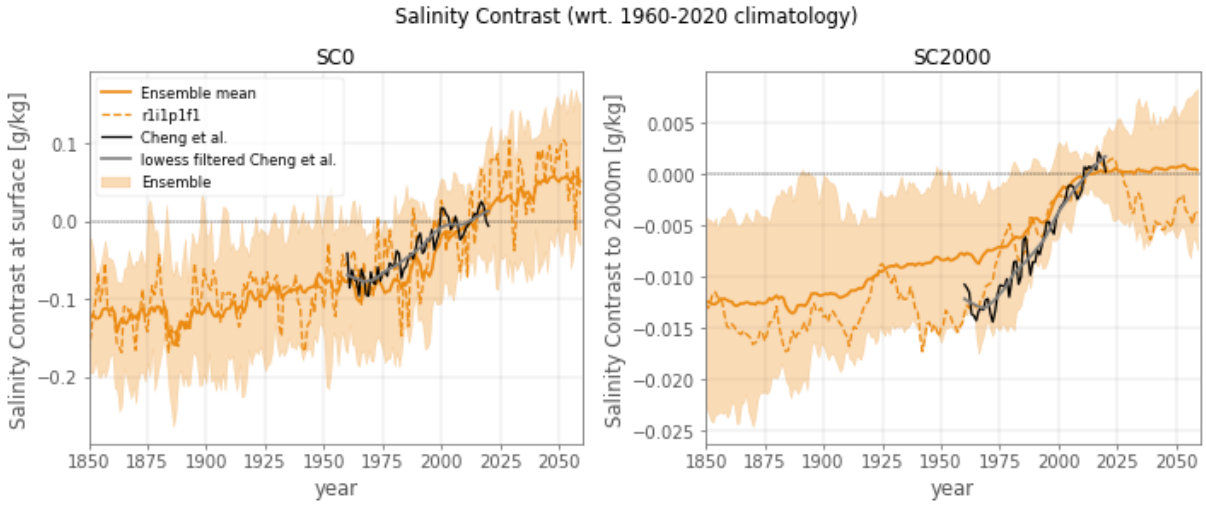

Figure IV.3: Salinity contrast at the surface (SCO, left) and in the upper 2000m (SC2000), computed in the large ensemble as in Cheng et al. [2020]. The observed salinity contrast time series were downloaded from Lijing Cheng's website: http://159.226.119.60/cheng/. The baseline is 2008-2018.

component (dotted blue line) responsible for almost 100% of the total signal until the late 20th century (SC0 in ALL), and a negative redistributed component (difference between the dotted and solid blue lines) which increases over the 21st century, showing that circulation changes induced by the freshwater flux perturbation itself are acting to weaken the "salty gets saltier, fresh gets fresher" fingerprint. Changes in the circulation caused by the wind stress perturbation are also acting to decrease SC0 (STRESS, or difference between BUOY and ALL), and the heat flux perturbation slightly increases SC0 in the second half of the 21st century. The impact of all these circulation changes only arise during the 21st century.

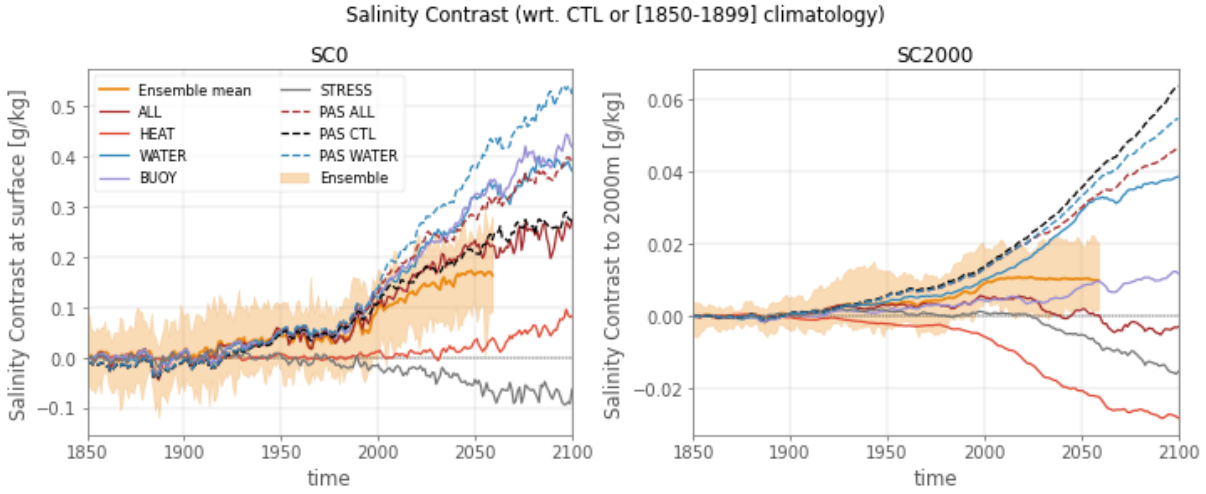

Figure IV.4: Salinity contrast at the surface (left) and in the upper 2000m (right), computed in the large ensemble and in the ocean-only experiments. The climatological high and low salinity areas are compute from the CTL mean state for the ocean-onyl experiments, and from the ensemble mean 1850-1899 mean state for the large ensemble.

Over the upper 2000m, a different picture emerges. The freshwater flux perturbation alone still causes a significant increase in SC2000 (larger than the ensemble in the 21st century), with a greater contribution from the added component, partially offset by the circulation changes in WATER (solid and dotted blue lines). However, the total SC2000 in ALL follows the increase of the ensemble mean until the 1970s,

pauses until the 2030s and then proceeds to progressively decline in the remainder of the simulation, a feature that seems to slightly move away from the response of the the large ensemble. This slower evolution of SC2000 in the ALL experiment and subsequent decline is explained by changes in the circulation induced predominantly by the heat flux perturbation (causing a slow decrease in the 20th century and a more rapid decline in the 21st century) and secondarily to the wind stress perturbation, starting to take effect around 2025. Changes in the circulation are thus very efficient at counteracting the increase in salinity contrast driven by the freshwater flux when considering the entire ocean in the upper 2000 m.

One notable feature is that we don't quite find the result of Zika et al. [2018], i.e. that the heat flux perturbation plays an important role in setting the SSS pattern amplification. Here, the effect of the heat flux is only slightly significant by 2100. One explanation is that they apply an idealized, much stronger radiative forcing, in which the salinity field might respond more quickly to the increased heat flux. Another explanation is that we don't use exactly the same metric. Indeed, the salinity contrast as proposed by Cheng et al. [2020] and applied here doesn't necessarily translate an exact pattern amplification: for example, a salinity increase in only high-salinity regions (such as the North Atlantic) could lead to increasing SC, even if the low-salinity regions keep their initial values, or only slightly change in either direction. Other indices have been constructed. Zika et al. [2018] use a water-mass transformation framework to construct their amplification index. Durack et al. [2012] use a regression between basin zonal mean SSS changes and climatological basin zonal mean SSS anomaly, to construct theirs. We could also apply these indices to our freshwater flux perturbation (the freshwater flux contrast computed similarly as SC indeed increases; not shown).

Other possibilities going forward include using pattern-based methods as in chapter II. The spatial fingerprint looked for could be the pattern of the passive salinity tracer, translating only the integrated signal from the freshwater flux forcing. However, these diagnostics don't help to really understand how the pattern amplification is weakened by circulation changes regionally. Thus, a more regional approach could be an interesting perspective. Fixed boxes cannot always be a good tool, as for the case of salinity, the forced signal implies dipoles of change, like in the SAMW/AAIW region. Tracking water-mass characteristic dynamically could be an interesting regional approach. For instance, the freshening of AAIW have been found to reflect the increased precipitations at southern high latitudes by the "pure freshening" process [Bindoff and Mcdougall, 1994, 2000, Banks and Bindoff, 2003, Lyu et al., 2020]. Seeing how these characteristics change when compared to the freshwater-only forced experiment could give more explicit indications as to the processes at play in weakening the fingerprint of the intensified hydrological cycle.

4 Key points

- In this chapter, I applied the numerical configuration presented in Chapter III to investigate the mechanisms causing thermohaline changes in the ocean to emerge from background internal variability, in the framework of the IPSL-CM6A-LR large ensemble.
- We first focused on temperature signals. We showed that in the long-term (by the end of the 21st century), our decomposition into individual surface flux forcings and into passive and redistributive components reproduces the main features found in previous studies that investigated these questions in the long-term response to more idealized forcings.
- We proposed a new analysis, looking at the balance of mechanisms in the transient response to climate change, focusing on geographical regions of the ocean associated with important ventilation pathways.
- In the mid-latitude Mode Waters of the Southern Ocean and North Atlantic, we find that although there is a large redistributive cooling in the North Atlantic induced by the heat flux perturbation by the late 21st century, the passive warming is the most important mechanism at the time when the total temperature change emerges from internal variability.
- In the open subpolar Southern Ocean, where AABW are formed and exported, there is passive uptake and transport of excess heat from the surface to the abyss, but this process is weakened by the decreasing overturning cell, induced by increasing buoyancy fluxes causing surface stratification. Instead, the increased stratification isolates the warmer subsurface waters, which increasingly gain heat. In the 20th century, both passive and redistributive effects are of equal importance, but in the 21st century, the passive uptake of heat does not keep increasing, and the redistributive warming takes the lead, with some delay from the surface winds, acting instead to destratify the water column.
- In the subpolar North Atlantic, where NADW are formed and exported, there is no signal before the 1980s. The passive uptake of excess heat starts in the early 21st century, but is almost entirely balanced by a redistributive cooling caused by AMOC weakening due to the heat flux perturbation. The small total warming by the late 21st century is found to be caused by circulation changes induced by the freshwater flux perturbation.
- Overall, these numerical experiments highlighted a number of physical mechanisms acting on a range of timescales during the transient response to anthropogenic climate change.
- We then presented some perspective work on the response of ocean salinity. We show that the passive tracer is a clear response to the hydrological cycle amplification, but that circulation changes act to weaken these patterns. We proposed a salinity contrast diagnostic at global scale, and more work is needed to investigate the balance of mechanisms at regional scale to understand the evolution of the total response.

Conclusion and discussion

Main results

Many aspects of the climate system are currently seeing long-term changes, unprecedented in their rates over many centuries to thousands of years [IPCC, 2021b]. As a result, every inhabited region over land is already affected by climate change. The ocean is not spared and has already experienced drastic changes in its physical and biochemical properties. The thermohaline structure of the ocean has been particularly affected: observations of the upper ocean since the mid-20th century show an unabated warming, and large-scale salinity changes coherent with an intensification of the hydrological cycle. There is still a lot we don't know about how temperature and salinity naturally vary in the ocean in the absence of human forcings, and much to be discovered about the deeper parts of the ocean, below 2000m where observations are still sparse today, and where long-term, global scale changes are missing from observational records.

To try and understand the responsibility of human activities in long-term oceanic changes and their projections, we can dive, with precautions, into the modelling world. By comparing simulations of the climate system since 1850 with and without anthropogenic forcings, we can map when, in different regions of the ocean, changes in temperature and salinity (and other variables) become greater than natural variations that would occur in the absence of human influence on the climate system. In other words, we can look when a deviation from background conditions occurs, for different variables and different regions of the ocean and on which time scales. We can investigate how these changes are manifested, and find out what their origin and driving physical processes could be.

This is what we have tried to broadly address in this thesis, with a variety of methods and frameworks. In an ensemble of climate models, we have extracted the dominant, externally-forced patterns of temperature and salinity changes found across models along surfaces of equal density. Accounting for the fact that models don't form their water-masses at the same densities as observed in the ocean, we found similar features and amplitude of multi-decadal changes in this density space. This framework focuses on upper ocean changes, under the mixed layer, essentially zooming in on thermocline, mode and intermediate waters of the global ocean. We revealed that changes in these water-masses were expected to emerge from natural climate variability between the last decades of the 20th century and the first decades of the 21st century for the ensemble median, with earlier emergence in the Southern Hemisphere than in the Northern Hemisphere. In particular, the cooling and freshening of the Subantarctic Mode Waters (SAMW) when looked in density space, that is observed in the southern Indian and Pacific basins (20ºS-40ºS), emerges decades earlier than the cooling and freshening of the northern Pacific subtropical mode waters (10ºN-30ºN). The Atlantic basin was found to present a different structure, with cooling

and freshening in the southern mid-latitudes but much weaker model agreement as to the emergence of this signal, and warming and salinification in the North Atlantic subtropical mode waters (20ºN-40ºN) emerging before 2020. The North Pacific subpolar gyre (40ºN-60ºN) shows warming and salinification, emerging in the 2010s-2020s. All these changes occur between 100-500m, sometimes reaching 1000m depth. Weaker but significant warming and salinification is also found across models and basins propagating deeper in the water column, between the 27.5 and 28 kg.m^{-3} γ_a (approximated neutral density) isopycnals in the upwelling sector of the Southern Hemisphere. These patterns emerge at the turn of the century in the multi-model median but are associated with larger inter-model spread than at mid-latitudes. In these water-masses, we find earlier emergence around 1500-2000m depth than in the upper ocean, and a northward extent of the emerging patterns at different latitudes across basins.

The hemispheric symmetry in the patterns of change in the Pacific and Indian basins are consistent with the single model study by Banks and Bindoff [2003], who found similar patterns along density surfaces in a climate change scenario, a feature that could not be explained by internal variability alone. They attributed the Indo-Pacific zonal mean changes mainly to surface warming causing a displacement of isopycnals in the water column, where vertical gradients of salinity and temperature vary regionally. This is also coherent with the broad-scale subduction of surface warming causing the observed changes, hypothesized by Durack and Wijffels [2010].

A second approach of this thesis consisted in shifting from the multi-model view to a single-model initial condition large ensemble, to 1) explore the time scales of temperature and salinity emergence in this model and better identify the role of different initial conditions of climate variability in modulating the emergence of the forced response; 2) investigate the mechanistic origin of these changes in the transient response to climate change, with the development of a numerical framework to attribute these changes to separate physical drivers. While the multi-model approach is a powerful tool to extract the most prominent information across models while limiting individual biases, focusing on a single model allows to dig into possible drivers of change and test hypotheses with numerical experiments.

The response of the IPSL-CM6A-LR large ensemble was tested against the multi-model mean in the density framework, revealing similar patterns of change and time scales of emergence, with a few regional differences in amplitude of change and in the density where these changes take place. Most significantly, the subtropical North Atlantic in the large ensemble exhibits an opposite sign of change than in the multi-model mean, and the subtropical freshening in the southern Pacific is almost absent. We then adopted a "regular" depth coordinate, more appropriate than γ_a to explore changes equally in the entire water column, including the vast deep and abyssal ocean. This also enables us to investigate changes in the temperature and salinity variables separately, and consider their total, effective change.

The largest changes in temperature and salinity are found in the first 1000m of the ocean, but the low noise levels of the deeper ocean reveal significant signal-to-noise ratios at depth, including in poorly-ventilated regions. The pathway generally associated with the export of AABW is the first to see detectable change, with the forced signal (estimated by the mean across 30 members) emerging in the mid-20th century for both temperature and salinity. This region is also associated with a century-wide spread between members, underlining that initial conditions play a significant role in determining when temperature and salinity definitively exceed the bounds of their unforced regime in these bottom waters. In other parts of the ocean and even at global scale, higher SNRs and earlier emergence is found for temperature than for salinity. In the upper ocean, the regional patterns of emerging temperature are coherent with the early emergence found in density space, globally organised around the main pathways of gyre and overturning circulation, with deeper penetration of high SNRs in the Southern Ocean mid-latitudes. The time scales of the upper ocean warming at global scale reflect that of the global mean surface temperature signal, with an early warming in the 20th century that is detectable in some but not all members, while the larger, more rapid change of the late 20th - early 21st century is detected in all members, within around a couple of decades of one another. The global pattern of temperature change in the zonal mean is detected earlier

when weighting by the local noise than when considering the signal alone, another evidence that the deep ocean in this model is particularly sensitive to climate change signals.

The reasons for these regional emerging patterns in the IPSL-CM6A-LR model were searched for by designing ocean-only experiments to reproduce the ocean response of the historical+ssp period, as forced by all surface flux perturbations (heat, freshwater, winds) of the coupled model during this period, or imposed separately. This novel numerical configuration allowed to properly investigate the balance of large-scale mechanisms in the transient response to climate change, while attempting to effectively separate internal variability from the forced response. The surface perturbations cause warming in almost all regions of the ocean, either by the direct input of excess heat flux into the ocean, or by the redistribution of internal ocean heat by circulation changes in response to these perturbations. To explain the different emerging patterns of temperature change in the coupled model, we found that the emergence of the upper ocean warming was generally driven by the passive uptake and storage of excess heat by the ocean circulation, with a minor role for circulation changes at the time when these signals emerge; while in the deeper ocean, circulation changes played an important role. Indeed, in the open subpolar Southern Ocean where AABW are generally formed in the model and exported, although the winds act to increase vertical mixing, destratify the water column and thus cool subsurface water-masses, increased freshwater and heat fluxes strongly stratify the surface (pre-dominantly from the surface freshening) and reduce vertical mixing, blocking the warmer subsurface layer from releasing its heat. It is the latter drivers, on top of the surface heat flux anomalies penetrating in the ocean as temperature anomalies, that are responsible for the an early (mid-20th century) rise of the forced temperature signal in the large ensemble, which is partly offset by the wind forcing later in the 20th century and continuing in the 21st century. In the subpolar North Atlantic, the decreasing overturning circulation cools the subsurface, almost completely counteracting the storage of excess heat. The residual warming in the ensemble is found to be mainly due to redistribution by the freshwater flux perturbation. The emergence of the total warming in the deep waters of the subpolar North Atlantic is found several decades after the subpolar Southern Ocean; and about 10 years later for the mid-latitude upper ocean warming of the North Atlantic compared to its Southern Ocean counterpart. This asymmetry is consistent with the hemispheric asymmetry in the ocean's storage of anthropogenic heat that has been linked to GHG forcing being partly counterbalanced by aerosol forcing in the 20th century in the Northern Hemisphere [Shi et al., 2018, Menary et al., 2020].

Overall, these results suggest the ocean is particularly sensitive to human-induced climate change, with its thermohaline structure already modified beyond the level of natural variations in large parts of its interior water-masses. This sensitivity is due to a balance of diverse processes that varies regionally. If climate model projections can be trusted for the future of the deep ocean, which can be questioned (see below), this could mean that the sparse observed changes already collected in the deep and abyssal changes could already be of anthropogenic origin. The prospect of deep Argo floats provides hope to obtain greater temporal and spatial sampling of the ocean below 2000m than is currently possible, with the perspective to solve interannual variations at these depths.

Implications for our cross-cutting questions

In the General Introduction, we laid out three questions that have constituted the scientific motivations of my thesis. Without claiming to provide straight answers, we will now try to discuss these points here based on the knowledge developed in this thesis.

What is the balance of mechanisms that makes the region associated with SAMW and AAIW such a key place for the detection of thermohaline changes of anthropogenic origin?

Across the studies presented in this thesis, we found using independent approaches that the Mode and Intermediate waters of the Southern Ocean stood out as one of the earliest emerging regions, with a

warming signal emerging from internal variability by the late decades of the 20th century. This confirms the results of several other studies that have independently found over the years significant multi-decadal changes in these water-masses in observations [Bindoff and Church, 1992, Johnson and Orsi, 1997, Wong et al., 1999, 2001, Bindoff and Mcdougall, 2000, Aoki et al., 2005, Gille, 2008, Durack and Wijffels, 2010, Helm et al., 2010] and coupled models [Banks et al., 2000, Downes et al., 2010, Sallée et al., 2013, Lyu et al., 2020], indicating a warming in SAMW and freshening in AAIW along pressure surfaces, or a cooling and freshening along deepening isopycnals. They point the origin of these changes to global surface warming associated with increased precipitation - evaporation in the source region of AAIW, expressed as warm and fresh surface anomalies, with a secondary role for changes in the winds acting to increase the downward Ekman pumping. These anomalies penetrate in the interior along the ventilation pathways of SAMW/AAIW, i.e. they are subducted below the deep winter mixed layer and exported equatorwards into the subtropical gyres. This highlights the sensitivity of these water-masses to thermodynamic changes, integrating long-term changes as they are formed and homogenized on large volumes, with detectable climate change signals before the 21st century.

Separating the air-sea fluxes into individual components, we found that the warming signal propagated deeper when the perturbation of the wind stress was included, corroborating earlier studies that found that the effects of the poleward and intensifying westerly winds, increasing the northward transport and subduction of heat, was a secondary but important ingredient of the amplitude of the warming in the long-term or equilibrium response [Fyfe et al., 2007, Liu et al., 2018, Shi et al., 2020]. However, in the transient response, changes in the wind stress start to affect subsurface temperature changes only from the 1980s, when the warming is already large enough to exceed internal variability thresholds. The dominant warming mechanism in the Southern Ocean mid-latitudes is found to be the uptake of excess heat at about 60ºS where old deep water upwells, and is transported northward and subducted by the background meridional overturning circulation (MOC). This is true in the transient response, and it is by this very effective process that the upper ocean is warmed in the 20th century onwards. Circulation changes play a secondary role, with an enhancement of the warming by the winds in the 21st century, almost completely compensated by a cooling due to increased freshwater fluxes. The residual redistribution effect is found to be caused by the heat flux perturbation itself, slightly offsetting the passive warming by increasing the stratification, reducing the overall ventilation of the region and preventing the heat from reaching as deeply as the passive process. The realism of the time scales found in our modelling study depends on the balance between the different perturbation components, their amplitude, and the representation of the overturning circulation, which, as we have seen here, controls most of the warming processes [Armour et al., 2016].

To sum up, SAMW/AAIW are a hot spot of anthropogenic warming with particularly high signal-to-noise ratios compared to other water-masses of the upper ocean. The importance for heat storage of these Southern Hemisphere water-masses compared to their Northern Hemisphere counterpart is due to a combination of aspects:

- They are formed over large volumes of water, which means they integrate the varying atmospheric conditions at their formation site; they are thus well-positioned to capture long-term trends in air-sea fluxes while removing the higher frequencies of natural variations.
- The residual-mean MOC of the Southern Ocean upwells old waters that haven't seen atmospheric conditions in decades to centuries; they surface at the southern flank of the ACC, where the atmosphere has warmed more rapidly than the ocean surface waters. This creates a very large uptake of heat that, instead of being stored locally, is transported northward by the upper branch of the residual-mean MOC to be stored in the SAMW that subduct north of the ACC. Thus, not only do these water-masses gain heat by local warming sources, but they capture the majority of the heat taken up at higher latitudes because of the background circulation.
- The northward convergence of heat in the SAMW is partially increased by the intensifying westerly winds in response to ozone and GHG forcings, starting in the late 20th century.

- Another notable difference with the Northern Hemisphere stemming from radiative forcings is the weaker effect of aerosol radiative cooling in the Southern Hemisphere, that possibly temporarily offsets the GHG-induced warming in the Northern Hemisphere, delaying the uptake of heat. This could further possibly explain why there are hemispheric asymmetries in the detection of ocean warming.

We have not addressed a variety of processes which are important for the upper ocean circulation, the subduction and ventilation of SAMW and AAIW, and the evolution of upper ocean warming. For instance, the horizontal resolution of global climate models ($\sim 1^{o}$) does not allow for finer processes to be resolved, such as the role of eddies in inducing advection and isopycnal mixing, which are instead parameterized and can be important for the net residual meridional overturning and for the ventilation of water-masses without net mass transport [Gent and Mcwilliams, 1990, Speer et al., 2000, Sallée et al., 2010, Abernathey and Ferreira, 2015]. Furthermore, we have adopted a zonal mean view, as is often done because it is a useful tool, but is also a simplification of Southern Ocean dynamics. Indeed, the subduction of SAMW and AAIW varies longitudinally, and is found in localized hot spots constrained by the bathymetry, with circumpolar variations of SAMW and AAIW characteristics [Sallée et al., 2010, Jones et al., 2016a]. Adopting a 3D framework would enable to see whether these hot spots are displaced, and whether that relates to the amount of warming that is found in the interior. Finally, while we have talked about SAMW and AAIW, we have not formally delineated them with dynamic criteria, such as the minimum in potential vorticity for SAMW and the salinity minimum for AAIW (e.g. Downes et al. [2010], Sallée et al. [2013], Hobbs et al. [2021], Roy et al. [2021]), as these properties can evolve in time in response to climate change. Such delimitation of water-masses can inform on the evolution of their volume, ventilation time and thermohaline properties.

What can we learn from climate models about deep and abyssal changes and their timing?

We have found thermohaline changes at depth in climate model simulations, emerging from internal variability sometimes earlier than in the upper ocean. These changes were found on density surfaces (warming and salinification) in the range of CDW, and on depth surfaces in the pathways associated with the export of AABW (warming and freshening), as well as in the weakly-ventilated shadow zones of the ocean interior (e.g. DeVries and Primeau [2011], Holzer et al. [2021] and see figure V.1), especially in the Pacific and Indian basins around 2000-4000m depth, with rapid and already emerged changes in both temperature and salinity. These changes are coherent with a small propagation of the surface warming at depth, along with a much larger warming due to the reorganization of the circulation in response to surface buoyancy fluxes at high latitudes, acting to decouple the surface from the deeper layers. It is interesting to see that, in contradiction with the idea that deep convection is a conduit to export surface warming downward, and that shutting down deep convection will possibly decrease the rate of heat uptake in climate models [Heuzé et al., 2015], we find that the warming in AABW by 2100 is mostly caused by the fact that deep convection shuts down and subsurface heat is trapped, with only a minor role for the excess heat passively transported by the decreased circulation. The fact that rapid changes are also found in areas of the ocean where it takes over 1200 years for these water-masses to get ventilated (figure V.1) is particularly fascinating at first sight, and suggests that some water-masses are getting geographically reorganized by transport and mixing processes.

Studying deep ocean properties in climate models can be tricky. We have shown that persistent drift can be present, largely impacting the mean state of the deep and abyssal ocean and its long-term changes, and should thus be removed when looking at trends. For salinity, we have seen that there is a persisting drift in some areas even after a careful dedrifting procedure, which might be an indication that the shape of the true drift in salinity might be more complex at local scale than a second order polynomial. This drift in temperature and salinity might affect the evaluation of climate models and their intercomparison. Indeed, thermohaline properties in the model are often compared to observations, averaged over a common period of time; however, the mean state in these variables drifts in the model. Furthermore, in some intercom-

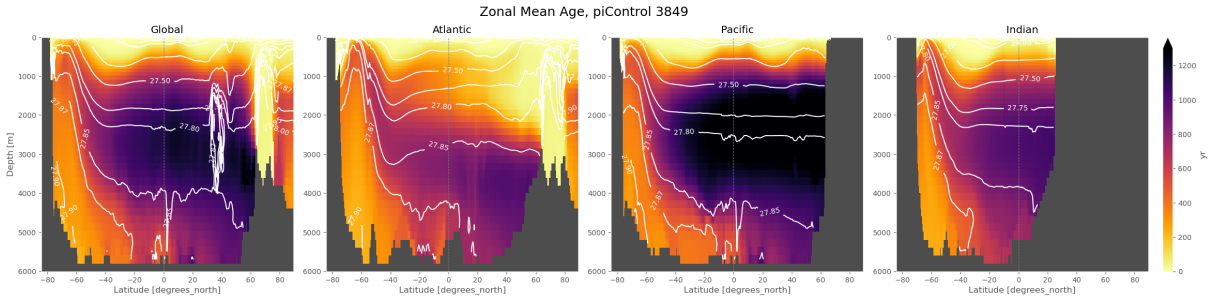

Figure V.1: Zonal mean Age tracer indicating time since surface contact, after over 2500 years of piControl run in the IPSL-CM6A-LR. White contours indicate climatological potential density.

parison studies looking at bottom waters and their formation processes (e.g. Heuzé [2021], Mohrmann et al. [2021]), only one member is used, but we have found that these water-masses and their associated processes are particularly sensitive to initial conditions (also corroborated by de Lavergne et al. [2014]), which casts doubts on the relevance of taking into account a single member when looking at processes such as deep convection in a limited time period.

To what extent can thermohaline changes in the deep and abyssal ocean be trusted in climate models? The bottom water-masses of the ocean and their near-surface formation site at high latitude are very weakly stratified compared to the rest of the ocean (Levitus and Boyer [1994], also see figure V.1). Because density gradients are weak in these parts of the ocean, it is not surprising that an anomalous and continuous buoyancy supply, even small in amplitude, can radically change the structure and characteristics of deep and bottom waters. For instance, the non-renewal of cold AABW or their export with modified characteristics is a coherent factor of rapid thermohaline structural changes in the bottom layers of the ocean. However, some high-latitude processes, where deep and bottom water-masses are formed, are not represented in climate models, or not well represented. For instance, climate models tend to form their bottom waters by open-ocean deep convection, while we know that in the real ocean it forms through dense water formation on the Antarctic continental shelf, which then overflows and sinks along the continental slope towards the abyss [Heuzé et al., 2013, Heuzé, 2021]. In addition, we expect the increasing glacial melt from the Antarctic ice shelves, which is not represented in the current generation of climate models, to have a large impact on the formation and export of AABW [Lago and England, 2019]. These important limitations of climate models hinder going too far in the interpretation of future change projected in AABW. However, investigating processes at play in AABW changes in climate models, and knowing about the main limitations in the representation of these water-masses, allow us to speculate on the direction of future changes. While AABW formation processes are arguably unrealistic in climate models, increases in stratification would also reduce formation of dense shelf water in continental shelf, and have therefore similar consequences than what is projected in climate models when forming AABW by deep convection. Similarly, increasing iceshelf meltwater as a response to climate change goes in the same direction as the increased freshwater flux already simulated in climate models, with possibly similar but larger effects, as basal melt implies large surface freshening. In summary, despite important limitations in the representation of bottom waters in climate models, current process-understanding tends to tell us that the direction of temperature changes projected by those models is robust.

To what extent can we trust time scales of change in deep water properties presented here? Even though we can provide some understanding with the processes already represented in the models, it is difficult to predict what will be - and already are - the time scales of such changes in the real world. The balance of complex processes driving these changes determines their timing. We know that models convect too much [Heuzé, 2021], which means that a decrease in deep convection in these models potentially drives too rapid warming in the bottom waters, with important consequences for climate sensitivity [Gjermundsen et al., 2021]. On the other hand, glacial melt is not included, which would possibly enhance the

warming response at depth, and its rapidity [Lago and England, 2019]. Furthermore, the time scale of this warming across models probably depends on the representation of deep convection in each model, and the timing of its decrease or complete shutdown. For example, IPSL-CM6A-LR has been found to not form any open-water polynias even before large climate signals have penetrated in the ocean (although only one member was investigated) [Mohrmann et al., 2021]. In models that do form open-water polynias (such as ACCESS-OM2, Dias et al. [2021]), the timing of the response may vary according to the frequency of such events, and their decrease with time. Moreover, we have seen that the timing of the bottom warming among a single model is extremely constrained by the initial conditions (large inter-model spread in the emergence of the warming signal). Finally, the IPSL-CM6A-LR model seems particularly sensitive to changes in these deep and abyssal regions, with early and significant warming in the ensemble mean. This can be explained by the low variability envelope (noise) found at depth which leads very easily to emerging signals. The realism of this noise estimate is unknown in observations, but it would be interesting to investigate whether this is a robust feature of climate models, by looking at other large ensembles, after having carefully removed any residual drift. The sensitivity of different processes under global warming to initial conditions in other large ensembles would be a particularly compelling point to address in future studies, as they largely control the thermal transient response of the deep ocean.

What does emergence mean in different methodological frameworks, how do they compare and what do we learn from them?

We have considered temperature and salinity changes in the ocean in different frameworks: in basin zonal mean along pressure and density levels, vertically-integrated, and in the T-S volumetric space. They all indicated long-term changes, with a different side view. Due to the thermohaline structure of the ocean, which is very stratified in the upper ocean and weakly stratified at depth, the "binning" methods chosen (density and T-S space) ended up zooming on upper ocean changes, leaving the largest volumes of the ocean to reside in just a few bins. Better bin resolution or adapted density definition could help better distinguishing these deeper parts. In a different way, vertically-integrated variables also favor the upper-ocean, since it is where the largest changes are found, in absolute values. Consequently, it is really with a zonal mean framework along pressure surfaces that we were able to uncover the spatial distribution of emerging signals in the deeper ocean. While this averaging method may be mixing different signals in the upper ocean, as seen for salinity changes at least in the IPSL-CM6A-LR model, it seems to reveal coherent changes in the deeper parts. Because of the very low simulated interannual variability in the deep and abyssal ocean, we detect particularly early emergence at local scales, confirmed by the earlier detection of the global fingerprint of the temperature SNR compared to absolute temperature values.

We did not find earlier signals along density surfaces compared to pressure surfaces within a same region and model. Zonally averaging along isopycnal surfaces may pick up more physically-consistent water-masses and changes than on pressure surfaces. But on multi-decadal time scales, decomposing thermohaline changes into isopycnal heave (vertical movements of isopycnals) and spice (changes along isopycnals) cannot be explained as a dynamic / thermodynamic (or adiabatic vs. diabatic) mechanistic decomposition, as the dominant signal is a downward displacement of density surfaces in the water-column in response to global warming. As discussed, there are however mechanistic reasons to look at these changes along both density and pressure surfaces, such as the idealized ventilation processes introduced by Bindoff and Mcdougall [1994], that have been useful to attribute early signs of ocean interior change in the observations to changes in air-sea fluxes that were not observable.

Beyond trying to find the best estimate of time of emergence or detection, what I learned throughout this thesis, is that the range of existing methodologies highlights what is probably more important to our understanding: the key physical processes acting on time scales of emergence. Indeed, the diagnostics of time of emergence or detection include many uncertainties, from the estimate of internal variability to the sensitivity to initial conditions, but also methodological uncertainties related to detection definitions and threshold criteria. We have seen that when the signal is slowly increasing, such as the 20th

century warming, there is a large sensitivity to initial conditions, even in the "best" places to look for anthropogenic change (such as SAMW/AAIW). Hence, although the forced signal might be extractable and detected early within a large ensemble (the ensemble mean), what is most interesting might not be that this forced signal emerged in 1950, 1955 or 1957, but what processes influence the emergence, the range over which individual members cross the same threshold, and how that compares across regions of the ocean. Individual members act as one possible realization of the climate; the observations are the actual only realization; they have both the forced signal, and the modulations by internal variability, but we don't know the "initial conditions" for the observations. Consequently, we can discuss a range of possible emergence and the sensitivity to internal variations in different regions or points in time. In some regions, the temperature and salinity changes have already been detected in the observations, but observations don't go back very far in time, so it is interesting to revisit these changes in models to know if they could have been detected earlier than on the observable period. This informs us on the ocean's sensitivity to changes in the climate system beyond what we observe. In other regions, changes are not yet detected, and the emergence diagnostics can provide a guess with a range of possible times when they may start to be detected. Better quantifying the uncertainties related to these ranges - model-to-model differences, internal variability, or scenario -, is important to understand what we can learn from these models.

Perspectives

In this section, I briefly present a few avenues for future work that have sparked my interest, before trying to conclude on the notion of emergence. Other perspectives for future work have been presented in the conclusion section of some chapters. For example, early work was presented in Chapter IV on the mechanisms of salinity contrast amplification and the role of ocean circulation in damping it.

Characterising forced changes in the ocean water-masses

We have largely (mis?)used the term "water-mass" in this thesis to designate broad areas of the ocean but we have never actually defined them based on dynamic characteristics or looked at their long-term changes. In Chapter I, we tried to inter-compare regional long-term changes in climate models by adapting the regions we looked at in each model, but this largely relied on an ad-hoc approach, and would benefit from more quantitative criteria. Indeed, water-masses can be displaced geographically, and their density and volume can also change in response to climate change, so neither fixed boxes along density or pressure surfaces are a good fit to actually follow their evolution (formation rate, volume, T-S characteristics, etc..). This was not the question that we aimed to tackle, but could be an interesting avenue: more appropriately track water-masses in time and investigate how their characteristics respond to climate change, whether they grow or completely disappear in response to different forcings [Downes et al., 2009, 2010, Sallée et al., 2013, Hobbs et al., 2021, Roy et al., 2021]. Furthermore, it is a promising approach for intercomparison analyses based on different models and observations, as water-masses across models are not always found at the same depth or density levels.

Attribution to different radiative forcings: experimenting with DAMIP

In the analysis of the IPSL-CM6A-LR response to climate change (Chapter II) and in the numerical framework presented in Chapters III and IV, we focused on the historical and ssp245 radiative forcings that included all anthropogenic external factors, largely because we had the large ensemble of members which was an essential tool to extract the forced response. However, to test the role of individual anthropogenic forcings and the hypotheses made on the delay of warming emergence in the North Atlantic compared to Southern Ocean because of anthropogenic aerosol cooling, it would be an interesting prospect to explore the DAMIP (Detection and Attribution Model Intercomparison Project) experiments that have run in response to individual forcings. Similar ocean-only experiments could then be run in response to

these individual forcings, although the forced component from the surface fluxes would not be as refined because of the smaller number of members than the historical-extended ensemble.

Quantifying different sources of uncertainty: towards a multi-large ensemble analysis

Diving into the analysis of a large ensemble of historical-extended simulations allowed to quantify the uncertainty and the sensitivity of the model's response to different initial conditions in internal phases of variability. The uncertainty of the ToE of ocean warming due to initial climate conditions was found to be large everywhere in the ocean in the 20th century, with some regions persisting longer than others. I am really curious to find out how these features hold in other large ensembles, and how this uncertainty compares to model-to-model uncertainty. A multi-large ensemble analysis seems like a promising avenue to better quantify the different sources of uncertainty associated with ocean interior changes, which has for now been mostly done for surface variable projections (e.g. Kumar and Ganguly [2018], Maher et al. [2020], Deser et al. [2020], Lehner et al. [2020]) or ocean potential ecosystem stressors [Frölicher et al., 2016], essentially applying the framework proposed by Hawkins and Sutton [2009], revisited to include better estimates of internal variability uncertainty with the use of large ensembles. Many other questions could be addressed in a multi-large ensemble analysis. For example, we have seen in the IPSL model that with 30 members, the historical ensemble spread replicated the interannual variability from the piControl. Is that true in other models? How many members are needed to isolate and detect anthropogenic changes across models? The CMIP6 archive, which now comprises several models with over 30 historical members, along with the dedicated simulations of Single Model Initial condition Large Ensembles (SMILEs), provides a large basis for such analyses.

Epilogue: some thoughts on the concept of Time of Emergence

ToE has received particular attention in the past decade for its implications for marine ecosystems [Bindoff et al., 2019]. The ToE for potential ecosystem stressors (temperature, pH, NPP, oxygen, etc...) gives indications at local scales on the exceedance of environmental thresholds than can be important for ecosystem habitats. Marine organisms are exposed to potential radical shifts in their environment. Their vulnerability to these shifts depends on their individual level of tolerance to variations in environment variables, and the velocity of the associated changes. Whether different organisms are vulnerable to such local hazards, and whether they are able to migrate are important considerations for their adaption to climate change.

These questions are also relevant for extreme events which have potentially large impacts on marine life: with every additional fraction of global warming, marine heat waves become more frequent and more intense [Bindoff et al., 2019]. Extreme events are another way to look at the emergence of long-term signals: instead of focusing on the evolution of mean state variables, the focus is put on the tail of the distribution.

ToE can be a way to grow our understanding of the impact of climate change. But beyond a precise time of emergent change, considering the evolution of signal to noise ratios is also a way to explore the different time scales of the processes at play in response to climate change, with potential impacts at different SNR levels. We have seen that some processes can be very efficient in causing an early but small rise in SNR, while others can take longer to occur but will cause more abrupt changes and thus larger amplitudes of SNR. Looking at emergent change can inform us on which mechanisms are capable of modifying the climate state, on which time scales, and where in the climate system. Considering a variety of variables highlights different ways climate signals are expressed.

One fundamental limitation of the ToE or SNR approach in climate models is that even if they can reproduce observed trends in physical changes, there is still much we don't know about internal variability in the real world, at interannual but also decadal to multi-decadal time scales. Constraining this knowledge

with long-enough observations is a way towards providing targeted information on whether observed trends emerge from the seasonal, interannual or decadal cycle. Repeated transects in the ocean have already provided knowledge on the emergence of 25-year trends from interannual variability [Auger et al., 2021]. Paleoclimate observations have also been useful to put multi-decadal observed trends from satellite measurements in the context of centennial-scale variability [Jones et al., 2016b].

Finally, I have found when telling the main story of this PhD to friends and family, that perhaps, ToE studies also have a "societal utility" in the message they convey in communicating with the general public: climate change has already affected the most remote and hidden places of the ocean, away from human life and from human exploration. These changes will continue to increase and have important consequences for us, such as sea level rise. But we have the power to limit the amplitude of such impacts, if we make the right choices as a society, and if we make them now.

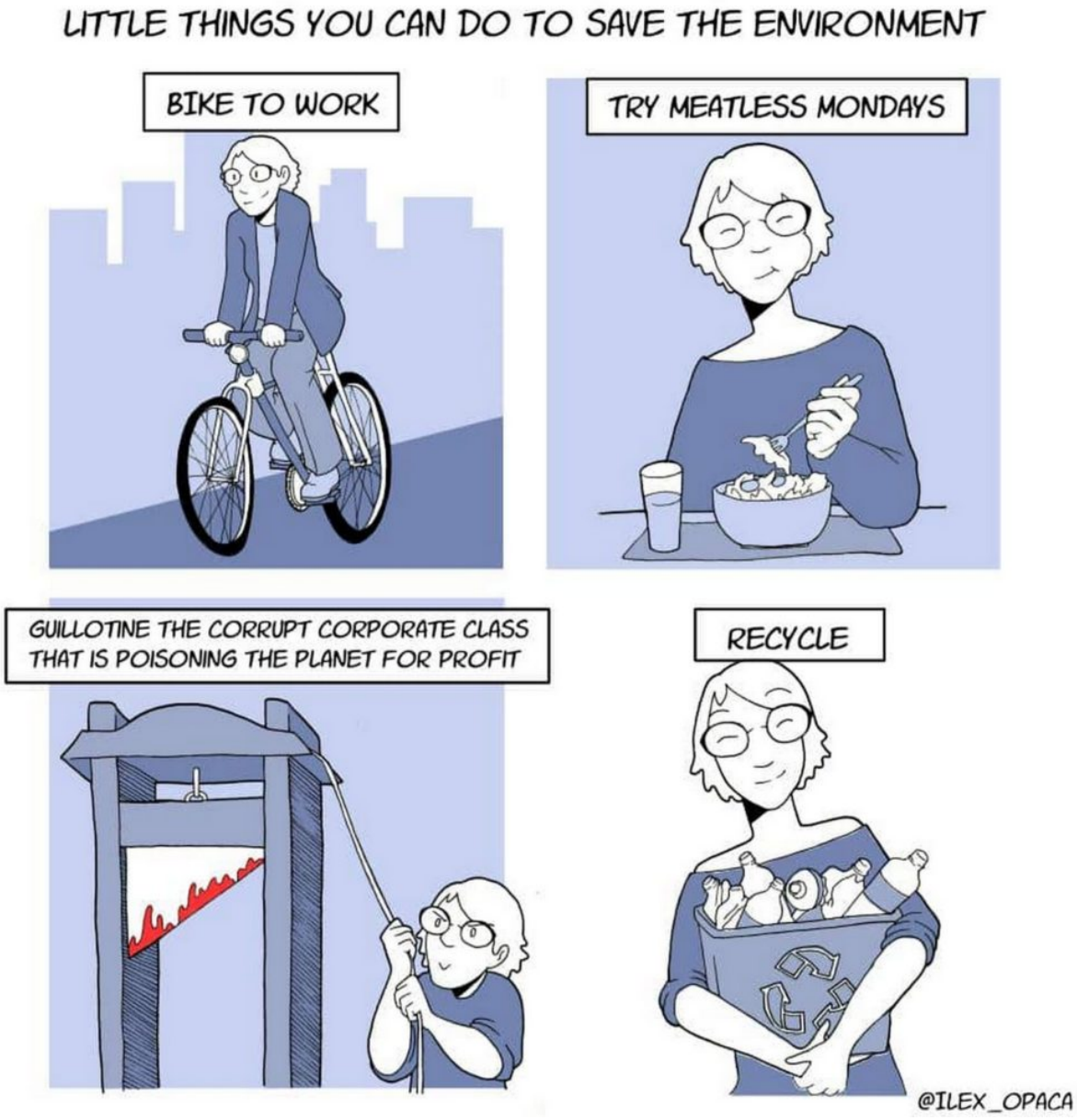
LITTLE THINGS YOU CAN DO TO SAVE THE ENVIRONMENT
BIKE TO WORK
TRY MEATLESS MONDAYS
GUILLOTINE THE CORRUPT CORPORATE CLASS THAT IS POISONING THE PLANET FOR PROFIT
RECYCLE
@ILEX_OPACA

Appendices

Appendix

A

Supplementary Material to the first paper

nature research

https://doi.org/10.1038/s41558-020-0878-x

Supplementary information

Human-induced changes to the global ocean water masses and their time of emergence

In the format provided by the authors and unedited

Human-induced changes to the global ocean water-masses and their time of emergence

Yona Silvy, Eric Guilyardi, Jean-Baptiste Sallée and Paul J. Durack

Corresponding author email: yona.silvy@icloud.com

Supplementary Information

Supplementary Figures

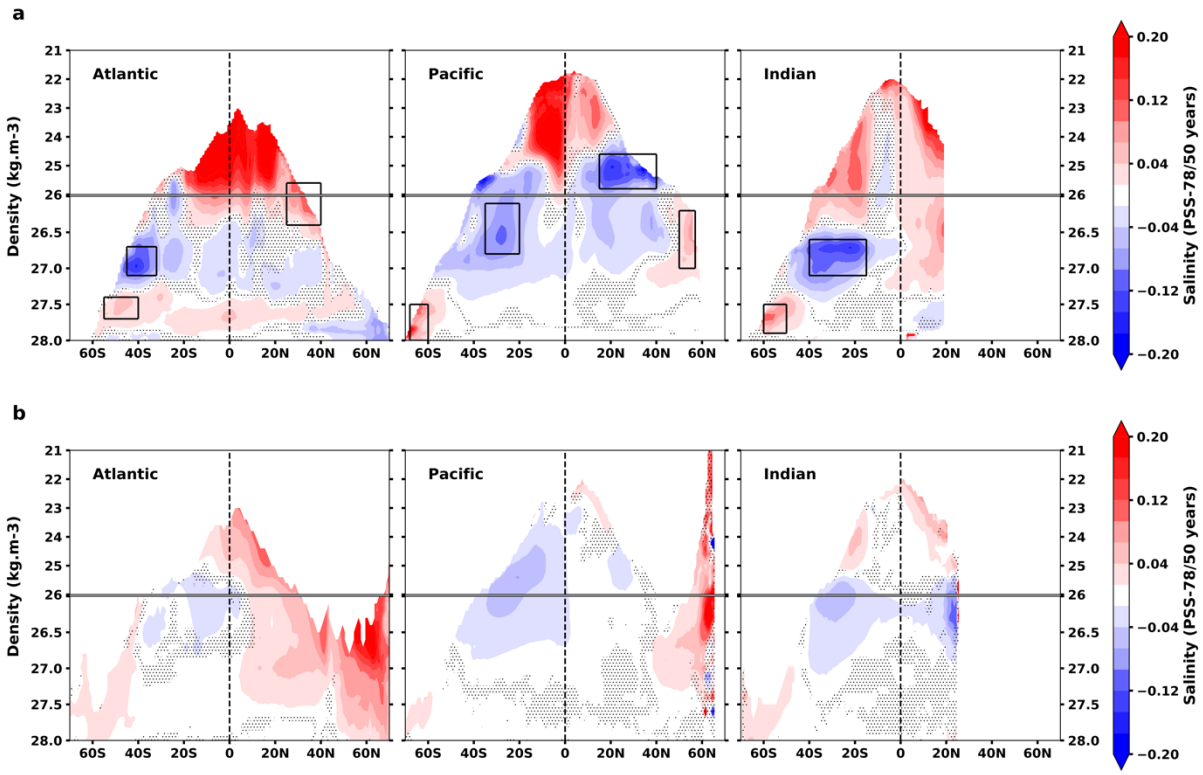

Supplementary Figure 1 Observed and simulated salinity changes analyzed on density surfaces between 1950 and 2008, shown in PSS-78/50 years (as in Figure 1 of the paper, in original density coordinate). (a) From Durack & Wijffels (2010)[1] observation-based analysis. Stipples show where the trend is not significant at the 90% confidence level. Black rectangles indicate the regions in which the trend is averaged for the computation of Figure 1c. (b) From the multi-model mean historical experiments. Stipples show the areas where less than 60% of models agree on the sign of the change.

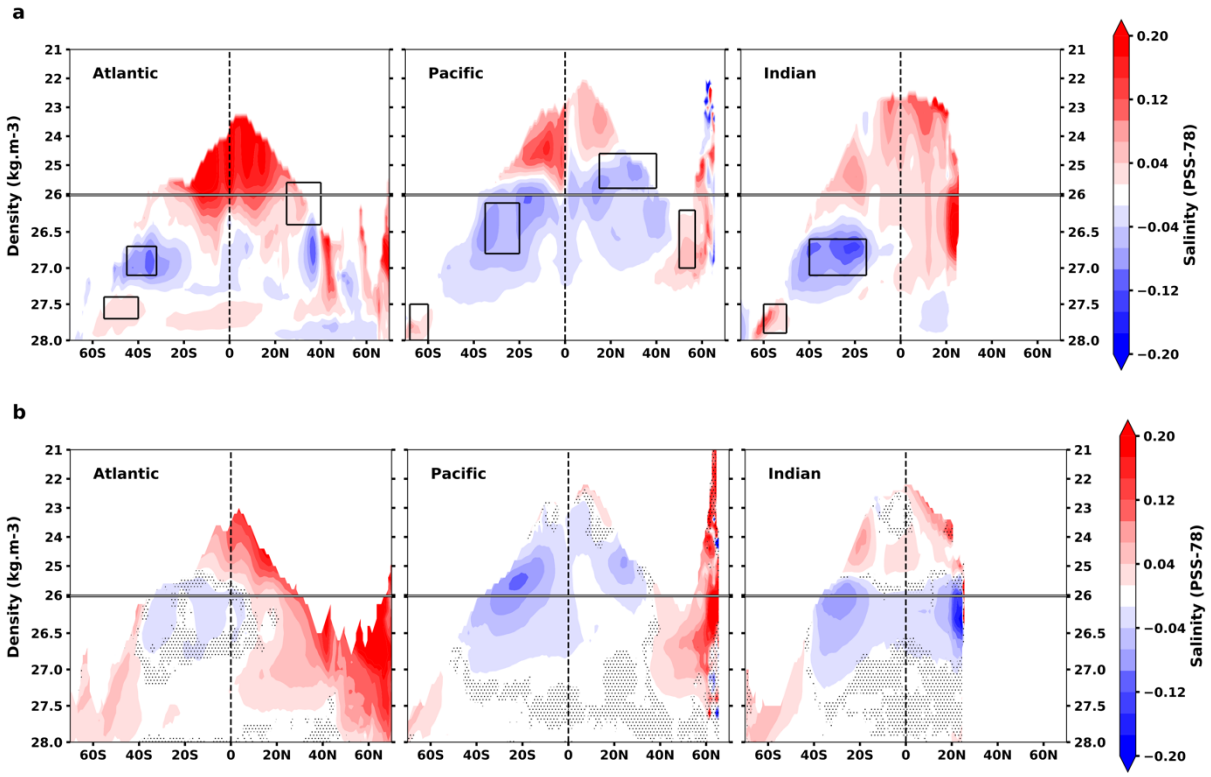

Supplementary Figure 2 Estimated and simulated salinity changes analyzed on density surfaces between 1950 and 2017. (a) From the EN4 observation-based analysis. Black rectangles indicate the regions in which the trend is averaged for the computation of Figure 1c (same coordinates as those used for the Durack & Wijffels 2010 dataset). (b) From the multi-model mean historical (1950-2005) + RCP8.5 (2006-2017) experiments. Stipples show the areas where less than 60% of models agree on the sign of the change.

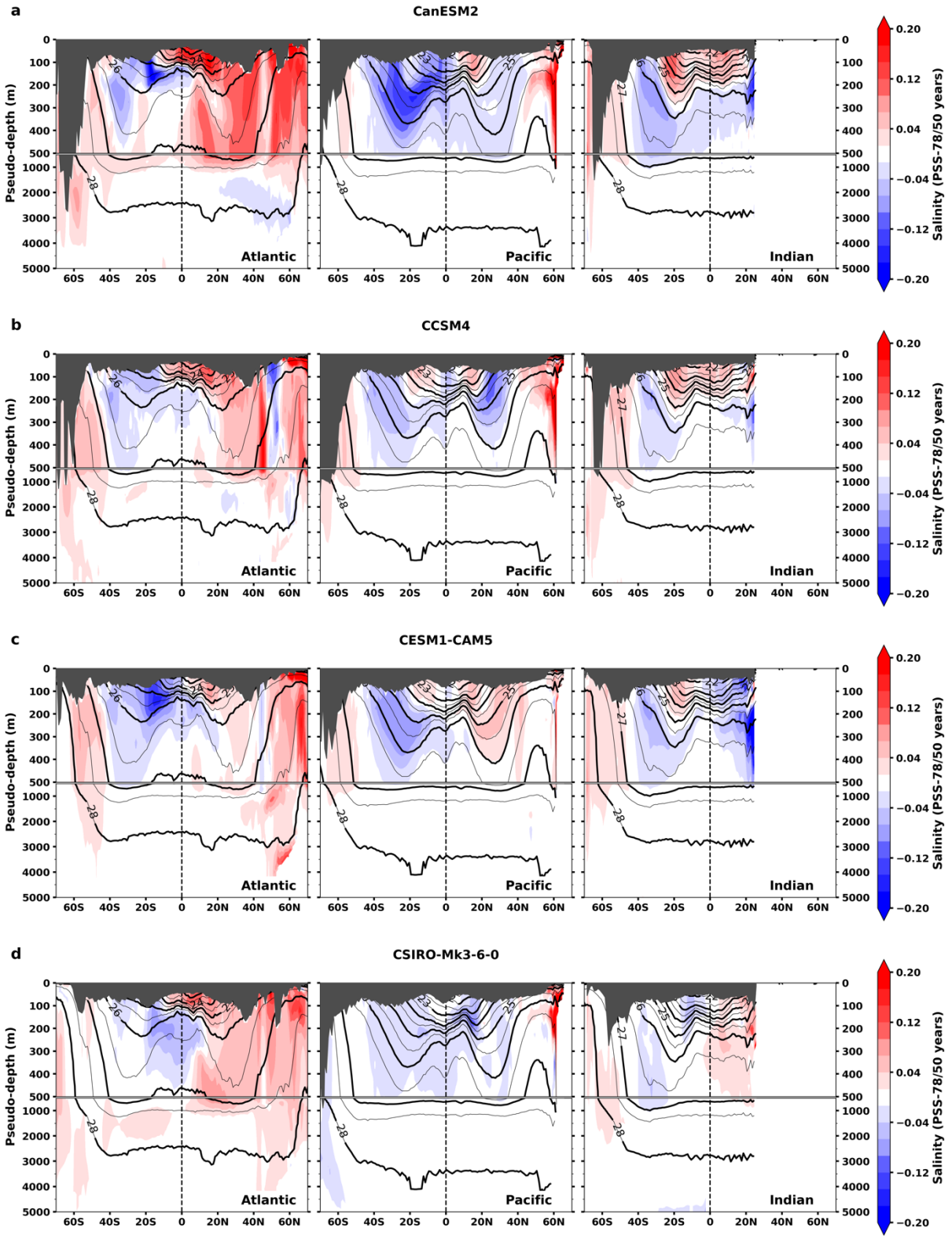
a
CanESM2
b
CCSM4
c
CESM1-CAM5
d
CSIRO-Mk3-6-0
Pseudo-depth (m)
Salinity (PSS-78/50 years)
Atlantic
Pacific
Indian
60S 40S 20S 0 20N 40N 60N
0 100 200 300 400 500 1000 2000 3000 4000 5000
0.20 0.12 0.04 −0.04 −0.12 −0.20

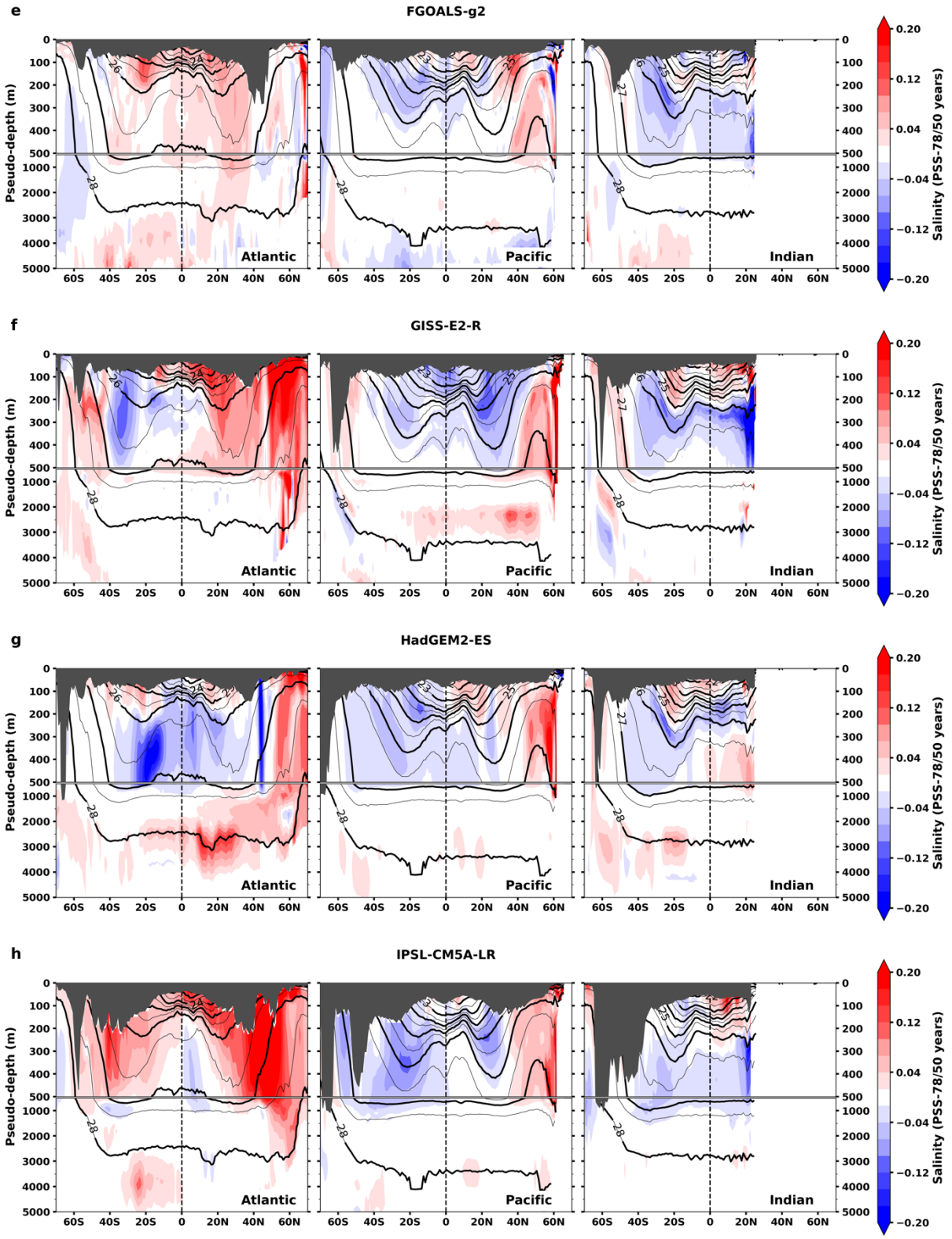
e
FGOALS-g2
f
GISS-E2-R
g
HadGEM2-ES
h
IPSL-CM5A-LR
Pseudo-depth (m)
Atlantic
Pacific
Indian
60S 40S 20S 0 20N 40N 60N
Salinity (PSS-78/50 years)
0.20
0.12
0.04
−0.04
−0.12
−0.20

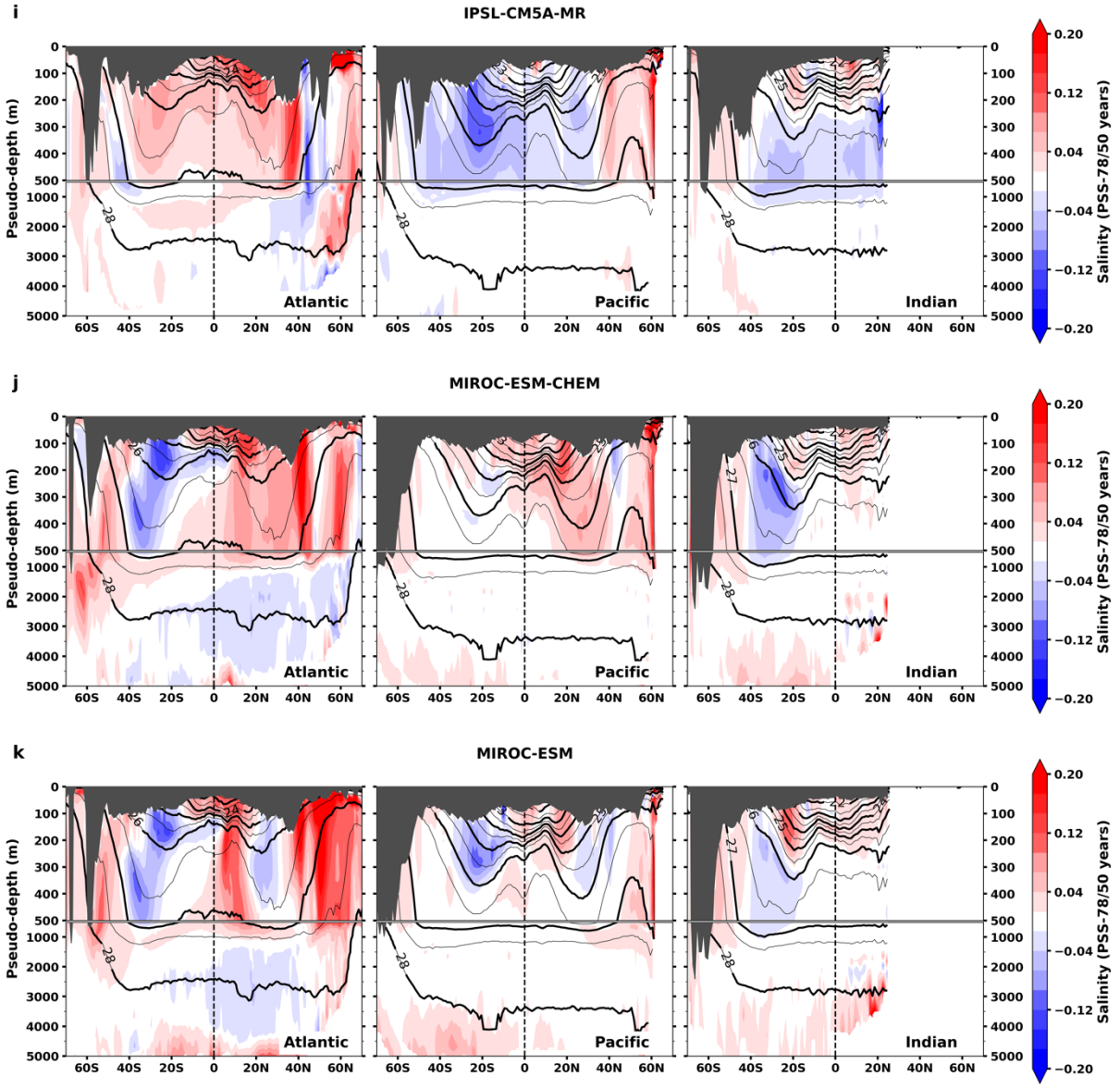

Supplementary Figure 3 Simulated salinity changes analyzed on density surfaces between 1950 and 2008, shown in PSS-78/50 years, for the 11 model ensemble means. The dark grey area at the surface corresponds to the ocean surface above the bowl.

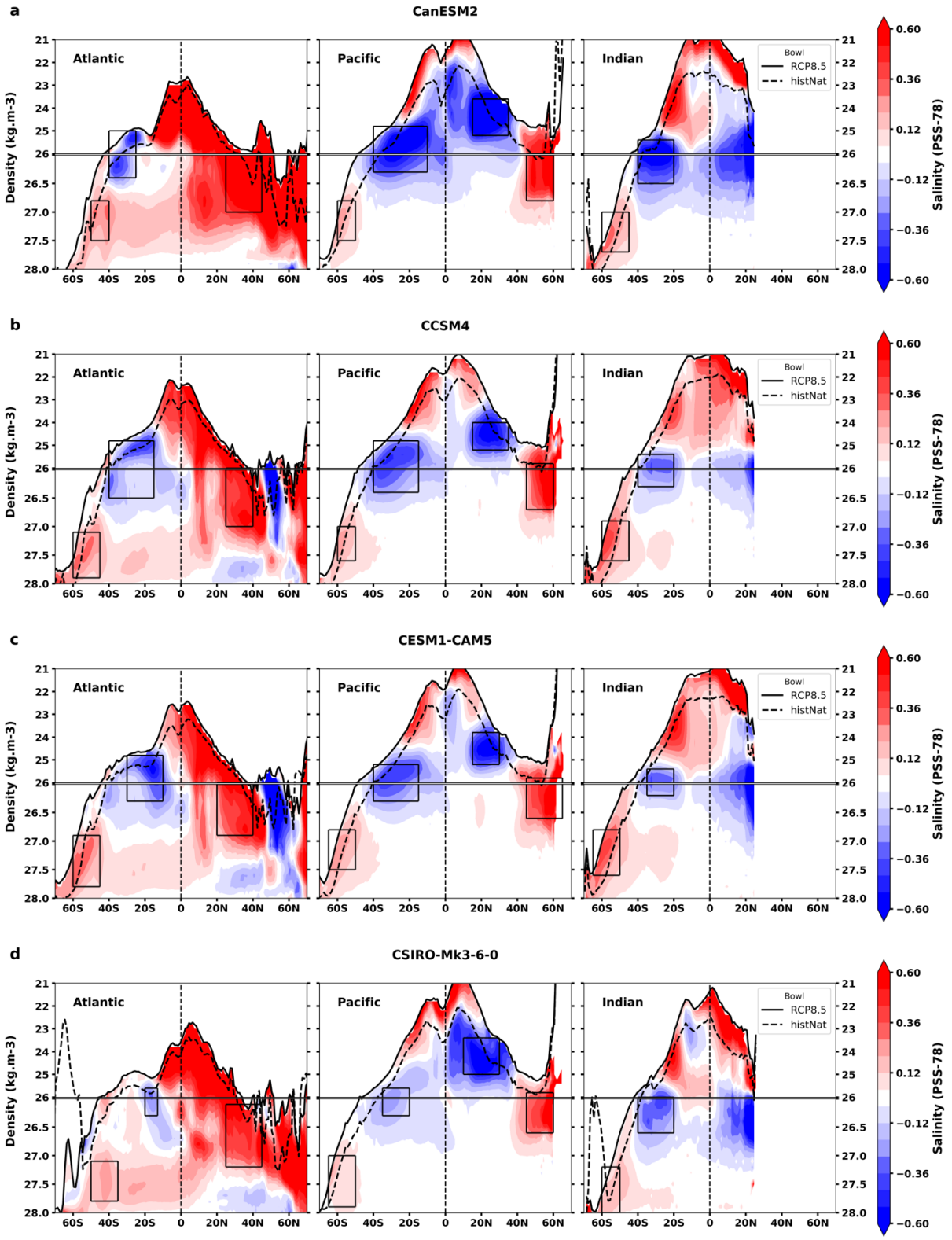
a
CanESM2
b
CCSM4
c
CESM1-CAM5
d
CSIRO-Mk3-6-0
Atlantic
Pacific
Indian
Bowl
RCP8.5
histNat
Density (kg.m-3)
Salinity (PSS-78)
60S 40S 20S 0 20N 40N 60N
21 22 23 24 25 26 26.5 27.0 27.5 28.0
0.60 0.36 0.12 −0.12 −0.36 −0.60

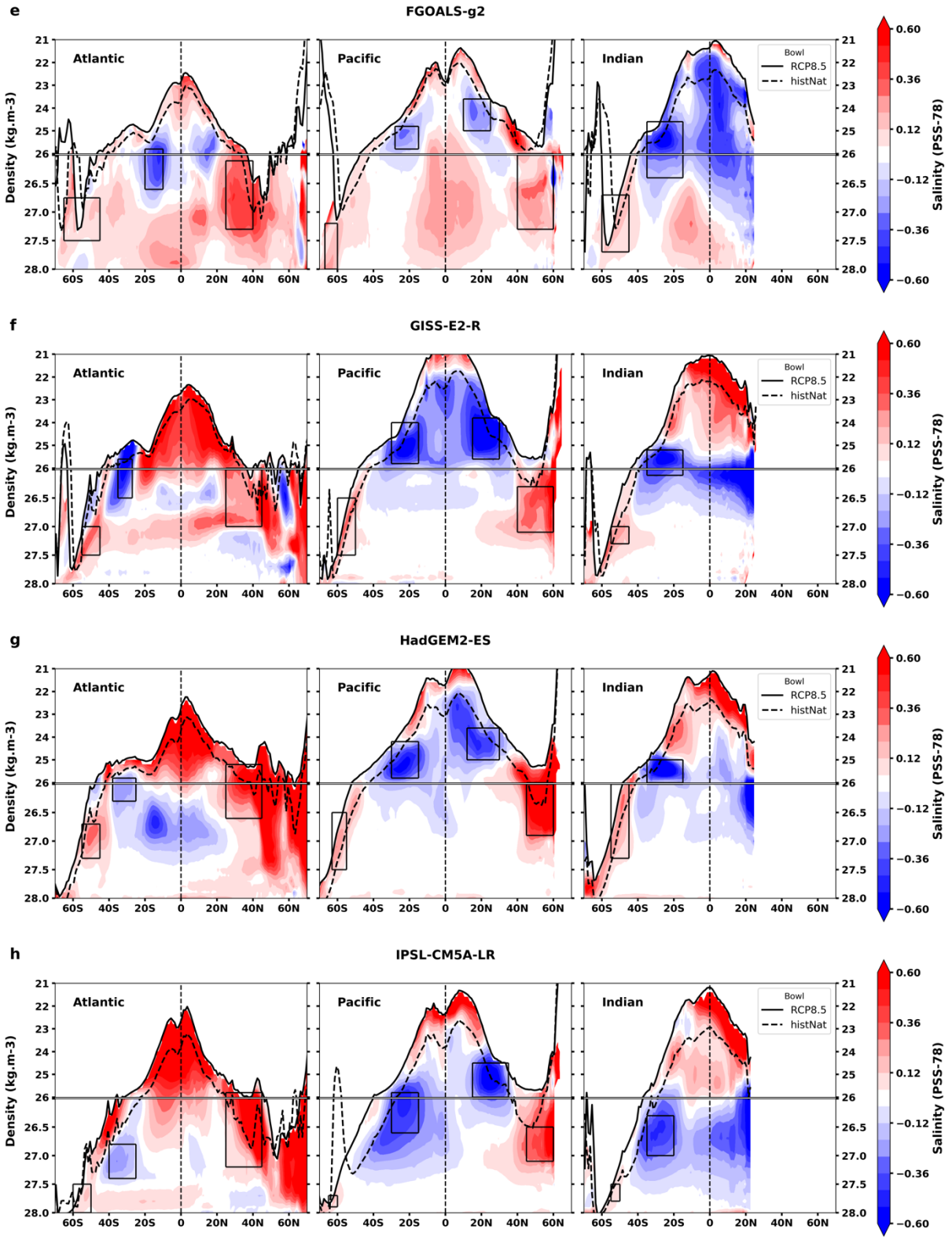
e
FGOALS-g2
f
GISS-E2-R
g
HadGEM2-ES
h
IPSL-CM5A-LR
Atlantic
Pacific
Indian
Bowl
RCP8.5
histNat
Density (kg.m-3)
Salinity (PSS-78)
21
22
23
24
25
26
26.5
27.0
27.5
28.0
60S
40S
20S
0
20N
40N
60N
0.60
0.36
0.12
−0.12
−0.36
−0.60

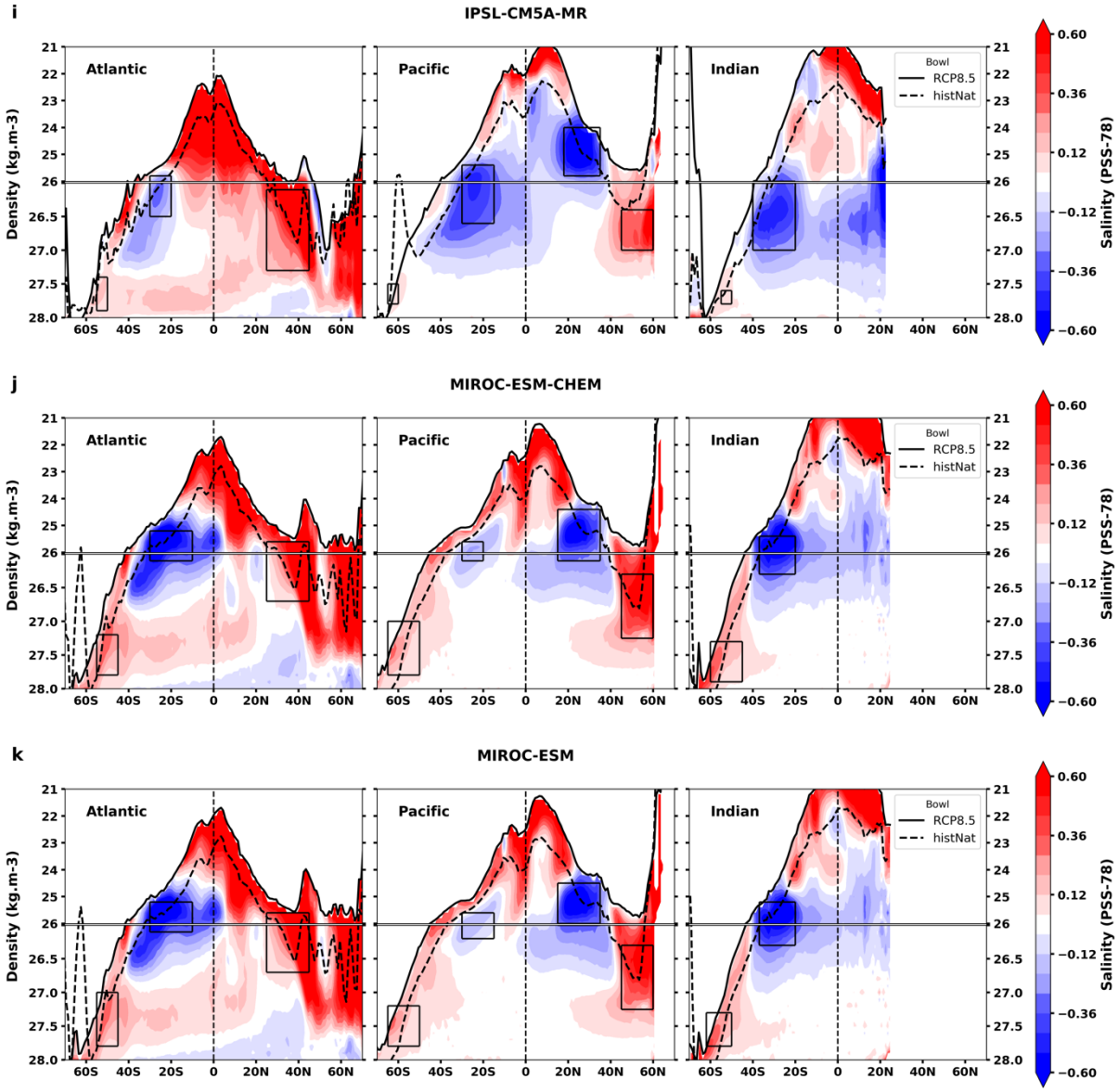

Supplementary Figure 4 Anthropogenic salinity change along density surfaces for the 11 model ensemble means, at the end of the 21st century (RCP8.5[2080-2100] - time average historicalNat). Black boxes represent where the regional time of emergence computation was done in each model for Figure 4 and Supplementary Figures 6, 8, 10, 11, 12 and 13. They also indicate where the 1950-2008 trends were calculated for the analysis of Figure 1c.

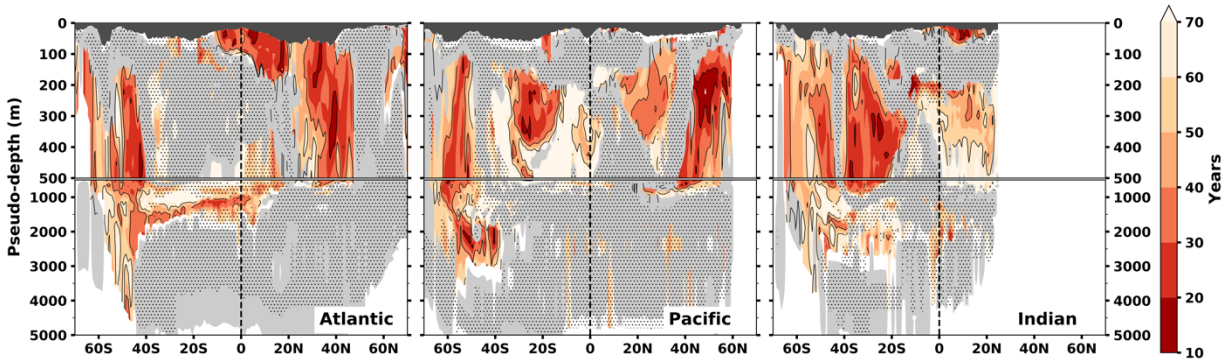

Supplementary Figure 5 25-75% inter-model range for the time of emergence of the anthropogenic salinity change, calculated for an ensemble of 11 models. Light grey regions mean no emergence of the 75th percentile of the distribution, while stippled regions show where the models don't agree on the sign of the signal (see Methods). The dark grey area at the surface corresponds to the ocean surface above the bowl.

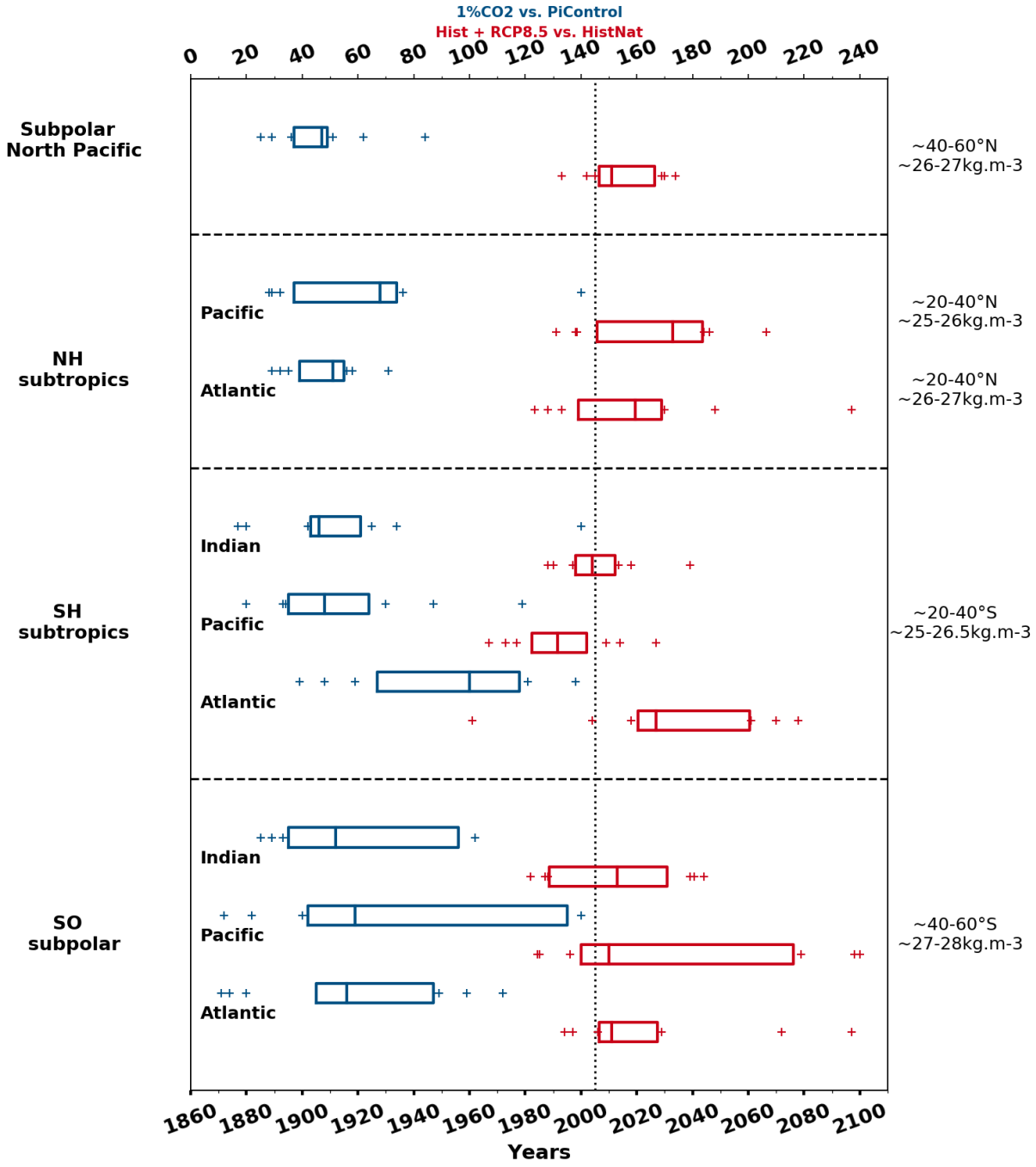

Supplementary Figure 6 Distribution of times of emergence. As in Figure 4 but as a function of time. Calculated from the anthropogenic (red) and pure CO2 (blue, from the 1pctCO2 experiment) signal for 9 regions of interest: the Southern Ocean subpolar range, the Southern Hemisphere subtropical range, the Northern Hemisphere subtropical range and the subpolar North Pacific. Boxes indicate 1st quartile, median and 3rd quartile.

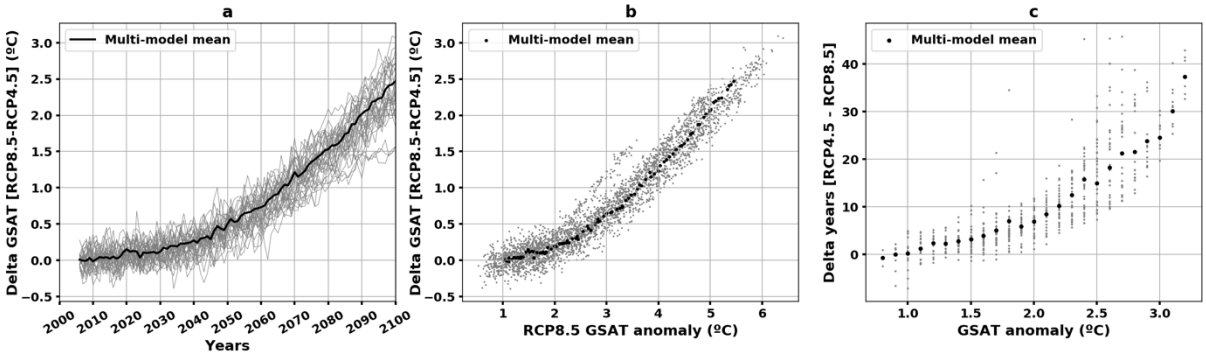

Supplementary Figure 7 Difference in Global Surface Air Temperature (GSAT) between the RCP8.5 and RCP4.5 scenario, as a function of time (a) and RCP8.5 warming (GSAT anomaly - b). Difference of years between the RCP4.5 and RCP8.5 scenarios at different levels of warming (c). Computed with the same model distribution as the rest of the study, with only 2 simulations missing out of 35 due to the absence of RCP4.5 data.

At a +2°C warming, there is only a 0.2°C – panel b - (or 8 years, panel c) difference between the two scenarios (for the multi-model mean, and the maximum of the distribution stays under 0.5ºC or 12 years). This value is smaller than the typical width of the boxplots in Figure 4 (or Supplementary Figure 6). Yet, our results show that the median signal emerges before 2020 (Figure 3a) and that by a +2°C warming, the majority of the inter-model distributions across regions have emerged (Figure 4). This means that the climate signal in most simulations and regions emerges before there is a significant difference in warming scenarios. We can therefore argue that a slower warming scenario will only potentially affect the later/warmer part of the distributions, which in most regions consists of a few (or even no) outliers, with the exception of the southern subtropical Atlantic where half of the distribution emerges after a +2°C warming. Thus, a slower warming scenario would simply delay the emergence of that part of the distribution.

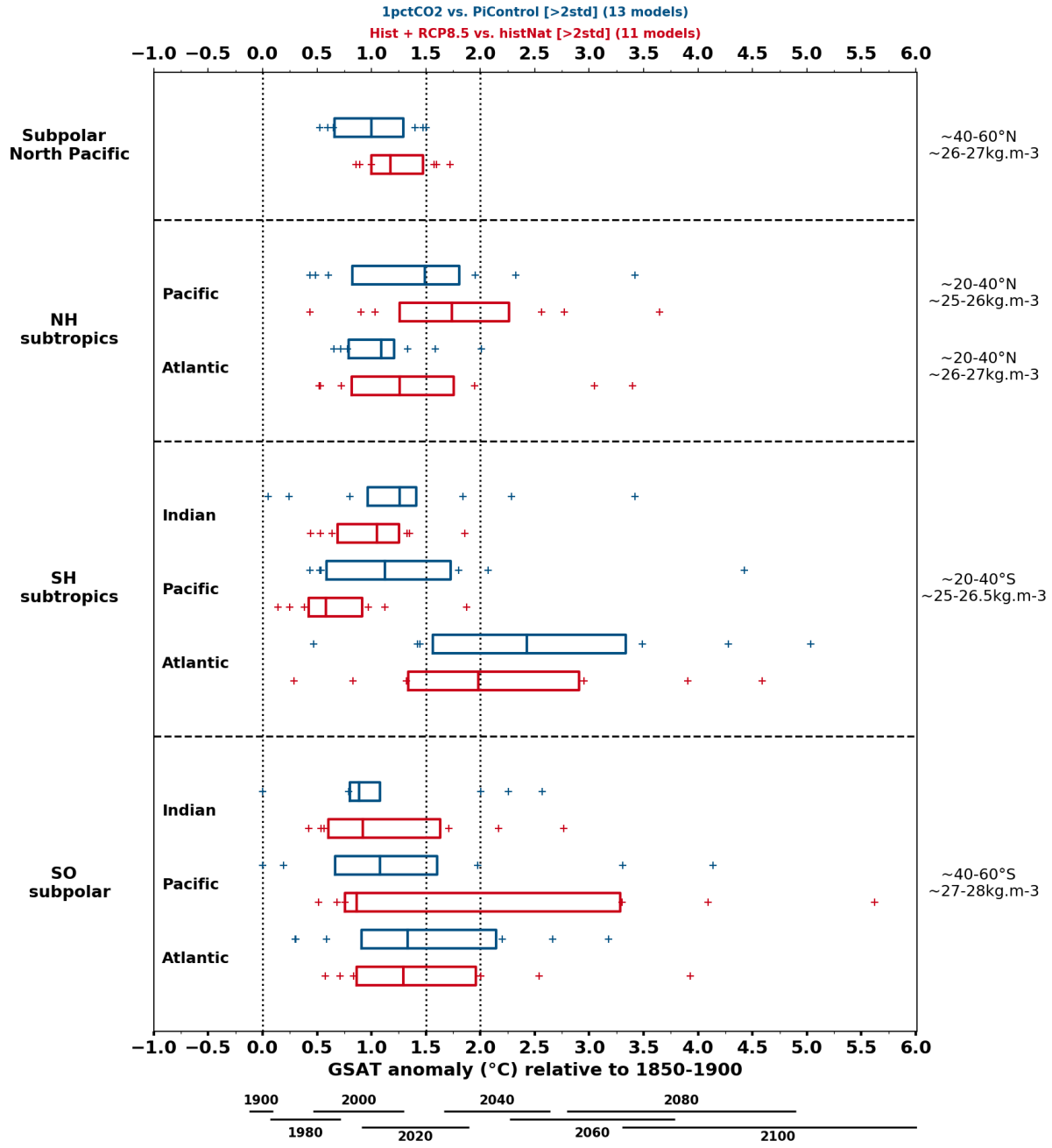

Supplementary Figure 8 Distribution of Global Surface Air Temperature at emergence. Calculated from the anthropogenic (red) and pure CO2 (blue, from the 1pctCO2 experiment) signal for 9 regions of interest: the Southern Ocean subpolar range, the Southern Hemisphere subtropical range, the Northern Hemisphere subtropical range and the subpolar North Pacific. Boxes indicate 1st quartile, median and 3rd quartile. Red boxes are as in Figure 4.

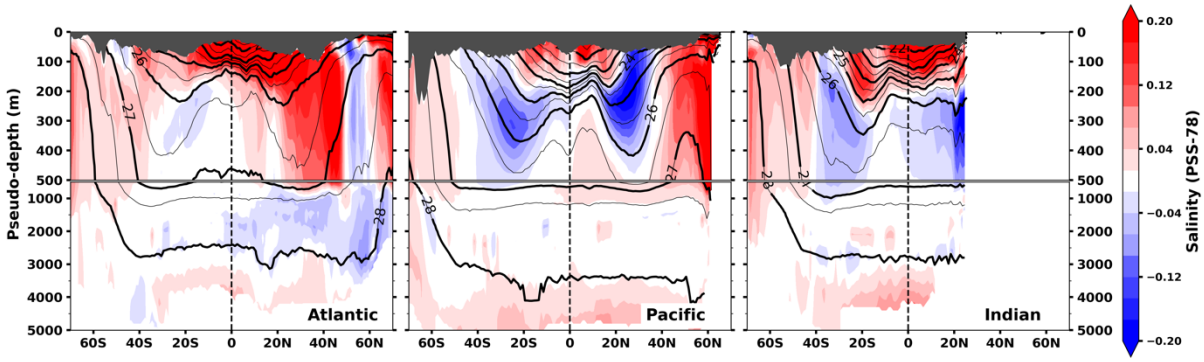

Supplementary Figure 9 Multi-model mean difference between a doubling of CO2 concentrations in the 1pctCO2 experiment, and the last 20 years of the piControl.

	hist+RCP8.5 vs. histNat	hist+RCP8.5 vs. PiControl	1pctCO2 vs. PiControl
ACCESS1-0	.	.	1
ACCESS1-3	.	.	1
BNU-ESM	.	.	1
CanESM2	5	5	.
CCSM4	6	6	1
CESM1-BGC	.	.	1
CESM1-CAM5	3	3	1
CNRM-CM5-2	.	.	1
CSIRO-Mk3-6-0	9	9	1
FGOALS-g2	1	.	.
GFDL-ESM2M	.	.	1
GISS-E2-R	3	.	.
HadGEM2-ES	2	2	1
IPSL-CM5A-LR	3	3	1
IPSL-CM5A-MR	1	1	1
IPSL-CM5B-LR	.	.	1
MIROC-ESM	1		.
MIROC-ESM-CHEM	1	1	.
TOTAL	**35**	**30**	**13**

Supplementary Table 1 CMIP5[2] models and number of members used in the ToE calculations

Supplementary Discussion

Sensitivity of ToE to noise definition

We chose a signal-to-noise ratio exceedance threshold of two, corresponding to a 95% confidence interval for the signal emergence. We tested how the ToE was affected for a threshold of one standard deviation instead (a less conservative choice, corresponding to a 67% confidence interval), as also discussed by e.g. Hawkins & Sutton (2012)[3], Lyu et al. (2014)[4], Rodgers et al. (2015)[5]. The regional anthropogenic ToE distributions are shown in Supplementary Figure 10 when using both one (light red) and two (dark red) standard deviations as the variability threshold. As expected, we find earlier times of emergence (corresponding to a weaker warming), with a shift in the distributions of about 10-20 years for the medians according to the regions (0.25-0.75ºC). Although this shift is not negligible, it doesn't change our understanding of the narrative, as one method is simply more conservative than the other. Displaying both methods allows for a larger distribution of probabilities, i.e. a larger spectrum of possible times of emergence in the real ocean.

The other sensitivity test was conducted by choosing the pre-industrial control (PiControl) instead of the historicalNat experiment in the definition of signal and noise of the anthropogenic ToE. As historicalNat includes external natural forcings and PiControl does not, a first guess resulting from using PiControl instead of historicalNat in ToE definition would be to obtain earlier times of emergence. However, the results are almost not changed by this choice (see Supplementary Figure 11), and overall, the distributions are well aligned, and this choice plays a secondary role in ToE sensitivity. This is in fact consistent with the use of the interannual noise, which is similar between the historicalNat and PiControl experiments. At decadal to multidecadal timescales, the noise levels might not be so close (possibly larger for historicalNat with the influence of strong volcanic eruptions during certain decades).

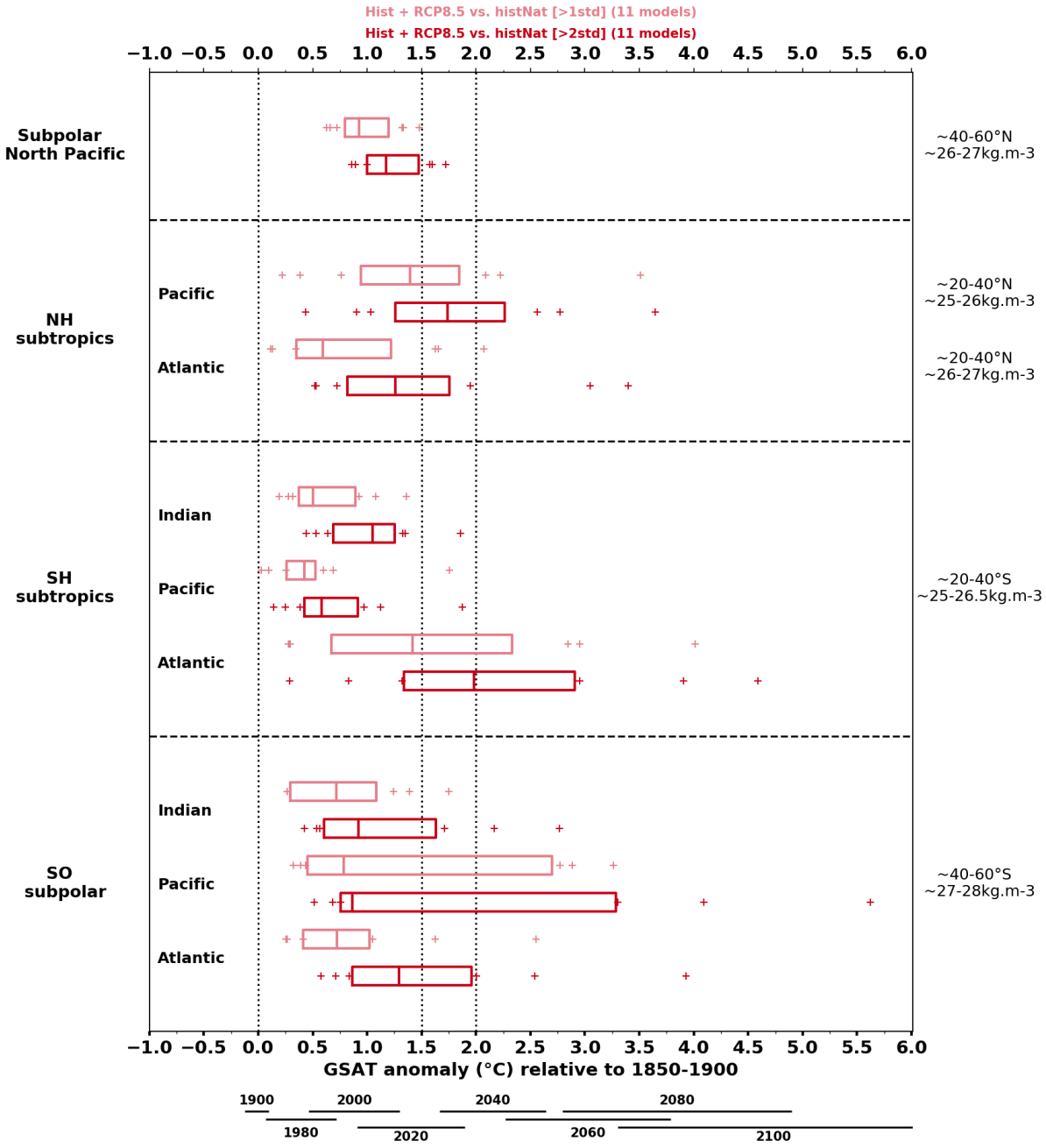

Supplementary Figure 10 Distribution of Global Surface Air Temperature at emergence. Calculated from the anthropogenic signal with 1 S/N as the ToE threshold (light red, 67% confidence interval) and 2 (dark red, as in Figure 4 of the paper, 95% confidence interval).

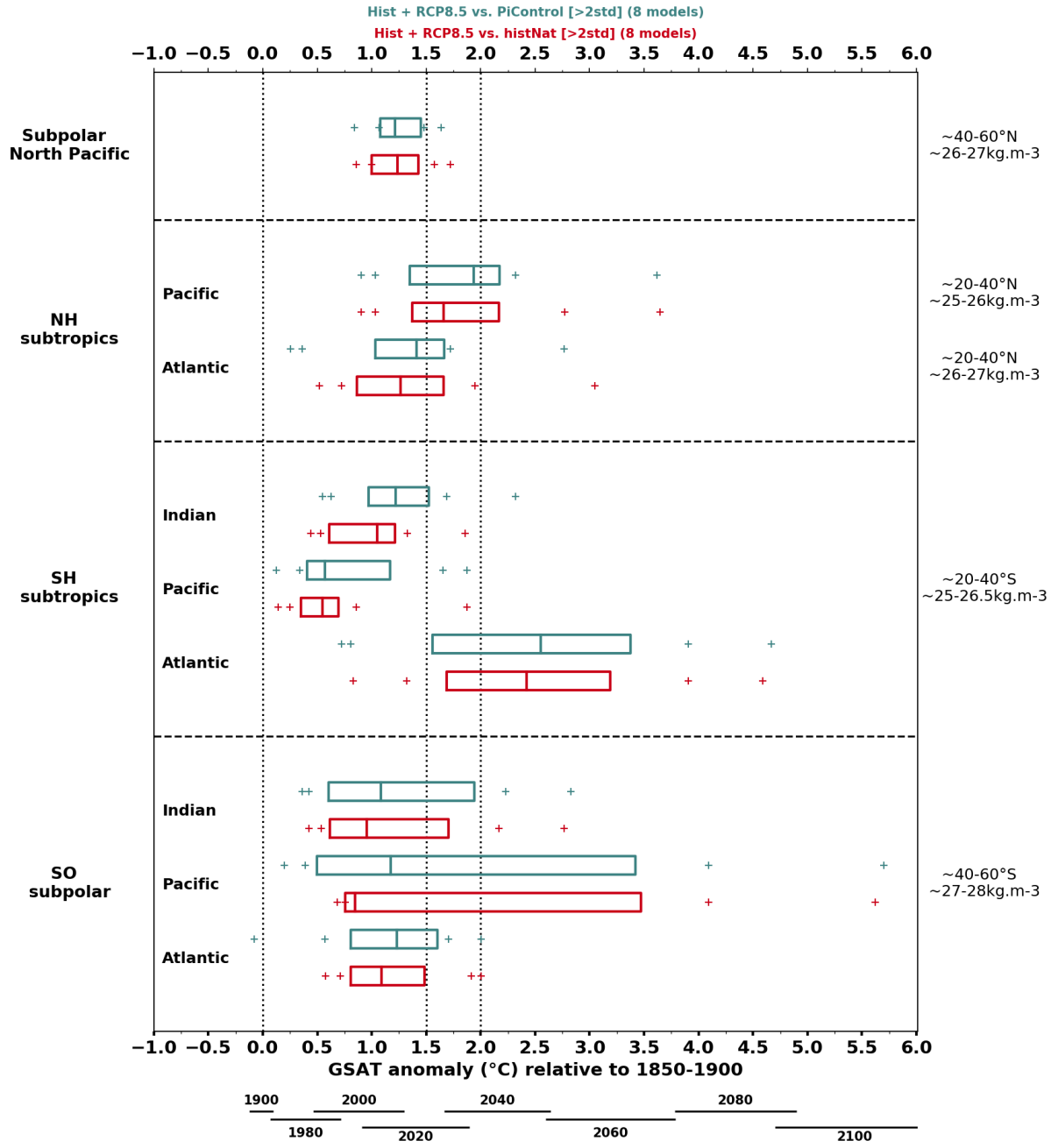

Supplementary Figure 11 Distribution of Global Surface Air Temperature at emergence. Calculated from the anthropogenic signal using historicalNat in the definition of signal and noise (red, as in Figure 4 of the paper) and piControl instead (turquoise, see Methods).

Relative contributions of signal and noise to the ToE spread

We now investigate the relative importance of signal and background noise in controlling the ToE spread within models and regions.

We first consider the inter-model spread within each region (Supplementary Figure 12) and find there are two possible opposite configurations of ToE/noise relationship across realizations. The first configuration is the absence of any discernible linear fit between the noise and ToE (e.g. Southern Subtropical Atlantic, Northern Subtropical Pacific). In the second configuration (e.g. Northern subtropical Atlantic, subpolar Southern Pacific), the noise explains the ToE at the 1st order (linear fit), and the signal explains it at the 2nd order (dispersion around the fit). The background noise being equal for all members of the same model in each region, the spread in ToE within several members of one model lies in the different initial conditions of the signal, thus exhibiting the role of internal variability of the climate system (e.g. opposite phases of an oscillation).

We now wish to answer the following question: is the spatial pattern of the noise controlling the ToE? To address that question, we compare ToE across regions, by considering the ToE/noise relationship separately for each model (Supplementary Figure 13). If the noise level controlled the ToE spread across regions within a model, then there would be a clear linear fit between the two. However, we find that except for a few models where there is indeed a discernable fit (e.g. FGOALS-g2, MIROC-ESM, MIROC-ESM-CHEM), ToE is not a clear function of the background noise level, i.e. the regions with the highest noise don't necessarily have the latest ToE.

We conclude that overall it is not (or not only) the background noise threshold (1 or 2 interannual standard deviations, i.e. the "bounds" of natural variability over a long time series) that predominantly explains the spread in the time of emergence but the signal, i.e. either the strength of the forced response, or the decadal to multi-decadal variability of the signal itself representing different phases of internal (unforced) or naturally-forced variability (no smoothing was applied on the annual values of the signal in this study). This is well illustrated by the fact that different members of the same model can have ToE differences of more than 20 years in the same region while having the same background noise level, which means the ToE is controlled by the different phases of internal variability of the signal (Supplementary Figure 14 – signal and noise time series).

Thus, uncertainties associated to inter-model spread of ToE may be reduced in the future by possible model improvements, but part of the spread won't be able to be narrowed due to

different representations of internal variability that modulates the response to anthropogenic forcing.

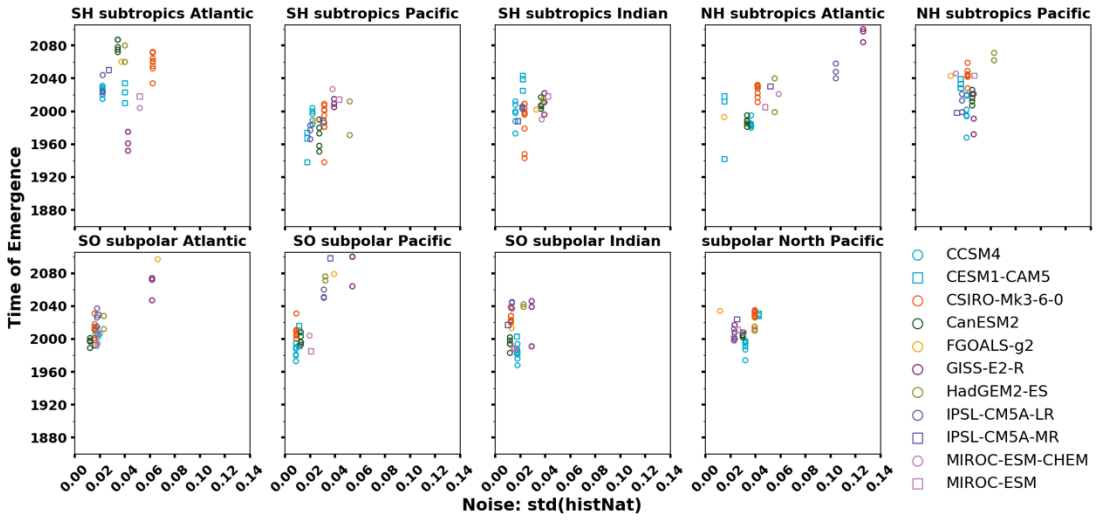

Supplementary Figure 12 Time of Emergence as a function of "noise" (i.e. the standard deviation of the historicalNat experiment), distribution of the models per region.

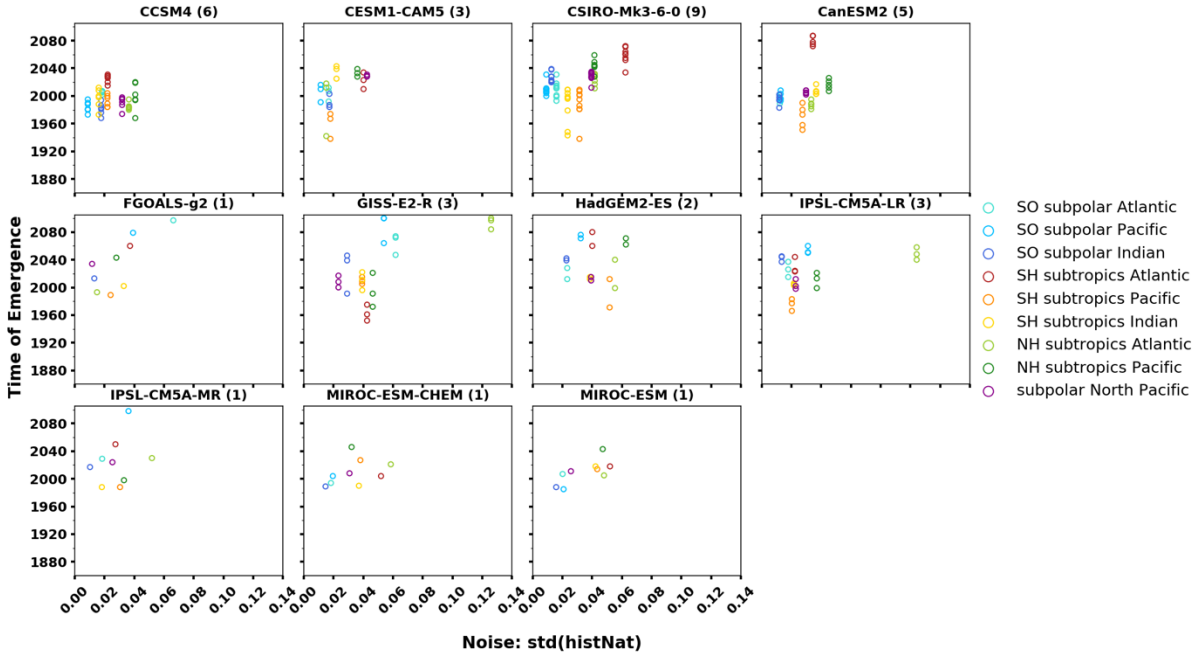

Supplementary Figure 13 Time of Emergence as a function of "noise" (i.e. the standard deviation of the historicalNat experiment), distribution of the regions per model.

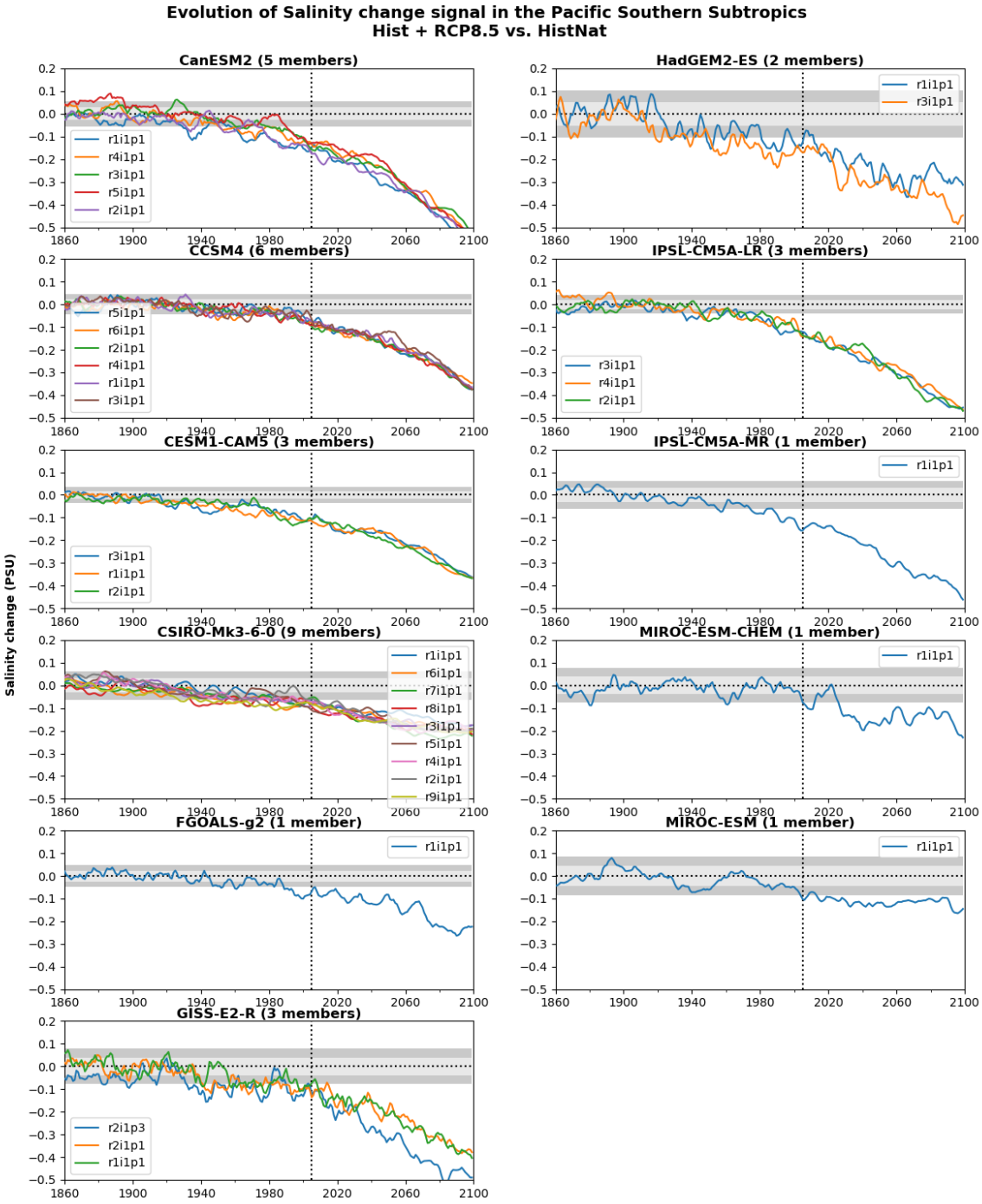

Supplementary Figure 14 Evolution of the anthropogenic salinity change signal in the Pacific southern subtropical region, for every model and member used in this study. The light grey area encompasses the interval plus or minus one standard deviation of the historicalNat ensemble mean, while the dark grey area encompasses plus or minus twice the standard deviation (i.e. the noise bounds).

References

1. Durack, P. J. & Wijffels, S. E. Fifty-Year Trends in Global Ocean Salinities and Their Relationship to Broad-Scale Warming. *J. Clim.* **23**, 4342–4362 (2010).

2. Taylor, K. E., Stouffer, R. J. & Meehl, G. A. An Overview of CMIP5 and the Experiment Design. *Bull. Am. Meteorol. Soc.* **93**, 485–498 (2012).

3. Hawkins, E. & Sutton, R. Time of emergence of climate signals. *Geophys. Res. Lett.* **39** (2012).

4. Lyu, K., Zhang, X., Church, J. A., Slangen, A. B. A. & Hu, J. Time of emergence for regional sea-level change. *Nat. Clim. Change* **4**, (2014).

5. Rodgers, K. B., Lin, J. & Frölicher, T. L. Emergence of multiple ocean ecosystem drivers in a large ensemble suite with an Earth system model. *Biogeosciences* **12**, 3301–3320 (2015).

Appendix

B

Ocean drift in the IPSL-CM6A-LR model: test points

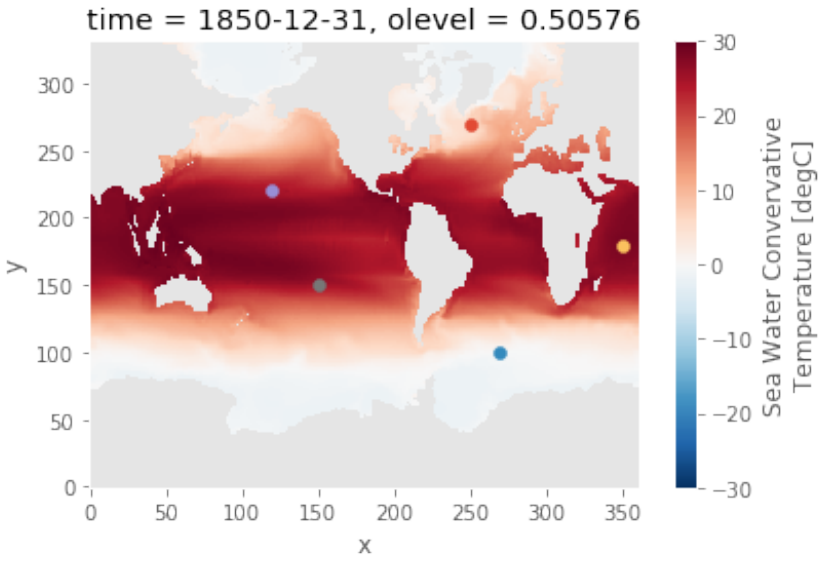

Figure B.1: Map of the test points shown below.

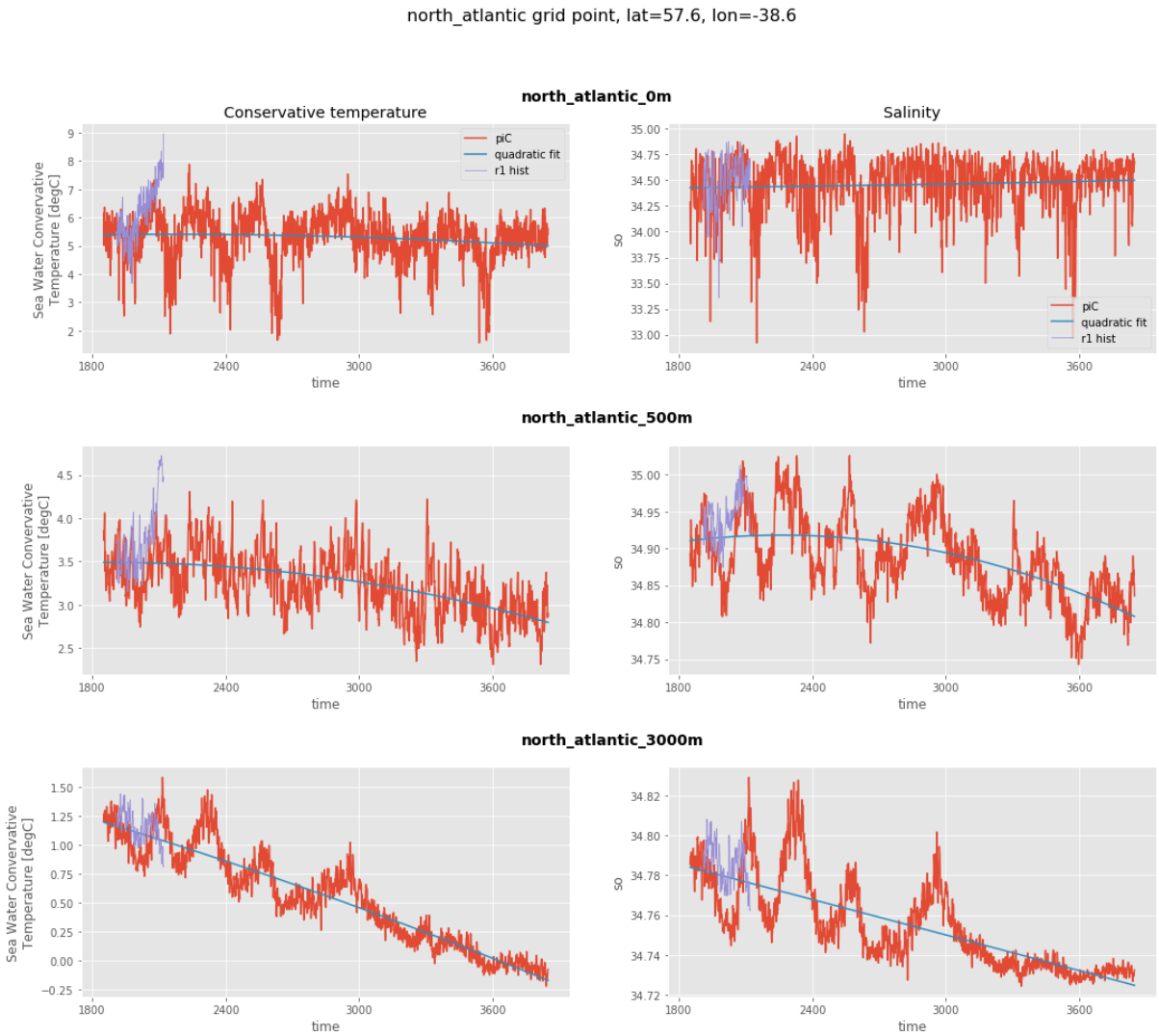

Figure B.2: Temperature (left) and salinity (right) for a grid point in the North Atlantic ocean (see map in figure B.1), at the surface (top), 500m (middle) and 3000m (bottom).

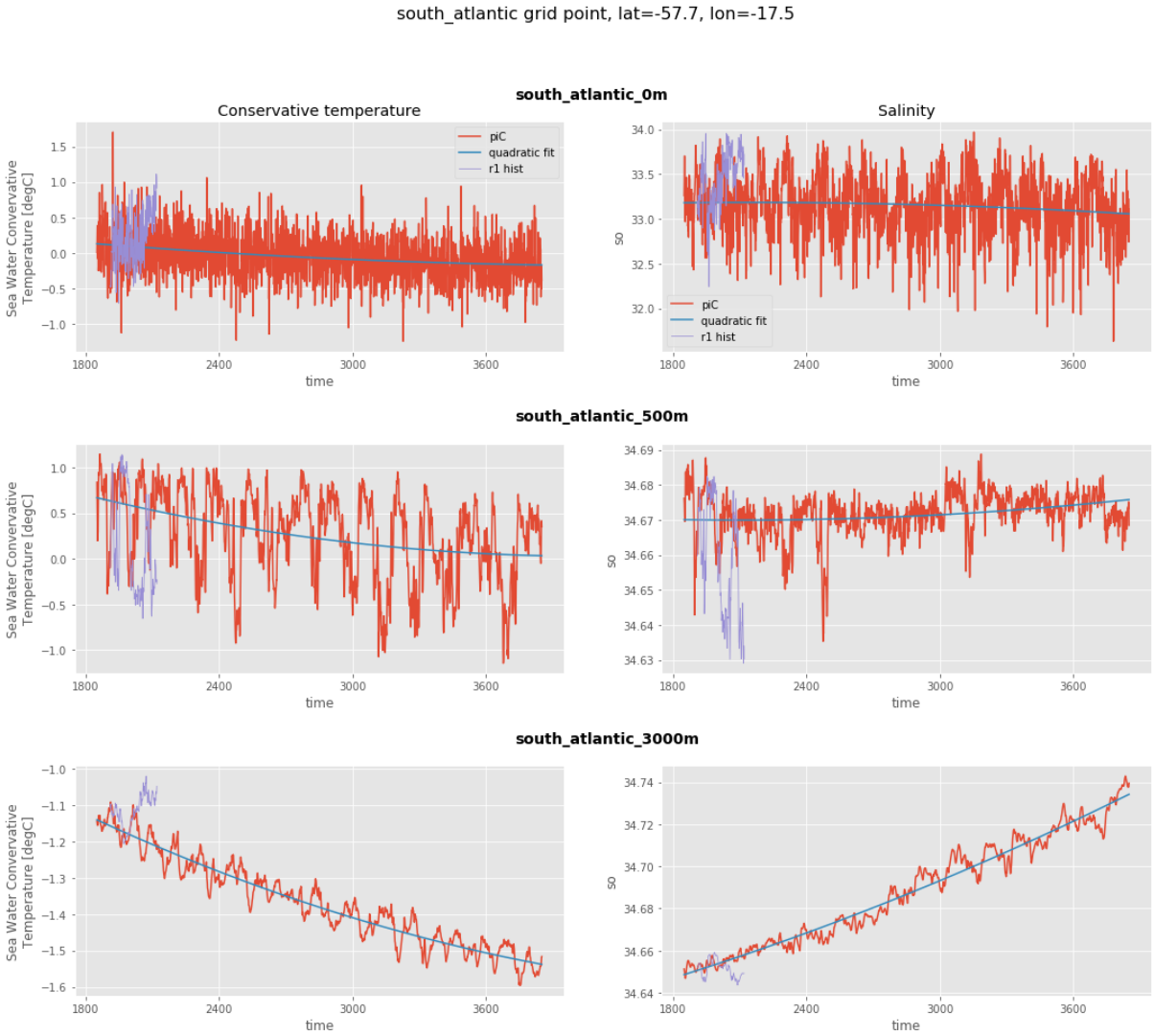

Figure B.3: Temperature (left) and salinity (right) for a grid point in the South Atlantic ocean (see map in figure B.1), at the surface (top), 500m (middle) and 3000m (bottom).

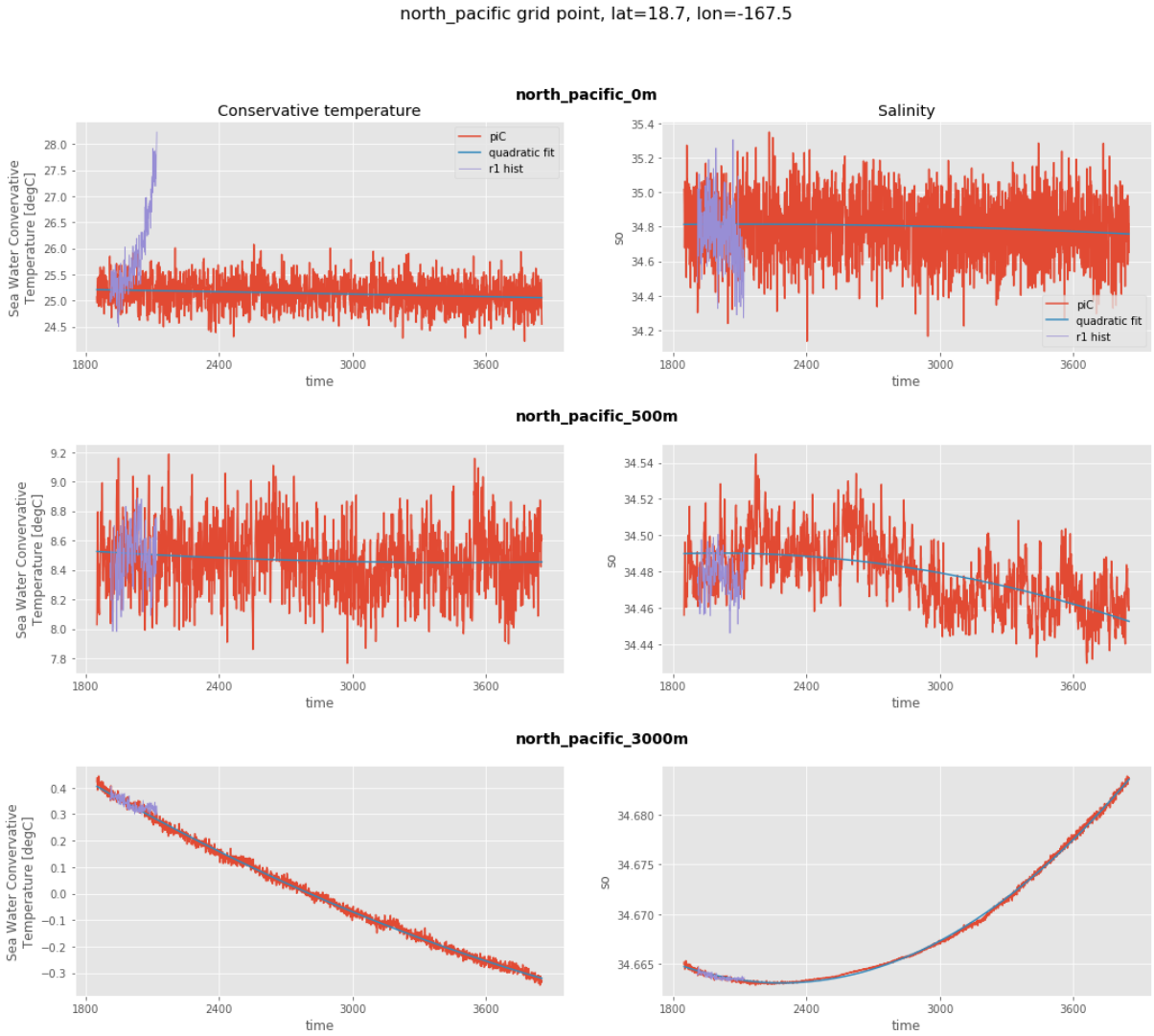

Figure B.4: Temperature (left) and salinity (right) for a grid point in the North Pacific ocean (see map in figure B.1), at the surface (top), 500m (middle) and 3000m (bottom).

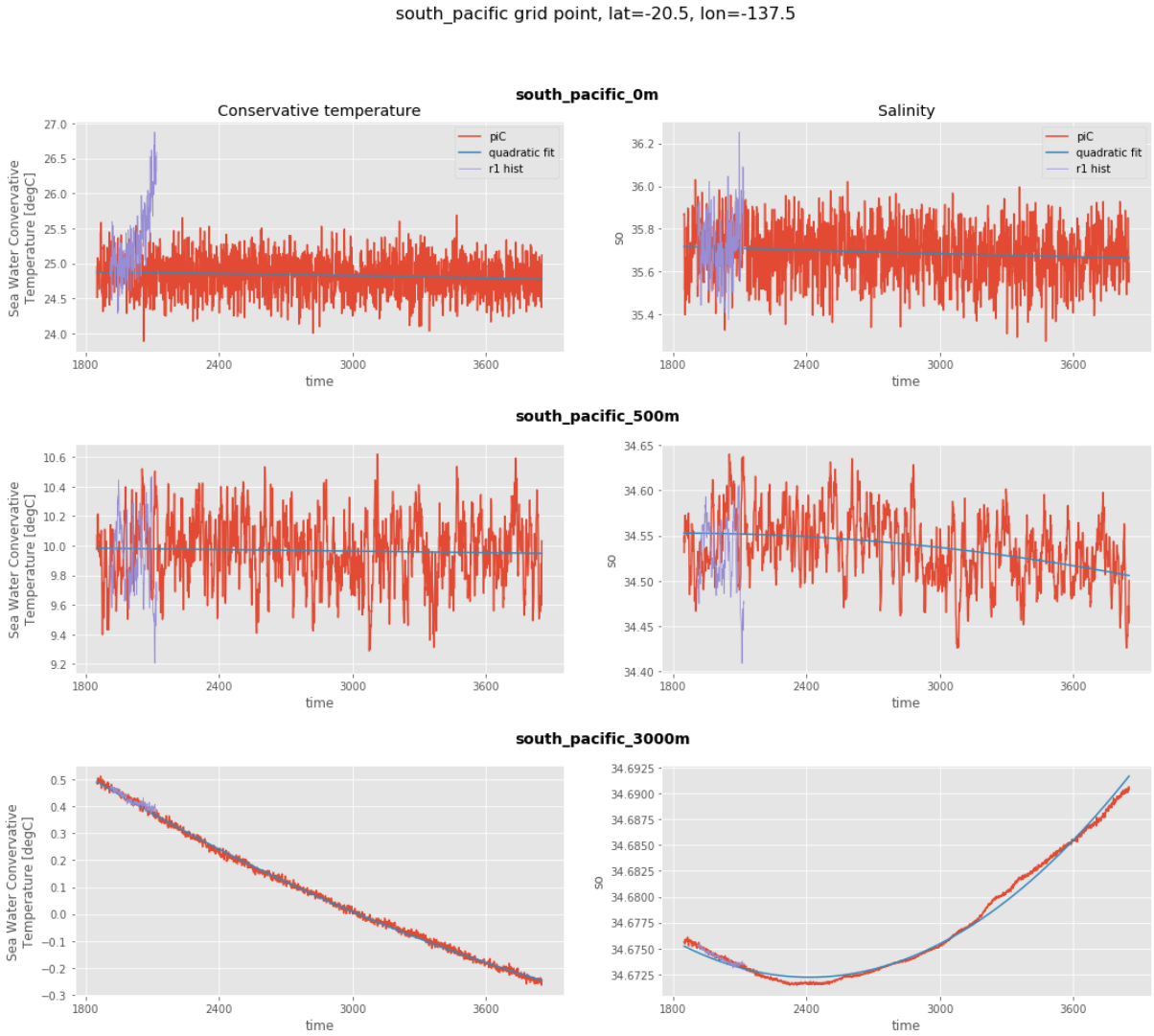

Figure B.5: Temperature (left) and salinity (right) for a grid point in the South Pacific ocean (see map in figure B.1), at the surface (top), 500m (middle) and 3000m (bottom).

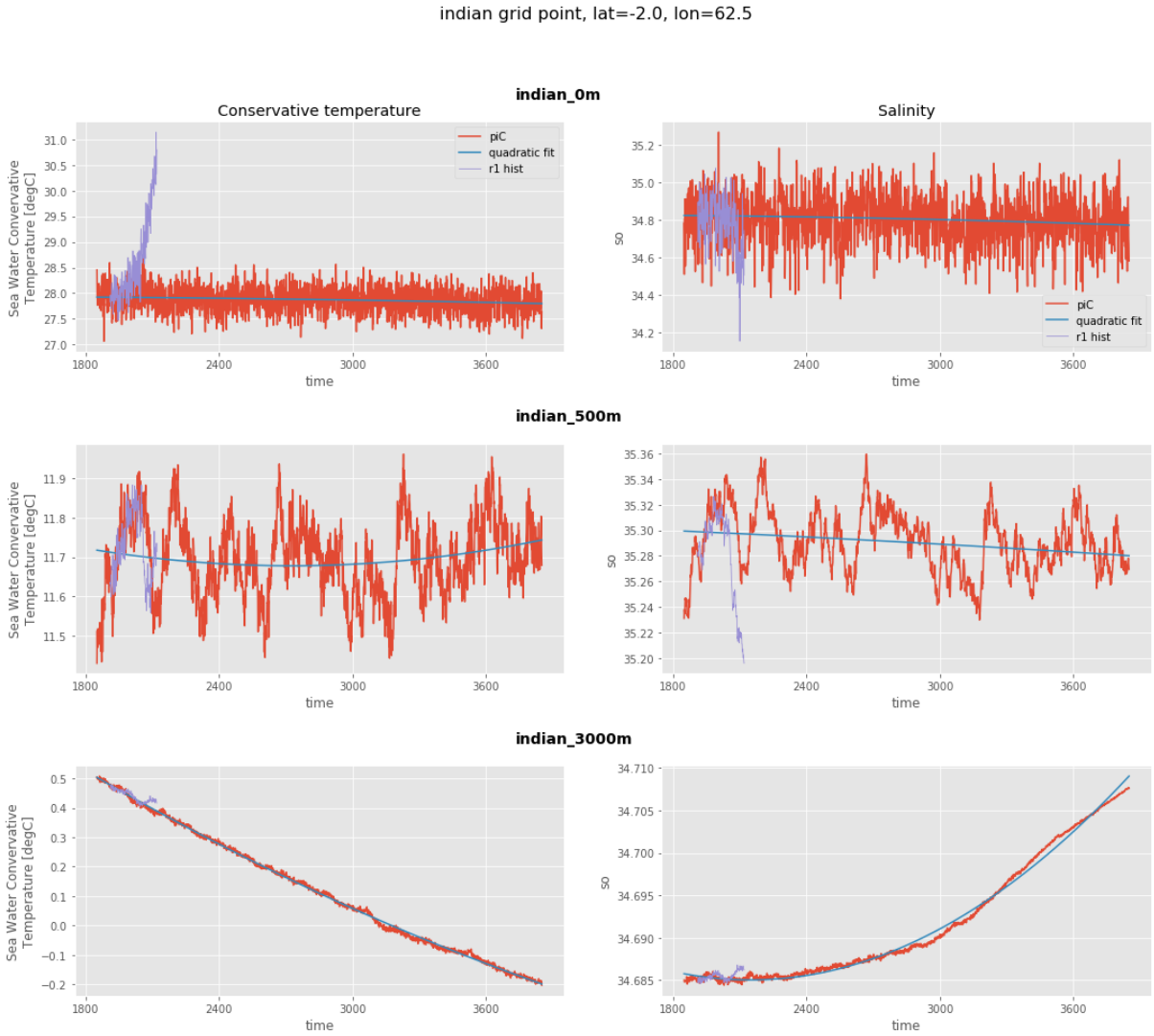

Figure B.6: Temperature (left) and salinity (right) for a grid point in the Indian ocean (see map in figure B.1), at the surface (top), 500m (middle) and 3000m (bottom).

Appendix

C Numerical configuration: sensitivity

1 Prescribed chlorophyll field

Here we show the difference in SST in the first year of simulation between CTL and piControl for different options of the prescribed chlorophyll field (see chapter III):

- nn_chldta=2: the surface chlorophyll from piControl is read and vertically interpolated (figure C.1)
- nn_chldta=2: the surface chlorophyll from an observed climatology is read and vertically interpolated (figure C.2)
- nn_chldta=0: the surface chlorophyll is imposed at the constant and uniform value of 0.05 mg.m^{-3} (figure C.3)
- nn_chldta=1: the surface chlorophyll from piControl is read (no vertical interpolation, figure C.4)
- nn_chldta=3: the full 3D chlorophyll from piControl is read (left column in figures C.1-C.4)

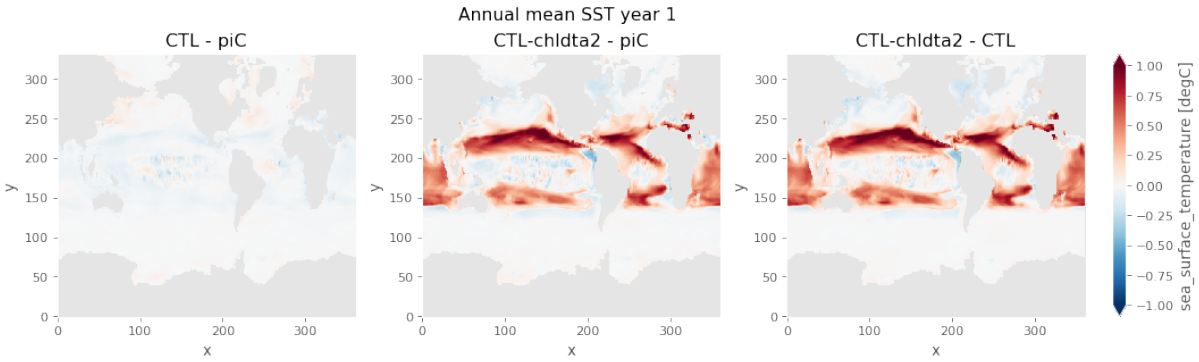

Figure C.1: Difference in SST in the 1st year between: (1st column) piControl and CTL when reading the 3D chlorophyll field from piControl; (2nd column) piControl and CTL when reading the 2D chlorophyll field from piControl vertically interpolated; (3rd column) the two CTL experiments mentioned above.

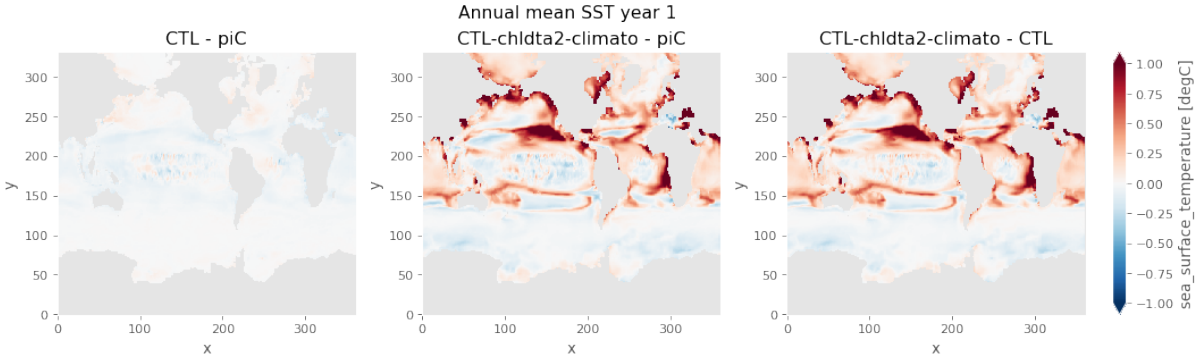

Figure C.2: Difference in SST in the 1st year between: (1st column) piControl and CTL when reading the 3D chlorophyll field from piControl; (2nd column) piControl and CTL when reading the 2D chlorophyll field from an observed climatology; (3rd column) the two CTL experiments mentioned above.

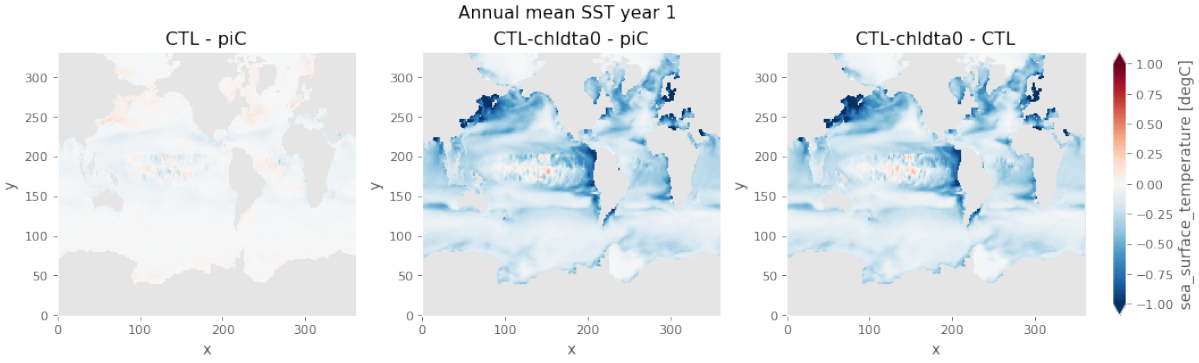

Figure C.3: Difference in SST in the 1st year between: (1st column) piControl and CTL when reading the 3D chlorophyll field from piControl; (2nd column) piControl and CTL when reading a constant and uniform chlorophyll field; (3rd column) the two CTL experiments mentioned above.

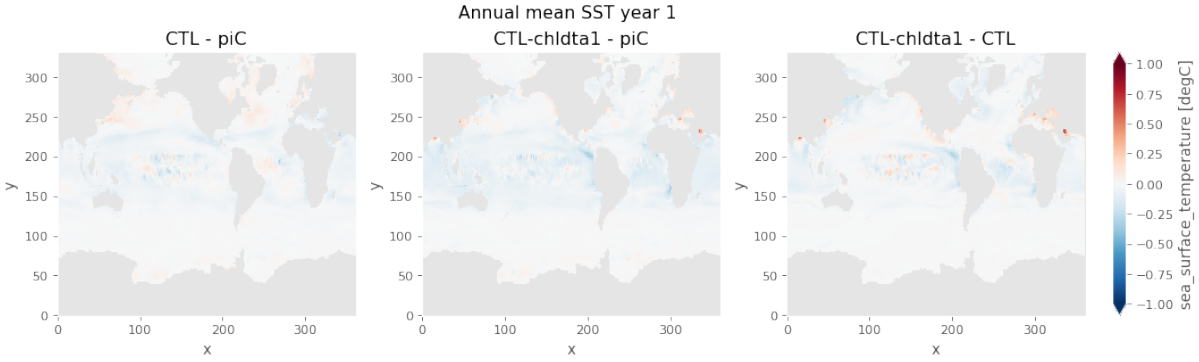

Figure C.4: Difference in SST in the 1st year between: (1st column) piControl and CTL when reading the 3D chlorophyll field from piControl; (2nd column) piControl and CTL when reading the 2D chlorophyll field from piControl without activating the vertical interpolation; (3rd column) the two CTL experiments mentioned above.

2 Temperature below freezing point in ocean-only simulations

Here we discuss two alternatives to the treatment of the freezing-point temperature tested on the entire 251 years for both CTL and ALL:

1. At each time step, the temperature is relaxed to the freezing point temperature in the mixed layer when it falls below freezing, with a 30-day relaxation period. This is equivalent to adding a positive heat flux in the ocean locally, thus not conserving heat in CTL relatively to piControl nor in ALL relatively to the historical+ssp245 ensemble. The question is to know whether this heat flux becomes large in time and if it has an impact on the rest of the ocean.
2. At each time step, we block the temperature to the freezing point temperature in the mixed layer when it falls below freezing, and we remove the equivalent heat flux in the non-solar heat flux qns distributed over the entire ocean surface, i.e. at each time step and every grid point: qns(x,y,t) = qns(x,y,t) - qfrz(t)/S with qfrz the equivalent heat flux added by blocking the temperature to the freezing point over the mixed layer, integrated vertically and horizontally, and S the ocean area. This redistribution of the added heat flux allows for the global conservation of heat relatively to the coupled experiments.

In the second option, over 150 years, the globally-averaged heat flux added and redistributed in qns due to temperatures falling below the freezing point is qfrz=0.06 $W.m^{-2}$ in CTL compared to the net incoming heat flux -0.14 $W.m^{-2}$ and rises to qfrz=0.12 $W.m^{-2}$ compared to the total -0.13 $W.m^{-2}$ over the entire simulation (251 years). In ALL, qfrz=0.12 $W.m^{-2}$ over the first 150 years compared to the net incoming heat flux 0.015 $W.m^{-2}$. Over the entire simulation, it rises to qfrz=0.16 $W.m^{-2}$ compared to a total 0.61 $W.m^{-2}$. This additional heat flux is thus globally non-negligible in both simulations and rises over time. Although the second option conserves heat, it implies a global cooling in the first layers of the ocean because of the redistribution of qfrz in qns, and a warming at depth to compensate for this surface cooling. This is shown in figures C.5, C.6 and C.7. The global SST cooling in the ALL experiment in this configuration is such that it leaves the range of the large ensemble (figure C.7, right). In CTL, the temperature drifts away from the piControl with the treatment of the freezing point in almost all layers of the ocean.

On the opposite, the first option (imposing a relaxation to the freezing point without any redistribution) induces a better SST anomaly pattern compared with the large ensemble (figure C.8) but a warming everywhere in the ocean in CTL and in ALL since heat is added, which makes the temperature in CTL drift away from piControl as well, much more than the "original" CTL experiment where temperature evolves freely (figure C.9). This additional heat flux amounts to 0.074 $W.m^{-2}$ in CTL and 0.11 $W.m^{-2}$ in ALL over the entire simulation (less than in the other option since here we relax instead of blocking the temperature), which is non-negligeable compared to qt=0.16 $W.m^{-2}$ in ALL. This relaxation makes the temperature in ALL warm faster and earlier than when letting the temperature evolve freely (i.e. when respecting the heat budget). This might have consequences on the kind of analyses we are interested in, e.g. the timing of departure of a warming signal from background climate variability.

To verify that the heat transport is not affected by the temperature below freezing and to better compare the freely-evolving case with the relaxation case, we show in figure C.10 the evolution of averaged temperature and salinity at different depths in the North Atlantic (in close contact with the ice-covered region where temperatures fall below freezing) and in a region farther away from the Arctic (the subtropical Southern Ocean, figure C.11). The differences in-between the two cases of the ALL experiment are not very large, confirming that the heat transport doesn't seem much affected by the temperatures below freezing. The freely-evolving case however is found to be better at reproducing the piControl than the relaxation test in the CTL experiment, even for salinity which seems to drift away from the piControl because of the temperature relaxation even in the subtropical Southern Ocean.

In summary, apart from better reproducing the SST anomaly pattern in the Arctic in the ALL experiment, preventing the temperature from falling (or falling too much) below the freezing point does not have other advantages. Letting the temperature evolve freely is found overall to not impact the response to anthropogenic climate change in other regions and to be better at reproducing the temporal evolution of the piControl, which ensures minimal drift from our reference simulation. We thus chose to run all the

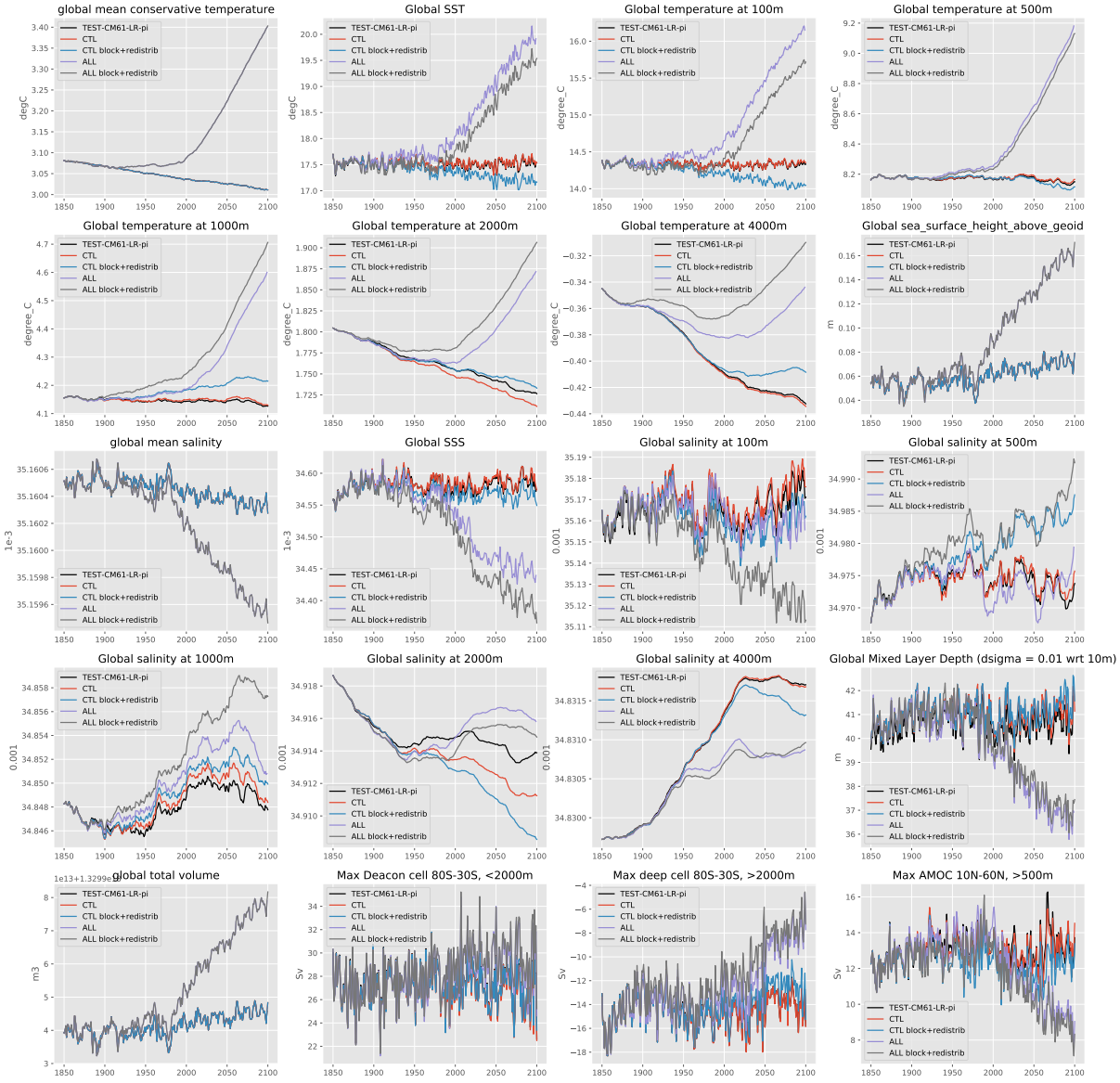

Figure C.5: Intermonitoring of 1D variables for the coupled piControl (black), the flux-forced CTL (red) and the ALL experiment (purple), compared with the CTL and ALL when blocking the temperature when it falls below the freezing point and redistributing the equivalent heat flux over the ocean area in the non-solar heat flux (blue and grey respectively).

experiments without any treatment of the temperature below freezing other than in the equation of state.

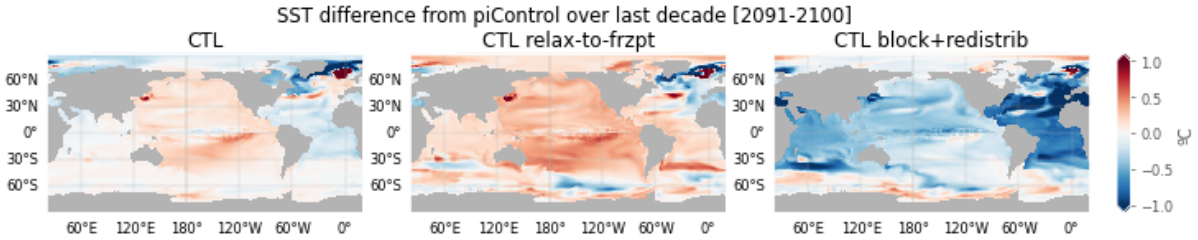

Figure C.6: SST difference in the CTL experiment from the coupled piControl, when temperature evolves freely (left), is relaxed to the freezing point when it falls below (middle), and is prevented from falling below the freezing point by blocking it and redistributing the associated heat flux over the ocean area (right).

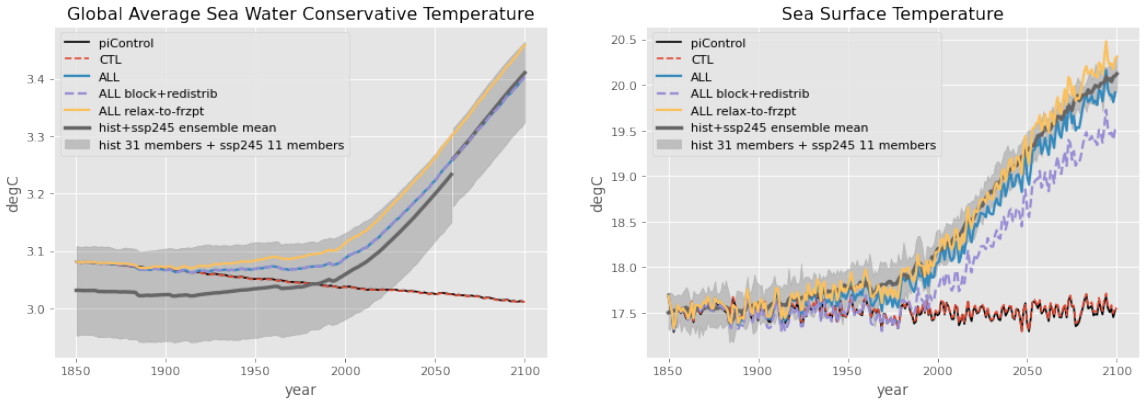

Figure C.7: Global mean temperature (left) and SST (right) for the IPSL-CM6A-LR ensemble (grey), piControl (black), CTL (dotted red), ALL (blue), ALL with relaxation to freezing point temperature (yellow) and ALL with blocking of the temperature to the freezing point and redistribution of the associated heat flux (dotted purple).

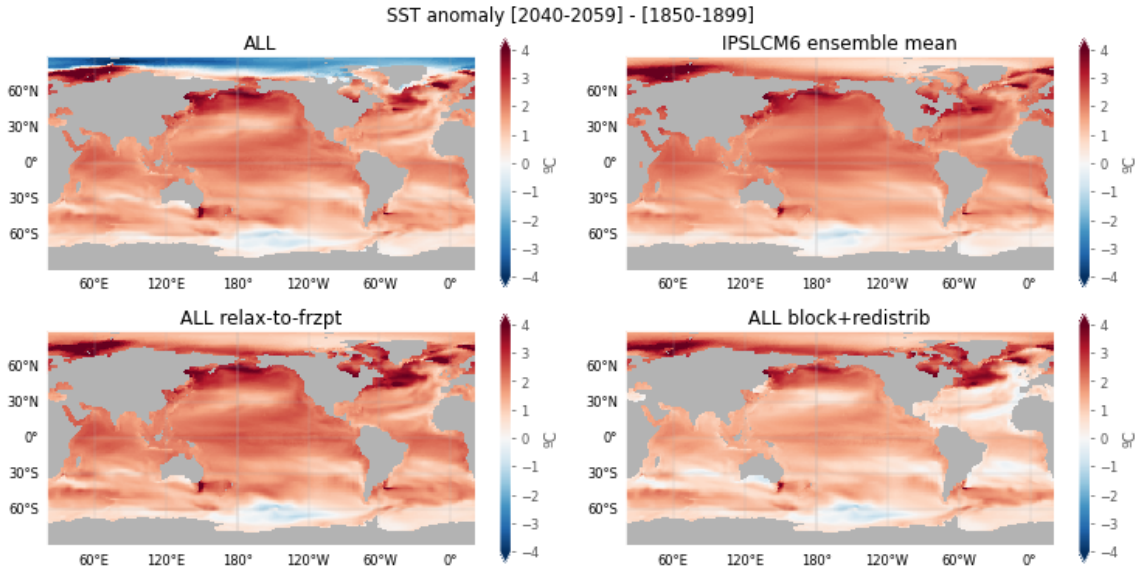

Figure C.8: SST anomaly in 2040-2059 relative to 1850-1899 in ALL when temperature evolves freely (top left), in the IPSL-CM6A-LR historical-EXT ensemble mean (top right), in ALL when the temperature below freezing point is relaxed to the freezing point (bottom left) and in ALL when temperature is blocked to the freezing point and the associated heat flux is redistributed over the ocean surface (bottom right).

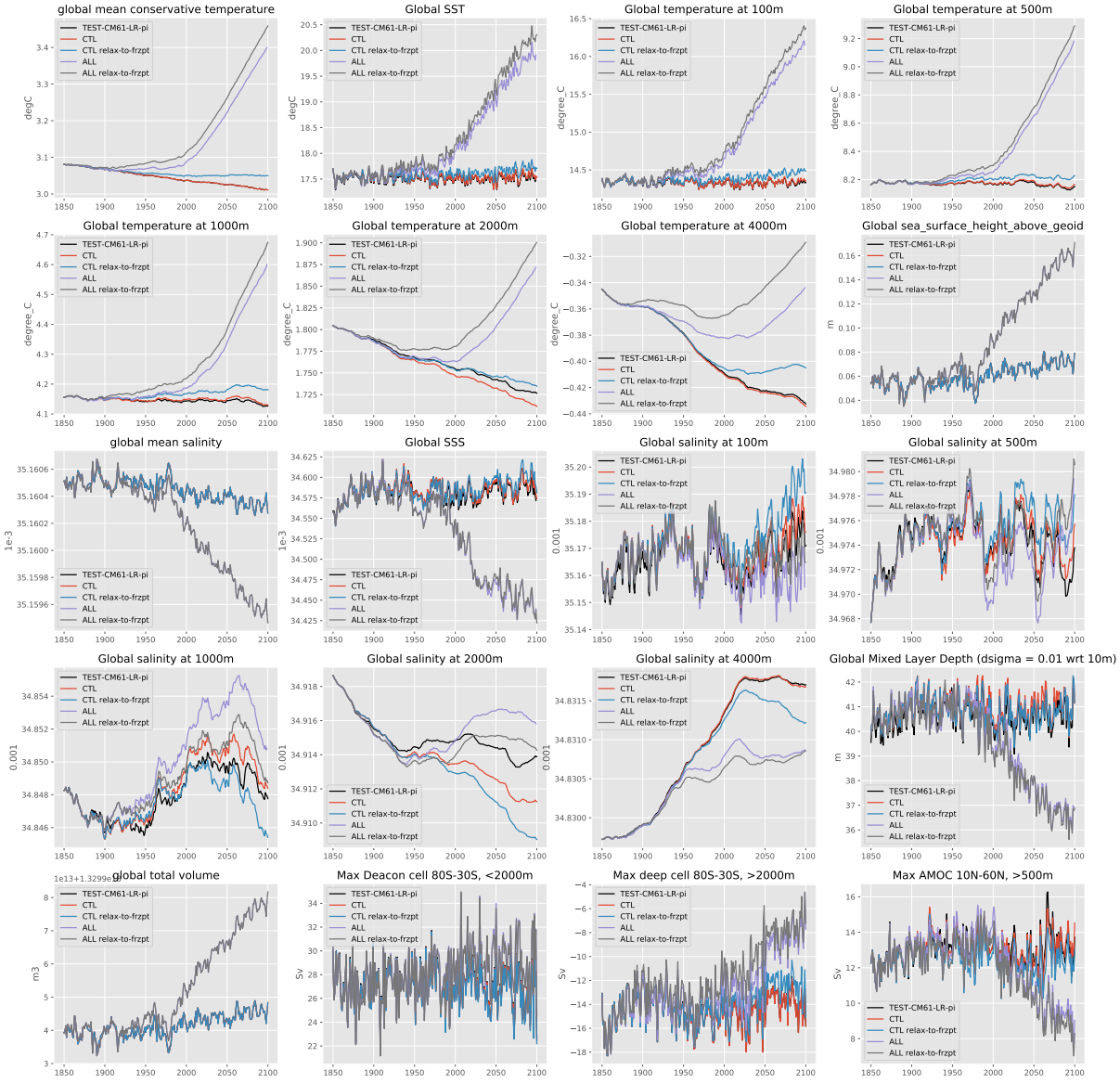

Figure C.9: Intermonitoring of 1D variables for the coupled piControl (black), the flux-forced CTL (red) and the ALL experiment (purple), compared with the CTL and ALL when relaxing the temperature when it falls below the freezing point to the freezing point temperature (blue and grey respectively).

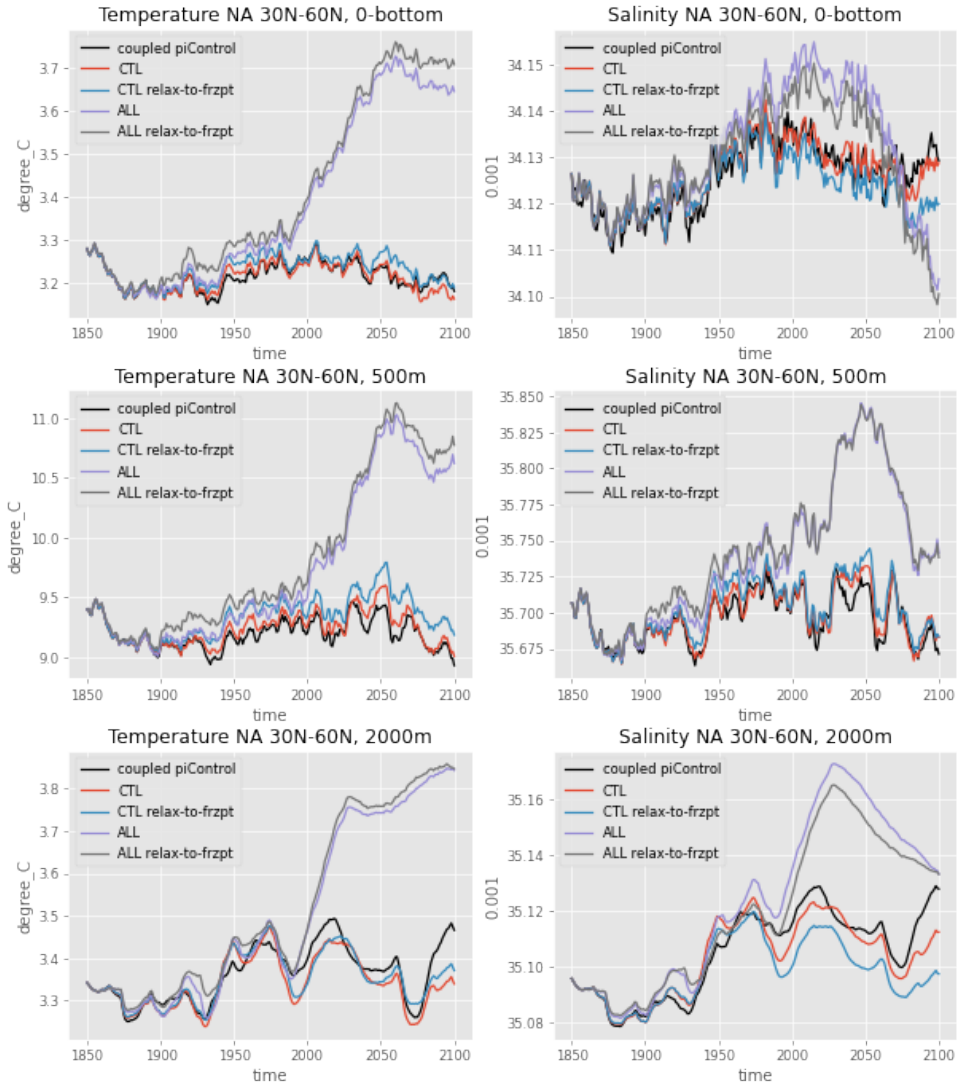

Figure C.10: Evolution of temperature and salinity in the North Atlantic (30N-60N) in the piControl (black), CTL and ALL when temperature evolves freely (red and purple), and in CTL and ALL when the temperature below freezing point is relaxed to the freezing point (blue and grey).

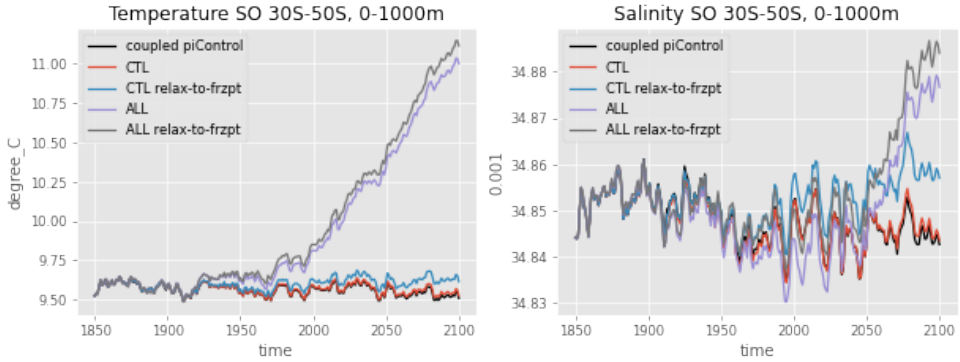

Figure C.11: Evolution of temperature and salinity in the Southern Ocean (30S-50S) top 1000m, in the piControl (black), CTL and ALL when temperature evolves freely (red and purple), and in CTL and ALL when the temperature below freezing point is relaxed to the freezing point (blue and grey).

Appendix

D

Supplementary Material to the second paper

Supplemental Material Figure 1

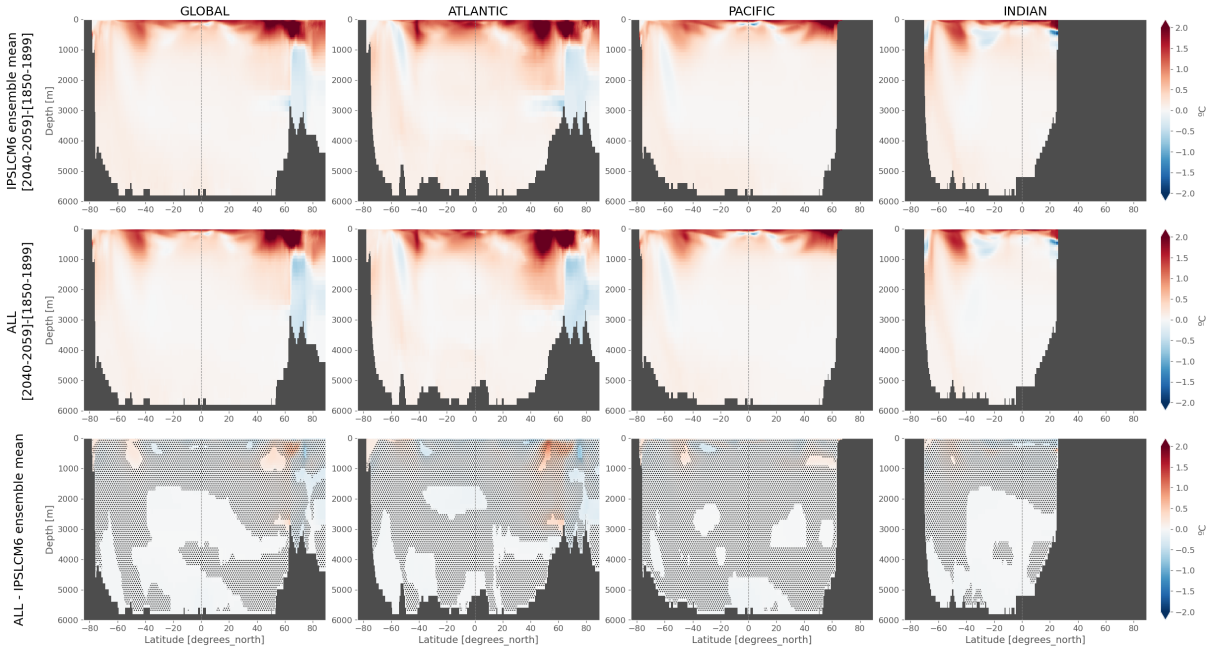

Figure D.1: Zonal mean temperature anomaly per basin in the IPSL-CM6A-LR ensemble mean (upper panels) and in the ALL experiment (lower panels), in 2040-2059 relative to 1850-1899. Their difference is shown in the lower panels (ALL-IPSLCM6), with stipples indicating where the difference is lower than twice the intermember standard deviation.

Supplemental Material Figure 2

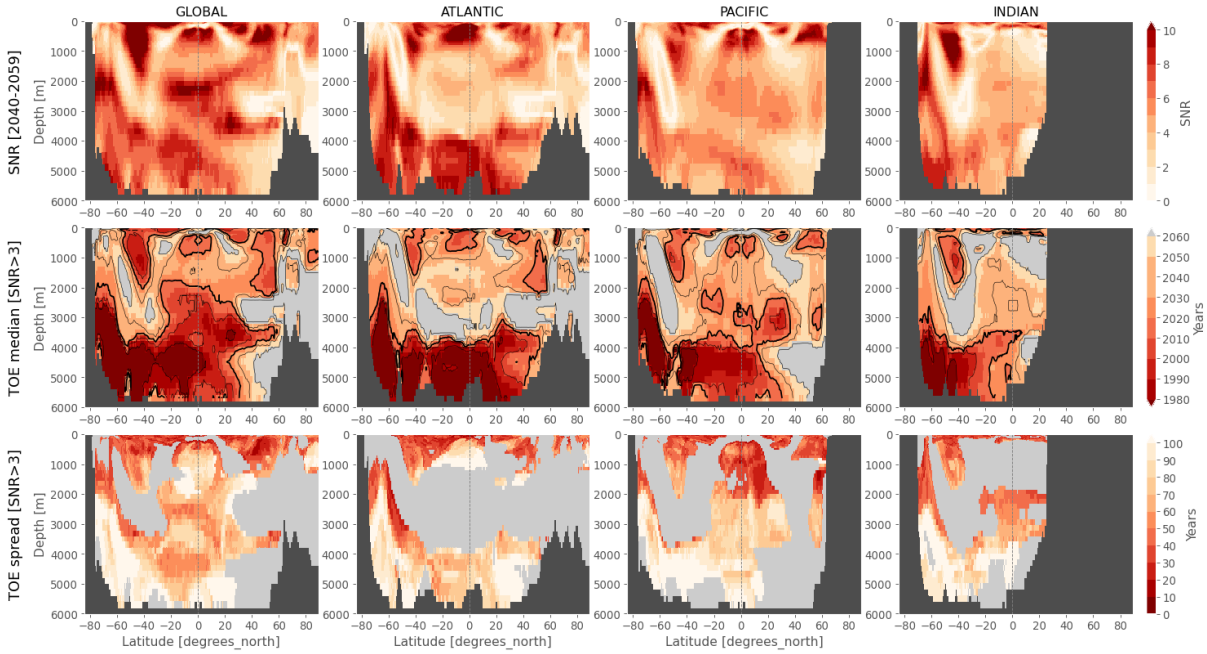

Figure D.2: Zonal mean temperature signal to noise ratio per basin in the ensemble mean averaged over 2040-2059 (upper panels). Ensemble median Time of Emergence when the SNR exceeds 3 and remains above it (middle panels). Grey regions indicate where the median has not emerged. The thick black contour indicates year 2020. (lower panels) Associated intermember spread (the spread is the difference between the maximum ToE and mimum ToE in the ensemble). Grey regions mean the maximum ToE is not defined (no emergence before 2059).

Supplemental Material Figure 3

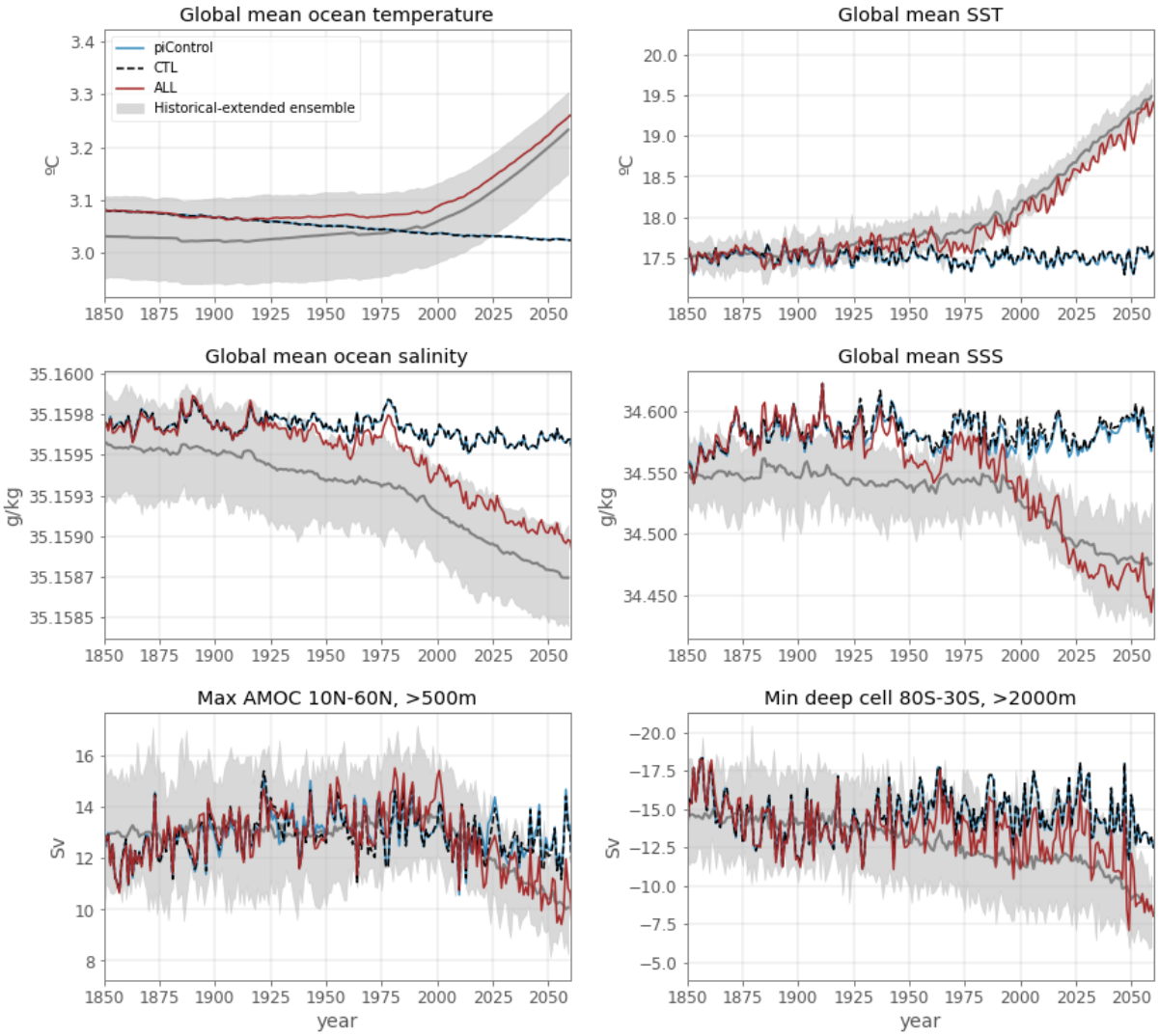

Figure D.3: Time series of global mean ocean temperature, salinity, SST, SSS, and indices of the AMOC and Southern Ocean deep overturning cell in the coupled piControl (blue), ocean-only CTL (dotted black), ocean-only ALL (dark red) and large ensemble (grey).

Supplemental Material Figure 4

Perturbation components in [2081-2100]

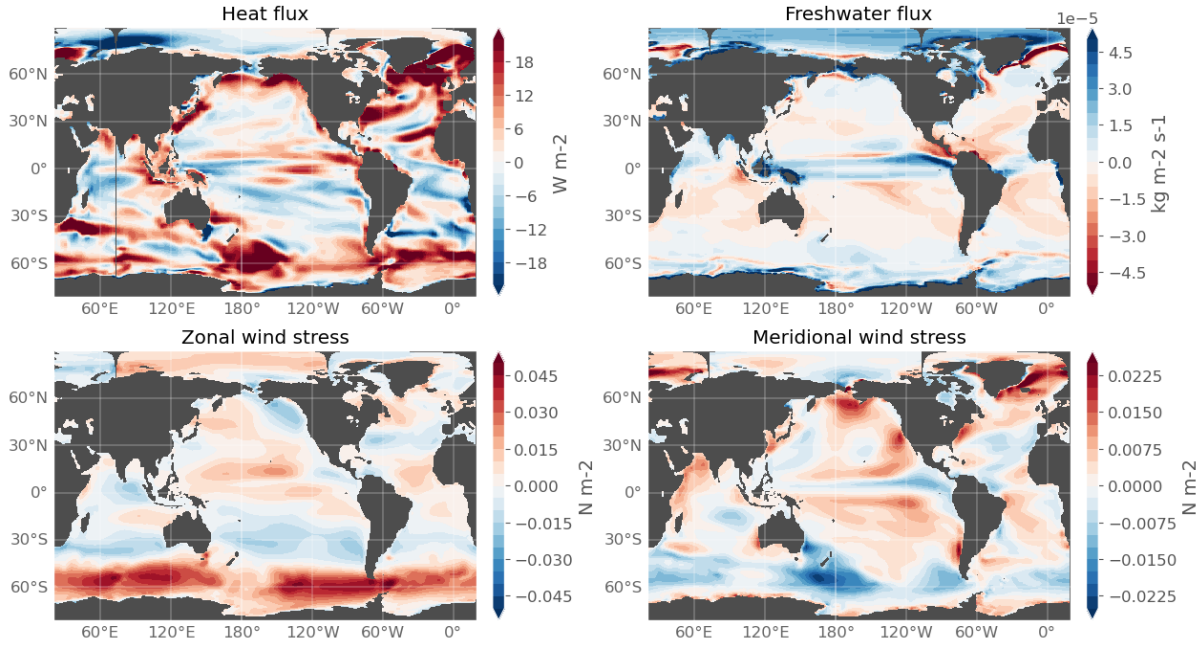

Figure D.4: Perturbation surfaces fluxes averaged in [2081-2100], computed as the ensemble mean anomaly relative to [1850-1899]. Heat flux (qt'+hflx_rnf'), freshwater flux (-emp'+runoffs'+iceshelf'), zonal wind stress (utau') and meridional wind stress (vtau').

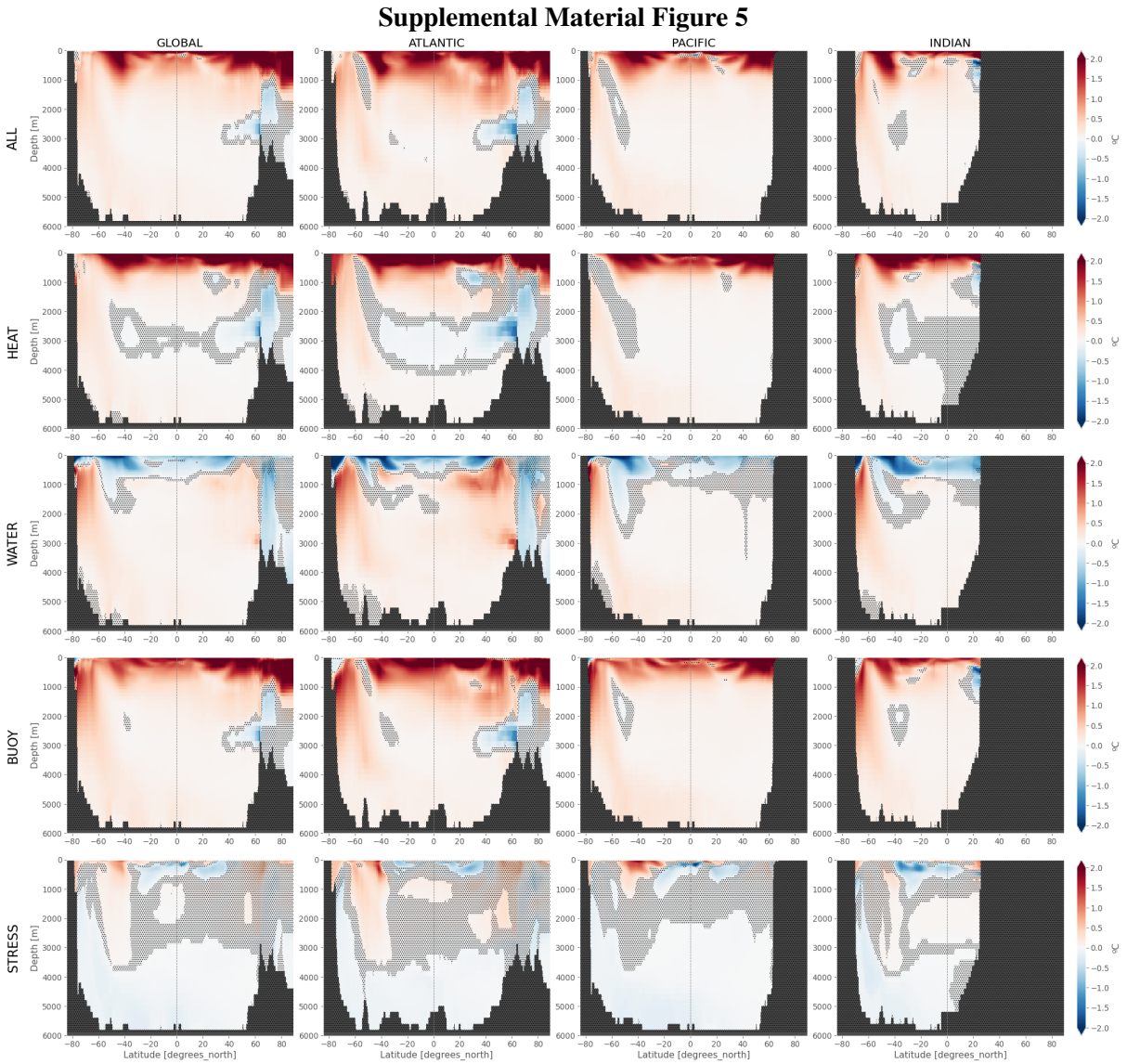

Figure D.5: Basin zonal mean temperature anomalies in each ocean-only experiment averaged in [2081-2100] relative to the same period in the CTL. Stipples indicated where the anomaly is lower than twice the interannual standard deviation of the CTL experiment.

Supplemental Material Figure 6

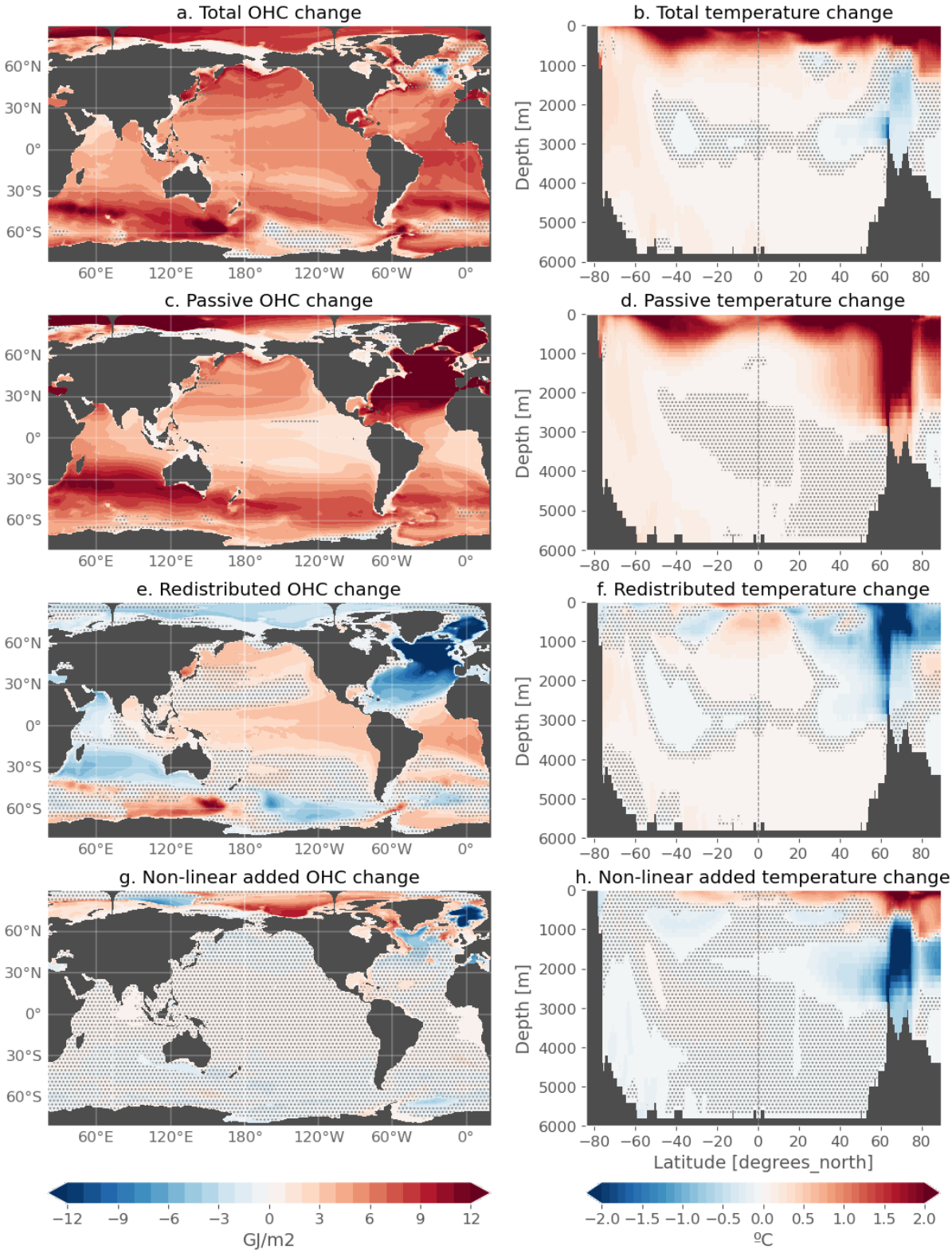

Figure D.6: Same as Figure 4 in the paper but for the HEAT experiment: ocean heat content and zonal mean temperature anomaly averaged in [2081-2100] relative to the CTL. (a,b) total change (c,d) passive component (e,f) redistributive component (g,f) non-linear added heat component (see text for the definition of these components). Stippled indicated where the anomaly is lower than twice the interannual standard deviation of the CTL experiment.

Supplemental Material Figure 7

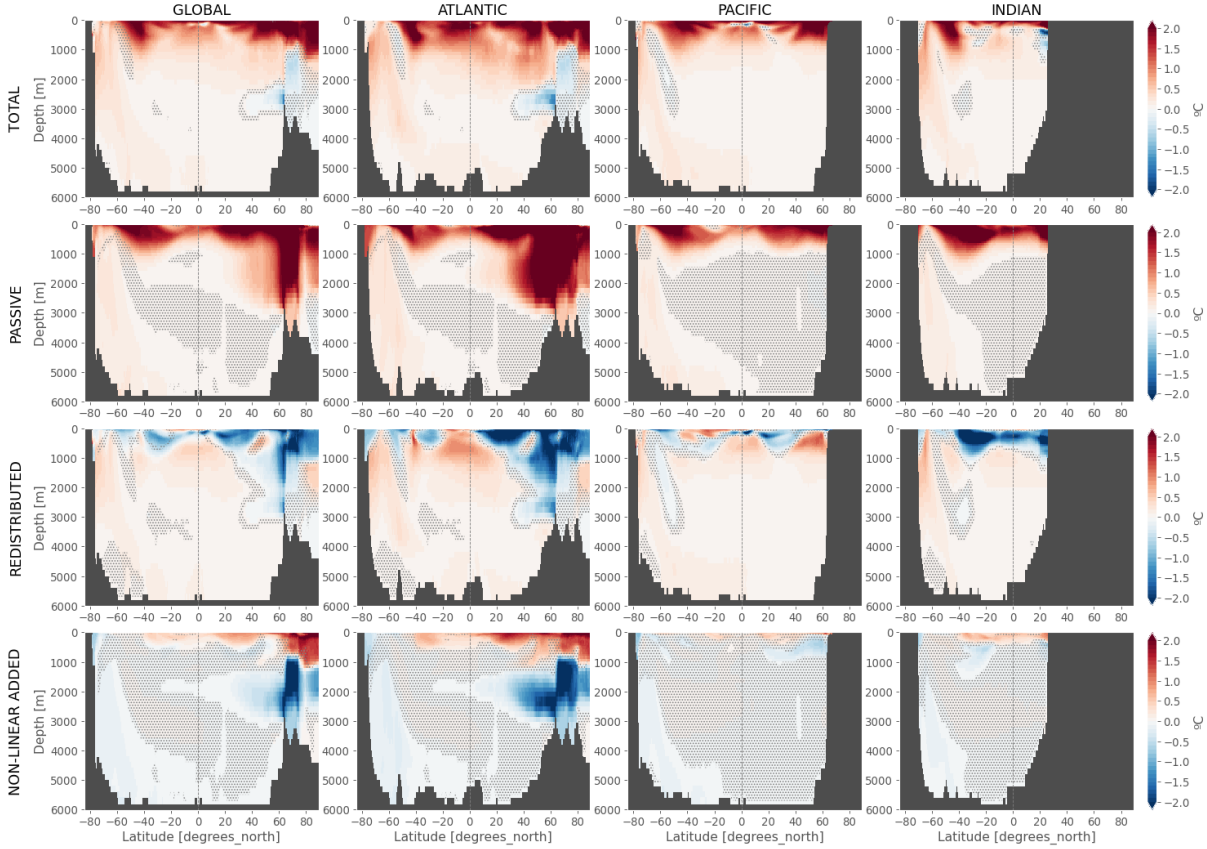

Figure D.7: As in Figure 4 of the paper but showing the global and basin zonal mean anomalies averaged in [2081-2100] in the ALL experiment relative to CTL. Total change (first row), passive component (second row), redistributed component (third row) and non-linear added heat component (fourth row).

Supplemental Material Figure 8

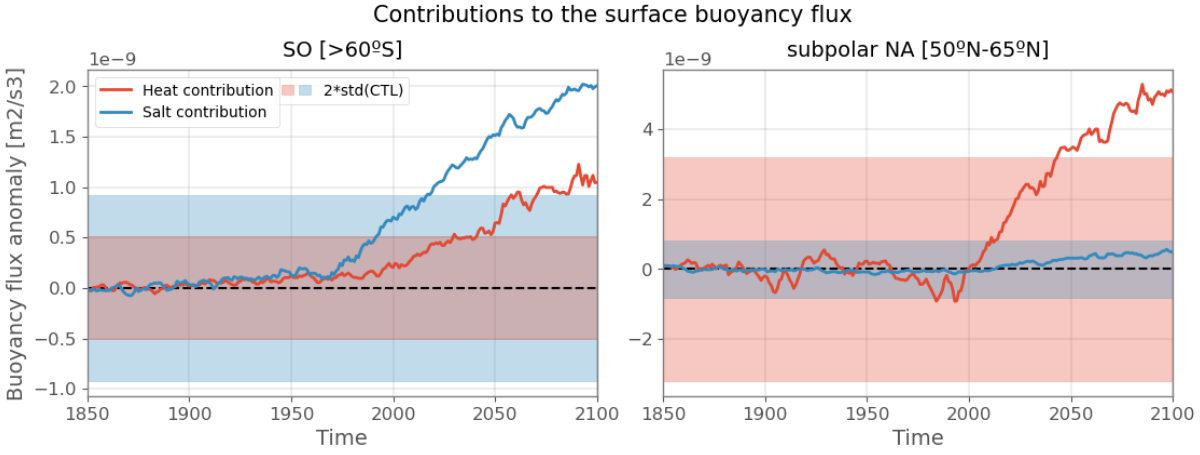

Figure D.8: Freshwater flux (blue) and heat flux (red) contributions to the surface buoyancy flux anomaly in the subpolar Southern Ocean (left) and North Atlantic (right), in the perturbed experiments. The anomaly is computed relative to 1850-1899, and a 5-year running mean is applied for visual purposes. The shadings indicate twice the interannual standard deviation of the freshwater (blue) and heat flux (red) contributions in the CTL experiment, an estimate of the internal variability.

Supplemental Material Figure 9

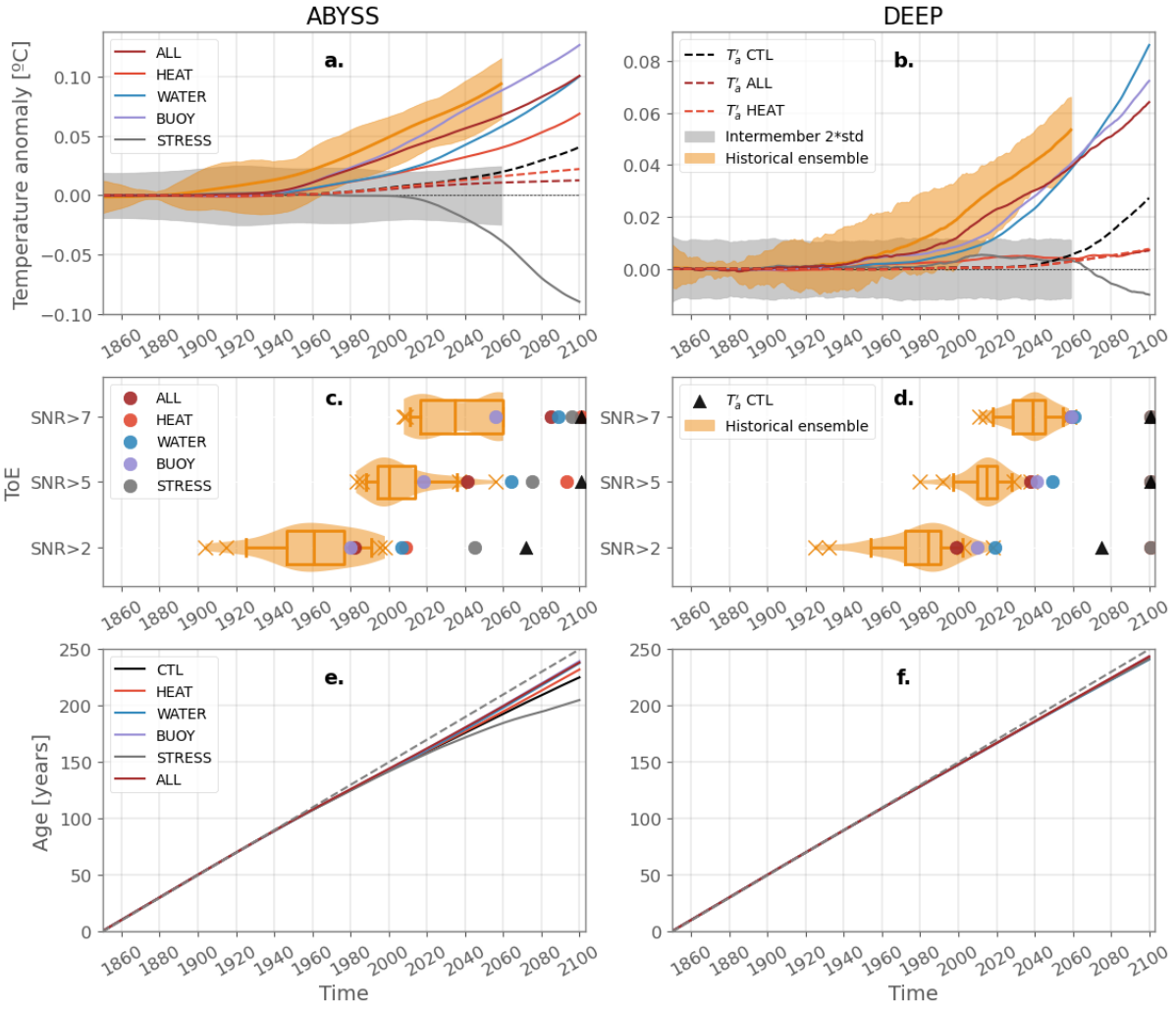

Figure D.9: As in Figures 7 and 8 of the paper, but for the abyssal and deep waters, defined as boxes in global zonal mean between 40ºS and 40ºN below 4000m (abyss) and between 2000m and 4000m (deep).

Supplemental Material Figure 10

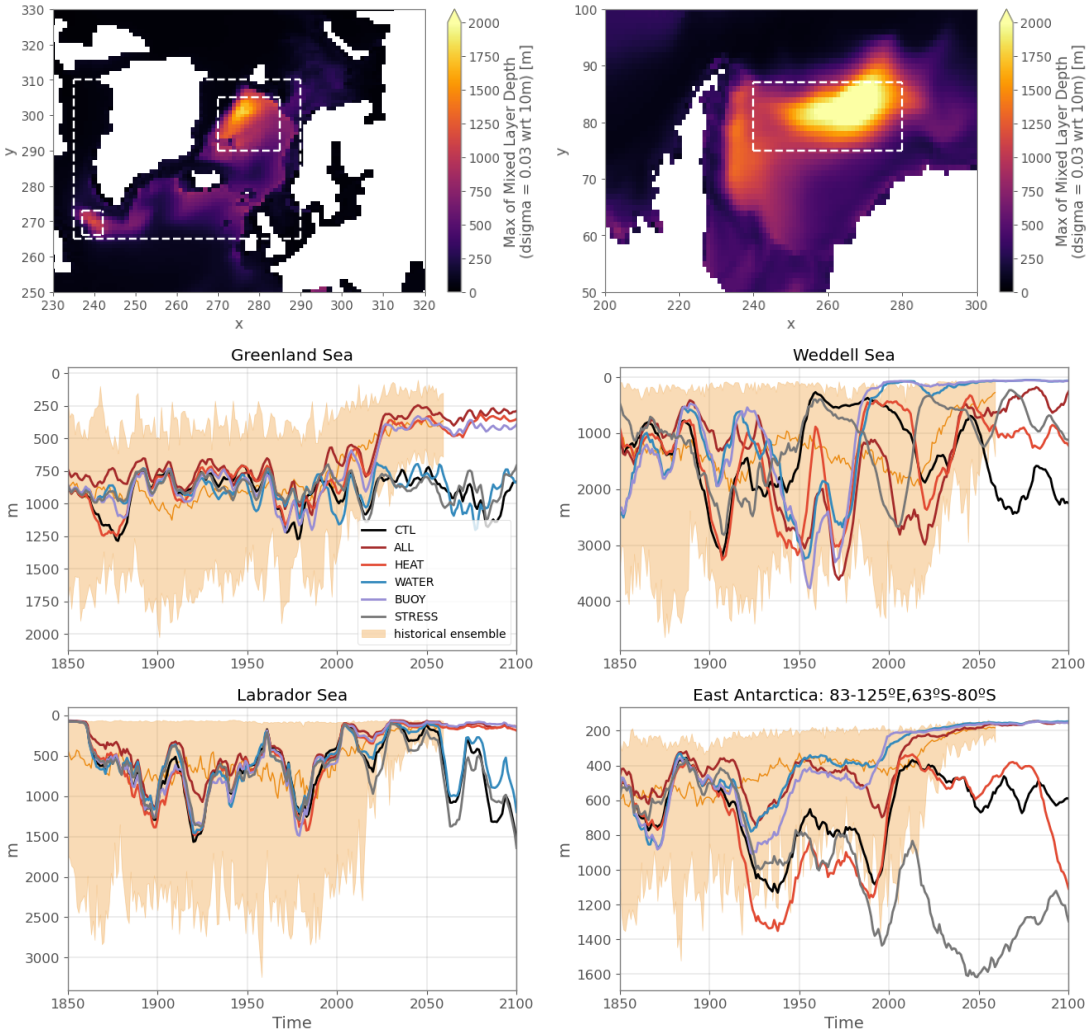

Figure D.10: As in Figure 9 of the paper, mixed layer depth (annual maximum), but with a more regional focus. Left column shows the MLD in the Greenland and Labrador Seas, as defined in the upper left panel (directly on the ORCA1 grid) showing the MLD in the CTL experiment. Right column shows the MLD in the Weddell Sea as defined in the upper right panel (directly on the ORCA1 grid), and in East Antarctica (latitude-longitude range given in the subplot title). These regions were chosen as hot spots of deep convection in the CTL.

Appendix

E

Supplementary salinity figures

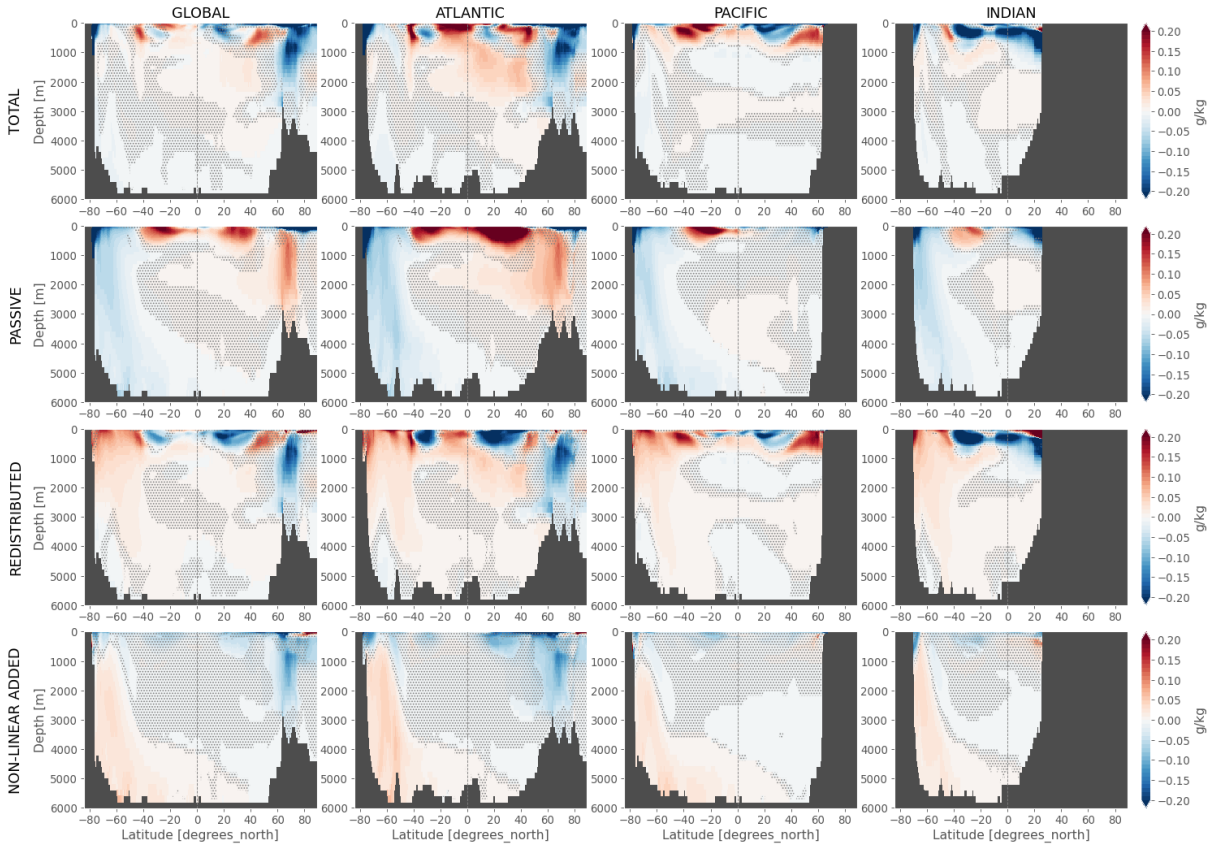

Figure E.1: Basin zonal mean salinity anomaly in the ALL experiment relative to CTL, for the total, passive, redistributed and non-linear added components, averaged over [2081-2100]. Stipples indicate where the anomaly is below twice the interannual standard deviation of the CTL.

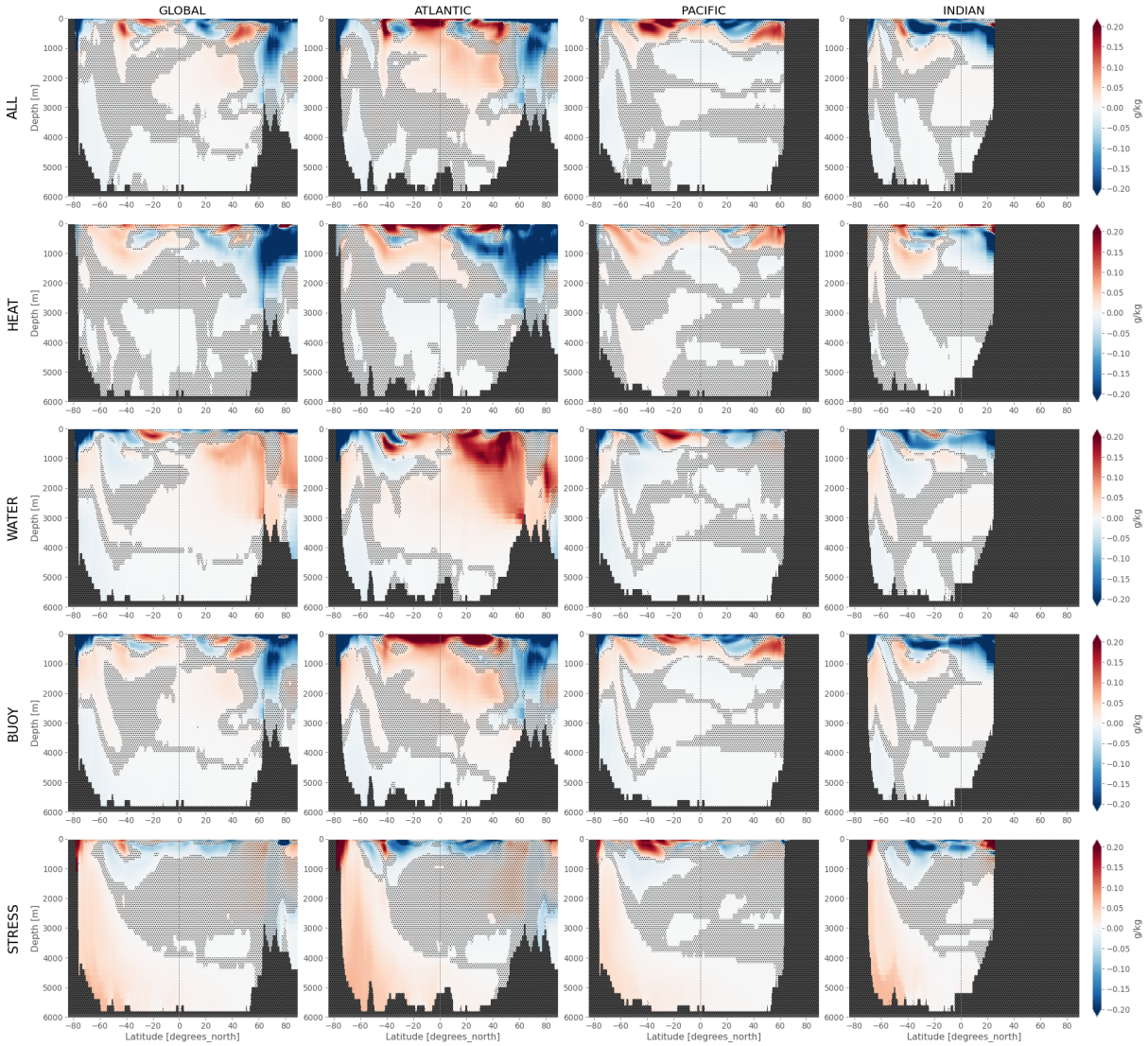

Figure E.2: Basin zonal mean salinity anomaly in the ocean-only perturbed experiments relative to CTL, averaged over [2081-2100]. Stipples indicate where the anomaly is below twice the interannual standard deviation of the CTL.

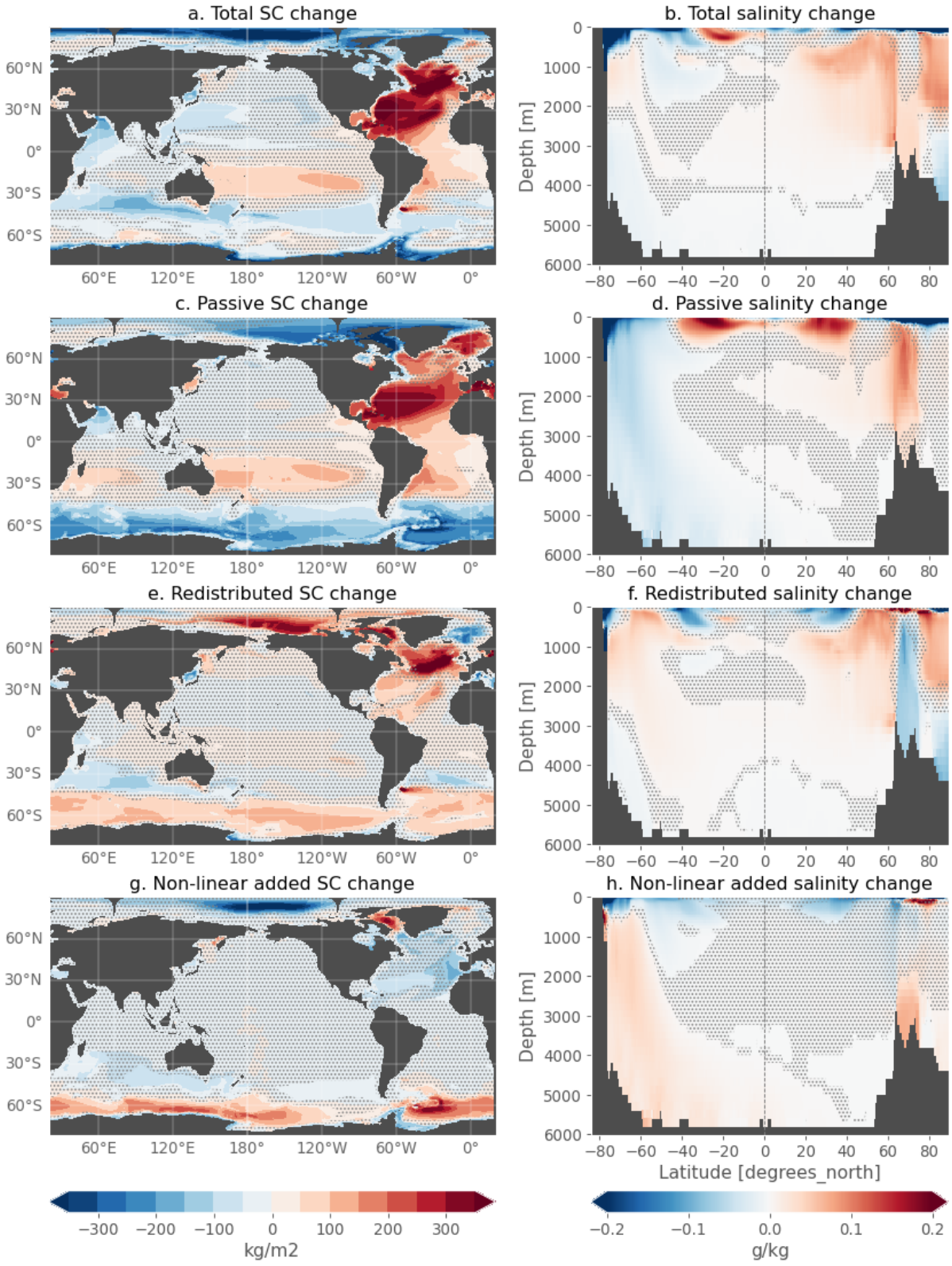

Figure E.3: Same as figure IV.2 but for the WATER experiment. Vertically-integrated salt content anomaly (left) and zonal mean salinity anomaly (right) in the WATER experiment relative to CTL, for the total, passive, redistributed and non-linear added components, averaged over [2081-2100]. Stipples indicate when the anomaly is below twice the interannual standard deviation of the CTL.

Appendix

F

Towards a low-carbon research at LOCEAN

One central object of this scientific work has been the ongoing climate change we are currently living, caused by human activities. Scientists and particularly the climate science community have played a key role in warning society about the risks of continually emitting greenhouse gases in the atmosphere. This same community still plays an important role in delivering the latest, up-to-date evaluation of climate change science and key climate projections, specifically in the successive IPCC reports. However, how the climate science and academic community in general has practised its research activities in the past decades has not been neutral for the climate system and has been been particularly carbon intensive. This, and the fact that greenhouse gas emissions have not stopped increasing after 30 years of IPCC reports, raise many questions concerning the responsibility of climate scientists in the climate crisis, questions that go beyond the point of this paragraph. Nonetheless, I have had the chance to work in a lab where this aspect has been collectively questioned and acted upon during my time here. A working group was constituted a few weeks after my arrival at the lab, so I was lucky to be able to join the discussions very early on and contribute to the efforts that took place here, and that served as an experiment for other labs to follow in their own way. The low-carbon transition at the lab level is now organized at the national scale, and constitutes a new topic of research, addressed by the organization Labos1.5 [1]. In this Appendix, I briefly present a few orders of magnitude of the carbon footprint associated with my PhD work, before presenting an overview of the experience that took place at LOCEAN.

1 Carbon footprint of the main activities of this thesis

Here, the goal is not to present a detailed carbon footprint that could be attributed to my PhD, but to give the orders of magnitude of the main emitting sectors in which I had some personal lever.

Train and air travel

My carbon footprint from travelling is presented in table F.1. It is computed from https://monpetitcarbone.fr. The footprint from air travel can be multiplied by at least 2 (large uncertainties on this factor remain) when taking into account the indirect effects of contrails on the radiative forcing. My travelling footprint is dominated by my flying trips, especially from the transatlantic flight. If I had taken the train to EGU 2019 instead of flying, I would have emitted 40 $kgCO_2e$, 5.8 times less than flying (in France, because of the low carbon content of electricity, the plane/train ratio is larger). At that time, booking European trains from the CNRS platform was not possible. Furthermore, flying still costs less than taking the train.

1. https://labos1point5.org

This is an example where a systemic and structural change is necessary. I will of course try to never fly again within European borders because it does not make sense anymore to me (+ avoiding as much as possible long-haul flights, which goes without saying). But this is my personal will. If taking the train was made easier and cheaper for everyone, it would provoke reductions in emissions beyond individual small steps. Beyond that, I also believe scientific conferences need to re-think their format. It saddens me that it took a global pandemic for these organizations to realize it was possible to do things differently and more inclusively. I won't expand on these points, nor on the inequalities behind flying because there is a lot to say, but I will point to a few papers that have already started addressing these issues (e.g. Ong et al. [2014], Le Quéré et al. [2015], Janisch and Hilty [2017], Kalmus [2019], Wynes et al. [2019], Burtscher et al. [2020], Klöwer et al. [2020], Glausiusz [2021]).

Table F.1: Carbon footprint from travels

Trip	Duration	Itinerary	Transport	Emissions
Winter school	1 week	Paris-Brest-Paris	Train	4 $kgCO_2e$
EGU 2019	1 week	Paris-Vienna-Paris	Plane	231 $kgCO_2e$
Visit	1 day	Paris-Reading-Paris	Train	18 $kgCO_2e$
CMIP6 workshop	2 days	Paris-Bordeaux-Paris	Train	4 $kgCO_2e$
OSM 2020	1 month	Paris-LA; Chicago-Paris	Plane	1320 $kgCO_2e$
TOTAL				**1577 $kgCO_2e$**
TOTAL with contrails x 2				**3128 $kgCO_2e$**

Numerical simulations

Between running the coupled model, the ocean-only model and the many (many many many) tests it took to get the numerical configuration developed in this thesis right, it took about a million cpu hours. A good order of magnitude for the energy usage of an hour of cpu time is 30Wh (storage included, representing about 10% of that figure) [2]. The carbon content of electricity in France is roughly 100 gCO_2e/kWh. One cpu hour thus emits $3gCO_2e$. Consequently, for one million hours, the carbon footprint of my numerical simulations amounts to **3 tCO_2e**.

When considering a factor of 2 for indirect effects of flying, we can see that the carbon footprints from travelling and from numerical modelling are almost equal. The footprint of numerical simulations (and more broadly of any electricity usage) strongly depends on the carbon content of electricity. The same simulations in Germany where coal is still strongly burnt for electricity production would have a footprint multiplied by about 4.

Other sectors

Personnal computer A laptop was bought at the beginning of the thesis (13" MacBook Pro): **160 $kgCO_2e$** [3].

Commuting I take the subway to work (RER), which amounts to 14 $kgCO_2e$ per year (in a normal COVID-free year).

2. Internal document: https://intranet.locean-ipsl.upmc.fr/mediawiki/index.php/Calcul_au_sens_des_centres_nationaux,_et_incluant_les_espaces_de_stockage_et_leur_utilisation

3. Base carbone ADEME : https://data.ademe.fr/datasets/base-carbone(r)

Meals Lunches enter the scope of the professional footprint. I have a vegetarian diet with very small amounts of dairy. ADEME gives 0.5 $kgCO_2e$ per vegetarian meal (on average, a meal is 2 $kgCO_2e$ across all diets, 7.2 $kgCO_2e$ when it is beef-dominant). For a year, the carbon footprint of my work lunches amounts to about 118 $kgCO_2e$ per year. For three years: **354 $kgCO_2e$**.

Lab functioning In the scope of my professional carbon footprint, should be included the footprint of lab functioning (energy use, building, etc..) divided by the number of people in the lab. This part is dominated by the building. This is not something I have a personal lever on, but amounts to about 0.5 tCO_2e per year.

2 Towards a low-carbon research at LOCEAN: an overview of the collective experience

This text is a collaborative contribution. Its first origin goes back to a Twitter thread written with J-B. Sallée, to share our experience with the Twitter academic community after the lab vote of September 2020[4]*. It was then extended and completed by other members of the Climactions community at LOCEAN.*

Through its research activities, LOCEAN has been contributing for years to the results that feed the IPCC reports, showing that climate change is a reality whose impacts are felt more and more strongly, here and elsewhere. The recent heat waves and Mediterranean flash floods are shattering evidence, among others, that France is not spared from the impacts of climate change, and that these impacts are perceptible, severe and intensifying.

Faced with this fact, France has committed, alongside 194 countries through the Paris Agreement in 2015, to reduce its greenhouse gas (GHG) emissions in order to keep global warming well below 2ºC. This is reflected in the "National Low-Carbon Strategy" (SNBC, Stratégie Nationale Bas Carbone) by carbon budgets set for a period of five years, broken down into objectives for all sectors of activity and to be carried out by all: citizens, local communities, companies. LOCEAN has about 190 employees, equivalent to a medium-sized company, one of the scales of action of the SNBC. How can it contribute to the general effort?

A chronological account (October 2018-September 2020)

In October 2018, following the release of the IPCC 1.5 Special Report, the climate walks, and the numerous corridor discussions, the "climactions" group was born at LOCEAN, aiming to gather individual initiatives into collective actions. A first estimate of the carbon footprint of the lab emanated from this group in early 2019: in 2018, LOCEAN staff emitted on average 9.5 tCO_2e/person (professional footprint only). This figure should be compared to the national average which was 11.2 tCO_2e/person in 2018, and which included both personal and professional activities. In the case of LOCEAN, half of these emissions are due to traveling (conferences, meetings, field work, etc.), with air travel accounting for 97% of this share.

The second half of the footprint is divided between oceanographic cruises, numerical modelling and lab functioning (equipment, purchases, heating, meals, etc.). The two largest sectors of emissions are related to specific activities at LOCEAN: ocean observations, and collaborations / capacity building in the South, one of our research supervising institutions being IRD (Institut pour la Recherche et le Développement).

This GHG assessment and its analysis are an essential step to identify the main emission sectors in order to reduce them. This scientific-based approach, with a quantification phase, has led to many formal

4. In French: https://twitter.com/YonaSilvy/status/1314492809416712193?s=20 and in English: https://twitter.com/jb_sallee/status/1315906614420017152?s=20

(seminars, laboratory councils, management committees, general assemblies of the lab or IPSL, etc.) and informal exchanges. This gave the opportunity to all the lab staff to think about and understand the topic during the year 2019.

In November 2019, the climactions group, supported financially by the lab, organized a two-day work retreat to develop proposals and a roadmap for reducing the LOCEAN carbon footprint. The twenty or so people who participated came back with 19 concrete propositions around 3 main themes:

- Systematically quantify our carbon footprint
- Reduce the footprint of our travels in a fair way, by reconsidering our practises
- Engage in a larger-scale reflection on the other sectors with our research institutions, funding agencies, (very) large infrastructures, partner labs and institutes on a national scale

Following new exchange times to share these reflections with all the staff of the lab, it appeared useful to organize a consultation of the lab on the reduction of the lab carbon footprint. An independent representative group was formed for the purpose, with links to the laboratory council. During the first semester of 2020, this groups of 7 people stimulated discussions within the lab teams and groups of personnel, which allowed to survey the staff and assess people's readiness to accept these propositions. They also engaged in numerous exchanges and discussions with the management committee and climactions.

At the beginning of summer 2020, a list of actions to be carried out emerged, including:

- The implementation, as soon as 2021, of measures to better monitor the lab's carbon footprint, with the obligation for each staff member to track his or her travel footprint on a dedicated tool (in compliance with data protection rules)
- To hold a vote on 3 measures:
    1. The lab's commitment on the principle to reduce our emissions on a trajectory compatible with the Paris Agreement, i.e. -50% by 2030
    2. To ban air travel for any journey that can be made in less than 5 hours by train (thus reinforcing the national travel directive in the public service which will be implemented in 2021)
    3. The introduction of an annual individual carbon quota on travels. This individual quota would decrease over time and allow a reduction of half of the travel-related GHG emissions by 2030. Several exemptions are provided for, such as field work, teaching, and long trips (>30 days). Early careers (PhDs, post-docs), also benefit from a non-quota journey every 2 years. A "carbon reserve" makes it possible to save unused quotas for future use, within a limited amount

Once these measures were validated by the laboratory council and the management committee, communication and information work was carried by the management (seminar) and the climaction group (informational and exchange website [5], seminar [6], production/posting of infographics concerning the issues at stake in the vote [7]) in preparation for the vote on 28-29 September 2020. A message from the laboratory council was drafted in order to draw the attention of the staff to the seriousness of the process that led to this vote.

The results of the vote (75% turnout, and over 80% of the votes in favor of the measures) provide a clear picture, on the basis of which the implementation of restrictive measures 2. and 3. should be possible by early 2021 under decent conditions. The turnout is particularly high compared to general lab elections.

5. https://colibris-wiki.org/empreinteClocean/?PagePrincipale
6. Video and slides available here: https://colibris-wiki.org/empreinteClocean/?TexteVote
7. See figure F.1 and https://colibris-wiki.org/empreinteClocean/?ElementsBilanCarboneLOCEAN

Feedback and originality of the approach

The adoption of GHG reduction measures at the lab level is only one step in a long process that has not, to date, delivered any actual emission reductions. Nevertheless, it is an important step that has required overcoming many obstacles and making important choices for the future. Among important elements that contributed to this first successes, we can mention:

- Permanently looking for an open, broad and sincere internal dialogue, inclusive of all categories of staff, especially young people on fixed-term contracts
- The collective attachment to collegial deliberation processes, in particular through the role of the laboratory council
- The willingness of the management to support the bottom-up approach
- The long-term commitment (2 years) of a dozen or so staff members within a larger group who frequently lent a hand
- The importance and diversity of personal motivations to reduce our emissions: a need for coherence in the face of the climate situation and the messages that our community delivers on this subject; the desire/need to live an ecological transformation in concrete terms; the potential for co-benefits for the collective functioning; the desire/need to slow down the pace at which our professional lives are conducted, due in particular to a large number of short trips; the conviction that the transformation of practises within the higher education and research system can produce ripple effects outside of its spectrum, ...
- Choosing to make the reduction process an *experiment* with, in particular, an annual meeting point (lab council) from 2022 onwards which will make it possible to assess the effectiveness of the measures in place, the difficulties they might cause, and ways to solve them / limit the negative impacts
- Choosing measures whose administrative implementation must not place an additional burden on our already overburdened administrative team
- The existence of a larger ecosystem of laboratories committed to transforming their practises, at IPSL, at the national scale and beyond

Among the decisive choices made, it is worth noting the choice to adopt binding measures while protecting the core of the lab's activities (due to the exemptions retained from the carbon quota mechanism). The debate on the nature of the measures to be put in place, incentives vs. constraints, sparked numerous, sometimes "lively" discussions. Despite the individual dimension of the constraints retained at LOCEAN, our binding approach has the advantage of setting up a common framework for the collective transformation of practises, which makes it possible to explicitly integrate equity issues (including by integrating exemptions such as the out-of-quota trip every two years for early careers). This is an important difference from a "carbon tax" type of incentive approach, which puts the burden of reducing on staff members who do not have the means to pay the tax.

Starting in 2021, LOCEAN's very frequent travellers will see some of their trips restricted, in particular short trips to participate in meetings, conferences.... The lab is aware of the fact that these trips have in the past contributed to the scientific dynamism of the entire lab. Being part of the pioneers implies taking a risk. However, this risk seems to us limited considering the possible optimization of some trips and especially the rapid generalization of videoconferencing. On this last point, the lab has for a long time had a voluntarist policy on the provision of good equipment. This effort will of course be pursued as well as the participation in the development and the diffusion of a virtual communication culture.

In a professional environment where there is a general consensus on the seriousness of climate change, LOCEAN's initiative allows to experiment with the quota/rationing approach, which could be one of the tools to drive transformations on a larger scale in the future.

The share of the lab's footprint that is not linked to travel will not be forgotten. It is already the subject

of reflections and actions, but most often raises the need for dialogue or coordination on a larger scale than LOCEAN alone, for example on the issue of observations at sea or numerical computing. In this respect, it seems important to us that other labs, supported by their funding agencies, commit to quantifying and reducing their carbon emissions. The deployment on October 15th 2020 of the "GHG1.5" tool [8] dedicated to calculating the carbon footprint of laboratories should greatly contribute to this in the near future.

8. https://labos1point5.org/ges-1point5

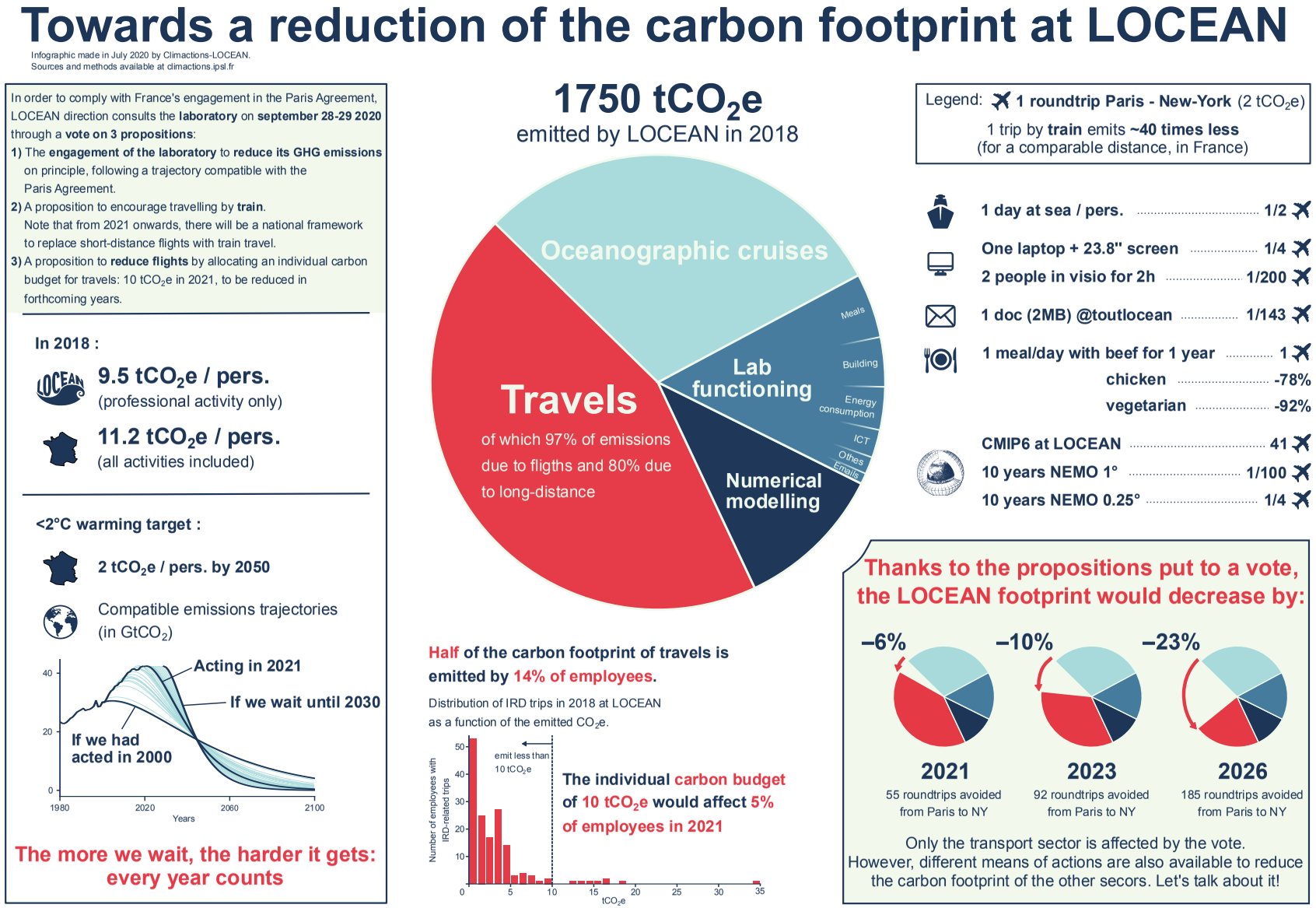

Figure F.1: Informational poster we made in summer 2020 before the vote.

Bibliography

R. Abernathey and D. Ferreira. Southern Ocean isopycnal mixing and ventilation changes driven by winds. *Geophysical Research Letters*, 42(23), Dec. 2015. ISSN 0094-8276, 1944-8007. doi: 10.1002/2015GL066238. URL https://onlinelibrary.wiley.com/doi/10.1002/2015GL066238.

J. P. Abraham, M. Baringer, N. L. Bindoff, T. Boyer, L. J. Cheng, J. A. Church, J. L. Conroy, C. M. Domingues, J. T. Fasullo, J. Gilson, G. Goni, S. A. Good, J. M. Gorman, V. Gouretski, M. Ishii, G. C. Johnson, S. Kizu, J. M. Lyman, A. M. Macdonald, W. J. Minkowycz, S. E. Moffitt, M. D. Palmer, A. R. Piola, F. Reseghetti, K. Schuckmann, K. E. Trenberth, I. Velicogna, and J. K. Willis. A review of global ocean temperature observations: Implications for ocean heat content estimates and climate change. *Reviews of Geophysics*, 51(3):450–483, Sept. 2013. ISSN 8755-1209, 1944-9208. doi: 10.1002/rog.20022. URL https://onlinelibrary.wiley.com/doi/10.1002/rog.20022.

N. J. Abram, R. Mulvaney, F. Vimeux, S. J. Phipps, J. Turner, and M. H. England. Evolution of the Southern Annular Mode during the past millennium. *Nature Climate Change*, 4(7):564–569, July 2014. ISSN 1758-678X, 1758-6798. doi: 10.1038/nclimate2235. URL http://www.nature.com/articles/nclimate2235.

M. R. Allen and W. J. Ingram. Constraints on future changes in climate and the hydrologic cycle. *Nature*, 419(6903):228–232, Sept. 2002. ISSN 0028-0836, 1476-4687. doi: 10.1038/nature01092. URL http://www.nature.com/articles/nature01092.

S. Aoki, N. L. Bindoff, and J. A. Church. Interdecadal water mass changes in the Southern Ocean between 30°E and 160°E. *Geophysical Research Letters*, 32(7):n/a–n/a, Apr. 2005. ISSN 00948276. doi: 10.1029/2004GL022220. URL http://doi.wiley.com/10.1029/2004GL022220.

K. C. Armour, J. Marshall, J. R. Scott, A. Donohoe, and E. R. Newsom. Southern Ocean warming delayed by circumpolar upwelling and equatorward transport. *Nature Geoscience*, 9(7):549–554, July 2016. ISSN 1752-0894, 1752-0908. doi: 10.1038/ngeo2731. URL http://www.nature.com/articles/ngeo2731.

S. Arrhenius. XXXI. On the influence of carbonic acid in the air upon the temperature of the ground. *The London, Edinburgh, and Dublin Philosophical Magazine and Journal of Science*, 41(251):237–276, Apr. 1896. ISSN 1941-5982, 1941-5990. doi: 10.1080/14786449608620846. URL https://www.tandfonline.com/doi/full/10.1080/14786449608620846.

M. Auger, R. Morrow, E. Kestenare, J.-B. Sallée, and R. Cowley. Southern Ocean in-situ temperature trends over 25 years emerge from interannual variability. *Nature Communications*, 12(1):514, Dec. 2021. ISSN 2041-1723. doi: 10.1038/s41467-020-20781-1. URL http://www.nature.com/articles/s41467-020-20781-1.

O. Aumont, C. Ethé, A. Tagliabue, L. Bopp, and M. Gehlen. PISCES-v2: an ocean biogeochemical model for carbon and ecosystem studies. *Geoscientific Model Development*, 8(8):2465–2513, Aug. 2015. ISSN 1991-9603. doi: 10.5194/gmd-8-2465-2015. URL https://gmd.copernicus.org/articles/8/2465/2015/.

M. Azaneu, R. Kerr, M. M. Mata, and C. A. E. Garcia. Trends in the deep Southern Ocean (1958-2010): Implications for Antarctic Bottom Water properties and volume export: trends in AABW hydrographic profiles. *Journal of Geophysical Research: Oceans*, 118(9):4213–4227, Sept. 2013. ISSN 21699275. doi: 10.1002/jgrc.20303. URL http://doi.wiley.com/10.1002/jgrc.20303.

A. Banerjee, J. C. Fyfe, L. M. Polvani, D. Waugh, and K.-L. Chang. A pause in Southern Hemisphere circulation trends due to the Montreal Protocol. *Nature*, 579(7800):544–548, Mar. 2020. ISSN 0028-0836, 1476-4687. doi: 10.1038/s41586-020-2120-4. URL http://www.nature.com/articles/s41586-020-2120-4.

H. Banks and R. Wood. Where to Look for Anthropogenic Climate Change in the Ocean. *Journal of Climate*, 15(8):879–891, Apr. 2002. ISSN 0894-8755. doi: 10.1175/1520-0442(2002)015<0879:WTLFAC>2.0.CO;2. URL https://journals.ametsoc.org/doi/full/10.1175/1520-0442%282002%29015%3C0879%3AWTLFAC%3E2.0.CO%3B2.

H. Banks, R. Wood, and J. Gregory. Changes to Indian Ocean Subantarctic Mode Water in a Coupled Climate Model as CO2 Forcing Increases. *Journal of Physical Oceanography*, 32:12, 2002.

H. T. Banks and N. L. Bindoff. Comparison of Observed Temperature and Salinity Changes in the Indo-Pacific with Results from the Coupled Climate Model HadCM3: Processes and Mechanisms. *Journal of Climate*, 16:11, 2003.

H. T. Banks and J. M. Gregory. Mechanisms of ocean heat uptake in a coupled climate model and the implications for tracer based predictions of ocean heat uptake. *Geophysical Research Letters*, 33(7), 2006. ISSN 1944-8007. doi: 10.1029/2005GL025352. URL https://agupubs.onlinelibrary.wiley.com/doi/abs/10.1029/2005GL025352.

H. T. Banks, R. A. Wood, J. M. Gregory, T. C. Johns, and G. S. Jones. Are observed decadal changes in intermediate water masses a signature of anthropogenic climate change? *Geophysical Research Letters*, 27(18):2961–2964, Sept. 2000. ISSN 00948276. doi: 10.1029/2000GL011601. URL http://doi.wiley.com/10.1029/2000GL011601.

T. P. Barnett. Penetration of Human-Induced Warming into the World's Oceans. *Science*, 309(5732):284–287, July 2005. ISSN 0036-8075, 1095-9203. doi: 10.1126/science.1112418. URL https://www.sciencemag.org/lookup/doi/10.1126/science.1112418.

T. P. Barnett, D. W. Pierce, and R. Schnur. Detection of Anthropogenic Climate Change in the World's Oceans. *Science*, 292 (5515):270–274, Apr. 2001. ISSN 00368075, 10959203. doi: 10.1126/science.1058304. URL http://www.sciencemag.org/cgi/doi/10.1126/science.1058304.

A. Baumgartner and E. Reichel. World Water Balance: Mean Annual Global, Continental and Maritime Precipitation, Evaporation and Run-Off. *Elsevier, Amsterdam*, 1975.

R. A. F. Bilbao, J. M. Gregory, N. Bouttes, M. D. Palmer, and P. Stott. Attribution of ocean temperature change to anthropogenic and natural forcings using the temporal, vertical and geographical structure. *Climate Dynamics*, 53:5389–5413, July 2019. ISSN 1432-0894. doi: 10.1007/s00382-019-04910-1. URL https://doi.org/10.1007/s00382-019-04910-1.

N. L. Bindoff and J. A. Church. Warming of the water column in the southwest Pacific Ocean. *Nature*, 357(6373):59–62, May 1992. ISSN 0028-0836, 1476-4687. doi: 10.1038/357059a0. URL http://www.nature.com/articles/357059a0.

N. L. Bindoff and T. J. Mcdougall. Diagnosing Climate Change and Ocean Ventilation Using Hydrographic Data. *Journal of Physical Oceanography*, 24(6):1137–1152, June 1994. ISSN 0022-3670. doi: 10.1175/1520-0485(1994)024<1137:DCCAOV>2.0.CO;2. URL https://journals.ametsoc.org/doi/abs/10.1175/1520-0485%281994%29024%3C1137%3ADCCAOV%3E2.0.CO%3B2.

N. L. Bindoff and T. J. Mcdougall. Decadal Changes along an Indian Ocean Section at 32ºS and Their Interpretation. *Journal of Physical Oceanography*, 30:16, 2000.

N. L. Bindoff, W. W. L. Cheung, and J. G. Kairo. Changing Ocean, Marine Ecosystems, and Dependent Communities. In *IPCC Special Report on the Ocean and Cryosphere in a Changing Climate*. 2019.

G. J. Boer, D. M. Smith, C. Cassou, F. Doblas-Reyes, G. Danabasoglu, B. Kirtman, Y. Kushnir, M. Kimoto, G. A. Meehl, R. Msadek, W. A. Mueller, K. E. Taylor, F. Zwiers, M. Rixen, Y. Ruprich-Robert, and R. Eade. The Decadal Climate Prediction Project (DCPP) contribution to CMIP6. *Geoscientific Model Development*, 9(10):3751–3777, Oct. 2016. ISSN 1991-9603. doi: 10.5194/gmd-9-3751-2016. URL https://gmd.copernicus.org/articles/9/3751/2016/.

C. J. W. Bonfils, B. D. Santer, J. C. Fyfe, K. Marvel, T. J. Phillips, and S. R. H. Zimmerman. Human influence on joint changes in temperature, rainfall and continental aridity. *Nature Climate Change*, 10(8):726–731, Aug. 2020. ISSN 1758-6798. doi: 10.1038/s41558-020-0821-1. URL https://doi.org/10.1038/s41558-020-0821-1.

R. Bonnet, O. Boucher, J. Deshayes, G. Gastineau, F. Hourdin, J. Mignot, J. Servonnat, and D. Swingedouw. Presentation and Evaluation of the IPSL-CM6A-LR Ensemble of Extended Historical Simulations. *Journal of Advances in Modeling Earth Systems*, page 25, 2021a. doi: 10.1029/2021MS002565.

R. Bonnet, D. Swingedouw, G. Gastineau, O. Boucher, J. Deshayes, F. Hourdin, J. Mignot, J. Servonnat, and A. Sima. Increased risk of near term global warming due to a recent AMOC weakening. *Nature Communications*, 12(1):6108, Dec. 2021b. ISSN 2041-1723. doi: 10.1038/s41467-021-26370-0. URL https://www.nature.com/articles/s41467-021-26370-0.

O. Boucher, J. Servonnat, A. L. Albright, O. Aumont, Y. Balkanski, V. Bastrikov, S. Bekki, R. Bonnet, S. Bony, L. Bopp, P. Braconnot, P. Brockmann, P. Cadule, A. Caubel, F. Cheruy, F. Codron, A. Cozic, D. Cugnet, F. D'Andrea, P. Davini, C. Lavergne, S. Denvil, J. Deshayes, M. Devilliers, A. Ducharne, J. Dufresne, E. Dupont, C. Éthé, L. Fairhead, L. Falletti, S. Flavoni, M. Foujols, S. Gardoll, G. Gastineau, J. Ghattas, J. Grandpeix, B. Guenet, L. Guez, E., E. Guilyardi, M. Guimberteau, D. Hauglustaine, F. Hourdin, A. Idelkadi, S. Joussaume, M. Kageyama, M. Khodri, G. Krinner, N. Lebas, G. Levavasseur, C. Lévy, L. Li, F. Lott, T. Lurton, S. Luyssaert, G. Madec, J. Madeleine, F. Maignan, M. Marchand, O. Marti, L. Mellul, Y. Meurdesoif, J. Mignot, I. Musat, C. Ottlé, P. Peylin, Y. Planton, J. Polcher, C. Rio, N. Rochetin, C. Rousset, P. Sepulchre, A. Sima, D. Swingedouw, R. Thiéblemont, A. K. Traore, M. Vancoppenolle, J. Vial, J. Vialard, N. Viovy, and N. Vuichard. Presentation and Evaluation of the IPSL-CM6A-LR Climate Model. *Journal of Advances in Modeling Earth Systems*, 12(7), July 2020. ISSN 1942-2466, 1942-2466. doi: 10.1029/2019MS002010. URL https://onlinelibrary.wiley.com/doi/abs/10.1029/2019MS002010.

N. Bouttes and J. M. Gregory. Attribution of the spatial pattern of CO2-forced sea level change to ocean surface flux changes. *Environmental Research Letters*, 9(3):034004, Mar. 2014. ISSN 1748-9326. doi: 10.1088/1748-9326/9/3/034004. URL https://iopscience.iop.org/article/10.1088/1748-9326/9/3/034004.

T. P. Boyer, S. Levitus, J. I. Antonov, R. A. Locarnini, and H. E. Garcia. Linear trends in salinity for the World Ocean, 1955–1998. *Geophysical Research Letters*, 32(1), 2005. ISSN 1944-8007. doi: 10.1029/2004GL021791. URL https://agupubs.onlinelibrary.wiley.com/doi/abs/10.1029/2004GL021791.

T. J. Bracegirdle, E. Shuckburgh, J.-B. Sallee, Z. Wang, A. J. S. Meijers, N. Bruneau, T. Phillips, and L. J. Wilcox. Assessment of surface winds over the Atlantic, Indian, and Pacific Ocean sectors of the Southern Ocean in CMIP5 models: historical bias, forcing response, and state dependence. *Journal of Geophysical Research: Atmospheres*, 118(2):547–562, Jan. 2013. ISSN 2169897X. doi: 10.1002/jgrd.50153. URL http://doi.wiley.com/10.1002/jgrd.50153.

T. J. Bracegirdle, G. Krinner, M. Tonelli, F. A. Haumann, K. A. Naughten, T. Rackow, L. A. Roach, and I. Wainer. Twenty first century changes in Antarctic and Southern Ocean surface climate in CMIP6. *Atmospheric Science Letters*, 21(9), Sept. 2020. ISSN 1530-261X, 1530-261X. doi: 10.1002/asl.984. URL https://onlinelibrary.wiley.com/doi/10.1002/asl.984.

W. Broeker. The Great Ocean Conveyor. *Oceanography*, 4(2):79–89, 1991. ISSN 10428275. doi: 10.5670/oceanog.1991.07. URL https://tos.org/oceanography/article/the-great-ocean-conveyor.

B. Bronselaer and L. Zanna. Heat and carbon coupling reveals ocean warming due to circulation changes. *Nature*, 584(7820): 227–233, Aug. 2020. ISSN 0028-0836, 1476-4687. doi: 10.1038/s41586-020-2573-5. URL http://www.nature.com/articles/s41586-020-2573-5.

B. Bronselaer, M. Winton, S. M. Griffies, W. J. Hurlin, K. B. Rodgers, O. V. Sergienko, R. J. Stouffer, and J. L. Russell. Change in future climate due to Antarctic meltwater. *Nature*, 564(7734):53–58, Dec. 2018. ISSN 0028-0836, 1476-4687. doi: 10.1038/s41586-018-0712-z. URL http://www.nature.com/articles/s41586-018-0712-z.

K. Bryan. Climate and the ocean circulation III. The ocean model. *Monthly Weather Review*, 97(11):806–827, 1969. doi: https://doi.org/10.1175/1520-0493(1969)097%3C0806:CATOC%3E2.3.CO;2.

L. Burtscher, D. Barret, A. P. Borkar, V. Grinberg, K. Jahnke, S. Kendrew, G. Maffey, and M. J. McCaughrean. The carbon footprint of large astronomy meetings. *Nature Astronomy*, 4(9):823–825, Sept. 2020. ISSN 2397-3366. doi: 10.1038/s41550-020-1207-z. URL https://www.nature.com/articles/s41550-020-1207-z.

L. Caesar, S. Rahmstorf, A. Robinson, G. Feulner, and V. Saba. Observed fingerprint of a weakening Atlantic Ocean overturning circulation. *Nature*, 556(7700):191–196, Apr. 2018. ISSN 0028-0836, 1476-4687. doi: 10.1038/s41586-018-0006-5. URL http://www.nature.com/articles/s41586-018-0006-5.

L. Caesar, G. D. McCarthy, D. J. R. Thornalley, N. Cahill, and S. Rahmstorf. Current Atlantic Meridional Overturning Circulation weakest in last millennium. *Nature Geoscience*, 14(3):118–120, Mar. 2021. ISSN 1752-0894, 1752-0908. doi: 10.1038/s41561-021-00699-z. URL http://www.nature.com/articles/s41561-021-00699-z.

G. S. Callendar. The artificial production of carbon dioxide and its influence on temperature. *Quarterly Journal of the Royal Meteorological Society*, 64(275):223–240, Apr. 1938. ISSN 00359009. doi: 10.1002/qj.49706427503. URL https://onlinelibrary.wiley.com/doi/10.1002/qj.49706427503.

R. Chemke, L. Zanna, and L. M. Polvani. Identifying a human signal in the North Atlantic warming hole. *Nature Communications*, 11(1):1540, Dec. 2020. ISSN 2041-1723. doi: 10.1038/s41467-020-15285-x. URL http://www.nature.com/articles/s41467-020-15285-x.

L. Cheng, K. E. Trenberth, J. Fasullo, T. Boyer, J. Abraham, and J. Zhu. Improved estimates of ocean heat content from 1960 to 2015. *Science Advances*, 3(3):e1601545, Mar. 2017. ISSN 2375-2548. doi: 10.1126/sciadv.1601545. URL http://advances.sciencemag.org/lookup/doi/10.1126/sciadv.1601545.

L. Cheng, J. Abraham, Z. Hausfather, and K. E. Trenberth. How fast are the oceans warming? *Science*, 363(6423):128–129, Jan. 2019. ISSN 0036-8075, 1095-9203. doi: 10.1126/science.aav7619. URL http://science.sciencemag.org/content/363/6423/128.

L. Cheng, K. E. Trenberth, N. Gruber, J. P. Abraham, J. T. Fasullo, G. Li, M. E. Mann, X. Zhao, and J. Zhu. Improved Estimates of Changes in Upper Ocean Salinity and the Hydrological Cycle. *Journal of Climate*, 33(23):10357–10381, Dec. 2020. ISSN 0894-8755, 1520-0442. doi: 10.1175/JCLI-D-20-0366.1. URL https://journals.ametsoc.org/doi/10.1175/JCLI-D-20-0366.1.

E.-S. Chung, B. Soden, B. J. Sohn, and L. Shi. Upper-tropospheric moistening in response to anthropogenic warming. *Proceedings of the National Academy of Sciences*, 111(32):11636–11641, Aug. 2014. ISSN 0027-8424, 1091-6490. doi: 10.1073/pnas.1409659111. URL http://www.pnas.org/cgi/doi/10.1073/pnas.1409659111.

J. Cole-Dai. Volcanoes and climate. *WIREs Climate Change*, 1(6):824–839, Nov. 2010. ISSN 1757-7780, 1757-7799. doi: 10.1002/wcc.76. URL https://onlinelibrary.wiley.com/doi/10.1002/wcc.76.

M. P. Couldrey, J. M. Gregory, F. Boeira Dias, P. Dobrohotoff, C. M. Domingues, O. Garuba, S. M. Griffies, H. Haak, A. Hu, M. Ishii, J. Jungclaus, A. Köhl, S. J. Marsland, S. Ojha, O. A. Saenko, A. Savita, A. Shao, D. Stammer, T. Suzuki, A. Todd, and L. Zanna. What causes the spread of model projections of ocean dynamic sea-level change in response to greenhouse gas forcing? *Climate Dynamics*, 56(1-2):155–187, Jan. 2021. ISSN 0930-7575, 1432-0894. doi: 10.1007/s00382-020-05471-4. URL http://link.springer.com/10.1007/s00382-020-05471-4.

M. F. Cronin, C. L. Gentemann, J. Edson, I. Ueki, M. Bourassa, S. Brown, C. A. Clayson, C. W. Fairall, J. T. Farrar, S. T. Gille, S. Gulev, S. A. Josey, S. Kato, M. Katsumata, E. Kent, M. Krug, P. J. Minnett, R. Parfitt, R. T. Pinker, P. W. Stackhouse, S. Swart, H. Tomita, D. Vandemark, A. R. Weller, K. Yoneyama, L. Yu, and D. Zhang. Air-Sea Fluxes With a Focus on Heat and Momentum. *Frontiers in Marine Science*, 6:430, July 2019. ISSN 2296-7745. doi: 10.3389/fmars.2019.00430. URL https://www.frontiersin.org/article/10.3389/fmars.2019.00430/full.

A. Dawson. eofs: A Library for EOF Analysis of Meteorological, Oceanographic, and Climate Data. *Journal of Open Research Software*, 4:e14, Apr. 2016. ISSN 2049-9647. doi: 10.5334/jors.122. URL http://openresearchsoftware.metajnl.com/articles/10.5334/jors.122/.

C. de Boyer Montégut. Mixed layer depth over the global ocean: An examination of profile data and a profile-based climatology. *Journal of Geophysical Research*, 109(C12):C12003, 2004. ISSN 0148-0227. doi: 10.1029/2004JC002378. URL http://doi.wiley.com/10.1029/2004JC002378.

C. de Lavergne, J. B. Palter, E. D. Galbraith, R. Bernardello, and I. Marinov. Cessation of deep convection in the open Southern Ocean under anthropogenic climate change. *Nature Climate Change*, 4(4):278–282, Apr. 2014. ISSN 1758-6798. doi: 10.1038/nclimate2132. URL https://www.nature.com/articles/nclimate2132.

D. Desbruyères, E. L. McDonagh, B. A. King, and V. Thierry. Global and Full-Depth Ocean Temperature Trends during the Early Twenty-First Century from Argo and Repeat Hydrography. *Journal of Climate*, 30(6):1985–1997, Mar. 2017. ISSN 0894-8755, 1520-0442. doi: 10.1175/JCLI-D-16-0396.1. URL http://journals.ametsoc.org/doi/10.1175/JCLI-D-16-0396.1.

D. G. Desbruyères, E. L. McDonagh, B. A. King, F. K. Garry, A. T. Blaker, B. I. Moat, and H. Mercier. Full-depth temperature trends in the northeastern Atlantic through the early 21st century. *Geophysical Research Letters*, 41(22):7971–7979, Nov. 2014. ISSN 00948276. doi: 10.1002/2014GL061844. URL http://doi.wiley.com/10.1002/2014GL061844.

D. G. Desbruyères, S. G. Purkey, E. L. McDonagh, G. C. Johnson, and B. A. King. Deep and abyssal ocean warming from 35 years of repeat hydrography. *Geophysical Research Letters*, 43(19):10,356–10,365, 2016. ISSN 1944-8007. doi: 10.1002/2016GL070413. URL https://agupubs.onlinelibrary.wiley.com/doi/abs/10.1002/2016GL070413.

C. Deser, A. Phillips, V. Bourdette, and H. Teng. Uncertainty in climate change projections: the role of internal variability. *Climate Dynamics*, 38(3):527–546, Feb. 2012. ISSN 1432-0894. doi: 10.1007/s00382-010-0977-x. URL https://doi.org/10.1007/s00382-010-0977-x.

C. Deser, F. Lehner, K. B. Rodgers, T. Ault, T. L. Delworth, P. N. DiNezio, A. Fiore, C. Frankignoul, J. C. Fyfe, D. E. Horton, J. E. Kay, R. Knutti, N. S. Lovenduski, J. Marotzke, K. A. McKinnon, S. Minobe, J. Randerson, J. A. Screen, I. R. Simpson, and M. Ting. Insights from Earth system model initial-condition large ensembles and future prospects. *Nature Climate Change*, 10(4):277–286, Apr. 2020. ISSN 1758-678X, 1758-6798. doi: 10.1038/s41558-020-0731-2. URL http://www.nature.com/articles/s41558-020-0731-2.

T. DeVries and F. Primeau. Dynamically and Observationally Constrained Estimates of Water-Mass Distributions and Ages in the Global Ocean. *Journal of Physical Oceanography*, 41(12):2381–2401, Dec. 2011. ISSN 0022-3670, 1520-0485. doi: 10.1175/JPO-D-10-05011.1. URL http://journals.ametsoc.org/doi/10.1175/JPO-D-10-05011.1.

F. B. Dias, R. Fiedler, S. J. Marsland, C. M. Domingues, L. Clément, S. R. Rintoul, E. L. Mcdonagh, M. M. Mata, and A. Savita. Ocean Heat Storage in Response to Changing Ocean Circulation Processes. *Journal of Climate*, 33(21):9065–9082, Nov. 2020. ISSN 0894-8755, 1520-0442. doi: 10.1175/JCLI-D-19-1016.1. URL https://journals.ametsoc.org/jcli/article/33/21/9065/353950/Ocean-Heat-Storage-in-Response-to-Changing-Ocean.

F. B. Dias, C. M. Domingues, S. J. Marsland, S. R. Rintoul, P. Uotila, R. Fiedler, M. M. Mata, N. L. Bindoff, and A. Savita. Subpolar Southern Ocean Response to Changes in the Surface Momentum, Heat, and Freshwater Fluxes under 2xCO2. *Journal of Climate*, 34(21):8755–8775, Nov. 2021. ISSN 0894-8755, 1520-0442. doi: 10.1175/JCLI-D-21-0161.1. URL https://journals.ametsoc.org/view/journals/clim/34/21/JCLI-D-21-0161.1.xml.

N. S. Diffenbaugh and A. Charland. Probability of emergence of novel temperature regimes at different levels of cumulative carbon emissions. *Frontiers in Ecology and the Environment*, 14(8):418–423, Oct. 2016. ISSN 15409295. doi: 10.1002/fee.1320. URL http://doi.wiley.com/10.1002/fee.1320.

N. S. Diffenbaugh and M. Scherer. Observational and model evidence of global emergence of permanent, unprecedented heat in the 20th and 21st centuries. *Climatic Change*, 107(3):615–624, Aug. 2011. ISSN 1573-1480. doi: 10.1007/s10584-011-0112-y. URL https://doi.org/10.1007/s10584-011-0112-y.

C. M. Domingues, J. A. Church, N. J. White, P. J. Gleckler, S. E. Wijffels, P. M. Barker, and J. R. Dunn. Improved estimates of upper-ocean warming and multi-decadal sea-level rise. *Nature*, 453(7198):1090–1093, June 2008. ISSN 1476-4687. doi: 10.1038/nature07080. URL https://www.nature.com/articles/nature07080.

S. M. Downes, N. L. Bindoff, and S. R. Rintoul. Impacts of Climate Change on the Subduction of Mode and Intermediate Water Masses in the Southern Ocean. *Journal of Climate*, 22(12):3289–3302, June 2009. ISSN 0894-8755, 1520-0442. doi: 10.1175/2008JCLI2653.1. URL http://journals.ametsoc.org/doi/abs/10.1175/2008JCLI2653.1.

S. M. Downes, N. L. Bindoff, and S. R. Rintoul. Changes in the Subduction of Southern Ocean Water Masses at the End of the Twenty-First Century in Eight IPCC Models. *Journal of Climate*, 23(24):6526–6541, Dec. 2010. ISSN 0894-8755, 1520-0442. doi: 10.1175/2010JCLI3620.1. URL http://journals.ametsoc.org/doi/abs/10.1175/2010JCLI3620.1.

C. O. Dufour, A. K. Morrison, S. M. Griffies, I. Frenger, H. Zanowski, and M. Winton. Preconditioning of the Weddell Sea Polynya by the Ocean Mesoscale and Dense Water Overflows. *Journal of Climate*, 30(19):7719–7737, June 2017. ISSN 0894-8755. doi: 10.1175/JCLI-D-16-0586.1. URL https://journals.ametsoc.org/doi/full/10.1175/JCLI-D-16-0586.1.

P. Durack. Ocean Salinity and the Global Water Cycle. *Oceanography*, 28(1):20–31, Mar. 2015. ISSN 10428275. doi: 10.5670/oceanog.2015.03. URL https://tos.org/oceanography/article/ocean-salinity-and-the-global-water-cycle.

P. J. Durack and S. E. Wijffels. Fifty-Year Trends in Global Ocean Salinities and Their Relationship to Broad-Scale Warming. *Journal of Climate*, 23(16):4342–4362, Aug. 2010. ISSN 0894-8755, 1520-0442. doi: 10.1175/2010JCLI3377.1. URL http://journals.ametsoc.org/doi/abs/10.1175/2010JCLI3377.1.

P. J. Durack, S. E. Wijffels, and R. J. Matear. Ocean Salinities Reveal Strong Global Water Cycle Intensification During 1950 to 2000. *Science*, 336(6080):455–458, Apr. 2012. ISSN 0036-8075, 1095-9203. doi: 10.1126/science.1212222. URL http://science.sciencemag.org/content/336/6080/455.

P. J. Durack, P. J. Gleckler, F. W. Landerer, and K. E. Taylor. Quantifying underestimates of long-term upper-ocean warming. *Nature Climate Change*, 4(11):999–1005, Nov. 2014a. ISSN 1758-6798. doi: 10.1038/nclimate2389. URL https://www.nature.com/articles/nclimate2389.

P. J. Durack, S. E. Wijffels, and P. J. Gleckler. Long-term sea-level change revisited: the role of salinity. *Environmental Research Letters*, 9(11):114017, Nov. 2014b. ISSN 1748-9326. doi: 10.1088/1748-9326/9/11/114017. URL https://doi.org/10.1088%2F1748-9326%2F9%2F11%2F114017.

K. Döös and D. J. Webb. The Deacon Cell and the Other Meridional Cells of the Southern Ocean. *Journal of Physical Oceanography*, 24(2), 1994.

K. Döös, J. Nilsson, J. Nycander, L. Brodeau, and M. Ballarotta. The World Ocean Thermohaline Circulation. *Journal of Physical Oceanography*, 42(9):1445–1460, Sept. 2012. ISSN 0022-3670, 1520-0485. doi: 10.1175/JPO-D-11-0163.1. URL http://journals.ametsoc.org/doi/abs/10.1175/JPO-D-11-0163.1.

V. W. Ekman. On the influence of the earth's rotation on ocean-currents. *Ark. Mat. Astron. Fys.*, 2:1–52, 1905.

D. G. Evans, J. D. Zika, A. C. Naveira Garabato, and A. J. G. Nurser. The imprint of Southern Ocean overturning on seasonal water mass variability in Drake Passage. *Journal of Geophysical Research: Oceans*, 119(11):7987–8010, Nov. 2014. ISSN 21699275. doi: 10.1002/2014JC010097. URL http://doi.wiley.com/10.1002/2014JC010097.

D. G. Evans, J. D. Zika, A. C. Naveira Garabato, and A. J. G. Nurser. The Cold Transit of Southern Ocean Upwelling. *Geophysical Research Letters*, 45(24):13,386–13,395, Dec. 2018. ISSN 0094-8276, 1944-8007. doi: 10.1029/2018GL079986. URL https://onlinelibrary.wiley.com/doi/abs/10.1029/2018GL079986.

V. Eyring, S. Bony, G. A. Meehl, C. A. Senior, B. Stevens, R. J. Stouffer, and K. E. Taylor. Overview of the Coupled Model Intercomparison Project Phase 6 (CMIP6) experimental design and organization. *Geoscientific Model Development*, 9(5): 1937–1958, May 2016. ISSN 1991-9603. doi: 10.5194/gmd-9-1937-2016. URL https://gmd.copernicus.org/articles/9/1937/2016/.

V. Eyring, N. P. Gillett, K. M. AchutaRao, R. Barimalala, M. Barreiro Parrillo, N. Bellouin, C. Cassou, P. J. Durack, Y. Kosaka, S. McGregor, S. Min, O. Morgenstern, and Y. Sun. Human Influence on the Climate System. In *Climate Change 2021: The Physical Science Basis. Contribution of Working Group I to the Sixth Assessment Report of the Intergovernmental Panel on Climate Change*. Cambridge University Press, 2021.

M. Fieux. *L'océan planétaire*. Les presses de l'ensta edition, 2010.

E. Foote. Circumstances affecting the Heat of the Sun's Rays. *The American Journal of Sciences and Art*, 22(66):382–383, 1856.

P. Forster, T. Storelvmo, K. Armour, W. Collins, J.-L. Dufresne, D. Frame, D. J. Lunt, T. Mauritsen, M. D. Palmer, M. Watanabe, M. Wild, and H. Zhang. The Earth's Energy Budget, Climate Feedbacks, and Climate Sensitivity. In *Climate Change 2021: The Physical Science Basis. Contribution of Working Group I to the Sixth Assessment Report of the Intergovernmental Panel on Climate Change*. Cambridge University Press, 2021.

B. Fox-Kemper, H. T. Hewitt, C. Xiao, G. Aðalgeirsdóttir, S. S. Drijfhout, T. L. Edwards, N. R. Golledge, M. Hemer, R. E. Kopp, G. Krinner, A. Mix, D. Notz, S. Nowicki, I. S. Nurhati, L. Ruiz, J.-B. Sallée, A. B. A. Slangen, and Y. Yu. Ocean, Cryosphere and Sea Level Change. In *Climate Change 2021: The Physical Science Basis. Contribution of Working Group I to the Sixth Assessment Report of the Intergovernmental Panel on Climate Change*. Cambridge University Press, 2021.

C. Frankignoul and K. Hasselmann. Stochastic climate models, Part II Application to sea-surface temperature anomalies and thermocline variability. *Tellus*, 29(4):289–305, Jan. 1977. ISSN 0040-2826, 2153-3490. doi: 10.3402/tellusa.v29i4.11362. URL https://www.tandfonline.com/doi/full/10.3402/tellusa.v29i4.11362.

C. L. E. Franzke and T. J. O'Kane, editors. *Nonlinear and Stochastic Climate Dynamics*. Cambridge university press edition, 2017.

P. Friedlingstein, M. O'Sullivan, M. W. Jones, R. M. Andrew, J. Hauck, A. Olsen, G. P. Peters, W. Peters, J. Pongratz, S. Sitch, C. Le Quéré, J. G. Canadell, P. Ciais, R. B. Jackson, S. Alin, L. E. O. C. Aragão, A. Arneth, V. Arora, N. R. Bates, M. Becker, A. Benoit-Cattin, H. C. Bittig, L. Bopp, S. Bultan, N. Chandra, F. Chevallier, L. P. Chini, W. Evans, L. Florentie, P. M. Forster, T. Gasser, M. Gehlen, D. Gilfillan, T. Gkritzalis, L. Gregor, N. Gruber, I. Harris, K. Hartung, V. Haverd, R. A. Houghton, T. Ilyina, A. K. Jain, E. Joetzjer, K. Kadono, E. Kato, V. Kitidis, J. I. Korsbakken, P. Landschützer, N. Lefèvre, A. Lenton, S. Lienert, Z. Liu, D. Lombardozzi, G. Marland, N. Metzl, D. R. Munro, J. E. M. S. Nabel, S.-I. Nakaoka, Y. Niwa, K. O'Brien, T. Ono, P. I. Palmer, D. Pierrot, B. Poulter, L. Resplandy, E. Robertson, C. Rödenbeck, J. Schwinger, R. Séférian, I. Skjelvan, A. J. P. Smith, A. J. Sutton, T. Tanhua, P. P. Tans, H. Tian, B. Tilbrook, G. van der Werf, N. Vuichard, A. P. Walker, R. Wanninkhof, A. J. Watson, D. Willis, A. J. Wiltshire, W. Yuan, X. Yue, and S. Zaehle. Global Carbon Budget 2020. *Earth System Science Data*, 12(4):3269–3340, Dec. 2020. ISSN 1866-3516. doi: 10.5194/essd-12-3269-2020. URL https://essd.copernicus.org/articles/12/3269/2020/.

T. L. Frölicher, J. L. Sarmiento, D. J. Paynter, J. P. Dunne, J. P. Krasting, and M. Winton. Dominance of the Southern Ocean in Anthropogenic Carbon and Heat Uptake in CMIP5 Models. *Journal of Climate*, 28(2):862–886, Jan. 2015. ISSN 0894-8755. doi: 10.1175/JCLI-D-14-00117.1. URL https://journals.ametsoc.org/doi/full/10.1175/JCLI-D-14-00117.1.

T. L. Frölicher, K. B. Rodgers, C. A. Stock, and W. W. L. Cheung. Sources of uncertainties in 21st century projections of potential ocean ecosystem stressors. *Global Biogeochemical Cycles*, 30(8):1224–1243, 2016. ISSN 1944-9224. doi: 10.1002/2015GB005338. URL https://agupubs.onlinelibrary.wiley.com/doi/abs/10.1002/2015GB005338.

J. C. Fyfe, O. A. Saenko, K. Zickfeld, M. Eby, and A. J. Weaver. The Role of Poleward-Intensifying Winds on Southern Ocean Warming. *Journal of Climate*, 20(21):5391–5400, Nov. 2007. ISSN 1520-0442, 0894-8755. doi: 10.1175/2007JCLI1764.1. URL http://journals.ametsoc.org/doi/10.1175/2007JCLI1764.1.

C. Garcia-Soto, L. Caesar, A. Cazenave, L. Cheng, A. Cheripka, P. J. Durack, K. Evans, D. Halpern, L. Jewett, S. Y. Kim, G. Li, I. Rigor, S. Schmidtko, J. Wang, and T. Zielinski. Trends in the physical and chemical state of the ocean (Chapter 5). In *The Second World Ocean Assessment. World Ocean Assessment II,*, volume I. Unites nations edition, 2021. URL https://www.un.org/regularprocess/sites/www.un.org.regularprocess/files/2011859-e-woa-ii-vol-i.pdf.

O. A. Garuba and B. A. Klinger. Ocean Heat Uptake and Interbasin Transport of the Passive and Redistributive Components of Surface Heating. *Journal of Climate*, 29(20):7507–7527, July 2016. ISSN 0894-8755. doi: 10.1175/JCLI-D-16-0138.1. URL https://journals.ametsoc.org/doi/10.1175/JCLI-D-16-0138.1.

O. A. Garuba and B. A. Klinger. The Role of Individual Surface Flux Components in the Passive and Active Ocean Heat Uptake. *Journal of Climate*, 31(15):6157–6173, May 2018. ISSN 0894-8755. doi: 10.1175/JCLI-D-17-0452.1. URL https://journals.ametsoc.org/doi/full/10.1175/JCLI-D-17-0452.1.

P. R. Gent and J. C. Mcwilliams. Isopycnal Mixing in Ocean Circulation Models. *Journal of Physical Oceanography*, 20(1): 150–155, Jan. 1990. ISSN 0022-3670, 1520-0485. doi: 10.1175/1520-0485(1990)020<0150:IMIOCM>2.0.CO;2. URL http://journals.ametsoc.org/doi/10.1175/1520-0485(1990)020<0150:IMIOCM>2.0.CO;2.

M. J. Gidden, K. Riahi, S. J. Smith, S. Fujimori, G. Luderer, E. Kriegler, D. P. van Vuuren, M. van den Berg, L. Feng, D. Klein, K. Calvin, J. C. Doelman, S. Frank, O. Fricko, M. Harmsen, T. Hasegawa, P. Havlik, J. Hilaire, R. Hoesly, J. Horing, A. Popp, E. Stehfest, and K. Takahashi. Global emissions pathways under different socioeconomic scenarios for use in CMIP6: a dataset of harmonized emissions trajectories through the end of the century. *Geoscientific Model Development*, 12(4):1443–1475, Apr. 2019. ISSN 1991-9603. doi: 10.5194/gmd-12-1443-2019. URL https://gmd.copernicus.org/articles/12/1443/2019/.

S. T. Gille. Warming of the Southern Ocean Since the 1950s. *Science*, 295(5558):1275–1277, Feb. 2002. ISSN 00368075, 10959203. doi: 10.1126/science.1065863. URL https://www.sciencemag.org/lookup/doi/10.1126/science.1065863.

S. T. Gille. Decadal-Scale Temperature Trends in the Southern Hemisphere Ocean. *Journal of Climate*, 21(18):4749–4765, Sept. 2008. ISSN 0894-8755. doi: 10.1175/2008JCLI2131.1. URL https://journals.ametsoc.org/doi/full/10.1175/2008JCLI2131.1.

F. Giorgi and X. Bi. Time of emergence (TOE) of GHG-forced precipitation change hot-spots. *Geophysical Research Letters*, 36(6):L06709, 2009. ISSN 1944-8007. doi: 10.1029/2009GL037593. URL https://agupubs.onlinelibrary.wiley.com/doi/abs/10.1029/2009GL037593.

A. Gjermundsen, A. Nummelin, D. Olivié, M. Bentsen, Ø. Seland, and M. Schulz. Shutdown of Southern Ocean convection controls long-term greenhouse gas-induced warming. *Nature Geoscience*, 14(10):724–731, Oct. 2021. ISSN 1752-0894, 1752-0908. doi: 10.1038/s41561-021-00825-x. URL https://www.nature.com/articles/s41561-021-00825-x.

J. Glausiusz. Rethinking travel in a post-pandemic world. *Nature*, 589(7840):155–157, Jan. 2021. ISSN 0028-0836, 1476-4687. doi: 10.1038/d41586-020-03649-8. URL http://www.nature.com/articles/d41586-020-03649-8.

P. J. Gleckler, B. D. Santer, C. M. Domingues, D. W. Pierce, T. P. Barnett, J. A. Church, K. E. Taylor, K. M. AchutaRao, T. P. Boyer, M. Ishii, and P. M. Caldwell. Human-induced global ocean warming on multidecadal timescales. *Nature Climate Change*, 2(7):524–529, July 2012. ISSN 1758-678X, 1758-6798. doi: 10.1038/nclimate1553. URL http://www.nature.com/articles/nclimate1553.

N. R. Golledge, E. D. Keller, N. Gomez, K. A. Naughten, J. Bernales, L. D. Trusel, and T. L. Edwards. Global environmental consequences of twenty-first-century ice-sheet melt. *Nature*, 566(7742):65–72, Feb. 2019. ISSN 0028-0836, 1476-4687. doi: 10.1038/s41586-019-0889-9. URL http://www.nature.com/articles/s41586-019-0889-9.

S. A. Good, M. J. Martin, and N. A. Rayner. EN4: Quality controlled ocean temperature and salinity profiles and monthly objective analyses with uncertainty estimates. *Journal of Geophysical Research: Oceans*, 118(12):6704–6716, Dec. 2013. ISSN 21699275. doi: 10.1002/2013JC009067. URL http://doi.wiley.com/10.1002/2013JC009067.

B. Goutorbe, J. Poort, F. Lucazeau, and S. Raillard. Global heat flow trends resolved from multiple geological and geophysical proxies. *Geophysical Journal International*, 187(3):1405–1419, Dec. 2011. ISSN 1365-246X, 0956-540X. doi: 10.1111/j.1365-246X.2011.05228.x. URL https://academic.oup.com/gji/article/187/3/1405/614806.

J. M. Gregory, H. T. Banks, P. A. Stott, J. A. Lowe, and M. D. Palmer. Simulated and observed decadal variability in ocean heat content. *Geophysical Research Letters*, 31(15), 2004. ISSN 1944-8007. doi: 10.1029/2004GL020258. URL https://agupubs.onlinelibrary.wiley.com/doi/abs/10.1029/2004GL020258.

J. M. Gregory, N. Bouttes, S. M. Griffies, H. Haak, W. J. Hurlin, J. Jungclaus, M. Kelley, W. G. Lee, J. Marshall, A. Romanou, O. A. Saenko, D. Stammer, and M. Winton. The Flux-Anomaly-Forced Model Intercomparison Project (FAFMIP) contribution to CMIP6: investigation of sea-level and ocean climate change in response to CO2 forcing. *Geoscientific Model Development*, 9(11):3993–4017, Nov. 2016. ISSN 1991-9603. doi: 10.5194/gmd-9-3993-2016. URL https://www.geosci-model-dev.net/9/3993/2016/.

S. M. Griffies, G. Danabasoglu, P. J. Durack, A. J. Adcroft, V. Balaji, C. W. Böning, E. P. Chassignet, E. Curchitser, J. Deshayes, H. Drange, B. Fox-Kemper, P. J. Gleckler, J. M. Gregory, H. Haak, R. W. Hallberg, P. Heimbach, H. T. Hewitt, D. M. Holland, T. Ilyina, J. H. Jungclaus, Y. Komuro, J. P. Krasting, W. G. Large, S. J. Marsland, S. Masina, T. J. McDougall, A. J. G. Nurser, J. C. Orr, A. Pirani, F. Qiao, R. J. Stouffer, K. E. Taylor, A. M. Treguier, H. Tsujino, P. Uotila, M. Valdivieso, Q. Wang, M. Winton, and S. G. Yeager. OMIP contribution to CMIP6: experimental and diagnosticprotocol for the physical component of the Ocean Model Intercomparison Project. *Geoscientific Model Development*, 9(9):3231–3296, Sept. 2016. ISSN 1991-9603. doi: 10.5194/gmd-9-3231-2016. URL https://www.geosci-model-dev.net/9/3231/2016/.

S. Groeskamp, J. D. Zika, T. J. McDougall, B. M. Sloyan, and F. Laliberté. The Representation of Ocean Circulation and Variability in Thermodynamic Coordinates. *Journal of Physical Oceanography*, 44(7):1735–1750, July 2014. ISSN 0022-3670, 1520-0485. doi: 10.1175/JPO-D-13-0213.1. URL http://journals.ametsoc.org/doi/abs/10.1175/JPO-D-13-0213.1.

S. K. Gulev, P. W. Thorne, J. Ahn, F. J. Dentener, C. M. Domingues, S. Gerland, D. Gong, D. S. Kaufman, H. C. Nnamchi, J. Quaas, J. A. Rivera, S. Sathyendranath, S. L. Smith, B. Trewin, K. von Shuckmann, and R. S. Vose. Changing State of the Climate System. In *Climate Change 2021: The Physical Science Basis. Contribution of Working Group I to the Sixth Assessment Report of the Intergovernmental Panel on Climate Change*. Cambridge University Press, 2021.

A. S. Gupta, N. C. Jourdain, J. N. Brown, and D. Monselesan. Climate Drift in the CMIP5 Models. *Journal of Climate*, 26(21): 8597–8615, Nov. 2013. ISSN 0894-8755, 1520-0442. doi: 10.1175/JCLI-D-12-00521.1. URL https://journals.ametsoc.org/jcli/article/26/21/8597/34545/Climate-Drift-in-the-CMIP5-Models.

K. Hanawa and L. D. Talley. Chapter 5.4 Mode waters. In G. Siedler, J. Church, and J. Gould, editors, *International Geophysics*, volume 77 of *Ocean Circulation and Climate*, pages 373–386. Academic Press, Jan. 2001. doi: 10.1016/S0074-6142(01)80129-7. URL http://www.sciencedirect.com/science/article/pii/S0074614201801297.

K. Hasselmann. On the signal-to-noise problem in atmospheric response studies, 1979.

F. A. Haumann, N. Gruber, and M. Münnich. Sea-Ice Induced Southern Ocean Subsurface Warming and Surface Cooling in a Warming Climate. *AGU Advances*, 1(2), June 2020. ISSN 2576-604X, 2576-604X. doi: 10.1029/2019AV000132. URL https://onlinelibrary.wiley.com/doi/10.1029/2019AV000132.

E. Hawkins and R. Sutton. The Potential to Narrow Uncertainty in Regional Climate Predictions. *Bulletin of the American Meteorological Society*, 90(8):1095–1108, Aug. 2009. ISSN 0003-0007, 1520-0477. doi: 10.1175/2009BAMS2607.1. URL https://journals.ametsoc.org/doi/10.1175/2009BAMS2607.1.

E. Hawkins and R. Sutton. Time of emergence of climate signals. *Geophysical Research Letters*, 39(1):L01702, Jan. 2012. ISSN 00948276. doi: 10.1029/2011GL050087. URL http://doi.wiley.com/10.1029/2011GL050087.

E. Hawkins, R. S. Smith, J. M. Gregory, and D. A. Stainforth. Irreducible uncertainty in near-term climate projections. *Climate Dynamics*, 46(11-12):3807–3819, June 2016. ISSN 0930-7575, 1432-0894. doi: 10.1007/s00382-015-2806-8. URL http://link.springer.com/10.1007/s00382-015-2806-8.

I. M. Held and B. J. Soden. Robust Responses of the Hydrological Cycle to Global Warming. *Journal of Climate*, 19(21): 5686–5699, Nov. 2006. ISSN 0894-8755. doi: 10.1175/JCLI3990.1. URL https://journals.ametsoc.org/doi/full/10.1175/JCLI3990.1.

K. P. Helm, N. L. Bindoff, and J. A. Church. Changes in the global hydrological-cycle inferred from ocean salinity. *Geophysical Research Letters*, 37(18), 2010. ISSN 1944-8007. doi: 10.1029/2010GL044222. URL https://agupubs.onlinelibrary.wiley.com/doi/abs/10.1029/2010GL044222.

S. A. Henson, C. Beaulieu, T. Ilyina, J. G. John, M. Long, R. Séférian, J. Tjiputra, and J. L. Sarmiento. Rapid emergence of climate change in environmental drivers of marine ecosystems. *Nature Communications*, 8:14682, Mar. 2017. ISSN 2041-1723. doi: 10.1038/ncomms14682. URL http://www.nature.com/doifinder/10.1038/ncomms14682.

C. Heuzé. North Atlantic deep water formation and AMOC in CMIP5 models. *Ocean Science*, 13(4):609–622, July 2017. ISSN 1812-0792. doi: 10.5194/os-13-609-2017. URL https://os.copernicus.org/articles/13/609/2017/.

C. Heuzé. Antarctic Bottom Water and North Atlantic Deep Water in CMIP6 models. *Ocean Science*, 17(1):59–90, Jan. 2021. ISSN 1812-0792. doi: 10.5194/os-17-59-2021. URL https://os.copernicus.org/articles/17/59/2021/.

C. Heuzé, K. J. Heywood, D. P. Stevens, and J. K. Ridley. Southern Ocean bottom water characteristics in CMIP5 models. *Geophysical Research Letters*, pages 1409–1414, 2013. ISSN 1944-8007. doi: 10.1002/grl.50287@10.1002/(ISSN)1944-8007.GRLCMIP5. URL https://agupubs.onlinelibrary.wiley.com/doi/abs/10.1002/grl.50287%4010.1002/%28ISSN%291944-8007.GRLCMIP5.

C. Heuzé, K. J. Heywood, D. P. Stevens, and J. K. Ridley. Changes in Global Ocean Bottom Properties and Volume Transports in CMIP5 Models under Climate Change Scenarios. *Journal of Climate*, 28(8):2917–2944, 2015. ISSN 0894-8755. doi: 10.1175/JCLI-D-14-00381.1. URL https://journals.ametsoc.org/doi/10.1175/JCLI-D-14-00381.1.

M. Hieronymus, J. Nilsson, and J. Nycander. Water Mass Transformation in Salinity–Temperature Space. *Journal of Physical Oceanography*, 44(9):2547–2568, Sept. 2014. ISSN 0022-3670, 1520-0485. doi: 10.1175/JPO-D-13-0257.1. URL http://journals.ametsoc.org/doi/abs/10.1175/JPO-D-13-0257.1.

S. Hirahara, M. Ishii, and Y. Fukuda. Centennial-Scale Sea Surface Temperature Analysis and Its Uncertainty. *Journal of Climate*, 27(1):57–75, Jan. 2014. ISSN 0894-8755, 1520-0442. doi: 10.1175/JCLI-D-12-00837.1. URL http://journals.ametsoc.org/doi/10.1175/JCLI-D-12-00837.1.

W. R. Hobbs, C. Roach, T. Roy, J.-B. Sallée, and N. Bindoff. Anthropogenic Temperature and Salinity Changes in the Southern Ocean. *Journal of Climate*, 34(1):215–228, Jan. 2021. ISSN 0894-8755, 1520-0442. doi: 10.1175/JCLI-D-20-0454.1. URL https://journals.ametsoc.org/view/journals/clim/34/1/jcliD200454.xml.

M. Holzer, T. DeVries, and C. de Lavergne. Diffusion controls the ventilation of a Pacific Shadow Zone above abyssal overturning. *Nature Communications*, 12(1):4348, Dec. 2021. ISSN 2041-1723. doi: 10.1038/s41467-021-24648-x. URL http://www.nature.com/articles/s41467-021-24648-x.

Y. Hong, Y. Du, X. Xia, L. Xu, Y. Zhang, and S.-P. Xie. Subantarctic Mode Water and its long-term change in CMIP6 models. *Journal of Climate*, pages 1–51, Sept. 2021. ISSN 0894-8755, 1520-0442. doi: 10.1175/JCLI-D-21-0133.1. URL https://journals.ametsoc.org/view/journals/clim/aop/JCLI-D-21-0133.1/JCLI-D-21-0133.1.xml.

S. Hosoda, T. Suga, N. Shikama, and K. Mizuno. Global surface layer salinity change detected by Argo and its implication for hydrological cycle intensification. *Journal of Oceanography*, 65(4):579–586, Aug. 2009. ISSN 1573-868X. doi: 10.1007/s10872-009-0049-1. URL https://doi.org/10.1007/s10872-009-0049-1.

F. Hourdin, C. Rio, J. Grandpeix, J. Madeleine, F. Cheruy, N. Rochetin, A. Jam, I. Musat, A. Idelkadi, L. Fairhead, M. Foujols, L. Mellul, A. Traore, J. Dufresne, O. Boucher, M. Lefebvre, E. Millour, E. Vignon, J. Jouhaud, F. B. Diallo, F. Lott, G. Gastineau, A. Caubel, Y. Meurdesoif, and J. Ghattas. LMDZ6A: The Atmospheric Component of the IPSL Climate Model With Improved and Better Tuned Physics. *Journal of Advances in Modeling Earth Systems*, 12(7), July 2020. ISSN 1942-2466, 1942-2466. doi: 10.1029/2019MS001892. URL https://onlinelibrary.wiley.com/doi/10.1029/2019MS001892.

F. Hourdin, D. Williamson, C. Rio, F. Couvreux, R. Roehrig, N. Villefranque, I. Musat, L. Fairhead, F. B. Diallo, and V. Volodina. Process-Based Climate Model Development Harnessing Machine Learning: II. Model Calibration From Single Column to Global. *Journal of Advances in Modeling Earth Systems*, 13(6), June 2021. ISSN 1942-2466, 1942-2466. doi: 10.1029/2020MS002225. URL https://onlinelibrary.wiley.com/doi/10.1029/2020MS002225.

S. Hu, S.-P. Xie, and W. Liu. Global Pattern Formation of Net Ocean Surface Heat Flux Response to Greenhouse Warming. *Journal of Climate*, 33(17):7503–7522, Sept. 2020. ISSN 0894-8755, 1520-0442. doi: 10.1175/JCLI-D-19-0642.1. URL https://journals.ametsoc.org/doi/10.1175/JCLI-D-19-0642.1.

B. Huang, P. W. Thorne, V. F. Banzon, T. Boyer, G. Chepurin, J. H. Lawrimore, M. J. Menne, T. M. Smith, R. S. Vose, and H.-M. Zhang. Extended Reconstructed Sea Surface Temperature, Version 5 (ERSSTv5): Upgrades, Validations, and Intercomparisons. *Journal of Climate*, 30(20):8179–8205, Oct. 2017. ISSN 0894-8755, 1520-0442. doi: 10.1175/JCLI-D-16-0836.1. URL http://journals.ametsoc.org/doi/10.1175/JCLI-D-16-0836.1.

S. Häkkinen, P. B. Rhines, and D. L. Worthen. Warming of the Global Ocean: Spatial Structure and Water-Mass Trends. *Journal of Climate*, 29(13):4949–4963, July 2016. ISSN 0894-8755, 1520-0442. doi: 10.1175/JCLI-D-15-0607.1. URL http://journals.ametsoc.org/doi/10.1175/JCLI-D-15-0607.1.

B. Ingleby and M. Huddleston. Quality control of ocean temperature and salinity profiles — Historical and real-time data. *Journal of Marine Systems*, 65(1-4):158–175, Mar. 2007. ISSN 09247963. doi: 10.1016/j.jmarsys.2005.11.019. URL https://linkinghub.elsevier.com/retrieve/pii/S0924796306002909.

Intergovernmental Panel on Climate Change. Summary for Policymakers. In *Global warming of 1.5°C. An IPCC Special Report on the impacts of global warming of 1.5°C above pre-industrial levels and related global greenhouse gas emission pathways, in the context of strengthening the global response to the threat of climate change, sustainable development, and efforts to eradicate poverty*. 2018. URL http://www.ipcc.ch/report/sr15/. OCLC: 1056192590.

IPCC. *Climate Change 2021: The Physical Science Basis. Contribution of Working Group I to the Sixth Assessment Report of the Intergovernmental Panel on Climate Change*. Cambridge University Press, 2021a.

IPCC. Summary for Policymakers. In *Climate Change 2021: The Physical Science Basis. Contribution of Working Group I to the Sixth Assessment Report of the Intergovernmental Panel on Climate Change*. Cambridge University Press, 2021b.

D. Irving, W. Hobbs, J. Church, and J. Zika. A Mass and Energy Conservation Analysis of Drift in the CMIP6 Ensemble. *Journal of Climate*, pages 1–43, Aug. 2020. ISSN 0894-8755, 1520-0442. doi: 10.1175/JCLI-D-20-0281.1. URL https://journals.ametsoc.org/doi/10.1175/JCLI-D-20-0281.1.

M. Ishii and M. Kimoto. Reevaluation of historical ocean heat content variations with time-varying XBT and MBT depth bias corrections. *Journal of Oceanography*, 65(3):287–299, June 2009. ISSN 0916-8370, 1573-868X. doi: 10.1007/s10872-009-0027-7. URL http://link.springer.com/10.1007/s10872-009-0027-7.

M. Ishii, A. Shouji, S. Sugimoto, and T. Matsumoto. Objective analyses of sea-surface temperature and marine meteorological variables for the 20th century using ICOADS and the Kobe Collection. *International Journal of Climatology*, 25(7):865–879, June 2005. ISSN 0899-8418, 1097-0088. doi: 10.1002/joc.1169. URL https://onlinelibrary.wiley.com/doi/10.1002/joc.1169.

M. Ishii, Y. Fukuda, S. Hirahara, S. Yasui, T. Suzuki, and K. Sato. Accuracy of Global Upper Ocean Heat Content Estimation Expected from Present Observational Data Sets. *SOLA*, 13(0):163–167, 2017. ISSN 1349-6476. doi: 10.2151/sola.2017-030. URL https://www.jstage.jst.go.jp/article/sola/13/0/13_2017-030/_article.

D. R. Jackett and T. J. McDougall. A Neutral Density Variable for the World's Oceans. *Journal of Physical Oceanography*, 27(2):237–263, Feb. 1997. ISSN 0022-3670, 1520-0485. doi: 10.1175/1520-0485(1997)027<0237:ANDVFT>2.0.CO;2. URL http://journals.ametsoc.org/doi/abs/10.1175/1520-0485%281997%29027%3C0237%3AANDVFT%3E2.0.CO%3B2.

T. Janisch and D. L. Hilty. Background Report for the 2017 Virtual Conference on University Air Miles Reduction. page 23, 2017.

S. Jayne, D. Roemmich, N. Zilberman, S. Riser, K. Johnson, G. Johnson, and S. Piotrowicz. The Argo Program: Present and Future. *Oceanography*, 30(2):18–28, June 2017. ISSN 10428275. doi: 10.5670/oceanog.2017.213. URL https://tos.org/oceanography/article/the-argo-program-present-and-future.

W. Jiang, G. Gastineau, and F. Codron. Multicentennial Variability Driven by Salinity Exchanges Between the Atlantic and the Arctic Ocean in a Coupled Climate Model. *Journal of Advances in Modeling Earth Systems*, 13(3), Mar. 2021. ISSN 1942-2466, 1942-2466. doi: 10.1029/2020MS002366. URL https://onlinelibrary.wiley.com/doi/10.1029/2020MS002366.

G. C. Johnson. Quantifying Antarctic Bottom Water and North Atlantic Deep Water volumes. *Journal of Geophysical Research*, 113(C5):C05027, May 2008. ISSN 0148-0227. doi: 10.1029/2007JC004477. URL http://doi.wiley.com/10.1029/2007JC004477.

G. C. Johnson and A. H. Orsi. Southwest Pacific Ocean Water-Mass Changes between 1968/69 and 1990/91*†. *Journal of Climate*, 10(2):306–316, Feb. 1997. ISSN 0894-8755, 1520-0442. doi: 10.1175/1520-0442(1997)010<0306:SPOWMC>2.0.CO;2. URL http://journals.ametsoc.org/doi/10.1175/1520-0442(1997)010<0306:SPOWMC>2.0.CO;2.

D. C. Jones, A. J. S. Meijers, E. Shuckburgh, J.-B. Sallée, P. Haynes, E. K. McAufield, and M. R. Mazloff. How does Subantarctic Mode Water ventilate the Southern Hemisphere subtropics? *Journal of Geophysical Research: Oceans*, 121(9):6558–6582, Sept. 2016a. ISSN 21699275. doi: 10.1002/2016JC011680. URL http://doi.wiley.com/10.1002/2016JC011680.

J. M. Jones, S. T. Gille, H. Goosse, N. J. Abram, P. O. Canziani, D. J. Charman, K. R. Clem, X. Crosta, C. de Lavergne, I. Eisenman, M. H. England, R. L. Fogt, L. M. Frankcombe, G. J. Marshall, V. Masson-Delmotte, A. K. Morrison, A. J. Orsi, M. N. Raphael, J. A. Renwick, D. P. Schneider, G. R. Simpkins, E. J. Steig, B. Stenni, D. Swingedouw, and T. R. Vance. Assessing recent trends in high-latitude Southern Hemisphere surface climate. *Nature Climate Change*, 6(10):917–926, Oct. 2016b. ISSN 1758-678X, 1758-6798. doi: 10.1038/nclimate3103. URL http://www.nature.com/articles/nclimate3103.

L. Jullion, A. C. Naveira Garabato, M. P. Meredith, P. R. Holland, P. Courtois, and B. A. King. Decadal Freshening of the Antarctic Bottom Water Exported from the Weddell Sea. *Journal of Climate*, 26(20):8111–8125, Oct. 2013. ISSN 0894-8755, 1520-0442. doi: 10.1175/JCLI-D-12-00765.1. URL http://journals.ametsoc.org/doi/10.1175/JCLI-D-12-00765.1.

P. Kalmus. Fly less to convey urgency. *Science*, 365(6460):1355–1355, Sept. 2019. ISSN 0036-8075, 1095-9203. doi: 10.1126/science.aaz5810. URL https://science.sciencemag.org/content/365/6460/1355.

J. E. Kay, C. Deser, A. Phillips, A. Mai, C. Hannay, G. Strand, J. M. Arblaster, S. C. Bates, G. Danabasoglu, J. Edwards, M. Holland, P. Kushner, J.-F. Lamarque, D. Lawrence, K. Lindsay, A. Middleton, E. Munoz, R. Neale, K. Oleson, L. Polvani, and M. Vertenstein. The Community Earth System Model (CESM) Large Ensemble Project: A Community Resource for Studying Climate Change in the Presence of Internal Climate Variability. *Bulletin of the American Meteorological Society*, 96(8):1333–1349, Aug. 2015. ISSN 0003-0007, 1520-0477. doi: 10.1175/BAMS-D-13-00255.1. URL https://journals.ametsoc.org/doi/10.1175/BAMS-D-13-00255.1.

K. M. Keller, F. Joos, and C. C. Raible. Time of emergence of trends in ocean biogeochemistry. *Biogeosciences*, 11(13):3647–3659, July 2014. ISSN 1726-4189. doi: 10.5194/bg-11-3647-2014. URL https://www.biogeosciences.net/11/3647/2014/.

S. Khatiwala, F. Primeau, and T. Hall. Reconstruction of the history of anthropogenic CO2 concentrations in the ocean. *Nature*, 462(7271):346–349, Nov. 2009. ISSN 0028-0836, 1476-4687. doi: 10.1038/nature08526. URL http://www.nature.com/articles/nature08526.

S. P. Khatiwala, T. Tanhua, S. E. Mikaloff Fletcher, M. Gerber, S. C. Doney, H. D. Graven, N. Gruber, G. A. McKinley, A. Murata, A. F. Rios, and C. L. Sabine. Global ocean storage of anthropogenic carbon. *Biogeosciences*, 10(4):2169–2191, 2013. doi: 10.3929/ethz-b-000067385. URL https://www.research-collection.ethz.ch/handle/20.500.11850/67385.

M. C. Kirchmeier-Young, F. W. Zwiers, and N. P. Gillett. Attribution of Extreme Events in Arctic Sea Ice Extent. *Journal of Climate*, 30(2):553–571, Jan. 2017. ISSN 0894-8755, 1520-0442. doi: 10.1175/JCLI-D-16-0412.1. URL https://journals.ametsoc.org/doi/10.1175/JCLI-D-16-0412.1.

M. Klöwer, D. Hopkins, M. Allen, and J. Higham. An analysis of ways to decarbonize conference travel after COVID-19. *Nature*, 583(7816):356–359, July 2020. ISSN 0028-0836, 1476-4687. doi: 10.1038/d41586-020-02057-2. URL http://www.nature.com/articles/d41586-020-02057-2.

S. Kobayashi, Y. Ota, Y. Harada, A. Ebita, M. Moriya, H. Onoda, K. Onogi, H. Kamahori, C. Kobayashi, H. Endo, K. Miyaoka, and K. Takahashi. The JRA-55 Reanalysis: General Specifications and Basic Characteristics. *Journal of the Meteorological Society of Japan. Ser. II*, 93(1):5–48, 2015. ISSN 0026-1165, 2186-9057. doi: 10.2151/jmsj.2015-001. URL https://www.jstage.jst.go.jp/article/jmsj/93/1/93_2015-001/_article.

G. Krinner, N. Viovy, N. de Noblet-Ducoudré, J. Ogée, J. Polcher, P. Friedlingstein, P. Ciais, S. Sitch, and I. C. Prentice. A dynamic global vegetation model for studies of the coupled atmosphere-biosphere system. *Global Biogeochemical Cycles*, 19(1), Mar. 2005. ISSN 08866236. doi: 10.1029/2003GB002199. URL http://doi.wiley.com/10.1029/2003GB002199.

D. Kumar and A. R. Ganguly. Intercomparison of model response and internal variability across climate model ensembles. *Climate Dynamics*, 51(1-2):207–219, July 2018. ISSN 0930-7575, 1432-0894. doi: 10.1007/s00382-017-3914-4. URL http://link.springer.com/10.1007/s00382-017-3914-4.

V. Lago and M. H. England. Projected Slowdown of Antarctic Bottom Water Formation in Response to Amplified Meltwater Contributions. *Journal of Climate*, 32(19):6319–6335, Oct. 2019. ISSN 0894-8755, 1520-0442. doi: 10.1175/JCLI-D-18-0622.1. URL http://journals.ametsoc.org/doi/10.1175/JCLI-D-18-0622.1.

V. Lago, S. E. Wijffels, P. J. Durack, J. A. Church, N. L. Bindoff, and S. J. Marsland. Simulating the Role of Surface Forcing on Observed Multidecadal Upper-Ocean Salinity Changes. *Journal of Climate*, 29(15):5575–5588, Aug. 2016. ISSN 0894-8755, 1520-0442. doi: 10.1175/JCLI-D-15-0519.1. URL http://journals.ametsoc.org/doi/10.1175/JCLI-D-15-0519.1.

W. G. Large and S. G. Yeager. The global climatology of an interannually varying air–sea flux data set. *Climate Dynamics*, 33 (2-3):341–364, Aug. 2009. ISSN 0930-7575, 1432-0894. doi: 10.1007/s00382-008-0441-3. URL http://link.springer.com/10.1007/s00382-008-0441-3.

C. Le Quéré, S. Capstick, A. Corner, D. Cutting, M. Johnson, A. Minns, H. Schroeder, K. Walker-Springett, L. Whitmarsh, and R. Wood. Towards a culture of low-carbon research for the 21stCentury, Mar. 2015. URL https://tyndall.ac.uk/sites/default/files/twp161.pdf.

J. L. Lean. Cycles and trends in solar irradiance and climate. *WIREs Climate Change*, 1(1):111–122, Jan. 2010. ISSN 1757-7780, 1757-7799. doi: 10.1002/wcc.18. URL https://onlinelibrary.wiley.com/doi/10.1002/wcc.18.

J. Y. Lee, J. Marotzke, G. Bala, L. Cao, S. Corti, J. P. Dunne, F. Engelbrecht, E. Fischer, J. C. Fyfe, C. Jones, A. Maycock, J. Mutemi, O. Ndiaye, S. Panickal, and T. Zhou. Future global climate: scenario-based projections and near-term information. In *Climate Change 2021: The Physical Science Basis. Contribution of Working Group I to the Sixth Assessment Report of the Intergovernmental Panel on Climate Change*. Cambridge University Press, 2021.

F. Lehner, C. Deser, and L. Terray. Toward a New Estimate of "Time of Emergence" of Anthropogenic Warming: Insights from Dynamical Adjustment and a Large Initial-Condition Model Ensemble. *Journal of Climate*, 30(19):7739–7756, Oct. 2017. ISSN 0894-8755, 1520-0442. doi: 10.1175/JCLI-D-16-0792.1. URL http://journals.ametsoc.org/doi/10.1175/JCLI-D-16-0792.1.

F. Lehner, C. Deser, N. Maher, J. Marotzke, E. M. Fischer, L. Brunner, R. Knutti, and E. Hawkins. Partitioning climate projection uncertainty with multiple large ensembles and CMIP5/6. *Earth System Dynamics*, 11(2):491–508, May 2020. ISSN 2190-4987. doi: 10.5194/esd-11-491-2020. URL https://esd.copernicus.org/articles/11/491/2020/.

S. Levitus. Warming of the World Ocean. *Science*, 287(5461):2225–2229, Mar. 2000. ISSN 00368075, 10959203. doi: 10.1126/science.287.5461.2225. URL https://www.sciencemag.org/lookup/doi/10.1126/science.287.5461.2225.

S. Levitus and T. P. Boyer. World Ocean Atlas 1994. Volume 4. Temperature. Technical report, United States, 1994. URL https://www.osti.gov/biblio/137203.

S. Levitus, J. I. Antonov, J. Wang, T. L. Delworth, K. W. Dixon, and A. J. Broccoli. Anthropogenic Warming of Earth's Climate System. *Science*, 292(5515):267–270, Apr. 2001. ISSN 00368075, 10959203. doi: 10.1126/science.1058154. URL http://www.sciencemag.org/cgi/doi/10.1126/science.1058154.

S. Levitus, J. Antonov, and T. Boyer. Warming of the world ocean, 1955–2003. *Geophysical Research Letters*, 32(2):L02604, 2005. ISSN 0094-8276. doi: 10.1029/2004GL021592. URL http://doi.wiley.com/10.1029/2004GL021592.

S. Levitus, J. I. Antonov, T. P. Boyer, R. A. Locarnini, H. E. Garcia, and A. V. Mishonov. Global ocean heat content 1955-2008 in light of recently revealed instrumentation problems. *Geophysical Research Letters*, 36(7), Apr. 2009. ISSN 00948276. doi: 10.1029/2008GL037155. URL http://doi.wiley.com/10.1029/2008GL037155.

S. Levitus, J. I. Antonov, T. P. Boyer, O. K. Baranova, H. E. Garcia, R. A. Locarnini, A. V. Mishonov, J. R. Reagan, D. Seidov, E. S. Yarosh, and M. M. Zweng. World ocean heat content and thermosteric sea level change (0-2000 m), 1955-2010. *Geophysical Research Letters*, 39(10), May 2012. ISSN 00948276. doi: 10.1029/2012GL051106. URL http://doi.wiley.com/10.1029/2012GL051106.

G. Li, L. Cheng, J. Zhu, K. E. Trenberth, M. E. Mann, and J. P. Abraham. Increasing ocean stratification over the past half-century. *Nature Climate Change*, 10(12):1116–1123, Dec. 2020. ISSN 1758-678X, 1758-6798. doi: 10.1038/s41558-020-00918-2. URL http://www.nature.com/articles/s41558-020-00918-2.

W. Liu, J. Lu, S.-P. Xie, and A. Fedorov. Southern Ocean Heat Uptake, Redistribution, and Storage in a Warming Climate: The Role of Meridional Overturning Circulation. *Journal of Climate*, 31(12):4727–4743, June 2018. ISSN 0894-8755, 1520-0442. doi: 10.1175/JCLI-D-17-0761.1. URL https://journals.ametsoc.org/doi/10.1175/JCLI-D-17-0761.1.

M. S. Lozier. Deconstructing the Conveyor Belt. *Science*, 328(5985):1507–1511, June 2010. ISSN 0036-8075, 1095-9203. doi: 10.1126/science.1189250. URL http://www.sciencemag.org/cgi/doi/10.1126/science.1189250.

K. Lyu, X. Zhang, J. A. Church, A. B. A. Slangen, and J. Hu. Time of emergence for regional sea-level change. *Nature Climate Change*, 4:1006–1010, 2014.

K. Lyu, X. Zhang, J. A. Church, and Q. Wu. Processes Responsible for the Southern Hemisphere Ocean Heat Uptake and Redistribution under Anthropogenic Warming. *Journal of Climate*, 33(9):3787–3807, May 2020. ISSN 0894-8755, 1520-0442. doi: 10.1175/JCLI-D-19-0478.1. URL http://journals.ametsoc.org/doi/10.1175/JCLI-D-19-0478.1.

G. Madec, R. Bourdallé-Badie, P.-A. Bouttier, C. Bricaud, D. Bruciaferri, D. Calvert, J. Chanut, E. Clementi, A. Coward, D. Delrosso, C. Ethé, S. Flavoni, T. Graham, J. Harle, D. Iovino, D. Lea, C. Lévy, T. Lovato, N. Martin, S. Masson, S. Mocavero, J. Paul, C. Rousset, D. Storkey, A. Storto, and M. Vancoppenolle. NEMO ocean engine. Oct. 2017. ISSN 1288-1619. doi: 10.5281/ZENODO.3248739. URL https://zenodo.org/record/3248739. Publisher: Zenodo Version Number: v3.6-patch.

N. Maher, S. McGregor, M. H. England, and A. S. Gupta. Effects of volcanism on tropical variability: EFFECTS OF VOLCANISM. *Geophysical Research Letters*, 42(14):6024–6033, July 2015. ISSN 00948276. doi: 10.1002/2015GL064751. URL http://doi.wiley.com/10.1002/2015GL064751.

N. Maher, S. Milinski, L. Suarez-Gutierrez, M. Botzet, M. Dobrynin, L. Kornblueh, J. Kröger, Y. Takano, R. Ghosh, C. Hedemann, C. Li, H. Li, E. Manzini, D. Notz, D. Putrasahan, L. Boysen, M. Claussen, T. Ilyina, D. Olonscheck, T. Raddatz, B. Stevens, and J. Marotzke. The Max Planck Institute Grand Ensemble: Enabling the Exploration of Climate System Variability. *Journal of Advances in Modeling Earth Systems*, 11(7):2050–2069, July 2019. ISSN 1942-2466, 1942-2466. doi: 10.1029/2019MS001639. URL https://onlinelibrary.wiley.com/doi/abs/10.1029/2019MS001639.

N. Maher, F. Lehner, and J. Marotzke. Quantifying the role of internal variability in the temperature we expect to observe in the coming decades. *Environmental Research Letters*, 15(5):054014, May 2020. ISSN 1748-9326. doi: 10.1088/1748-9326/ab7d02. URL https://iopscience.iop.org/article/10.1088/1748-9326/ab7d02.

I. Mahlstein, R. Knutti, S. Solomon, and R. W. Portmann. Early onset of significant local warming in low latitude countries. *Environmental Research Letters*, 6(3):034009, July 2011. ISSN 1748-9326. doi: 10.1088/1748-9326/6/3/034009. URL http://stacks.iop.org/1748-9326/6/i=3/a=034009?key=crossref.4f6f298120b5f9acd1127c399bd39515.

I. Mahlstein, R. W. Portmann, J. S. Daniel, S. Solomon, and R. Knutti. Perceptible changes in regional precipitation in a future climate. *Geophysical Research Letters*, 39(5):L05701, 2012. ISSN 1944-8007. doi: 10.1029/2011GL050738. URL https://agupubs.onlinelibrary.wiley.com/doi/abs/10.1029/2011GL050738.

S. Manabe and R. T. Wetherald. The Effects of Doubling the CO2 Concentration on the climate of a General Circulation Model. *Journal of Atmospheric Sciences*, 32(1):3–15, 1975. doi: https://doi.org/10.1175/1520-0469(1975)032%3C0003:TEODTC%3E2.0.CO;2.

G. J. Marshall. Trends in the Southern Annular Mode from Observations and Reanalyses. *Journal of Climate*, 16:10, 2003.

J. Marshall and K. Speer. Closure of the meridional overturning circulation through Southern Ocean upwelling. *Nature Geoscience*, 5(3):171–180, Mar. 2012. ISSN 1752-0894, 1752-0908. doi: 10.1038/ngeo1391. URL http://www.nature.com/articles/ngeo1391.

J. Marshall, J. R. Scott, K. C. Armour, J.-M. Campin, M. Kelley, and A. Romanou. The ocean's role in the transient response of climate to abrupt greenhouse gas forcing. *Climate Dynamics*, 44(7-8):2287–2299, Apr. 2015. ISSN 0930-7575, 1432-0894. doi: 10.1007/s00382-014-2308-0. URL http://link.springer.com/10.1007/s00382-014-2308-0.

M. S. McCartney. Subantarctic mode water. In *A voyage of discovery: George Deacon 70th Anniversary Volume*, pages 103–119. Supplement to Deep-Sea Research, Pergamon Press, Oxford, angel, m. v. edition, 1977.

T. J. McDougall. Neutral Surfaces. *Journal of Physical Oceanography*, 17(11):1950 – 1964, 1987. doi: 10.1175/1520-0485(1987)017<1950:NS>2.0.CO;2. URL https://journals.ametsoc.org/view/journals/phoc/17/11/1520-0485_1987_017_1950_ns_2_0_co_2.xml. Place: Boston MA, USA Publisher: American Meteorological Society.

T. J. McDougall and D. R. Jackett. The material derivative of neutral density. *Journal of Marine Research*, 63(1):159–185, Jan. 2005. ISSN 00222402, 15439542. doi: 10.1357/0022240053693734. URL http://www.ingentaselect.com/rpsv/cgi-bin/cgi?ini=xref&body=linker&reqdoi=10.1357/0022240053693734.

A. Meijers, D. Munday, T. Roy, and J.-B. Sallée. Southern Ocean water mass properties and circulation under CMIP6 climate forcing. other, pico, Mar. 2021. URL https://meetingorganizer.copernicus.org/EGU21/EGU21-8222.html.

M. B. Menary, J. Robson, R. P. Allan, B. B. B. Booth, C. Cassou, G. Gastineau, J. Gregory, D. Hodson, C. Jones, J. Mignot, M. Ringer, R. Sutton, L. Wilcox, and R. Zhang. Aerosol-Forced AMOC Changes in CMIP6 Historical Simulations. *Geophysical Research Letters*, 47(14), July 2020. ISSN 0094-8276, 1944-8007. doi: 10.1029/2020GL088166. URL https://onlinelibrary.wiley.com/doi/10.1029/2020GL088166.

V. V. Menezes, A. M. Macdonald, and C. Schatzman. Accelerated freshening of Antarctic Bottom Water over the last decade in the Southern Indian Ocean. *Science Advances*, 3(1):e1601426, Jan. 2017. ISSN 2375-2548. doi: 10.1126/sciadv.1601426. URL https://www.science.org/doi/10.1126/sciadv.1601426.

B. Meyssignac, T. Boyer, Z. Zhao, M. Z. Hakuba, F. W. Landerer, D. Stammer, A. Köhl, S. Kato, T. L'Ecuyer, M. Ablain, J. P. Abraham, A. Blazquez, A. Cazenave, J. A. Church, R. Cowley, L. Cheng, C. M. Domingues, D. Giglio, V. Gouretski, M. Ishii, G. C. Johnson, R. E. Killick, D. Legler, W. Llovel, J. Lyman, M. D. Palmer, S. Piotrowicz, S. G. Purkey, D. Roemmich, R. Roca, A. Savita, K. v. Schuckmann, S. Speich, G. Stephens, G. Wang, S. E. Wijffels, and N. Zilberman. Measuring Global Ocean Heat Content to Estimate the Earth Energy Imbalance. *Frontiers in Marine Science*, 6, 2019. ISSN 2296-7745. doi: 10.3389/fmars.2019.00432. URL https://www.frontiersin.org/articles/10.3389/fmars.2019.00432/full.

J. Mignot, F. Hourdin, J. Deshayes, O. Boucher, G. Gastineau, I. Musat, M. Vancoppenolle, J. Servonnat, A. Caubel, F. Chéruy, S. Denvil, J. Dufresne, C. Ethé, L. Fairhead, M. Foujols, J. Grandpeix, G. Levavasseur, O. Marti, M. Menary, C. Rio, C. Rousset, and Y. Silvy. The tuning strategy of IPSL-CM6A-LR. *Journal of Advances in Modeling Earth Systems*, Apr. 2021. ISSN 1942-2466, 1942-2466. doi: 10.1029/2020MS002340. URL https://onlinelibrary.wiley.com/doi/10.1029/2020MS002340.

U. Mikolajewicz and R. Voss. The role of the individual air-sea flux components in CO2-induced changes of the ocean's circulation and climate. *Climate Dynamics*, 16(8):627–642, Aug. 2000. ISSN 1432-0894. doi: 10.1007/s003820000066. URL https://doi.org/10.1007/s003820000066.

M. Mohrmann, C. Heuzé, and S. Swart. Southern Ocean polynyas in CMIP6 models. *The Cryosphere*, 15(9):4281–4313, Sept. 2021. ISSN 1994-0424. doi: 10.5194/tc-15-4281-2021. URL https://tc.copernicus.org/articles/15/4281/2021/.

C. Mora, A. G. Frazier, R. J. Longman, R. S. Dacks, M. M. Walton, E. J. Tong, J. J. Sanchez, L. R. Kaiser, Y. O. Stender, J. M. Anderson, C. M. Ambrosino, I. Fernandez-Silva, L. M. Giuseffi, and T. W. Giambelluca. The projected timing of climate departure from recent variability. *Nature*, 502(7470):183–187, Oct. 2013. ISSN 1476-4687. doi: 10.1038/nature12540. URL https://www.nature.com/articles/nature12540.

M. A. Morales Maqueda. Polynya Dynamics: a Review of Observations and Modeling. *Reviews of Geophysics*, 42(1):RG1004, 2004. ISSN 8755-1209. doi: 10.1029/2002RG000116. URL http://doi.wiley.com/10.1029/2002RG000116.

A. K. Morrison, D. W. Waugh, A. M. Hogg, D. C. Jones, and R. P. Abernathey. Ventilation of the Southern Ocean Pycnocline. *Annual Review of Marine Science*, 14(1):null, 2022. doi: 10.1146/annurev-marine-010419-011012. URL https://doi.org/10.1146/annurev-marine-010419-011012. _eprint: https://doi.org/10.1146/annurev-marine-010419-011012.

W. Munk and C. Wunsch. Abyssal recipes II: energetics of tidal and wind mixing. *Deep Sea Research Part I: Oceanographic Research Papers*, 45(12):1977–2010, Dec. 1998. ISSN 09670637. doi: 10.1016/S0967-0637(98)00070-3. URL https://linkinghub.elsevier.com/retrieve/pii/S0967063798000703.

W. H. Munk. On the wind-driven ocean circulation. *Journal of the Atmospheric Sciences*, 7(2):80–93, 1950. doi: https://doi.org/10.1175/1520-0469(1950)007%3C0080:OTWDOC%3E2.0.CO;2.

W. H. Munk. Abyssal recipes. *Deep Sea Research and Oceanographic Abstracts*, 13(4):707–730, Aug. 1966. ISSN 00117471. doi: 10.1016/0011-7471(66)90602-4. URL https://linkinghub.elsevier.com/retrieve/pii/0011747166906024.

V. Naik, S. Szopa, B. Adhikary, P. Artaxo, T. Berntsen, W. D. Collins, S. Fuzzi, L. Gallardo, A. Kiendler-Scharr, Z. Klimont, H. Liao, N. Unger, and P. Zanis. Short-lived climate forcers. In *Climate Change 2021: The Physical Science Basis. Contribution of Working Group I to the Sixth Assessment Report of the Intergovernmental Panel on Climate Change*. Cambridge University Press, 2021.

E. Newsom, L. Zanna, S. Khatiwala, and J. M. Gregory. The Influence of Warming Patterns on Passive Ocean Heat Uptake. *Geophysical Research Letters*, 47(18):11, 2020. doi: https://doi.org/10.1029/2020GL088429.

D. Ong, T. Moors, and V. Sivaraman. Comparison of the energy, carbon and time costs of videoconferencing and in-person meetings. *Computer Communications*, 50:86–94, Sept. 2014. ISSN 01403664. doi: 10.1016/j.comcom.2014.02.009. URL https://linkinghub.elsevier.com/retrieve/pii/S0140366414000620.

M. D. Palmer, S. A. Good, K. Haines, N. A. Rayner, and P. A. Stott. A new perspective on warming of the global oceans. *Geophysical Research Letters*, 36(20):L20709, 2009. ISSN 1944-8007. doi: 10.1029/2009GL039491. URL https://agupubs.pericles-prod.literatumonline.com/doi/abs/10.1029/2009GL039491.

L. Patara, C. W. Böning, and T. Tanhua. Multidecadal Changes in Southern Ocean Ventilation since the 1960s Driven by Wind and Buoyancy Forcing. *Journal of Climate*, 34(4):1485–1502, Feb. 2021. ISSN 0894-8755, 1520-0442. doi: 10.1175/JCLI-D-19-0947.1. URL https://journals.ametsoc.org/view/journals/clim/34/4/JCLI-D-19-0947.1.xml.

C. G. Piecuch, R. M. Ponte, C. M. Little, M. W. Buckley, and I. Fukumori. Mechanisms underlying recent decadal changes in subpolar North Atlantic Ocean heat content. *Journal of Geophysical Research: Oceans*, 122(9):7181–7197, Sept. 2017. ISSN 2169-9275, 2169-9291. doi: 10.1002/2017JC012845. URL https://onlinelibrary.wiley.com/doi/10.1002/2017JC012845.

D. W. Pierce, T. P. Barnett, K. M. AchutaRao, P. J. Gleckler, J. M. Gregory, and W. M. Washington. Anthropogenic Warming of the Oceans: Observations and Model Results. *Journal of Climate*, 19(10):1873–1900, May 2006. ISSN 0894-8755, 1520-0442. doi: 10.1175/JCLI3723.1. URL http://journals.ametsoc.org/doi/abs/10.1175/JCLI3723.1.

D. W. Pierce, P. J. Gleckler, T. P. Barnett, B. D. Santer, and P. J. Durack. The fingerprint of human-induced changes in the ocean's salinity and temperature fields. *Geophysical Research Letters*, 39(L21704), 2012.

S. G. Purkey and G. C. Johnson. Warming of Global Abyssal and Deep Southern Ocean Waters between the 1990s and 2000s: Contributions to Global Heat and Sea Level Rise Budgets*. *Journal of Climate*, 23(23):6336–6351, Dec. 2010. ISSN 1520-0442, 0894-8755. doi: 10.1175/2010JCLI3682.1. URL http://journals.ametsoc.org/doi/10.1175/2010JCLI3682.1.

S. G. Purkey and G. C. Johnson. Global Contraction of Antarctic Bottom Water between the 1980s and 2000s*. *Journal of Climate*, 25(17):5830–5844, Sept. 2012. ISSN 0894-8755, 1520-0442. doi: 10.1175/JCLI-D-11-00612.1. URL http://journals.ametsoc.org/doi/10.1175/JCLI-D-11-00612.1.

S. G. Purkey and G. C. Johnson. Antarctic Bottom Water Warming and Freshening: Contributions to Sea Level Rise, Ocean Freshwater Budgets, and Global Heat Gain*. *Journal of Climate*, 26(16):6105–6122, Aug. 2013. ISSN 0894-8755, 1520-0442. doi: 10.1175/JCLI-D-12-00834.1. URL http://journals.ametsoc.org/doi/10.1175/JCLI-D-12-00834.1.

S. G. Purkey, G. C. Johnson, L. D. Talley, B. M. Sloyan, S. E. Wijffels, W. Smethie, S. Mecking, and K. Katsumata. Unabated Bottom Water Warming and Freshening in the South Pacific Ocean. *Journal of Geophysical Research: Oceans*, 124(3):1778–1794, Mar. 2019. ISSN 2169-9275, 2169-9291. doi: 10.1029/2018JC014775. URL https://onlinelibrary.wiley.com/doi/10.1029/2018JC014775.

S. Rathore, N. L. Bindoff, H. E. Phillips, and M. Feng. Recent hemispheric asymmetry in global ocean warming induced by climate change and internal variability. *Nature Communications*, 11(1):2008, Dec. 2020. ISSN 2041-1723. doi: 10.1038/s41467-020-15754-3. URL http://www.nature.com/articles/s41467-020-15754-3.

N. A. Rayner. Global analyses of sea surface temperature, sea ice, and night marine air temperature since the late nineteenth century. *Journal of Geophysical Research*, 108(D14):4407, 2003. ISSN 0148-0227. doi: 10.1029/2002JD002670. URL https://onlinelibrary.wiley.com/doi/10.1029/2002JD002670.

B. K. Reichert, R. Schnur, and L. Bengtsson. Global ocean warming tied to anthropogenic forcing. *Geophysical Research Letters*, 29(11):20–1–20–4, 2002. ISSN 1944-8007. doi: 10.1029/2001GL013954. URL https://agupubs.onlinelibrary.wiley.com/doi/abs/10.1029/2001GL013954.

M. Rhein, S. R. Rintoul, S. Aoki, E. Campos, D. Chambers, R. A. Feely, S. Gulev, G. C. Johnson, S. A. Josey, A. Kostianoy, C. Mauritzen, D. Roemmich, L. Talley, and F. Wang. Observations: Ocean. In Intergovernmental Panel on Climate Change, editor, *Climate Change 2013: The Physical Science Basis. Contribution of Working Group I to the Fifth Assessment Report of the Intergovernmental Panel on CLimate Change*, pages 255–316. Cambridge University Press, Cambridge, 2013. ISBN 978-1-107-41532-4. doi: 10.1017/CBO9781107415324.010. URL https://www.cambridge.org/core/product/identifier/CBO9781107415324A018/type/book_part.

A. Ribes and L. Terray. Application of regularised optimal fingerprinting to attribution. Part II: application to global near-surface temperature. *Climate Dynamics*, 41(11-12):2837–2853, Dec. 2013. ISSN 0930-7575, 1432-0894. doi: 10.1007/s00382-013-1736-6. URL http://link.springer.com/10.1007/s00382-013-1736-6.

S. R. Rintoul. Rapid freshening of Antarctic Bottom Water formed in the Indian and Pacific oceans. *Geophysical Research Letters*, 34(6):L06606, Mar. 2007. ISSN 0094-8276. doi: 10.1029/2006GL028550. URL http://doi.wiley.com/10.1029/2006GL028550.

S. R. Rintoul. The global influence of localized dynamics in the Southern Ocean. *Nature*, 558(7709):209–218, June 2018. ISSN 0028-0836, 1476-4687. doi: 10.1038/s41586-018-0182-3. URL http://www.nature.com/articles/s41586-018-0182-3.

K. B. Rodgers, J. Lin, and T. L. Frölicher. Emergence of multiple ocean ecosystem drivers in a large ensemble suite with an Earth system model. *Biogeosciences*, 12(11):3301–3320, June 2015. ISSN 1726-4189. doi: 10.5194/bg-12-3301-2015. URL https://www.biogeosciences.net/12/3301/2015/.

D. Roemmich, J. Church, J. Gilson, D. Monselesan, P. Sutton, and S. Wijffels. Unabated planetary warming and its ocean structure since 2006. *Nature Climate Change*, 5(3):240–245, Mar. 2015. ISSN 1758-6798. doi: 10.1038/nclimate2513. URL https://www.nature.com/articles/nclimate2513.

F. Roquet, G. Madec, T. J. McDougall, and P. M. Barker. Accurate polynomial expressions for the density and specific volume of seawater using the TEOS-10 standard. *Ocean Modelling*, 90:29–43, June 2015. ISSN 14635003. doi: 10.1016/j.ocemod.2015.04.002. URL https://linkinghub.elsevier.com/retrieve/pii/S1463500315000566.

C. Rousset, M. Vancoppenolle, G. Madec, T. Fichefet, S. Flavoni, A. Barthélemy, R. Benshila, J. Chanut, C. Levy, S. Masson, and F. Vivier. The Louvain-La-Neuve sea ice model LIM3.6: global and regional capabilities. *Geoscientific Model Development*, 8(10):2991–3005, Oct. 2015. ISSN 1991-9603. doi: 10.5194/gmd-8-2991-2015. URL https://gmd.copernicus.org/articles/8/2991/2015/.

T. Roy, J. B. Sallée, L. Bopp, and N. Metzl. Diagnosing CO2 emission-induced feedbacks between the Southern Ocean carbon cycle and the climate system: A multiple Earth System Model analysis using a water mass tracking approach. *Journal of Climate*, pages 1–62, Sept. 2021. ISSN 0894-8755, 1520-0442. doi: 10.1175/JCLI-D-20-0889.1. URL https://journals.ametsoc.org/view/journals/clim/aop/JCLI-D-20-0889.1/JCLI-D-20-0889.1.xml.

J.-B. Sallée. Southern Ocean Warming. *Oceanography*, 31(2), June 2018. ISSN 10428275. doi: 10.5670/oceanog.2018.215. URL https://tos.org/oceanography/article/southern-ocean-warming.

J.-B. Sallée, K. Speer, S. Rintoul, and S. Wijffels. Southern Ocean Thermocline Ventilation. *Journal of Physical Oceanography*, 40(3):509–529, Mar. 2010. ISSN 0022-3670. doi: 10.1175/2009JPO4291.1. URL https://journals.ametsoc.org/doi/full/10.1175/2009JPO4291.1.

J.-B. Sallée, E. Shuckburgh, N. Bruneau, A. J. S. Meijers, T. J. Bracegirdle, Z. Wang, and T. Roy. Assessment of Southern Ocean water mass circulation and characteristics in CMIP5 models: Historical bias and forcing response. *Journal of Geophysical Research-Oceans*, 118(4):1830–1844, Apr. 2013. ISSN 2169-9275. doi: 10.1002/jgrc.20135. WOS:000320324100014.

J.-B. Sallée, V. Pellichero, C. Akhoudas, E. Pauthenet, L. Vignes, S. Schmidtko, A. N. Garabato, P. Sutherland, and M. Kuusela. Summertime increases in upper-ocean stratification and mixed-layer depth. *Nature*, 591(7851):592–598, Mar. 2021. ISSN 0028-0836, 1476-4687. doi: 10.1038/s41586-021-03303-x. URL http://www.nature.com/articles/s41586-021-03303-x.

B. D. Santer, J. C. Fyfe, S. Solomon, J. F. Painter, C. Bonfils, G. Pallotta, and M. D. Zelinka. Quantifying stochastic uncertainty in detection time of human-caused climate signals. *Proceedings of the National Academy of Sciences*, page 201904586, Sept. 2019. ISSN 0027-8424, 1091-6490. doi: 10.1073/pnas.1904586116. URL http://www.pnas.org/lookup/doi/10.1073/pnas.1904586116.

M. Saunois, A. R. Stavert, B. Poulter, P. Bousquet, J. G. Canadell, R. B. Jackson, P. A. Raymond, E. J. Dlugokencky, S. Houweling, P. K. Patra, P. Ciais, V. K. Arora, D. Bastviken, P. Bergamaschi, D. R. Blake, G. Brailsford, L. Bruhwiler, K. M. Carlson, M. Carrol, S. Castaldi, N. Chandra, C. Crevoisier, P. M. Crill, K. Covey, C. L. Curry, G. Etiope, C. Frankenberg, N. Gedney, M. I. Hegglin, L. Höglund-Isaksson, G. Hugelius, M. Ishizawa, A. Ito, G. Janssens-Maenhout, K. M. Jensen, F. Joos, T. Kleinen, P. B. Krummel, R. L. Langenfelds, G. G. Laruelle, L. Liu, T. Machida, S. Maksyutov, K. C. McDonald, J. McNorton, P. A. Miller, J. R. Melton, I. Morino, J. Müller, F. Murguia-Flores, V. Naik, Y. Niwa, S. Noce, S. O'Doherty, R. J. Parker, C. Peng, S. Peng, G. P. Peters, C. Prigent, R. Prinn, M. Ramonet, P. Regnier, W. J. Riley, J. A. Rosentreter, A. Segers, I. J. Simpson, H. Shi, S. J. Smith, L. P. Steele, B. F. Thornton, H. Tian, Y. Tohjima, F. N. Tubiello, A. Tsuruta, N. Viovy, A. Voulgarakis, T. S. Weber, M. van Weele, G. R. van der Werf, R. F. Weiss, D. Worthy, D. Wunch, Y. Yin, Y. Yoshida, W. Zhang, Z. Zhang, Y. Zhao, B. Zheng, Q. Zhu, Q. Zhu, and Q. Zhuang. The Global Methane Budget 2000–2017. *Earth System Science Data*, 12(3):1561–1623, July 2020. ISSN 1866-3516. doi: 10.5194/essd-12-1561-2020. URL https://essd.copernicus.org/articles/12/1561/2020/.

S. Schlunegger, K. B. Rodgers, J. L. Sarmiento, T. L. Frölicher, J. P. Dunne, M. Ishii, and R. Slater. Emergence of anthropogenic signals in the ocean carbon cycle. *Nature Climate Change*, 9:719–725, Aug. 2019. ISSN 1758-6798. doi: 10.1038/s41558-019-0553-2. URL https://www.nature.com/articles/s41558-019-0553-2.

S. Schmidtko, K. J. Heywood, A. F. Thompson, and S. Aoki. Multidecadal warming of Antarctic waters. *Science*, 346(6214): 1227–1231, Dec. 2014. ISSN 0036-8075, 1095-9203. doi: 10.1126/science.1256117. URL https://www.sciencemag.org/lookup/doi/10.1126/science.1256117.

J.-R. Shi, S.-P. Xie, and L. D. Talley. Evolving Relative Importance of the Southern Ocean and North Atlantic in Anthropogenic Ocean Heat Uptake. *Journal of Climate*, 31(18):7459–7479, Sept. 2018. ISSN 0894-8755, 1520-0442. doi: 10.1175/JCLI-D-18-0170.1. URL https://journals.ametsoc.org/doi/10.1175/JCLI-D-18-0170.1.

J.-R. Shi, L. D. Talley, S.-P. Xie, W. Liu, and S. T. Gille. Effects of Buoyancy and Wind Forcing on Southern Ocean Climate Change. *Journal of Climate*, 33(23):10003–10020, Dec. 2020. ISSN 0894-8755, 1520-0442. doi: 10.1175/JCLI-D-19-0877.1. URL https://journals.ametsoc.org/doi/10.1175/JCLI-D-19-0877.1.

A. Silvano, S. R. Rintoul, B. Peña-Molino, W. R. Hobbs, E. van Wijk, S. Aoki, T. Tamura, and G. D. Williams. Freshening by glacial meltwater enhances melting of ice shelves and reduces formation of Antarctic Bottom Water. *Science Advances*, 4(4): eaap9467, Apr. 2018. ISSN 2375-2548. doi: 10.1126/sciadv.aap9467. URL https://www.science.org/doi/10.1126/sciadv.aap9467.

A. Silvano, A. Foppert, S. R. Rintoul, P. R. Holland, T. Tamura, N. Kimura, P. Castagno, P. Falco, G. Budillon, F. A. Haumann, A. C. Naveira Garabato, and A. M. Macdonald. Recent recovery of Antarctic Bottom Water formation in the Ross Sea driven by climate anomalies. *Nature Geoscience*, 13(12):780–786, Dec. 2020. ISSN 1752-0894, 1752-0908. doi: 10.1038/s41561-020-00655-3. URL http://www.nature.com/articles/s41561-020-00655-3.

Y. Silvy, E. Guilyardi, J.-B. Sallée, and P. J. Durack. Human-induced changes to the global ocean water masses and their time of emergence. *Nature Climate Change*, Aug. 2020. ISSN 1758-6798. doi: 10.1038/s41558-020-0878-x. URL https://doi.org/10.1038/s41558-020-0878-x.

N. Skliris, R. Marsh, S. A. Josey, S. A. Good, C. Liu, and R. P. Allan. Salinity changes in the World Ocean since 1950 in relation to changing surface freshwater fluxes. *Climate Dynamics*, 43(3-4):709–736, Aug. 2014. ISSN 0930-7575, 1432-0894. doi: 10.1007/s00382-014-2131-7. URL https://link.springer.com/article/10.1007/s00382-014-2131-7.

N. Skliris, J. D. Zika, G. Nurser, S. A. Josey, and R. Marsh. Global water cycle amplifying at less than the Clausius-Clapeyron rate. *Scientific Reports*, 6:38752, Dec. 2016. ISSN 2045-2322. doi: 10.1038/srep38752. URL https://www.nature.com/articles/srep38752.

B. M. Sloyan and I. V. Kamenkovich. Simulation of Subantarctic Mode and Antarctic Intermediate Waters in Climate Models. *Journal of Climate*, 20(20):5061–5080, Oct. 2007. ISSN 1520-0442, 0894-8755. doi: 10.1175/JCLI4295.1. URL http://journals.ametsoc.org/doi/10.1175/JCLI4295.1.

D. A. Smeed, G. D. McCarthy, S. A. Cunningham, E. Frajka-Williams, D. Rayner, W. E. Johns, C. S. Meinen, M. O. Baringer, B. I. Moat, A. Duchez, and H. L. Bryden. Observed decline of the Atlantic meridional overturning circulation 2004–2012. *Ocean Science*, 10(1):29–38, Feb. 2014. ISSN 1812-0792. doi: 10.5194/os-10-29-2014. URL https://os.copernicus.org/articles/10/29/2014/.

D. A. Smeed, S. A. Josey, C. Beaulieu, W. E. Johns, B. I. Moat, E. Frajka-Williams, D. Rayner, C. S. Meinen, M. O. Baringer, H. L. Bryden, and G. D. McCarthy. The North Atlantic Ocean Is in a State of Reduced Overturning. *Geophysical Research Letters*, 45(3):1527–1533, Feb. 2018. ISSN 0094-8276, 1944-8007. doi: 10.1002/2017GL076350. URL https://onlinelibrary.wiley.com/doi/10.1002/2017GL076350.

D. M. Smith and J. M. Murphy. An objective ocean temperature and salinity analysis using covariances from a global climate model. *Journal of Geophysical Research*, 112(C2):C02022, Feb. 2007. ISSN 0148-0227. doi: 10.1029/2005JC003172. URL http://doi.wiley.com/10.1029/2005JC003172.

S. Solomon. Stratospheric ozone depletion: A review of concepts and history. *Reviews of Geophysics*, 37(3):275–316, Aug. 1999. ISSN 87551209. doi: 10.1029/1999RG900008. URL http://doi.wiley.com/10.1029/1999RG900008.

S. Solomon, D. J. Ivy, D. Kinnison, M. J. Mills, R. R. Neely, and A. Schmidt. Emergence of healing in the Antarctic ozone layer. *Science*, 353(6296):269–274, July 2016. ISSN 0036-8075, 1095-9203. doi: 10.1126/science.aae0061. URL https://www.sciencemag.org/lookup/doi/10.1126/science.aae0061.

K. Speer and E. Tziperman. Rates of Water Mass Formation in the North Atlantic Ocean. *Journal of Physical Oceanography*, 22 (1):93–104, Jan. 1992. ISSN 0022-3670, 1520-0485. doi: 10.1175/1520-0485(1992)022<0093:ROWMFI>2.0.CO;2. URL http://journals.ametsoc.org/doi/abs/10.1175/1520-0485%281992%29022%3C0093%3AROWMFI%3E2.0.CO%3B2.

K. Speer, S. R. Rintoul, and B. Sloyan. The Diabatic Deacon Cell. *Journal of Physical Oceanography*, 30:11, 2000.

H. Stommel. The westward intensification of wind-driven ocean currents. *Transactions, American Geophysical Union*, 29(2): 202, 1948. ISSN 0002-8606. doi: 10.1029/TR029i002p00202. URL http://doi.wiley.com/10.1029/TR029i002p00202.

H. Stommel. A survey of ocean current theory. *Deep Sea Research (1953)*, 4:149–184, Jan. 1957. ISSN 01466313. doi: 10.1016/0146-6313(56)90048-X. URL https://linkinghub.elsevier.com/retrieve/pii/014663135690048X.

A. Storto, M. A. Balmaseda, E. de Boisseson, B. S. Giese, S. Masina, and C. Yang. The 20th century global warming signature on the ocean at global and basin scales as depicted from historical reanalyses. *International Journal of Climatology*, page joc.7163, May 2021. ISSN 0899-8418, 1097-0088. doi: 10.1002/joc.7163. URL https://onlinelibrary.wiley.com/doi/10.1002/joc.7163.

P. A. Stott, R. T. Sutton, and D. M. Smith. Detection and attribution of Atlantic salinity changes. *Geophysical Research Letters*, 35(21), Nov. 2008. ISSN 0094-8276. doi: 10.1029/2008GL035874. URL http://doi.wiley.com/10.1029/2008GL035874.

S. Sun and J. E. Hansen. Climate Simulations for 1951–2050 with a Coupled Atmosphere–Ocean Model. *Journal of Climate*, 16:20, 2003.

H. U. Sverdrup. Wind-Driven Currents in a Baroclinic Ocean; with Application to the Equatorial Currents of the Eastern Pacific. *Proceedings of the National Academy of Sciences of the United States of America*, 33(11):318–326, Nov. 1947. ISSN 0027-8424 1091-6490. doi: 10.1073/pnas.33.11.318.

N. C. Swart, S. T. Gille, J. C. Fyfe, and N. P. Gillett. Recent Southern Ocean warming and freshening driven by greenhouse gas emissions and ozone depletion. *Nature Geoscience*, 11(11):836–841, Nov. 2018. ISSN 1752-0894. doi: 10.1038/s41561-018-0226-1. WOS:000448672100009.

D. Swingedouw, J. Mignot, P. Ortega, M. Khodri, M. Menegoz, C. Cassou, and V. Hanquiez. Impact of explosive volcanic eruptions on the main climate variability modes. *Global and Planetary Change*, 150:24–45, Mar. 2017. ISSN 09218181. doi: 10.1016/j.gloplacha.2017.01.006. URL https://linkinghub.elsevier.com/retrieve/pii/S0921818116300352.

L. D. Talley and M. E. Raymer. Eighteen_degree_water_variability.pdf. *Journal of Marine Research*, 40:757–775, 1982.

K. E. Taylor, R. J. Stouffer, and G. A. Meehl. An Overview of CMIP5 and the Experiment Design. *Bulletin of the American Meteorological Society*, 93(4):485–498, Apr. 2012. ISSN 0003-0007, 1520-0477. doi: 10.1175/BAMS-D-11-00094.1. URL http://journals.ametsoc.org/doi/abs/10.1175/BAMS-D-11-00094.1.

L. Terray, L. Corre, S. Cravatte, T. Delcroix, G. Reverdin, and A. Ribes. Near-Surface Salinity as Nature's Rain Gauge to Detect Human Influence on the Tropical Water Cycle. *Journal of Climate*, 25(3):958–977, Feb. 2012. ISSN 0894-8755, 1520-0442. doi: 10.1175/JCLI-D-10-05025.1. URL http://journals.ametsoc.org/doi/abs/10.1175/JCLI-D-10-05025.1.

D. W. J. Thompson and S. Solomon. Interpretation of Recent Southern Hemisphere Climate Change. *Science*, 296(5569):895–899, May 2002. ISSN 00368075, 10959203. doi: 10.1126/science.1069270. URL https://www.sciencemag.org/lookup/doi/10.1126/science.1069270.

D. W. J. Thompson, S. Solomon, P. J. Kushner, M. H. England, K. M. Grise, and D. J. Karoly. Signatures of the Antarctic ozone hole in Southern Hemisphere surface climate change. *Nature Geoscience*, 4(11):741–749, Nov. 2011. ISSN 1752-0894, 1752-0908. doi: 10.1038/ngeo1296. URL http://www.nature.com/articles/ngeo1296.

A. Todd, L. Zanna, M. Couldrey, J. Gregory, Q. Wu, J. A. Church, R. Farneti, R. Navarro-Labastida, K. Lyu, O. Saenko, D. Yang, and X. Zhang. Ocean-Only FAFMIP: Understanding Regional Patterns of Ocean Heat Content and Dynamic Sea Level Change. *Journal of Advances in Modeling Earth Systems*, 12(8), Aug. 2020. ISSN 1942-2466, 1942-2466. doi: 10.1029/2019MS002027. URL https://onlinelibrary.wiley.com/doi/10.1029/2019MS002027.

K. B. Tokarska, G. C. Hegerl, A. P. Schurer, A. Ribes, and J. T. Fasullo. Quantifying human contributions to past and future ocean warming and thermosteric sea level rise. *Environmental Research Letters*, 14(7):074020, July 2019. ISSN 1748-9326. doi: 10.1088/1748-9326/ab23c1. URL https://iopscience.iop.org/article/10.1088/1748-9326/ab23c1.

K. E. Trenberth and J. M. Caron. Estimates of Meridional Atmosphere and Ocean Heat Transports. *Journal of Climate*, 14:11, 2001.

K. E. Trenberth, J. Fasullo, and L. Smith. Trends and variability in column-integrated atmospheric water vapor. *Climate Dynamics*, 24(7-8):741–758, June 2005. ISSN 0930-7575, 1432-0894. doi: 10.1007/s00382-005-0017-4. URL http://link.springer.com/10.1007/s00382-005-0017-4.

D. Turk, H. Wang, X. Hu, D. K. Gledhill, Z. A. Wang, L. Jiang, and W.-J. Cai. Time of Emergence of Surface Ocean Carbon Dioxide Trends in the North American Coastal Margins in Support of Ocean Acidification Observing System Design. *Frontiers in Marine Science*, 6, Mar. 2019. ISSN 2296-7745. doi: 10.3389/fmars.2019.00091. URL https://www.frontiersin.org/article/10.3389/fmars.2019.00091/full.

J. Tyndall. I. The Bakerian Lecture.—On the absorption and radiation of heat by gases and vapours, and on the physical connexion of radiation, absorption, and conduction. *Philosophical Transactions of the Royal Society of London*, 151:1–36, Dec. 1861. ISSN 0261-0523, 2053-9223. doi: 10.1098/rstl.1861.0001. URL https://royalsocietypublishing.org/doi/10.1098/rstl.1861.0001.

G. K. Vallis. *Atmospheric and oceanic fluid dynamics: fundamentals and large-scale circulation*. Cambridge university press, Cambridge, 2nd ed edition, 2017. ISBN 978-1-107-06550-5.

N. T. Vinogradova and R. M. Ponte. In Search of Fingerprints of the Recent Intensification of the Ocean Water Cycle. *Journal of Climate*, 30(14):5513–5528, July 2017. ISSN 0894-8755, 1520-0442. doi: 10.1175/JCLI-D-16-0626.1. URL http://journals.ametsoc.org/doi/10.1175/JCLI-D-16-0626.1.

G. Walin. On the relation between sea-surface heat flow and thermal circulation in the ocean. *Tellus*, 34(2):187–195, Apr. 1982. ISSN 00402826, 21533490. doi: 10.1111/j.2153-3490.1982.tb01806.x. URL http://tellusa.net/index.php/tellusa/article/view/10801.

L. Wang, K. Lyu, W. Zhuang, W. Zhang, S. Makarim, and X. Yan. Recent Shift in the Warming of the Southern Oceans Modulated by Decadal Climate Variability. *Geophysical Research Letters*, 48(3), Feb. 2021. ISSN 0094-8276, 1944-8007. doi: 10.1029/2020GL090889. URL https://onlinelibrary.wiley.com/doi/10.1029/2020GL090889.

D. W. Waugh, A. McC. Hogg, P. Spence, M. H. England, and T. W. N. Haine. Response of Southern Ocean Ventilation to Changes in Midlatitude Westerly Winds. *Journal of Climate*, 32(17):5345–5361, Sept. 2019. ISSN 0894-8755, 1520-0442. doi: 10.1175/JCLI-D-19-0039.1. URL http://journals.ametsoc.org/doi/10.1175/JCLI-D-19-0039.1.

E. Weller, S.-K. Min, M. D. Palmer, D. Lee, B. Y. Yim, and S.-W. Yeh. Multi-model attribution of upper-ocean temperature changes using an isothermal approach. *Scientific Reports*, 6(1):26926, June 2016. ISSN 2045-2322. doi: 10.1038/srep26926. URL http://www.nature.com/articles/srep26926.

S. Wijffels, D. Roemmich, D. Monselesan, J. Church, and J. Gilson. Ocean temperatures chronicle the ongoing warming of Earth. *Nature Climate Change*, 6(2):116–118, Feb. 2016. ISSN 1758-678X, 1758-6798. doi: 10.1038/nclimate2924. URL http://www.nature.com/articles/nclimate2924.

R. G. Williams, A. Katavouta, and V. Roussenov. Regional Asymmetries in Ocean Heat and Carbon Storage due to Dynamic Redistribution in Climate Model Projections. *Journal of Climate*, 34(10):3907–3925, May 2021. ISSN 0894-8755, 1520-0442. doi: 10.1175/JCLI-D-20-0519.1. URL https://journals.ametsoc.org/view/journals/clim/34/10/JCLI-D-20-0519.1.xml.

M. Winton, S. M. Griffies, B. L. Samuels, J. L. Sarmiento, and T. L. Frölicher. Connecting Changing Ocean Circulation with Changing Climate. *Journal of Climate*, 26(7):2268–2278, Apr. 2013. ISSN 0894-8755, 1520-0442. doi: 10.1175/JCLI-D-12-00296.1. URL http://journals.ametsoc.org/doi/10.1175/JCLI-D-12-00296.1.

A. P. S. Wong, N. L. Bindoff, and J. A. Church. Large-scale freshening of intermediate waters in the Pacific and Indian oceans. 400:440–443, 1999. doi: 10.1038/22733. URL https://doi.org/10.1038/22733.

A. P. S. Wong, N. L. Bindoff, and J. A. Church. Freshwater and Heat Changes in the North and South Pacific Oceans between the 1960s and 1985–94. *Journal of Climate*, 14(7):1613–1633, Apr. 2001. ISSN 0894-8755, 1520-0442. doi: 10.1175/1520-0442(2001)014<1613:FAHCIT>2.0.CO;2. URL http://journals.ametsoc.org/doi/10.1175/1520-0442(2001)014<1613:FAHCIT>2.0.CO;2.

L. Worthington. The water masses of the world ocean: some results of a fine-scale census. In *Evolution of physical oceanography*. 1981.

S. Wynes, S. D. Donner, S. Tannason, and N. Nabors. Academic air travel has a limited influence on professional success. *Journal of Cleaner Production*, 226:959–967, July 2019. ISSN 0959-6526. doi: 10.1016/j.jclepro.2019.04.109. URL http://www.sciencedirect.com/science/article/pii/S0959652619311862.

P. Xie and G. K. Vallis. The passive and active nature of ocean heat uptake in idealized climate change experiments. *Climate Dynamics*, 38(3):667–684, Feb. 2012. ISSN 1432-0894. doi: 10.1007/s00382-011-1063-8. URL https://doi.org/10.1007/s00382-011-1063-8.

R. Yamaguchi and T. Suga. Trend and Variability in Global Upper-Ocean Stratification Since the 1960s. *Journal of Geophysical Research: Oceans*, 124(12):8933–8948, Dec. 2019. ISSN 2169-9275, 2169-9291. doi: 10.1029/2019JC015439. URL https://onlinelibrary.wiley.com/doi/abs/10.1029/2019JC015439.

L. Yu, S. A. Josey, F. M. Bingham, and T. Lee. Intensification of the global water cycle and evidence from ocean salinity: a synthesis review. *Annals of the New York Academy of Sciences*, page nyas.14354, May 2020. ISSN 0077-8923, 1749-6632. doi: 10.1111/nyas.14354. URL https://onlinelibrary.wiley.com/doi/abs/10.1111/nyas.14354.

L. Zanna, J. M. Brankart, M. Huber, S. Leroux, T. Penduff, and P. D. Williams. Uncertainty and scale interactions in ocean ensembles: From seasonal forecasts to multidecadal climate predictions. *Quarterly Journal of the Royal Meteorological Society*, 2019a. ISSN 1477-870X. doi: 10.1002/qj.3397@10.1002/(ISSN)1477-870X.25-Years-of-Ensemble-Forecasting. URL https://rmets.onlinelibrary.wiley.com/doi/abs/10.1002/qj.3397%4010.1002/%28ISSN%291477-870X.25-Years-of-Ensemble-Forecasting.

L. Zanna, S. Khatiwala, J. M. Gregory, J. Ison, and P. Heimbach. Global reconstruction of historical ocean heat storage and transport. *Proceedings of the National Academy of Sciences*, 116(4):1126–1131, Jan. 2019b. ISSN 0027-8424, 1091-6490. doi: 10.1073/pnas.1808838115. URL https://www.pnas.org/content/116/4/1126.

J. D. Zika, M. H. England, and W. P. Sijp. The Ocean Circulation in Thermohaline Coordinates. *Journal of Physical Oceanography*, 42(5):708–724, May 2012. ISSN 0022-3670, 1520-0485. doi: 10.1175/JPO-D-11-0139.1. URL http://journals.ametsoc.org/doi/abs/10.1175/JPO-D-11-0139.1.

J. D. Zika, N. Skliris, A. J. G. Nurser, S. A. Josey, L. Mudryk, F. Laliberté, and R. Marsh. Maintenance and Broadening of the Ocean's Salinity Distribution by the Water Cycle. *Journal of Climate*, 28(24):9550–9560, Dec. 2015. ISSN 0894-8755, 1520-0442. doi: 10.1175/JCLI-D-15-0273.1. URL http://journals.ametsoc.org/doi/10.1175/JCLI-D-15-0273.1.

J. D. Zika, N. Skliris, A. T. Blaker, R. Marsh, A. J. G. Nurser, and S. A. Josey. Improved estimates of water cycle change from ocean salinity: the key role of ocean warming. *Environmental Research Letters*, 13(7):074036, July 2018. ISSN 1748-9326. doi: 10.1088/1748-9326/aace42. URL https://doi.org/10.1088%2F1748-9326%2Faace42.

J. D. Zika, J. M. Gregory, E. L. McDonagh, A. Marzocchi, and L. Clément. Recent Water Mass Changes Reveal Mechanisms of Ocean Warming. *Journal of Climate*, 34(9):3461–3479, May 2021. ISSN 0894-8755, 1520-0442. doi: 10.1175/JCLI-D-20-0355.1. URL https://journals.ametsoc.org/view/journals/clim/34/9/JCLI-D-20-0355.1.xml.

Emergence des changements de température et de salinité dans l'océan intérieur en réponse au changement climatique : échelles de temps et mécanismes

Résumé : Le changement climatique d'origine humaine impacte déjà toutes les régions habitées de la planète. 90% de l'excès de chaleur associé aux activités humaines a été absorbé par l'océan depuis les années 1970, atténuant en grande partie le réchauffement atmosphérique, mais impactant fortement les sociétés humaines et la vie marine. Dans cette thèse, j'explore à l'aide d'ensembles de modèles de climat et de simulations numériques dédiées, où et quand les changements de température et de salinité dans l'océan intérieur deviennent assez grands pour être différenciés de la variabilité interne, ainsi que les mécanismes physiques associés. Nous trouvons ainsi que le signal climatique dans les masses d'eau de l'océan supérieur émerge entre la fin du XX^{ème} et les premières décennies du XXI^{ème} siècle. Les eaux modales des moyennes latitudes de l'hémisphère Sud émergent plus tôt que leurs homologues de l'hémisphère Nord. Le réchauffement associé à ces échelles de temps est principalement du à une absorption de chaleur transportée passivement dans l'océan intérieur. Dans les profondeurs de l'océan, les changements de circulation jouent un rôle plus important aux échelles de temps d'émergence du signal climatique. Le gain de flottabilité en surface dans les régions subpolaires provoque un ralentissement de la circulation méridienne de retournement. Cela réchauffe les eaux intérieures et abyssales de l'Océan Austral dès le milieu du XX^{ème}, venant s'ajouter au faible transport passif de chaleur, alors que cela le contre dans les profondeurs de l'Atlantique Nord et retarde l'émergence. Bien que les modèles de climat passent à côté de certains aspects importants de la réponse océanique au changement climatique, ils permettent d'apporter des éléments sur l'équilibre de processus en jeu, et suggèrent que l'influence humaine impacte déjà de grandes parties de l'océan.

Mots clés : Changements thermohalins, émergence, signal anthropique, océan intérieur, modélisation

Emergence of temperature and salinity changes in the ocean interior in response to climate change: time scales and mechanisms

Abstract : Human-induced climate change is already affecting every inhabited region of the planet. Yet, over 90% of the excess heat associated with human activities has been absorbed by the ocean since the 1970s, which acts to largely damp atmospheric warming, but has large impacts on human societies and marine life. In this thesis, I explore when and where thermohaline changes in the ocean interior become large enough to be unambiguously set apart from internal variability and investigate their associated physical drivers, using ensembles of climate models and dedicated numerical experiments. We find that the climate signal in the upper ocean water-masses emerges between the late 20th century and the first decades of the 21st. The Southern Hemisphere mid-latitude Mode Waters emerge before their Northern Hemisphere counterparts. The associated warming at these timescales is mostly caused by the uptake of heat from the atmosphere, passively transported into the ocean interior. In the deeper parts of the ocean, circulation changes play a more important role in the emergence timescales of the climate signals. Increased buoyancy gain at the surface in the subpolar areas cause a slowdown in the meridional overturning circulation. This warms the subsurface and abyssal waters in the Southern Ocean as soon as the mid-20th century, adding up to the weaker passive uptake of heat, but counteracts it in the deep North Atlantic over the 21st, delaying the emergence. Although climate models miss some important aspects of the ocean response to climate change, they allow to shed light on the balance of processes at play, and suggest anthropogenic influence has already spread to large parts of the ocean.

Keywords : Thermohaline changes, emergence, anthropogenic signal, ocean interior, modelling